Application and Policy Evaluation of New Energy and Materials

Lead Guest Editor: Yanmei Li
Guest Editors: Song Jiang and Wei Liu

Application and Policy Evaluation of New Energy and Materials
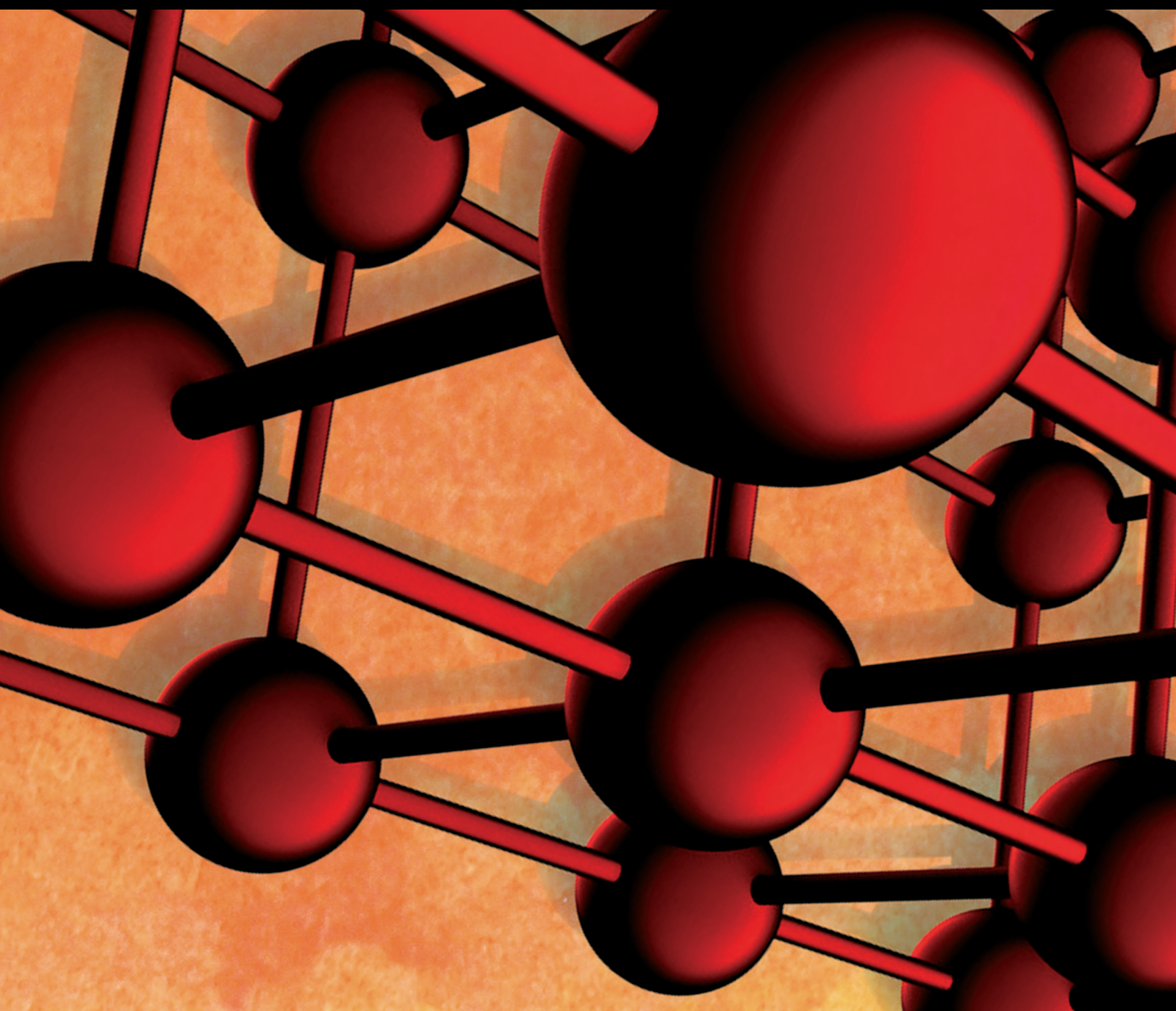
Application and Policy Evaluation of New Energy and Materials

Lead Guest Editor: Yanmei Li
Guest Editors: Song Jiang and Wei Liu

Contents

Contents

Research Article

Effect of Repeated Weld Repairs on Microstructure and Mechanical Properties of Heat-Affected Zone in CA6NM Stainless Steel

Peng Liu [iD],[1,2] **Jien Ma** [iD],[1] **Youtong Fang** [iD],[1] **Bowen Xu** [iD],[1] **and Lin Qiu** [iD][1]

[1]*College of Eledtrical Engineering, Zhejiang University, Hangzhou, Zhejiang 310000, China*
[2]*Shenyang Blower Group Co.,Ltd.,, Shenyang, Liaoning 110869, China*

Correspondence should be addressed to Jien Ma; majien@zju.edu.cn

The low-carbon martensitic stainless steel CA6NM is widely used in the impellers of hydroelectric and nuclear power units due to its advantages of high hardness, corrosion fatigue strength, and good fracture toughness. In order to analyze the number of repair welding times on the properties of heat-affected zone (HAZ, the most unstable area of welded joint property) in CA6NM, the microstructure and mechanical properties of HAZ with once-repaired welds (1R) and twice-repaired welds (2R) were tested. Through data analysis, the following conclusions are drawn for welded joints: (1) the grain size of HAZ with a different number of repair welding processes is smaller than that of the base material; (2) the density of texture concentration is reduced and the directionality is not obvious; (3) the density of twins and dislocations are increased; (4) the hardness and impact energy of HAZ of the 1R and 2R specimens are higher than that of the base material.

1. Introduction

With the development of society and the progress of science and technology, the demand for electricity is consistently increasing. At present, access to social electricity is mainly dependent on fossil resources. In the process of transforming these resources into electricity for use by various industries in society, a large variety and amount of toxic and hazardous substances are generated, which will pollute the environment. With the increase of environmental pollution and the greenhouse effect, the frequency of extreme weather is also on the rise. These phenomena have brought significant risks to people's lives and property. Therefore, many countries are investigating new clean energy resources to reduce pollution and improve the living environment. As a new type of clean energy, nuclear energy technology has been paid attention to around the globe, and relevant investments have gradually increased. Accordingly, the installed capacity of nuclear power generation has shown an increasing trend in various countries. Although nuclear power generation is a clean energy resource, the safe operation of nuclear power plants and nuclear radiation protection remain issues of general concern. These have promoted the continuous development of nuclear power generation technology and the improvement of the construction and operation of nuclear power plants.

Nuclear pump is a key component of a nuclear power plant, and its quality is directly related to the safe operation of such power plant. The main body of a nuclear pump consists of a pump casing and an impeller. Based on the current standards, the impeller is usually cast from CA6NM stainless steel. This is because this material has high hardness and corrosion fatigue strength, good fracture toughness, and excellent weldability at room temperature and below [1]. During the casting process, the metal liquid will flow quickly in the mold and have a violent reaction with the mold. Although the casting process can be optimized, this process will inevitably produce certain defects, such as porosity and inclusion. Therefore, all castings have relevant standards regarding the allowed number and size of defects contained

within them during the acceptance process. When the size of defects exceeds the standard requirements, certain repair measures should be taken to remove those defects and make the product meet the requirements. Therefore, repair welding technology is widely used in casting procedures. [2, 3].

Since CA6NM stainless steel is formed by casting, a large number of scholars have carried out research on its as-cast structure and properties, especially its corrosion resistance [4, 5]. With the increasing number of applications where CA6NM stainless steel needs to be connected, its welding method and technology has also attracted scholars' attention. Sarafan et al. [6] used EB to weld 60 mm thick CA6NM with a single pass without filler metal. The welded joint of CA6NM exhibited a narrow fusion zone and a series of distinct yet very small heat-affected zones (HAZ) with different microstructural characteristics. Mirakhorli et al. [7] used laser-arc welding to weld 10 mm thick CA6NM in a butt joint. The evaluation of the mechanical properties of welded joint after 600°C and 1 h post-weld tempering indicated that, according to ASTM, the ultimate tensile strength and Charpy impact energy values of welded joint were acceptable. The effect of interpass temperature on microstructure, impact toughness, and fatigue crack propagation of CA6NM joints were researched, which were welded by GTAW using AWS410NiMo filler metal [8]. The research results showed that the formation of ferrite δ under a low interpass temperature can promote an increase in impact toughness and a decrease in the fatigue crack propagation when compared with the sample welded under a higher interpass temperature. The FCAW was used to weld CA6NM steel, and the effect of post welding heat treatment on the microstructure and mechanical properties of welded joint were studied [9]. The results showed that despite the nearly identical toughness values of the weld metal for AW and PWHT samples, the PWHT material showed finely dispersed retained austenite at an amount near 10 vol.%. It can be inferred from the above results that the welding process of CA6NM basically includes commonly used welding methods, which have achieved good results. However, in the repair process of castings, it is often impossible to repair products with satisfactory performance by welding once; therefore, multiple repair welding is necessary to meet the requirements. At present, changes in the properties of CA6NM stainless steel after repeated weld repairs, i.e., the effects on its microstructure and mechanical properties, are unknown. However, there have been relevant studies on the influence of multiple repair welding on the microstructure and properties of welded joints. Carpenter et al. [10] investigated the effect of multiple repair welding procedures on quenched and tempered steel for naval vessels. The findings showed that, compared to the original toughness, the application of multiple repeat welds or the multiple simulation of the same sub-HAZ thermal cycle did neither deteriorate toughness nor noticeably altered the final microstructure. Sun [11–15] repaired Q345C several times and tested the hardness and impact toughness of the welded joints after multiple repair welding cycles. The results indicated that, after 10 repair welding sessions, the hardness

and impact energy of the welded joint decreased, but these could still meet the needs of the project. The microstructure and mechanical properties of 7N01 aluminum alloy welded joint were studied for multiple repair welds. [16] As a result, the hardness of DC CMT was weaker than the pulsed MIG, and the DC CMT could effectively reduce the hot cracking sensitivity and alleviate the degradation of joint performance. To analyze the effect of multiple repair welding on the performance of CA6NM stainless steel welded joints, this study uses GTAW to perform multiple repair welds on CA6NM stainless steel and subsequently examines and analyzes the microstructure and properties of the welded joint. The repair welding area includes the weld, the base material, and the HAZ, and the weakest position in these areas is expected to be the HAZ. Therefore, the aims of this paper are mainly the analysis of microstructure and properties of the HAZ under multiple repair welding and the exploration of the relevant mechanisms to guide subsequent production.

2. Experimental Method

In this study, GTAW is used to prepare the 1R and 2R specimens. The welding current is 180 A, the welding voltage is 17 V, and the welding speed is 85–100 mm/min. The chemical composition of CA6NM, determined by Handhold Energy Dispersive XRF spectrometer and welding wire (ER410NiMo), is shown in Table 1.

The CA6NM steel is repair-welded once and twice, respectively, and marked as 1R and 2R. After the repair welding process, the test plate is processed into the corresponding test sample. The pick-up location of the performance sample is shown in Figure 1. For comparative analysis, the base material is also processed into the same test sample as the repair-welded samples, as required. The microstructure of the sample is observed by metallographic microscope (OM, Olympus BX-6). The phase composition is observed by X-ray diffraction (XRD, Shimadzu 7000). The grain orientation field is examined by emission scanning electron microscope (FESEM, Geminisem300) and transmission electron microscope (TEM, JEM-2000). The hardness of the welded joint is tested by a Rockwell hardness tester (HR-150A). The size of the Charpy impact specimen is 10 mm × 10 mm×55 mm. The impact energy is tested by an impact tester (JB-300B).

3. Results and Discussion

The phase composition of the repair welding area was analyzed, and the results are shown in Figure 2. It can be established from the XRD pattern of the base material region that the base material is basically composed of a Ni-Cr-Fe phase with body-centered cubic (BCC) structure. After repair welding, the phase composition in the heat-affected zone obviously changes compared with the base material. The phase composition in the HAZ includes Ni-Cr-Fe, NiC_x, and $Fe_{0.64}Ni_{0.36}$, whether for once-repaired weld or twice-repaired weld. The Ni-Cr-Fe phase is the matrix, and B and C are precipitates. In contrast, the diffraction peak

TABLE 1: Chemical composition of CA6NM and ER410NiMo (wt.%).

	C	Si	Mn	S	P	Cr	Ni	Mo
CA6NM	0.04	0.58	0.60	0.010	0.020	13.60	4.10	0.55
ER410NiMo	0.02	0.40	0.60	0.002	0.021	12.10	4.61	0.47
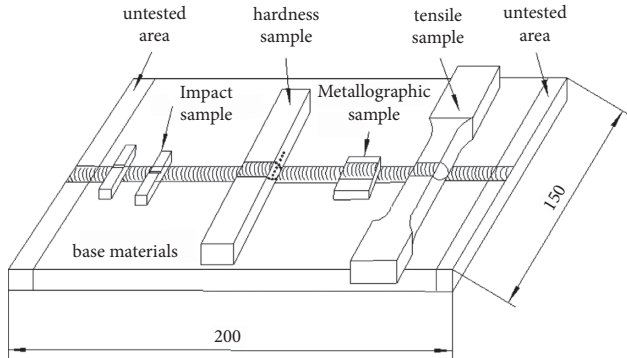
FIGURE 1: Schematic diagram of processed samples.

intensity of NiCx in the twice-repaired weld is improved to a certain extent, which indicates that the precipitation amount of NiCx has been increased. This phenomenon indicates that more carbides are formed in the HAZ in two repair welding cycles, which will improve the hardness of the HAZ to a certain extent.

The microstructure of welded joints with a different number of welding repairs is shown in Figure 3. In the figure, the distribution from left to right represents the base material, the heat-affected zone, and the weld, respectively. The fusion lines can be vaguely seen both in the once-repaired weld and the twice-repaired weld. The fusion line is arc-shaped without obvious precipitate, which indicates a good fusion of welded joints. The microstructures of weld, heat-affected zone, and base material are different because of the different action processes of welding heat input. The weld is formed by the fusion and solidification of the filling material and the base material. The microstructure of the weld is equiaxed grain, which is quite different from the lath martensite beam of the base material. The heat-affected zone (HAZ) is between the base material and the weld. The metallurgical reaction process of the heat-affected zone is complex and the microstructure morphology is very characteristic. Therefore, the heat-affected zone is usually the weak zone of the welded joint. The microstructures of the heat-affected zone in Figure 3 have limited magnification, and the difference between the two cannot be clearly observed. So, high-power metallographic analysis of the HAZ was carried out, and the results are shown in Figure 4. It can be found that the base material is still lath martensite structure, and the martensite is mainly distributed in bundles, as shown in Figure 4(a). The bundles are arranged in different directions and their structure is relatively dense. After repair welding, the martensite beam basically disappears, and the heat-affected zone is replaced by equiaxed grains. Comparing the once-repaired weld and the twice-repaired weld, the grain size of the HAZ of the twice-repaired weld is slightly smaller, and the carbide

precipitation is increased. This has a positive effect on improving the performance of HAZ and enhancing the overall bearing capacity of welded joint.

In order to accurately judge the change of grain size before and after repair welding, EBSD technology is used to count the grain size, and the results are shown in Figure 5. It can be found that the grain size has changed significantly. Firstly, the size of most of the crystal grains in the three states is less than $10 \, \mu m$. With the increasing number of repair welding procedures, the percentage of grains over $10 \, \mu m$ in diameter decreases gradually. Secondly, the grain size of the HAZ becomes significantly refined after repair welding, and the proportion of grains smaller than $5 \, \mu m$ exceeds 61%. The proportion of grains in the HAZ less than $10 \, \mu m$ in once-repaired weld reaches 93.25% and that in the HAZ less than $10 \, \mu m$ in twice-repaired weld reaches 95.53%. The average grain diameter of 1R specimen is $5.32 \, \mu m$, which shows a decrease of 16.7% compared to that of the base material. The average grain diameter of 2R specimen is $5.13 \, \mu m$, which is 19.6% smaller than that of the base material, as shown in Table 2. The findings reveal that repair welding can refine the grains in the HAZ.

Apart from statistics on grain size, EBSD can also analyze the growth characteristics and distribution characteristics of crystals in the HAZ. The grain distribution and corresponding pole figures of the 0R specimen and the HAZ of the 1R and 2R specimens are shown in Figure 6. In the 0R specimen, the preferred texture orientation is in the (101) plane. The texture concentration density of the 0R specimen in the {100}, {110}, and {111} crystal plane families are shown in Figure 6(b). It can be found that the maximum texture concentration density reaches 11.48, which appears in the {110} crystal plane families. By observing the EBSD of the HAZ of 1R specimen in Figure 6(c), it can be found that the grain morphology has changed significantly, and the grains have no obvious orientation. The texture concentration density of the HAZ in the 1R specimen is 4.39, which is only one third of the 0R specimen, and the texture randomness is stronger. Higher texture randomness will lead to more obstacles to slip and improve the toughness of materials [17–20]. There is still no obvious texture orientation in the HAZ in the 2R specimen, and the texture concentration density is also reduced to 3.51. This phenomenon occurs mainly because the repair welding area is re-liquefied and re-solidified during the repair welding process. This process will cause the molten pool metal to recrystallize and nucleate, causing the original grain growth to be disrupted, and the inhibition of the formation of martensite bundles with a certain orientation. In addition, since the temperature of the base metal around the repair welding area is lower, it is easy to produce a larger degree of undercooling, which further promotes the formation of equiaxed crystals. The results show that repair welding can effectively reduce the
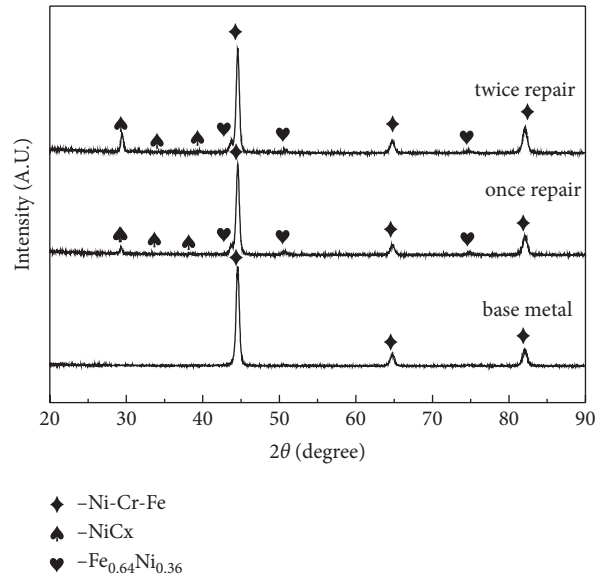
Figure 2: XRD patterns of specimen.

(a)

(b)
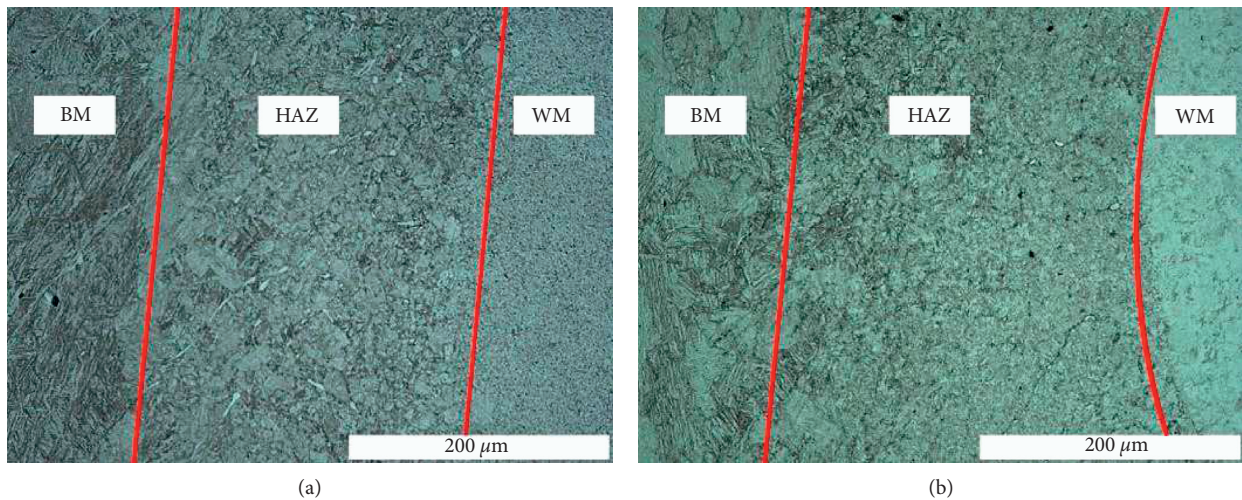
Figure 3: Microstructure of welded joints after a different number of welding procedures: (a) once-repaired weld and (b) twice-repaired weld.

texture concentration density, which is consistent with the research results of Hassan et al. [21].

In order to observe the crystal morphology of the HAZ under a different number of repair welds more clearly, transmission electron microscopy is performed, and the results are shown in Figure 7. Figure 7(a) shows the complete shape of lath martensite in the 0R specimen with a width of 200–500 nm. The martensitic laths in the same beam are distributed in a parallel position. The martensitic beam is divided by high-angle grain boundaries. When plastic deformation occurs under force, the grain of the material will slip. If the slip zone moves to the high-angle grain boundary, it takes more energy to cross the grain boundary, thereby the strength of materials will be improved [22]. In Figure 7(b), it can be found that there are a large number of dislocations on the lath produced during the casting process. These dislocations form dislocation walls or networks, which divide the lath into different regions, but no subgrain boundaries have been formed. As seen in Figure 7(c), the morphology has changed from the original lath shape to a block shape, and the grain size of block ferrite is about 500 nm. High-density dislocations can be detected on the grain surface, especially near the grain boundary. These dislocations are formed by the collision between adjacent grains during the growth process of the crystal and the volume change during the post-weld cooling process, which results in the change of thermal stress, and the generation of steps or stress on the crystal surface. Figure 7(d) shows that the grain size is finer than that of the 1R specimen, and there are a large number of pearlite lamellae, which plays a positive role in improving the mechanical properties of the material. Twins and dislocations in the white circle can also be seen in Figure 7(d). It has been known that the grains in the HAZ of the 2R specimen have been refined, which leads to the increase of

(a)

(b)

(c)
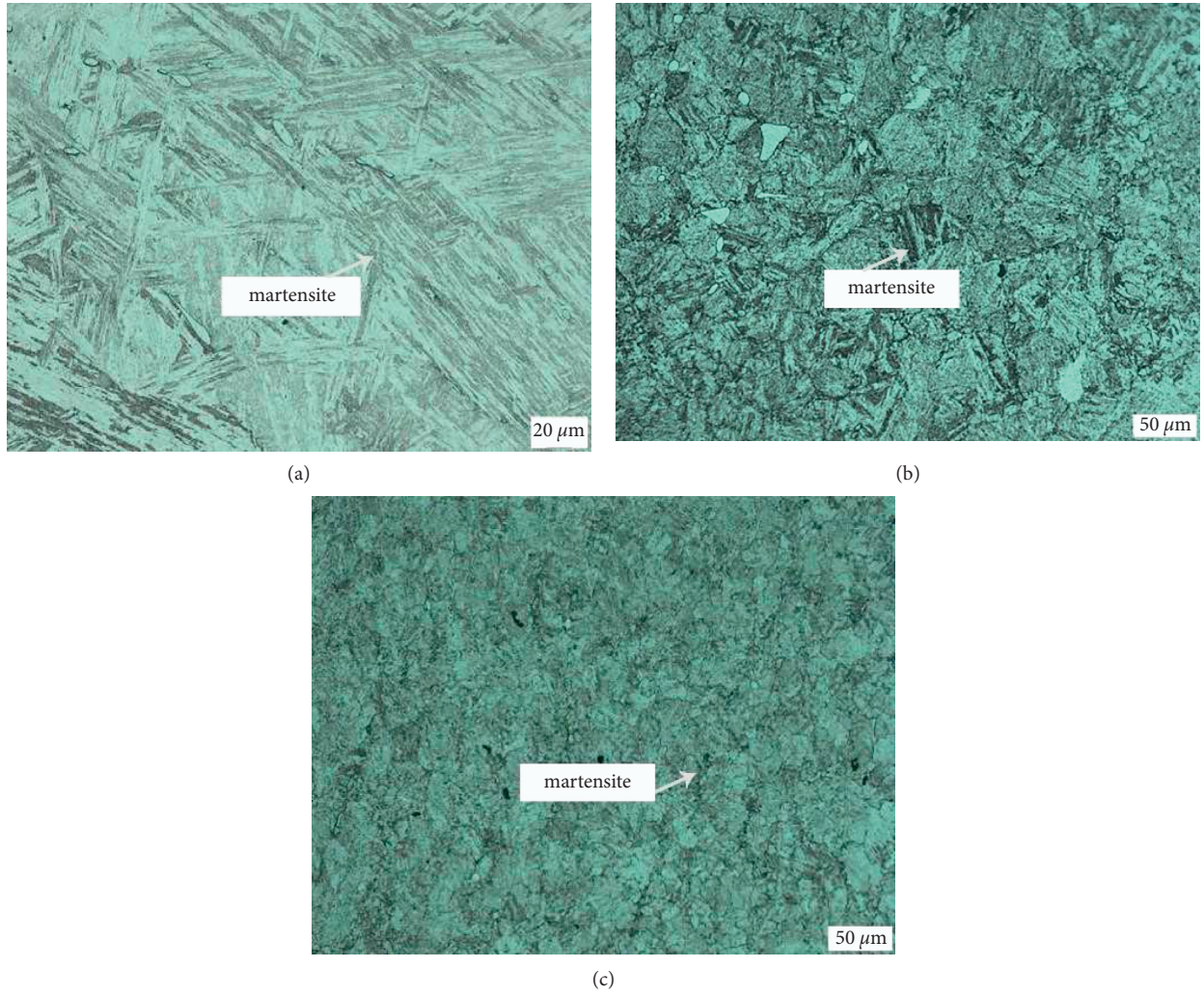
Figure 4: Microstructure of the heat-affected zone in welded joint between samples. (a) Base material, (b) once-repaired HAZ, and (c) twice-repaired HAZ.
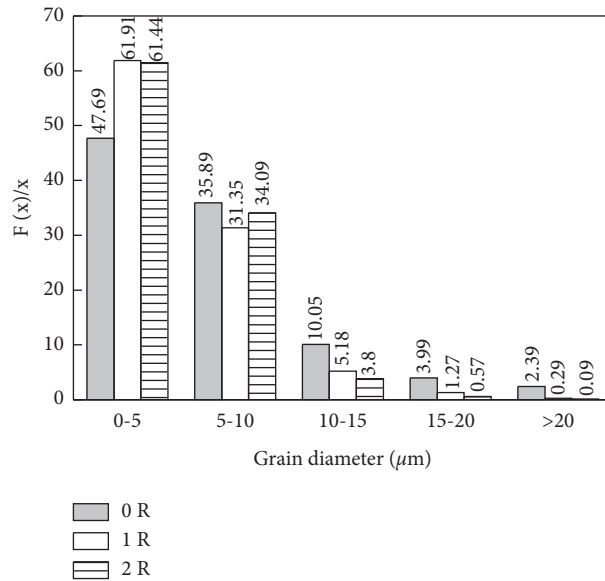
Figure 5: Grain size of HAZ with different numbers of repair welds.

TABLE 2: Average diameter of grains after different number of repair welds.

Repair times	Average diameter (μm)	Average area (μm^2)	Number of grains
0	6.3941	46.544	627
1	5.3275	28.214	1024
2	5.1378	25.069	1053

(a)

(b)

(c)

(d)

FIGURE 6: Continued.

(e)

(f)
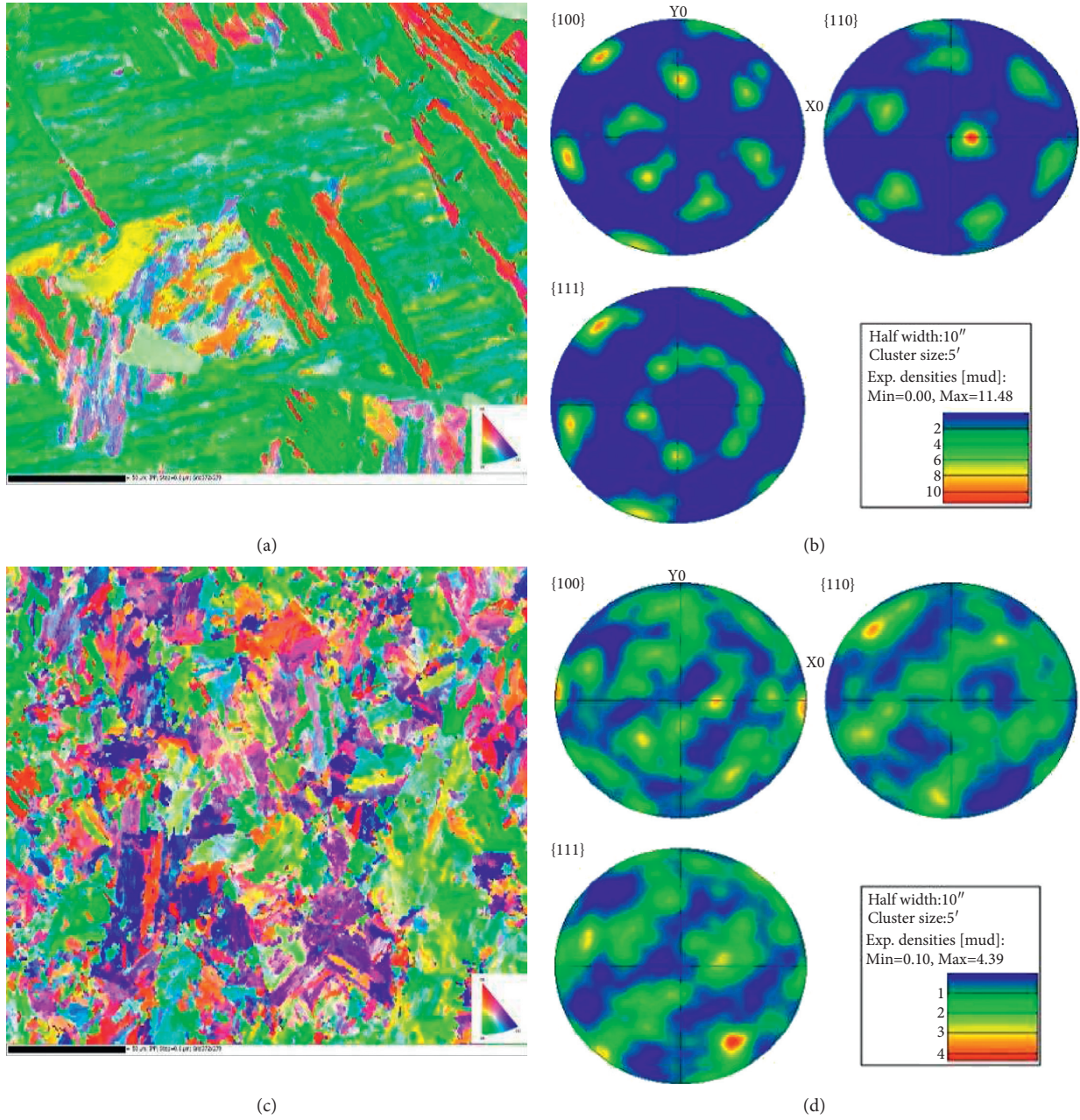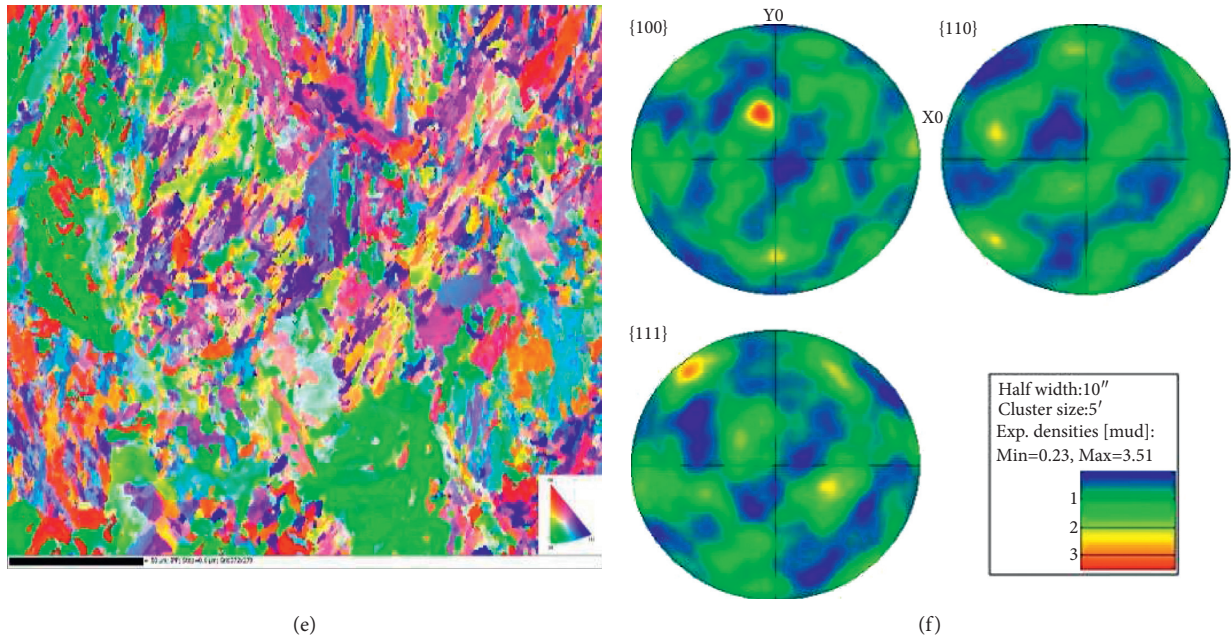
Figure 6: EBSD morphology and pole figure of specimen. (a) EBSD morphology of 0R specimen. (b) Pole figure of 0R specimen. (c) EBSD morphology of 1R specimen. (d) Pole figure of 1R specimen. (e) EBSD morphology of 2R specimen. (f) Pole figure of 2R specimen.

(a)

(b)

(c)

(d)
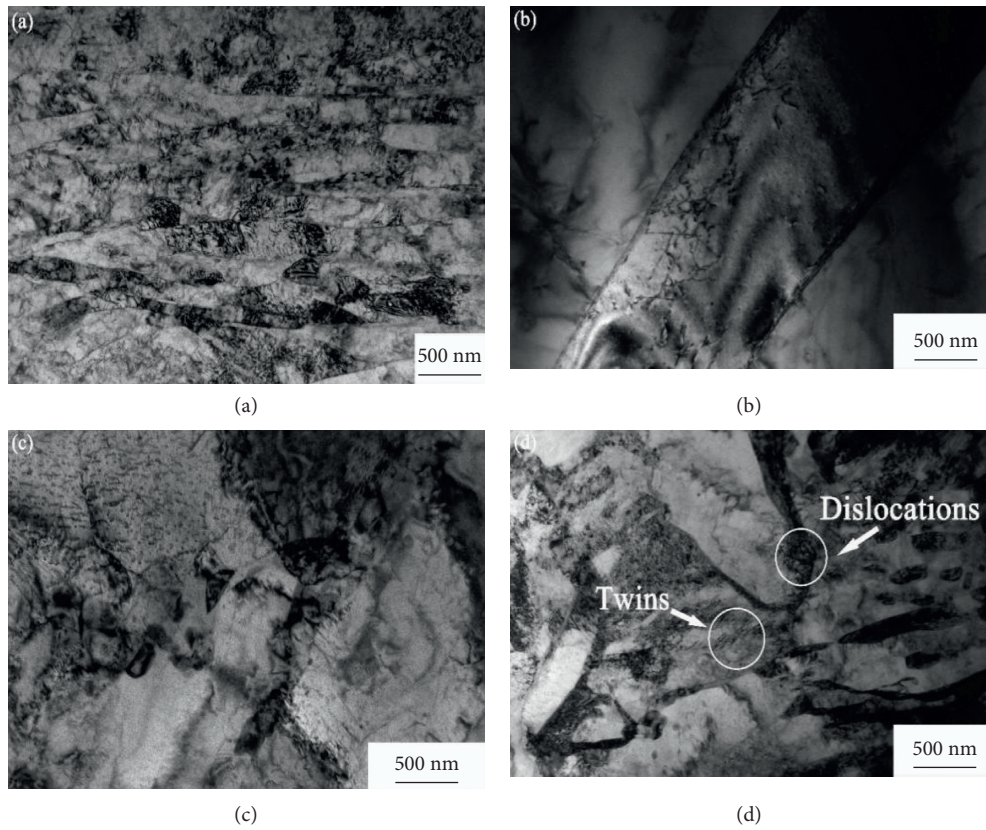
Figure 7: Morphology of microstructure by TEM. (a) 0R specimen (15000X). (b) 0R specimen (20000X). (c) 1R specimen (25000X). (d) 2R specimen (20000X).
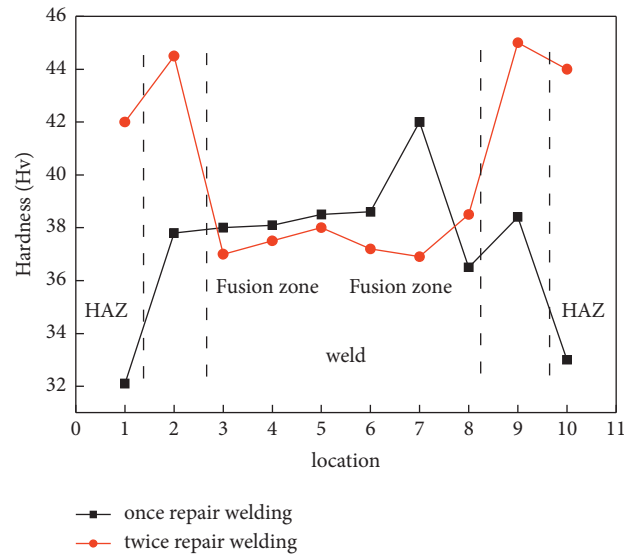
FIGURE 8: Hardness of welded joint with a different number of repair welding times.

density and energy of grain boundary. At the same time, the increase of plastic deformation resistance caused by the obstruction of grain boundary to dislocation movement will enhance the mechanical properties of the HAZ of the 2R specimen.

In view of the direct relationship between structure and performance, the change of microstructure will inevitably affect the macromechanical properties of the material. To analyze the changes in the performance of the welded joints under different repair welding times, the hardness of the welded joints was first tested and analyzed, and the results are shown in Figure 8. It can be seen that the hardness data of the weld are relatively uniform, and the hardness of the HAZ changes greatly. For the hardness of the weld, the once-repaired weld shows a slightly larger value than the twice-repaired weld, and for the hardness of the HAZ, the twice-repaired weld is significantly greater than that of the once-repaired weld. To more clearly reflect the effect of repair welding times on the hardness of the HAZ, the surface and profile hardness of the HAZ were tested, with the results shown in Figure 9. For the surface hardness of the HAZ, the hardness of 1R is opposite to the hardness of 0R, and it is significantly lower than the hardness of 2R, as shown in Figure 9(a). With respect to the profile of the HAZ, the difference in hardness between the three states is still quite obvious. The hardness of 1R is higher than that of 2R, and the hardness of 2R is greater than that of 0R, shown as Figure 9(b). The average surface hardness of the HAZ under 1R and 2R is 0.45% and 26.58% higher, and the average profile hardness is 8.08% and 30.75% higher than that of the 0R specimen, respectively.

The impact energy curves of the HAZ under a different number of repair welding times are shown in Figure 10. There are three curves in the figure, which represent the variation of the impact toughness of HAZ with temperature under a different number of repair welding times. As the test temperature decreases, the impact energy of the HAZ shows

a downward trend, which does not correlate with the number of repair welding times. This change law reflects the basic properties of the material. As the temperature decreases, the toughness of the material gradually diminishes until brittle fracture occurs. Under the same temperature conditions, the impact energy values of the once-repaired weld and the twice-repaired weld are not much different, but are still higher than that of the 0R.

Impact fracture contains a lot of information, which is beneficial to explain the change of material impact toughness. For this reason, this paper also detects and analyzes the fracture of the impact sample. However, due to the large number of impact samples in this test, only representative 20°C and −60°C are selected for comparison. The results are shown in Figure 11. It can be seen from the figure that, at 20°C, there are a large number of dimples in the impact fracture, and the fracture mode of the sample is ductile fracture, which is consistent with the impact energy data, as shown in Figures 10(a)–10(c). When the experimental temperature is −60°C, the impact fracture changes very obviously, and a large number of cleavage planes or quasi-cleavage planes appear at the fracture, as shown in Figures 10(d)–10(f). This phenomenon is consistent with the deterioration of impact toughness. Comparing the fracture morphology under a different number of repair welding times, it can be found that whether it is 20 degrees or −60 degrees, the number of dimples in the 1R and 2R repair welding fractures is higher than 0R, and the size is smaller. This should be the reason why the impact energy of 1R and 2R is higher than 0R. During welding, the weld zone is heated above the liquidus line to melt the filler and part of the base metal to form a molten pool. Since the HAZ is between the base metal and the weld, its temperature is not as high as that of the weld, but its temperature is also heated to above A_{C3}. At this time, the structure of the HAZ is also completely austenitized and then begins to cool gradually and solidify. Due to the small volume of the molten pool and

(a)

(b)
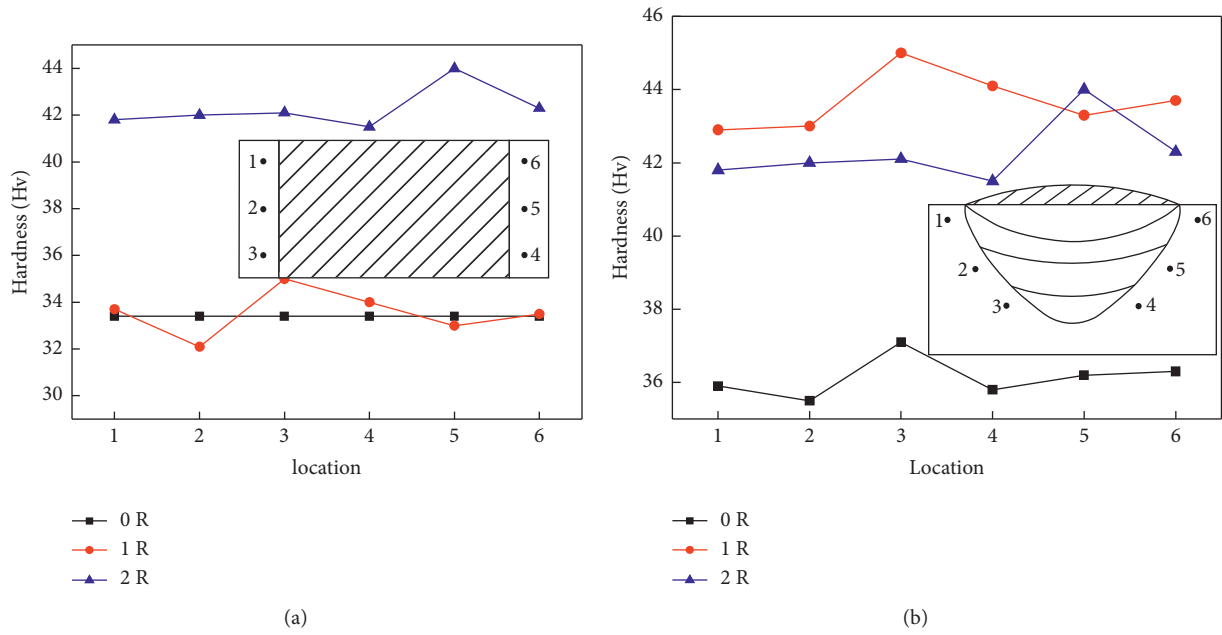
FIGURE 9: Hardness of HAZ. (a) Hardness of surface. (b) Hardness of profile.
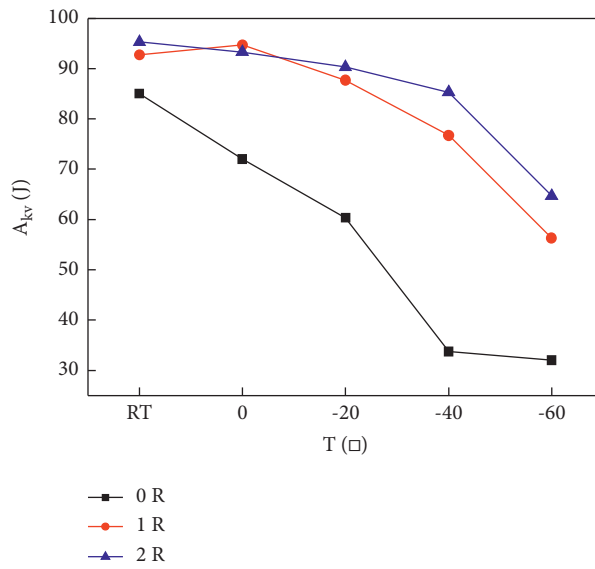
FIGURE 10: Impact energy of repair welding area.

(a)

(b)

(c)
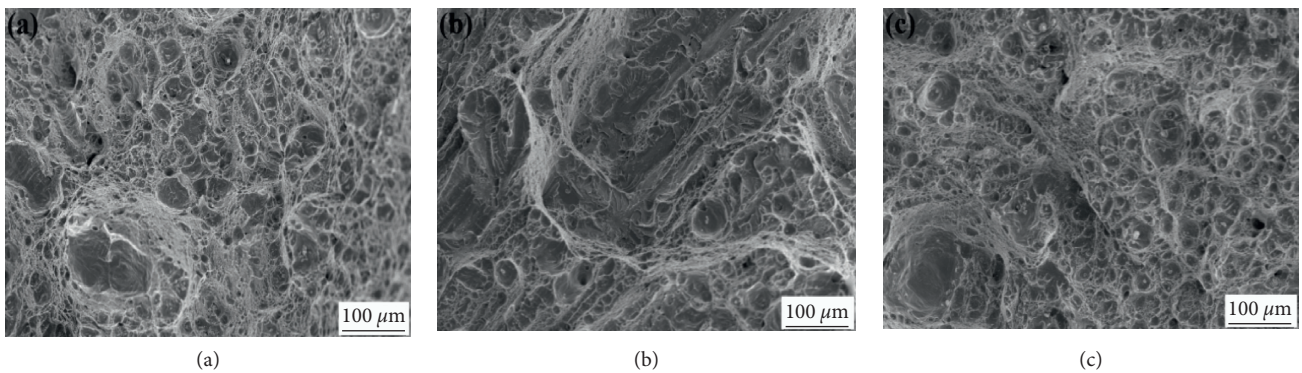
FIGURE 11: Continued.

(d)

(e)

(f)
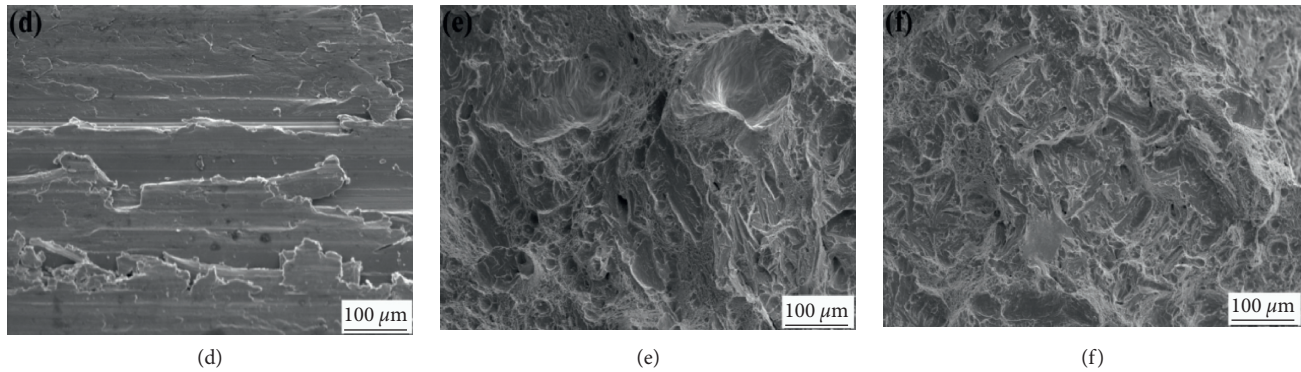
FIGURE 11: Impact fracture of the heat-affected zone. (a) 0R 20°C, (b) 1R 20°C, (c) 2R 20°C, (d) 0R −60°C, (e) 1R −60°C, and (f) 2R −60°C.

the fast heat dissipation rate, the liquid molten pool and the HAZ exist for a shorter period, and the nucleation and growth process of crystal grains is different from the traditional as-cast state. The degree of undercooling in the HAZ is large, and the grain growth time is short. This process is equivalent to normalize or refine the grain, consistently with the research results of Vega. O.E. [23–26] Thus, hardness and toughness are improved through a fine grain strengthening mechanism. These are in good agreement with the grain size data in Figure 5. During the second repair welding process, the previous weld pass is reheated. At this time, the secondary repair welding is relative to the annealing treatment of the original primary repair welding bead. This can relieve stress and homogenize the structure, which can in turn improve the toughness of the material. Therefore, the dual role of repair welding twice in grain refinement strengthening and remelting annealing is more beneficial to the improvement of toughness and strength.

4. Conclusions

In this study, the microstructure and mechanical properties of the CA6NM stainless steel heat-affected zone under a different number of repair welding times have been tested and analyzed, and the evolution of the microstructure has been studied. Based on the analysis of the above data, the following conclusions are drawn:

(1) Repair welding changes the phase composition of CA6NM. In addition to the original as-cast structure of Ni-Cr-Fe, the repair welding zone also contains carbide precipitation NiC_x and second-phase $Fe_{0.64}Ni_{0.36}$. The precipitation of carbide and second phase increase the strength and hardness of the welded joint.

(2) After repair welding, the martensite beam basically disappears, and the heat-affected zone is replaced by equiaxed grains. Compared with the once-repaired weld and the twice-repaired weld, the grain size of the HAZ of the twice-repaired weld is slightly smaller, and the carbide precipitation is increased. This has a positive effect on improving the performance of HAZ and improving the overall bearing capacity of welded joint.

(3) The texture of repair welding area is no longer directional and showing crystal orientation behavior, and the texture density decreased by 69.43%. Dislocations and lamellar pearlites are detected, and the grain refining effect is more obvious. The average grain diameter of 1R and 2R specimen shows 16.7% and 19.6% reduction, respectively.

(4) The increase of hardness has little fluctuation, but material toughness has been greatly improved when the CA6NM is repair-welded once or twice. The average surface hardness of the HAZ under 1R and 2R is 0.45% and 26.58% higher than that of the 0R, respectively, which is mainly due to the carbide phase in the HAZ. The grain refinement strengthening and remelting annealing effects are more beneficial to improving material toughness in the twice-repaired weld.

Data Availability

No data were used to support this study.

Conflicts of Interest

The authors declare that there are no conflicts of interest with any financial organizations regarding the material reported in this manuscript.

References

[1] J. H. Liu, H. Dong, R. Zhu, and S. Q. Li, "Study on transformation of CaO-Al₂O₃-SiO₂-MgO system inclusions in ZG06Cr13Ni4Mo stainless steel," *Journal of Iron and Steel Research*, vol. 18, no. S2, pp. 341–346, 2011.

[2] V. I. Gladshtein, "Improvement of repair weld quality in low-alloy steel turbine casing components," *Power Technology and Engineering*, vol. 47, no. 1, pp. 61–67, 2013.

[3] T. Schuchardt, S. Müller, and K. Dilger, "Remanufacturing of die casting dies made of hot-work steels by using the wire-based electron-beam welding with an in situ heat treatment," *Welding in the World*, vol. 63, no. 6, pp. 1669–1679, 2019.

[4] C. V. Roa, J. A. Valdes, F. Larrahondo, and S. A. Rodríguez, "Comparison of the resistance to cavitation erosion and slurry erosion of four kinds of surface modification on 13-4 CA6NM

hydro-machiney steel," *Journal of Materials Engineering and Performance*, vol. 30, p. 6, 2021.

[5] A. Allenstein, C. Lepienski, A. D. A. Buschinelli, and S. F Brunatto, "Improvement of the cavitation erosion resistane for low-temperature plasma nitrided CA6NM martensitic stainless steel," *wear*, vol. 309, no. 1-2, pp. 159–165, 2014.

[6] S. Sarafan, P. Wanjara, H. Champliaud, and D. Thibault, "Characteristics of an autogenous single pass electron beam weld in thick gage CA6NM steel," *International Journal of Advanced Manufacturing Technology*, vol. 78, no. 9-12, pp. 1523–1535, 2015.

[7] F. Mirakhorli, X. Cao, X.-T. Pham, P. Wanjara, and J.-L. Fihey, "Post-weld tempered microstructure and mechanical properties of hybrid laser-arc welded cast martensitic stainless steel CA6NM," *Metallurgical and Materials Transactions B*, vol. 47, no. 6, pp. 3245–3256, 2016.

[8] R. R. de Gouveia, A. G. M. Pukasiewicz, A. R. Capra, S. L. Henke, and P. C. Okimoto, "Effect of interpass temperature on microstructure, impact toughness and fatigue crack propagation in joints welded using the GTAW process on steel ASTM A743-CA6NM," *Welding International*, vol. 29, no. 6, pp. 433–440, 2015.

[9] R. d. P. Silva, M. I. S. T. Faria, L. F. C. B. d. Almeida, C. A. Nunes, D. Vieira, and W. Borges Júnior, "Microstructure and mechanical properties of ASTM A743 CA6NM steel welded by FCAW process," *Materials Research*, vol. 20, no. 6, pp. 1622–1629, 2017.

[10] K. R. Carpenter, P. Dissanayaka, Z. Sterjovski, and H Li, "The effect of multiple repair welds on a quenched and tempered steel for naval vessels," *Welding in the World*, vol. 65, pp. 1–16, 2021.

[11] D. P. Koistinen and R. E. Marburger, "A general equation prescribing the extent of the austenite-martensite transformation in pure iron-carbon alloys and plain carbon steels," *Acta Metallurgica*, vol. 7, no. 1, pp. 59-60, 1959.

[12] Z. Gao, C. Wang, and Y. Liu, "Evaluation of cavitation erosion-corrosion process of Q235 and ZG06Cr13Ni4Mo with various applied potentials," *International Journal of Electrochemical Science*, vol. 10, no. 8, pp. 6487–6499, 2015.

[13] Y. Yin, P. Kang, R. Zhang, Lu Chao, X. Mengzhi, and Z. Yuan, "Effect of heat treatment on microstructure and properties of VG10 and 3Cr13 dissimilar welded joints," *China Welding*, vol. 30, no. 01, pp. 21–29, 2020.

[14] H. T. Yu, W. Z. Ming, and Y. G. Hui, "Welding quality control of large francis runner in baihetan hydropower station," *Electromechanical technology of hydropower station*, vol. 44, no. 1, pp. 50–52, 2021.

[15] W. Sun, "Effect of multiple repair welding on mechanical properties of Q345C steel welded joints," *Welding technology*, vol. 49, no. 5, pp. 39–42, 2020.

[16] Z. Liang, Y. Li, S. Zhao, and D Wang, "Multiple repair welding of 7N01 alumimum alloy with pulsed MIG and DC CMT welding," *Transactions fo the china welding institution*, vol. 35, pp. 27–32, Article ID 201435, 2014.

[17] Y. Chino, K. Sassa, A. Kamiya, and M Mabuchi, "Enhanced formability at elevated temperature of a cross-rolled magnesium alloy sheet," *Materials Science and Engineering A*, vol. 441, no. 1, pp. 349–356, 2006.

[18] D. Thibault, P. Bocher, M. Thomas, M Gharghouri, and M Côté, "Residual stress characterization in low transformation temperature 13%Cr–4%Ni stainless steel weld by neutron diffraction and the contour method," *Materials Science and Engineering A*, vol. 527, no. 23, pp. 6205–6210, 2010.

[19] K. R. Carpenter, P. Dissanayaka, Z. Sterjovski et al., "The effects of multiple repair welds on a quenched and tempered steel for naval vessels," *Welding in the World*, vol. 65, no. 10, pp. 1997–2012, 2021.

[20] M. Shojaati, S. F. Kashani Bozorg, M. Vatanara, M. Yazdizadeh, and M. Abbasi, "The heat affected zone of X20Cr13 martensitic stainless steel after multiple repair welding: microstructure and mechanical properties assessment," *International Journal of Pressure Vessels and Piping*, vol. 188, no. 3, Article ID 104205, 2020.

[21] A. J. Hassan, T. Boukharouba, D. Miroud, and T Nacer-Eddine, "Evolution of microstructural and mechanical properties of AISI 316 during continuous drive friction welding process," *China Welding*, vol. 29, no. 4, pp. 7–12, 2021.

[22] Y. Yoshida, L. Cisar, S. Kamado, and Y. Kojima, "Effect of microstructural factors on tensile properties of an ECAE-processed AZ31 magnesium alloy," *Materials Transactions*, vol. 44, no. 4, pp. 468–475, 2003.

[23] T. A. Davis, L. Bichler, F. D'Elia, and N. Hort, "Effect of TiBor on the grain refinement and hot tearing susceptibility of AZ91D magnesium alloy," *Journal of Alloys and Compounds*, vol. 759, pp. 70–79, 2018.

[24] J. W. Cahn and J. E. Taylor, "A unified approach to motion of grain boundaries, relative tangential translation along grain boundaries, and grain rotation," *Acta Materialia*, vol. 52, no. 16, 2004.

[25] O. E. Vega, J. M. Hallen, A. Villagomez, and A. Contreras, "Effect of multiple repairs in girth welds of pipelines on the mechanical properties," *Materials Characterization*, vol. 59, no. 10, pp. 1498–1507, 2008.

[26] M. Kang, M. Jiang, S. Sridar, W Xiong, Z Xie, and J Wang, "Effect of multiple repair welding on crack susceptibility and mechanical properties of inconel 718 alloy casting," *Journal of Materials Engineering and Performance*, vol. 31, no. 17, pp. 1–8, 2021.

Hindawi

Research Article

Device for Simulating Fluid Microgravity Environment Based on Magnetic Compensation Method and Research on Magnetic Fluid Lubrication Performance of Oil Film Bearing

Han Peng, Linjian Shangguan [ID], and Hai Zhang

School of Mechanical Engineering, North China University of Water Resource and Electric Power, Zhengzhou 450045, Henan, China

Correspondence should be addressed to Linjian Shangguan; shangguanlinjian@ncwu.edu.cn

At present, with the rapid development of the material market, the requirements of high performance and high precision of materials are increasingly exposed. Nanomagnetic fluid materials are more and more widely used in oil film bearings, but their compressive strength and performance are insufficient, which is difficult to meet the current requirements of material chemical properties. First of all, a device for simulating a microgravity environment with magnetic compensation is fabricated. Then, in the microgravity environment, according to the different proportions of magnetic solid particles, the base carrier liquid and the surfactant are mixed to produce nanomagnetic fluid and the nanomagnetic fluid with different composition proportions is prepared by adjusting the proportion of ferrous and ferric ions. Finally, the lubrication performance of oil film-bearing magnetic fluid with different composition ratios was tested. The results show that when the ratio of Fe^{2+} to Fe^{3+} is between $11:20$ and $13:20$, the MHD (magnetohydrodynamics) lubrication performance of oil film bearing is in the peak region. When the ratio is $3:5$, the best lubrication performance can be achieved. When it is slightly higher than this ratio, the oxidation rate is accelerated due to more ferrous ions. Although it can have a good lubrication effect, it is easy to cause the overall fluidity of oil film-bearing magnetic fluid to deteriorate. Therefore, the oil film bearing nano-MHD with the ratio of $3:5$ ferrous to ferric has the best lubrication performance in the microgravity environment simulated by magnetic compensation. Experiments have shown that when the magnetic fluid is heated in a magnetic field, the temperature gradient will cause the magnetization to change, which makes the magnetic force experienced by the liquid in each part different, causing convection. Therefore, by selecting the direction of the magnetic field and the heating surface, by applying an external magnetic field or promoting convection, or suppressing convection, convection in the opposite direction to the natural convection of gravity can also be realized. Moreover, magnetism can immediately promote high-temperature boiling, generate bubbles, and eliminate the generation of bubbles to promote heat transfer. With the above effects, the heat conduction between the heating wall and the liquid can be controlled, and its practical and potential application fields are very wide.

1. Introduction

In recent years, magnetic fluid lubrication technology has developed rapidly at home and abroad because of its many advantages. According to the characteristics of the relatively uniform magnetic field distribution of the Helmholtz coil, a suitable alternating magnetic field generator is designed. When the load is large, the pressure on the bearing surface makes the bearing produce elastic deformation. On the other

hand, the temperature rise will also cause large thermal deformation of the bearing. The deformation of the bearing will cause the change of oil film distribution, which will affect the lubrication performance. Therefore, under the condition of heavy load, it is necessary to consider the influence of bearing deformation on lubrication performance.

In the research of MHD coil, Kakutani analyzed the MHD lubricated coil in detail and gave the coil design parameters suitable for different parts of the tumor lubrication through

simulation [1]. Romig has developed the first lubrication prototype in China, which has been applied to magnetic field research after several iterations [2]. The research and preparation of magnetic fluid are also developing rapidly. Ziemer and Bush made a horizontal comparison of magnetic medium parameters and proposed optimization methods for different magnetic medium parameters [3]. Smith et al. summarized more than 30 studies on magnetic nanoparticles in the past five years and believed that the field is trying to minimize the side effects of lubrication on healthy cells [4]. Murakami and Okuno heat the tubular metal implants in the magnetic fluid through the magnetic fluid, but only when the magnetic fluid tissue of the lesion is relatively regular [5]. Su et al. confirmed that the warm moistening method above 42°C had an obvious killing effect on human MHD cells (QBC939). They also perfused hot saline into canine MHD by placing a catheter, but the temperature control was not accurate enough and the puncture was difficult [6]. Zhao et al. established the FMBD model of axial piston pump through AMESim and virtual platform, considering the influence of bearing and fluid vibration, and studied the noise transmission mechanism of axial piston pump combined with the test bench [7].

On bearing lubrication, Ahmad et al. conducted a theoretical study on the influence of the exciting force caused by the oil pressure in the plunger cavity on the vibration of the axial piston pump and built a test bench to verify the correctness of the theory [8]. Gülhan et al. simplified the structure of the axial piston pump, especially built a test bench for studying the oil film characteristics of the slipper pair, and measured the oil film thickness under different speeds and pressures under actual working conditions [9]. Based on the three-dimensional fractal theory, Smith et al. analyzed the nonlubricated contact of the rough surface and established the normal contact lubrication degree model of the fixed mechanical joint surface, and based on this model, the normal contact lubrication degree of the fixed mechanical joint surface under light load can be well predicted [10]. The above researches are mostly based on the elastohydrodynamic lubrication model, that is, the solid contact only has elastic deformation, and the lubrication is hydrodynamic lubrication, which often ignores the elasticity and elastoplasticity of the microconvex body when the actual contact pair bears medium and heavy load. The method in the overview only considers the elastic deformation of the object and does not consider its own bearing capacity in the actual process, which is one-sided.

This paper studies the device of magnetic compensation method to simulate fluid microgravity environment and the magnetic fluid lubrication performance of oil film bearing. First of all, a device for simulating a microgravity environment with magnetic compensation is fabricated. Then, in the microgravity environment, according to the different proportions of magnetic solid particles, the base carrier liquid and the surfactant are mixed to produce nanomagnetic fluid, and the nanomagnetic fluid with different composition proportions is prepared by adjusting the proportion of ferrous and ferric ions. Finally, the lubrication performance of oil film-bearing magnetic fluid with different composition ratios was tested.

2. Contact Lubrication and Amplitude Conversion of Nano-MHD

2.1. Dynamic Contact and Surface Activity Adjustment Method of Nanomagnetic Fluid. The fluid oil film is a kind of material that is sandwiched between two opposite sliding surfaces and has lubrication performance to achieve an antiwear effect. For the axial piston pump, the oil film characteristics between slippers are directly related to the overall performance and reliability life of the pump [11]. An axial plunger pump is a plunger pump in which the reciprocating direction of the piston or plunger is parallel to the central axis of the cylinder. An axial piston pump is a swashplate type axial piston pump that uses an oil distribution plate to distribute oil, the cylinder body rotates, and the variable head is variable. The pump adopts the optimal oil film thickness design of hydrostatic balance, so that the cylinder block and the oil distribution plate, the sliding shoe, and the variable head are operated under pure liquid friction. It has a simple structure, small volume, low noise, high efficiency, and long life. Longhe has the advantages of self-priming ability. The key parameter of oil film characteristics is viscosity, which directly affects the bearing capacity and leakage of oil film of slipper pair, and the most important factor of viscosity is temperature [12]. The purpose of this paper is to strengthen the pressure resistance of oil film bearings, expand the application range of oil film bearings, and meet the current social demand for materials. The temperature control system of the test bench can realize any variable temperature or constant temperature control required by the oil film test system of the slipper pair [13]. Therefore, temperature control is very important for the experimental study of fluid lubrication characteristics.

Under high preload, the average dynamic contact lubricity of nano-MHD increases with the increase of amplitude, but the overall value between the two kinds of interface is relatively similar. The main reason is that when the contact load increases, the actual contact area of the solid increases correspondingly, and the lubricant decreases [14, 15]. At this time, the dynamic contact lubricity of microconvex body plays a major role; therefore, it is approximate to the dynamic lubrication degree of the solid-solid nano-MHD interface [16, 17]. At the same time, it can be found that the theoretical model of solid-liquid interface is in good agreement with the experimental data, which verifies the correctness of the established model [18, 19]. The contact damping of the solid-liquid interface is much larger than that of the solid-consolidation interface, which is not of the same order of magnitude. With the increase of amplitude, the contact damping of the solid-liquid interface increases, while the increase of the solid-liquid interface is small [20]. In the low amplitude range, the solid-liquid interface data is smaller than the model, and in the high amplitude range, it is more consistent [21]. Due to the special location of the MHD tumor, it is necessary to strictly control the lubrication range and temperature to avoid irreversible damage to the surrounding normal MHD tissue. However, there are some defects in the above lubrication methods, such as fuzzy treatment area and nontreatment area, or high temperature, and easy to injure healthy tissue [22].

At low pressure, the slow development of the arc root will not only make the arc stagnate on the pantographed slide for a longer time but also cause the arc stretching speed to be slow due to the slow development and the arc length to maintain at a small level, and the arc is difficult to extinguish. The longer stagnation of arc root on the electrode under low pressure and the increase of arc duration due to the slow change of arc length make the arc corrode the pantograph catenary system electrode more seriously under low pressure [23]. At the same time, the temperature characteristics and shape characteristics of the arc under different gas pressures are analyzed. With the decrease of gas pressure, the overall temperature of the arc is slightly lower than that of the high gas pressure, but the decrease is not significant. It is worth noting that the diameter of the arc at lower air pressure is obviously larger than that at the higher air pressure, and the corresponding arc volume is also increased [24]. This is because, with the decrease of air pressure, the dynamic viscosity of the air decreases to a certain extent, which enhances the fluidity of the arc and increases the expansion degree of the arc column [25]. The increase of arc volume leads to the slow development of arc motion under the action of crosswind [26].

In addition, the stability of surfactants at high temperatures is poor, so a stable and efficient dispersant is needed to achieve the stable suspension of nanoparticles. Ionic liquids (ILs) have attracted researchers' attention because of their good stability at high temperatures, and they have good compatibility. It is reported that ionic liquids can also increase the critical micelle concentration of other additives in the base solution, so the mixed nanofluids with high-temperature stability can be obtained by compounding other surfactants with ionic liquids [27, 28]. From the point of view of the grinding process, although the cooling and lubrication conditions in the grinding zone can be improved to the maximum by adding nanoparticles, the penetration efficiency of grinding fluid is still difficult to be guaranteed due to the existence of the air barrier effect in the grinding process [29]. The internal cooling technology improves the structure of the tool so that the grinding fluid can directly wash the grinding area through the internal channel of the grinding wheel, which greatly improves the utilization rate of the grinding fluid, which is of great help to quickly reduce the temperature of the grinding area. The pressure term in the momentum equation and the product term of velocity and pressure in the energy equation are split, and then, a hybrid upwind scheme is constructed. In addition, the new convection pressure flux splitting method is that there is no pressure term in the convection flux. The mixed upwind scheme based on the convection pressure flux splitting method is simple in form and can capture contact discontinuities accurately. However, the "Ruby" phenomenon and postshock oscillation still appear in some problems. A new accurate and robust flux difference splitting scheme is constructed based on the Zha-Bilgen convection pressure flux splitting method. The pressure subsystem has a complete set of linearly independent eigenvectors, so the traditional flux difference splitting scheme can be constructed for calculation. The weak hyperbolic convection subsystem is calculated by the flux difference splitting scheme with the generalized eigenvector

method. In order to improve the resolution of contact discontinuities, the BVD algorithm is used to reduce the density difference in the dissipation term of convective flux. Stability analysis and numerical experiments show that the new flux difference splitting scheme has better robustness and higher resolution than the roe scheme.

The surface morphology of the workpiece was obtained by traditional grinding fluid and mixed nanofluid. When the liquid supply pressure is low, deep processing lines appear on the surface of the workpiece, and the furrow is very obvious, which leads to local pits due to the phenomenon of material bonding. However, with the increase of liquid supply pressure in China's mechanical engineering, the surface of the workpiece is better improved, the furrow becomes shallower, smoother, and more regular, and the phenomenon of material bonding is reduced. This shows that increasing the supply pressure can effectively prevent the surface defects caused by the adhesion of wear debris, which is conducive to improving the processing performance. Compared with the surface morphology observed under different cooling and lubrication conditions at the same supply pressure, the surface morphology obtained by mixing nanofluids is more regular. The results show that the mixed nanofluids are helpful to improve the lubrication condition and surface quality of the grinding zone. When the feed pressure is 1 MPa, the profile fluctuation value of the two cooling media is 11.38 under the condition of traditional grinding fluid μ m. However, the profile fluctuation value decreases to 8.433 under the condition of mixed nanofluid grinding μ m. This is because the mechanism of grinding fluid in the grinding zone is boundary lubrication, and the lubrication effect mainly depends on the lubricating film. Compared with traditional grinding fluid, the mixed nanofluids are easier to form a lubricating film in the grinding zone, which avoids the direct contact between the abrasive particles and the workpiece. The existence of nanoparticles improves the bearing capacity of the lubricating film; under the physical synergism between ionic liquid and nanoparticles, the mixed nanofluids show excellent lubrication performance, which can effectively reduce the adhesion between grains and workpiece, and reduce the profile fluctuation of the machined surface. Therefore, better surface quality can be obtained by mixing nanofluids.

2.2. Algorithm for Normal Contact Lubrication and Amplitude Conversion of Nano-MHD.
When the normal surface pressure is h and Y, respectively, and the excitation frequency is f, the experimental results of the solid-liquid interface are compared with the theoretical model:

$$
\begin{aligned}
H_i &= F\left(\sum_{j=i}^{k} \omega_{ij} y_j - \theta_i\right) - C * Y, i \neq j, \\
Y_r &= \|G_I - G_O\|_2.
\end{aligned}
\tag{1}
$$

Under low preload, the increasing trend of solid-liquid interface is relatively more obvious, and the dynamic contact lubrication degree of solid-liquid interface is greater than that of solid-solid interface s: under the same amplitude,

$$S_{ikjl} = \begin{cases} \dfrac{n}{\Delta_{ikjl}} \sqrt{\displaystyle\sum_{s=1}^{n} \left(x_{ik}(G) - x_{jl}(G)\right)^2 \Delta_{ikjl}(Y)} & \Delta_{ikjl} > 0; \\ \\ 0 & \Delta_{ikjl} < 0 \end{cases} \tag{2}$$

$$\frac{Y}{H} = \sum_{S-1}^{U} \sum_{d-1}^{K} f_s, \, DV_s, \, d.$$

By comparing the experimental data of solid-liquid interface with the theoretical simulation, it can be seen that there is a small jump in the experimental data, but the overall trend is consistent with the theoretical derivation:

$$R(D_i, w_j) = R(d_i)P(w_j|d_i); T(w_j|d_i) = \sum_{k=1}^{K} T(w_j|z_k)P(z_k|d_i),$$

$$T = \{P_1|D, L, f_2, Q, d, l \quad P_2|f_1, \mu P_3|N, M, I\}. \tag{3}$$

When the normal surface pressure is R and t, respectively, and the excitation amplitude is p, the dynamic contact lubrication degree changes with the excitation frequency Z:

$$R = \sum_{i=1}^{g} \left\{ P_i | \sum_{j=1}^{k} p_j^{(i)} \right\},$$

$$\sqrt{T} = \frac{|R^g \cap R^r||Z_0 - Z|}{R^g \cup R^r}. \tag{4}$$

2.3. Magnetic Fluid Reynolds Equation of Oil Film Bearing.
Reynolds' equation is the governing equation to study the film pressure produced by lubrication film in the process of lubrication. The general form is as follows:

$$\eta(x) = 2n \ln(L) + n \ln(h) + n\left\{ \frac{n + tr(S)}{n - 2 - tr(S)} \right\} * DV, \tag{5}$$

$$U(d_i, w_j) = P(d_i)P(w_j|d_i); P(w_j|d_i) = \sum_{k=1}^{K} b(w_j|z_k)P(z_k|d_i), \tag{6}$$

where η indicates the viscosity of the lubricant, in PA s. U is the velocity of the upper surface in M/s. P is the hydro-dynamic pressure in PA. H is the thickness of the oil film, in μ m. In a small area, the surface is simplified to a plane. Each texture unit is a square with length L, and there is a diamond texture with diagonal length B in it. The initial clearance of friction pair is H_0, the depth of microtexture is HP, and the oil film thickness between friction pairs can be expressed as follows:

$$L_i = IR * \beta(hp_i, v_i) + \sum_{j=1}^{p} \beta_j(x, y)x_{ij} + \varepsilon_j \beta_j, \tag{7}$$

where (x, y) denotes any point in the element. Δ indicates rhombic texture region. Dimensionless can reduce the number of variables in the process of solving, and also the solutions expressed by dimensionless parameters are universal. The dimensionless parameters are defined as follows, where P_0 is atmospheric pressure. By substituting the above equation into equations (6) and (7), the dimensionless Reynolds equation and film thickness equation can be obtained, respectively:

$$L(Y_i, y_i) = -\frac{1}{n} \sum_{i=1}^{n} [Y_i \log(y_i) + (1 - Y_i)\log(1 - y_i)], \tag{8}$$

$$p_0(\varepsilon) = \begin{cases} 0, & x_{ik}(\Lambda) = \dfrac{N}{A}, \quad x_{jl}(\varepsilon) = \dfrac{N}{A}; \\ \\ 1, & x_{ik}(\Lambda) = Y_i \log(y_i) + (1 - Y_i)\log(1 - y_i), \quad x_{jl}(\varepsilon) = \dfrac{N}{A}, \end{cases} \tag{9}$$

where Λ indicates the operating condition of the friction pair. By substituting the above difference results into

equation (9), the discrete form can be obtained as follows:

$$N(A) = K(y(T-1), \ldots, y(t-n), u(T-d-\phi), \ldots, u(k-d-n)),$$
$$Y(T) = K(y(k2-1), u(\rho 2 - c2 - 1)), \tag{10}$$

where ρ_2, C_2, and K_2 are the thermophysical parameters of MHD mixed with tumor tissue. φ represents the volume fraction of magnetic fluid in tumor tissue, and $\varphi = 003$ is the typical dose of the magnetic field. The thermophysical parameters of MHD are also replaced by the structure of MHD particles.

3. Preparation and Performance Test of Magnetic Fluid

3.1. Research Content. First of all, a device for simulating a microgravity environment with magnetic compensation is fabricated. The compensation device is an important part of the flat-topped long-pulse magnetic field device and is equivalent in the flat-topped phase of the magnetic field to a controlled current source to compensate for the magnet current. Its main functions are the fast and accurate acquisition of pulsed magnet currents, control of power devices (IGBT), fault handling, and human-machine interaction. The magnetic field generated by a pulsed magnet has a linear field; the magnetic field generated by the pulsed magnet has a linear relationship between field strength and current. Then, in the microgravity environment, according to the different proportions of magnetic solid particles, the base carrier liquid and the surfactant are mixed to produce nanomagnetic fluid, and the nanomagnetic fluid with different composition proportions is prepared by adjusting the proportion of ferrous and ferric ions. Finally, the lubrication performance of oil film-bearing magnetic fluid with different composition ratios was tested.

3.2. Preparation of Magnetic Fluid. In this paper, the nanomagnetic fluid used magnetic solid particles, base carrier liquid, and surfactant. Therefore, the focus of this study is to simulate the MHD lubrication model systematically, in order to make full use of the characteristics of MHD lubrication, such as good thermal uniformity, warm lubrication, adjustable parameters, and temperature control. In order to improve the reliability and safety of lubrication, the appropriate alternating magnetic field was designed, the accurate distribution of temperature field was obtained, the possible problems were discussed, and the treatment effect and safety were evaluated.

The lubrication coefficient includes thermal uniformity, temperature lubrication, active parameters, and temperature control. In the experiment, you can use the controlled variable method to implement one by one to find the specific relationship.

In order to prepare magnetic fluid, a TC4 bar was purchased and processed Φ 31.7 mm. For the blank sample with the size of 10 mm, the metallographic sandpaper with the particle size of 200, 400, 800, 1500, and 2000 was selected to polish the sample to RA < 0.2 μ m. We use an ultrasonic cleaning machine to clean for 10 min and air dry. The ylp-

d20 fiber laser was used to process the microtexture on the surface of the disk specimen. Through the preliminary setting test and continuous debugging, the laser output power was 6 W and the scanning speed was 100 mm/s. After laser processing, the workpiece is polished again with metallographic sandpaper, the material around the microtexture is cleaned, and the melted recast material is cleaned with acetone solution and dried.

Under certain conditions, the separated molecules or atoms are condensed, and the process of nucleation and growth of the condensate is controlled to obtain nanoparticle materials. Based on this principle, the metal carbonyl compound thermal decomposition method can prepare the ferromagnetic metal particle material S.8.0. Metal carbonyls are unstable and can be decomposed with changes in pressure and temperature. In the evaporator, the metal carbonyls vaporize and volatilize and are diluted by inert gas into the reaction vessel at a temperature of 25°C, and the metal carbonyls will decompose.

The preparation of the magnetic fluid base fluid uses ordinary kerosene, and the surfactant is selected as oleic acid. The whole process of the experiment is divided into dissolution, filtration, reaction, heating, separation, and other stages, and finally, a black shiny Fe304 kerosene-based magnetic fluid is obtained.

4. Results and Discussion

4.1. Magnetic Fluid Lubrication Performance. Figure 1 shows the relationship between the texture parameters and the coefficient of friction at temperatures of 30, 35, 38, 40, 43, and 50 degrees. Due to the extremely small size of the nanoparticles, when the friction subsurface is worn to form a crater, the nanoparticles gather at the dent to fill the wear in time, so that the friction subsurface is always in a flat state, by selecting the appropriate nanoparticles, so that the temperature-pressure reaction with the friction subsurface is firmly attached to the friction subsurface, so that the entire friction system has a self-healing function and thus has a friction reduction antiwear effect.

The effect of texture parameters on friction coefficient at different temperatures is shown in Figure 1. The lubricating fluid with a viscosity of 0.05 PAS was prepared by base carrier fluid and 9% NaCl. The surface motion parameters of the normal human hip joint were selected. The load was about 35 N, and the rotation speed was 83 R/min. The pressure sensor of the testing machine is 215b, the measuring range is 200 kg, and the sensitivity is 1.504 MV/v. The friction and wear tests were carried out in the form of a lubrication pool under simulated hydrodynamic lubrication for 30 min.

When the frequency is 100 kHz, the peak value of alternating current is 10 A, and the coil turns are 380, the distribution of magnetic field generated by Helmholtz coil is

shown in Figure 2. Electromagnetic exposure refers to the fact that the equipment of the information system can radiate through the ground wire, power line, etc. during operation, resulting in electromagnetic leakage. The magnetic field distribution refers to the distribution law of the magnetic field strength around the magnet. It can be seen that the magnetic field distribution near the magnetic fluid is more uniform; even if the patient's body moves forward and backward, left and right slightly, it can meet the requirements of magnetic fluid lubrication. It is worth noting that the magnetic field intensity decreases rapidly outside the coil device, and the electromagnetic exposure safety risk of patients' brains and nearby medical staff is low. The Helmholtz coil has a pair of identical current-carrying circular coils parallel to each other and coaxial, with current flowing in the same direction. Therefore, it is of great practical value in production and scientific research and is also commonly used as a measurement standard for weak magnetic fields.

The magnetic fluid is dense and sparse, and the electric field distribution is shown in Figure 3. The electric field intensity of the air in the magnetic fluid cavity is higher than that of the surrounding biological tissues, and the electric field intensity in the common bile duct outside the liver is about 190 V/m. The electric field intensity in the right hepatic duct is about 150 V/m, while that in the left hepatic duct is only 80 V/m. The location of one-dimensional magnetic field intensity distribution is along the direction of the common bile duct in the bearing magnetic fluid; that is, the magnetic field intensity at $x = 150$ mm is 9208 A/m. The uniformity of magnetic field distribution in space is the guarantee of safety and stability of MHD lubrication. Taking $x = 150$ mm as the center point, the variation range of magnetic field intensity in the range of 75 mm is not more than 0.3%. Compared with the single coil, the uniformity is greatly improved, and there is also a larger space suitable for lubrication.

Taking the magnetic field intensity $H = 9208$ A/m at the magnetic fluid as the external condition, the actual lubrication performance P of different attribute parameters of Fe_3O_4 magnetic medium under this condition is simulated and calculated by MATLAB. Magnetic fluid is a new kind of lubricant. It uses an external magnetic field to keep the magnetic fluid in the lubricated part without leakage. For example, mine wheel bearings are sometimes immersed in water, and water should be prevented from eroding the grease in the bearing and causing loss. Permanent magnets can be installed in the bearing to magnetize the rolling elements and form a magnetic field in the contact area between the rolling elements and the bearing ring. We keep the magnetic fluid lubricant in the bearing, so that the bearing is always in good lubrication conditions, thereby greatly improving the life of the bearing. The actual lubrication performance is related to the nanoparticle radius r, magnetic anisotropy parameter K, and viscosity coefficient of Fe_3O_4 magnetic fluid η and volume fraction φ as shown in Table 1. There are many kinds of magnetic fluids used in MHD lubrication, including ferrite magnetic nanoparticles Fe_3O_4 and Fe_3O_4. γ- Fe_2O_3 is a magnetic material approved by the US Food and Drug Administration and can be used in the human body. In this study, water-based Fe_3O_4 nanomagnetic fluid was used with a high Curie temperature of 120°C.

As shown in Figure 4, the actual lubrication performance is strongly dependent on the size of Fe_3O_4 nanoparticles and reaches the maximum value near $R = 9.5$ nm and then begins to decline. The reason is that when the radius of nanoparticles changes, the composite relaxation time also changes dynamically. When $r = 9.5$ nm, the Neill relaxation time is close to the brown relaxation time, and the composite relaxation time is the largest. When $R < 9.5$ nm, the relaxation is dominant, and the composite relaxation time and relaxation loss heat decrease. When $r > 9.5$ nm, the relaxation dominates, the equilibrium susceptibility decreases, and the actual lubrication performance decreases again.

As shown in Figure 5, in order to understand the lubrication of magnetic fluid under different lubrication performance in advance, this study carried out 8 times the simulation in advance; that is, when the actual lubrication performance of magnetic fluid is 5×105, 1×106, 1.5×106, and 2×106 w/m³, the corresponding temperature data of MHD in hepatic hilum and MHD in the liver were obtained.

The lubrication time is 500 s, and the temperature of each point is summarized, as shown in Table 2. It can be seen that the temperature in the tumor is directly proportional to the actual lubrication performance of the magnetic fluid, the temperature in the center of the tumor is slightly higher than that in the edge, and the temperature in the corresponding point of the magnetic fluid model in the porta hepatis is slightly lower than that of the magnetic fluid model outside the liver. The optimal temperature range of MHD lubrication is 42~46°C. Therefore, as long as the minimum temperature of the tumor edge is above 42°C, it means that the magnetic fluid tissue can be effectively lubricated. According to the maximum temperature of 46°C, it can be preliminarily determined that when the actual lubrication performance of the magnetic fluid is at 1 and when the flow rate is about 106 w/m³, it can meet the requirement of MHD lubrication.

The temperature required by the warm lubrication method and the simulation results of the Helmholtz coil is shown in Figure 6. Under the alternating magnetic field of 9208 A/M and 100 kHz, the calculated lubrication performance of the Fe_3O_4 magnetic nanoparticles is $P0 = 1.844 \times 106$ w/m³ multiplied by the correction factor α. After the actual lubrication performance, $P = 1.014$. The SAR value of MHD is 4381.5 w/kg. The biological heat transfer module of COMSOL software was used to simulate the solution, and the free tetrahedral mesh was used to generate unit meshes. The research step was set as 1 s, and the total time was 500 s.

As shown in Figure 7, the magnetic anisotropy parameter is 1. The actual lubrication performance reaches the maximum at 104 J/m³. The viscosity coefficient generally refers to the viscosity of the magnetic fluid-based carrier fluid. Nanomagnetic particles are dispersed in the base carrier fluid. Good fluidity enables them to enter the human tissue smoothly, and the viscosity coefficient is greater than 1. After $10 - 3$ kg/(MS), the actual lubrication performance
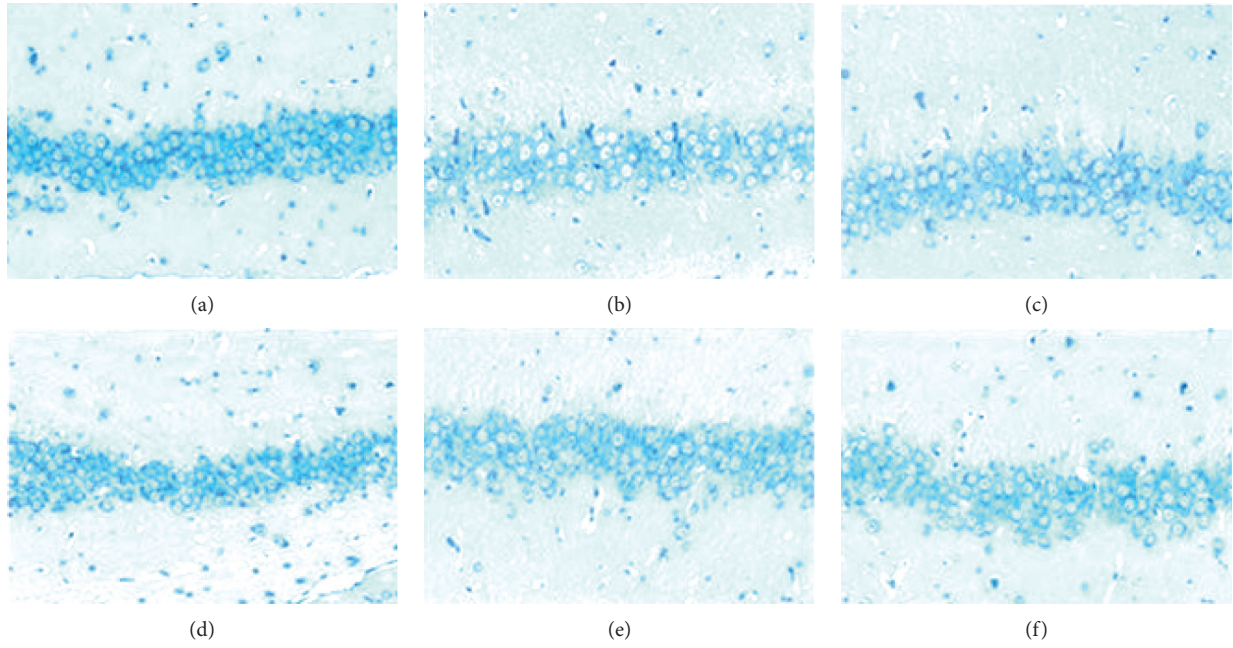
FIGURE 1: Influence of texture parameters on friction factor at different temperatures. (a) 30°C. (b) 35°C. (c) 38°C. (d) 40°C. (e) 43°C. (f) 50°C.
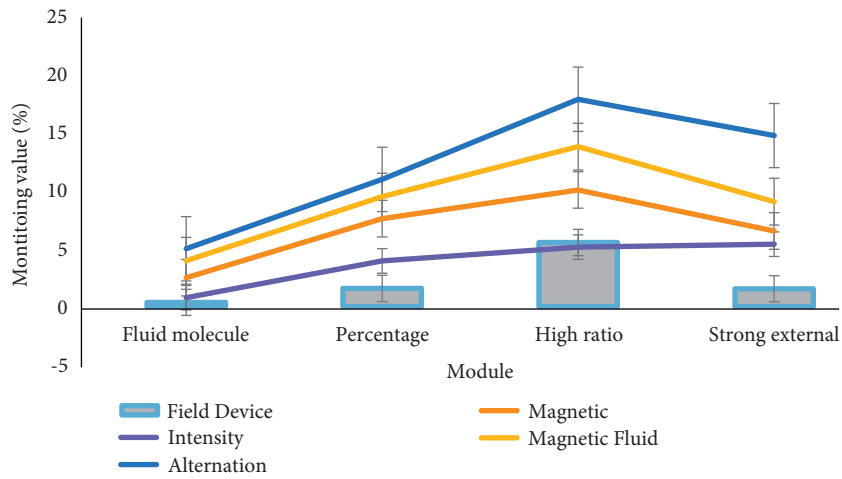
FIGURE 2: Distribution of the magnetic field generated by the Helmholtz coil.
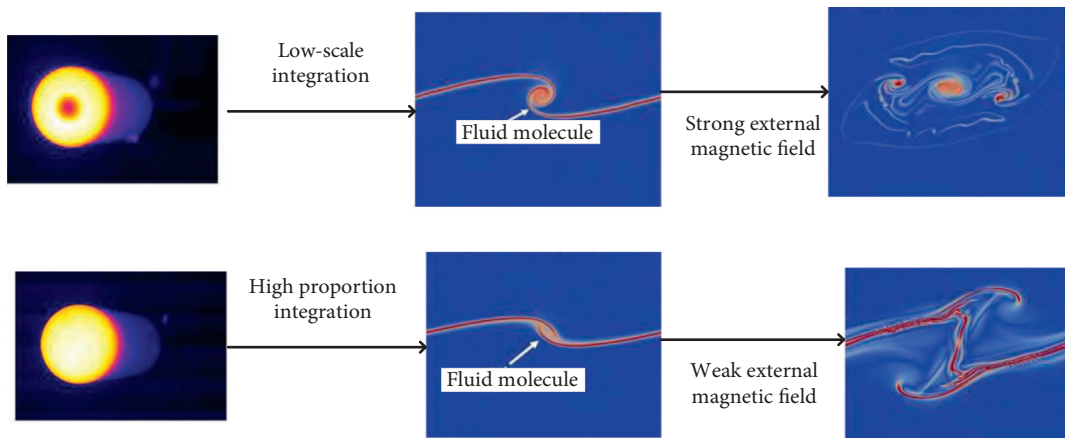
FIGURE 3: Magnetic fluid dense and sparse electric field distribution.

TABLE 1: The relationship between viscosity coefficient η and volume fraction φ.

Item	Intensity	Magnetic	Field device	Magnetic fluid	Alternation
P	0.76	1.71	0.35	1.45	1.04
φ	3.91	3.63	1.55	1.89	1.48
K	5.09	4.91	5.49	3.72	4.06
r	5.35	1.13	1.52	2.52	5.67
External	1.26	4.32	4.35	4.4	2.75
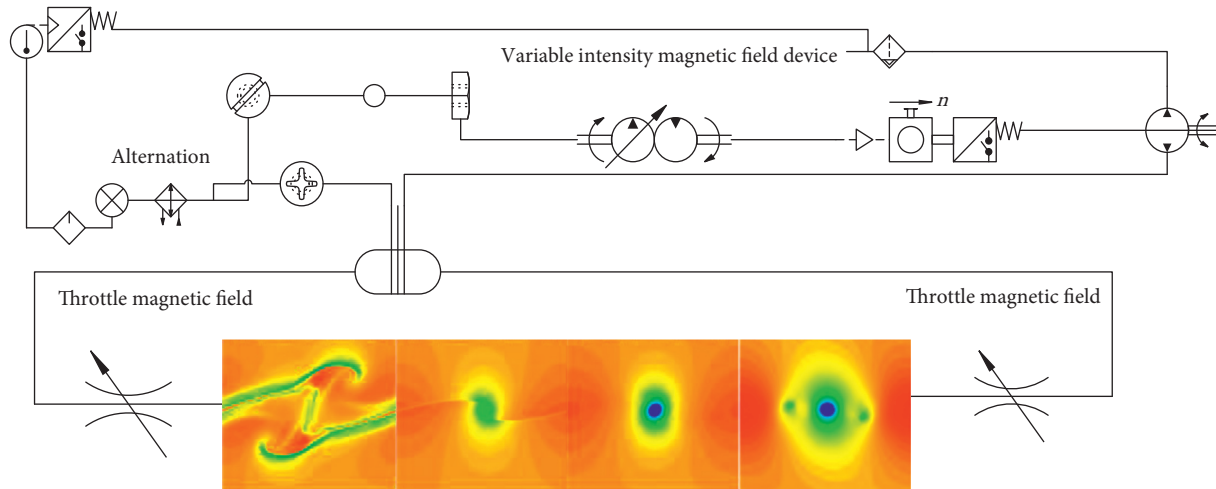
FIGURE 4: Dependence of actual heating power on nanoparticles.

tends to be stable. The actual lubrication performance is also in direct proportion to the volume fraction of the magnetic fluid. In a certain range, the lubrication degree of the tumor area can be increased or decreased by adjusting the volume fraction appropriately. The change of viscosity coefficient due to temperature change is not considered in this study.

The bearing deformation is evaluated by predicting the lubrication performance of small bearings, as shown in Table 3. Although the one-dimensional and two-dimensional bearing deformation models have high computational efficiency, the thermohydrodynamic lubrication model is extended to the thermoelastic hydrodynamic lubrication model when the size of the tilting pad journal bearing is large. Based on the model, a direct lubricated two-pad tilting pad journal bearing with a diameter of 890 mm is studied.

The results of the thermoelastic hydrodynamic lubrication model are shown in Figure 8. The static performance of tilting pad journal bearing under high speed and heavy load is studied and compared with the experimental results. A new 900 mm three-pad tilting pad journal bearing was optimized and verified. Through the coupling analysis of the thermal hydrodynamic lubrication program and commercial structural mechanics software, the influence of bearing thermal stress and deformation is considered. In this paper, the experimental study of a five-pad tilting pad journal bearing with directional lubrication is carried out under different oil supply flow conditions. By comparing with the theoretical results, it is found that speed has a great influence on the transition from rich oil to lean oil.

Table 4 shows the steady-state and dynamic performance of tilting pad journal bearing under the condition of too much lubricating oil and too low lubricating oil. The thermoelastic hydrodynamic lubrication models of tilting pad journal bearings are mostly solved by self-programming with finite difference method or finite element method. Because the programming code is not open source and not easy to copy, it limits the wide application of simulation tools in the industry. The great beauty of open source is that it is not dependent on a single vendor; everyone can modify the code to meet their own needs, and millions of "their needs" come together to make a great product. Using commercial software can make researchers pay more attention to physical phenomena than complex numerical methods. By combining COMSOL multiphysics and MATLAB, Hibachi's method is realized, which provides a new idea to solve the thermoelastic hydrodynamic model of coating cylinder line contact.

As shown in Table 5, under low preload, with the increase of excitation frequency, the dynamic contact lubricity of the solid-liquid interface keeps approximately unchanged, because the inherent properties (Poisson's ratio, elastic modulus) of the interface material remain unchanged, while the dynamic contact lubricity of the solid-liquid interface has an obvious increasing trend, and the variation laws of the two interfaces are consistent with the simulation results; however, the simulation results of the solid-liquid interface are slightly larger than the experimental data.

As shown in Figure 9, in the range of 80 Hz–100 Hz, the data value drops precipitously, which is inconsistent with the overall trend. It may be caused by the resonance between the excitation frequency and the experimental platform. Under high preload, with the increase of
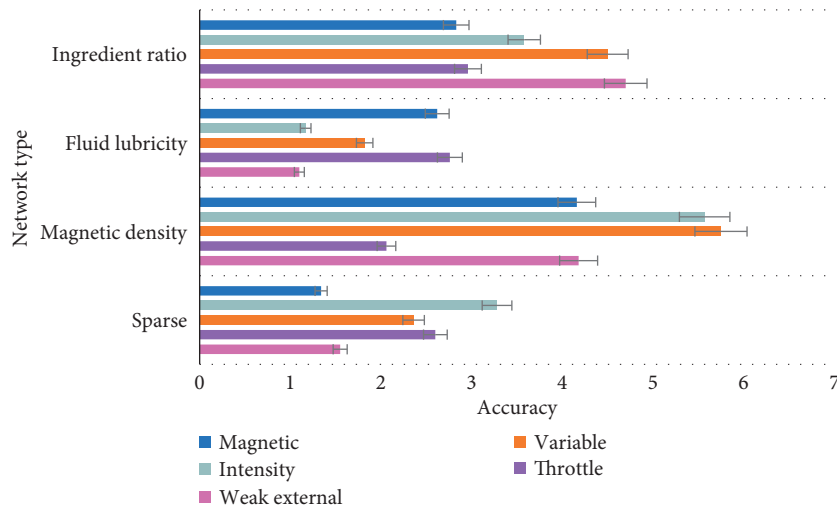
FIGURE 5: Lubrication of ferrofluid cancer.

TABLE 2: Lubrication time and temperature at each point.

Time (second)	Weak external	Throttle	Variable	Intensity	Magnetic
100	1.55	2.6	2.36	3.28	1.34
300	4.18	2.06	5.75	5.57	4.16
500	1.1	2.76	1.82	1.17	2.62
750	4.7	2.96	4.5	3.58	2.83
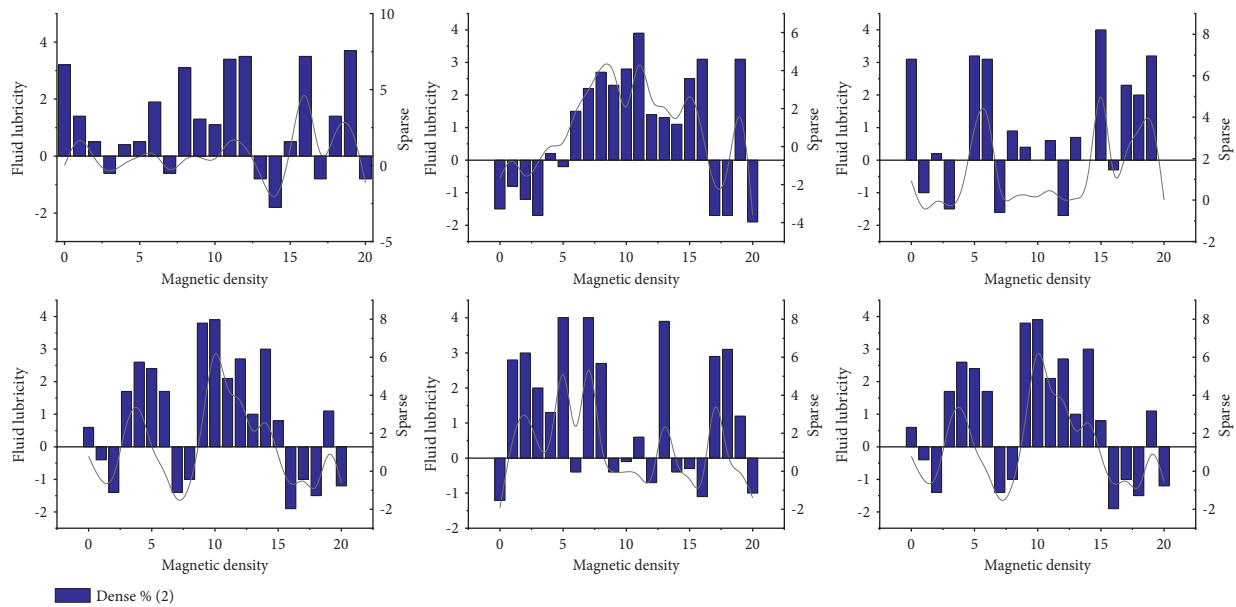
FIGURE 6: The relationship between ingredient ratio and lubricity.

excitation frequency, the change trend of solid-liquid interface and solid-consolidation interface is almost the same, but the solid-liquid interface still has a small increase, which is in good agreement with the theoretical model simulation. The differences in the range of 80 Hz–100 Hz are also caused by resonance.

As shown in Figure 10, when the ratio of Fe^{2+} to Fe^{3+} is between $11:20$ and $13:20$, the MHD lubrication performance of oil film bearing is in the peak region. When the ratio is $3:5$, the best lubrication performance can be achieved. When it is slightly higher than this ratio, the oxidation rate is accelerated due to more ferrous ions. Although it can have a good lubrication effect, it is easy to cause the overall fluidity of oil film-bearing magnetic fluid to deteriorate. Therefore, the oil film-bearing nano-MHD with the ratio of $3:5$ ferrous to ferric has the best lubrication performance in the microgravity environment simulated by magnetic compensation.
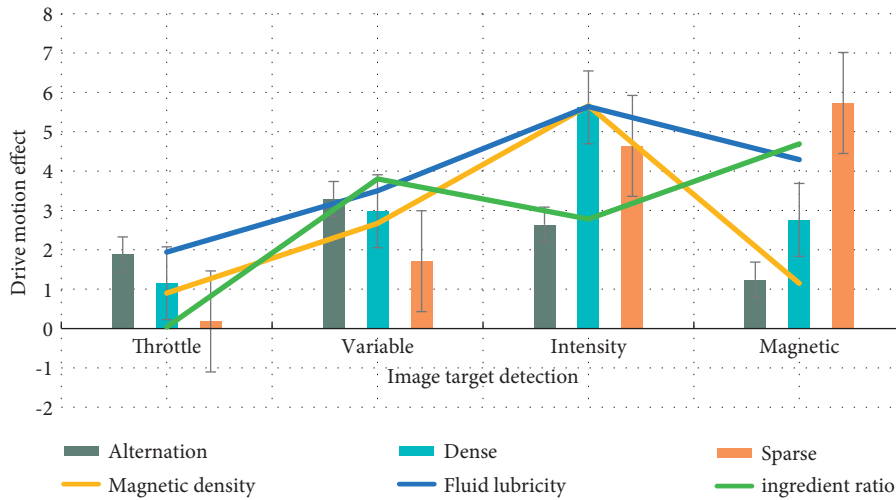
FIGURE 7: Volume fraction of magnetic fluid.

TABLE 3: Lubrication performance and bearing deformation of small bearings.

Item	Alternation	Dense	Sparse	Magnetic density	Fluid lubricity	Ingredient ratio
Throttle	1.88	1.15	0.18	0.9	1.94	0.04
Variable	3.29	2.98	1.71	2.67	3.5	3.8
Intensity	2.64	5.62	4.64	5.66	5.64	2.78
Magnetic	1.24	2.76	5.73	1.15	4.29	4.69
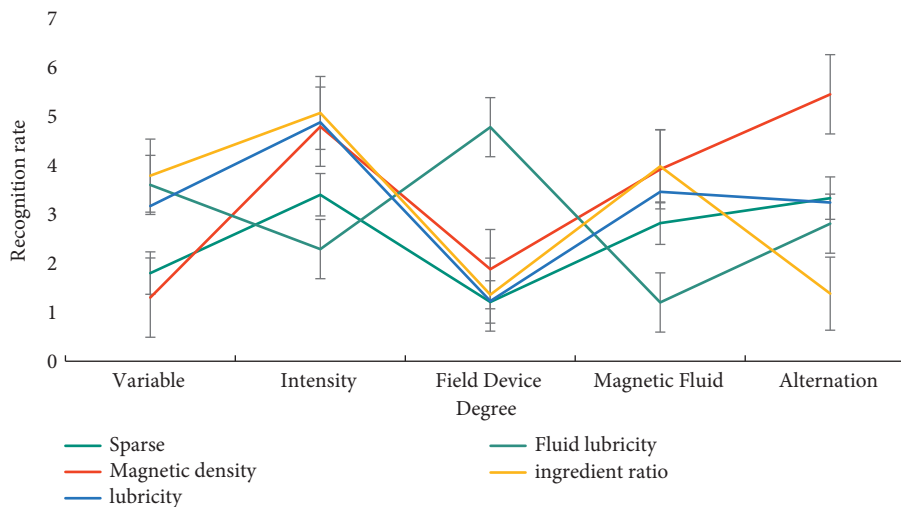
FIGURE 8: Thermoelastic hydrodynamic lubrication model results.

In the state of magnetic fluid lubrication, the amount of adhesive wear that occurs is the least. Different from the dry friction state and the traditional lubrication state, the surface is relatively smooth and smooth. The greater the load, the greater the amount of wear, and the maximum wear depth is 43.02 μm, 50.58 μm, and 150.1 μm, respectively. Under different load conditions, the wear depth of babbitt alloy under the magnetic fluid lubrication state is the smallest and the wear amount is the lowest. Under the traditional lubrication state, the friction and wear morphology has been improved, and the average friction coefficient is greatly reduced, mainly because the dry friction changes to wet friction and the lubricating oil plays a lubricating effect. In the state of magnetic fluid lubrication, the average friction coefficient is the lowest. The main reason may be that the nanomagnetic particles in the magnetic fluid fill the grooves and pits on the surface to play a certain role in repairing, and the nanoadditives in the magnetic fluid are in the process of wear. A series of physical and chemical reactions occur to form an oxide film on the friction surface, thereby effectively improving its friction and wear conditions.

TABLE 4: Steady state and dynamic performance of tilting pad sliding bearing.

Degree of occlusion	Sparse	Magnetic density	Fluid lubricity	Ingredient ratio	Lubricity
Variable	1.8	1.3	3.6	3.79	3.17
Intensity	3.4	4.79	2.29	5.07	4.88
Field device	1.21	1.88	4.78	1.36	1.23
Magnetic fluid	2.82	3.92	1.2	3.98	3.46
Alternation	3.33	5.45	2.81	1.38	3.24
Dense	4.11	4.26	4.39	6.73	1.73

TABLE 5: Approximate degree of dynamic contact lubricity of the joint surface.

Item	Alternation	Dense	Sparse	Magnetic density	Fluid lubricity
High ratio	3.83	1.14	3.66	3.39	1.21
External	2.41	5.84	2.82	3.17	2.31
Weak external	5.28	3.08	3.78	4.82	2.19
Throttle	2.3	2.43	4.06	3.64	1.15
Variable	4.62	1.22	6.34	6.71	6.25
Intensity	3.52	3.13	2.58	6.52	6.93
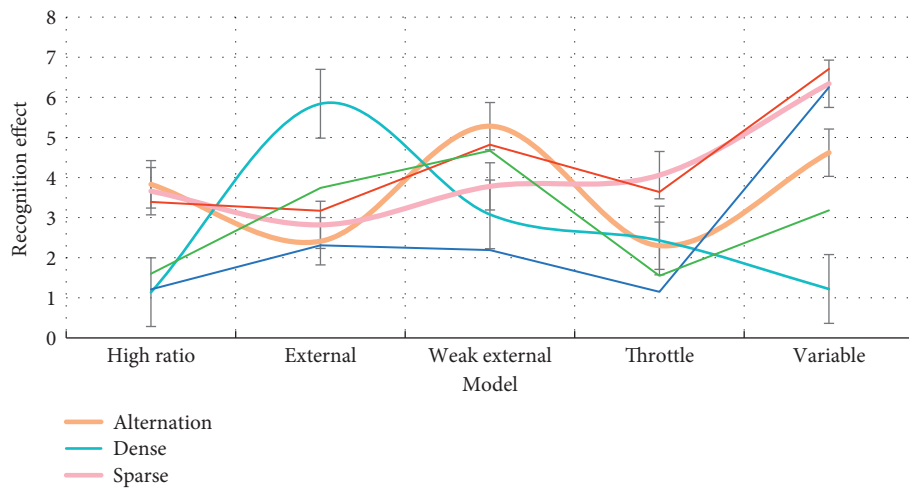
FIGURE 9: Excitation frequency and experimental platform resonance.
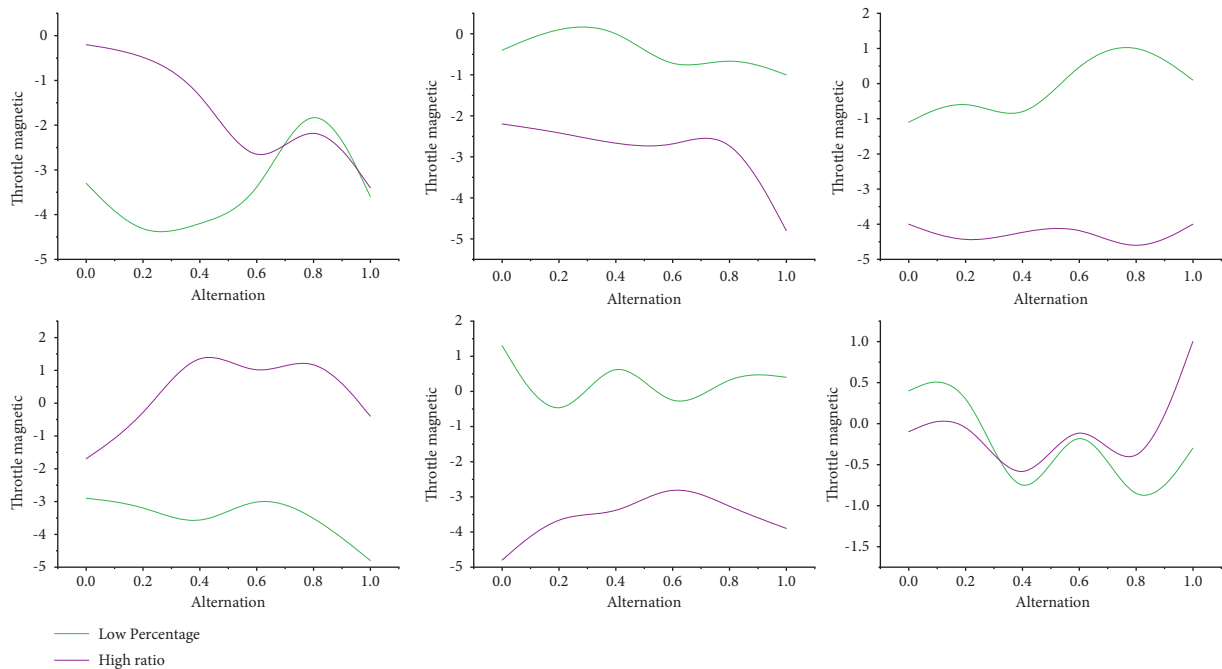
FIGURE 10: Influence of variable intensity magnetic field device on magnetic fluid.

4.2. Discussion. The purpose of this paper is to study the variation and relationship of oil film thickness, temperature distribution, pressure distribution, power loss, viscosity temperature characteristics, and leakage under constant temperature and variable temperature, vibration, and nonvibration conditions. Through the numerical simulation and friction and wear test, it can be concluded that the rhombic microtexture has the best parameters, which provides the basis for the subsequent optimization of texture parameters. The upper and right edges of the oil film bearing are closer to the magnetic field coil, so the magnetic fluid strength is higher. The temperature rise caused by the eddy current effect is more obvious here. In the vicinity of human skin tissue, the temperature increased by 4~5°C, and the temperature of other parts did not change significantly. In the process of changing with time, the temperature rises rapidly at the beginning and reaches the peak after about 10 minutes. It is worth noting that there is no obvious cumulative effect of heat during the long lubrication process of 30 min; that is, the temperature remains stable after reaching equilibrium and does not rise all the time. In the region of MHD lubrication, the temperature fluctuation caused by eddy heat is very small, which only increases by 0.1°C. Therefore, it can be considered that the eddy heat generated by the Helmholtz coil type magnetic field generator in this study will not cause harm to the human body under fixed parameters and has little influence on the temperature distribution in the tumor area of magnetic induction lubrication.

5. Conclusions

In this paper, the relationship between the parameters of Fe_3O_4 magnetic fluid and its lubrication performance is analyzed, and it is substituted into Pennes biological heat transfer equation as an external heat source term. Based on the finite element method, the model is meshed to obtain the distribution of electromagnetic field and thermal field in the MHD treatment area. When the frequency is 100 kHz, the peak value of alternating current is 10 A, the number of turns is 380, the amplitude of the magnetic field generated by the Helmholtz coil in MHD is 9208 A/m, and the distribution is relatively uniform. Based on the Reynolds equation, the hydrodynamic lubrication theoretical analysis model of biomimetic microtexture is established. The influence of texture size and texture depth on friction coefficient is solved by MATLAB. It is concluded that changing texture parameters can affect the friction performance of friction pairs, and the friction coefficient first increases and then decreases with the increase of microtexture size and depth. Under the condition of fluid lubrication, the experimental results are consistent with the numerical simulation results. By changing the parameters of microtexture, the friction behavior of the friction interface can be adjusted to achieve friction reduction. The different material properties, such as radius of nanoparticles, viscosity coefficient, magnetic anisotropy constant, and volume fraction, will lead to the change of the heating effect. It can meet the requirements of the warm lubrication method commonly used in MHD

lubrication. There are also many shortcomings in this article. For example, due to the limitations of realistic conditions, this experiment was done hurriedly, and many details were not considered. This problem needs follow-up improvement.

Data Availability

No data were used to support this study.

Conflicts of Interest

The authors declare that there are no conflicts of interest.

Acknowledgments

References

[1] T. Kakutani, "Axially symmetric stagnation-point flow of an electricallyconducting fluid under transverse magnetic field," *Journal of thePhysical Society of Japan*, vol. 15, no. 4, pp. 688–695, 2020.

[2] M. F. Romig, "The influence of electric and magnetic fields on heattransfer to electrically conducting fluids," *Advances in Heat Transfer*, vol. 1, no. 4, pp. 267–354, 2020.

[3] R. W. Ziemer and W. B. Bush, "Magnetic field effects on bow shock stand-offdistance," *Physical Review Letters*, vol. 1, no. 2, pp. 58-59, 2020.

[4] D. R. Smith, D. E. Gildfind, P. A. Jacobs et al., "Magneto-hydrodynamic drag measurements in an expansion tunnel with argon test gas," *AIAA Journal*, vol. 58, no. 10, pp. 4495–4504, 2020.

[5] T. Murakami and Y. Okuno, "High-performance nonequilibrium-plasmamagnetohydrodynamic electrical power generator using slightlydivergent channel configuration: II. Experiment," *Journal of Physics D: Applied Physics*, vol. 41, no. 12, pp. 23–25, 2018.

[6] C. B. Su, Y. H. Li, and B. Q. Chen, "Experimental investigation of MHD flowcontrol for the oblique shock wave around the ramp in low-temperaturesupersonic flow," *Chinese Journal of Aeronautics*, vol. 22, no. 1, pp. 22–32, 2020.

[7] W. Zhao, Z. L. Jiang, T. Saito, J. M. Lin, H. R. Yu, and K. Takayama, "Performance of a detonation drivenshock tunnel," *Shock Waves*, vol. 14, no. 4, pp. 53–59, 2019.

[8] Z. Ahmad, S. Lv, Z. Tang, A. Shah, and X. Chen, "Methoxy poly (ethylene glycol)-block-poly (glutamic acid)-graft-6-(2-nitroimidazole) hexyl amine nanoparticles for potential hypoxia-responsive delivery of doxorubicin," *Journal of Biomaterials Science, Polymer Edition*, vol. 27, no. 1, pp. 40–54, 2016.

[9] A. Gülhan, B. Esser, U. Koch et al., "Experimental verification ofheat-flux mitigation by electromagnetic fields in partially-ionized-argonflows," *Journal of Spacecraft and Rockets*, vol. 46, no. 2, p. 274, Article ID 28338, 2019.

[10] D. R. Smith, D. E. Gildfind, D. J. Mee, C. M. James, and B. V. Allsop, "Magnetohydrodynamic dragforce

measurements in an expansion tunnel using a stress wave forcebalance," *Experiments in Fluids*, vol. 61, no. 8, pp. 11–15, 2020.

[11] L. Qiu, X. Han, T. Peng et al., "Design and experiments of a high fieldelectromagnetic forming system," *IEEE Transactions on Applied Superconductivity*, vol. 22, no. 3, pp. 37–39, 2019.

[12] R. H. Levy, "A simple MHD flow with hall effect," *AIAA Journal*, vol. 1, no. 3, p. 698, Article ID 69948, 2020.

[13] M. Kawamura, A. Matsuda, H. Katsurayama et al., "Experimental on dragenhancement for a blunt body with electrodynamic heat shield," *Journal of Spacecraft and Rockets*, vol. 46, no. 6, pp. 1171–1177, 2019.

[14] M. Kawamura, Y. Nagata, H. Katsurayama, H. Otsu, K. Yamada, and T. Abe, "Magnetoaerodynamicforce on a magnetized body in a partially ionized flow," *Journal ofSpacecraft and Rockets*, vol. 50, no. 2, pp. 347–351, 2019.

[15] B. Gao, N. Xu, and P. Xing, "Shock wave induced nanocrystallization during the high current pulsed electron beam process and its effect on mechanical properties," *Materials Letters*, vol. 237, no. 15, pp. 180–184, 2019.

[16] S. V. Bobashev, Y. P. Golovachev, G. A. Kurbatov et al., "Experimental andnumerical investigation into the supersonic flow of a weakly ionizedplasma around a dihedral angle: magnetohydrodynamic control of theflow pattern and heat fluxes toward the wall," *Technical Physics*, vol. 54, no. 1, pp. 33–41, 2019.

[17] X. Xianzhen, H. Yangdong, W. Lianying, and W. Xi, "Experimental and modeling of vapor–liquid equilibria for mixed electrolyte solution systems," *Journal of Chemical & Engineering Data*, vol. 61, no. 7, pp. 2311–2320, 2016.

[18] R. J. Nowak and M. C. Yuen, "Heat transfer to a hemispherical body in asupersonic argon plasma," *AIAA Journal*, vol. 11, no. 11, pp. 1463-1464, 2020.

[19] X. Xianzhen, H. Yangdong, W. Lianying, and C. Xia, "A new model in correlating and calculating the solid-liquid equilibrium of salt-water systems," *Chinese Journal of Chemical Engineering*, vol. 24, no. 8, pp. 1056–1064, 2016.

[20] L. E. Hooks and R. C. Lewis, "Simplified magnetoaerodynamic flow relationsfor axisymmetric blunt bodies," *AIAA Journal*, vol. 5, no. 4, pp. 644–650, 2020.

[21] M. D. Ladyzhenskii, "Hypersonic flow past a body inmagnetohydrodynamics," *Journal of Applied Mathematics andMechanics*, vol. 23, no. 6, pp. 1427–1443, 2020.

[22] P. S. Lykoudis, "The Newtonian approximation in magnetic hypersonicstagnation-point flow," *Journal of the Aerospace Sciences*, vol. 28, no. 7, pp. 541–546, 2020.

[23] R. W. Porter and A. B. Cambel, "Theoretical aspects of blunt bodymagnetoaerodynamics. NASA Report N-1-66, 196660 Poggie J, Gaitonde DV. Magnetic control of flow past a blunt body:Numerical validation and exploration," *Physics of Fluids*, vol. 14, no. 5, pp. 1720–3161, 2020.

[24] R. P. H. Berton, "Analytic model of a resistive magnetohydrodynamic shock without Hall effect," *Journal of Fluid Mechanics*, vol. 842, no. 4, pp. 273–322, 2018.

[25] M. Brio and C. C. Wu, "An upwind differencing scheme for the equations ofideal magnetohydrodynamics," *Journal of Computational Physics*, vol. 75, no. 2, pp. 400–422, 2020.

[26] G. C. Zha, Y. Shen, and B. Wang, "An improved low diffusion E-CUSP upwindscheme," *Computers & Fluids*, vol. 48, no. 1, pp. 214–220, 2019.

[27] D. G. Maciel and E. Sávio, "Magnetic field applied to thermochemicalnon-equilibrium reentry flows in 2D–five species," *International Journal of Computational Fluid Dynamics*, vol. 29, no. 6, pp. 376–399, 2019.

[28] X. Xu, Y. Hu, L. Wu, and S. Zhang, "Experimental and modeling of vapor-liquid equilibria for electrolyte solution systems," *Journal of Chemical & Engineering Data*, vol. 59, no. 11, pp. 3741–3748, 2014.

[29] B. Ju and D. C. Barnes, "The Effect of Nonzero B on the numericalsolution of the magnetohydrodynamic equations," *Journal of Computational Physics*, vol. 35, no. 3, pp. 426–430, 2020.

Research Article

Preparation of Au-Ag Bimetals and Large-Size Porous Gold Nanostructured Materials

Xuewen Chen [1,2]

^{1}*Guangdong Engineering Polytechnic, Guangzhou 510520, China*
^{2}*Guangzhou Metals Association, Guangzhou 510520, China*

Correspondence should be addressed to Xuewen Chen; lxd@hhtc.edu.cn

Gold, silver, and other precious metals are very important nonferrous metals and have been widely applied in fields such as electronics, medicine, metallurgy, pharmaceuticals, and transportation. Adjustable properties of precious metals are mainly attributed to controlled synthesis of precious metals by structure, size, composition, and morphology. Synthesis of binary metals focuses on coordination of physical and chemical properties of metal elements in components, with the aim to give full play to the advantages of the two metals. Gold (Au) and silver (Ag) have similar lattice constants, which provide important theoretical basis for obtaining the binary bimetallic nanostructure of the two metals by coreduction at room temperature. Ag–Au alloy was prepared at different molar ratios of Ag^+/Au^{III}, and the bimetallic nanomaterials obtained had similar Ag/Au ratios to the molar ratio at reaction. This suggested that the bimetallic nanomaterials reacted completely, with the maximum average size in $Ag_{90.1}$–$Au_{9.9}$ and the minimum average size in $Ag_{83.2}$–$Au_{16.8}$ and $Ag_{66.9}$–$Au_{33.1}$. Due to the deficiency of conventional etching agents, the "regrowth etching" method was proposed in this study. Specifically, with Au^I as the etching agent, the porous gold nanomaterials with the size of more than 300 nm were successfully prepared, achieving the regrowth etching effect and a good structural stability. According to the analysis based on the catalytic reduction reaction with p-nitrophenol, the properties of the large-size porous gold nanomaterials were related to the quantity and size of pores.

1. Introduction

1.1. Overview of Nanomaterial and Nanotechnology. Nanostructured material, "nanomaterial" for short, is a generic term for superfine granular materials with at least one dimension in the nanoscale. According to the definition adopted by the European Commission on October 18, 2011, "nanomaterial" means a natural, incidental, or manufactured material containing particles, in an unbound state or as an aggregate or as an agglomerate , where, for 50% or more of the particles in the number size distribution, one or more external dimensions is in the size range 1 nm–100 nm. The European Commission suggests that basic particles of most nanomaterials are within this range, though materials beyond this range may also have the characteristics of nanomaterials. The definition aims to make the standard clear: a low threshold of nanoparticles will cover up the nanoproperties of the whole material, and 50% is an appropriate threshold. In addition, using the quantity ratio of nanoparticles instead of mass ratio as the measurement standard of nanomaterials can reflect the characteristics of nanomaterials better, because some nanomaterials have a very low density but still can show obvious characteristics of nanomaterials in the case of low mass ratio. Nanomaterials can be roughly divided into four categories: nanopowder, nanofiber, nanofilm, and nanoblock. Among them, the nanopowder features the longest development history and most mature technology and is the basis for the production of the other three.

Nanotechnology is a technology to study the properties and applications of materials with structural sizes ranging from 1 nm to 100 nm. With the invention of scanning tunneling microscope in 1981, a new science with length 1 nm–100 nm as the research object was born, whose

ultimate goal is to construct products with specific functions directly from atoms or molecules. Therefore, nanotechnology is actually a kind of science and technology that uses single atoms or molecules to make matters.

1.2. Precious Metal Nanomaterials and Their Properties. Precious metals generally refer to eight nonferrous metal elements, including gold, silver, and platinum group (including ruthenium, rhodium, palladium, osmium, iridium, and platinum). They are used in optoelectronics, energy, chemical, biomedical, and ceramic fields because of their unique optical, electrical, catalytic, and physicochemical properties. By adjusting the physical parameters and properties such as structure, morphology, size, and composition of precious metal nanocrystals, specific properties can be effectively obtained, realizing the application of precious metal nanomaterials. Precious metal nanomaterials refer to the new materials containing precious metals, whose size is less than 100 nm (or containing corresponding size of nanophase) obtained from precious metal products developed and produced by using nanotechnology.

Nanomaterials are powders, fibers, films, or blocks in the nanoscale. Scientific experiments have proved that when normal matter is processed to an extremely fine nanoscale, there will be specific surface effect, volume effect and quantum effect, and its optical, thermal, electrical, magnetic, mechanical, and even chemical properties will change significantly accordingly. Because of their small size, nanomaterials have very high surface energy and chemical activity and many special functions. Therefore, nanomaterials have superior properties that ordinary materials do not have.

Like nanomaterials, precious metal nanomaterials also have a series of special physical and chemical properties. The melting point of precious metal nanomaterials is obviously lower than that of conventional precious metal materials, which is due to the large specific surface area, high surface energy and interfacial energy, and less internal energy needed for melting of nanoparticles. The same is true of silver, gold, and platinum group metal nanoparticles. Precious metal nanoparticles have excellent catalytic activity and selectivity because of their larger specific surface area, higher surface energy, and surface crystal defects.

1.3. Preparation and Application of Precious Metal Nanomaterials. With the gradual weakening of the monetary function of precious metals such as gold, silver, platinum, and palladium, the industrial application of precious metals has increased rapidly. One of the reasons is that high and new technologies such as nanotechnology are constantly combined with traditional deep processing technology of precious metals, which has greatly expanded the application scope and quantity of precious metals in industry.

The preparation methods of precious metal nanomaterials can be divided into two categories: one is top-down, using macro- to submicroscopic methods, such as grinding, peeling, and etching; the other is bottom-up, using microscopic to submicroscopic methods, such as

chemical synthesis, polymerization, and self-assembly. The former method mostly involves physical operations, while the latter involves chemical reactions. As there are many preparation methods of precious metal nanoparticles, and the preparation is easy, it has become one of the many advantages for precious metal nanoparticles to be widely studied and used.

At present, the research and application of nanotechnology mainly focus on materials and preparation, microelectronics and computer technology, medicine and health, aerospace and aviation, environment and energy, biotechnology, and agricultural products. Nanotechnology occupies a core position in the research and application of new materials. The equipment made of nanomaterials boasts of lighter weight, stronger hardness, longer life, lower maintenance cost, and more convenient design. Nanomaterials can also be used to produce materials with specific properties or materials that do not exist in nature, and to produce biomaterials and biomimetic materials.

Along with the constant development of modern science and technology, nanomaterials have played an increasingly important role in many fields. In particular, precious metal nanomaterials have attracted much attention because of their excellent physical and chemical properties [1]. The size and morphology of nanomaterials mainly depend on preparation methods. According to some study reports, synthesis of precious metallic nanocrystallines was controllable, and small-size monometallic nanomaterials had a high activity and excellent properties, but a poor stability, whereas large-size nanomaterials featured a stable structure, but their internal components were hard to interact [2–5]. Therefore, the regrowth etching technique was adopted in this study to etch Au/Ag bimetallic nanomaterials, in the expectation of obtaining porous gold nanomaterials with a stable structure and large size. The specific study is as follows.

2. Materials and Methods

2.1. Instruments and Reagents

(1) The used instruments were as follows: ultrasonic apparatus, electronic scale, scanning electron microscope, beaker, stirrer, liquid ultraviolet spectrophotometer, centrifuge, transmission electron microscope, and cuvette

(2) The used reagents were as follows: silver nitrate, ammonium hydroxide, anhydrous ethanol, chloride acid (all were analytically pure), sodium borohydride, ascorbic acid, polyvinylpyrrolidone (PVP), p-nitrophenol, and deionized water

3. Methods

3.1. Preparation of Bimetallic Nanoparticles. After 4 mL of silver nitrate solution was mixed with 0.4 g of polyvinylpyrrolidone, the solution was dissolved in 5 mL of deionized water and stirred for 10 min. After the solution was confirmed to be clear, 2 mL of ammonium hydroxide

was added and stirred for 2 min. Then, 2 mL of auric chloride solution was added to the mixture, and the total amount of Ag and Au must be 3μmol. After 1 mL of vitamin C was added and reacted for 15 min, the sample was cleaned with deionized water and then dispersed into 3 mL of deionized water for later use.

3.2. Synthesis of Au Nanoparticles. 4 mL of chloroauric acid solution and 0.4 g polyvinylpyrrolidone were added into 5 mL of deionized water and then fully stirred. After 1 mL vitamin C was added, the color of the solution changed accordingly. After reaction for 15 min, the solution was cleaned with deionized water and then dispersed into deionized water for later use.

3.3. Preparation of Porous Nano-Au

(1) Appropriate amount of the vitamin C solution was added into the chloroauric acid solution. After the solution became transparent and colorless, the Au^I solution was obtained. After the prepared Ag-Au bimetallic nanoparticles were mixed with the Au^I solution, the color would gradually change. Samples were collected at room temperature and cleaned and centrifuged with ammonium hydroxide and ionized water. The product obtained was dispersed into deionized water for later use.

(2) By Fe^{3+} etching approach, the prepared Ag-Au bimetallic nanoparticles were mixed with 20 mM of ferric nitrate, and the color of the solution gradually faded. After reaction for half an hour, the samples were collected, cleaned with deionized water, and centrifuged. The product obtained was dispersed into deionized water for later use.

(3) By ammonium hydroxide erosion approach, the prepared Ag-Au bimetallic nanoparticles were mixed with appropriate amount of ammonium hydroxide. After reaction for 12 h, the samples were collected, cleaned, and centrifuged. The final product was dispersed into deionized water for later use.

(4) By catalytic reduction with nitrophenol, 1 mL of p-nitrophenol and 1 mL of sodium borohydride were mixed. Then, the prepared Au-based nanoreactor was injected into the reaction system to obtain 3 mL of mixed solution. Finally, the mixed solution was placed in a quartz cuvette for an absorbance test, until the solution became colorless.

4. Results

4.1. Preparation of Bimetallic Precursor. Based on the closely matched lattice constants of Ag and Au, nucleation and growth rates of Ag and Au were adjusted to reduce Ag-Au alloy. The morphology of bimetallic nanomaterials obtained at different molar ratios (10 : 1, 5 : 1, and 2 : 1) of Ag^+/Au^{III} was observed by scanning electron microscope (SEM) as shown in Figure 1. In the chemical element components, the corresponding ratios of Ag to Au were 90.1 : 9.9, 83.2 : 16.8,

and 66.9 : 33.1, respectively, which were close to the molar ratios at the reaction, indicating that the bimetallic nanomaterials obtained reacted completely.

After the average particle size of bimetallic nanomaterials above was determined, it was found that bimetallic nanomaterials synthesized at different molar ratios had certain differences. The average size of $Ag_{90.1}-Au_{9.9}$, $Ag_{83.2}-Au_{16.8}$, and $Ag_{66.9}-Au_{33.1}$ is as shown in Figure 2, with the maximum average size in $Ag_{90.1}-Au_{9.9}$ and the minimum average size in $Ag_{83.2}-Au_{16.8}$ and $Ag_{66.9}-Au_{33.1}$.

According to the analysis of SEM images and electron diffraction images of $Ag_{66.9}-Au_{33.1}$, the particles were polycrystalline, as shown in Figure 3(a). Based on dark-field transmission electron microscope images and bimetallic element distribution mapping images of $Ag_{66.9}-Au_{33.1}$, Ag and Au elements were widely distributed, as shown in Figures 3(b) and 3(c).

5. Analysis of Etching Results

5.1. Conventional Etching Agent. Conventionally, ammonium hydroxide, nitric acid, ferric nitrate, and other oxidizing agents were adopted for etching. For example, ammonium hydroxide and ferric nitrate were adopted for etching for Ag–Au bimetal generally. However, in the process of operation, Fe^{3+} and ammonium hydroxide were difficult to etch Ag in Ag–Au bimetal as expected. Through reaction between ferric nitrate and $Ag_{66.9}-Au_{33.1}$, the SEM image of the final product is shown in Figure 4(a). The analysis suggested that the whole structure of the product was collapsed and deformed, which was difficult to better maintain the porous gold structure. According to Figure 4(b) EDX image, the product had a significant Ag signal. The product featured a hollow structure, but with Ag uncleaned completely, which might be related to Au's involvement in Fe^{3+} reaction. With ammonium hydroxide as the etching agent, SEM and EDX images of the final product are shown in Figures 4(c) and 4(d). In the aerobic environment, ammonium hydroxide as a corrosive agent could react with Ag atoms to form $[Ag(NH^3)2]^+$, making an etching effect. However, this study found that the product obtained after reaction with $Ag_{66.9}-Au_{33.1}$ did not achieve a good etching effect. The reason might be related to the slow reaction, and there was still as significant Ag signal.

5.2. Special Etching Agent: Au^I. It is difficult for the conventional etching agent to have a stable structure, and Au in residual components is not enough to maintain the large-size porous structure and results in obvious collapse and deformation. Therefore, a new-type etching agent that could obtain porous structures while providing complete etching is urgently needed, which is also an important way to obtain porous Au. Based on this, Au^{III} was first adopted as the etching agent in this study for the purpose of stabilizing the product structure. However, the following chemical reactions occurred simultaneously during the experiment:

(a)   (b)   (c)
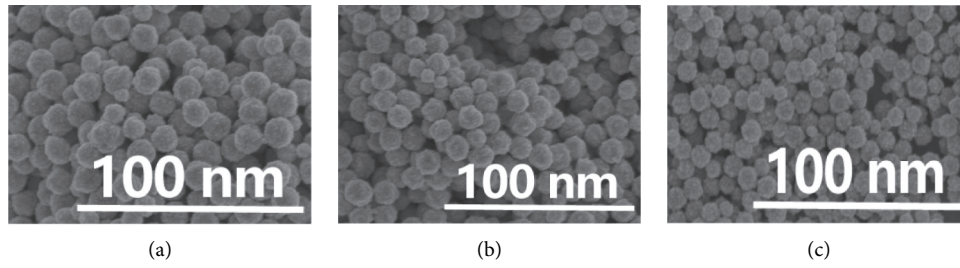
FIGURE 1: Low-power SEM images of product of Ag^+/Au^{III} at different molar ratios (a) 10 : 1; (b) 5 : 1; (c) 2 : 1.
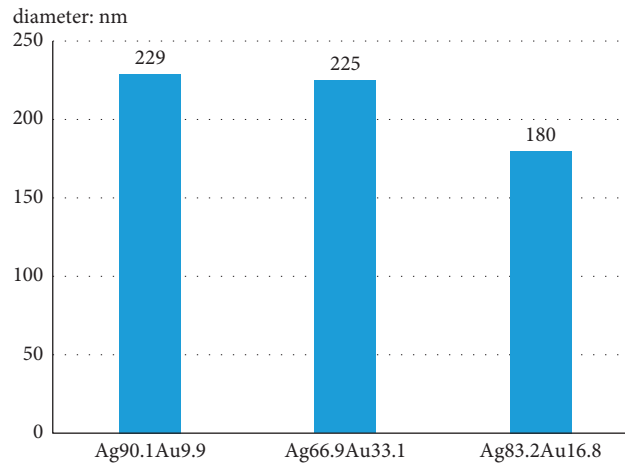
FIGURE 2: Average size of products of Ag^+/Au^{III} at different molar ratios.

(a)   (b)   (c)
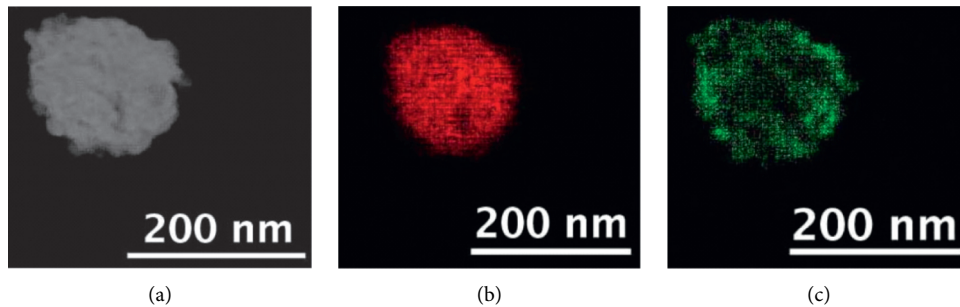
FIGURE 3: HADDF-STEM images and bimetallic element distraction mapping images of $Ag_{66.9}-Au_{33.1}$: (a) HADDF-STEM image; (b) Ag; (c) Au.

$$3Ag + Au^{III} = 3Ag^+ + Au, \qquad (1)$$

$$2Au + Au^{III} = 3Au^I, \qquad (2)$$

$$Ag + Au^I = Au^+ + Au. \qquad (3)$$
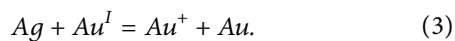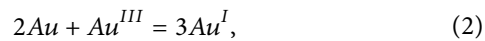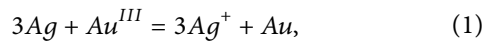
These reactions will inevitably lead to failure obtaining a good structure. Different oxidized states of Au have distinctive electrode potentials. Compared with Au^{III}, Au^I has a lower valence state but a higher oxidizability and could avoid reactions (1) and (2). Therefore, Au^I is more suitable than Au^{III} as the etching agent for preparing porous gold nanostructures.

After $Ag_{90.1}-Au_{9.9}$, $Ag_{83.2}-Au_{16.8}$, and $Ag_{66.9}-Au_{33.1}$ were etched with Au^I, the three porous gold nanomaterials were identified as sample 1, sample 2, and sample 3, respectively, as shown in SEM images in Figure 5. There were significant differences in morphology, quantity, and pore diameter of the porous materials with different bimetallic compositions.

After the average size of the previously mentioned three etched porous nanostructures was determined, it was found that the average particle sizes of sample 1 ($Ag_{90.1}-Au_{9.9}$), sample 2 ($Ag_{83.2}-Au_{16.8}$), and sample 3 ($Ag_{66.9}-Au_{33.1}$) were 500 nm, 400 nm, and 300 nm, respectively. This suggested that the materials obtained by Au^I etching had a larger size, which accorded with the effect of regrowth etching, as shown in Figure 6.

(a)   (b)   (c)   (d)
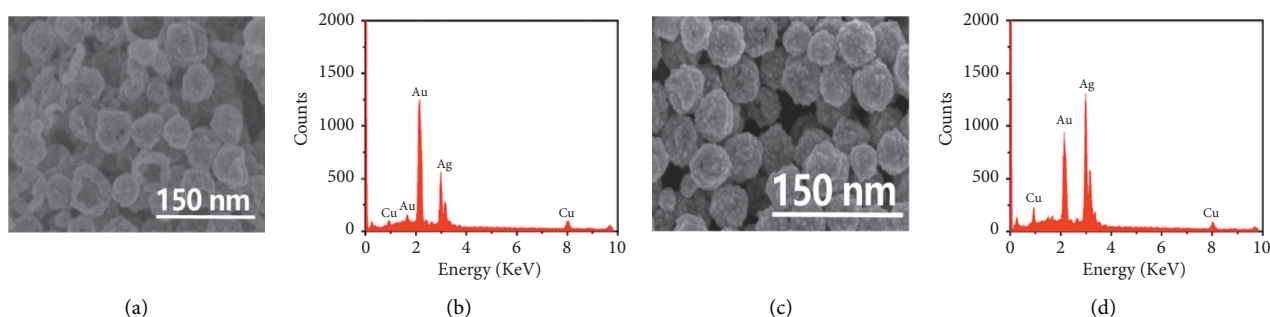
FIGURE 4: SEM and EDX images of product obtained with conventional etching agent: (a) SEM image; (b) EDX image; (c) SEM image; (d) EDX image.

(a)   (b)   (c)
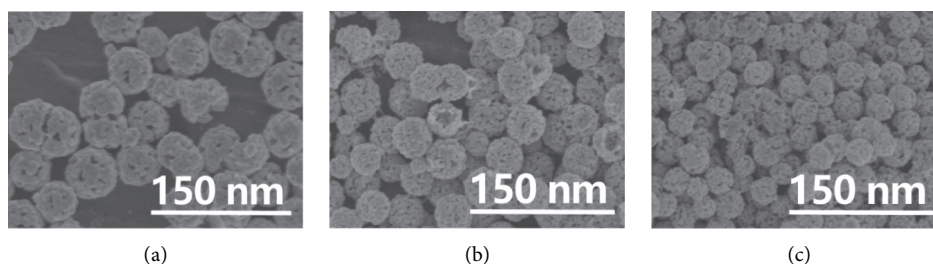
FIGURE 5: Porous nanostructures obtained by Au^I etching: (a) $Ag_{90.1}$–$Au_{9.9}$; (b) $Ag_{83.2}$–$Au_{16.8}$; (c) $Ag_{66.9}$–$Au_{33.1}$.

TEM images of the products of the three samples after etching showed they all had the single-particle porosity. SAED images of $Ag_{66.9}$–$Au_{33.1}$ showed the particle was polycrystalline. Precursor $Ag_{90.1}$–$Au_{9.9}$ contained the highest property of Ag. Among the new samples obtained after etching, there were about 6 and 50 nm diameter pores in a single particle. Among precursor $Ag_{83.2}$–$Au_{16.8}$ samples, there were about 22 and 16 nm diameter pores in a single particle. Among $Ag_{66.9}$–$Au_{33.1}$ samples with less Ag, there were about 35 and 11 nm diameter pores in a single particle. This indicated the different appearances of the final porous materials due to the difference in structural sites of Ag element in bimetallic components. Dark-field TEM images of porous materials obtained from $Ag_{66.9}$–$Au_{33.1}$ showed no Ag residue in porous gold nanomaterials, as shown in Figure 7.

The specific process of regrowth etching may be analyzed as follows. The replacement reaction between Ag atoms and Au^I occurred on the P surface. With the disappearance of Ag, Au grew on the bimetallic surface, and pores occurred on the surface. As the pores on the surface were diffused into the inner layer, their concentration increased, which led to the formation of a cavity. When Ag atoms and Au atoms in the inner layer were diffused to the surface layer, they reached a stable structure with the lowest energy, which improved the contact rate between Ag and Au^I in the reaction liquid. Therefore, the original bimetallic structure disappeared, and the porous gold nanostructure was obtained finally.

6. Catalytic Property of p-Nitrophenol

Metal-based nanomaterials as a catalyst could promote p-nitrophenol reduction at the room temperature to a certain extent. Therefore, a typical catalytic reduction was
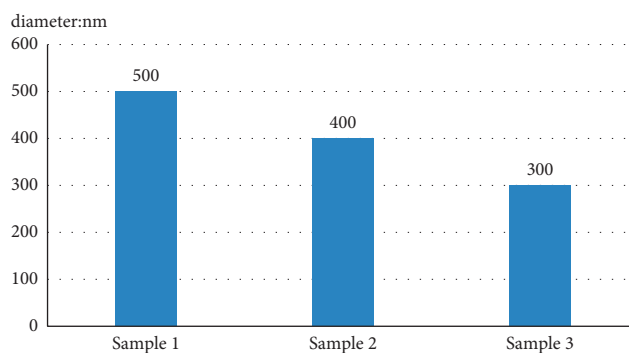
FIGURE 6: Average size of products obtained from three samples by Au^I etching.

also adopted in this study to verify the properties of the Au-based nanomaterials obtained. In general, p-nitrophenol will not be reduced without a catalyst, even if a large amount of sodium borohydride is adopted. Nitrophenyl nitrate ions were formed in the solution, and their characteristic main peak was at about 400 nm. However, after the effective catalyst was added, the main peak decreased, and the characteristic peak of p-nitrophenol was observed at about 292 nm.

6.1. Catalysis with p-Nitrophenol. With sample 3 as the catalyst and porous nanoreactor as the reaction site, the UV absorbance spectrum after catalytic reduction with p-nitrophenol is shown in Figure 8(a). The whole process of p-nitrophenol reduction and aminophenol generation was complete in the porous reactor. During the 4 min of complete reaction, the main peak in the UV spectrum decreased
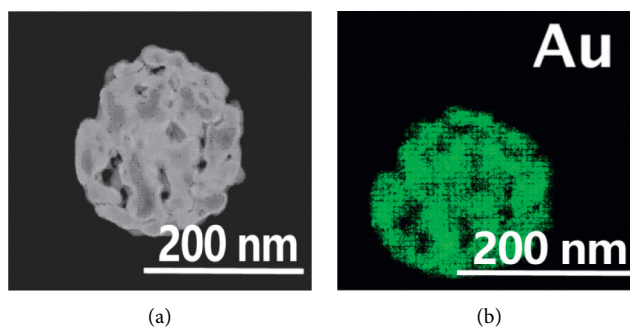
Figure 7: Dark-field TEM image of sample 3 and EDX mapping image of element Au: (a) TEM image; (b) EDX mapping image.
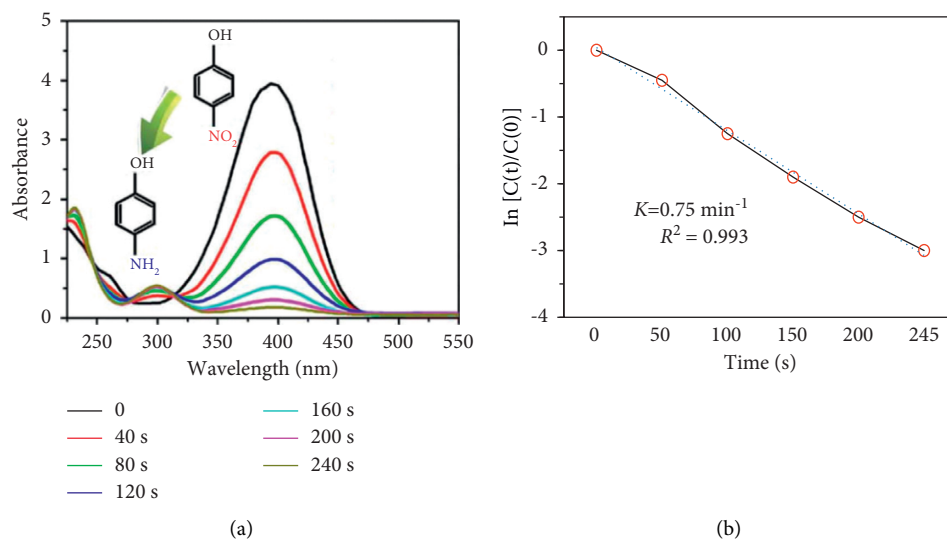
Figure 8: UV absorbance curves and catalytic time linear graph of sample 3 as catalyst: (a) UV absorbance curves; (b) relationship between $\ln[C(t)/C(0)]$ and time.

significantly, p-nitrophenols were all reduced, and the color of the solution became colorless and transparent. Figure 8(b) shows the kinetic process of sample 3. The results showed that $\ln[C(t)/C(0)]$ was positively correlated with time, which accorded with the first-order reaction.

6.2. Comparison of Catalytic Results. In order to understand the catalytic property of porous gold nanomaterials prepared in this study, nitrophenol catalytic reduction tests were conducted for Au particles, three bimetals, and the first two corresponding products, respectively. The results showed that, with the increase of Au content in the components, the bimetallic materials showed a more significant catalytic effect, with a significantly shorter time required. Among the porous samples, the large-pore-diameter sample 1 had a worse catalytic effect, whereas small-pore-diameter samples 2 and 3 had a better catalytic effect, as shown in Figure 9.

The catalytic time of Au was more than 2 h, while the catalytic times required by $Ag_{90.1}$–$Au_{9.9}$; $Ag_{83.2}$–$Au_{16.8}$; $Ag_{66.9}$–$Au_{33.1}$ were 31 min, 18 min, and 16 min, respectively. Therefore, the time required by porous materials was significantly shorter. Specifically, the times required by samples 1 and 2 were 10 min and 6 min, respectively. This suggested

that the properties of porous gold nanomaterials were related to the quantity and size of pores.

7. Discussion

Energy, materials, and information are important pillars of modern science and technology, among which material technology is the key to solve energy and environment problems [6]. Nanotechnology plays a very important role in such fields as medicine, optics, and catalysis. Gold and silver are the most common precious metals. New precious metal materials prepared by nanotechnology have special physical and chemical properties and become an important part of nanotechnology studies [7]. Some studies reported that hollow, porous, or framed precious metal nano-materials differed greatly from solid nanoparticles in terms of structure, with a larger effective contact area, lower overall density, and better liquid fluidity [8–10]. Therefore, in the actual synthesis process, these nanomaterials as the catalytic reaction reactor can effectively increase the con-tact area and involve gas and liquid more easily, so as to promote the reaction [11]. Due to their excellent properties, porous materials are widely used in various fields. In
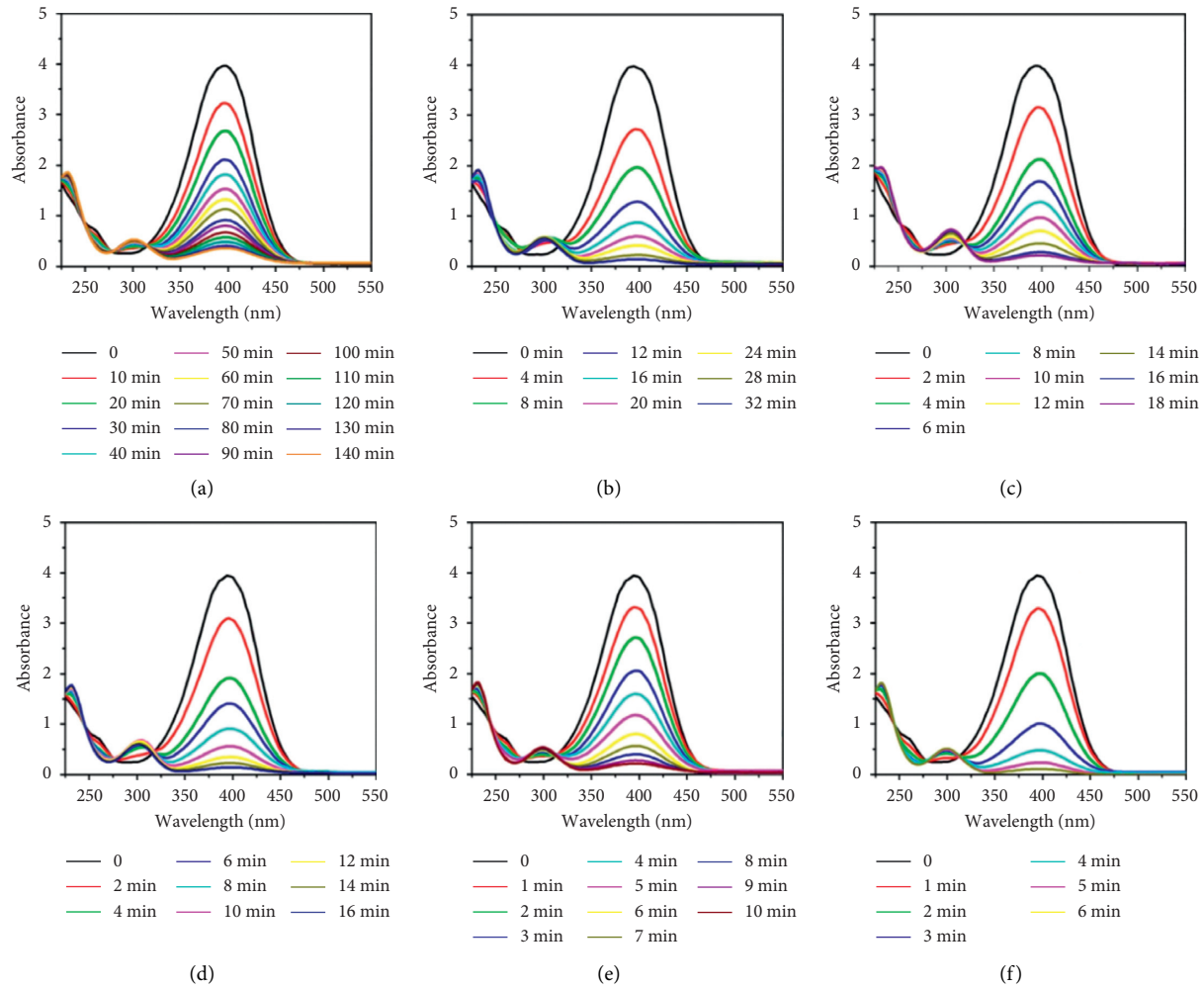
FIGURE 9: UV absorbance spectrum of catalytic reduction with different Au-based catalysts: (a) Au particle; (b) $Ag_{90.1}$–$Au_{9.9}$; (c) $Ag_{83.2}$–$Au_{16.8}$; (d) $Ag_{66.9}$–$Au_{33.1}$; (e) sample 1; (f) sample 2.

appropriate solutions, metal salt can be reduced to obtain monometal nanostructures. Accordingly, two different metals can be reduced to get bimetallic nanostructures. However, because of the differences between the two metals in chemical properties and reduction potential, it is difficult to control their reduction and nucleation processes simultaneously [12]. Coreduction synthesis, replacement synthesis, and thermal decomposition synthesis are the most commonly used methods for preparing bimetallic nanomaterials.

Etching bimetallic materials by replacement reaction is a widely used and effective approach to obtain monometallic porous nanostructures at present. During the whole process of operation, metal A with the reduction property is adopted as the template, and metal B ion with the oxidization property is adopted as the etching agent in general. While B grows towards the outer layer, A atom in the inner layer is also diffused outward. Finally, B deposits on the surface of A and forms a shell [13]. In this way, the alloy of hollow spheres is obtained. During this process, the etching agent not only adjusts the inner cavity but also modifies the outer shell [14]. According to the application advantages of replacement

reaction, during the specific process of operation, bimetallic materials can be etched to prepare large-size monometallic nanomaterials, such as Au nanotubes, Au nanocages, and Au/Pt. These etched precursors all have a frame-like structure [15]. In brief, hollow Ag/Au nanoshells are transformed into porous nanocages. In practice, it is difficult to prepare large-size spherical porous nanostructures (with a diameter of more than 100 nm). For instance, monometallic M template is generally adopted for Au nanomaterials, and the Au-M nanoshell structure is formed after displacement reaction. Then, residual metal A is cleaned by etching. However, it is difficult to obtain large-size spherical porous materials by this operation [16]. The challenges mainly exist in the following aspects. First, although the size increases after replacement reaction, it cannot be further increased. Second, the increase in the size of the selected etching templates causes the decrease in the composition etched materials and structural stability and the possibility of collapse. Third, the porous gold structures obtained by bimetallic etching are prone to have silver residues, and the reactants may cause blocking when passing through pores [17].

Based on this, the "regrowth etching" method was proposed in this study, with the aim to reduce collapse caused by structural instability. First, Ag-Au bimetallic materials were prepared through adjustment of the nucleation and growth rates of Ag and Au. Although all of the prepared $Ag_{90.1}$–$Au_{9.9}$, $Ag_{83.2}$–$Au_{16.8}$, and $Ag_{66.9}$–$Au_{33.1}$ bimetallic nanomaterials reacted completely, Ag was high in the precursor and occupied more sites. Then, Au^I was adopted as the etching agent to further trigger the replacement reaction with Ag, which not only obtained large-size porous gold nanomaterials with a better stability but also effectively avoided collapse and deformation. The catalytic reduction reaction with p-nitrophenol confirmed that hollow porous materials have a more advantageous catalytic activity. The enhanced diffusion effect of porous structure is mainly manifested as follows. First, the large-volume-fraction interface in the structure provides an important way for short-cycle diffusion. Second, the particle interfaces and cavities after the replacement reaction have high-density defects. Third, due to the driving force, the stress and deformation in the crystals enhance the diffusion effect. Fourth, pores in materials lead to capillary phenomenon, which is more significant in materials with small-diameter pores in general. Because porous nanomaterials are a reaction site, the fluid transfer process is mainly completed through the pores. Small-size pores are easy to be blocked by reactants or products, while a large number of pores can provide multiple channels to transfer these substances, so as to effectively reduce pore blocking. At present, it is generally believed that nanomaterials with a large number of 10 nm-diameter pores have a good catalytic effect and are excellent catalytic materials [18].

In conclusion, the regrowth etching method was adopted in this study to successfully prepare large-size porous gold nanomaterials with a good structural stability. The properties of porous gold nanomaterials were improved through adjustment of the size and quantity of pores to a certain degree. Applied as a catalytic reaction site, these materials have more outstanding properties than solid particles and are expected to play important roles in disease detection, catalysis, and biomedicine.

8. Conclusion

Ag–Au alloy was prepared at different molar ratios of Ag^+/Au^{III}, and the bimetallic nanomaterials obtained had similar Ag/Au ratios to the molar ratio at reaction. This suggested that the bimetallic nanomaterials reacted completely, with the maximum average size in $Ag_{90.1}$–$Au_{9.9}$ and the minimum average size in $Ag_{83.2}$–$Au_{16.8}$ and $Ag_{66.9}$–$Au_{33.1}$.

Due to the deficiency of conventional etching agents, the "regrowth etching" method was proposed in this study. Specifically, with AuI as the etching agent, the porous gold nanomaterials with the size of more than 300 nm were successfully prepared, achieving the regrowth etching effect and a good structural stability.

According to the analysis based on the catalytic reduction reaction with p-nitrophenol, the properties of the large-size porous gold nanomaterials were related to the quantity and size of pores.

Data Availability

The data used to support the findings of this study are included within the article.

Conflicts of Interest

The authors declare that they have no conflicts of interest to declare.

References

[1] Yu. Guan, *Study of Preparation and Catalysis of Titanium Dioxide Nanoribbon-Supported Bimetallic Catalyst and its Photocatalytic Property*, Shandong University, Shandong, 2013.

[2] F. Shaojie, D. Zhao, F. Xie, W. Xiufang, and Z. Jun, *Study of Synthesis and Structural Adjustment of Inorganic Nanomaterials and Their Functions*, Anhui Jianzhu University, Hefei, China, 2017.

[3] Qi Zhou, Z. Li, and B. Zheng, "Preparation of nanoporous bimetallic oxide NiCo2O4 and its electrochemical property," *Chinese Journal of Inorganic Chemistry*, vol. 34, no. 6, pp. 1103–1109, 2018.

[4] Y. Li, M. Zhang, X. Wang, and W. Li, "Advance in studies of preparation method of nanoporous metals and their mechanical properties," *Journal of Aeronautical Materials*, vol. 38, no. 05, pp. 10–23, 2018.

[5] G. Tao, Z. Cheng, D. Zhang, and F. Hang, "Preparation of CO-doped zinc oxide porous materials derived from bimetallic MOF and their gas-sensitive properties," *Journal of Functional Materials*, vol. 51, no. 9, pp. 9185–9192, 2020.

[6] X. Hu, Y. Yin, W. Liu et al., "Preparation of cobalt phosphide @ iron-zinc bimetallic phosphide multistage nano-composites and their electrocatalytic water decomposition properties," *Chinese Journal of Catalysis*, vol. 40, no. 7, pp. 1093–1104, 2019.

[7] M. Mceachran, D. Keogh, B. Pietrobon et al., "Ultrathin gold nanoframes through surfactant-free templating of faceted pentagonal silver nanoparticles," *Journal of the American Chemical Society*, vol. 133, no. 21, pp. 8066–8069, 2011.

[8] J. Li, *Construction of Transition Metal-Based Three-Dimensional Nanostructures and Their Electrochemical Properties*, Qingdao University of Science and Technology, Shandong, 2019.

[9] T. Zhang, *Preparation of Porous Precious Metal Alloy Nanomaterials and Their Optical/Electrocatalytic Properties*, Anhui: University of Science and Technology of China, Huainan, China, 2019.

[10] C. Tian, *Study of Synthesis of Nanoporous Metal/Graphene Composites and Their Electrochemical Properties*, China University of Mining and Technology, Beijing, China, 2019.

[11] W. Shaozhen, K. Wang, H. Long et al., "A highly efficient, clean-surface, porous platinum electrocatalyst and the inhibition effect of surfactants on catalytic activity," *Chemistry - A European Journal*, vol. 19, no. 1, p. 416, 2013.

[12] Qi Zhou, B. Zheng, Z. Li, W. Yafei, and F. Jiwei, "Dealloying preparation of nanoporous bimetallic oxide NiMoO4 and its electrochemical properties," *Chinese Journal of Inorganic Chemistry*, vol. 33, no. 8, pp. 1416–1422, 2017.

[13] H. Luo, C. Xu, H. Wu, and Z. Yun, "Preparation of silicon/carbon composites derived from organic frameworks of cobalt-iron bimetals and their electrochemical properties," *Sichuan Nonferrous Metals*, no. 2, pp. 48–51, 2020.

[14] S. Zheng, Z. Ma, H. Yuan, L. Jinping, and W. Xiaoguang, "Study of preparation of self-supported nanoporous Al-doped NiCu-S electrode and its electrolyzed water hydrogen evolution," *Journal of Taiyuan University of Technology*, vol. 52, no. 1, pp. 29–37, 2021.

[15] X. Tan, A. Tahini Hassan, and C. Smith Sean, "Conductive boron-doped graphene as an ideal material for electrocatalytically switchable and high-capacity hydrogen storage," *ACS applied materials & interfaces*, vol. 48, 2016.

[16] C. Sundaram, L. Yao, L. Deng et al., "Recent advances in metal sulfides: from controlled fabrication to electrocatalytic, photocatalytic and photoelectrochemical water splitting and beyond," *Chemical Society Reviews*, vol. 48, no. 15, pp. 4178–4280, 2019.

[17] Z. Yan, D. Wu, and Z. Wang, "Advance in studies of preparation of nanoscale zero-valent iron and its application," *Applied Chemical Industry*, vol. 68, no. 03, Article ID 012052, 2021.

[18] Y. X. Bao, B. W. Hao, X. Wang, and X. W. Lou, "One-pot synthesis of cubic PtCu3 nanocages with enhanced electrocatalytic activity for the methanol oxidation reaction," *Journal of the American Chemical Society*, vol. 134, no. 34, pp. 13934–13937, 2012.

Research Article

Analysis of Foundation Pit Design of Metro Station in Complex Environment

Yunchao Tao (ID)

Urban Rail Transit Engineering Company Limited of China Railway 15th Bureau, Luoyang 47100, China

Correspondence should be addressed to Yunchao Tao; taoyunchaocr15g@163.com

The complex engineering geological conditions and the surrounding environmental conditions of the existing subway lines and adjacent buildings have significantly deepened the difficulty of metro station foundation pit design and construction. Based on the foundation pit project of Luboyuan Station of Nanjing Metro Line 9, this study chooses a reasonable foundation pit support design scheme to carry out related research by analyzing the site geological environmental conditions. Through the analysis and evaluation of the engineering geological conditions of the engineering site, the engineering geological problems that may occur in the process of construction are given. According to the lithologic characteristics of the site strata, the hydrogeological conditions, and the features of the underground engineering structure, the design of the foundation pit supporting system is optimized and analyzed. The results show that making full use of the geological features of strata and adopting effective support methods can ensure the safety of foundation pit construction, reduce the cost of engineering description, and shorten the construction period, which can be used as a reference for similar projects and construction.

1. Introduction

With the high development of urbanization, the high concentration of population, and the rapid growth of motor vehicle ownership, the phenomenon of urban traffic congestion is becoming more and more serious. At present, traffic carrying capacity is a binding condition for urban development [1–4]. Rail transit has the advantages of convenience, high speed, and enormous power and has become an essential part of the urban modern, high-quality, comprehensive three-dimensional traffic network. It can greatly improve the problem of urban traffic congestion [5–7]. At the same time, the new development concept under the traffic-guided development (TOD, transit-oriented development) mode, rail transit led the urban development pattern, has undergone new changes, not only to reshape the urban space form, but also to change the urban planning and market space [8]. Therefore, the transportation department has been promoting the high-speed and high-quality development of urban rail transit.

By 2020, 10 subway lines have been opened in Nanjing, including Line 1 to Line 4, Line 10, Line S1, Line S3, and Line S7 to Line S9, forming a subway network covering 11 municipal districts in Nanjing [9, 10]. As shown in Figure 1, the operating mileage of 378 km ranks sixth in the country, and Nanjing has become the first city in China to open subways in all districts and counties, sharing 53.82% of the city's public transport. However, because Nanjing straddles the Yangtze River, three bedrock uplifts, and two sag basins in the central city, the Qinhuai River runs through from south to north [11]. According to the division of main engineering geological zones and distinct soil layers in the Nanjing area, Hongzhong Xu, and others, the engineering geological conditions are mainly classified as the floodplain of the Yangtze River (distributed primarily on the banded area with a certain width on both sides of the Yangtze River), the ancient channel of the Qinhuai River, and multistage river terraces, and the soil layer parameters are pretty different from each other [12]. Zheng et al. [13] believe that there are three types of geomorphological units
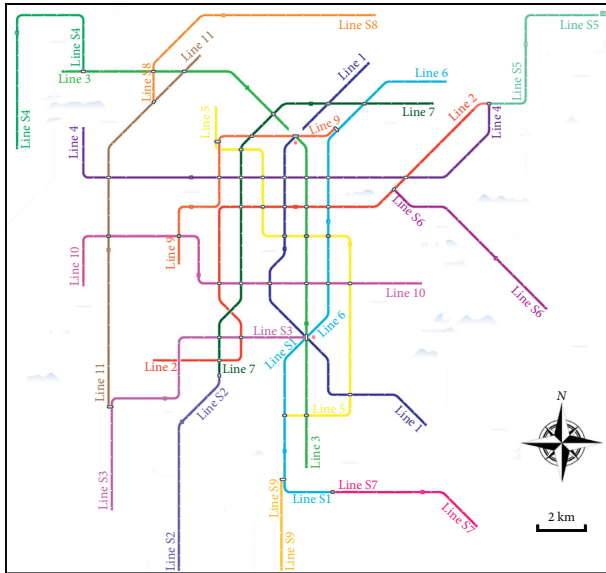
Figure 1: Planning map of Nanjing Metro Line from 2019 to 2023.

in the Nanjing area: tectonic denudation low mountain and hilly area, inter-hillock depression area, and river valley plain area, with various engineering geological and hydrogeological conditions, and the subway tunnel is a linear project passing through different geomorphological units. The engineering geological and hydrogeological properties of each team are very different. Nanjing's complex engineering geological conditions and the surrounding environmental conditions of existing subway lines and adjacent buildings have considerably deepened the difficulty of design and construction. At present, the new mileage of the Nanjing subway is slower than that of other provincial capitals.

The shallow layer in the Nanjing area mostly belongs to the water-rich soft soil foundation, and the shield construction is usually used to dig the subway tunnel. The open excavation method is used to carry out the station construction [14–17]. The open-cut subway station needs to build the foundation pit retaining structure first and then excavate the bottomless foundation pit [18–20]. However, the subway station is generally located in the bustling area of the city, with a concentrated population, dense buildings, and many underground pipelines [21, 22]. The excavation of the bottomless foundation pit of the station can easily lead to the displacement of the surrounding soil and land subsidence. The support design and construction of the foundation pit should be considered to bring great risks to the surrounding environment [23, 24]. In recent years, in the construction of deep foundation pit engineering in the Jiangsu and Zhejiang areas, major engineering accidents have been caused due to complex site engineering geological conditions, complex surrounding environmental conditions, and improper selection of supporting structures, resulting in a large number of economic losses. A diaphragm wall is widely used as the retaining structure of a deep foundation pit because of its slight vibration, high stiffness, and good anti-seepage.

Of the 760 subway stations built along the southeast coast in the past 20 years, 650 have adopted diaphragm walls as foundation pit retaining structures. Taking the deep foundation pits of 48 subway stations collected in Nanjing, for example, only 21 foundation pits are protected by underground diaphragm walls, bored piles cover another 26, and one project uses SMW piles [25, 26]. Most of the projects that select diaphragm walls as bottomless foundation pit retaining structures are located in the floodplain of the Yangtze River and the ancient channel of the Qinhuai River. A bored cast-in-place pile is often used in the retaining design of a deep foundation pit under the condition of a river terrace. Therefore, although some technical standards and specifications can guide local subway construction, the construction experience of similar projects still needs to be used as a reference in the actual design.

However, the difference in physical and mechanical properties of regional soil layer cannot be blindly copied. It may cause unnecessary waste to blindly select the support mode without sufficient consideration, or unilaterally improve the safety factor of support. It is imperative to make rational use of the geological structure characteristics of rock and soil and the surrounding environmental conditions to reduce the project cost-effectively, solve the technical problems of foundation pit construction, and speed up the construction speed and other factors [27, 28].

In this study, taking the foundation pit design of Luboyuan Station in the fourth project of Nanjing Metro Line 9 as an example, through the analysis and evaluation of the engineering geological conditions of the project site, this study gives the engineering geological problems that may occur in the process of construction. According to the onsite lithologic characteristics of strata, the hydrogeological conditions, and the structural elements of underground engineering, the design of the foundation pit supporting structure is optimized and analyzed.

2. General Situation of the Project

2.1. Project Overview. The first phase of Line 9 is a local line in the northwest direction of the network, starting from Danxia Road Station in the north and Binjiang Park Station in the south, passing through three administrative districts: Xuanwu District, Gulou District, and Jianyu District. The total length of the line is 19.68 km, all underground lines, with a total of 16 stations, including 9 transfer stations, with an average station spacing of 1.26 km (see Figure 2).

The Luboyuan Station of this project is an underground three-story island platform station with a double-column three-span box frame structure. The open-cut method is adopted for construction. The station hall is on the first underground floor, the equipment is on the second underground floor, and the platform is on the third underground floor (see Figure 3).

2.2. Surrounding Environment. The main underground pipelines affecting the construction of the main enclosure structure of Luboyuan Station are as follows: buried 4.6 m
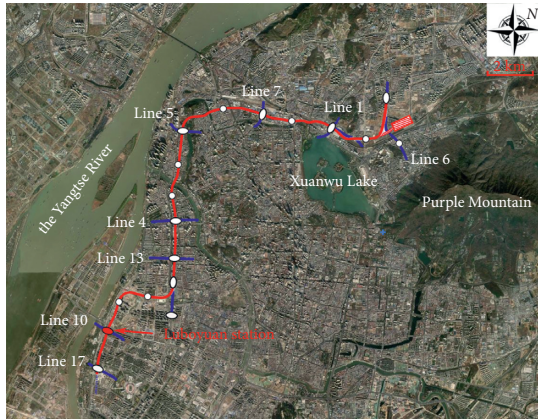
Figure 2: General plan of the first-phase project of Nanjing Metro Line 9.
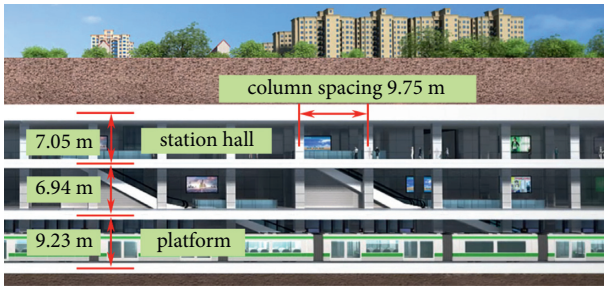
Figure 3: Luboyuan Station profile based on BIM technology.

220 kV power pipe, buried deep 1.2 m 380 V power pipe, buried deep 2.85 m DN800 rain pipe, and buried 4.6 m communication optical cable. The main underground pipelines affecting the construction of the auxiliary enclosure structure of Luboyuan Station are as follows: buried 4.6 m 220 kV power pipe, buried 2.85 m DN800 rain pipe, buried 2.85 m DN400 rain pipe, and buried 1.2 m DN1400 water supply pipe. Ground green water pipes, street lamp power lines, signal light communication lines, and other small scattered pipelines in the site shall be abolished on the spot.

The northwest side of the station is Nanjing China Greening Expo Park, the southwest side is Yuanjiang Fishing Port, and the southeast and northeast sides are green open spaces (see Figure 4). The adjacent buildings also include the Luboyuan Station of Line 10 (underground second-floor station, T-type transfer) and the underground comprehensive pipe corridor of the Yangtze River Rapid Avenue Reconstruction Project (underground first floor, about 7 m from the main body of the station).

2.3. Geology and Hydrology. The landform of Luboyuan Station belongs to the geomorphological unit of Ningzhen Yangqiu hills and plain area and river valley plain. The site is distributed on the south side of the Yangtze River, and the terrain is flat and open. The station is arranged along the Yangtze River Avenue, which is about 82 m wide. The ground along the line is relatively flat, and the present
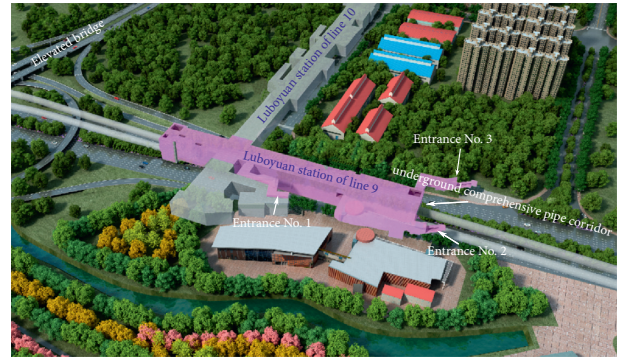
Figure 4: Surroundings of the station.

ground elevation is between 5.1 m and 5.7 m. The near surface mainly consists of Holocene (Q4) artificial filling, silty clay, and muddy silty clay (mixed with silt and silt). The groundwater in this site is mainly pore phreatic water, and due to the great difference in permeability between the weak clayey soil layer in the upper and middle and lower parts of the site and the sandy soil and gravel-bearing silty clay at the bottom, the groundwater in sandy soil layer and gravel-bearing silty clay has micro-pressure-bearing property. In addition, there is a small amount of bedrock fissure water in the bedrock weathering zone.

3. Analysis of Engineering Geological Conditions

3.1. Division of Engineering Geological Strata. To find out in detail the regional geological, hydrogeological, and engineering geological conditions of the site area, the suitability of foundation types and construction methods is analyzed and evaluated, the possible geotechnical problems are predicted, and a large number of field and laboratory tests are carried out. According to the geological survey and survey data combined with the geomorphological unit, the geomorphological type of this site belongs to the geomorphology of the Yangtze River floodplain, and the engineering geological division belongs to the Yangtze River floodplain engineering geological area (subarea). The artificial filling is widely distributed on the surface of the field area, followed by clay, silty clay, muddy silty clay (mixed with silt and silty sand), silty clay (mixed with silt and silty sand), silty sand, medium-coarse sand, and gravel. The underlying bedrock is the sandy mudstone of the Cretaceous Pukou Formation. The rock surface does not fluctuate much, and the burial depth is about 50 m to 53 m. The rock and soil in the site are divided into 16 layers by engineering geological. This layered scheme has many quantities and complex contents, which is not conducive to the use of designers. In this study, according to the age, genesis, state characteristics, and buried depth of rock and soil layer, the strata in the excavation depth of the foundation pit are divided into 6 layers, as shown in Figure 5 and Table 1.

The exploration holes in this survey are mainly arranged in a "Z" shape crossing 3~5 m outside the outline of the main structure, and the interval of the exploration holes is about

plain filling soil   silty sand (medium dense)
miscellaneous soil   silty sand (dense)
muddy silty clay   silty clay with silty sand
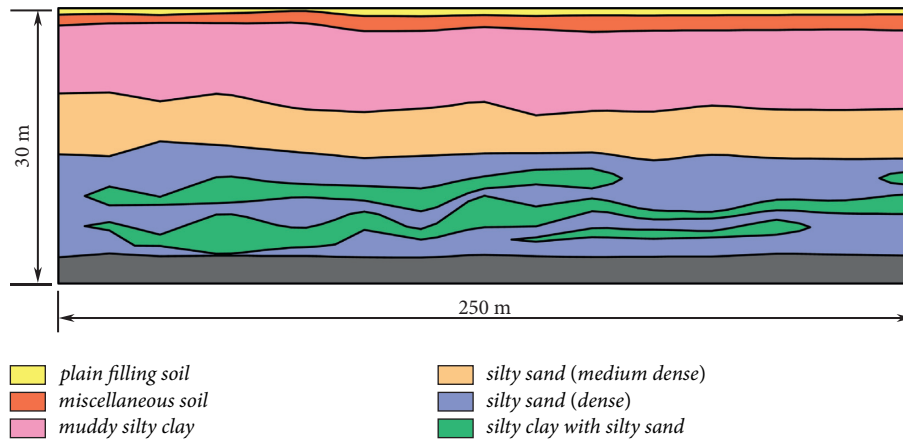
FIGURE 5: Longitudinal geological profile of Luboyuan Station.

TABLE 1: A list of stratigraphic distribution in Luboyuan Station.

The cause of the times	Stratum name	Feature	Thickness (m)
Q$_4^{ml}$	Miscellaneous soil	Miscellaneous colors, mainly grayish-yellow and gray; loose to slightly dense; mainly composed of construction waste, containing a large number of bricks, stones, concrete blocks, and a small amount of silty clay; the surface is partially concrete floor	1.00~4.10
	Plain filling soil	Grayish-yellow, grayish-brown; loose to slightly dense; mainly composed of clayey soil, see shells and screw fragments, mixed lime, and a small amount of macadam	0.60~2.20
Q$_4^{al+l}$	Muddy silty clay	Gray, grayish-brown; flow plastic; soil quality is uneven, with horizontal bedding, sandwiched with silt and a thin layer of silty sand, showing thousands of layers of cake; the middle and lower part of the sand content is gradually higher, with high pressure, occasionally see shell fragments and rotten plants	0.80~22.40
	Silty sand (medium dense)	Gray, bluish-gray; medium dense; poor gradation; mineral composition is mainly quartz, feldspar, see mica debris, local sandwiched with a thin layer of silty clay	1.80~15.00
	Silty sand (dense)	Gray, bluish-gray; dense; poor gradation; mineral composition is mainly quartz, feldspar, see mica debris, local sandwiched with a thin layer of silty clay	1.30~17.40
	Silty clay with silty sand	Grayish brown; soft plastic; soil quality is uneven, with horizontal bedding; the thickness of the single layer is about 5 mm to 20 m, the thickness of the single layer is about 2~5 mm silt and silty sand, and the thickness ratio is about 4:1	0.90~3.1

20 m. The exploration holes on the inner side of the station structure are added, with the hole spacing not greater than 24 m. A total of 50 exploration holes are arranged, including 16 control holes, 34 general holes, and 11 test holes.

The physical and mechanical properties of the rock and soil mass of the site are shown in Figure 6 and Table 2. It can be seen from the table that the upper soil has low strength, general compressibility, pore ratio and permeability, poor uniformity, and poor engineering geological performance, and belongs to aquitard. It is a weakly permeable layer. The central soil has low strength, high compressibility, extremely poor engineering geological performance, and uneven permeability. The permeability in the horizontal direction is significantly greater than that in the vertical direction, belonging to the weak permeable layer. The lower part has general strength, low compressibility, and general engineering geological performance and belongs to the medium permeable layer. The bottom soil has low strength, medium and high compressibility, and poor engineering geological

performance. Due to the inclusion of a large amount of silt, the permeability in the horizontal direction is obviously greater than that in the vertical direction, which is a weakly permeable layer.

3.2. Evaluation of Engineering Stability and Main Problems. The depth of the foundation pit of the main body of the station is about 26.20 m, the depth of the foundation pit of the ancillary structure (entrance, air shaft, etc.) is about 12.10 m, and the buried depth is large; there are no buildings in the upper part, and the groundwater level is high. The main basement of the station is located in the lower soil, and the engineering geological performance of this layer is general; the substrates of ancillary structures are all located in the middle soil, muddy silty clay, and silty sand, and this layer is a soft soil layer, which is easy to produce an uneven settlement, so the comprehensive evaluation of the stability of the foundation is insufficient.

FIGURE 6: Borehole samples.

TABLE 2: Physical and mechanical property index of stratum soil in Luboyuan Station.

Stratum name	Water content (%)	Density (g/cm³)	Void ratio	Liquidity index	Compression modulus (MPa)	Cohesion (kPa)	Internal friction angle (°)	Permeability coefficient (cm/s)
Miscellaneous soil	31.9	1.93	0.867	0.54	5.84	—	—	—
Plain filling soil	31.9	1.91	0.892	0.59	4.18	—	—	0.14×10^{-6}
Muddy silty clay (with microscale sand)	39.2	1.80	1.105	1.22	3.36	14.4	15.9	0.87×10^{-6}
Silty sand	23.2	1.94	0.703	—	13.18	2.9	31.4	1.76×10^{-3}
Silty sand	26.9	1.88	0.810	—	11.11	2.8	31.0	1.30×10^{-3}
Silty clay with silty sand	32.0	1.83	0.962	0.96	3.94	17.2	20.4	1.38×10^{-6}

Considering that the foundation pit of the station is close to the buildings under construction and municipal roads, there are many underground pipelines, and the surrounding environment is more complex. In the excavation depth, the soil is extremely loose, and the soil structure and self-stability are poor; it is easy to be disturbed and collapse, and lateral displacement deformation occurs. The main problems of foundation pit construction are slope instability, pit bottom uplift, piping, quicksand, and surrounding buildings, roads, underground pipelines, and facilities. Combined with the geological conditions, the hydrological conditions, and the excavation depth of foundation pit and surrounding environment, the main retaining structure of the project adopts diaphragm wall + internal support, the maintenance structure of ancillary structure adopts soil mixing wall (SMW) pile + internal support, and the internal clearance can be supported by concrete and steel. The support system should not only meet the requirements of bearing capacity but also meet the requirements of deformation.

4. Foundation Pit Engineering Design

4.1. Underground Diaphragm Wall Design. The original ground elevation of the station is 5.18 m to 5.78 m, the enclosure structure is 1200 mm thick underground diaphragm wall, the inner and outer sides of the diaphragm wall are reinforced by Φ850@600 triaxial mixing piles (Figure 7), and the reinforcement depth is 20 m. Strongly weathered sandy mudstone (waterproof layer) is inserted into the bottom of the diaphragm wall to form a closed foundation pit to cut off underground diving and micro-confined water supply. The pipe well is used to drain in the hole, the groundwater level is lowered to 1 m below the excavation surface of the foundation pit, and observation wells are arranged outside the pit, which can be used as recharge wells if necessary. The foundation pit supporting the structure of Luboyuan Station adopts 1200 mm thick diaphragm wall, a total of 84 pieces, and H-shaped steel joints; the average length of the wall is 54 m, and the toe of the wall is located in the strongly weathered sandy mudstone layer. C35 underwater concrete is adopted for underground diaphragm wall,
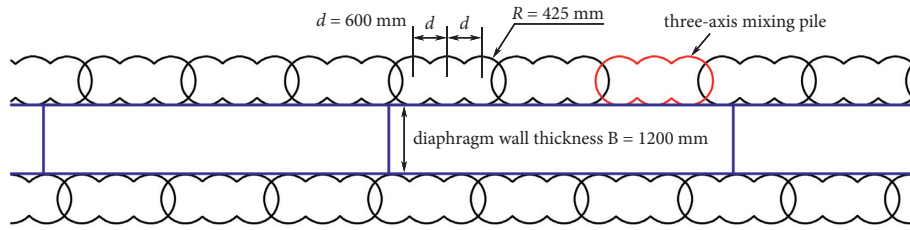
FIGURE 7: Schematic diagram of groove wall reinforcement.

with the compressive strength of 16.7 MPa and an elastic modulus of 31500 MPa, and the concrete impermeability grade is not less than P6.

4.2. Support System Design. The standard section of the central foundation pit is provided with seven braces along with the depth of the foundation pit. The first and fifth are reinforced concrete braces, the second, third, and fourth are steel braces of Φ609, and the sixth and seventh are steel braces of Φ800. The support arrangement of the east-west end well is the same as the standard section except that the distance between the vertical layouts of the support is different. The horizontal spacing of the first concrete support is about 9 m, and a closed reinforced concrete ring beam is arranged at the top of the ground diaphragm wall, and the concrete ring beam is used as the girder of the first support and the anti-floating top beam of the main structure at the same time. The horizontal spacing of the second, third, fourth, fifth, sixth, and seventh supports is 3 m. The steel plate at the end of the support is embedded in the ground diaphragm wall, and the steel support acts directly on the ground wall without setting a steel girder. There is a row of 460 mm × 460 mm temporary lattice columns in the middle, and the lattice foundation adopts "850 bored cast-in-place piles." The ancillary structure of the station is an underground single-story structure, and the excavation depth of the foundation pit is 9.5 m to 9.8 m. The enclosure structure adopts Φ850@600SMW construction method pile + internal support system (2 vertical braces, the first is a concrete brace and the second is steel bracing), and Φ700@500 biaxial mixing piles reinforce the bottom of the pit. The reinforced concrete inner support can give full play to the characteristics of high compressive bearing capacity, small deformation, and significant stiffness of the substantial material, which plays an important role in reducing the horizontal displacement of the enclosure and ensuring the overall stability of the enclosure, and reduces the cost of technical construction measures at the same time, as shown in Figure 8. C35 concrete is adopted for reinforced concrete inner support, with compressive strength of 11.9 MPa and elastic modulus of 28000 MPa.

4.3. Soil Excavation Design. The primary foundation pit of Luboyuan Station is divided into two small foundation pits due to the transfer of Line 10. The 160 m small foundation pit at the south end uses step excavation to carry out earthwork (see Figure 9). The excavation direction is carried
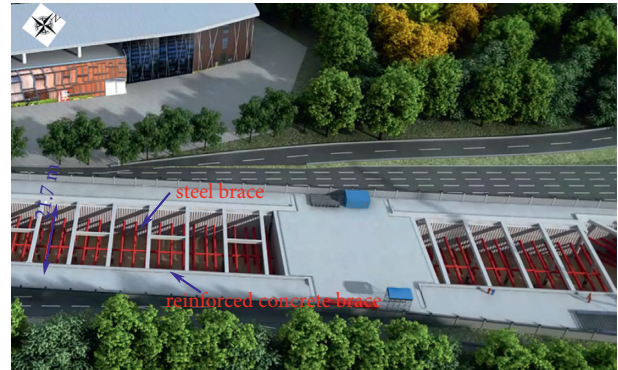
FIGURE 8: BIM schematic diagram of support system.

out from south to north (to ensure the shield receiving site). Finally, the remaining earthwork collection, vertical transportation, centralized accumulation, and outward transportation are carried out near the transfer node. The 55 m small foundation pit at the north end is carried out earthwork by vertical excavation; according to the working condition of the enclosure, the site in the northwest corner of the foundation pit is relatively spacious, and the vertical transportation operation point and temporary Earth accumulation area can be set up; the Earth is transported vertically by clam grab or car hoist, and the excavator in the foundation pit cooperates to collect the earthwork to the northwest corner; the distance between steel supports is optimized, and the hoisting shaft of excavator is set up.

4.4. Main Technical Difficulties and Measures. The construction of foundation pit excavation, dewatering, and structure will cause a disturbance, uneven settlement, and noise pollution and hinder the regular operation of the existing line, and the requirements of production management and control are high because of the transfer between the Luboyuan Station and the current Line 10; foundation pit excavation, dewatering, structure, and other construction will affect the existing line. When the underground diaphragm wall passes through the silt and silty sand layer, it is straightforward to cause defects such as collapse, mud entrainment, and hole, and it is difficult to form a groove; it is straightforward to cause defects such as limit invasion, displacement, and forking, and it is challenging to control verticality; it is easy to cause defects such as joint winding and leakage, and common handling is complex. Located in the floodplain stratum of the Yangtze River, it is not easy to control the effect of dewatering. Too heavy
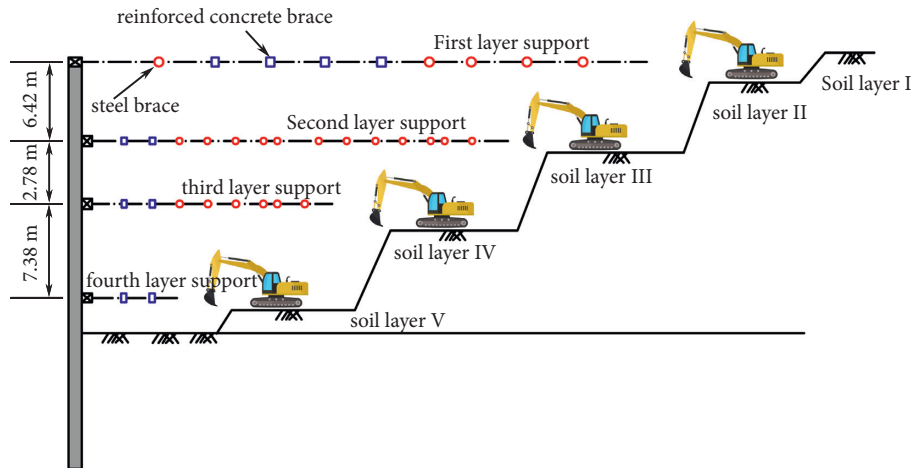
Figure 9: Profile of earthwork excavation.

precipitation is easy to cause land subsidence, settlement, and cracking of surrounding structures, too easy-to-cause foundation pit water level cannot go down, and excavation is difficult.

To ensure the safety of the existing line, the quality control of the joints of the diaphragm wall, and the effect of foundation pit excavation and dewatering, it has been worked out that if the necessary joint treatment of the enclosure structure is done well, the slotting machine is used to chisel off part of the concrete of the old diaphragm wall to ensure the integrity of the concrete structure. In the process of grooving construction of the underground wall, we should focus on controlling the verticality of the grooving and strengthening the training of the technical level of the grooving driver to ensure that the verticality of each underground wall meets the requirements of 0.3% of the code. After each underground continuous wallis grooved, the perpendicularity must be detected by ultrasonic detector. The construction of the lower groove wall from the verticality ultrasonic testing data is adjusted timely; the monitoring and analysis of the water level and water quantity in the dewatering operation are strengthened, the problems found in time are dealt timely, and the number of pumping wells and pumping flow, and dewatering as needed are adjusted, to ensure the safety of foundation pit and environment and other detailed construction plan measures.

5. Results and Analysis

The foundation pit design scheme proposed in this study is used for construction. At the same time, the wall settlement of underground diaphragm wall, wall deformation of diaphragm wall, reinforcement internal force of diaphragm wall, surface settlement around the station, and axial force of steel support are monitored. The monitoring data are processed and analyzed, and the results are summarized as follows:

(1) The maximum settlement rate of diaphragm wall is 0.02 mm/d, the maximum monthly settlement is 0.65 mm, and the maximum cumulative settlement is 9.25 mm.

(2) The inclination of the diaphragm wall of the foundation pit is monitored. The maximum monthly inclination value is 1.5 mm, and the cumulative maximum deviation is 8.6 mm (the warning value is 25 mm).

(3) The reinforcement internal force of the diaphragm wall is monitored. The maximum stress of the reinforcement is 15.7 kN, which is located 18.6 m below the top surface of the diaphragm wall.

(4) The surface settlement around the station is monitored. The maximum monthly settlement is 1.3 mm, and the maximum cumulative settlement is 9.1 mm.

(5) The maximum axial force of steel brace is 1564 kN, and the axial force of single steel pipe brace does not exceed its ultimate stability bearing capacity.

According to the above analysis, based on the foundation pit deformation control standard in Nanjing, the results show that the bearing capacity and deformation of the supporting structure are within the allowable range, so the support scheme is feasible for the project.

6. Conclusions

Taking the foundation pit design of Luboyuan Station in the fourth project of Nanjing Metro Line 9 as an example, through the analysis and evaluation of the engineering geological conditions of the project site, this study gives the engineering geological problems that may occur in the process of construction. According to the on-site lithologic characteristics of strata, the hydrogeological conditions, and the structural elements of underground engineering, the design of the foundation pit supporting structure is optimized and analyzed. The conclusions of the study are as follows:

(1) According to the characteristics of large groundwater level, the poor distribution of soil particles, easy-to-occur geological disasters such as piping and quicksand, and the highly complex underground structure, the excavation method of the four-layer

basin is adopted. This construction method speeds up the construction cycle of the foundation pit and solves the great difficulties brought by the structure to the foundation pit support.

(2) Because the foundation pit's excavation depth is the largest, involving silt layer and fine silt layer, the confined water head is high, and soil's lateral pressure is high. Therefore, the combined supporting structure strengthened by underground diaphragm wall + internal support + triaxial mixing pile floor can effectively control the lateral deformation of soil and groundwater infiltration.

(3) The use of this scheme successfully realized the safe and rapid construction of deep foundation pit projects, avoided large-scale disturbances of the surrounding water and soil, greatly saved energy consumption such as fuel and electricity, and played an important role in protecting the surrounding environment.

Data Availability

The data used to support the findings of this study are available from the corresponding author upon request.

Conflicts of Interest

The authors declare that there are no conflicts of interest regarding the publication of this study.

References

[1] H. Nadrian, H. Mahmoodi, M. H. Taghdisi et al., "Public health impacts of urban traffic jam in sanandaj, Iran: a case study with mixed-method design," *Journal of Transport & Health*, vol. 19, Article ID 100923, 2020.

[2] M. F. Geronimo, E. G. H. Martinez, E. D. F. Vazquez, J. J. F. Godoy, and G. F. Anaya, "A multiagent systems with Petri Net approach for simulation of urban traffic networks," *Computers, Environment and Urban Systems*, vol. 89, Article ID 101662, 2021.

[3] M. Grote, B. Waterson, and F. Rudolph, "The impact of strategic transport policies on future urban traffic management systems," *Transport Policy*, vol. 110, pp. 402–414, 2021.

[4] Y. X. Wu, H. M. Lyu, S. L. Shen, and A. Zhou, "A three-dimensional fluid-solid coupled numerical modeling of the barrier leakage below the excavation surface due to dewatering," *Hydrogeology Journal*, vol. 28, pp. 1449–1463, 2020.

[5] L. Tian, H. Zhang, and J. Wu, "Data preprocessing based on wavelet and its application in settlement monitoring for urban subway," in *Proceedings of the 2010 International Conference on Mechanic Automation and Control Engineering*, pp. 4892–4895, Wuhan, China, June 2010.

[6] H. Z. Xu, W. S. Cui, and W. J. Hu, "Deformation behavior of deep excavations of Nanjing subway station in different engineering geological conditions," *Journal of Disaster Prevention and Mitigation Engineering*, vol. 38, no. 4, pp. 599–607, 2018.

[7] P. Mao, J. Li, L. Xiong et al., "Characterization of urban subway microenvironment exposure - a case of Nanjing in

China," *International Journal of Environmental Research and Public Health*, vol. 16, no. 4, p. 625, 2019.

[8] P. Zhao, X. Z. Li, J. J. Liu, D. Zhang, and J. Li, "Monitoring and analysis of the subway tunnel wall temperature and surrounding rock/soil heat absorption ratio," *Building and Environment*, vol. 194, Article ID 107657, 2021.

[9] Z. P. Li, M. K. Li, and Q. H. Huang, "Study of construction technique for the Nanjing subway station under the Nanjing railway station," *Chinese Journal of Rock Mechanics and Engineering*, vol. 24, pp. 1061–1066, 2005, in Chinese.

[10] H. Xu, P. Sun, and W. Cui, "MSD synthetic system stiffness and deformation prediction of support structure for deep excavation in Nanjing subway," *Journal of China University of Mining and Technology*, vol. 47, pp. 907–912, 2018.

[11] W. Xu, "Analysis the in and out of the hole region's soil reinforcement technology of the Nanjing subway shield," *Open Journal of Transportation Technologies*, vol. 2, no. 2, pp. 108–116, 2013.

[12] K. H. Lu and X. Y. Gu, "Space-time evolution of subway vulnerability based on hypergraph space," *Mathematical Problems in Engineering, Hindawi*, vol. 2020, Article ID 2045838, 10 pages, 2020.

[13] J. Zheng, C. G. She, C. H. Yan, and B. Zhang, "Engineering geological mechanism on deformation of nanjing metro tunnel in operating," *Journal of Engineering Geology*, vol. 25, no. 1, pp. 199–208, 2017, in Chinese.

[14] Y. X. Wu, S. L. Shen, H. M. Lyu, and A. Zhou, "Analyses of leakage effect of waterproof curtain during excavation dewatering," *Journal of Hydrology*, vol. 583, Article ID 124582, 2020.

[15] Y. X. Wu, H. M. Lyu, J. Han, and S.-L. Shen, "Dewatering–induced building settlement around a deep excavation in soft deposit in Tianjin, China," *Journal of Geotechnical and Geoenvironmental Engineering*, vol. 145, no. 5, Article ID 05019003, 2019.

[16] K. Elbaz, S. L. Shen, Y. Tan, and W. C. Cheng, "Investigation into performance of deep excavation in sand covered karst: a case report," *Soils and Foundations*, vol. 58, no. 4, pp. 1042–1058, 2018.

[17] K. Hermsmeyer, K. Miyagawa, S. T. Kelley et al., "Reactivity-based coronary vasospasm independent of atherosclerosis in rhesus monkeys," *Journal of the American College of Cardiology*, vol. 29, no. 3, pp. 671–680, 1997.

[18] W. Wang, H. Zhao, J. Deng, X. Zhang, and Y. Zhang, "Study on soil reinforcement param in deep foundation pit of marshland metro station," *Heliyon*, vol. 5, no. 11, Article ID e02836, 2019.

[19] J. J. Wu, L. M. Peng, J. W. Li et al., "Rapid safety monitoring and analysis of foundation pit construction using unmanned aerial vehicle images," *Automation in Construction*, vol. 128, Article ID 103706, 2021.

[20] S. H. Ye, Z. F. Zhao, and D. Q. Wang, "Deformation analysis and safety assessment of existing metro tunnels affected by excavation of a foundation pit," *Underground Space*, vol. 6, no. 4, pp. 421–431, 2021.

[21] X. Y. Cui, M. G. Ye, and Y. Zhuang, "Performance of a foundation pit supported by bored piles and steel struts: a case study," *Soils and Foundations*, vol. 58, no. 4, pp. 1016–1027, 2018.

[22] J. Zhang, R. Xie, and H. Zhang, "Mechanical response analysis of the buried pipeline due to adjacent foundation pit excavation," *Tunnelling and Underground Space Technology*, vol. 78, pp. 135–145, 2018.

[23] H. S. Sun, Y. D. Chen, J. H. Zhang, and T. Kuang, "Analytical investigation of tunnel deformation caused by circular foundation pit excavation," *Computers and Geotechnics*, vol. 106, pp. 193–198, 2019.

[24] A. Benin, A. Konkov, V. Kavkazskiy, A. Novikov, and N. Vatin, "Evaluation of deformations of foundation pit structures and surrounding buildings during the construction of the second scene of the state academic mariinsky theatre in saint-petersburg considering stage-by-stage nature of construction process," *Procedia Engineering*, vol. 165, pp. 1483–1489, 2016.

[25] H. Y. Zhuang, G. X. Chen, Z. H. Hu, and C. Qi, "Influence of soil liquefaction on the seismic response of a subway station in model tests," *Bulletin of Engineering Geology and the Environment*, vol. 75, no. 3, pp. 1169–1182, 2016.

[26] C. F. Zuo, D. G. Tang, and D. P. Li, "Research on building deformation caused by the excavation of subway station," in *Proceedings of the 2015 International Conference on Architectural, Civil and Hydraulics Engineering*, pp. 494–502, Guangzhou, China, November 2015.

[27] Y. You, C. H. Yan, B. T. Xu, S. Liu, and C. Che, "Optimization of dewatering schemes for a deep foundation pit near the Yangtze River, China," *Journal of Rock Mechanics and Geotechnical Engineering*, vol. 10, no. 3, pp. 555–566, 2018.

[28] C. F. Zeng, G. Zheng, X. F. Zhou, X.-L. Xue, and H.-Z. Zhou, "Behaviours of wall and soil during pre-excavation dewatering under different foundation pit widths," *Computers and Geotechnics*, vol. 115, Article ID 103169, 2019.

Research Article

Mathematical Model for Charpy Impact Energy of V-Notch Specimens

Wei Wang, Ping Wang, Xuesong Liu, Zhibo Dong, and Hongyuan Fang [ID]

State Key Laboratory of Advanced Welding and Joining, Harbin Institute of Technology, Harbin 150001, China

Correspondence should be addressed to Hongyuan Fang; one4321@126.com

Firstly, by analyzing the response of Charpy V-notch specimen impacted by pendulum, the relationship between specimen geometry, material properties, and impact energy is established and simplified, and the mathematical model for evaluating impact energy of specimens with different sizes is established. Then, the effectiveness of the model through a series of impact tests is verified. Theoretical analysis and experimental results show that the relationship between ligament length and impact energy is quadratic, while the relationship between ligament thickness and impact energy is linear. In the derivation process, the intrinsic impact toughness is used to evaluate the toughness of materials. The mathematical model makes it possible to evaluate the impact energy of specimens with different sizes and provides a theoretical basis for evaluating the impact resistance of structures.

1. Introduction

Impact energy characterizes the ability of a structure to consume energy through deformation and fracture under impact load. The impact energy A_k, a value measured by the Charpy impact test, is mainly used to control the quality of metallurgical and thermal processing products and determine the ductile-brittle transition temperature of materials [1]. However, the determination of the A_k value is required to use specimens with a certain standard size. The comparison between the impact energy of specimens of different sizes or nonstandard sizes is disapproved. Since it partly depends on the geometry of specimens, impact energy cannot be regarded as a mechanical property of the material itself. Meanwhile, the relationship between impact energy and specimen size is not clear, which cannot be applied to evaluate the impact bearing capacity of structures whose sizes are not the same as standard specimens.

Several methods have been proposed to isolate the impact of collision energy on geometry. Traditionally, impact toughness α_k, the quotient of the impact energy, and the cross-sectional area of the notch are used as the parameters to evaluate the toughness of material. However, for material with plastic deformation, energy consumption does not

occur on the notched section only, and energy consumption across the section is not uniform, indicating that the impact toughness is not relevant and accurate enough as a mechanical parameter of material. Mikhail et al. [2] studied the influence of different specimen sizes on the impact test results and presented a procedure for transforming data from subsize specimens to data from full-size specimens. Sokolove et al. [3] studied the correlation between the ductile-brittle transition temperatures measured with impact specimens of different sizes, developed a procedure for transforming data from subsize and the full-size specimens, and turned out a good agreement. Lucon et al. [4] found that there is a linear relation between the impact energy and the specimen size by studying the results of the impact test between the small-size specimen and the full-size specimen. Schill et al. [4] studied the correlation between the impact energy of a certain ferritic steel small-size specimen and a full-size standard impact specimen and evaluated the estimation effects of various conversion formulas. Konopik et al. [5] established the conversion relation between the impact test results of small-size impact specimens and full-size standard impact specimens based on the test results. Yang et al. [6] used GA-NN combined model to predict the Charpy impact energy, and R. Muscat et al. [7] used

membership function modeling to predict the Charpy impact energy of heat-treated steel more accurately. Chaouadi and Fabry [8] did a preliminary study on the relation between the impact energy and the size of the simply supported rectangular cross-section structure under impact load, and the result of the study is that the impact energy is proportional to the section modulus in bending. Sreenivasan and Mannan [9] studied the impact energy of specimens with different cross-sectional shapes. He further verified that the impact energy is proportional to the section modulus in bending of rectangular cross-section structures and found that the regularity is not significant for nonrectangular cross-sections. Inspired by summarizing the existing research, we try to find the functional relationship between the impact sample size and the impact energy measurement results, so as to estimate the impact energy of any size sample.

In this study, based on the load-bearing form of the V-notch specimens subjected to the pendulum lateral impact, and the response process of structural deformation and failure, a mathematical model containing impact energy, mechanical properties, and geometrical parameters of the structure was established. In this way, the influence of specimen geometry to impact energy is extracted, and a new mechanical property to describe the impact load-bearing capability of a material is defined. Finally, the regression analyses based on impact test results of two kinds of steel were performed to verify the rationality of the model.

2. Mathematical Model to Evaluate Impact Energy

2.1. Dynamic Response Process of V-Notched Specimen Subjected to Lateral Impact. The deformation mode of V-notch specimen subjected to lateral impact, as shown in Figure 1, can be regarded as a dynamic 3-point bending. After impacted by the pendulum, the dynamic response process of the specimen mainly includes three parts before completely broken: elastic deformation, plastic deformation, and crack propagation. Based on the plane assumption and the analysis of the stress-strain state of the bending deformation, during the elastic deformation, the kinetic energy of the pendulum is transformed into elastic potential energy, which is distributed in the entire specimen. In the plastic deformation stage, the plastic deformation locally occurs near the section which contains the impact position. The point at the tip of the V-notch has the maximum tensile stress and strain. When the bending deformation develops to a certain extent, cracks should occur at this point. After crack initiation, the crack shall propagate in the direction most conducive to its propagation until the sample is completely broken.

Through the analysis of the dynamic response process of the specimen after the impact, it can be known that the resistance capability of the specimen structure to impact load is related to the bending resistance in the elastic and plastic deformation stage and the energy absorption during the crack propagation.
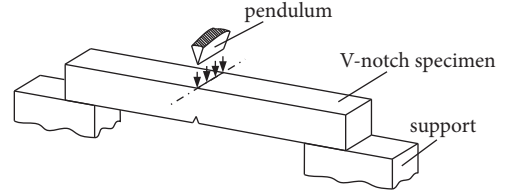
Figure 1: V-notch specimen struck by a pendulum transversely.

2.2. Construction of Mathematical Model of V-Notch Impact Energy. Based on the above analysis, it can be concluded that the impact energy consists of three parts: the elastic deformation energy E_e, the plastic deformation energy of the structure E_p, and the energy consumed by crack propagation in fracture section E_c. The impact energy of the specimen can be expressed as the sum of these energies, that is,

$$A = E_e + E_p + E_c. \tag{1}$$

In the bending process, energy consumed in the deformation process is the product of bending moment and deflection angle increment. Meanwhile, the stress of the material will change due to strain strengthening effect and strain rate effect, which will lead to the real-time change of the bending moment which resists the deformation. Therefore, bending moment can be regarded as a function of deflection angle $M(\theta)$. The energy consumed by crack propagation is the sum of the energy consumed by each area unit on the fracture section. The energy consumed on the area unit can be expressed as a function of position $\gamma(x, y)$. To sum up, each item at the right side of equation (1) can be expressed as

$$E_e = 2 \int_0^{\theta_s} M(\theta) \mathrm{d}\theta, \tag{2}$$

$$E_p = 2 \int_{\theta_s}^{\theta_r} M(\theta) \mathrm{d}\theta, \tag{3}$$

$$E_c = \iint_S \gamma(x, y) \mathrm{d}x \, \mathrm{d}y. \tag{4}$$

Among them, $M(\theta)$ is the real-time bending moment of the specimen during bending deformation; $\gamma(x, y)$ is the energy consumed on the area units at different locations of the cross-section when the crack grows; θ_s is the rotation angle of the specimen at the end of the elastic deformation; θ_f is the angle of the specimen when crack initiated at the backside of the specimen; S is the area of the crack propagation section.

Thus, equation (1) can be expressed as

$$A = 2 \int_0^{\theta_s} M(\theta) \mathrm{d}\theta + 2 \int_{\theta_s}^{\theta_r} M(\theta) \mathrm{d}\theta + \iint_S \gamma(x, y) \mathrm{d}x \, \mathrm{d}y. \tag{5}$$

In the elastic deformation stage, for the simply supported rectangular cross-section structure, the bending moment of the cross-section is

$$M(\theta) = \sigma_{\max}(\theta)\frac{wh^2}{6}. \tag{6}$$

Among them, $\sigma_{\max}(\theta)$ is the maximum stress on the section, in the elastic stage; its size is related to the bending deformation; w is the width of the cross-section of the notch center; h is the thickness of the cross-section of the notch center.

Substituting equation (6) to equation (2) gives

$$E_e = \frac{wh^2}{3}\int_0^{\theta_s}\sigma_{\max}(\theta)\mathrm{d}\theta. \tag{7}$$

In the elastic stage, the maximum stress and strain on the notch cross-section increase linearly with the deflection angle until the elastic limit is reached, so it can be obtained from equation (7) that

$$E_e = \frac{wh^2\sigma_s\theta_s}{6}. \tag{8}$$

Among them, σ_s is the yield strength of the material.

According to mechanics of materials, the deflection angle at the end of elastic deformation stage is

$$\theta_s = \frac{\sigma_s L}{4hE}. \tag{9}$$

Among them, L is the span between the support ends of the simply supported structure. E is young's modulus of the material.

Substituting equation (9) into equation (8), the energy dissipation in the elastic stage is

$$\begin{aligned}E_e &= 2\int_0^{\theta_s}M(\theta)\mathrm{d}\theta \\ &= \frac{wh\sigma_s\varepsilon_s L}{24},\end{aligned} \tag{10}$$

where ε_s is the strain when the material reaches the elastic limit.

Regarding α_e as an elastic index reflects the ability of material to absorb energy in elastic stage,

$$\alpha_e = \frac{\sigma_s\varepsilon_s}{24}. \tag{11}$$

Substituting equation (11) into equation (10) gives

$$E_e = \alpha_e whL. \tag{12}$$

When the maximum stress on the cross-section reaches the yield strength of the material, the elastic deformation generally turns into plastic deformation. After entering the plastic deformation stage, considering strain strengthening effects and strain rate effect, mechanical properties of the material show a high degree of nonlinear characteristics during the dynamic deformation process [10]. Therefore, the real bending moment at the bending section changes in real time, behaving as a function of deflection angle θ. The real-time bending moment of cross-section in plastic deformation stage can be written as a product of correction coefficient $k_r(\theta)$ and the ultimate plastic moment of cross-section M_p, that is,

$$M(\theta) = k_r(\theta)M_p. \tag{13}$$

The ultimate plastic bending moment M_p is calculated by the static yield strength of the material and the geometric size of the notched section, reflecting the ultimate bending moment when the material on the section theoretically yields completely under static bending. M_p does not change in the deformation process. The actual change of bending moment during deformation is considered by multiplying the correction coefficient function $k_r(\theta)$.

Substituting equation (13) to equation (3), we can get

$$E_p = 2M_p\int_{\theta_s}^{\theta_r}k_r(\theta)\mathrm{d}\theta. \tag{14}$$

It is difficult to obtain the analytical form of the strain strengthening effect and strain rate effect of the material in the process of plastic deformation, but the integral result can be replaced by the average value multiplied by the total deformation, that is,

$$\int_{\theta_s}^{\theta_r}k_r(\theta)\mathrm{d}\theta = k_{\mathrm{ave}}\Delta\theta. \tag{15}$$

Among them, k_{ave} is the mean value in the process of change $k_r(\theta)$.

Substituting equation (15) to equation (14), it gives

$$E_p = 2k_{\mathrm{ave}}M_p\Delta\theta. \tag{16}$$

For a rectangular cross-section structure, the ultimate moment of the section is

$$M_p = \frac{\sigma_s wh^2}{4}. \tag{17}$$

Different from elastic deformation, the plastic deformation of the specimen after impact is limited to a local position. The plastic area of a rectangular cross-section specimen is assumed to be two symmetrically distributed triangles, as shown in Figure 2.

When plastic deformation occurs, the relation between deflection angle increment $\Delta\theta$ and curvature k is

$$\kappa \approx \frac{2\Delta\theta}{l_h}, \tag{18}$$

where l_h is the largest length of plastic area, as shown in Figure 2.

It should be noted that the local length of plastic area l_h shall change during the deformation. However, for mathematical simplicity, some fixed values of l are recommended. In the case of rectangular cross-section beam, l_h roughly equals to the thickness of bending section [11,12].

The relation between the maximum strain in the bending section and the curvature is
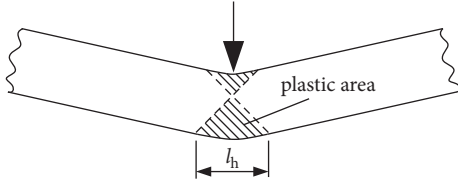
FIGURE 2: Plastic area at the impact point of a rectangular cross-section specimen.

$$\varepsilon_{\max} = \kappa z_{\max} = \kappa \frac{h}{2}, \tag{19}$$

where $z_{\max}$ is the distance from the notch to the neutral surface.

If $\varepsilon_{\max}$ increases to fracture strain ε_f, crack initiation occurs, and fracture strain ε_f is a mechanical property of material itself. Let $\varepsilon_{\max} = \varepsilon_f$; from equation (18) and (19), the deflection angle increment when crack initiation occurs can be derived

$$\Delta\theta = f\left(\varepsilon_f\right) = \varepsilon_f \frac{l_h}{h}. \tag{20}$$

From equations (16)~(20), the energy consumed by plastic deformation can be derived

$$E_p = 2 \int_{\theta_s}^{\theta_r} M(\theta) \mathrm{d}\theta = k_{\mathrm{ave}} \sigma_s \varepsilon_f \frac{whl_h}{2}. \tag{21}$$

Let

$$\alpha_t = k_{\mathrm{ave}} \sigma_s \varepsilon_f. \tag{22}$$

So, equation (21) can be written as

$$E_p = \alpha_t \frac{whl_h}{2}. \tag{23}$$

Among them, α_t is the intrinsic impact toughness, which is defined by equation (22) to reflect the toughness of material itself in the dynamic process.

Similarly, the average value is used to simplify the expression of energy consumed during crack propagation, which can be written as the product of average energy per unit area and fracture cross-sectional area. Therefore, equation (4) can be simplified as follows:

$$E_c = 2 \iint_S \gamma(x, y) \mathrm{d}x\, \mathrm{d}y = 2\gamma_{\mathrm{ave}} wh. \tag{24}$$

Among them, γ_{ave} is the average energy consumption per unit area during crack propagation, reflecting the ability of the material to resist crack propagation.

Substituting equations (12), (23), and (24) to equation (5), the simplified mathematical model of the impact work for rectangular cross-section structure can be obtained

$$A = \alpha_e whL + \alpha_t \frac{whl_h}{2} + 2\gamma_{\mathrm{ave}} wh. \tag{25}$$

Taking the local length of plastic deformation $l_h \approx h$ [11,12], we substitute it to equation (25) and derive

$$A \approx \alpha_t \frac{wh^2}{2} + (2\gamma_{\mathrm{ave}} + \alpha_e L)wh. \tag{26}$$

3. Experimental Verification of Impact Work Mathematical Model

The mathematical model described by equation (26) was verified by the impact experiments of 921A and Q235B steel.

3.1. Impact Test Equipment and Test Materials. In order to verify the validity of equation (26), a series of impact tests on rectangular cross-section specimens with different sizes and regression analyses of the impact test results were carried out.

The impact test was conducted at room temperature, and JB-300B pendulum impact tester was selected to carry out impact loading on the specimen. The geometry of the specimens is shown as Figure 3. The span between supports L was 40 mm; the length of all specimens was 55 mm. To control the crack position, a V-notch, whose angle is 45° and depth is 2 mm, was made at the center of each specimen. The radius of curvature at the bottom of the notch is 0.25 mm. Ligament length h is the width of specimen which really takes part in the baring. All specimens were processed by wire cutting and polished to make the roughness meet ASTM A370 standard requirements. Oil pollution was removed with acetone.

Ultra-high strength steel 921A is chosen for impact test in this study; its basic mechanical properties are measured as shown in Table 1.

Three impact tests were conducted on each impact specimen of the same size and material, and the average of the three tests was taken as the final result.

3.2. Analysis of Impact Test Results. The impact test results of specimens made of 921A steel are shown in Table 2.

According to the physical meaning of each parameter in equation (26), boundary conditions of parameters were given in Table 3 for the regression analysis. The intrinsic impact toughness α_t and average energy consumption per unit area γ_{ave} must be positive. The value of α_e can be calculated by substituting the yield strength and yield strain of each material in equation (11).

Nonlinear double independent variable regression analyses were conducted with software Mathematica, and the analysis results are shown in Table 4. The R-square value is close to 1, indicating the effectiveness of fitting. However, the value of γ_{ave} is close to 0, and the P value is close to 1, showing that the value of γ_{ave} is extremely insignificant. Compared with the energy dissipating during elastic deformation and the plastic deformation energy, the surface
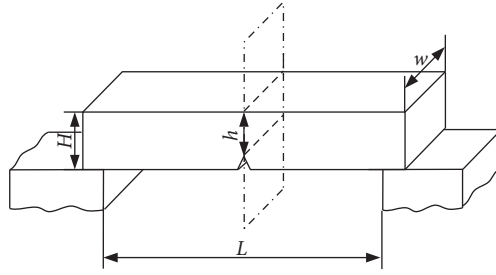
Figure 3: Dimensions of impact specimen.

Table 1: Basic mechanic properties of tested materials.

Material (A)	σ_s (MPa)	σ_b (MPa)	e (%)
921	665	729	25.5

Table 2: Impact test results of 921A steel.

Specimen number	w (mm)	h (mm)	A (J)
A1	10	3	30
A2	10	4	46
A3	10	6	102
A4	10	6	108
A5	10	6.5	110
A6	10	7	130
A7	10	8	202
A8	10	8	210
A9	10	9	248
A10	6	8	88
A11	6.5	8	96
A12	8	8	120
A13	9.5	8	166
A14	10	8	202
A15	12	8	228

Table 3: Boundary conditions constrained by physical significance.

α_t (mJ/mm^3)	α_e (mJ/mm^3)	γ_{ave} (mJ/mm^2)
>0	0.0554	>0

Table 4: Regression analysis results.

	Fitting result	P value	R-squared
α_t	579.765	0.0002	
α_e	0.0554	—	0.989375
γ_{ave}	0.00034	9.99482	

energy of materials used in this research is much smaller than the first two with a couple of orders of magnitude differences [13]. Therefore, as a result of regression analysis, the insignificance of γ_{ave} is reasonable, suggesting that γ_{ave} may be ignored under low accuracy requirement.

Substituting sizes of the specimens and the fitting results of α_e and α_t to equations (12) and (23), respectively, we found out that for materials with appreciable plasticity, the energy absorbed by plastic deformation is much larger than that of elastic deformation, which was commonly accepted by existing researches [14].

Substituting the fitting results of 921A steel into equation (26), we obtained the relationship between a and H (Figure 4(a)) and the relationship between a and w (Figure 4(b)). Meanwhile, impact test results were also marked in the corresponding coordinates for comparison, as shown in Figure 4.

It can be seen from Figure 4 that the results of impact test were all distributed near the curve base on equation (26). The average difference between the results evaluated with equation (26) and those obtained by impact tests is 10.54%. Considering the considerable discreteness of impact test itself, the

(a)

(b)
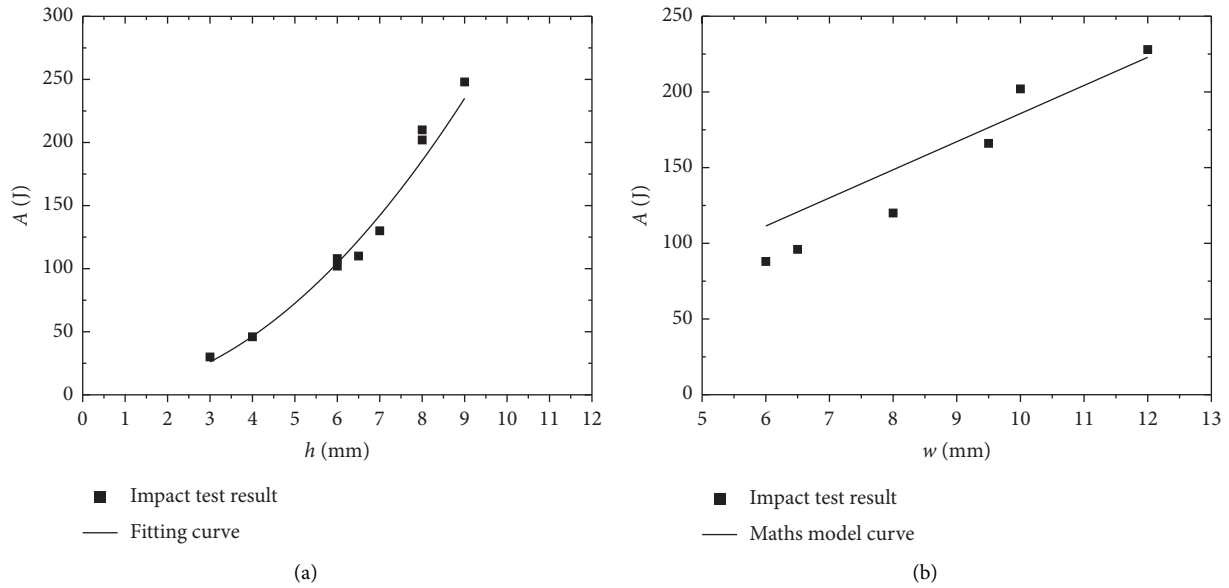
FIGURE 4: Comparison of evaluations based on model and impact test results for 921 steel. (a) A1~A9 specimen impact test results. (b) A10~A15 specimen impact test results.

accuracy and validity of the mathematical model described by equation (26) can be acceptable. Furthermore, the relation between ligament length h and impact energy A was quadratic approximately and the relationship between thickness W and impact energy a is approximately linear, which is in good agreement with the mathematical model [15].

4. Discussion

The mathematical model of impact energy illuminated the relation between mechanical properties of the material itself, the geometric dimensions of the structure, and the impact work. Thus, it is possible to estimate the impact energy of different size structures with known mechanical properties parameters of the materials. If the impact energy of a certain structure is taken as an index to evaluated impact bearing capability of the structure, this model can be used as a design basis or a tool of reliability evaluation [16].

Furthermore, the commonly used parameters A_k and α_k are influenced by the geometry of specimen. Thus, the comparison of A_k or α_k between specimens of different or nonstandard sizes cannot reflect their difference in toughness [17]. The intrinsic impact toughness α_t in this paper has no relation with the geometry of specimen, which can be regarded as a mechanical property of material itself. Furthermore, α_t can be obtained by regression analysis based on the mathematical model constructed in this paper [18]. Considering the convenience of impact test, α_t has the potential to be applied to evaluate the toughness of materials such as K_{Ic} and K_{Id}.

It is worth noting that the mathematical model of impact energy in this paper is established for materials with obvious plasticity. For materials with little plasticity, the mathematical model proposed in this study is not applicable [18]. The mathematical model proposed in this study did not consider the inertia effect of the structure under higher rate impact which needs to be further studied.

5. Conclusion

(1) By analyzing the dynamic response process of the V-shaped gap reduced by the transverse impact of the placed hammer, a mathematical model can be established to estimate the impact energy of different size fragments. This study reveals that the impact energy is linearly related to the width of the notch cross-section. The rules related to the second-time nonlinearity of the thickness have been verified by a series of impact defects.

(2) The inherent impact toughness is independent of the size and geometry of the material, which can be called the inherent impact toughness of the material itself. When comparing the volumes of different materials, it is no longer necessary to use specimens of the same standard size for impact test.

(3) When the structure is used below the ductile-brittle transition temperature and high-speed impact load, the mathematical model established in this study cannot be used in theory, which needs to be considered in the structural inertia.

Data Availability

The labeled dataset used to support the findings of this study are available from the corresponding author upon request.

Conflicts of Interest

The authors declare no conflicts of interest.

Acknowledgments

References

[1] K. K. Mathur, A. Needleman, and V. Tvergaard, "3D analysis of failure modes in the Charpy impact test," *Modelling and Simulation in Materials Science and Engineering*, vol. 2, no. 3A, pp. 617–635, 1994.

[2] Y. Nakamura, M. Yamaguchi, and M. Okubo, "Instrumented charpy impact test of epoxy resin filled with irregular-shaped silica particles," *Polymer Engineering & ence*, vol. 33, no. 5, pp. 279–284, 2010.

[3] H. Kurishita, H. Kayano, M. Narui, M. Yamazaki, Y. Kano, and I. Shibahara, "Effects of V-Notch dimensions on Charpy impact test results for differently sized miniature specimens of ferritic steel," *Materials Transactions, JIM*, vol. 34, no. 11, pp. 1042–1052, 1993.

[4] Y. Takashima, M. Ohata, and F. Minami, "Evaluation method for fracture mechanics-based material toughness from Charpy impact test," *Materials Science Forum*, vol. 512, pp. 61–66, 2006.

[5] C. H. Lee, H. S. Shin, K. T. Park, and S. H. Yang, "Evaluation of the applicability of structural steels to cold regions by the Charpy impact test," *Journal of Korean Society of Steel Construction*, vol. 23, no. 4, pp. 483–491, 2011.

[6] K. Toshiro, Y. Isamu, and N. Mitsuo, "Evaluation of dynamic fracture toughness parameters by instrumented Charpy impact test," *Engineering Fracture Mechanics*, vol. 24, no. 5, pp. 773–782, 1986.

[7] S. H. Kim, Y. W. Park, S. S. Kang, and H. D. Chung, "Estimation of fracture toughness transition curves of RPV steels from Charpy impact test data," *Nuclear Engineering and Design*, vol. 212, no. 1-3, pp. 49–57, 2002.

[8] R. Chaouadi and A. Fabry, "On the utilization of the instrumented Charpy impact test for characterizing the flow and fracture behavior of reactor pressure vessel steels," *From Charpy To Present Impact Testing*, vol. 30, pp. 103–117, 2002.

[9] P. R. Sreenivasan and S. L. Mannan, "Plastic n-factor for three-point bend specimens: analysis of instrumented Charpy impact test results for AISI 308 weld and AISI 316 stainless steels," *International Journal of Fracture*, vol. 101, no. 3, pp. 215–228, 2000.

[10] N. S. Cannon and D. S. Gelles, "Charpy impact test results from low activation alloys irradiated to 10 dpa at 365°C," *Journal of Nuclear Materials*, vol. 186, no. 1, pp. 68–76, 1991.

[11] H. Kikuchi, M. Harada, K. Ara, Y. Kamada, S. Kobayashi, and S. Takahashi, "Development of apparatus for magnetic measurements of Charpy impact test pieces," *Journal of Materials Processing Technology*, vol. 181, no. 1-3, pp. 190–193, 2007.

[12] M. M. Shokrieh, M. A. Torabizadeh, and A. Fereidoon, "Dynamic failure behavior of glass/epoxy composites under low temperature using Charpy impact test method," *Indian Journal of Engineering & Materials ences*, vol. 18, no. 3, pp. 211–220, 2011.

[13] O. S. Lee and S. K. Hong, "Dynamic fracture characteristics of highly brittle materials by using instrumented Charpy impact test," *KSME International Journal*, vol. 11, no. 5, pp. 513–520, 1997.

[14] T. Iwadate and H. Takemata, "Prediction method of fracture toughness KIC transition curve from Charpy V-Notch impact test results," *Journal of the Society of Materials Science, Japan*, vol. 41, no. 467, pp. 1241–1247, 1992.

[15] G. V. Kozlov, R. A. Shetov, and A. K. Mikitayev, "Determination of the limit of forced elasticity in the Charpy impact test," *Polymer Science U.S.S.R.* vol. 29, no. 9, pp. 2205–2207, 1987.

[16] K. Seo, F. Nogata, and J.-i. Masaki, "The absorbed energy in Charpy impact test for specimens with mechanical heterogeneity," *Journal of the Society of Materials Science, Japan*, vol. 35, no. 399, pp. 1405–1410, 1986.

[17] J. A. Wang and N. Rao, "New methodologies for developing radiation embrittlement models and trend curves of the Charpy impact test data," *Journal of ASTM International*, vol. 1, no. 9, p. 19, 2004.

[18] T. Otsuka, K. Hashizume, and M. Sugisaki, "Charpy impact test of oxidized and hydrogenated zircaloy using a thin strip specimen," *Journal of Nuclear Science and Technology*, vol. 41, no. 3, pp. 247–251, 2004.

Research Article

Study on Mesoscale Damage Evolution Characteristics of Irregular Sandstone Particles Based on Digital Images and Fractal Theory

Lujing Zheng,[1,2] Lulin Zheng ●,[1] Yujun Zuo,[1] Hao Liu,[1,3,4] Bin Chen,[1] Zhonghu Wu,[5] Wenjibin Sun,[1] and Yingle Wang[1]

[1]*College of Mining, Guizhou University, Guiyang 550025, China*
[2]*Guizhou Jinfeng Mining Limited, Southwest of Guizhou, Guizhou 562204, China*
[3]*College of Resource and Environmental Engineering, Guizhou University, Guiyang 550025, China*
[4]*Department of Civil and Environmental Engineering, Technical University of Catalonia (UPC), 08034 Barcelona, Spain*
[5]*College of Civil Engineering, Guizhou University, Guiyang 550025, China*

Correspondence should be addressed to Lulin Zheng; zhenglulin1983@126.com

To study the mesoscale damage evolution law of irregular sandstone particles, based on RFPA2D and digital image processing technology, a real mesostructure numerical model of irregular sandstone particles is established to simulate the breakage process of particles, the effects of loading conditions and mesoscale heterogeneity on irregular sandstone particle damage are studied, and the calculation method of fractal dimension of irregular rock particles mesoscale fracture is proposed. The results show that the fracture damage degree (ω) and fractal dimension (D) maximum values of the constrained particles are 0.733 and 1.466, respectively, and the unconstrained particles are 0.577 and 1.153, respectively. The final failure mode of constrained particles is more complicated than unconstrained particles, the damage is more serious, and the fracture is more complete. Thus, the larger values of D yield a more complicated final failure mode of the particles. Consequently, with the larger ω, the final damage is more serious, and the breakage effect is comparatively better. The study is of great significance for exploring the laws of rock particle breakage and energy consumption, rock breakage mechanism, and searching for efficient and energy-saving rock-breaking methods.

1. Introduction

Crushing is the process of turning a large piece of material into a small piece of material under external force, which is widely used in the mineral industry. The crushing operation is the first step to reduce the particle size of the ore or to dissociate useful minerals from the monomer in the ore in the crushing process, which aims to reduce the particle size. So far, it is an urgent problem to understand the fracture process and damage mechanism of particles from the mechanical point of view [1]. Therefore, revealing the mechanism of particle breakage has practical engineering significance for seeking efficient and energy-saving rock breakage methods and guiding energy saving and consumption reduction in mines.

Evertsson's study shows that the breakage of brittle materials such as rock is a complicated process; revealing the breakage process of a single particle under load is an important step in understanding particle fragmentation [1]. The breakage of materials is traditionally considered to be a single-particle breakage without considering the confinement conditions; the breakage of materials can be determined by Griffith's theory of brittle fracture [2]. However, the breakage behavior of single particles under without confinement conditions is not the same as that under with confinement conditions; when stress is applied to confinement particles, the stress distribution on the surface will be more complicated. Therefore, it is necessary to accurately model the breakage condition of a single particle when studying the breakage behavior of the particles, which will be

affected by multiple loads from adjacent particles [3]. Therefore, in the simulation of particle breakage, the confinement conditions should be considered to better understand the breakage process between particles. However, usually, the breakage behavior of rock particles is affected by their loading conditions, shape, and size [3]. Due to the complexity of the problem, there are many difficulties in analyzing the breakage process and damage evolution of rock particles. With the development of computer technology, numerical simulation methods seem to provide the possibility of revealing the mechanism of particle breakage [4]. Tang et al. developed the RFPA2D software based on the mesodamage mechanics theory, simulated the breakage process of rock particles under different loading conditions, and verified that RFPA2D is a suitable tool to study particle breakage [5]. Based on RFPA2D (dynamic version), Zuo et al. studied the breakage process of single-particle rock under impact load and discussed the crushing effect and energy consumption law of rock particles under different impact loads [6]. Zhou et al. developed a combined discrete-finite element method to simulate the breakage behavior of single particles and verified the reliability of the method [7]. Based on the FDEM method, Wei et al. studied the fracture behavior of single-particle breaking under rotational point loading [8].

The above scholars have made a lot of achievements in revealing the mechanism of particle fragmentation, but these studies ignore the real mesostructure of rock particles. A rock's mechanical properties are closely related to its mesostructure such that the breakage processes and macroscopic mechanical properties are dependent on the mesoscale behavior and mesostructure of the materials. Therefore, the establishment of numerical models that can reflect the real mesostructure of rock particles is a strong guarantee for the numerical calculation to obtain reliable results, which is of great significance for revealing the breakage mechanism of rock particles. With the development of computer graphics hardware and image processing software, digital image processing (DIP) technology has been applied to the study of rock mechanics[9]. Liu et al. used digital image processing technology to characterize the mesouniformity of sandstone, established a numerical model considering the real mesostructure of sandstone, and analyzed its fracture process [10]. Liang et al. using a digital image and 3D reconstruction technology obtained the structural parameters, for example, the quantity of 3D voids, the degree of voids, the appropriation of voids along the height direction, and the coefficient of variation of the proportion of the coarse aggregate area [11]. Li et al. analyzed the fractal characteristics of coal by digital image processing technology and systematically studied the pores and cracks of coal under different pressures [12]. Yue et al. combined digital images and the finite element method (FEM) to study heterogeneous geotechnical materials. With this method, they were able to truly characterize the heterogeneous characteristics of porous materials and study their mechanical properties [13]. By combining digital image processing technology with the original RFPA2D numerical simulation system, Yu et al. established an RFPA2D-DIP

numerical model based on the real mesostructure of rock and carried out numerical simulations of three kinds of conventional rock mechanics tests for rock specimens [14]. Wu et al. established a numerical model of shale mesoscale by combining digital images with finite element software and analyzed its fracture mode and fractal characteristics under uniaxial compression [15]. However, the above research results are based on the knowledge gained from the rule test pieces; few attempts have been made to study the breakage process in rock particles by establishing a numerical model based on the real mesostructure of irregular rock particles under different loading conditions.

Based on the above problems, this paper uses digital image processing technology to characterize the spatial distribution of minerals in irregular sandstone particles, so as to obtain the real mesostructure of the particles and map it to the finite element mesh, combined with RFPA2D-DIP software to establish a real mesostructure numerical model of irregular sandstone particles. The mesoscale breakage process of sandstone particles under different loading conditions is simulated, the effects of different loading conditions and mesononuniformity on breakage of irregular sandstone particles are studied, and the fractal characteristics, damage evolution, and acoustic emission distribution of breakage process of rock particles in numerical experiments are discussed.

2. Background Theory

2.1. DIP Technique. Digital image processing (DIP) is a new field that categorically studies and analyzes the theory, technology, and application of digital images. It widely involves transforming the required research objects into digital images and then carrying out sophisticated computer processing to enhance the quality of digital images and extracting the image information using computer-aided software to obtain useful research results about the subject of investigation. A pixel can be defined as the smallest element with an area formed when longitudinal and transverse scan lines intersect each other. A pixel normally consists of 0–255 values representing three primary color components, red (R), green (G), and blue (B). In order to explain the image information mathematically, three discrete functions are required, and hence each pixel becomes a function of red (R), green (G), and blue (B). The HSI space, which refers to hue, saturation, and intensity (brightness), is most related to our intuitive perception of color and it more naturally reflects the sensation of the color of human perception. The hue component refers to the names that we give to colors, red, green, yellow, orange, purple, and so on, and its values range from 0 to 360 that represent the dominant reflected wavelength of the color of the object under investigation. The saturation component S describes a color in terms of pale versus vivid with values 0 to 1 and is a representation of purity of color. The intensity component represents luminance and describes whether a color is light or dark. The HSI space is utilized because it provides a comparatively better understanding of colors. Based on variation in color and gray-scale value, the spatial distribution and geometrical

shape of the mesocomponents of materials are determined by DIP technology. This technology is utilized to produce an enhanced image representing the nonuniformity of the material of rock by classification of segmentation thresholds based on color and brightness of different media inside the rock. A 2-dimensional CT slice is shown in Figure 1(b), which is obtained through high-resolution CT scanning of a sandstone sample at Tianjin Sanying Company. The digital image represents the true colors of the stone sample, that is, a 24-bit digital image of a sandstone stone sample with a joint filled with calcite. For the purpose of studying the evolution process of breakage and damage of irregular particles, irregular CT slices were obtained by performing image processing in Figures 1(b) and 1(c).

Since the color variation in the digital image is not very obvious, so the image was processed further to improve the appearance of the imagery to assist in visual interpretation and analysis. According to previous research, the I value in the HIS color space is selected as the image segmentation threshold [10, 14]. The locality where the AA′ scan line moves through the imagery is shown in Figure 1(c), and alongside the scan line AA′, a graphical representation of the development in the value of I is shown in Figure 1(d). A comparison between the medium through which the scan lines passed and the change of the curve was analyzed, and many tests were performed on ImageJ software to find a segmentation threshold that was 150. Consequently, the value of I can be categorized into two subsections 0 to 150 for sandstone and 150 to 255 for the calcite filled in the joint. Therefore, the internal medium of the sandstone is divided into two categories based on the variation in the I values. Figure 1(e) is a digital representation of the mesostructure image obtained by digital image processing. The geometrical and spatial distribution of the sandstone and calcite two of the sandstone sample can be clearly seen in the picture. Sandstone is represented with red, while calcite is represented with gray, respectively. It can be seen from Figure 1(e) that digital image processing technology can better characterize the heterogeneity of sandstone.

2.2. Representation of Damage on the Mesoscopic Scale via Constitutive Relationship.

In RFPA2D, by assuming strain equivalence and based on the variation in elastic modulus, the damage variable is defined precisely [16]. A constitutive relationship after an external force causes damage to the sample material under investigation can be expressed as [6, 17, 18]

$$E = (1 - \omega)E0, \tag{1}$$

where ω is damage variable, E_0 represents the elastic modulus when the material is not damaged, E represents the elastic modulus when the material is damaged.

The tensile strength of the sandstone is very less than its compressive strength, so we chose the Mohr-Coulomb failure/shear strength and maximum tensile stress as criteria for element failure [17]. And its mesodamage constitutive relationship is shown in Figure 2. Initially, the stress-strain curve is linear, so the damage would be none, $D = 0$. When the mesoelement under uniaxial tension reaches the maximum tensile strain, brittle damage occurs. The primary failure mode of brittle rocks is tensile-induced failure [19, 20]. As soon as the tensile stress approaches f_t (tensile strength) of the element, damage takes place as per the main damage criteria. The function of tensile damage is expressed as [21]

$$F^- (\sigma) = \sigma_3 + f_t = 0, \tag{2}$$

where the principal stress vector is represented by σ. The third quadrant of Figure 3 illustrates that the constitutive relationship for the mesoscopic element under uniaxial tension can be expressed as [9, 18]

$$\omega = \begin{cases} 0, & \varepsilon_{t0} \leq \varepsilon < 0, \\ 1 - \dfrac{\lambda \varepsilon_{t0}}{\varepsilon}, & \varepsilon_{tl} \leq \varepsilon < \varepsilon_{t0}, \\ 1, & \varepsilon < \varepsilon_{tl.} \end{cases} \tag{3}$$

where λ represents the mesoscopic element's residual intensity coefficient, described as $f_{tr} = \lambda f_t$ (where mesoscopic element's uniaxial tensile strength is given by f_t, whereas f_{tr} is the residual strength at the element's initial tensile failure), and element's ultimate tensile strain is given by ε_{tl}. When the element's uniaxial tensile strain goes to ultimate tensile strain, then the element goes to tensile fracture state. η is defined as the ultimate strain coefficient, specifically expressed by $\varepsilon_{tl} = \eta \varepsilon_{t0}$. ε_{t0} is tensile strain corresponding to elastic limit that can be named as tensile failure strain threshold, which is calculated as [17]

$$\varepsilon_{t0} = -\frac{f_t}{E_o}. \tag{4}$$

When a mesoscopic element is exposed to uniaxial compression, as illustrated in the first quadrant of Figure 2, the Mohr-Coulomb criteria for damage are used as the second criterion, which defines element damage under compressive or shear stress conditions [22]:

$$F^+ (\sigma) = \sigma_1 - \sigma_3 \frac{1 + \sin \varphi}{1 - \sin \varphi} - f_c = 0, \tag{5}$$

where friction angle is given by φ, principal stresses are given by σ_1 and σ_3, and uniaxial compressive strength is given by f_c. ε element's damage variable under uniaxial compression may be given as [23, 24]

$$\omega = \begin{cases} 0, & \varepsilon \leq \varepsilon_{t0}, \\ 1 - \dfrac{\lambda \varepsilon_{t0}}{\varepsilon}, & \varepsilon \geq \varepsilon_{t0,} \end{cases} \tag{6}$$

where the coefficient of residual strength is given by λ, described as $f_{tr}/f_t = f_{cr}/f_c = \lambda$, whereas at the elastic limit, compressive strain is given by ε_{t0} that can be determined as [23, 24]

CT scan

(a) Sandstone samples

(b) Two-dimensional CT slice

Image Processing

(c) Irregular CT slice

threshold segmentation

(e) Image resulting from
thershold segmentation

■ calcite
■ sandstone

(d) Variation in the I value along scan line AA′
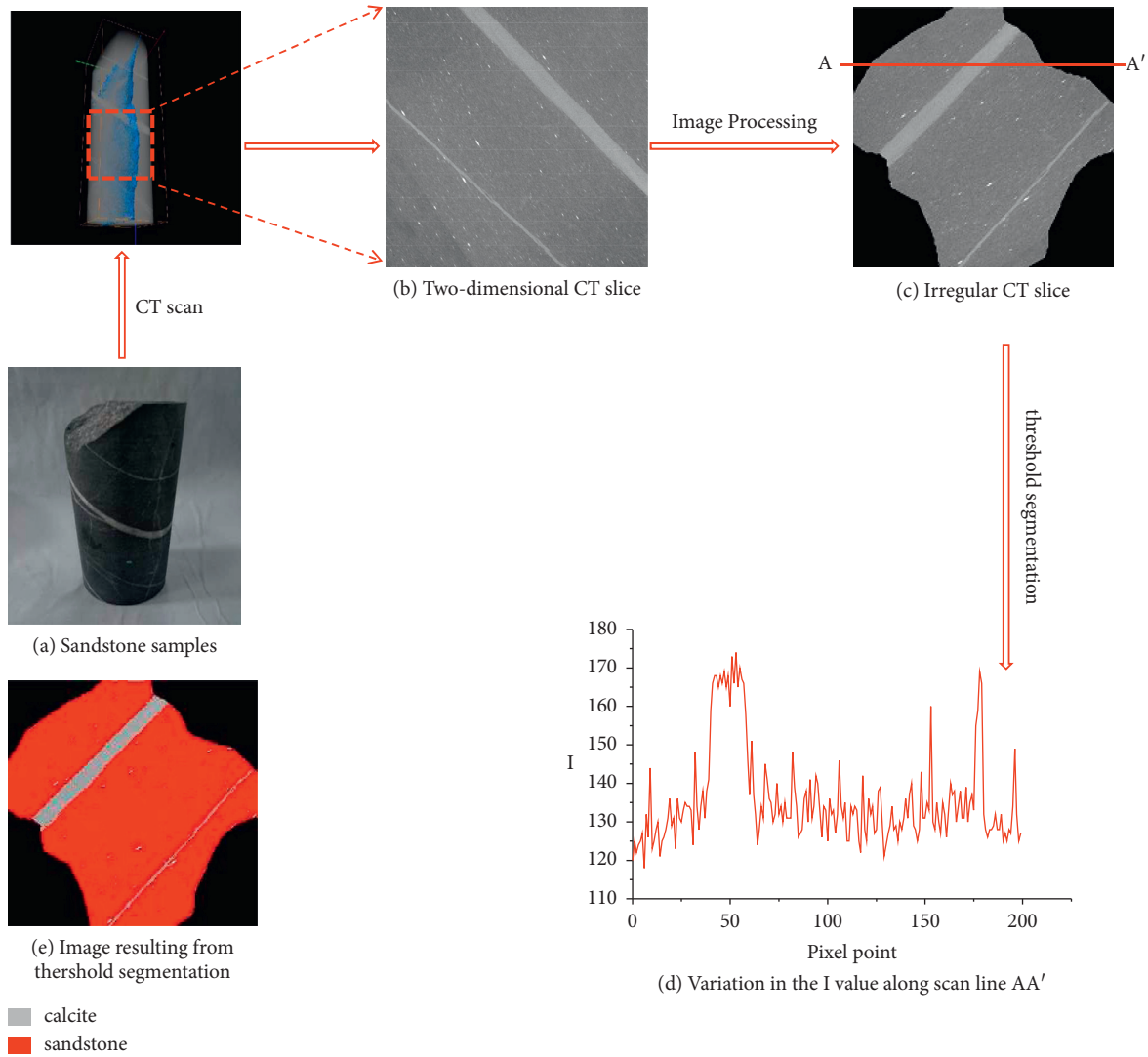
FIGURE 1: Irregular particle digital image processing process. (a) Sandstone samples. (b) Two-dimensional CT slice. (c) Irregular CT slice. (d) Variation in the I value along scan line AA′. (e) Image resulting from threshold segmentation.

f_c is compressive strength
f_{cr} is compressive residual strength
ε_{c0} is elastic compressive strain limit

f_t is tensile strength
f_{tr} is tensile residual strength
ε_{t0} is elastic tensile strain limit
ε_{tl} is tensile strain limit
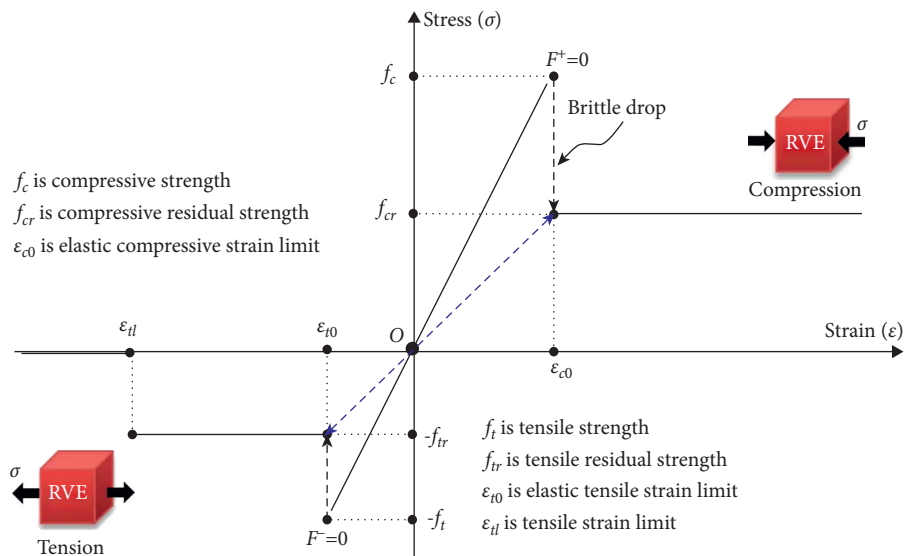
FIGURE 2: Constitutive relationship of mesoscale damage of element.

Step 42   Step 57   Step 72   Step 101   Step 116

(a)

(b)
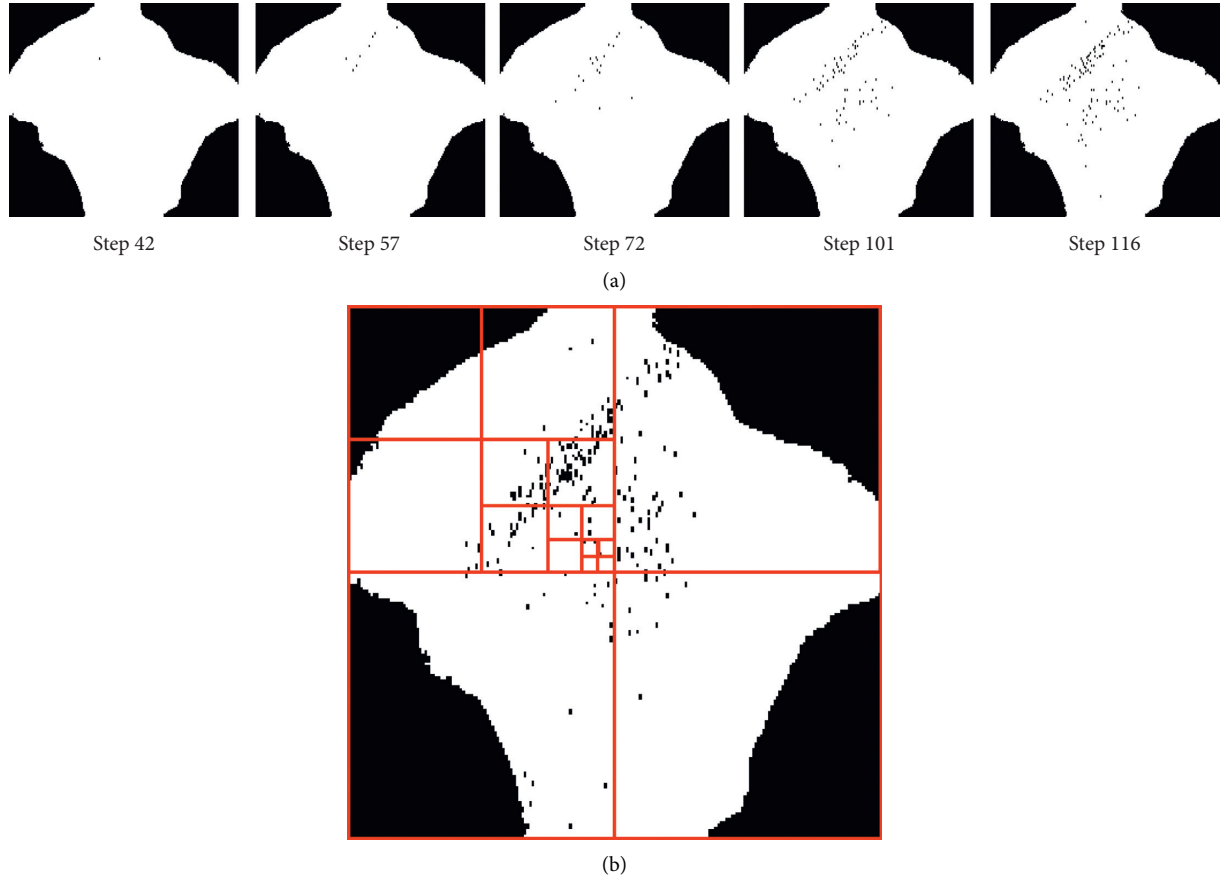
FIGURE 3: The calculation process of the box dimension of the rock mesodamage area. (a) Damage evolution of sandstone particles in the form of a binary image (with confinement). (b) Schematic diagram of the box division process.

$$\varepsilon_{c0} = -\frac{f_c}{E_o}. \tag{7}$$

2.3. Using the Box-Counting Method and Fractal Analysis of Images.

B.B. Mandelbrot proposed fractal damage theory. This theory studies and describes irregular, highly complex, unstable phenomena in nature. The fractal theory is able to describe complex objects in the physical world quantitatively and can be used to reveal the damage mechanism in a rock mass. Its calculation methods include the box dimension, Hausdorff dimension, and information dimension algorithms. Since the box-counting dimension can intuitively reflect the degree of occupancy of the target in the study area and it is easy to calculate and measure, it has been used widely in various fields. In this study, the box dimension calculation with the self-similarity method has been selected, which is defined as [25, 26]

$$Ds = \lim_{k \longrightarrow \infty} \frac{\lg Nr_k(A)}{\lg 1/r_k}, \tag{8}$$

where the self-similar fractal dimension of the damaged region is Ds and the developed reducing sequence with the element's square box size is r_k. The least number of grids necessary for covering the target set A with a square box of size r_k is $Nr_k(A)$.

Based on the research foundation of fractal theory, this paper aims to use box dimension to study and analyze the fractal of mesoscale failure element area of irregular sandstone particles with different loading conditions. The fractal dimension of the mesoscale failure element area of irregular sandstone particles with different loading conditions at different stress levels is calculated, and the corresponding damage degree of the medium is determined. A binary image in Figure 3(a) is a representation of the mesoscale fracture evolution of irregular sandstone particles under different loading steps. Since the size of the box and pixel is relatable, the actual size of the pixel is equal to the minimum size of the box. Therefore, the smaller size of the box yields higher image resolution and accuracy of the calculation result. The resolution of the image is 500×500 pixels in this paper. The resolution of the image is 500×500 pixels in this paper.

Figure 3(b) is the box covering various regions, which is dividing the mesoelement failure area into a small square grid with r_k side length (the length of each image pixel is described as 1 in this paper); then count the number Nr_k of all boxes comprising failure element region. A dichotomy is used to construct r_k in this paper. If the failure element distribution in this area satisfies the fractal features, the formula shows that "when the $r_k \longrightarrow 0$, $\lg Nr_k/\lg r_k \longrightarrow D$, it can be seen that the fractal dimension of the failure element field (acoustic emission field) in this area is D. Hence, in the

double logarithmic coordinate system, the data points ($\lg r_k$; $\lg Nr_k$) are linearly fitted by the least square method, and the straight line equation" can be found:

$$\lg Nr_k = D\lg r_k + b. \tag{9}$$

In the expression above, the box-counting dimension of the field of the failure element in the area is expressed in terms of D. Based on the above principle, Matlab programming is used to automatically mesh and statistics the acoustic emission evolution image of the mesoscale failure of the rock particle, and calculate the corresponding fractal dimension. The process for calculation is demonstrated in Figure 4.

3. Establishment of Numerical Model

For better comprehension of the fracture behavior and damage evolution characteristics of such rock particles, it is necessary to simulate the fracture evolution process of irregularly shaped particles under different loading conditions. Revealing the fracture process of a single particle under load conditions is an important step in understanding particle fragmentation. However, usually, the fracture behavior of single particles is affected by their loading conditions, shape, and size [3]. Therefore, DIP techniques (see Section 2.1) are combined with finite element modeling. In the finite element method, the research objects need to be divided into many small grids. Since many pixels make up a digital image, pixels can be regarded as mesh in finite elements (Figure 5). The entire characterization image can be transformed into several finite element grids, and then the material parameters are assigned to each material component according to the characterized color. The nonuniform coefficients of the different components are inputted into the numerical model. Thereby, a numerical model considering the real mesostructure of the material is established.

This study uses the rock failure process analysis system (RFPA2D) for numerical simulation; RFPA2D can simulate the microscopic failure evolution and failure process of rock through two-dimensional FEM. Thorough and detailed descriptions can be found elsewhere about this simulator [27]. Here, we incorporate digital image processing into the rock failure process analysis code (RFPA2D) and establish a quasiactual model. RFPA takes the rock heterogeneity into account [10, 28], culminating in the RFPA2D-DIP numerical simulation system [22, 28, 29]. The constitutive model of damage to the element is shown in Section 2.2. The numerical model consists of two materials: a sandstone matrix and a calcite mineral. In the numerical calculation, taking into account the nonuniformity of the material, we assume that the mechanical parameters of the matrix elements of sandstone and calcite obey the Weibull distribution function and is expressed as [6, 30, 31]

$$f(u) = \frac{m}{u_o}\left(\frac{u}{u_o}\right)^{m-1}\exp\left(-\frac{u}{u_o}\right)^m, \tag{10}$$

where u represents the parameter of the mechanical properties of the material medium, the average value of the mechanical property parameters is represented by u_0, m represents the property parameter of the distribution function, reflecting the uniformity of the material medium, and $f(u)$ is the statistical distribution density of the mechanical properties of the material. In the model, the heterogeneity of calcite and sandstone is considered, and the Monte-Carlo method is used to assign the mechanical parameters of the mesoelements [32, 33].

Figure 5 exemplifies the finite element model (FEM) based on an irregular CT slice. The mechanical parameters of each mesomedium in Table 1 are quoted from previous research results [10, 34]. Figure 6 is a mechanical loading model of two irregular particles based on DIP technology and RFPA2D software under different loading conditions. A 5 mm thick loading plate is fixed on the top and bottom of the particle test piece, the loading plate has uniform elasticity, the elastic modulus is 200 GPa, Poisson's ratio is 0.25, and the compressive strength is 1000 GPa [6]. P is the axial pressure of the model. The whole process adopts constant displacement loading control method and uses plane stress analysis to simulate the test. The initial displacement is 0.0002 mm, the single-step increment is 0.0004 mm, Q is the horizontal constraint, and Q is 0.5 MPa.

4. Results and Discussion

4.1. Stress Distribution Characteristics and Confinement Effect. Figure 7 shows the elastic modulus and internal maximum principal stress distribution in the initial stage of the specimen loading. In Figure 7, the brighter the area, the greater the stress, and vice versa. It can be seen from Figure 7(b) that the internal stress distribution is not uniform due to the existence of mesouniformity, and the unconstrained particles lead to the concentrated stress distribution due to the small contact area between the upper and lower end faces and the loading plate. And the stress concentration on both sides of the constrained particles is caused by the constant confinement on both sides. There is significant stress concentration between the sandstone and the calcite at the interface (a weak structural plane). This shows that the existence of calcite veins in sandstone and the heterogeneity of the mesostructure have a significant influence on the stress distribution.

Due to the different loading conditions, the irregular particles produced significantly different mechanical responses during the breakage process. As shown in Figures 8 and 9, the presence of confinement increases the initial stiffness of the particles compared to the particles without confinement, resulting in an increase in particle strength. There are obvious brittle-ductile transition processes in load-displacement curves under different loading conditions, and the load-displacement curve of the stationary phase of the constrained particle showed strong jagged fluctuations during the loading process, which is caused by the complex stress response caused by the microfracture inside the particle. In the subsequent breakage process, more acoustic emission signals are generated and more energy is released, which shows better ductility than unconstrained particles. This result seems to support the research conclusion of Tang et al. [5]. With confinement, particles are in breakage in a
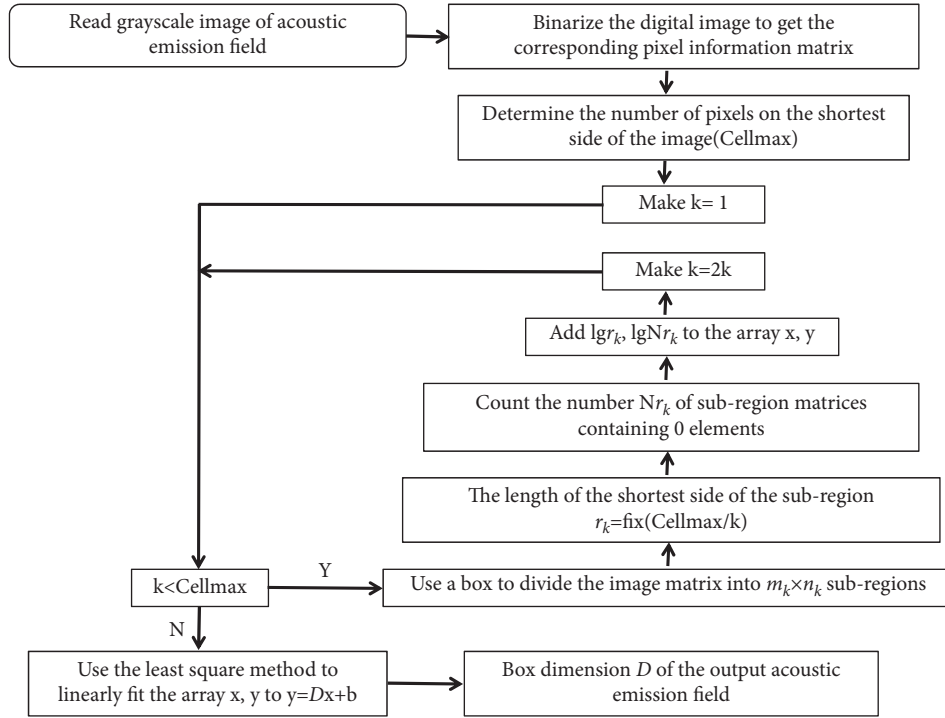
Figure 4: Schematic diagram of box dimension calculation based on acoustic emission field.

node
element

□ calcite
■ sandstone
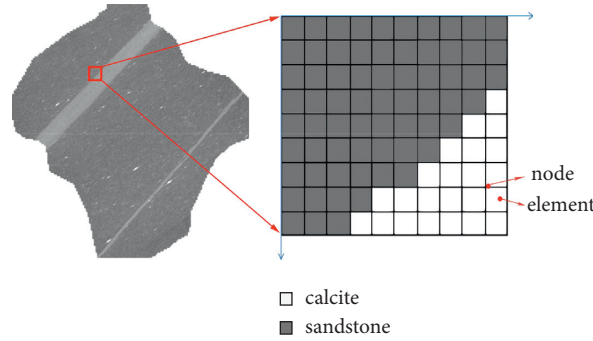
Figure 5: Finite element conversion process of sandstone particle digital image.

Table 1: Material parameters of a rock sample.

Material	Elastic modulus (GPa)	Compressive strength (MPa)	Poisson ratio	Compression-tension ratio	Internal friction angle (C°)
Sandstone	108.2	118	0.16	14	35
Calcite	80.5	101	0.30	10	30
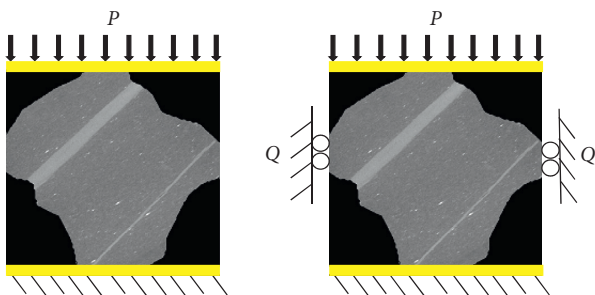
Figure 6: Mechanical loading diagram of the numerical model.

more ductile manner, and the maximum load required for failure is 245 N higher than the maximum load required for without confinement particles, which is about 11.9% of the maximum load, and without confinement, particles are in breakage in a more brittle manner.

4.2. Acoustic Emission Evolution Characteristics.
The evolution process of rock mass damage is essentially the use of dissipated energy to form damage, leading to loss of strength. The release of elastic energy stored in the rock mass unit is the internal cause of the sudden failure of the rock mass unit.

Without
confinement

(a)

Without
confinement

(b)

With
confinement

(c)

With
confinement

(d)
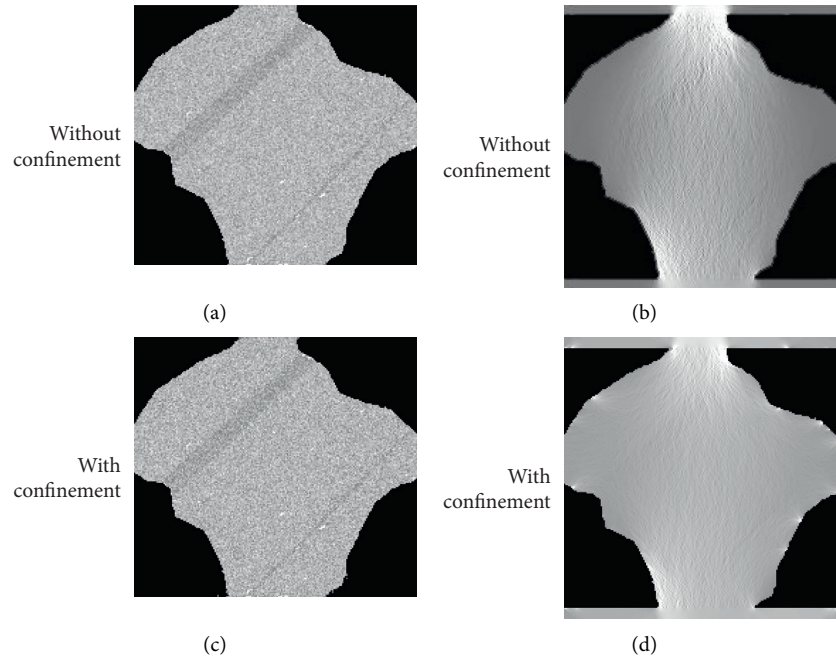
FIGURE 7: Distribution of the elastic modulus and maximum principal stress of the specimen during the initial loading.
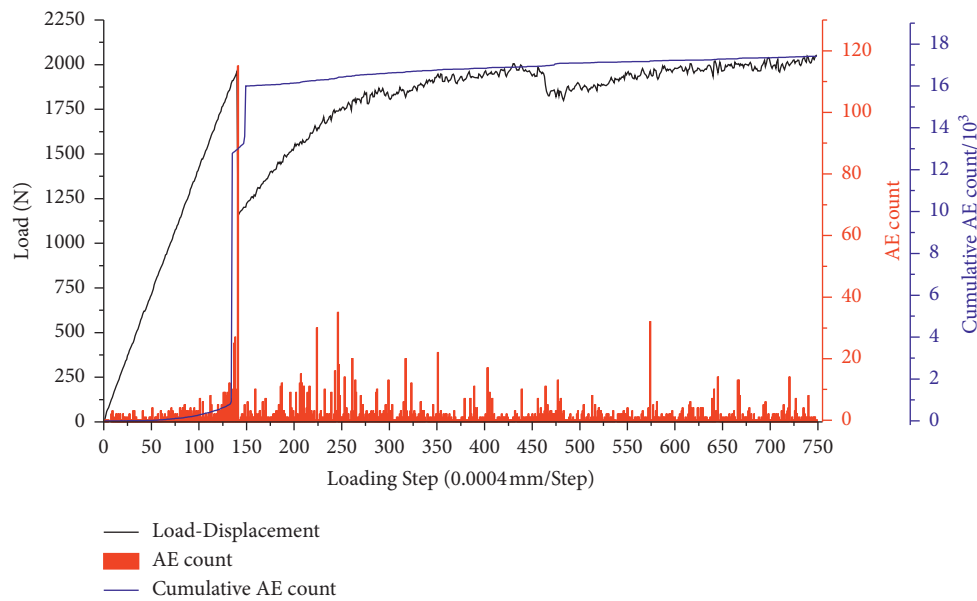
FIGURE 8: Load-AE and cumulative AE displacement curves of a particle under diametral loading with confinement.

Acoustic emission refers to the elastic wave emitted by the rapid release of local energy of the rock under the action of a load and is an effective tool for studying the internal damage evolution process of the rock. In RFPA2D, due to the failure of the sample element, elastic energy stored in the deformation process is released. Assume that the failure of every sample element represents the source of the acoustic emission. By recording the energy release for respective damaged elements and their number, RFPA2D is able to simulate the acoustic emission activity [5]. Figures 8 and 9 are trend graphs of load-displacement, AE count, and cumulative AE count varying

with loading step under different loading conditions. In the figure, it can be seen that the load-displacement curve is synchronized with the AE-load step change. For the without confinement particle specimens, in the early stage of loading (steps 1–132), there are fewer acoustic emission events, the AE signal is relatively weak, the stress is in the linear elastic stage, and the cumulative acoustic emission events show a gentle change and microcracks initiate. The cumulative acoustic emission events show linear growth in the middle (steps 132–139) loading period; after the loading reaches the maximum load, the acoustic emission events are the most, the
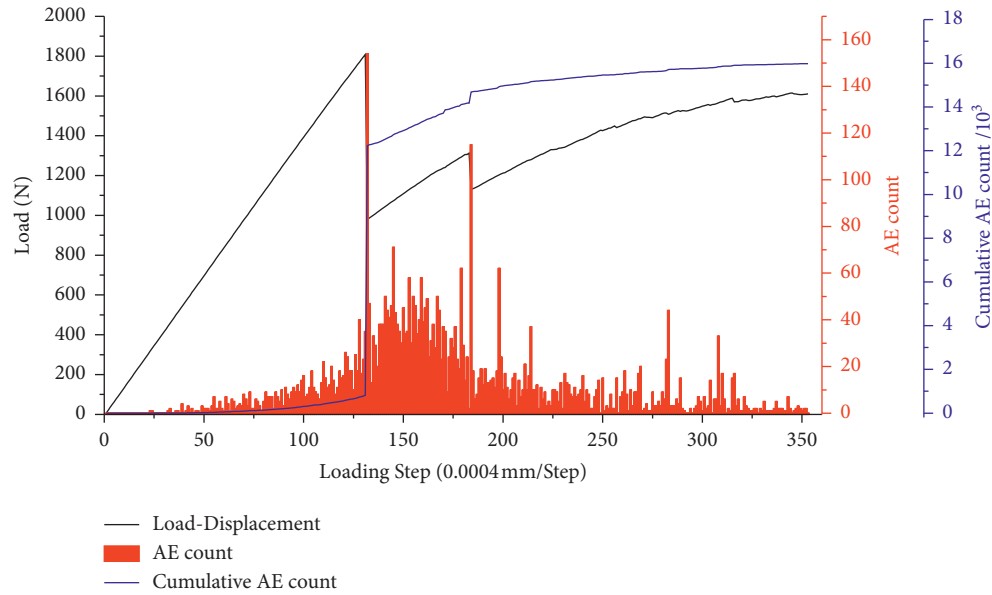
FIGURE 9: Load-AE and cumulative AE displacement curves of a particle under diametral loading without confinement.

AE signal is the strongest, a strong load drop phenomenon occurred, and the cracks extended and expanded sharply until they penetrated; the particles break (steps 132–139 in Figure 10) to form a macrofragmentation zone and consume most of the energy of the whole fracture process. In the later stage of loading (steps 139–350), in addition to the phenomenon of load drop again in step 189, the cumulative acoustic emission event showed a gentler change with a smaller change, and the particles completely broke. For the with confinement particle specimens, in the early stage of loading (steps 1–141), there are fewer acoustic emission events, the AE signal is relatively weak, the stress is in the linear elastic stage, there are obvious cracks, and the cumulative acoustic emission events show a gentle change. The cumulative acoustic emission event showed a sharp change in the middle of loading (steps 141–147), the acoustic emission event produced a jump growth when the maximum load is reached, the signal is extremely strong, there is a strong load drop phenomenon, and the particles break (steps 141–147 in Figure 10) to form a macrofragmentation zone and consume most of the energy of the whole fracture process. The load decreases and the AE value decreases significantly after the particle breakage at the later stage of loading (steps 147–749), but because the particle still has a certain residual strength, it still has a certain bearing capacity, and with the increase of the axial load, the original cracks further expanded and many new cracks were produced at the same time the cumulative change of the acoustic emission event is small. The particles completely break at this time. Accumulated acoustic emission events indicate that, with confinement particles consuming more energy during the breakage phase than without confinement particles (Figure 8), the greater the energy given to the particles, the finer the particles they produce and the better the final breakage effect.

4.3. Analysis of the Crack Propagation and Fracture Evolution of the Particle.

Figure 10 is the evolution diagram of acoustic emission and elastic modulus of irregular particle specimen's breakage process under different loading conditions. In the acoustic emission diagram, white indicates that the element has a compression-shear failure in the current loading step, black indicates that the elements have been completely damaged in the current loading step, and yellow indicates that the element has a tensile failure in the current loading step.

The figure clearly indicates that, in the unconstrained particle specimen, the initiation of cracks starts at the middle of the calcite veins. The initial crack and the horizontal plane of the specimen are about 45° angle from the cementation of the calcite vein and the sandstone (weak surface) and extend along the right upper part of the calcite vein. As the axial stress increases, the crack changes its propagation direction and grows steadily along the direction of the maximum principal stress. It can be seen from the acoustic emission evolution diagram that cracks initiation and expansion are caused by tensile failure. A large amount of tensile failure occurred inside the specimen when loaded to step 139, which led to the penetration of cracks. This is due to the low tensile strength of sandstone. In the without confinement compression state, the tensile stress first reaches the tensile strength and eventually forms a tensile failure. With confinement particle specimen, Tang et al. showed that the cracks were mainly caused by the progressive instability near the upper load point and then started in the shear zone between the upper load point and the lower-left load point [5]. However, due to the fact that the real mesostructure and mesoheterogeneity of particles are considered in this paper, the crack is formed along the middle part of the calcite vein and extends along the direction of maximum principal stress. A second tensile crack is formed along the lower-left part of the calcite vein when loading to step 145; with the
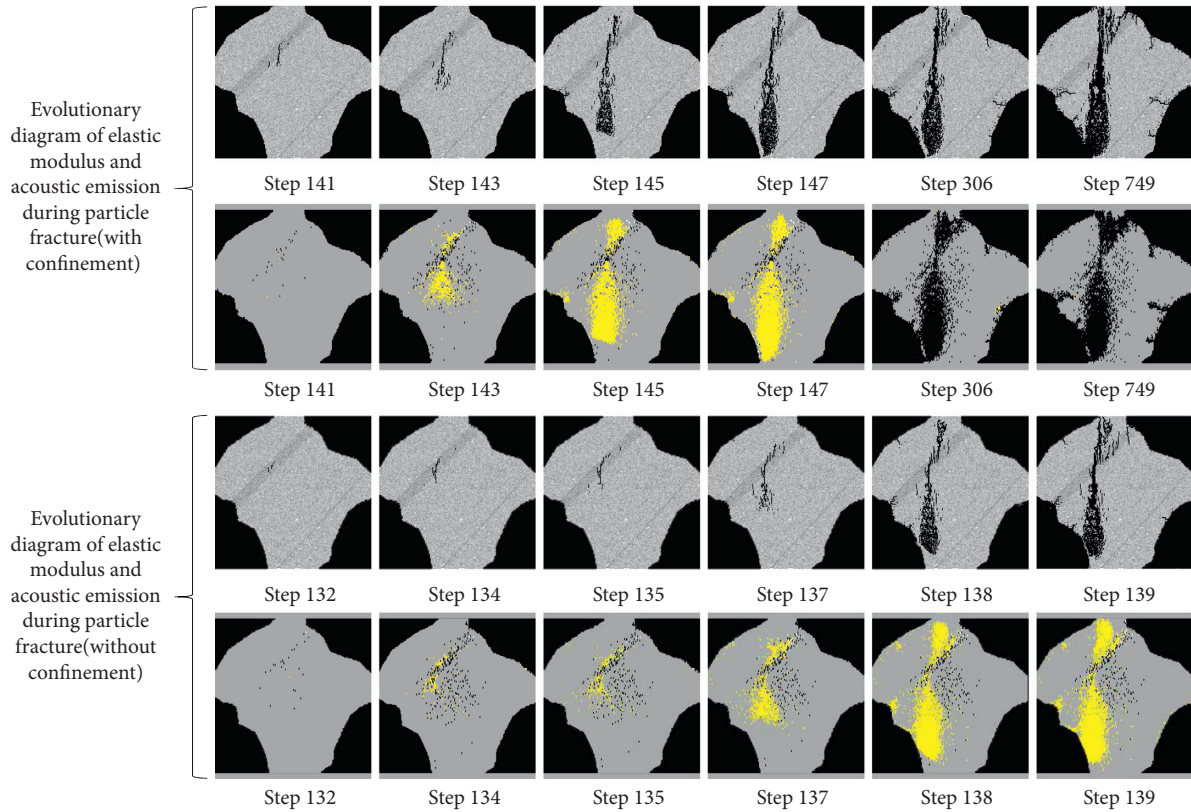
FIGURE 10: Evolutionary diagram of acoustic emission and elastic modulus of irregular particles during fracture.

increase of axial stress and the influence of confinement, a large amount of tensile failure occurred inside the specimen when loaded to step 147, which led to the penetration of the main crack and eventually formed tensile failure. Although the breakage of the particles under both loading conditions is tensile type failure, the with confinement particles show a more destructive nature, which is consistent with the study of Tang et al. [5].

Whiten et al. proposed two breakage functions to describe two different breakage modes; the first is the "catastrophic" breakage mode which produces a small number of coarse particles, and the second is to produce fine particles between the contact point between the liner of the crusher and the particles and the adjacent loading point [35]. Our study shows that the particles produce two different sizes of particles during the breakage: one is coarse particles due to tensile failure and the other is fine particles due to shear or compression failure near the load point (Figure 10). However, our results seem to be consistent with these conclusions.

4.4. Fractal Characteristics and Mesoscale Fracture Damage Degree Based on Box Dimensions.

The microfracture evolution can be described quantitatively using the damage variable; however, the damage variable does not adequately reflect the spatial distribution of microfractures, and yet the spatial relationships of microfractures are directly related to the macroscopic fracture of the sample. Xie et al. showed that

the fracture process of rock has self-similarity, which is manifested by the fact that the fracture process has fractal characteristics [36]. Every microfracture is accompanied by a measurable transient elastic wave generated by the rapid release of sound energy, known as acoustic emission. These acoustic emissions can be used to characterize the entire failure process of a rock, and hence the acoustic emission of rock failure has fractal features. Thus, using the fractal dimension determined from the acoustic emission field as the characteristic parameter to illustrate the evolution of mesoscale damage of the rock particles quantitative analysis of the evolution of mesoscale failure of the rock particles, damage evolution, and macrodamage characteristics of the mesoelement of the material can be done effectively. This data can be used to develop a relationship between the mesoscale fracture damage degree of the rock ω (hereinafter referred to as "fracture damage degree") and the fractal dimension value D corresponding to the "acoustic emission field," which can be expressed as

$$\omega = \frac{D - D0}{D^{\max} - D0}, \qquad (11)$$

where D is the fractal dimension of the damaged area of the mesoscopic element of the rock particles after stress loading; D_0 is the fractal dimension of the initial damage area of the mesoscopic element of the rock particles before stress loading; $D^{\max}$ is the fractal dimension when the mesoscopic element of the rock particles reaches the maximum damage area, for plane problems, $D^{\max} = 2$, and for three-
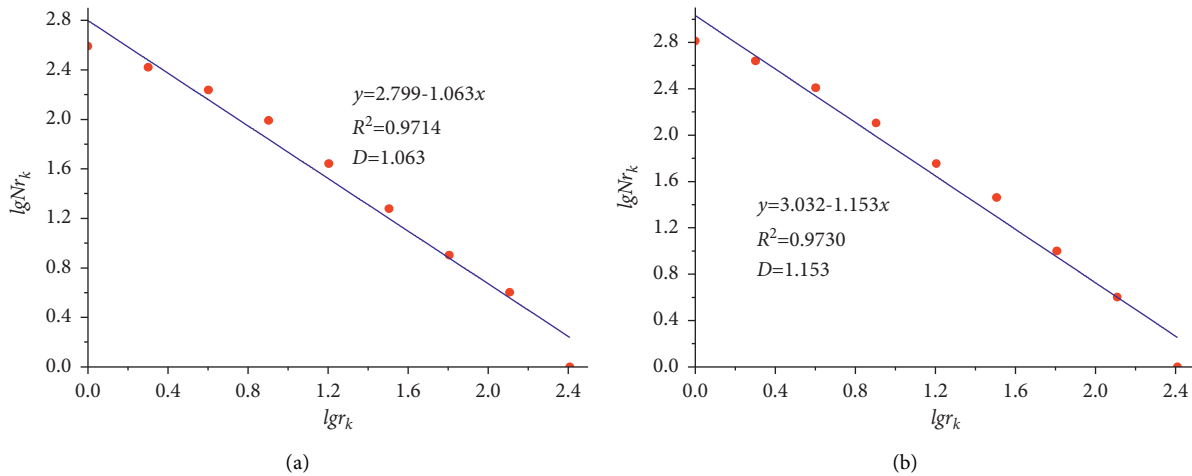
FIGURE 11: Calculation results of fractal dimension of the irregular particle (without confinement).

dimensional problems, $D^{max} = 3$. It can be seen from (11) that, before stress loading, $\omega = 0$; that is, the degree of material damage is 0. When the rock particles are in complete failure under the action of stress, it reaches $D = D_{max}$, then $\omega = 1$, and the material damage degree is 1.

In order to study the fractal characteristics of the mesoscale fracture evolution of irregular sandstone particles, the fractal dimension (see Section 2.3 in this paper) will be used to characterize the damage degree and load of rock particle breakage. Based on MATLAB platform, the fractal dimension under different stress conditions is calculated. Figure 11 shows the fractal fitting diagrams of irregular particle (without confinement) breakage when the stress level is 90% and 100%, respectively. The correlation coefficients are $R^2 = 0.9714$ and $R^2 = 0.9730$, respectively, indicating that the fractal dimension has a high degree of confidence, and its values are $D = 1.603$ and $D = 1.153$, respectively. Table 2 shows the fractal dimensions and damage degree of the sample under different stress conditions.

Figure 12 shows the relationship between different stress levels and fractal dimensions of the specimen under different loading conditions, and Figure 13 shows the relationship between the fracture damage degree and the different stress levels of the specimen under different loading conditions. It can be seen from Figures 12 and 13 that, under different load conditions, as the stress increases, the internal damage for the sandstone particles continues to accumulate, the fracture damage degree and fractal dimension are constantly increasing, and their changes are synchronized. The load of the particle damage area and fractal dimension are positively correlated, and the increase of fractal dimension is synchronized with the change of damage. Figure 13 describes and corroborates the effect of loading conditions on particle damage degree from the perspective of the fractal. Under different loading conditions, sandstone particles are in the elastic stage when the stress level is 10%, both the fracture damage degree and the fractal dimension value are 0, indicating that there is no damage inside the sandstone particles. The fractal dimension of the particles under different

loading conditions will increase rapidly when the stress level is lower than 50%, in which the fractal dimension of the without confinement particles is generally higher than that of the with confinement particles, which is due to the existence of confinement increases the initial stiffness of the particles, resulting in an increase in the strength of the with confinement particles and a smaller amount of microfracture with a random and isolated distribution in the whole sample under the same stress conditions. The deformation of the sample is more uniform, and the interaction between the microcracks is not obvious, which reflects the low degree of damage of the sample and the random characteristics of material properties, and its damage shows a certain lag. Finally, at a stress level of 100%, the degree of fracture damage is 0.733, and the fractal dimension value of the with confinement particles is 1.466. The fractal dimension value of the without confinement particles is 1.153 when the stress level is 100%, and the fracture damage degree is 0.577, all of which are smaller than the with confinement particles. The reason for further analysis shows that the final failure mode of with confinement particles is more complicated than that of without confinement particles, the breakage is more complete, and the damage is more serious, so the damage degree and the fractal dimension are larger. Therefore, the greater the degree of fracture damage is, the more severe the particle will eventually fracture, and the better the crushing effect, the larger the value of the fractal dimension and the more complex the particle's final failure mode.

Figure 14 shows the adequate relationship between the fractal dimension of particle breakage and load at different stress levels under different loading conditions, the correlation coefficients are $R^2 = 0.9872$ and $R^2 = 0.9624$, respectively, and the fitting relationship expressions are $P = 180 + 1319.44D^{1.49}$ and $P = 188 + 1347.69D$, respectively. The breakage load of without confinement particles and the fractal dimension approximately follow the power exponential relationship; the breakage load of the with confinement particles and the fractal dimension approximately follow a linear relationship. As shown in Figure 14, with the

TABLE 2: The fractal dimension value and damage degree of the specimen under different stress conditions.

Numerical sample		Stress level									
		10%	20%	30%	40%	50%	60%	70%	80%	90%	100%
Without confinement	D	0	0.182	0.416	0.588	0.688	0.837	0.878	0.971	1.063	1.153
	ω	0	0.091	0.226	0.294	0.344	0.419	0.439	0.485	0.532	0.577
With confinement	D	0	0.153	0.288	0.563	0.686	0.860	0.913	0.980	1.070	1.466
	ω	0	0.077	0.144	0.282	0.343	0.430	0.457	0.490	0.535	0.733
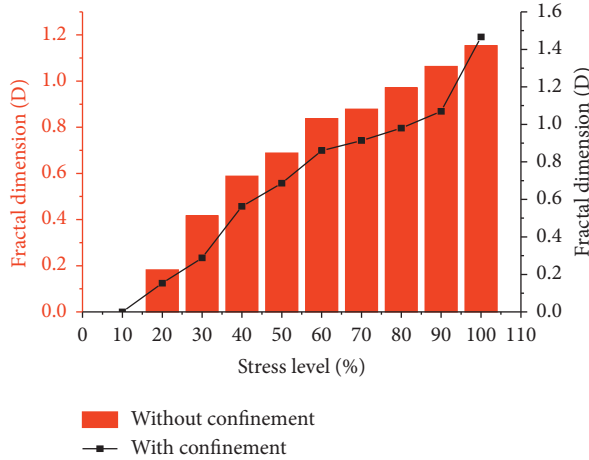
FIGURE 12: Relationship between stress levels and corresponding fractal dimensions.

FIGURE 14: Relationship between diametral load and fractal dimension under different loading levels.

FIGURE 13: Relationship between damage degree and different stress levels.

increase of the fractal dimension, the load of sandstone particles continues to increase. This is due to the development, expansion, and penetration of different-scale cracks within the particles, which lead to the destruction of the particles; it is the result of the initial mesoscopic damage in the internal particle structure developing to the macroscopic breakage. The higher the breakage load is, the more developed the internal cracks of the particle are, and the more the damage elements will be generated, the larger the

fracture damage degree and fractal dimension are; the fracture damage degree and fractal dimension can better characterize the damage evolution process of sandstone particle mesoscale fracture. Therefore, the load of particle crushing can be quantitatively described by the fractal dimension, and the fracture damage degree can be used to characterize the damage of the particle.

In summary, the fractal dimension can be used to characterize the complexity of irregular particle failure and can be used to predict failure strength, and the degree of damage can be characterized by the fracture damage degree. Therefore, it is very effective to apply fractal theory to rock particle fragmentation; we can use the method of this paper to calculate the fracture damage degree and fractal dimension to analyze the damage mechanical characteristics of irregular particles, which provides a new way to quantitatively evaluate the damage degree and crushing effect of irregular particles under load.

5. Conclusion

(1) A box dimension program for mesoscale failure analysis of irregular rock particles was developed based on the MATLAB platform, and the calculation method of fractal dimension of irregular rock particles mesoscale failure is proposed. This method can quantitatively describe the damage evolution process of irregular rock particles.

(2) The maximum fracture damage degree and fractal dimension of with confinement particles are 0.733 and 1.466, respectively, and the without confinement particles are 0.577 and 1.153, respectively. The final failure mode of with confinement particles is more

complicated than that of without confinement particles, the breakage is more complete, and the damage is more serious. Therefore, the greater the degree of fracture damage is, the more severe the particle will eventually fracture, and the better the crushing effect, the larger the value of the fractal dimension and the more complex the particle's final failure mode.

(3) The fractal model of irregular rock particles breakage under different loading conditions is established; that is, the fractal dimension of with confinement particles and load are approximately linear, and the fractal dimension of without confinement particles and load are approximately powered exponential relationship. Fractal dimension can be used quantitatively to describe a load of particle breakage under different loading conditions to explore the inherent law of rock particle breakage.

Data Availability

The data used to support the findings of this study are available from the corresponding author upon request.

Conflicts of Interest

The authors declare no conflicts of interest.

Acknowledgments

References

[1] C. M. Evertsson, "Cone crusher performance," Ph.D. thesis, Chalmers University of Technology, Gothenburg, Sweden, 2000.

[2] V. S. Vutukri, R. D. Lama, and S. S. Saluja, *Handbook on Mechanical Properties of Rocks*, pp. 87–140, Trans Technical Publications, Stafa-Zurich, Switzerland, 1974.

[3] O. Tsoungui, D. Vallet, and J. C. Charmet, "Numerical model of crushing of grains inside two-dimensional granular materials," *Powder Technology*, vol. 105, pp. 190–198, 1999.

[4] G. R. McDowell and O. Harireche, "Discrete element modelling of soil particle fracture," *Géotechnique*, vol. 52, no. 2, pp. 131–135, 2002.

[5] C. A. Tang, X. H. Xu, S. Q. Kou, P.-A. Lindqvist, and H. Y. Liu, "Numerical investigation of particle breakage as applied to mechanical crushing—part I: single-particle breakage," *International Journal of Rock Mechanics and Mining Sciences*, vol. 38, no. 8, pp. 1147–1162, 2001.

[6] Y. J. Zuo, Q. Zhang, T. Xu, Z.-H. Liu, Y.-Q. Qiu, and W.-C. Zhu, "Numerical tests on failure process of rock particle under impact loading," *Shock and Vibration*, vol. 2015, pp. 1–12, 2015.

[7] Bo Zhou, D. Wei, Ku Quan, J. Wang, and A. Zhang, "Study on the effect of particle morphology on single particle breakage using a combined finite-discrete element method," *Computers and Geotechnics*, vol. 122, pp. pp1–12, 2020.

[8] D. Wei, B. Zhao, D. Dias-da-Costa, and Y. Gan, "An FDEM study of particle breakage under rotational point loading," *Engineering Fracture Mechanics*, vol. 212, pp. 221–237, 2019.

[9] Y. Wang, X. Shang, and K. Peng, "Relocating mining microseismic earthquakes in a 3-D velocity model using a windowed cross-correlation technique," *IEEE Access*, vol. 8, pp. 37866–37878, 2020.

[10] H. Liu, Y. J. Zuo, Z. H. Wu, and W. Sun, "Fractal analysis of mesoscale failure evolution and microstructure characterization for sandstone using DIP, SEM-EDS, and micro-CT," *International Journal of Geomechanics*, vol. 21, no. 9, Article ID 04021153, 2021.

[11] C. Liang, Y. Wang, G. Tan, L. Zhang, Y. Zhang, and Z. Yu, "Analysis of internal structure of cement-stabilized macadam based on industrial CT scanning," *Advances in Materials Science and Engineering*, vol. 2020, no. 2, pp. pp1–10, 2020.

[12] Y. Li, Y. Zhao, Y. Jiang, Bo Zhang, H. Song, and B. Liu, "Characteristics of pore and fracture of coal with bursting proneness based on DIC and fractal theory," *Energies*, vol. 13, 2020.

[13] X. Y. Shang, Y. Wang, and R. Y. Miao, "Acoustic emission source location from P-wave arrival time corrected data and virtual field optimization method," *Mechanical Systems and Signal Processing*, vol. 163, Article ID 108129, 2022.

[14] Q. Yu, W. Zhu, C. Tang, and T. Yang, "Impact of rock microstructures on failure processes-Numerical study based on DIP technique," *Geomechanics and Engineering*, vol. 7, no. 4, pp. 375–401, 2004.

[15] Z. H. Wu, Y. J. Zuo, S. Y. Wang et al., "Numerical simulation and fractal analysis of mesoscopic scale failure in shale using digital images," *Journal of Petroleum Science and Engineering*, vol. 145, pp. 592–599, 2016.

[16] J. Lemaitre, *Evaluation of Dissipation and Damage in Metals Submitted to Dynamic Loading, Mechanical Behavior of Materials*, National Technical Reports Library, Guthrie, Gregory, 1972.

[17] C. A. Tang, L. G. Tham, S. H. Wang, H. Liu, and W. H. Li, "A numerical study of the influence of heterogeneity on the strength characterization of rock under uniaxial tension," *Mechanics of Materials*, vol. 39, no. 4, pp. 326–339, 2007.

[18] W. C. Zhu, J. Liu, C. A. Tang, X. D. Zhao, and B. H. Brady, "Simulation of progressive fracturing processes around underground excavations under biaxial compression," *Tunnelling and Underground Space Technology*, vol. 20, no. 3, pp. 231–247, 2005.

[19] C.-l. Wang, Z. Chen, Z.-f. Liao et al., "Experimental investigation on predicting precursory changes in entropy for dominant frequency of rockburst," *Journal of Central South University*, vol. 27, no. 10, pp. 2834–2848, 2020.

[20] Q. Xie, C. X. Jiang, and J. M. Ling, *Meso-Mechanics of Rock-Experiment and Analysis*, Southwest Jiaotong University Press, Chengdu, China, 1997, in Chinese.

[21] G. Li and C.-A. Tang, "A statistical meso-damage mechanical method for modeling trans-scale progressive failure process of rock," *International Journal of Rock Mechanics and Mining Sciences*, vol. 74, pp. 133–150, 2015.

[22] Z. Li, L. Li, B. Huang et al., "Numerical investigation on the propagation behavior of hydraulic fractures in shale reservoir based on the DIP technique," *Journal of Petroleum Science and Engineering*, vol. 154, pp. 302–314, 2017.

[23] S. Wang, S. Sloan, D. Sheng, and C. Tang, "Numerical analysis of the failure process around a circular opening in rock," *Computers and Geotechnics*, vol. 39, pp. 8–16, 2012.

[24] S. Wang, S. Sloan, C. Tang, and W. Zhu, "A numerical investigation of the failure mechanism around tunnels in transversely isotropic rock masses," *Tunnelling and Underground Space Technology*, vol. 32, pp. 231–244, 2012.

[25] H. Xie, *Fractals in Rock Mechanics*, A A Balkema, Rotterdam, Netherlands, 1993.

[26] J. Li, Q. Du, and C. Sun, "An improved box-counting method for image fractal dimension estimation," *Pattern Recognition*, vol. 42, no. 11, pp. 2460–2469, 2009.

[27] C. A. Tang, "Numerical simulation of progressive rock failure and associated seismicity," *International Journal of Rock Mechanics and Mining Sciences*, vol. 34, no. 2, pp. pp249–261, 1997.

[28] Q. Yu, W. Zhu, C. a. Tang, and T. Yang, "Impact of rock microstructures on failure processes - numerical study based on DIP technique," *Geomechanics and Engineering*, vol. 7, no. 4, pp. 375–401, 2014.

[29] H. Liu, L. Zheng, Y. Zuo et al., "Study on mesoscopic damage evolution characteristics of single joint sandstone based on micro-CT image and fractal theory," *Shock and Vibration*, vol. 2021, Article ID 6547028, 2021.

[30] W. Weibull, "A statistical distribution function of wide applicability," *Journal of Applied Mechanics*, vol. 18, pp. 293–297, 1951.

[31] C. A. Tang, H. Liu, P. K. K. Lee, Y. Tsui, and L. G. Tham, "Numerical studies of the influence of microstructure on rock failure in uniaxial compression - part I: effect of heterogeneity," *International Journal of Rock Mechanics and Mining Sciences*, vol. 37, no. 4, pp. 555–569, 1997.

[32] F. Rossi, A. D. Carlo, and P. Lugli, "Microscopic theory of quantum-transport phenomena in mesoscopic systems: a Monte Carlo approach," *Physical Review Letters*, vol. 80, no. 15, 1998.

[33] R. Y. Rubinstein and D. P. Kroese, *Simulation and the Monte Carlo Method*, 707. John Wiley and Sons, USA, 2011.

[34] H. Diao, "Rock mechanical properties and brittleness evaluation of shale reservoir," *Acta Petrologica Sinica*, vol. 29, no. 9, pp. 3300–3306, 2013.

[35] W. J. Whiten, "The simulation of crushing plants with models developed using multiple spline regression," *Journal of the South African Institute of Mining and Metallurgy*, pp. 257–264, 1972.

[36] H. Xie, *An Introduction to Fractal - Rock Mechanics*, Science Press, Beijing, China, (in Chinese), 1996.

Research Article

Discussion on the Design and Performance of the Whole Packaging Box of Environmentally Friendly Packaging Materials

Mengwei Xie [ID] [1,2]

[1]*Design and Manufacturing Collaborative Innovation Center, China Academy of Art, Hangzhou 310012, Zhejiang, China*
[2]*Art Academy, Yunnan Minzu University, Kunming 650504, Yunnan, China*

Correspondence should be addressed to Mengwei Xie; 20191083@caa.edu.cn

More and more designers and companies in the packaging industry begin to pay attention to research on environmentally friendly packaging design. From studying the additional functions of packaging to starting to study the environmentally friendly materials of packaging, as well as the "zero-pollution" packaging advocated today, the traditional form and mode of packaging has changed. This article aims to study the design of the overall packaging box of environmentally friendly packaging materials and discuss its performance. In this paper, the platform construction method and the modulus definition classification method are used to calculate the positive axis stiffness of the single-layer board. The effect of coating process on the wear resistance of paper-based materials was studied, the wear resistance of box board base paper and coated box board under different temperatures and different humidity conditions was compared, and the optimal design variable value range was set. The experimental results show that after the first level of optimization, the overall mass of the structure is reduced from the initial 39.42 kg to 31.18 kg and the optimization efficiency is 20.90%; the maximum relative deformation of the flap structure has increased from 0.143 mm to 0.198 mm, despite having the maximum tension. The opening displacement has increased, but it still meets the sealing deformation requirements. The design and performance discussion of the overall packaging box of environmentally friendly packaging materials have been completed relatively well.

1. Introduction

With the development of social science, designers are no longer restricted by materials, technology, and money. People work hard to explore and explore all aspects of design, but designers often fall into misunderstandings and start to make novel designs, for example, design new materials with various functions and physical effects, such as new ceramic materials, new metal materials, optical fiber materials, and packaging materials. More product packaging on the market is addicted to excessive product stimulus consumption, and more designs begin to enjoy sensory stimulation. At present, the basic task of the designer is to create a more logical way of use for the public to care for nature and human development. In recent years, packaging has become a way to select and process products to enhance the brand. In this process, the final recycling becomes an important goal. Packaging design can play an important role in improving resource recovery and solving high energy consumption production. The concept of green packaging has been adopted by many designers at home and abroad, but few packaging designs can be made using this concept. At present, various designers have done a lot of case studies and studies on structures and materials and have explored various aspects from recycling to reducing packaging costs, so as to create a more realistic, healthier, and more meaningful future for mankind. The "zero-pollution" packaging design was born and developed.

With the rapid development of high and new technology, the requirements for the performance of new materials have also become higher and higher, which puts forward higher requirements for the development of materials science itself. New materials refer to newly developed or developing structural materials with excellent properties and

functional materials with special properties. To design a new type of material that meets the expected requirements and manufacture it through advanced processes and technologies, it is necessary to have a deep understanding of the relationship between the material's microstructure and macroscopic properties and theoretically assume a material system with a specific structure and function. The microstructure of a material refers to the structure of the atoms, ions, and molecules that make up a substance, and there is a great relationship between the macroscopic properties. Changes in the microstructure will lead to changes in the macroscopic properties of the material. For example, C60 and diamonds: the same material is composed of carbon atoms but constitutes two different substances. In the context of the rapid development of computer-aided technology, computer simulation is a way of materials science. The method is to simulate the composition, microstructure, process, and performance of the material based on computer simulation; computer simulation has become an important technical means to solve practical problems in materials science. Combined with a powerful computing system and a variety of specific algorithm simulation techniques, researchers have been able to achieve unprecedented detailed simulation and extremely precise research on the internal conditions of materials. The advantage of using computer simulation to conduct in-depth research on materials is that it cannot only simulate various experimental processes and understand the relationship between the internal microstructure of the material and the macroscopic material properties, but also can predict its macroscopic properties before the actual preparation of new materials. This provides theoretical guidance for the design of excellent new materials. When calculating materials, first choose an appropriate method based on the objects, conditions, requirements, and other factors to be calculated. To make a good choice, you must understand the classification of material calculation methods. The performance of a material depends to a large extent on the microstructure of the material, and the use of the material is different, and the microstructure scale that determines its performance will vary greatly. This kind of simulation experiment in material science research is more economical, efficient, and flexible than the experiment itself and can play its unique role in occasions where the experiment itself is difficult to achieve or cannot be carried out, especially in understanding the microstructure and its unique simulation experiment method. It is irreplaceable.

In recent years, many domestic and foreign scholars have conducted in-depth discussions and researches on this issue. Neves et al. studied the relationship between the compression deformation ability of the corrugated sandwich panel and its plastic vibration absorption ability and established a mathematical model of material friction and wear. But his research did not discuss the friction and wear mechanism of materials [1]. Wang studied the performance of corrugated cartons under vertical dynamic loads; dynamic load refers to the load on the body under the influence of vibration, environment, and other factors during the movement. He simplified the loaded cartons into a spring system and proposed that the main

reason for the failure of cartons during transportation is the dynamic load caused by vibration. But his research did not get the dynamic behavior of paper packaging and the corresponding formula [2]. Vahid and Iman have verified through a large number of experiments that when the input frequency of the corrugated box vibration is close or equal to the resonance frequency of the carton system, the dynamic load of the corrugated box will increase exponentially, which can be said to be a step closer to the foundation of the predecessors. But their research did not propose the corresponding algorithm and formula [3]. Nurul et al. successively proposed and developed the Holm-Archard model. The Holm-Archard model is an important tool for studying mold wear, steady-state deformation, adhesive wear models, and numerical analysis of wheel wear. This formula was originally used to analyze the mechanism of material adhesion wear, but later it was proved that the formula has similar expressions for other wear methods [4]. Wang et al. established an abrasive wear model based on the plastic deformation of the material. The strain range of the model is generated by a tapered wear surface. They also proposed that there is a critical strain value. If the critical value is exceeded, wear debris will be generated [5]. The research of Dissanayake et al. found that the ultrasonic wave is applied in the moving plane to make it vibrate. When the vibration frequency is given by the ultrasonic wave reaching 20 MHz or more, the friction decreases. However, his research did not carry out SEM observation on the worn surface of the material and the morphology of the abrasive [6]. The photosensitive coating material is a relatively important material on the packaging surface. It causes the color change of the photochromic material after being exposed to sunlight/ ultraviolet rays; when it loses sunlight/ultraviolet rays, it will return to its original color. Puscaselu uses the paper strip contact drum method to measure the friction coefficient between paper-based materials. In his research, the photoelectric counting technology is used to measure the friction coefficient of the photosensitive coating surface of the blueprint material. But his research did not study the improvement of the performance and coating of paper-based materials from the aspect of microscopic materials [7].

The innovations of this paper are as follows. (1) The concept of zero-pollution packaging design is proposed, which combines the production process and application of plastic profiles with the concept of green environmental protection to meet the development needs of the new era. (2) According to the assumption of invariance of the straight normal, the strain at the middle distance z in the laminate is defined, and the Cauchy equation is used, which greatly improves the data accuracy of the algorithm. (3) In the discussion section, the relationship between materials and packaging design is proposed, and aesthetic ideas such as the perception of the visual beauty of materials in packaging design are perceived, and the humanities content and the science and engineering thinking content are combined, making the research introduction very comprehensive.

2. Design and Performance of the Overall Packaging Box of Environmentally Friendly Packaging Materials

2.1. Concept of "Zero-Pollution" Packaging Design. Zero pollution can also be understood as "zero-waste" [8]. It originally came from the concept of zero waste proposed in the field of waste recycling [9]. This concept can be applied to packaging design and can also be applied to modern green environmental protection design concepts. This is actually one of the designs they support. This method supports the redesign of packaging material resources [10], reducing or not generating packaging waste. On this basis [11], the concept of zero-pollution packaging design came into being, considering the final problem from the source of the design [12]. The point is such that when the packaging function of the product packaging is completed, the packaging can also become a part of the product, achieving the purpose of not generating any garbage in the packaging and solving the problem of packaging pollution [13] and so making continuous use of pollution-free packaging [14].

The zero-pollution packaging design covers the whole process of packaging basic products, from materials, structure, and decoration to the final packaging waste, with functional optimization as the main goal [15]. Zero-pollution packaging design is currently a method and development direction for people to solve environmental pollution problems in the field of packaging design. Its main purpose is to help society solve the pollution problem [16]; it can balance the contradiction between human development and the natural environment and find the best way [17]. Zero-pollution packaging has been tried abroad. For example, as edible wrapping paper, Japan has developed a wrapping paper made of chitosan polysaccharides extracted from shell materials. The Coca-Cola Company designed a self-melting ice bottle. The label on the bottle can protect consumers' hands and can be used as a wristband after use. The packaging materials are edible and easy to evaporate, having modern high-tech materials. They are solved through the daily human behavior after packaging and use, so as to solve the problems and contradictions in life and try to provide consumers with safety and convenience, bringing greater benefits [18]. The so-called zero-pollution package puts safety first. In addition to the basic functions of zero-pollution packaging to ensure packaging protection and safe transportation, all insignificant decorative elements must also be carefully removed [19]. Zero-pollution packaging not only has no waste pollution after packaging but also minimizes the structure and decorative elements of packaging materials, reduces unnecessary external transformations, reduces costs, and saves resources [20].

"Zero-pollution" packaging design is made to disappear the moment the product is used, besides the development direction of the so-called "zero-waste" packaging, so that the packaging itself can become a product. After the packaging function is used, according to the various environmental recycling characteristics of packaging materials, we will try to reduce the environmental impact of waste packaging pollution to "zero". The starting point of zero-pollution packaging design is not only to give people more beautiful and practical packaging, but, more importantly, it can arouse people's positive emotions and reduce the difficulties they face [21]. In the past, packaging designers only focused on the role of graphic agents in packaging design, but, now, designers realize that they can take the design as a whole and establish emotional connections with consumers and the market [22]. On the surface, the function of packaging is protecting the product, but this is also the easiest standard to meet. Faced with the current lack of environmental and social resources, it is the responsibility of packaging designers to awaken the environmental awareness of consumers and the entire society [23]. Zero-pollution packaging design can capture the emotional bond between consumers and society and remind designers to explore what improvements and research are being made on current product packaging design [24]. The overall plan of the plastic profile packaging line is shown in Figure 1.

2.2. Production Process and Application of Plastic Profile. Extrusion molding is a method in which materials are continuously passed through a die in a flowing state by heating and pressurizing in an extruder, also known as "extrusion". Compared with other molding methods, it has the advantages of high efficiency and low unit cost. The extrusion method is mainly used for the molding of thermoplastics and can also be used for some thermosetting plastics. The extruded products all have continuous profiles, such as tubes, rods, wires, plates, films, wire, and cable coatings. In addition, it can also be used for mixing, plasticizing, granulating, coloring, blending, etc. of plastics. Plastic profiles are plastic products with irregular cross-sections made by extrusion molding methods. They have a wide range of applications [25], especially plastic doors and windows. Plastic profiles are generally extruded through a plastic extruder, and the production process is shown in Figure 2.

The plastic film keyboard made of the finally obtained plastic profile section is shown in Figure 3.

2.3. Material Selection of Composite Packaging Boxes. The composite packaging box should be selected according to the specific performance requirements of the packaging box, and a composite material that combines a suitable reinforcement material and a matrix material should be selected. The properties of composite materials composed of different raw materials are also different, so the correct choice of materials is an important basis for designing composite packaging boxes.

At present, most of the reinforcing materials used in foreign composite packaging boxes are glass fiber, some of which are carbon fiber, and the matrix material is mostly epoxy resin or unsaturated polyurethane resin. Glass fiber is a kind of inorganic nonmetallic materials with excellent performance. There are many kinds of them. The advantages are good insulation, strong heat resistance, good corrosion
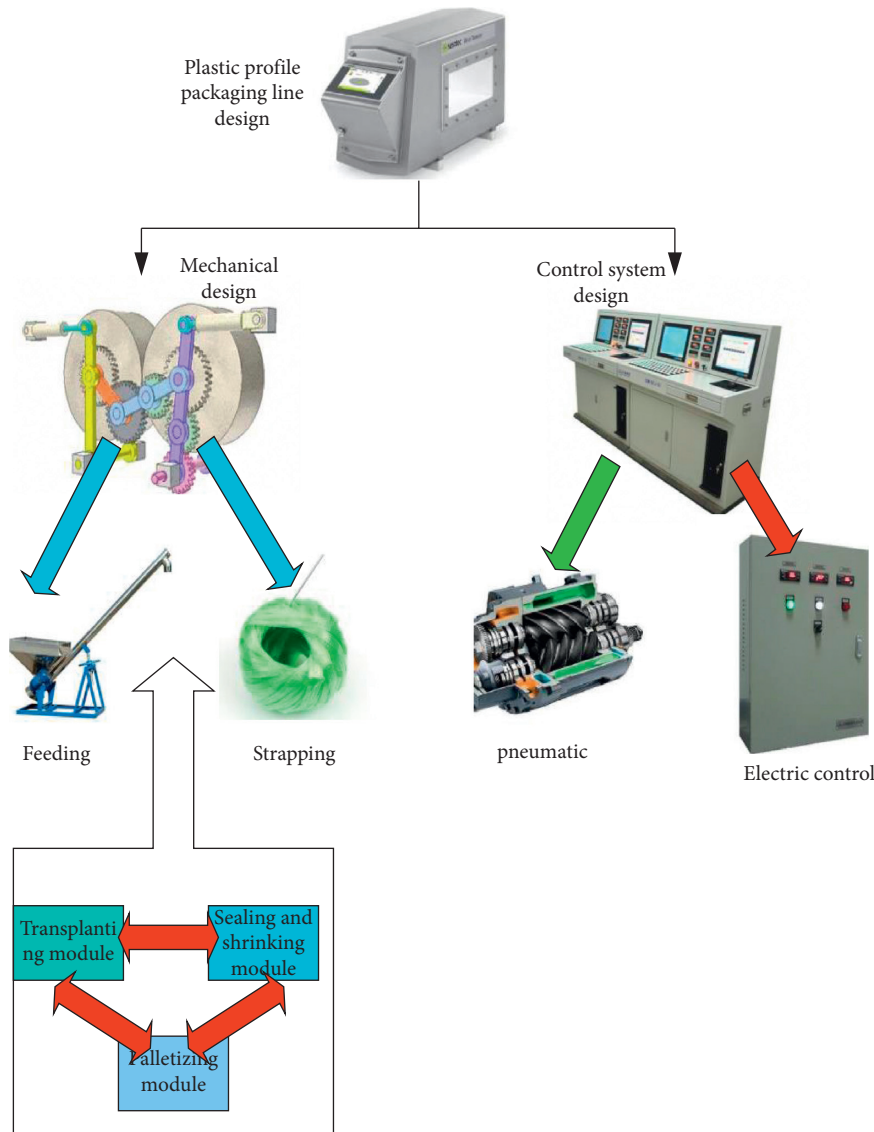
FIGURE 1: Plastic profile line diagram of the overall package.

resistance, and high mechanical strength. Carbon fiber is a special fiber composed of carbon elements. It has the characteristics of high temperature resistance, friction resistance, electrical conductivity, thermal conductivity, and corrosion resistance. Glass fiber was chosen because of its low price and good quality. Carbon fiber was chosen because it has better material properties than glass fiber and is suitable for more important occasions. Epoxy resin is chosen mainly because of its wide variety, easy hardening, strong adhesion, and low shrinkage. The cured epoxy resin has excellent mechanical and electrical properties and stable chemical properties. Since there are many types of glass fibers and epoxy resins, there are a large number of different combinations. In this paper, alkali-free glass fiber/epoxy resin composite material is selected as the raw material for the structural design of the packaging box. The following are the parameters related to the mechanical properties of materials, listing the performance parameters of such composite materials. In the design process of FRP packaging

boxes, the reasonable choice of raw materials determines whether the casting process is feasible; on the contrary, the casting process also limits the materials. Therefore, in the initial stage of designing FRP packaging boxes, it is necessary to consider choosing a suitable casting process [26].

When designing the structure of the composite material, the suitability of the respective casting process of the composite material should be fully considered. The casting process of composite materials mainly includes manual casting, RTM casting, vacuum casting, die casting, winding casting, and autoclave casting. The performance of the composite product is greatly affected by the casting process, and the appropriate casting process should be selected according to the shape of the composite component and the performance of the raw material [27]. The shape of the glass fiber reinforced plastic packaging box is a thin-wall reinforced closed structure, and manual pouring or vacuum pouring process can be selected. In the case of using the same raw materials, the strength, stiffness, and other physical
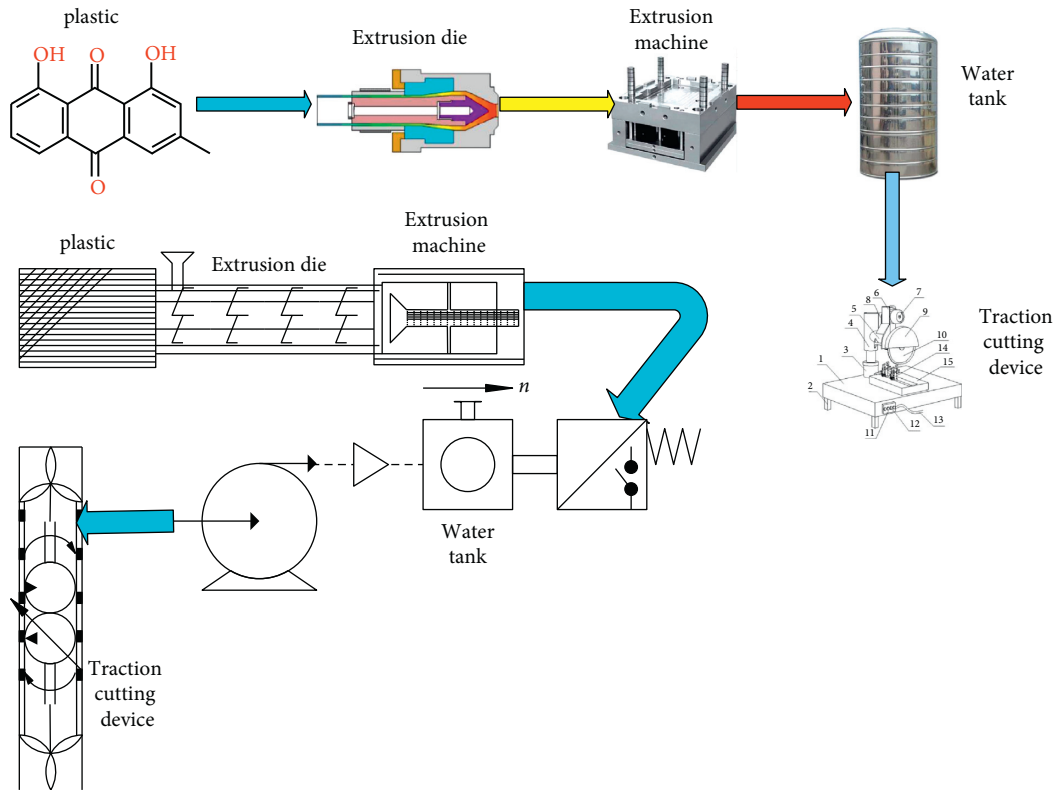
FIGURE 2: Plastic profile extrusion line.
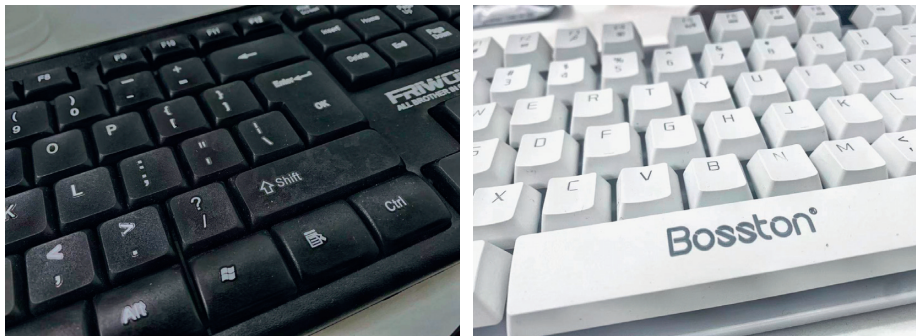
FIGURE 3: Plastic special-shaped membrane keyboard.

properties of the parts using the vacuum injection molding process can be increased by 30% to 50% or more than the parts using the vacuum injection molding process. Therefore, the vacuum injection molding process is preferred [28].

2.4. Positive Axis Stiffness of the Single-Layer Board. The positive axis stiffness of a single-layer board is the stiffness performance of the single-layer composite material on the positive axis. The positive axis stiffness has three forms of engineering elastic constant, modulus component, and compliance component, and these three forms can be converted mutually. The modulus component is the coefficient of the stress-strain relationship, usually used to find the stress from the strain, and is a set

of basic constants for calculating the stiffness of the laminate. According to the stress-strain matrix relationship of the single-layer board, the modulus component is defined as

$$\begin{bmatrix} \sigma_1 \\ \sigma_2 \\ \sigma_3 \end{bmatrix} = \begin{bmatrix} Q_{11} & Q_{12} & 0 \\ Q_{12} & Q_{22} & 0 \\ 0 & 0 & Q_{66} \end{bmatrix} \begin{bmatrix} \varepsilon_1 \\ \varepsilon_2 \\ \gamma_{12} \end{bmatrix}. \qquad (1)$$

It is stipulated that the angle θ rotating from the off-axis x to the positive axis 1 is positive when turning counterclockwise and negative when turning clockwise. If $m = \cos\theta$, $n = \sin\theta$, then

$$\begin{bmatrix} \varepsilon_1 \\ \varepsilon_2 \\ \gamma_{13} \end{bmatrix} = \begin{bmatrix} m^2 & n^2 & mn \\ n^2 & m^2 & -mn \\ -2mn & 2mn & m^2 - n^2 \end{bmatrix} \begin{bmatrix} \varepsilon_x \\ \varepsilon_y \\ \gamma_{xy} \end{bmatrix}. \tag{2}$$

$$[\varepsilon_1] = [T_\varepsilon][\varepsilon_x]. \tag{3}$$

From (1) to (3),

$$\begin{aligned} \{\sigma_x\} &= [T_\sigma]^{-1}[Q][T_\varepsilon]\{\varepsilon_K\} \\ &= |\overline{Q}|\{\varepsilon_x\}. \end{aligned} \tag{4}$$

$$\begin{bmatrix} \sigma_x \\ \sigma_y \\ \tau xy \end{bmatrix} = \begin{bmatrix} \overline{Q}_{11} & \overline{Q}_{12} & \overline{Q}_{16} \\ \overline{Q}_{12} & \overline{Q}_{22} & \overline{Q}_{26} \\ \overline{Q}_{16} & \overline{Q}_{26} & \overline{Q}_{66} \end{bmatrix} \begin{bmatrix} \sigma_1 \\ \sigma_2 \\ \tau_{12} \end{bmatrix}. \tag{5}$$

According to the assumption of invariance of the straight normal, the strain defining the distance to the midplane z in the laminate can be expressed as

$$\varepsilon_z = \frac{\partial w(x, y, z)}{\partial z} = 0,$$

$$Y_{zx} = \frac{\partial u(x, y, z)}{\partial z} + \frac{\partial w(x, y, z)}{\partial x} = 0, \tag{6}$$

$$Y_{yz} = \frac{\partial v(x, y, z)}{\partial z} + \frac{\partial w(x, y, z)}{\partial y} = 0.$$

Integrating z, respectively, we can get

$$w(x, y, z) = w(x, y),$$

$$u(x, y, z) = u_0(x, y) - z\frac{\partial w(x, y)}{\partial x}, \tag{7}$$

$$v(x, y, z) = v_0(x, y) - z\frac{\partial w(x, y)}{\partial y}. \tag{8}$$

Substituting (8) into the Cauchy equation, we can get

$$\varepsilon_x = \frac{\partial u_0}{\partial x} - z\frac{\partial^2 w}{\partial x^2},$$

$$\varepsilon_y = \frac{\partial v_0}{\partial y} - z\frac{\partial^2 w}{\partial y^2}, \tag{9}$$

$$\gamma_{xy} = \left(\frac{\partial u_0}{\partial y} + \frac{\partial v_0}{\partial x}\right) - 2z\frac{\partial^2 w}{\partial x\partial y}.$$

It can be expressed in matrix form as

$$\begin{bmatrix} \varepsilon_x \\ \varepsilon_y \\ \gamma_{xy} \end{bmatrix} = \begin{bmatrix} \varepsilon_x^0 \\ \varepsilon_y^0 \\ \gamma_{xy}^0 \end{bmatrix} + z\begin{bmatrix} \chi_x \\ \chi_y \\ \chi_{xy} \end{bmatrix}. \tag{10}$$

Among them,

$$\{\chi\} = \begin{bmatrix} \chi_x \\ \chi_y \\ \chi_{xy} \end{bmatrix} = -\begin{bmatrix} \dfrac{\partial^2 w}{\partial x^2} \\[2mm] \dfrac{\partial^2 w}{\partial y^2} \\[2mm] 2\dfrac{\partial^2 w}{\partial x\partial y} \end{bmatrix}. \tag{11}$$

Here, ε_x^0, ε_x^0, and γ_{xy}^0 are the midplane strains of the laminate, and substituting $\{\varepsilon\}$ into $\{\sigma\} = |Q|\{\varepsilon\}$, we get

$$\begin{bmatrix} \sigma_x \\ \sigma_y \\ \tau_{xy} \end{bmatrix}_k = \begin{bmatrix} \overline{Q}_{11} & \overline{Q}_{12} & \overline{Q}_{16} \\ \overline{Q}_{12} & \overline{Q}_{22} & \overline{Q}_{26} \\ \overline{Q}_{16} & \overline{Q}_{26} & \overline{Q}_{66} \end{bmatrix}_k \left(\begin{bmatrix} \varepsilon_x^0 \\ \varepsilon_y^0 \\ \gamma_{xy}^0 \end{bmatrix} + z\begin{bmatrix} \chi_x \\ \chi_y \\ \chi_{xy} \end{bmatrix} \right). \tag{12}$$

The resultant external force and the resultant external moment can be expressed as

$$\begin{bmatrix} N_x \\ N_y \\ N_{xy} \end{bmatrix} = \sum_{k=1}^{N} \int_{Z_{k-1}}^{Z_k} \begin{bmatrix} \sigma_x^{|k|} \\ \sigma_y^{|k|} \\ \sigma_{xy}^{|k|} \end{bmatrix} \mathrm{d}z,$$

$$\begin{bmatrix} M_x \\ M_y \\ M_{xy} \end{bmatrix} = \sum_{k=1}^{N} \int_{Z_{k-1}}^{Z_k} \begin{bmatrix} \sigma_x^{|k|} \\ \sigma_y^{|k|} \\ \sigma_{xy}^{|k|} \end{bmatrix} z\mathrm{d}z. \tag{13}$$

The parameters in the formula can be determined by experiments.

3. Experiment and Analysis of the Design and Performance of the Overall Packaging Box of Environmentally Friendly Packaging Materials

3.1. Problem Description and Model Establishment. Since the actual packaging structure is more complicated, including specific connection forms, such as screws and fins, and the actual packaging model does not form a closed space between each surface, a simplified model of the overall packaging is created based on MSC. Dytran large-scale commercial software is used for transition dynamics, including the introduction of fluid and solid finite element models, material composition relationships, application of acceleration loads, fluid-solid coupling surface, and integral step control and the appearance of a set of basic analysis programs for extracting impact loads. The specific flow chart is shown in Figure 4.

The packaging model defined in this chapter is a simplification of the actual model. Since the actual packaging structure is a thin-walled structure, its thickness is much smaller than the dimensions in the length and width directions. Therefore, in the finite element modeling, shell elements are used to simulate the structure. The packaging material adopts unidirectional board AS4/3502, the single-
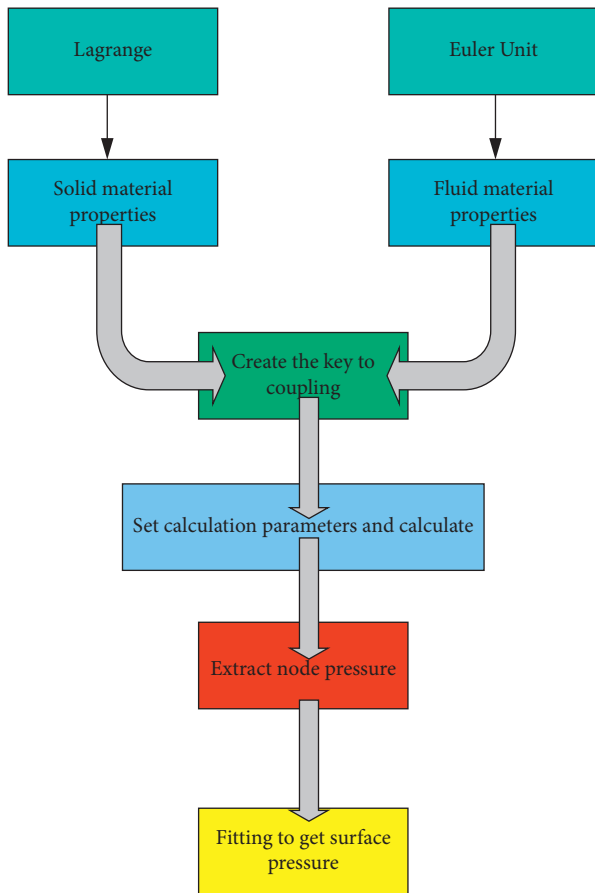
Figure 4: Impact load extraction flow chart.

Table 1: Material parameters of AS4-3502.

Parameter name	Material parameters	Value	Unit
Longitudinal modulus of elasticity	E_1	127500	MPa
Transverse elastic modulus	E_2	11300	MPa
In-plane shear modulus	G_{12}	6000	MPa
Principal Poisson's ratio	μ_{12}	0.3	-
Density	ρ	1.58	g/mm^3
Single-layer thickness	t	0.117	mm
Longitudinal tensile strength	X_t	1164	MPa

Table 2: Material parameters of AS4/3602.

Parameter name	Material parameters	Value	Unit
Longitudinal compressive strength	X_c	1060	MPa
Lateral tensile strength	Y_t	42	MPa
Transverse compressive strength	Y_c	207	MPa
In-plane shear strength	S	69	MPa

Table 3: Packaging layer and thickness distribution.

Area	Laying plan	Thickness/mm
Packing box siding	$[\pm 45/90]$	5.382
Packing frame ribs	$[45/0_3/-45/90_2]$	3.978
Cover structure	$[45/0/-45/90]_3$	8.424
Cover ribs	$[\pm 45/(0_3/45/90_3/-45)_3]$	7.956

layer thickness is 0.117 mm, the wall boards are the same, and the symmetrical layout is adopted. The materials of the total lining and the edging are all single-layer materials AS4/3502, using symmetrical plates. Material performance parameters are shown in Table 1.

The material parameters of AS4/3602 are shown in Table 2.

The thickness and layering plan of the components of the composite package are shown in Table 3.

3.2. Influence of the Coating Process on the Wear Resistance of Paper-Based Materials. By testing the dynamic friction coefficient of the surface when the cardboard and GCr steel balls are rubbed, the ability of the paper-based packaging material to resist the friction and wear of metal products under different process conditions is analyzed, and the best wear-resistant coating parameters are obtained, thereby developing a coating with wear-resistant function, cloth modified cardboard. The surface of the first-class cowhide noodle box paperboard is made with sulfate carpenter with two layers or one layer. It is suitable for the manufacture of corrugated cardboard for most product packaging. Because of its universality and representativeness, it is used to test the wear resistance of paper-based packaging materials. The chemical composition of the cardboard used in the experiment is shown in Table 4.

The surface friction coefficient of the coated cardboard gradually becomes uniform with time. This is because the coating makes the surface of various quantitative cardboards form a dense coating layer, which changes the original loose and porous paper surface. With the surface being smooth and flat, the coefficient of friction on the surface of all kinds of coated cardboard will be closer. The comparison of the friction coefficient values of different quantitative uncoated and coated box paperboards is shown in Figure 5.

The comparison of the abrasion resistance of the base paper of the box board and the coated box board at different temperatures is shown in Figure 6.

The comparison of the abrasion resistance of cardboard base paper and coated modified paper under different relative humidity conditions is shown in Figure 7.

The uncoated box board paper base of coated box board has much better wear resistance. At RH 50%, the coefficient of friction of coated cardboard is 49% lower than that of uncoated cardboard. At RH 90%, the coefficient of friction of coated cardboard is 60% lower than that of uncoated cardboard. This means that the higher the relative humidity, the higher the coefficient of friction of the coated paperboard. The abrasion resistance of the uncoated base paper is better than that of the uncoated base paper. This is because the superficial layer of the coated boxboard is filled with

TABLE 4: Chemical constituents of the first-class kraft faced liner.

Chemical name	CAS registry number	EC number	Content (%)
Wood fiber	65996-61-4	265-995-8	97
Starch	9005-25-8	232-679-6	1
Styrene-acrylate copolymer	24981-13-3	—	1
Polyacrylamide	9003-5-8	—	1
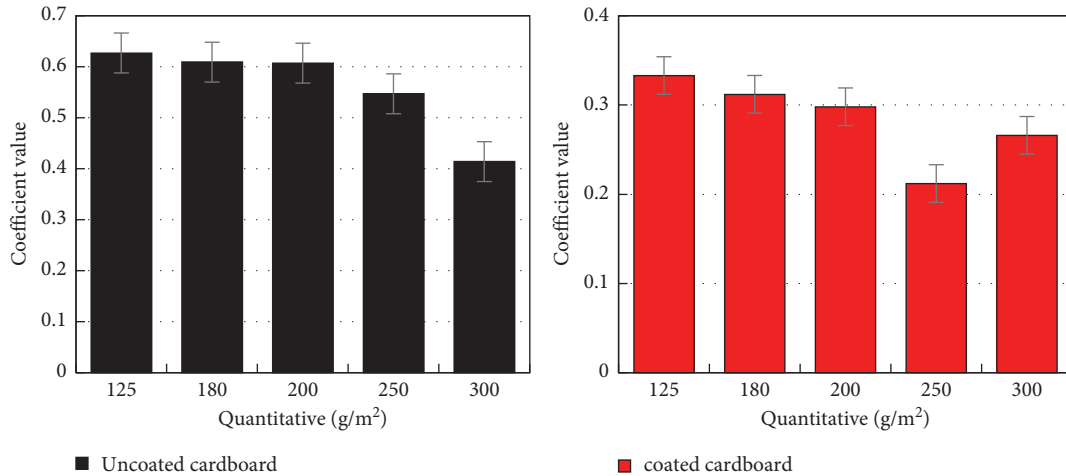
FIGURE 5: Values of friction coefficient of uncoated and coated cardboard in different quantitative paperboards.
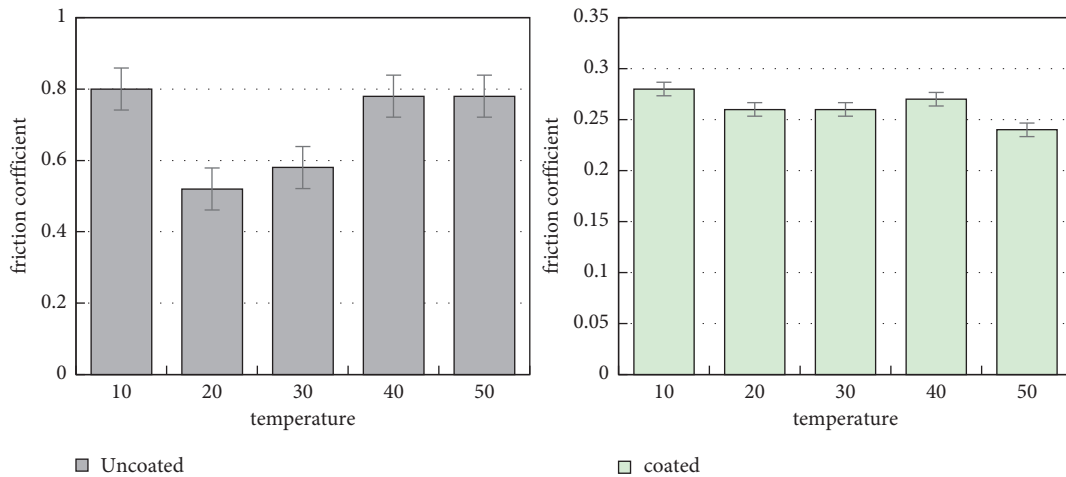
FIGURE 6: Abrasion resistance of box board base paper and coated box board at different temperatures.

paint, and a smooth and dense continuous coating film is formed on the surface. The paper fibers are not easy to absorb moisture in the air, so the abrasion resistance is significantly enhanced compared with the uncoated paper.

The buffer performance analysis is shown in Figure 8.

As the compressive load increases, the energy absorption efficiency of the material gradually increases first and then stabilizes. After stability, the relationship between the maximum energy absorption efficiency of each group of samples is NS + UNF > NS + AF.

The preparation of biomass buffer packaging material products is shown in Figure 9.

3.3. Packaging and Sealing Performance.

The following will analyze the number of horizontal screws (this article refers to half of the total number of screws in the horizontal direction) and the effect of vertical screws on the maximum relative deformation of the cover under dangerous load conditions. The results are shown in Figure 10.

Obviously, the smaller the number of screws in the two directions, the larger the screw spacing, and the smaller the restriction of the screw on the sealing performance; due to the nonuniformity of the load, the maximum relative deformation is not linear with the number of screws. With the increase in the number of screws, the tendency of the
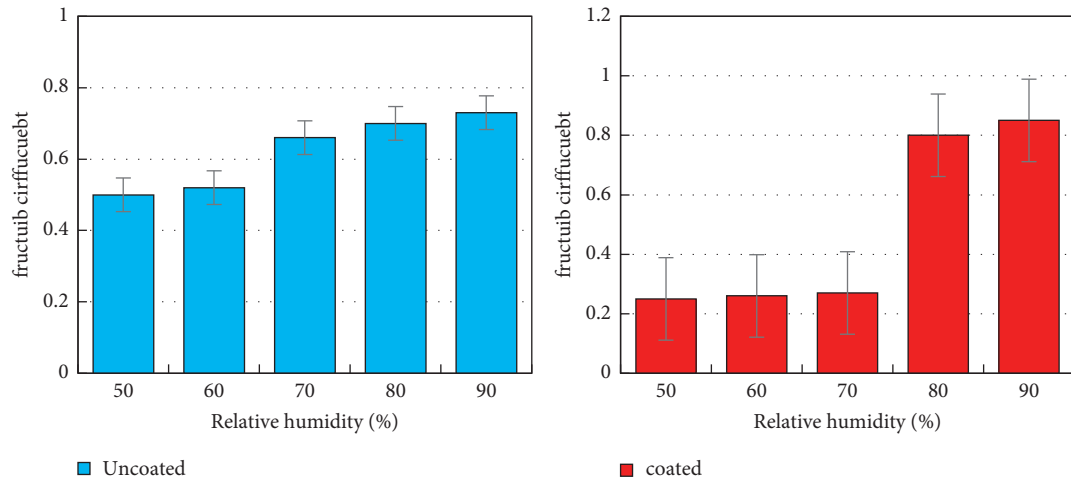
Figure 7: Abrasion resistance of cardboard base paper and coated modified paper under different relative humidity conditions.
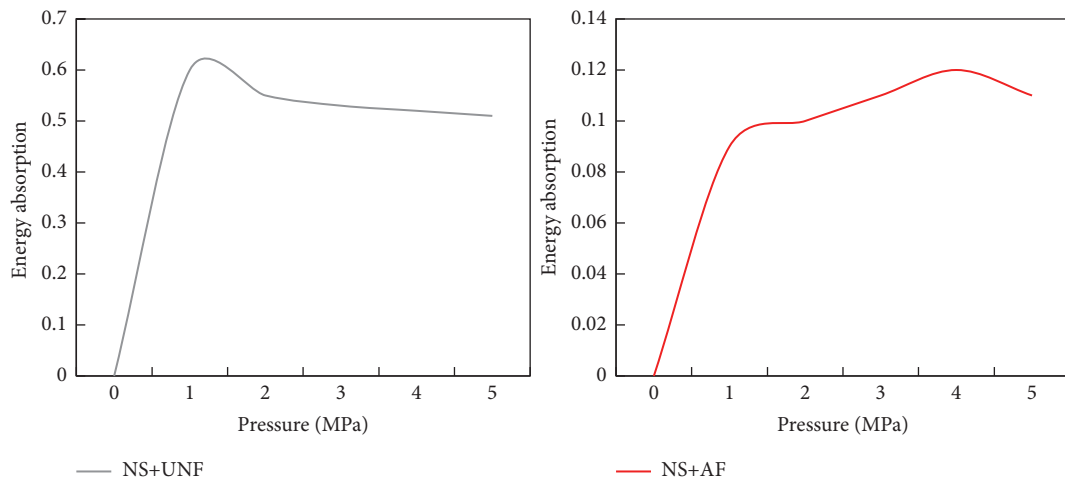
Figure 8: Buffer performance analysis.
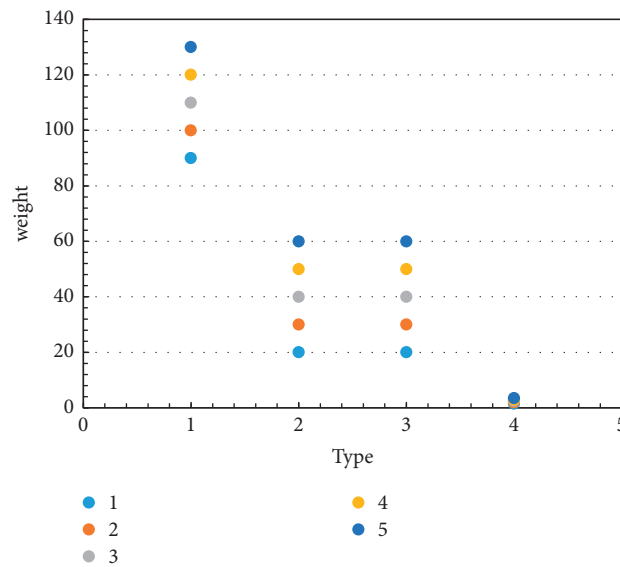
Figure 9: Preparation of biomass buffer packaging material products.
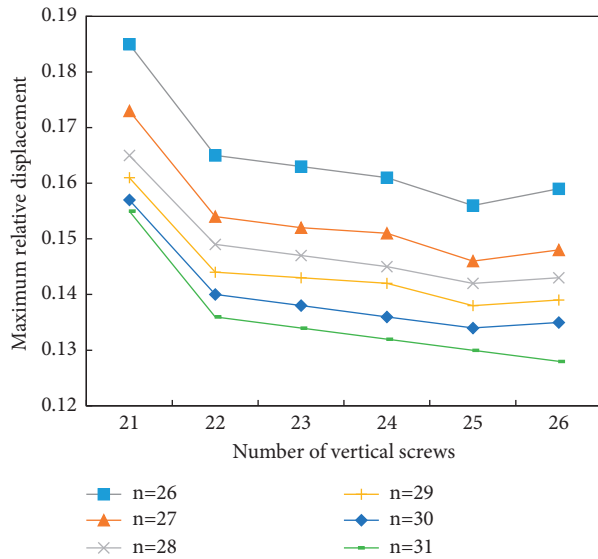
Figure 10: Diagram of the number of screws in the horizontal direction under dangerous load conditions.

maximum relative deformation to become smaller is gradually decreasing.

The value ranges of the optimized design variables are shown in Table 5.

After the first level of optimization, the overall mass of the structure was reduced from the initial 39.42 kg to 31.18 kg, and the optimization efficiency was 20.90%. The maximum relative deformation of the lid structure increased from 0.143 mm to 0.198 mm, although the maximum opening displacement increased, but still meeting the sealing deformation requirements.

4. Discussion on the Design and Performance of the Overall Packaging Box of Environmentally Friendly Packaging Materials

4.1. Relationship between Materials and Packaging Design. Packaging materials are materials selected for manufacturing packaging, packaging and printing containers, packaging and transportation, and other products that meet packaging requirements. The selection and use of packaging materials must consider various packaging factors. For example, food packaging must be nontoxic and tasteless, and the physical and chemical properties of the packaging must be stable and will not chemically react with the food. For the packaging of goods that must be moisture-proof, the packaging material must have good insulation and waterproof properties. If the packaging is fragile, the material must be stable and not easily deformed. In addition, factors such as the transportation of packaging materials, sales arrangements, and market demand for commodities must also be considered.

In the packaging design process, materials and packaging have a very close relationship: from prepackaging design to material selection and then from material selection to design

thinking design, designers can have a great influence. In the selection and integration of packaging materials, the designer's design style and personal feelings can be understood from the packaging materials. Therefore, the material is the extension and sublimation of the packaging. Packaging design is a technical issue as well as a very comprehensive issue. This is not only a question of art, but also a question of science and technology. It also covers design, materials science and engineering, social marketing, marketing management, consumer psychology, etc. In addition to making products safe and beautiful, it is also a powerful marketing tool. Packaging design refers to the selection of appropriate materials and the use of certain technologies to design the container structure, shape, and decoration of product packaging.

Packaging materials are materials produced to meet packaging needs and are materials that implement packaging styles. The continuous advancement of science has given birth to the invention and creation of new materials and technologies. There are more and more packaging materials, including traditional packaging materials as well as more innovative high-tech materials. Packaging materials can be classified according to source, use, development, and classification. According to reports, there are two types of packaging materials: one is natural materials, such as wood, bamboo, and rattan. The other is man-made materials, such as plastic, glass, and metal. According to the use, it can be divided into two categories: one is the main packaging materials, such as paper, plastic, metal, wood, ceramics, glass, bamboo, rubber, leather, fabrics, fiber materials, and composite materials. The other is auxiliary packaging materials, such as copper plating, moisture-proof and anti-corrosive materials, inks and coatings, adhesives, and other materials that play an auxiliary role in the packaging process and packaging modeling. Different packaging materials have different aesthetic characteristics and also produce different emotions in touch and vision. Designers must first understand the types of materials and then show the beauty of the materials.

Material is an eternal theme in design. Materials are the basis for human survival and construction: after humans seek better physical properties and functions of materials, they meet more needs through construction activities. The external characteristics of the material have a special expressive force in the external application of packaging design and play a direct and effective role. To make packaging products more artistic, it is necessary to fully understand and master the aesthetics of packaging materials. And it is applicable to all aspects of packaging design. A long time ago, people focused on the perfect combination of practicality and aesthetics, realized the important position of materials in design creation, reflected the importance of perceiving the beauty of materials in design, and had a deeper understanding of the beauty of material selection. For packaging design, the use of packaging materials is not only its material basis, but also one of the important contents of aesthetic research and application. The increasing development of science and technology and the abundance of materials have put forward a great demand for the selection and application

TABLE 5: Design variable value space.

Variable name	Initial value	Ranges
Number of horizontal screws	28	{26, 27, 28, 29, 30, 31}
Number of vertical screws	23	{21, 22, 23, 24, 25 ,26}
Stiffener web height	42	40–50
Width of ribs	16	15–22
Thickness of cover plate in 0° direction	1.170	0.1–2.0
The thickness of the cover plate in the direction of 45°	0.936	0.1–2.0
Thickness of cover plate in 90° direction	1.170	0.1–2.0
Packaging thickness at 0°	0.819	0.1–2.0
Packaging thickness at 45°	0.702	0.1–2.0
Packaging thickness at 90°	0.469	0.1–2.0
Thickness of ribs	1.404	0.1–2.0
The thickness of the ribs in the direction of 45°	0.585	0.1–2.0
Thickness of ribs in 90° direction	1.404	0.1–2.0

of packaging design materials. There are man-made materials, natural materials, composite materials, and individual materials. These have a wide range of applications and development efficiency in packaging technology.

4.2. Perceiving the Visual Beauty of Materials in Packaging Design. As a direct and practical marketing method, packaging gives people a visual experience and conveys an easy-to-understand and practical visual language. Eyes are the human body's sensory organs that receive the largest amount of information outside the body. Through the eyes, the most direct, rapid, and accurate perception of packaging materials can be achieved. When stimulated by the information of packaging design materials, vision will form physiological to psychological stimuli and will form different points and consciousness. Through the surface of the packaging design material, the customer visually perceive information, including the color, shape, and design presented by the material, making them produce different emotions.

Among the characteristics of materials, color is the first characteristic that expresses the material, and it is also the first element perceived by all human sensory organs. If you want to whiten and highlight the product, color plays an important role and has a strong appearance and visual charm. The color integrated into packaging materials is the unit of physiological stimulation, psychological stimulation, and aesthetic perception in human visions, and it is also an organic combination of natural characteristics, social characteristics, and artistic beauty. Therefore, the color of packaging materials expresses the beauty of art and provides consumers with the beauty of visual language. The color of the material directly affects the basic packaging style, making it easier for people to communicate with it emotionally. All materials have colors. The color varies with the material, and the material also has a unique visual effect due to the color. The colors of packaging materials are divided into solid colors and additional colors. The inherent color of the material is the natural color of the material itself, and the packaging design has an inherent beauty of value due to the beautiful color of the material, showing a simple and heartfelt feeling. The additional paint is made by processing

paint on the surface of natural materials, which can enhance, attenuate, or change the original color and can reasonably improve the relationship between the material and the packaged product according to the consumer or the actual environment. The relationship highlights the accuracy of packaging information delivery.

Color can not only directly attract attention but also can even guide people's psychological emotions. In order to gain the attention of consumers, the packaging of fructose food and beverages generally uses bright colors such as orange and yellow to bring people a sense of beauty, vitality, and happiness. Green and blue mainly give people a feeling of peace, calm, tranquility, and relaxation. These two colors are commonly found in food, energy-saving, and medical packaging materials. In order to meet the needs of consumers, foods often choose high-purity red, yellow, and orange series to reflect the color, fragrance, and taste. In packaging design, in addition to examining the color coordination of materials, it is also necessary to examine whether the feel of the color itself is consistent with the characteristics of the product. The warm and cold colors give people a strong psychological impact, while the pure colors give people the feeling of being generous and noble and spotless. The order of beauty is used in the packaging design to combine and match the colors of the materials, so that the weight, contrast, and direction of the colors convey visual information, so as to use the enjoyment of beauty in people's psychology. Combining the new elements of modern colors, we analyze the color aesthetic law of packaging design, meet the possible requirements of packaging design, and design better and more suitable packaging design products.

4.3. Economy of Material Beauty in Packaging Design. The beauty and economy of materials in packaging design refers to the comprehensive evaluation of the amount of packaging materials used in the product and the degree of conservation of energy and resources consumed in the production and processing of packaging materials. Nowadays, affected by the increasing proportion of the added value of packaging design in the total value of the product, cumbersome styles, luxurious materials, and bulky packaging have followed one after another, causing packaging design materials to be

distorted. The economy of material beauty in packaging design includes two aspects: convenience and simplicity of material use.

"Appropriate" is the most beautiful and accurate means of reasoning. A successful packaging product does not mean that the rarer the material and the higher the price, the better. The most appropriate should be based on the value of the product, the needs of consumers, and the environment in which they are used. "Appropriate packaging refers to a reasonable and appropriate packaging product. It is to fully explore the functional role of packaging. The protective function of packaging must be fully considered. The quantity of materials, cost prices, and complete labels must be fully considered." Appropriate packaging adjustment function and cost are very important. According to the product packaging, appropriate specific standards are established for the manufacturer, using appropriate packaging methods, packaging materials, material use, and appropriate packaging development. Ecobeauty needs a simple and convenient product packaging structure to improve the quality of product manufacturing while having mass production.

In order to eliminate the harmful effects of excessive packaging of products, the General Administration of Quality Supervision, Inspection and Quarantine and other relevant departments jointly formulated the provisions of GB 23350–2009 "Requirements for Restricting Excessive Packaging of Goods, Food and Cosmetics". Appropriate guidance and restrictions on the correct use of packaging materials have been made at all levels. Therefore, when designing packaging materials, the choice of materials must be based on the unique characteristics and economic benefits of the product.

5. Conclusions

The experimental results show that the overall packaging box design and performance discussion of environmentally friendly packaging materials proposed in this paper have improved airtightness, environmental protection, and capacity compared with the design of traditional packaging materials. The design method selected in this article has a good retention rate in terms of statistical indicators. The article introduces the relevant content of zero-pollution packaging, calculates the positive axis stiffness of the single-layer board, and studies the stiffness performance of the single-layer composite material on the positive axis. Through the material constitutive relationship, acceleration load application, fluid-solid coupling surface, and integration step control, a set of basic analysis processes for extracting impact load is derived. The actual model is simplified to a packaging model, and good experimental results are obtained. Experimental data show that after the first level of optimization, the overall mass of the structure is reduced from the initial 39.42 kg to 31.18 kg, and the optimization efficiency is 20.90%; the maximum relative deformation of the flap structure has increased from 0.143 mm to 0.198 mm, although having the maximum tension. The opening displacement has increased, but it still meets the sealing deformation requirements. The shortcomings of this article are

that the amount of data collected in the sample is relatively limited and the requirements of different aspects of the designed packaging may not be comprehensive. In future research, the experimental samples can be expanded to obtain the credibility of the research results. In addition, the article's introduction to algorithm comparison is not comprehensive enough, and there is no increase in citations and explanations of other algorithms for comparison. In future experiments, relevant content can be added to make the article more reasonable.

Data Availability

No data were used to support this study.

Conflicts of Interest

The author declares no conflicts of interest in this study.

Acknowledgments

References

[1] A. C. Neves, M. M. Moyne, C. Eyre, and B. P. Casey, "Acceptability and societal impact of the introduction of bioplastics as novel environmentally friendly packaging materials in Ireland," *Cleanroom Technology*, vol. 2, no. 1, pp. 127–143, 2020.

[2] Y. Wang and Y. Wang, "Research on the application of environmentally friendly packaging materials in the sustainable development of logistics," *IOP Conference Series: Earth and Environmental Science*, vol. 781, no. 3, pp. 25–32, 2021.

[3] G. Vahid and S. G. Iman, "Development of photo-modified starch/kefiran/TiO$_2$ bio-nanocomposite as an environmentally-friendly food packaging material," *International Journal of Biological Macromolecules*, vol. 116, no. 2, pp. 1082–1088, 2018.

[4] F. Nurul, J. Krishnan, B. Debes et al., "Green composites made of bamboo fabric and poly (lactic) acid for packaging applications—a review," *Materials*, vol. 9, no. 6, pp. 55–65, 2016.

[5] Q. Wang, J. Yang, P. Liu, and L. Li, "Facile one-step approach to manufacture environmentally friendly poly(vinyl alcohol) bead foam products," *Industrial & Engineering Chemistry Research*, vol. 60, no. 7, pp. 2962–2970, 2021.

[6] D. Dissanayake, D. Weerasinghe, T. Perera et al., "A sustainable transparent packaging material from the arecanut leaf sheath," *Waste and Biomass Valorization*, vol. 7, no. 3, pp. 1–18, 2021.

[7] Puscaselu, Gheorghita, Roxana et al., "The application of the peleg model in order to obtain completely soluble materials for food product packaging," *Journal of Applied Packaging Research*, vol. 10, no. 1, pp. 6-7, 2018.

[8] S. H. Jo, T. H. Ryu, H. Kwon et al., "Ecological characteristics and environmentally friendly control strategies of pochazia shantungensis (Hemiptera: ricaniidae) in korea," *Journal of the Faculty of Agriculture, Kyushu University*, vol. 61, no. 2, pp. 299–311, 2016.

[9] A. K. . Bolhassan, "Sweden takes lead on eco-friendly food packaging," *Paper Asia*, vol. 35, no. 1, pp. 2–5, 2019.

[10] C. Aversa, M. Puopolo, and M. Barletta, "Tailor-made bioplastics for environmentally friendly food packaging: a methodological approach to a challenging problem," *Encyclopedia of Renewable and Sustainable Materials*, vol. 4, no. 8, pp. 605–616, 2020.

[11] U. Hasanah, E. P. S. Dewi, U. Santoso, and S. Supriyadi, "Physical and chemical characteristic of young coconut leaves (cocos nucifera l.) as traditional packaging," *Indonesian Food and Nutrition Progress*, vol. 17, no. 2, pp. 33–44, 2021.

[12] A. K. Gain, L. Zhang, and M. Z. Quadir, "Thermal aging effects on microstructures and mechanical properties of an environmentally friendly eutectic tin-copper solder alloy," *Materials & Design*, vol. 110, no. 15, pp. 275–283, 2016.

[13] M. Combrzyński, A. P. Matwijczuk, A. Wójtowicz et al., "Potato starch utilization in ecological loose-fill packaging materials—sustainability and characterization," *Materials*, vol. 13, no. 6, pp. 13–90, 2020.

[14] A. Masek, M. Latos, M. Piotrowska, and M. Zaborski, "The potential of quercetin as an effective natural antioxidant and indicator for packaging materials," *Food Packaging and Shelf Life*, vol. 16, no. 9, pp. 51–58, 2018.

[15] M. Joyce, L. Pal, and T. Tran, "Production of polyhydroxyalkanoates (PHA)-based renewable packaging materials using photonic energy: a bench and pilot-scale study," *Octobr 2018*, vol. 17, no. 10, pp. 557–565, 2018.

[16] B. Geueke, K. Groh, and J. Muncke, "Food packaging in the circular economy: overview of chemical safety aspects for commonly used materials," *Journal of Cleaner Production*, vol. 193, no. 9, pp. 491–505, 2018.

[17] T. Giro, K. Beloglazova, G. Rysmukhambetova et al., "Xanthan-based biodegradable packaging for fish and meat products," *Foods and Raw Materials*, vol. 8, no. 1, pp. 67–75, 2020.

[18] M. Mironescu, A. S. Lazea, M. E. P. Barbinta et al., "Green design of novel starch-based packaging materials sustaining human and environmental health," *Polymers*, vol. 13, no. 8, pp. 1190–1198, 2021.

[19] Y. Zhang, L. Zhan, B. Xie et al., "Decomposition of packaging materials and recycling GaAs from waste ICs by hydrothermal treatment," *ACS Sustainable Chemistry & Engineering*, vol. 7, no. 16, pp. 98–101, 2019.

[20] R. M. Raybaudi, J. M. Mosqueda, R. F. Soliva, and O. B. Martín, "Combinational edible antimicrobial films and coatings," *Antimicrobial Food Packaging*, vol. 8, no. 11, pp. 633–646, 2016.

[21] A. Lisitsyn, A. Semenova, V. Nasonova et al., "Approaches in animal proteins and natural polysaccharides application for food packaging: edible film production and quality estimation," *Polymers*, vol. 13, no. 10, pp. 1592–1598, 2021.

[22] Y. Xu, X. Liu, Q. Jiang et al., "Development and properties of bacterial cellulose, curcumin, and chitosan composite biodegradable films for active packaging materials," *Carbohydrate Polymers*, vol. 260, no. 2, pp. 117–778, 2021.

[23] B. Bayram, G. Ozkan, T. Kostka, E. Capanoglu, and T. Esatbeyoglu, "Valorization and application of fruit and vegetable wastes and by-products for food packaging materials," *Molecules*, vol. 26, no. 13, pp. 4031-4032, 2021.

[24] M. B. Latos and A. Masek, "Biodegradable polyester materials containing gallates," *Polymers*, vol. 12, no. 3, pp. 77-78, 2020.

[25] M. Lamb, V. Rouillard, and J. Milverton, "An evaluation of the mechanical performance of extruded wheat starch loose fill," *Packaging Technology and Science*, vol. 32, no. 2, pp. 99–101, 2019.

[26] S. B. Tsai, M. F. Chien, Y. Xue et al., "Using the fuzzy dematel to determine environmental performance: a case of printed circuit board industry in taiwan," *PLoS One*, vol. 10, no. 6, Article ID e0129153, 2015.

[27] S. B. Tsai, Y. C. Lee, and J. J. Guo, "Using modified grey forecasting models to forecast the growth trends of green materials," *Proceedings of the Institution of Mechanical Engineers - Part B: Journal of Engineering Manufacture*, vol. 228, no. 6, pp. 931–940, 2014.

[28] J. Zhao, J. Huang, Y. Xiang et al., "Effect of a protective coating on the surface integrity of a microchannel produced by microultrasonic machining," *Journal of Manufacturing Processes*, vol. 61, pp. 280–295, 2021.

Research Article

Nanomaterial Antibacterial Technology in the Design of Antibacterial Fabrics for Sports Clothing

Yuan Feng (ID)

Sports Department, University of Shanghai for Science and Technology, Shanghai 200093, China

Correspondence should be addressed to Yuan Feng; fengyuan@usst.edu.cn

In recent years, nanomaterials have been widely used in sports equipment, and their application in sportswear has also attracted wide attention. This research mainly discusses the application of nanomaterial antibacterial technology in the design of antibacterial fabrics for sports apparel. The method of adding nano-TiO_2 to the antibacterial textiles varies with the type of fiber or fabric, and the finishing method also changes accordingly. For chemical fibers, the method of blending spinning is mainly used. By adding nano-antibacterial particles in the spinning solution, the polymer is ejected from the spinneret to make antibacterial fibers. This processing method is characterized by good antibacterial durability. The preparation of antimite finishing agent is mainly the dispersion of nanopowder. The selection of the best dispersant is mainly determined by measuring the change of the volume sedimentation rate of TiO_2 after 5 days under different dosage and pH value of each dispersant. Then, the particle size of nano-TiO_2 and Ag in different dispersing conditions was tested by TEM, and finally, the best dispersing agent and dispersing process were determined. The optimum of nano-antimite and antibacterial finishing agent is as follows: the dispersing agent is TW-80, the amount of anhydrous ethanol in dispersing medium is 5 times that of powder, the amount of dispersing agent is 1.5 times that of powder, the pH value is 7, and the stirring time is not less than 30 min. In the preparation of nano-antimite and antibacterial finishing agent, nanomaterials were used. The weight of nano-TiO_2 powder was 20 grams and that of Ag was 20 grams. The dispersion medium (absolute ethanol) was 100 mL of dispersant. The amount of TW-80 was 30 g, the amount of citric acid was 60 g, the emulsion was very stable, and there was only a small amount of precipitation after being static for 5 days. Considering the characteristics of silk knitted fabric, this experiment uses the exhaustion method in the finishing process to finish the silk knitted fabric. After 50 times of washing, the antibacterial rate of *Staphylococcus aureus* and *Escherichia coli* reached 95.13% and 87.44%, respectively. This study provides guidance for the application of nanomaterials in the antibacterial field of sports clothing.

1. Introduction

With the continuous improvement of people's living standards, people began to develop functional products that can inhibit the reproduction of microorganisms or kill bacteria, that is, fibers and textiles that can prevent bacteria and odors. Nanomaterials are widely used. For traditional industries such as textile and light industry, the development of nanomaterials is relatively late, but people's trust and attention to nanomaterials make more and more new nanoproducts in traditional industries continue to launch. In particular, in businesses and enterprises, to be invincible in the fierce market competition, it is necessary to take two methods: one is to continuously improve the performance and price of old products, and the other is to innovate constantly and develop new products with new features [1].

With the improvement of people's living standards, the pursuit of quality of life tends to be environmentally friendly and healthy, so new antibacterial clothing fabrics are widely used. In this study, nano-Ag/TiO_2 inorganic antibacterial powder with both advantages was selected to finish cotton fabric, and a kind of cotton fabric with antibacterial function was studied, which can be not only used as sports clothing fabric, but also widely used as medical substrate. It provides theoretical and experimental basis for the application of the antibacterial powder in the textile field.

Yanyan et al. believe that multifunctional carbon-based nanomaterials (MCBNs) with unparalleled optical,

electronic, and thermal properties have attracted more and more interest and show the greatest promise in the field of biomolecular imaging and therapy. Therefore, carbon-based nanomaterials have a large number of potential applications in the field of biomedicine, such as bioimaging, drug delivery, and tumor treatment. This research only stayed on the theoretical level and did not use experiments for exploration [2]. Sustainable and cost-effective energy production has become the key to meeting current energy needs. Paul et al. believe that inexpensive, scalable, efficient, and reliable catalysts must be developed. This research only presented the description of 3D porous carbon electrode, and the research process is not very clear [3]. Carbon-based nanomaterials have been developed for photothermal cancer treatment, but it is still a huge challenge to manufacture their multifunctional counterparts with simple methods, good biocompatibility and dispersion, and efficient cancer treatment methods. Li et al. have developed an alternative multifunctional nanoplatform based on carbon silica nanocapsules with gold nanoparticles (Au@CSN) in the cavity for cancer treatment. The encapsulated chemical doxorubicin can be released from Au@CSN with mesoporous and hollow structure by means of near-infrared light and pH stimulation. Although this research is conducive to spatiotemporal therapy to reduce off-target toxicity, the research method is too cumbersome [4]. Nanocapsules with efficient photothermal conversion and excellent biocompatibility realize the synergistic effect of photothermal and chemotherapy. Exercise under hypoxic conditions represents the extra stress associated with normoxic exercise. Santos et al. believe that hypoxia can induce oxidative stress inflammation, which may be exacerbated after exercise. In addition, vitamin E supplementation may reduce oxidative stress and inflammation caused by hypoxia during exercise. They evaluated the effect of vitamin E supplementation (250 mg) on inflammatory parameters and cell damage after hypoxic exercise at a simulated altitude of 4200 m. Nine volunteers were supplemented with vitamin E 1 hour before exercise, and performed three 60-minute exercises (with maximum oxygen uptake being 70%) under normoxia, hypoxia, and hypoxia + vitamin, interspersed for 1 week. Blood was collected before exercise, immediately after exercise, and 1 hour after exercise to measure inflammatory parameters and cell damage. This research only judged the influence of oxygen content on physical health and did not analyze the exercise time in detail [5].

Other research mainly discusses the application of nanomaterial antibacterial technology in sports apparel [6]. The preparation of antimite finishing agent is mainly the dispersion of nanopowder. Then, the particle sizes of nano-TiO_2 and Ag of the determined optimal dispersant under different dispersing process conditions were tested by transmission electron microscopy (TEM), and the best dispersant and dispersion process were finally determined. The best process of nano-antimite and antibacterial finishing agent is as follows: the dispersant is TW-80, the amount of dispersion medium containing anhydrous ethanol is 5 times the amount of powder, the amount of dispersant is 1.5 times the amount of powder, the PH value is 7, and the mixing

time is not less than 30 min. The preparation of nano-antimite and antibacterial finishing agent adopts the method of nanomaterial compounding: 20 grams of nano-TiO_2 powder, 20 grams of Ag, 100 mL of dispersion medium (absolute ethanol), 30 g of dispersant TW-80, and 60 g of citric acid. The prepared emulsion is very stable after standing for 5 days with only a small amount of precipitation. Considering the characteristics of silk knitted fabrics, in this experiment, the exhaustion method is used in the finishing process to finish the silk knitted fabrics.

2. Nanomaterial Antibacterial Effects

2.1. Nanomaterials. The full dispersion of nanoparticles is the key and difficult point of the research, which directly gives full play to the antibacterial and antimite effects of nanoparticles. This is the problem to be solved in this experiment [7]. In practical application, there are many factors that affect the full dispersion of nanoparticles, such as mixing method, mixing time, and dispersion medium, as well as the influence of temperature and humidity of the test environment and human factors, so it is key in the preparation of antimite finishing agent to determine the best dispersion process by a large number of repeated experiments [8, 9]. The pore size of nanomaterials is expressed as follows:

$$Eg_{os} - Eg_{ref} = \Delta Eg \approx \frac{h^2 \pi^2}{2R^2} \times \frac{1}{\mu} - \frac{1.8e^2}{\varepsilon R}. \tag{1}$$

Among them, $E_{g_{ref}}$ represents the initial potential energy of the nanoparticle, R is the longest radius, and μ is the corresponding particle size coefficient. The surface coefficient of nanoparticles will change correspondingly during the preparation process [10].

$$c_\tau = \tau_0 + \alpha g b \rho^{1/2} = \tau_0 + \alpha g b \rho^{p-N},$$

$$\tau = \left[\frac{Gb}{2\pi L(1-v)} \right] \left\{ 1 - \frac{v}{2}(3 - 4\cos^2 \phi) \right] \ln\left(\frac{L}{\eta}\right) - 1 + \frac{V}{2} \right\}. \tag{2}$$

Among them, c_τ is the surface coefficient, and τ_0 is the value of the initial strain force. After that, other forms of micromechanical peeling were obtained. This improves the quality and quantity of multifunctional nanomaterials prepared by micromechanical peeling to various degrees in terms of the number of control layers or the improvement of the edge structure [11, 12]. An organic film can be formed by adding a corresponding physical coating on the surface of the nanoparticles. The organic film sensitivity value is expressed as follows:

$$m = \frac{\sqrt{3}k_B T}{aGb^3} \left[\ln\left(\frac{V}{b^3}\right) - 1.63 \right]^{-1} + \rho V. \tag{3}$$

Among them, m represents the event sensitivity coefficient, and k_B is the correlation value of the sensitivity coefficient. Due to the small diameter of the nanoparticle, the surface area increases sharply, the surface energy is higher,

and the number of surface atoms is far more than that of non-nanomaterials of the same mass. The activity of nanomaterials is expressed as follows [13]:

$$V\% = \frac{[A]_{\text{sample}} - [A]_{\text{blank}}}{[A]_{\text{positivecontrol}} - [A]_{\text{blank}}} \times 100\%. \tag{4}$$

Among them, $[A]_{\text{sample}}$ is the quality of the sample, and $[A]_{\text{blank}}$ is the quality of the blank control. Nanomaterial carriers can improve the transparency of biological cell membranes and the compatibility of compounds [14, 15].

$$EE\% = C_{\text{sample}} \times \frac{V}{M_{\text{drug}}} \times 100\% + C_{\text{sample}} \times V_{\text{min}},$$

$$DL\% = C_{\text{sample}} \times \frac{V}{\left(C_{\text{sample}} \times V + M_{\text{micelle}}\right)} \times 100\%. \tag{5}$$

Here, C_{sample} is the DOX concentration measured with the nanoparticles loaded with drugs and the osmotic pressure value of $EE\%$ nanoparticles [16].

2.2. Nano-Antibacterial Effects.

The antimite and antibacterial research of nanotextiles is still in the further improvement stage. The particle sizes of nanomaterials on cotton knitted garments are all greater than 150 nanometers, beyond the basic requirement of nanomaterials that the particle size should be less than 100 nanometers in order to give full play to the characteristics of nanomaterials, so the antibacterial ability is low, with no resistance to washing, mainly because of the nanomaterials. They are not organically combined with the cotton fiber raw materials in knitted garments, so the washing resistance is low, and they can only be washed less than 10 times, which has no practical value [17, 18]. Therefore, the research and development of practical nano-mite-proof and antibacterial cotton knitted garments have become an urgent matter, which has greater practical significance and wider market application prospects. At the same time, it is also the focus of this research to ensure that the finished clothing has excellent antimite and antibacterial properties. The washing fastness of the nano-antimite and antibacterial finishing agent is also the focus of this research. The mixture is used to ensure the washing fastness of antimite and antibacterial clothing with no changes in its various properties (such as air permeability, skin affinity, strength, feel, and color). *Staphylococcus aureus* and *Escherichia coli* are shown in Figure 1.

The amount of information transmitted by nanomaterials to signals is KL [19]; namely,

$$KL = -\log_2 P(L_i). \tag{6}$$

Then, the information entropy is [20]

$$H(L) = -\sum_{i=1}^{n} P(L_i)\log_2 P(L_i). \tag{7}$$

The research and development of functional textile products with antibacterial properties, while maintaining the good feel and wearability of the fabric itself, not only are a requirement for technology, but also conform to the needs of contemporary people for the health function of textile products. While preventing diseases, this is consistent with people's promotion of healthy and relaxed lifestyles. In addition, there is a signal exchange between information X and Y; then [21],

$$R\left(\frac{X}{Y}\right) = -\sum_{i=1}^{n} \sum_{j=1}^{m} M(X_i Y_j)\log_2 N\left(\frac{X_i}{Y_j}\right),$$

$$RP(t_j) = \sqrt{\frac{1}{n} \sum_{i=1}^{n} \left[TP(t_j) - HP_i(t_j)\right]^2}. \tag{8}$$

Among them, t_j is the time of the current processing period, and n is the total number of items remaining after the previous processing. Polyethylene (lactic acid) is copolymerized with mesoporous multifunctional nanomaterials [22]. The organic film sensitivity value is expressed as follows:

$$V = \frac{k_B T}{AGB^3} \left[\ln\left(\frac{V}{B^3}\right) - 2\right]^{-1} + \rho V. \tag{9}$$

Among them, V represents the sensitivity coefficient. In the study of conduction rate, resistance is a frequently considered issue [23, 24].

$$Z_{\text{in}} = \sqrt{\frac{\mu_r}{\varepsilon_r^3}}\tanh\left[-j\left(\frac{2\pi}{c}\right)\right] + \left(\sqrt{\frac{\mu_r}{\varepsilon_r}} fd\right) \sum_{i=1}^{n} M. \tag{10}$$

When the correlation coefficient Z_{in} of resistance is constant, the size of the conductivity depends on the radius of a single molecule. In the use of related nanomaterials, it is usually necessary to consider the quality of its energy absorption R_L (dB) [25].

$$R_L(\text{dB}) = -20\log_{10}\left[\left|(Z_{\text{in}} - 1)(Z_{\text{in}} + 1)\right|\right] \sum_{i=1}^{n} \frac{M}{Z_1 Z_2}. \tag{11}$$

Information processing is carried out in sections, and each section needs to be refined. The absorption of energy can indirectly show the performance of related materials. After the preparation of nanomaterials, the concept of corresponding coefficients needs to be introduced at this time [26].

$$Q_g = \frac{\Delta P}{P_a - \Delta P} + \sum_{i=1}^{N} (Z_M - Z_N)(Z_2 - Z_1). \tag{12}$$

Keep the conduction rate Q_g unchanged, and when the change value of the air pressure increases, the sensitivity performance of the nanomaterials will increase accordingly. The mechanical properties of nanomaterials largely depend on the length of the diameter [27].

$$\varepsilon_{NH} = A_{NH}\frac{D\Omega}{KTd^2}\frac{\sigma}{}(Z_M - Z_N)\sum_{i=1}^{n}(D_2 - D_1)|X_M + X_N|,$$

$$\varepsilon_{c0} = \frac{D_{Gb}\Omega\delta\sigma}{KTd^3}\sum_{i=1}^{n}(Z_M - Z_N)|X_2 - X_1|. \tag{13}$$

When the conductivity is constant, the change between the maximum value ε_{NH} and the minimum value ε_{c0} of the diameter has the most obvious effect on the stress change of the nanomaterials [28, 29].

$$M_k(T) = \sum_{i=1}^{N} u_k(T) \times \delta(T - \tau_1) \times p_k(T) \times g_{ki}(T) \times M. \tag{14}$$

In information transmission, signal transmission usually requires a certain process, and the transmission cycle T will also be affected by related factors [30].

$$W_p(t) = \sum_{k=1}^{M} \left[W_k(t) \times l_k(t) \right] = \sum_{k=1}^{M} \left[\sum_{i=1}^{M} \delta(t - t_{ki}) \right] (t_k + k_i). \tag{15}$$

The potential energy of repulsion when the attached layer is compressed is

$$U_R^e = N_S K T \theta \infty \left(\frac{1-h}{l} \right), \tag{16}$$

where N_s represents the number of molecules adsorbed per unit area; $\theta\infty$ represents the extent to which the surface is covered by molecules when $H = \infty$; and H represents the distance between the two surfaces close to each other [31, 32].

3. Nano-Antibacterial Sportswear Experiment

3.1. Preparation of Nano-Antimite Finishing Agent.
The preparation of antimite finishing agent is mainly the dispersion of nanopowders. The full dispersion of nanoparticles is related to factors such as pH value, dispersant dosage, stirring method, and dispersion medium, so in the dispersion experiment, mainly start from the above aspects. To solve the dispersion problem, the experiment is mainly divided into two parts: the first is the choice of dispersant. This is because there are many types of dispersants, and an optimal dispersant that can fully disperse the nanopowder must be selected. The second is determining the best dispersant. Dispersant experiments were carried out to get the best dispersion process.

3.1.1. Design Ideas.
The following design ideas were considered: retrieval of related literature $\longrightarrow$ design experimental plan $\longrightarrow$ experiment $\longrightarrow$ best experimental plan $\longrightarrow$ experiment $\longrightarrow$ several dispersants with relatively good dispersion effect $\longrightarrow$ experiment $\longrightarrow$ best dispersant and dispersion medium $\longrightarrow$ experiment $\longrightarrow$ determining the best dispersion process.

3.1.2. Experimental Instruments and Reagents.
The following experimental instruments and reagents were used:

> BME100LX high-shear mixing emulsifier (Shanghai Weiyu Electromechanical Manufacturing Co., Ltd.).

TEM-200CX transmission electron microscope (School of Materials Science) (the main reagent information is shown in Table 1).

Nano-TiO$_2$ (particles of 50–80 nm) (Jiangsu Changtai Nanometer Material Co., Ltd.).

Nano-Ag (particle size of 20 nm) (Beijing Saiterui Nano Co., Ltd.).

The selection of the above dispersants is based on the dispersion theory and initial preliminary experiments. Among the above several dispersants, citric acid, SDS, SDBS, and SD-03 are ionic dispersants, mainly based on the electric double layer theory for nanometer. The particles are dispersed. PEG, TW-80, and OP are nonionic dispersants, which are mainly based on the theory of steric stability to disperse nanoparticles.

Experimental steps are as follows: weigh Ag and TiO$_2$ $\longrightarrow$ add water $\longrightarrow$ stir $\longrightarrow$ add dispersant $\longrightarrow$ stir $\longrightarrow$ adjust PH value $\longrightarrow$ stir $\longrightarrow$ stand still $\longrightarrow$ observe the dispersion effect.

3.2. Best Dispersant and Dispersion Process Selection.
The choice of the best dispersant is mainly determined by measuring the change in the volume sedimentation rate of TiO$_2$ after 5 days of standing for each dispersant under different dosage and pH conditions. Then, the determined optimal dispersant and the nanometer TiO$_2$ and Ag particle size under different dispersing process conditions were tested by TEM, and the best dispersant and dispersion process were finally determined.

3.2.1. Selection of Ionic Dispersant.
Disperse SDS, SDBS, and SD-03 ionic dispersants according to the process in Table 1, then put them in a graduated cylinder under the same conditions, let them stand for 5 days, and then calculate the sedimentation rate relative to the entire system. The smallest value corresponds to the dispersant and dispersant dosage.

The minimum sedimentation rate of the dispersant SDS is 0.045%, the corresponding dispersant dosage is 0.5%, and the minimum sedimentation rate of the dispersant SDBS is 0.046%, which is similar to the minimum sedimentation rate of the dispersant SDS, which corresponds to the dispersion. The dosage of the dispersant is 0.2%, the dispersion effect of the dispersant SD-03 is the worst, and its minimum sedimentation rate is 0.086%, which corresponds to a dispersant dosage of 1%. Change the PH value of the above dispersant at its optimal dosage, and also put it for 5 days to observe the volume sedimentation rate.

Among the three ionic dispersants used in the experiment, the dispersant SDBS had the best dispersion effect, the best dosage was 0.2%, and the best PH value was 10; the worst dispersion effect was that of the dispersant SD-03. The particle dispersion effect is best when pH = 10.

The above is the selection of the best ionic dispersant. Use the same experimental method to select the best nonionic dispersant, then compare the dispersion effect of the
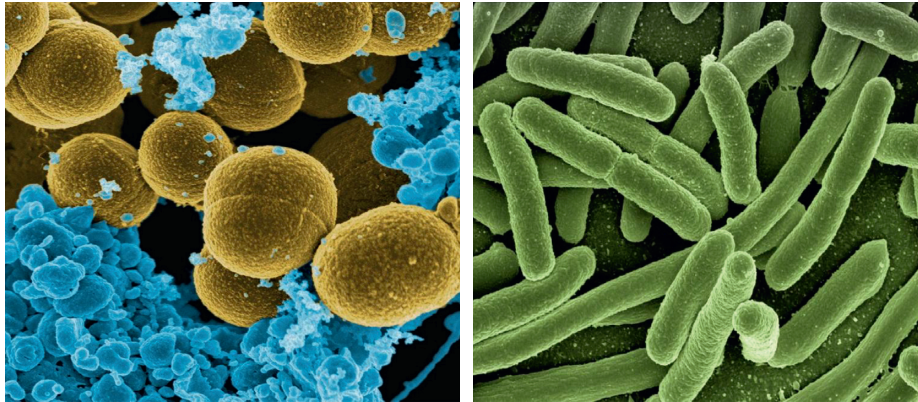
FIGURE 1: *Staphylococcus aureus* and *Escherichia coli* (http://alturl.com/uc3j5 and http://alturl.com/fmpiu).

TABLE 1: Main reagent information.

Drug name	Analytically pure	Factory
Citric acid	Analytically pure	Bengbu Chemical Reagent Factory
SDS	Chemically pure	Hedong District Hongyan Chemical Reagent Factory
SDBS	—	Yifa Chemical Reagent Factory
SD-03	Chemically pure	A chemical research institute
PEG	Chemically pure	Kemeou Chemical Reagent Development Center
TW-80	Chemically pure	Zonghengxing Industry and Trade Co., Ltd., Chemical Reagent Company
OP	Analytically pure	Yifa Chemical Reagent Factory
Absolute ethanol	Analytically pure	Chemical reagent factory
Ethylene glycol	Analytically pure	Zongheng Xinggong Chemical Reagent Company

ionic dispersant and nonionic dispersant, and finally select the best dispersant and dispersion process.

3.2.2. Selection of Nonionic Dispersant.
The dispersing principle of nonionic dispersant is to form an adsorption layer on the surface of the particles, so that the particles are dispersed. Therefore, the amount of dispersant is much larger than that of particle-type dispersants, and it is no longer nanopowder. Furthermore, its pH value is no longer the main influencing factor, so the pH value is set to 7 in the experiment.

Comparing the volume sedimentation rate of PEG, TW-80, OP, and nonionic dispersant, we can find that the overall volume sedimentation rate of dispersant TW-80 is very small, the smallest can reach 0.015%, and the corresponding dispersant dosage is 1.5 times the amount of nanopowder. Combining the above dispersants, we can find that the best dispersing effect is the nonionic dispersant TW-80, and its optimum dosage is 1.5 times the amount of nanopowder. It can be seen from the TEM photo that the dispersant TW-80 has the best dispersion effect when the amount of dispersant is 1.5 times the amount of TiO_2.

3.2.3. Determination of pH.
The best process of nano-antimite and antibacterial finishing agent is as follows: the dispersant is TW-80. The pH value is 7, and the mixing time is not less than 30 min.

3.3. Nano-Antimite and Antibacterial Finishing Agent.
In order to achieve the expected goal, i.e., to kill bacteria and repel mites and to decompose their residual nuclei and remains, we used the way of nanomaterials compounding. Nano-Ag is a contact antibacterial agent, which kills the bacteria by destroying the sulfhydryl group of the enzyme protein in the bacteria by the free Ag+. Nano-TiO_2 is a photocatalytic antibacterial agent. It kills bacteria and decomposes organic matter by decomposing various bacteria or organic matter into small inorganic molecules such as CO_2 and H_2O through the highly oxidizing HO• and •O_2.

The weight of nano-TiO_2 powder is 20 grams and Ag is 20 grams, the volume of dispersion medium (absolute ethanol) is 100 mL, the amount of dispersant TW-80 is $20 \times 1.5 = 30$ g, the amount of citric acid is $20 \times 3 = 60$ g, and pH = 7. Stirring time is 30 min, and stirring speed is 6000 r/min. The emulsion prepared is very stable, and there is only a small amount of precipitation after standing for 5 days. The TEM photos of nano-TiO_2 and Ag under the best dispersion process are shown in Figure 2.

3.4. Nanometer Antimite and Antibacterial Silk Knitted Garment Finishing

3.4.1. Finishing Method.
For natural fibers, since functional powder cannot be added in the fiber production process, only postprocessing methods can be used. Processing techniques include exhaustion method, padding method,

(a)

(b)
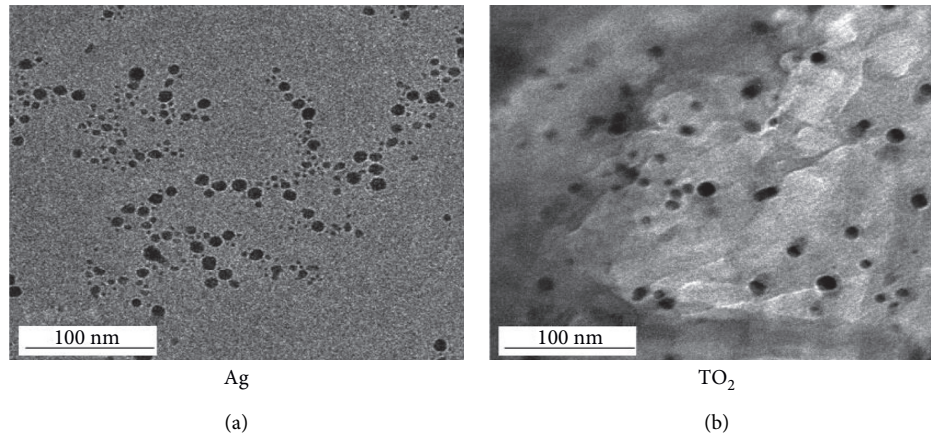
Figure 2: TEM images of nano-TiO_2 and Ag under the best dispersion process (from http://alturl.com/7j8ad).

and coating method. Considering the characteristics of the silk knitted fabric itself, in this experiment, the exhaustion method is used in the finishing process to finish the silk knitted fabric as follows:

(1) Laboratory apparatus: IR12P infrared dyeing instrument, LD-3624 sample shaping dryer

(2) Medicine: adhesive (Shanghai Fujikawa Chemical Co., Ltd.), detergent: German soap (MT9906017)

(3) Fabric: silk knitted fabrics of various colors (Zhejiang Xinyang Knitting Apparel Company)

(4) Process formula is as follows:

> #1 finishing solution formula: compound finishing dosage 0.5%; TiO_2 : Ag, respectively, 1 : 0, 1 : 1, 1 : 2, 1 : 5, 1 : 10, 0 : 1; adhesive 4%; liquor ratio 1 : 10.
> #2 finishing solution formula: compound finishing dosage 1%; TiO_2 : Ag, respectively, 1 : 0, 1 : 1, 1 : 2, 1 : 5, 1 : 10, 0 : 1; adhesive 4%; liquor ratio 1 : 10.
> #3 finishing solution formula: composite finishing dosage 2%; TiO_2 : Ag, respectively, 1 : 0, 1 : 1, 1 : 2, 1 : 5, 1 : 10, 0 : 1; adhesive 4%; liquor ratio 1 : 10.

3.4.2. Process Flow. The process flow is summarized as follows: fabric washing ⟶ dehydration ⟶ immersion of the fabric in a dyeing cup filled with finishing liquid- ⟶ heating up (reaching 40°C within 10 min) ⟶ keeping warm (30 min) ⟶ prebaking at 90°C for 5 min ⟶ baking at 120°C for 2 min ⟶ washing.

3.4.3. Washing Method. Follow the Japanese Industrial Standards (JIS) washing method. Use household alkaline detergents (polyoxyethylene alkyl ether and sodium α-olefin xanthate, 9 : 1 compound) in household washing machines with a bath ratio of 1 : 30. Washing at 40°C for 5 minutes and two washings with water for 2 minutes at room temperature constitute a cycle.

4. Discussion

4.1. Bacteriostatic Test Analysis. The effect of different composite finishing agents is shown in Figure 3, with different amounts of composite finishing agent: 0.5%, 1%, and 2%. Taking into account the high price of nanopowder, from the perspective of enterprise cost, the ratio of TiO_2 and Ag is 1 : 1, 1 : 2, and 1 : 3, respectively, to finish the fabric, and then the shaking flask method is used to carry out the antibacterial test.

When the dosage of the composite finishing agent is 0.5%, the TiO_2 : Ag ratio is 1 : 3, 1 : 2, and 1 : 1, and the finished fabrics are numbered #1, #2, and #3. That is to say, the household alkaline detergent polyoxyethylene alkyl ether and α-olefin yellow sodium are compounded in a ratio of 9 : 1. After 20 washings, the antibacterial effect was measured by the shaking flask method. After shaking for 5 hours by the shaking flask method, the antibacterial situation of the finished fabric is shown in Table 2.

During the test, when the ratio of TiO_2 to Ag is 1 : 3, the antibacterial effect is the best, reaching more than 94%. After washing the fabric 20 times, the antibacterial effect on gold can be stabilized above 97%. By gradually narrowing the scope of the method, the final determination of the best process is as follows: the amount of composite finishing agent is 0.5%, and the ratio of TiO_2 and Ag is 1 : 3. The antibacterial situation of the fabric after 20 washings is shown in Table 3.

In the study, the sample "nano-mite-proof silk knitted garment fabric" (after washing 50 times) was used for 6 hours, and the antibacterial rate against *Staphylococcus aureus* (ATCC6S38) reached more than 50.0%; the sample "nano-mite-proof silk knitted garment fabric" (after washing 50 times in water) acts for 6 hours, and its antibacterial rate against *Escherichia coli* reaches over 50.0%. The antibacterial effect of "nano-mite-proof silk knitted garment fabric" on *Staphylococcus aureus* is shown in Table 4.

Under the condition of the test temperature of 20 ± 2°C, the nanometer antimite silk knitted garment fabrics submitted for inspection have been used for 6 hours, and the antibacterial rate against *Staphylococcus aureus* (ATCC6538)
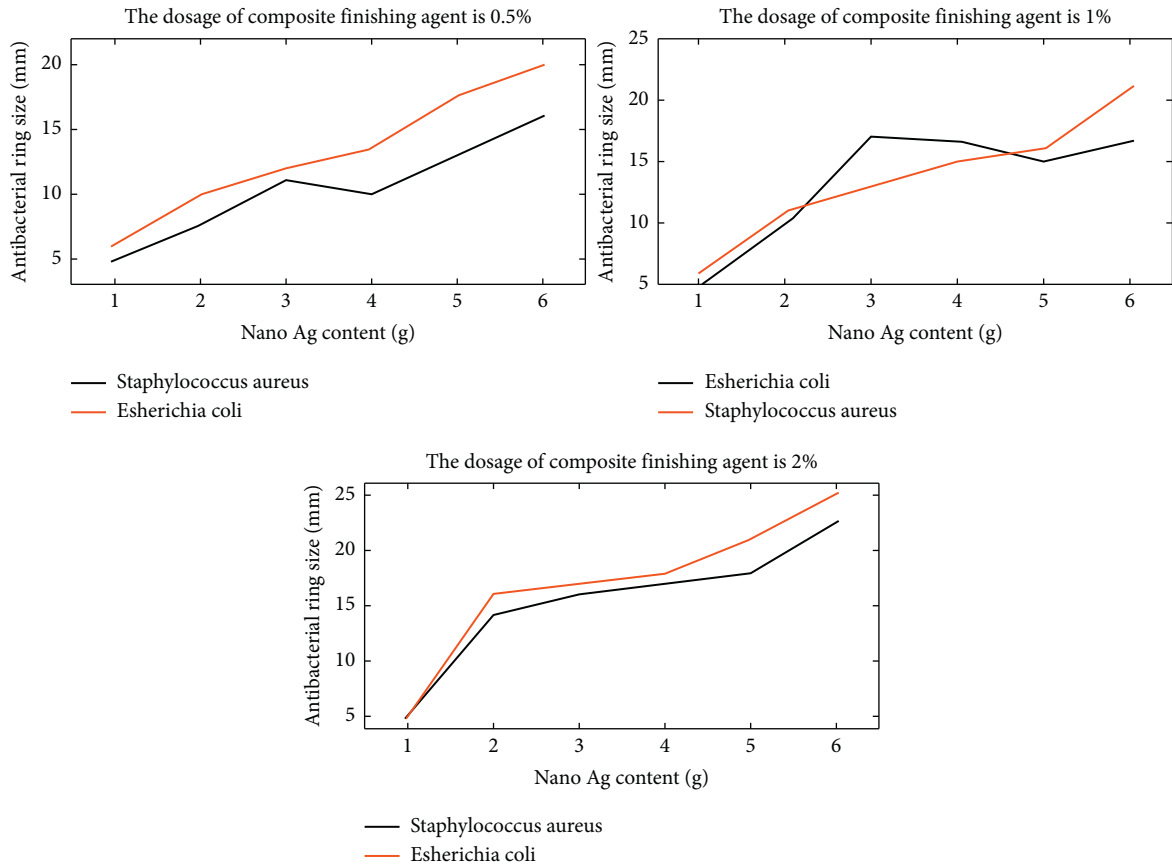
FIGURE 3: Different amounts of composite finishing agent.

is above 90%. The antibacterial effect of "nano-mite-proof silk knitted garment fabric" on *Escherichia coli* is shown in Table 5.

4.2. Fabric Performance Test Analysis.

During the test, each sample is tested 10 times, and then the average value is calculated. The area of presser foot is $100 \, mm^2$, the diameter of presser foot is 10.28 mm, the pressure is 200 N, and the pressure time is 10 s. It can be seen from the data of the average diameter of the contrast samples in Figure 4 that the thickness of the fabric before and after finishing does not change at all. The comparison of the average diameter of the fabric thickness is shown in Figure 4.

Air permeability is an important indicator of the comfort of wearing clothing. The finished fabric and the original sample are tested on 5 samples, and the average value is calculated. It can be seen that the air permeability of the finished fabric is the same or slightly better. The air permeability comparison is shown in Figure 5.

The better the drape of the fabric, the better the material. It can be seen from Figure 6 that the drape of the finished fabric is better than the original or remains unchanged, and there is no sample with worse drape than the original. The drape of the fabric is shown in Figure 6.

Breaking strength and elongation at break are important indexes reflecting the mechanical properties of fabrics. It can be seen from Table 6 that there is no obvious change in the indexes of fabric strength before and after finishing; that is to say, the antibacterial and antimite fabric developed in this study has little effect on bursting strength and tensile length. The strength of reactive fabric is shown in Table 6.

The difference between this experiment and the previous experiment is that this experiment is conducted to deal with the clothing, not the piece of clothing, so there may be some problems that did not appear in the sample experiment. In the experiment, we try to choose different colors, different raw materials, and different fabrics for the selection of silk knitwear. The purpose is to verify the antibacterial properties of different materials and the impact on their properties and lay the foundation for the next batch production of enterprises. Different clothing properties are shown in Table 7.

Before and after finishing, the experiment condition temperature in the constant temperature box is $25 \pm 1°C$, and the relative humidity of the dryer is $75 \pm 2\%$. Nano-antimite and antibacterial knitted garments have an effect of 10 minutes, and the antibacterial rate against *Staphylococcus aureus* (ATCC6538) reaches more than 99.04%. After washing 50 times, the antibacterial rate against *Staphylococcus aureus* (ATCC6538) reached over 95.13%, and the antibacterial rate against *Escherichia coli* (8099) reached over 87.44%. The antibacterial effect of nanometer antimite and antibacterial knitted garments is shown in Figure 7.

TABLE 2: The antibacterial situation of the finished fabric after shaking for 5 hours by the shaking flask method.

Bacteria	Swatch	Diluent and bacterial concentration (cfu/tablet)		Bacteria concentration	Inhibition rate
	Numbering	100	10^{-1}	(cfu/mL)	(%)
	Original sample	Uncountable	Uncountable	5.23×10^5	—
Golden yellow	#1	468	48	5.22×10^5	99.90
Staphylococcus	#2	491	52	4.91×10^5	99.87
	#3	499	53	3.94×10^5	97.48
Large intestine	#1	Uncountable	462	3.57×10^5	97.26
Bacillus	#2	Uncountable	487	4.01×10^5	96.8

TABLE 3: Bacteriostasis of fabric after 20 washings.

Bacteria	Swatch	Diluent and bacterial concentration (cfu/tablet)		Bacteria concentration	Inhibition rate
	Numbering	100	10^{-1}	(cfu/mL)	(%)
	Original sample	Uncountable	Uncountable	5.23×10^5	—
Golden yellow	#1	Uncountable	348	5.23×10^5	98.85
Staphylococcus	#2	Uncountable	452	4.82×10^5	98.13
	#3	Uncountable	453	4.01×10^5	98.25
Large intestine	#1	Uncountable	Uncountable	3.59×10^5	97.21
Bacillus	#2	Uncountable	Uncountable	3.99×10^5	96.74

TABLE 4: Antibacterial effect of nano-antimite silk knitted garment fabrics on Staphylococcus aureus.

The average bacteriostatic rate and range of different action time (%)		
	1 h	6 h	12 h
	33.49	54.65	64.19
Average number of colonies and range of positive control group (cfu/tablet)	(32.99–33.90)	(53.33–55.40)	(63.41–64.88)
	5.77×10^4	5.37×10^4	5.13×10^4
	4.85×10^4–6.66×10^4	4.35×10^4–6.2×10^4	4.10×10^4–6.11×10^4

TABLE 5: Antibacterial effect of "nano-mite-proof silk knitted garment fabric" on Escherichia coli.

The average bacteriostatic rate and range of different action time (%)		
	1 h	6 h	12 h
	85.88	91.79	94.19
Average number of colonies and range of positive control group (cfu/tablet)	(85.21–86.64)	(91.50–92.17)	(93.41–94.88)
	5.68×10^4	5.36×10^4	4.13×10^4
	4.5×10^4–6.69×10^4	4.25×10^4–6.38×10^4	3.10×10^4–5.11×10^4
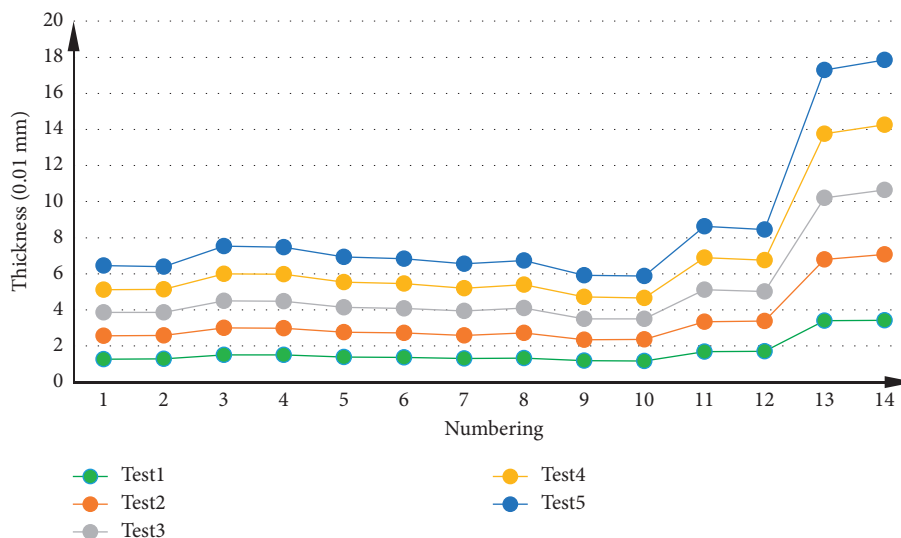
FIGURE 4: Comparison of average diameter of fabric thickness.
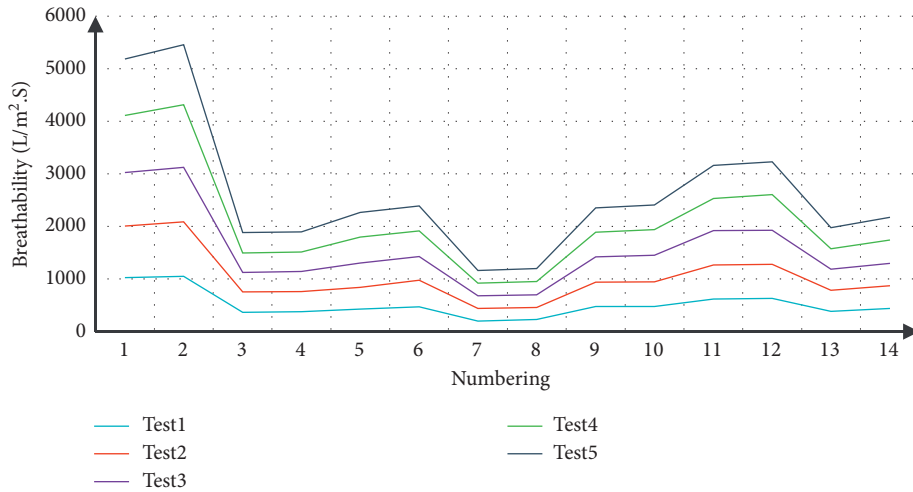
Figure 5: Air permeability comparison.
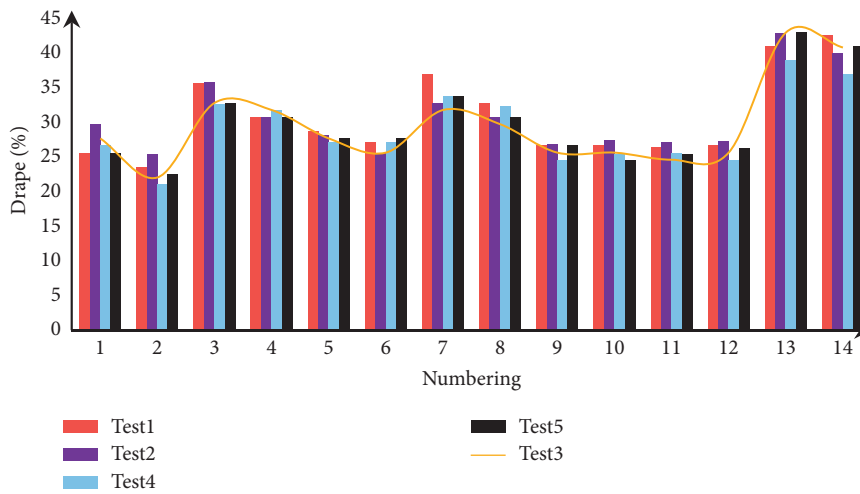
Figure 6: Drapability of fabric.

Table 6: Reaction fabric strength.

Sample		1	2	3	4	5
Unorganized	Breaking strength (N)	402	412	431	421	359
	Stretching length (mm)	48	51	49	49	52
Organized	Breaking strength (N)	432	445	434	459	467
	Stretching length (mm)	49	55	45	51	53

Table 7: Different clothing properties.

Fabric color	Material	Organization	Weight	Quantity (piece)
Light blue	Spandex + filament	6 + 6 rib	302	1
Dark camel	Filament	Jacquard	136	1
Red	Silk + cashmere	Flat needle	226	1
Blue	Spandex + spun silk	Jacquard	266	2
Color stripes	Spun silk	Flat needle	256	2
Green	Spun silk	Jacquard	189	2
Light stone cyan	Filament	Flat needle	276	1
Black	Spandex + spun silk	Flat stitch	236	1
Dark gray	Filament + spandex	Flat needle	348	1
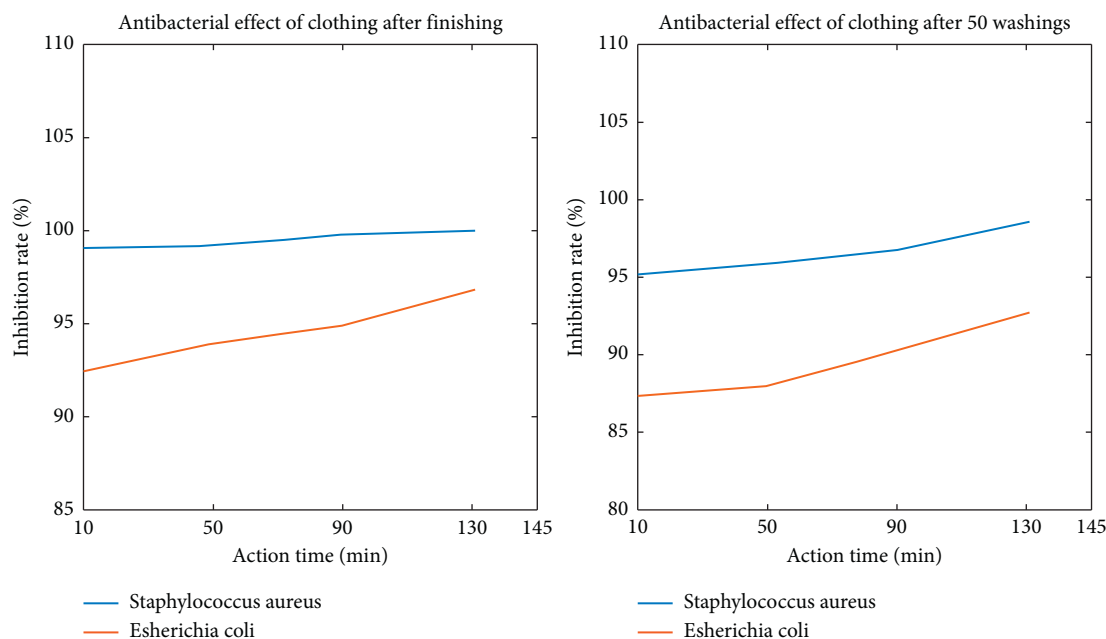
Figure 7: Nano-antimite and antibacterial knitted garment.

5. Conclusion

As a green and environmentally friendly photocatalyst, TiO_2 has been used in air pollution treatment and water pollution treatment due to its stable chemical properties and low price. In addition, TiO_2 is a kind of inorganic antibacterial agent; because of its long-lasting and broad-spectrum antibacterial properties, it does not easily produce drug resistance and has the advantages of thorough sterilization and no toxic side effects to the human body. It is used in the antibacterial finishing of textiles. In order to improve the photocatalytic performance of TiO_2, this study has carried out sulfur and nitrogen codoping modification to prepare cotton fabrics loaded with doped TiO_2 visible light catalytic durability antibacterial fabric, and its antibacterial properties were studied. This study involves the best antibacterial material, the best dispersant, the best dispersion process, the best finishing process, and the best plan considering the actual selection of the enterprise. Finally, the most effective antimite and antibacterial cotton knitted fabric is obtained. The results show that nano-Ag and TiO_2 have outstanding antibacterial effect and the composite finishing agent is composed of photocatalysis and contact finishing agent, so its antibacterial effect is no longer affected by environmental conditions and will be more thorough. The best effect will be achieved when the ratio of Ag and TiO_2 is $3:1$. Dispersion is the key of nano-antimite and antibacterial finishing agent. In this study, through searching a large number of literature studies and referring to the research results of dispersion at home and abroad, the dispersion theory which can fully disperse nanoparticles was summarized. After a series of fabric mechanical properties and fabric style tests, this study revealed that cotton knitwear finished by nano-antimite and antibacterial finishing agent has good antimite and antibacterial effect and washing fastness. In future work, the dispersion problem is still the key of nanomaterials. The full dispersion of nanoparticles still needs to be further improved to make the obtained nanosolution more effective. Therefore, the dispersion process and finishing process still need to be further improved in the actual production of enterprises, so as to get the best antibacterial performance with the least investment.

Data Availability

The data that support the findings of this study are available from the author upon reasonable request.

Conflicts of Interest

The author declares no potential conflicts of interest with respect to the research, authorship, and/or publication of this article.

References

[1] B. Gao, N. Xu, and P. Xing, "Shock wave induced nano-crystallization during the high current pulsed electron beam process and its effect on mechanical properties," *Materials Letters*, vol. 237, no. 15, pp. 180–184, 2019.

[2] Z. Yanyan, W. Minghao, W. Mingjie, J. Zhu, and X. Zhang, "Multifunctional carbon-based nanomaterials: applications in biomolecular imaging and therapy," *ACS Omega*, vol. 3, no. 8, pp. 9126–9145, 2018.

[3] R. Paul, F. Du, L. Dai et al., "3D heteroatom-doped carbon nanomaterials as multifunctional metal-free catalysts for integrated energy devices," *Advanced Materials*, vol. 31, no. 13, Article ID 18055981, 2019.

[4] L. Li, C. Chen, H. Liu et al., "Multifunctional carbon-silica nanocapsules with gold core for synergistic photothermal and chemo-cancer therapy under the guidance of bimodal

imaging," *Advanced Functional Materials*, vol. 26, no. 24, pp. 4252–4261, 2016.

[5] S. A. Santos, E. T. Silva, A. V. Caris, F. S. Lira, S. Tufik, and R. V. T. dos Santos, "Vitamin E supplementation inhibits muscle damage and inflammation after moderate exercise in hypoxia," *Journal of Human Nutrition and Dietetics*, vol. 29, no. 4, pp. 516–522, 2016.

[6] Y. Zhang, Y. Li, and C. Bai, "Microstructure and oxidation behavior of Si-MoSi 2 functionally graded coating on Mo substrate," *Ceramics International*, vol. 43, no. 8, pp. 6250–6256, 2017.

[7] Y. Zhang, W. Ni, and Y. Li, "Effect of siliconizing temperature on microstructure and phase constitution of Mo-MoSi2 functionally graded materials," *Ceramics International*, vol. 44, no. 10, pp. 11166–11171, 2018.

[8] L. Zhang, T. Liu, and Y. Chen, "Magnetic conducting polymer/mesoporous SiO2 yolk/shell nanomaterials: multifunctional nanocarriers for controlled release of doxorubicin," *RSC Advances*, vol. 6, no. 11, pp. 8572–8579, 2016.

[9] L. Qiu, Z. He, and D. Li, "Multifunctional cellular materials based on 2D nanomaterials: prospects and challenges," *Advanced Materials*, vol. 30, no. 4, pp. 17048501–170485015, 2018.

[10] G. Yang, H. Gong, T. Liu, X. Sun, L. Cheng, and Z. Liu, "Mesoporous silica-coated WS2@Fe3O4 nanosheets as a multifunctional theranostic nanocarrier for combination therapy of cancer," *Nanomedicine: Nanotechnology, Biology and Medicine*, vol. 12, no. 2, p. 523, 2016.

[11] N. Shadjou and M. Hasanzadeh, "Application of graphene and mesoporous silica nanomaterials on the orthopaedic implants: recent advances," *Materials Technology*, vol. 31, no. 13, pp. 806–811, 2016.

[12] Q. Ban, T. Bai, X. Duan, and J. Kong, "Noninvasive photothermal cancer therapy nanoplatforms via integrating nanomaterials and functional polymers," *Biomaterials Science*, vol. 5, no. 2, pp. 190–210, 2017.

[13] A. Peyvandi, I. Harsini, L. Ahmed Sbia et al., "Performance evaluation of precast concrete beams reinforced with multifunctional graphite nanomaterials," *PCI Journal*, vol. 61, no. 1, pp. 29–38, 2016.

[14] S. Raghav, R. Painuli, and D. Kumar, "Multifunctional nanomaterials for multifaceted applications in biomedical arena," *International Journal of Pharmacology*, vol. 13, no. 7, pp. 890–906, 2017.

[15] X. Li, T. Zhao, L. Sun et al., "The applications of conductive nanomaterials in the biomedical field," *Journal of Biomedical Materials Research. Part A*, vol. 104, no. 1, pp. 322–339, 2016.

[16] S. Marchesan, L. Ballerini, and M. Prato, "Nanomaterials for stimulating nerve growth," *Science*, vol. 356, no. 6342, pp. 1010-1011, 2017.

[17] C. Upendra, Q. Yiru, and J. F. Lovell, "Targeted nanomaterials for phototherapy," *Nanotheranostics*, vol. 1, no. 1, pp. 38–58, 2017.

[18] C.-F. He, C.-F. He, S.-H. Wang et al., "Advances in biodegradable nanomaterials for photothermal therapy of cancer," *Cancer Biology & Medicine*, vol. 13, no. 3, pp. 299–312, 2016.

[19] T. C. Jackson, B. O. Patani, and M. B. Israel, "Nanomaterials and cell interactions: a review," *Journal of Biomaterials and Nanobiotechnology*, vol. 08, no. 4, pp. 220–228, 2017.

[20] Z. Zhang and M. R. King, "Nanomaterials for the capture and therapeutic targeting of circulating tumor cells," *Cellular and Molecular Bioengineering*, vol. 10, no. 1, pp. 275–294, 2017.

[21] L. Yuxuan, W. Lijun, L. Yuan et al., "Immunosensors based on nanomaterials for detection of tumor markers," *Journal of Biomedical Nanotechnology*, vol. 14, no. 1, pp. 44–65, 2018.

[22] X. Luo, W. Wang, J. R. Dorkin et al., "Poly(glycoamidoamine) brush nanomaterials for systemic siRNA delivery in vivo," *Biomaterials science*, vol. 5, no. 1, pp. 38–40, 2016.

[23] Y.-G. Bi, D. Di Liu, X.-M. Liu, and S.-Q. Zhou, "Adsorption of Cu2+ from aqueous solution using PEG modified hydroxyapatite nanomaterials as adsorbent," *Journal of Biobased Materials and Bioenergy*, vol. 11, no. 4, pp. 364–371, 2017.

[24] T. M. Becker, J. Heinen, D. Dubbeldam, L.-C. Lin, and T. J. H. Vlugt, "Polarizable force fields for CO2 and CH4 adsorption in M-MOF-74," *Journal of Physical Chemistry C*, vol. 121, no. 8, pp. 4659–4673, 2017.

[25] T. Inprasit, K. Motina, P. Pisitsak, and P. Chitichotpanya, "Dyeability and antibacterial finishing of hemp fabric using natural bioactive neem extract," *Fibers and Polymers*, vol. 19, no. 10, pp. 2121–2126, 2018.

[26] N. A. Raouf, N. M. A. Enazi, I. B. M. Ibraheem, R. M. Alharbi, and M. M. Alkhulaifi, "Antibacterial and anti-hyperlipidemic activities of the green alga Cladophora koeiei," *Beni-Suef University Journal of Basic and Applied Sciences*, vol. 7, no. 1, pp. 158–164, 2018.

[27] C. H. Lim, K. Kim, and Y. Cheong, "Factors affecting sportswear buying behavior: a comparative analysis of luxury sportswear," *Journal of Business Research*, vol. 69, no. 12, pp. 5793–5800, 2016.

[28] B. Woo-Yeul, K. K. Byon, C. Young-Hwan, and C. W. Park, "Millennial consumers' perception of sportswear brand globalness impacts purchase intention in cause-related product marketing," *Social Behavior & Personality An International Journal*, vol. 45, no. 8, pp. 1319–1335, 2017.

[29] D. Baumann-Pauly, A. G. Scherer, and G. Palazzo, "Managing institutional complexity: a longitudinal study of legitimacy strategies at a sportswear brand Company," *Journal of Business Ethics*, vol. 137, no. 1, pp. 31–51, 2016.

[30] J. T. Kalkhoven and M. L. Watsford, "The relationship between mechanical stiffness and athletic performance markers in sub-elite footballers," *Journal of Sports Sciences*, vol. 36, no. 2, pp. 1022–1029, 2018.

[31] J. Drager, J. Rasio, and A. Newhouse, "Athletic pubalgia (sports hernia): presentation and treatment," *Arthroscopy: The Journal of Arthroscopic & Related Surgery*, vol. 36, no. 12, pp. 2952-2953, 2020.

[32] T. A. Hanson, M. R. Bryant, and K. J. Lyman, "Intercollegiate athletic programs, university brand equity and student satisfaction," *International Journal of Sports Marketing & Sponsorship*, vol. 21, no. 1, pp. 106–126, 2019.

Research Article

Wind Speed Forecast Based on the LSTM Neural Network Optimized by the Firework Algorithm

Bilin Shao [ID],[1] Dan Song [ID],[1] Genqing Bian [ID],[2] and Yu Zhao [ID][1]

[1]*School of Management, Xi'an University of Architecture and Technology, Xi'an 710055, China*
[2]*School of Information and Control Engineering, Xi'an University of Architecture and Technology, Xi'an 710055, China*

Correspondence should be addressed to Dan Song; 674355101@qq.com

Wind energy is a renewable energy source with great development potential, and a reliable and accurate prediction of wind speed is the basis for the effective utilization of wind energy. Aiming at hyperparameter optimization in a combined forecasting method, a wind speed prediction model based on the long short-term memory (LSTM) neural network optimized by the firework algorithm (FWA) is proposed. Focusing on the real-time sudden change and dependence of wind speed data, a wind speed prediction model based on LSTM is established, and FWA is used to optimize the hyperparameters of the model so that the model can set parameters adaptively. Then, the optimized model is compared with the wind speed prediction based on other deep neural architectures and regression models in experiments, and the results show that the wind speed model based on FWA-improved LSTM reduces the prediction error when compared with other wind speed prediction-based regression methods and obtains higher prediction accuracy than other deep neural architectures.

1. Introduction

As a green renewable energy source, wind power has an immeasurable commercial development prospect, and the research on related forecasting technologies is also more important. However, the randomness, volatility, and intermittency of wind resources have brought great troubles and challenges to the stable operation of the power system. Traditional wind power forecasting technologies are no longer sufficient to solve the above problems. For this reason, it is urgent to introduce cutting-edge artificial intelligence technology. Artificial intelligence is a branch of computer science dedicated to the research and development of theories, methods, technologies, and application systems for simulating, extending, and expanding human intelligence. In recent years, the rapid development of artificial intelligence-related machine learning, deep learning, and other technologies has provided new ideas for the research and implementation of high-precision wind power prediction technology and brought new development opportunities.

Wind power prediction relies on wind speed estimation. Due to the cyclical, daily pattern, and high stochastic variability, accurate prediction of wind power is too complicated. Therefore, it is clear that efficient transformation and application of the wind energy resources require exact and complete information on the wind features of the region, and local and regional climates, topography, and impediments include buildings; all affect wind energy. In the last decades, scholars have proposed different prediction methods based on the time series of historical wind speed and in general, these models can be divided generally into four types: physical, statistical, intelligence learning model, and hybrid model.

Physical approaches, which are based on a detailed physical description of the atmosphere, used meteorological data such as air temperature, topography, and pressure to predict wind speed, thus leading to intricate calculations and high costs [1]. Statistical methods, such as Autoregressive Integrated Moving Average (ARIMA) model, Seasonal ARIMA (SARIMA), Generalized Autoregressive Conditional Heteroskedasticity (GARCH) model, and Monte

Carlo Simulation [2], predict wind speed on the premise of linear assumption and are more accurate than physical methods [3, 4]. However, the variation of wind speed contains significant nonlinear and chaotic characteristics, and it is usually difficult to accurately and effectively predict the future wind speed simply by applying these methods or models. In addition, statistical methods require a large amount of data for learning and modeling and are more suitable for ultrashort-term wind power prediction. Intelligent learning methods, such as Support Vector Regressor (SVR), Decision Tree Regressor (DTR), Multivariate Linear Regression (MLR), Artificial Neural Network (ANN), train and predict the wind speed data with better performance in the fitting of the nonlinear changes of wind speed [5–7]. SVR, MLR, and DTR have advantages in sparsity and generalization and solving nonlinearity prediction problems, but its key parameters mainly rely on manual selection [8–11]. ANN [12, 13] has the advantages of good nonlinear fitting and strong self-learning ability, but it is unstable, slow convergence rate is easy to fall into the local optimal value, and it is difficult to obtain its network structure including the number of hidden layers. The wind speed prediction model based on Convolutional Neural Networks (CNN) can consider the temporal and spatial correlation of wind speed, to make the ultrashort-term prediction of the spatial distribution of wind speed [14–16].

Wind speed is affected by many factors, and a single prediction model cannot fully include all these factors. Particularly in extreme weather cases, a single model does not have sufficient learning, which may lead to a large deviation in the prediction. The combined prediction method takes into account the respective advantages of different models at the same time, optimally combining a variety of single models and giving play to the advantages of each model can significantly improve the accuracy of prediction [17–20]. Combination prediction methods mainly include weighted combination prediction and fusion combination prediction [21]. The key lies in the determination of the weight coefficient. The combination method of the fixed weight coefficient [22] is simple and easy to realize. The combination method of the variable weight coefficient [17] is strong adaptability and high accuracy. The fusion combination is optimized by other prediction methods in different prediction stages, including input data stabilization, model parameter optimization, and output error correction. Based on empirical mode decomposition (EMD) [22–25], variational mode decomposition (VMD) [26–29], analytical mode decomposition (AMD) [30, 31], the wavelet decomposition [14, 25, 32], and so on, the wind speed sequence data was preprocessed to make the data stable. Better prediction results are achieved. In addition, the Hilbert–Huang transform (HHT) [33], fast correlation filter [34], principal component analysis (PCA) [35], and so on extracted the input features of wind speed data and obtained good prediction results by optimizing the short-term wind speed prediction model combined with other prediction methods. It is an important way to optimize the parameters of the model by using an intelligent algorithm. According to the characteristics of the wind speed data, the intelligent

algorithm is used to determine the parameters adaptively during the training process to improve the learning ability and generalization ability of the model. Genetic algorithm [36], particle swarm optimization algorithm [27], and cuckoo algorithm [37] are used to optimize the hybrid model combining the parameters and threshold values of BPNN, LSTM, SVM, and other intelligent learning models, which can overcome the problem of low prediction accuracy of a single model and improve the accuracy of wind speed prediction. The prediction results of the traditional method are substituted into the error model to correspond to the superposition and correct the error, which has strong universality and is not limited to the specific prediction process [38–41].

In this paper, based on the measured data of a wind turbine in a power plant and the analysis of wind power time series, the combined prediction method is proposed. Firstly, a wind speed prediction model based on LSTM is established. Then, from the perspective of model hyperparameter optimization, the fireworks algorithm (FWA) is used to automatically search for the best hyperparameter combination suitable for wind speed data. Finally, the optimized FWA-LSTM is used to predict and analyse the wind speed data, and its feasibility and effectiveness are verified.

This paper is organized as follows: in Section 2, we constructed a wind speed prediction model based on LSTM; in Section 3, we studied the firework algorithm, hyperparameters optimization of LSTM by the firework algorithm, and optimized LSTM wind speed prediction algorithm based on firework algorithm. In addition, experimental environment configuration and parameter settings, wind speed prediction results based on the proposed method, and the comparison are discussed; and finally, the main conclusions are drawn in Section 5.

2. Wind Speed Prediction Model Based on LSTM

2.1. LSTM Neural Network Model. The traditional neural network model will lose the remote information, and it is difficult to learn the long-distance dependent information. LSTM is an improvement of the recurrent neural network, which aims to overcome the defects of the recurrent neural network in processing long-term memory. The LSTM introduced the concept of cellular states, which determine which states should be preserved and which should be forgotten. The basic principle of LSTM is shown in Figure 1.

As shown in Figure 1, X_t is the input at time t, h_{t-1} is the output of the hidden layer at time $t - 1$, and C_{t-1} is the output of the historical information at time $t - 1$; f, i, and o are, respectively, the forgetting gate, input gate, and output gate at time t, and e is the internal hidden state, namely, the transformed new information. LSTM conducts parameter learning for them in the training. C_t is the updated historical information at time t, and h_t is the output of the hidden layer at time t.

Firstly, the input x_t at time t and the output h_{t-1} of the hidden layer are copied into four copies, and different weights are randomly initialized for them, so as to calculate the forgetting gate f, input gate i, and output gate o, as well as the internal hidden state e. Their calculation methods are
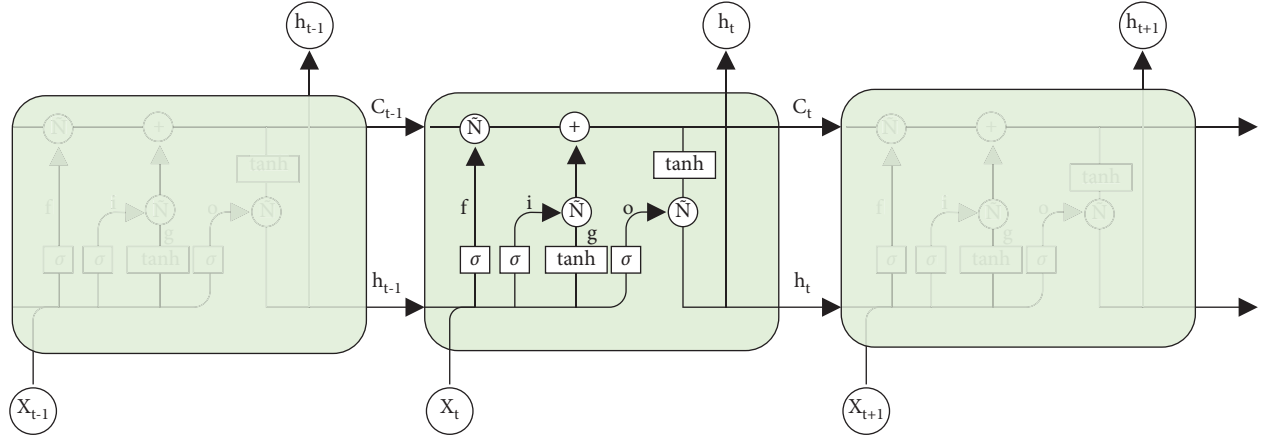
FIGURE 1: Basic principle of LSTM.

shown in formulas (1)–(4), where W is the parameter matrix from the input layer to the hidden layer, U is the self-recurrent parameter matrix from the hidden layer to the hidden layer, r is the bias parameter matrix, and σ is the sigmoid function so that the output of the three gates remains between 0 and 1:

$$f = \sigma\left(W_f x_t + U_f h_{t-1} + r_f\right), \tag{1}$$

$$i = \sigma\left(W_i x_t + U_i h_{t-1} + r_i\right), \tag{2}$$

$$o = \sigma\left(W_o x_t + U_o h_{t-1} + r_o\right), \tag{3}$$

$$g = \sigma\left(W_g x_t + U_g h_{t-1} + r_g\right). \tag{4}$$

Secondly, forgetting gate f and input gate i are used to control how much historical information C_{t-1} is forgotten and how much new information e is saved, to update the internal memory cell state C_t. The calculation method is as follows:

$$C_t = f_t \otimes C_{t-1} \oplus i \otimes e. \tag{5}$$

Finally, output gate o is used to control how much C_t information of the internal memory unit is output to the implicit state h_t, and its calculation method is shown as follows:

$$h_t = o \otimes \tanh\left(C_t\right). \tag{6}$$

2.2. Wind Speed Prediction Model Based on LSTM. The process of using LSTM to predict wind speed data is shown in Figure 2. It mainly includes wind speed data preparation and preprocessing (data resampling and null filling), data normalization, data division, prediction model establishment and evaluation, and data prediction.

First, the wind speed data is modeled as a nonnegative matrix X of an $N \times T$, where N represents the number of wind speed monitoring points, T represents the number of time slots sampled, and each column in the wind speed data matrix represents the wind speed value at different points in a specific time interval.

Wind speed prediction can obtain the predicted value of the future time through the historical time series, $X(i, j)$ represents the scale of $N \times T$ flow matrix, $x_{n,t}$ represents the wind speed value of row n and column t. Wind speed prediction is defined by a series of historical wind speed data $(x_{n,t-1}, x_{n,t-2}, x_{n,t-3}, \ldots, x_{n,t-1})$ to predict the wind speed at time t in the future. In the wind speed prediction model based on LSTM (Figure 2), it is assumed that the wind speed at a certain point in the t-slot is predicted, the input of the model is $(x_{n,t-1}, x_{n,t-2}, x_{n,t-3}, \ldots, x_{n,t-1})$, and the output is the predicted value $\hat{x}_t$ of the wind speed at the t-slot at this point.

(1) Wind speed data preparation and preprocessing: to meet the time-frequency (seconds, minutes, hours, days, etc.) requirements of wind speed data prediction, it is necessary to resample the original data, that is, to convert the time series from one frequency to another through downsampling or upsampling. In addition, if there are null values in the resampled data sequence, the null values need to be filled. Here, we use the machine learning method—the K-Nearest Neighbours (KNN)—to fill with null values of wind speed data.

(2) Data normalization: the range standardization method is used to process the wind speed data so that the sample data value is between 0 and 1. The calculation method of the range standardization method is shown as follows:

$$X_{\text{nor}} = \frac{X - X_{\min}}{X_{\max} - X_{\min}}. \tag{7}$$

In formula (7), $X_{\max}$ represents the maximum value of wind speed data and $X_{\min}$ represents the minimum value of wind speed data.

(3) Data division: the wind speed data after preprocessing and normalization is divided into a training set and a test set according to a simple cross-validation method. While keeping the wind speed data sequence unchanged, fivefold cross-validation is used to divide into the training set and the test set, which are used for the training and prediction of the LSTM wind speed prediction model, respectively.
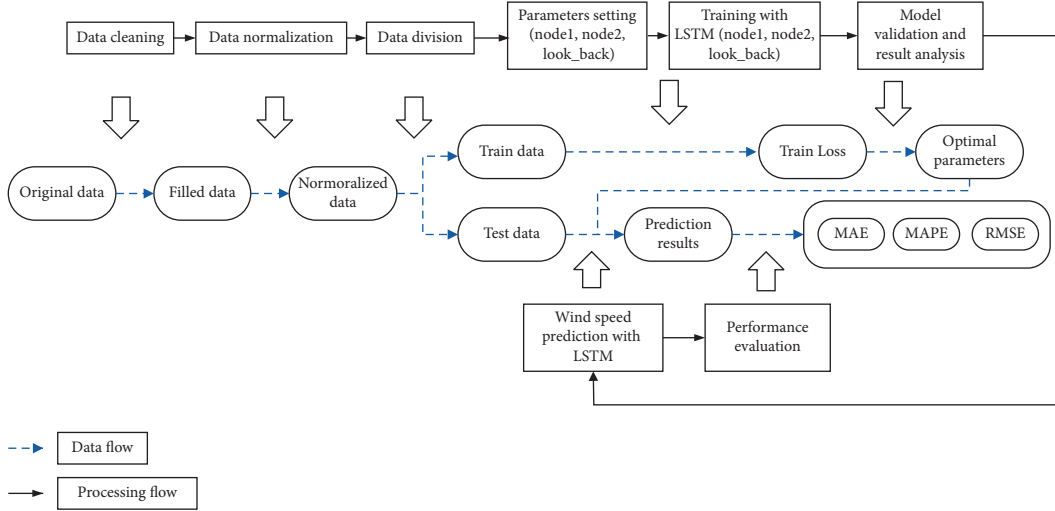
FIGURE 2: General schematic diagram for LSTM-based wind speed prediction.

(4) Construct an LSTM wind speed prediction model: define an LSTM neural network and set the parameters, including time step, network layer number, number of neurons in each layer, dropout, activation function, return value type and number, hidden layer dimension size, learning rate, batch size, and values for the number of iterations.

(5) Compile the network: set the optimizer, error measurement indicators, and training record parameters and compile the constructed LSTM wind speed prediction model.

(6) Evaluate the network: the training set data is substituted into the model for training, the error of the established prediction model is evaluated, and the parameter settings of the model are fine-tuned according to the result to obtain a better prediction effect.

(7) Forecast and evaluation: use the optimized wind speed prediction model to make predictions, compare the prediction results with the real data, and calculate the error.

3. The LSTM Wind Speed Prediction Model Optimized by the Firework Algorithm

3.1. The Firework Algorithm. The fireworks algorithm (FWA) [42–44] is a simple-rule, fast-convergence-speed swarm intelligence optimization algorithm. It searches the solution space mainly by the sparks generated by the firework explosions, and the fireworks and the sparks from the explosion formed the whole crowd. In this algorithm, the firework is seen as a feasible solution in the solution space of the optimization problem, and the process of firework explosion to generate sparks is the way of searching the neighbourhood. FWA includes the following steps: initialization, calculating the fitness, generating sparks by firework explosions, and calculating the optimal solution.

Firstly, FWA sets a series of initial parameter values including the number of fireworks population N, the explosion range control parameter $\widehat{A}$, the maximum number of sparks m, the number of variant sparks $\widehat{m}$, the parameters a and b that limit the number of sparks produced by the explosion, The minimum normal value ε of zero, and the solution space boundaries B_u and B_i, where B_u is the upper boundary and B_i is the lower boundary. The firework algorithm mainly uses random initialization to generate N initial fireworks in the solution space.

Secondly, calculate the fitness value of each firework, and generate sparks based on the fitness value. The calculation for generating the number of sparks in FWA is shown as follows:

$$S_i = m \frac{Y_{\max} - f(x_i) + \varepsilon}{\sum_{i=1}^{N} (Y_{\max} - f(x_i)) + \varepsilon}. \tag{8}$$

In formula (8), S_i is the number of sparks produced by the ith firework, m is a constant which limits the total number of sparks produced, $Y_{\max}$ is the objective function value of the firework with the worst fitness of the current population, $f(x_i)$ is the fitness function of the firework x_i, and ε is the minimum number of the machine.

The calculation of FWA explosion amplitude is shown as follows:

$$A_i = \widehat{A} \frac{f(x_i) - Y_{\min} + \varepsilon}{\sum_{i=1}^{N} (f(x_i) - Y_{\min}) + \varepsilon}. \tag{9}$$

In formula (9), A_i is the explosion amplitude of the ith firework, that is, the explosion radius, $\widehat{A}$ is a constant which represents the maximum explosion amplitude, and $Y_{\min}$ is the fitness value of the firework with the best current population fitness value.

Thirdly, according to the actual firework attributes and the actual situation of the search problem, sparks are generated in the radiation space of the firework. To ensure the diversity of the population, the fireworks need to be appropriately mutated, such as Gaussian mutation.

The calculation of the Gaussian mutation algorithm in FWA is shown as follows:

$$x_i^k = x_i^k \times g. \tag{10}$$

In formula (10), x_i^k is the position of the ith individual on the kth dimension and g is the value of the Gaussian distribution function where $g \sim (1, 1)$.

Finally, calculate the optimal solution of the population and decide whether the termination condition is met. If it satisfies the requirements, stop the search; else, continue iterating.

In the entire population, the spark with the best fitness value is selected and retained as the next-generation fireworks, and the remaining sparks are selected by roulette. The probability of each spark being selected is calculated as follows:

$$P(x_i) = \frac{R(x_i)}{\sum_{j \in k} R(x_i)}. \tag{11}$$

In formula (11), $P(x_i)$ is the probability of the ith spark and $R(x_i)$ is the sum of the distance between the x_i and the candidate fireworks except for x_i.

Compared with particle swarm optimization (PSO) and genetic algorithm (GA), the fireworks algorithm has higher convergence and solving accuracy and has been applied to solve many practical optimization problems, of which parameter optimization is an important aspect [45–47].

3.2. Hyperparameter Optimization of LSTM by the Firework Algorithm. The hyperparameter selection of the LSTM model has an important influence on the prediction accuracy of the model. The existing hyperparameter selection generally adopts the empirical method. The empirical method is arbitrary and blind in the choice of parameters without universality. Therefore, combining multiple hyperparameters into a multidimensional solution space and traversing the solution space to obtain the optimal parameter combination can reduce the randomness and blindness of parameter selection. The selection of multiple hyperparameters is often carried out in a larger solution space, and a better performance optimization algorithm is needed to quickly obtain the global optimal solution. Therefore, the firework algorithm with global optimization and fast convergence speed is adopted to optimize the LSTM model's hyperparameters to improve the scientificity of model parameter selection and thus improve the prediction accuracy of the model.

Suppose that n hyperparameters of the LSTM wind speed prediction model need to be optimized, and each firework represents a set of hyperparameters in the solution space. Assuming that there are q sets of hyperparameter combinations in the n-dimensional continuous search space, for the ith hyperparameters $i(i = 1, 2, \ldots, q)$ in the spark, the n-dimensional current position vector $x^i(k) = [x_1^i \ x_2^i \ \ldots x_n^i]^T$ represents the current value of the ith group of hyperparameters in the solution space, and the n-dimensional velocity vector $v^i(k) = [v_1^i \ v_2^i \ \& \ v_n^i]^T$ represents the search direction of the group of hyperparameters.

The goal of wind speed prediction is to make the predicted value close to the actual value, that is, the error between the predicted value and the actual value is as small as possible, so the Root Mean Square Error (RMSE) of the training data in the wind speed prediction model is selected as the objective function. Let fitness = RMSE; then, the objective function is to minimize RMSE. The calculation method of RMSE is as follows:

$$\text{RMSE} = \sqrt{\frac{1}{n} \sum_{i=1}^{n} (y_i - \widehat{y}_i)^2}. \tag{12}$$

In formula (12), $\widehat{y}_i$ is the predicted value, $\widehat{y} = \{\widehat{y}_1, \widehat{y}_2, \ldots, \widehat{y}_i\}$, y is the true value, $y = \{y_1, y_2, \ldots, y_i\}$.

According to the firework algorithm, two important hyperparameters of the LSTM wind speed prediction model are optimized: the time step and the number of neurons in each layer. Two LSTM models, single-layer and double-layer LSTM, are used as the research objects to optimize the hyperparameters. Use node to represent the number of neurons and look_back to represent the time step. For a single-layer LSTM model, fitness = RMSE (node, look_back); for a two-layer LSTM model, fitness = RMSE (node 1, node 2, look_back).

According to the FWA process (as shown in Figure 3), the process of the hyperparameters optimization of the LSTM wind speed prediction model mainly includes six steps:

> Step 1: initialize the parameters of FWA: set the initial firework population size, namely, the number of hyperparameter combinations N, the explosion range control parameter $\widehat{A}$, the maximum number of sparks m, and the number of variant sparks $\widehat{m}$ and limit the number of sparks produced by the explosion parameters a and b, the minimum normal value ε that tends to zero, and the solution space boundaries B_u and B_i, where B_u is the upper boundary and B_i is the lower boundary. Using random initialization, N initial fireworks are generated in the solution space. Set the maximum number of iterations *item_max* and the preset error *Pre_error*.

> Step 2: calculate the fitness of each firework; that is, calculate the fitness value of the objective function of each group of hyperparameters. According to the fitness value, the explosion operator, the number of sparks, the explosion amplitude, and the offset value are calculated. Each firework explosion generates sparks of the hyperparametric group, and the sparks beyond the boundary are mapped according to the rules. At the same time, a certain number of Gaussian variation sparks of the hyperparametric group are generated by using Gaussian variation.

> Step 3: set the optimal objective function value F_i of each group of hyperparameters. For the ith group of hyperparameters, compare its current objective function value current_fitness with F_i. If it is less than F_i, use current_fitness as the best objective function value F_i of the ith group of hyperparameters; that is, let F_i = current_fitness.
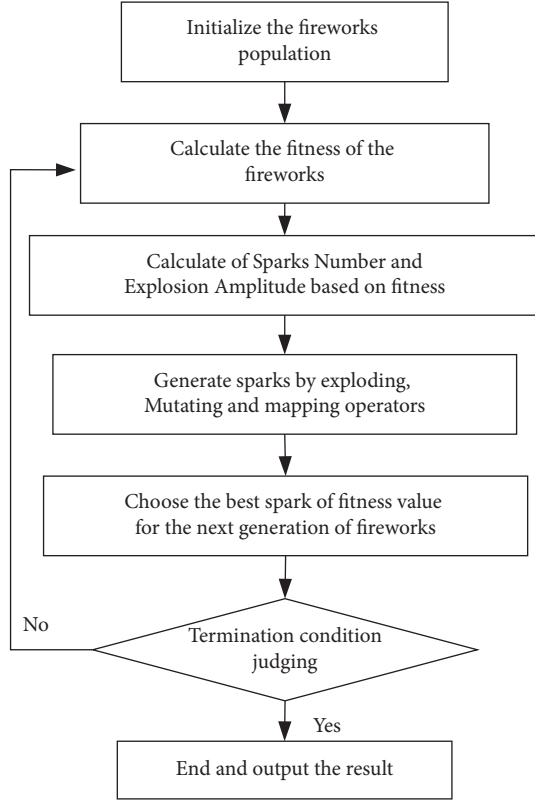
FIGURE 3: Process of FWA.

Step 4: set the global optimal value F_g. For the ith group of hyperparameters, compare F_i with F_g. If it is less than F_g, use F_i as the optimal value F_g of the current population; that is, let $F_g = F_i$.

Step 5: update the explosion range and spark number of each group of hyperparameters according to formulas (8) and (9).

Step 6: check the termination conditions. If the set conditions (preset error or maximum number of iterations) are not reached, return to Step 2 to continue execution.

3.3. Optimized LSTM Wind Speed Prediction Algorithm Based on the Firework Algorithm. According to the wind speed prediction steps based on LSTM and the process of the FWA hyperparameter optimization, the call relationship between them can be obtained as in Figure 4.

It is obtained that the wind speed prediction algorithm based on LSTM optimized by FWA—the FWA-LSTM wind speed prediction algorithm—is derived. The pseudocode of the algorithm is shown in Algorithm 1.

Algorithm 1 firstly preprocesses the wind speed data, normalizes and divides the data to obtain a training set and a test set, then establishes the LSTM wind speed prediction model, and uses FWA to optimize the LSTM hyperparameters to obtain the optimal parameter combination; finally, the parameters are substituted into the model to complete the prediction and error calculation of wind speed data.
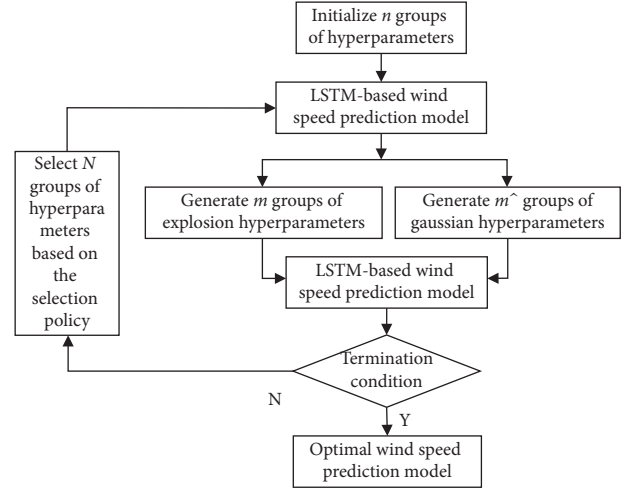
FIGURE 4: The specific calling relationship between the FWA hyperparameter optimization and the LSTM-based wind speed prediction model.

4. Experimental Evaluations

4.1. Experimental Environment Configuration and Parameter Settings. This study selects the measured wind speed data of a wind farm in 2015, starting from January 1, 2015, to December 31, 2015, with an interval of 1 hour, each containing 8759 data packets. This paper selects some data segments for model analysis.

For the prediction results of the network model, three error analysis indicators are used to verify the prediction accuracy, namely, Root Mean Square Error (RMSE), Mean Absolute Error (MAE), and Mean Absolute Error (Mean Absolute Percentage Error, MAPE). The calculation methods of MAE and MAPE are shown in equations (13) and (14).

$$\text{MAE} = \frac{1}{n} \sum_{i=1}^{n} |y_i - \widehat{y}_i|, \tag{13}$$

$$\text{MAPE} = \frac{1}{n} \sum_{i=1}^{n} \left| \frac{y_i - \widehat{y}_i}{y_i} \right| \times 100\%. \tag{14}$$

It can be seen from formula (12) that the smaller the value of RMSE, the smaller the average error between the prediction result and the actual data, the higher the prediction accuracy of the model, and the better the prediction performance of the model. Similarly, it can be seen from formulas (13) and (14) that the more MAE and MAPE values tend to 0, the better the prediction effect of the model is and the more perfect the model is. on the contrary, the larger the values, the greater the error and the worse the prediction effect of the model.

To fully verify the prediction effect of the LSTM wind speed prediction model on the wind speed data after FWA optimization, the optimized model prediction results were compared with the typical LSTM prediction results, other neural network models, and regression prediction methods. As shown in the firework algorithm [45, 46], the initial

(1) Wind speed data preparation and preprocessing;
(2) Normalize the raw data;
(3) Divide training set and test set;
(4) Construct LSTM wind speed prediction model. Set partial parameters and fix the number n of optimized parameter;
(5) FWA parameter initialization (fireworks population size P, solving space dimension d, maximum number of iterations $iter\_max$, explosion amplitude range control parameter $\hat{A}$, the maximum number of sparks m, the number of variation sparks $\hat{m}$, the parameters a and b that limit the number of sparks produced by the explosion, the minimum normal value ε that tends to zero, the solution space boundaries B_u and B_i);
(6) Initialize the values of n-dimensional parameter combinations of P groups randomly in the solution space;
(7) Initialize the global optimal parameter combination gbest_parameters, the partial optimal parameter combination pbest_parameters, and the best fitness function value Pg;
(8) While the end condition is false:
(9)   Apply the n-dimensional parameter combinations of P groups, respectively, to the LSTM network flow prediction model for training, and calculate the current fitness function value;
(10)   Get the current best fitness value P_i and the corresponding parameter combination pbest_parameters;
(11)   if $F_i < F_g$
(12) $F_g = F_i$;
(13)   gbest_parameters = pbest_parameters;
(14)   end if
(15)   for each parameter combination
(16)   Calculate the search direction and position of the new parameter combination according to formulas (8) and (9);
(17)   Fix the updated parameter in the selected values;
(18)   end for
(19)   The number of iterations+1;
(20) end while
(21) Return the gbest_parameters;
(22) gbest_parameters is introduced into LSTM wind speed prediction model to predict test data and calculate prediction error.

ALGORITHM 1: FWA-LSTM wind speed prediction algorithm.

number of fireworks $N = 5$, the size of the fireworks population $P = 50$, the preset maximum explosion amplitude $\hat{A} = 40$, the maximum number of sparks $m = 20$, the number of mutant sparks $\hat{m} = 5$, the constants $a = 0.04$, $b = 0.8$, and the maximum number of generations is set to 100.

4.2. Wind Speed Prediction Results Based on FWA-LSTM

4.2.1. Data Processing

(1) Data resampling: Figure 5 shows wind speed data after null filling by the KNN algorithm.

(2) Data normalization: the range standardization method (equation (7)) is used to process the wind speed data so that the sample data value is between 0 and 1. The processing result is shown in Figure 6.

(3) Data division: the normalized data is divided into train set and test set according to the simple cross-validation method. The first 80% of the data is used as training data for the training of the LSTM network model. The remaining 20% of the data is used as prediction data to verify the efficiency of the model.

4.2.2. Wind Speed Prediction Based on Basic LSTM

(1) Define the network: this prediction uses a four-layer LSTM model with one input layer, two hidden layers, and one output layer.

The specific connection method of the three-layer LSTM is as follows: the first layer of LSTM receives input with time steps of 1, data_dim = 3, and the number of neurons is 64; the second layer uses the results of the first input layer as input for training and passes its output to the next hidden layer. The number of neurons is the same as that of the first layer, and the third layer of the hidden layer (Dense) uses the first layer of LSTM. The output of the third layer is the input; the output layer of the third layer takes the output of the second hidden layer as the input and is connected to a fully connected layer. A one-dimensional vector with a length of 200 output from the fully connected layer is the final output result, which represents the predicted value of 200 data points in the future. To prevent LSTM from overfitting, a dropout layer is added between the first layer and the hidden layer for regularization. After repeated testing, it is found that the accuracy of the training set is the highest when dropout = 0.25.

(2) Compile the network: LSTM network compilation uses adaptive moment estimation (Adam) algorithm as the optimizer and a mean square error loss function as the objective function.

(3) Fitting the network: the LSTM network is trained on 1600 pieces of train data and 200 pieces of valid data are used for validation. The number of iterations epochs = 50, look_back = {1, 5, 10}, and batch_size = 128.
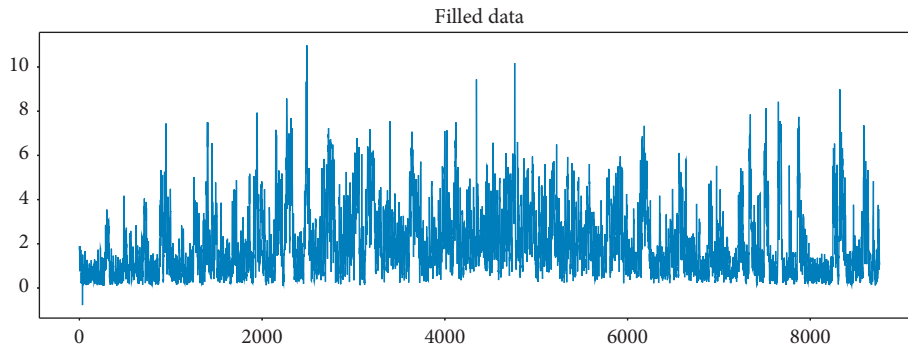
FIGURE 5: Wind speed data after null filling.
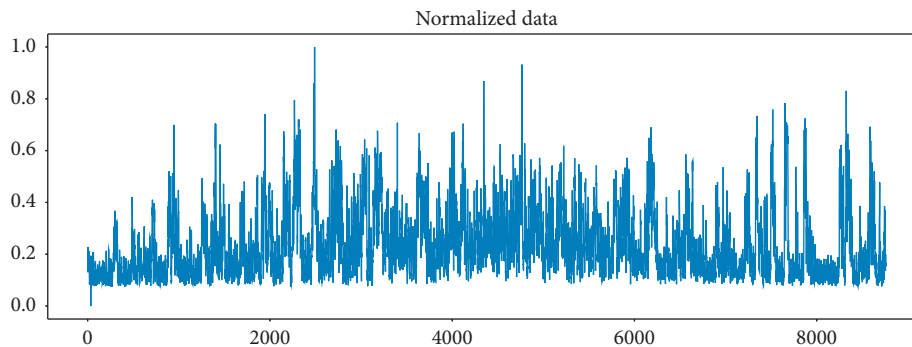
FIGURE 6: Wind speed data after normalization.

(4) Network evaluation: when look_back takes 1, 5, and 10, respectively, and the number of hidden layers (LN) is 1 and 2, respectively, the loss data of the model training process are shown in Figure 7.

According to Figure 7, the loss of each training shows a downward trend, indicating that the model is effective.

(5) Wind speed forecasting: 200 pieces of test data are predicted and the results are shown in Figure 8. TestOriginal_result represents the original data; testPredict_result_101, testPredict_result_105, and testpredict_110, respectively, represent the prediction results when LN = 1, look_back takes 1, 5, and 10, respectively. TestPredict_result_201, testPredict_result_205, and testpredict_210, respectively, represent the prediction results when LN = 2, and look_back takes 1, 5, and 10, respectively.

(6) Error of the prediction mode: LSTM models corresponding to different parameter combinations were used for wind speed prediction, and errors (RMSE, MAE, MAPE) of each model validation set were compared (see Table 1).

It can be concluded that, for the wind speed data, the prediction effect of the parameter combination set by the empirical method is unstable and cannot achieve the optimal prediction performance. Therefore, the fireworks algorithm (FWA) is adopted to optimize the model; that is, an intelligent algorithm is used to efficiently obtain the parameter combination with the optimal prediction effect.

4.2.3. Hyperparameter Optimization according to FWA. To show the process of the optimal parameter value of the LSTM wind speed model determined by the firework algorithm, Figure 9 shows the changes in the number of nodes and the time step during the optimization process of the FWA-LSTM12 model.

Figure 9 shows that, for the prediction of wind speed data, the fitness value tends to be stable starting from the 9th iteration; that is, the FWA to optimize the LSTM-based wind speed prediction model converges easily.

The changes in the number of nodes and time steps in the optimization process of the FWA-LSTM23 model are shown in Figure 10.

It can be seen from Figure 10 that the optimal parameters of the FWA-LSTM model are set to node 1 = 5, node 2 = 2, and look_back = 5. Therefore, in the prediction of wind speed data used in this article, the best configuration of the LSTM model is that the number of neurons in the first layer is set to 5, the number of neurons in the second layer is set to 2, and the time step is set to 5.

4.3. Result Analysis. To evaluate the prediction performance of the LSTM model after parameter optimization by FWA, wind speed data samples at 200-time points are used for verification. Firstly, the basic LSTM and PSO-LSTM (LSTM optimized by the particle swarm optimization) are tested for comparison. Figure 11 shows the prediction results of these three methods.

It can be seen from Figure 11 that the prediction effects of FWA-LSTM and PSO-LSTM models are similar and both better than the basic LSTM method. To compare the
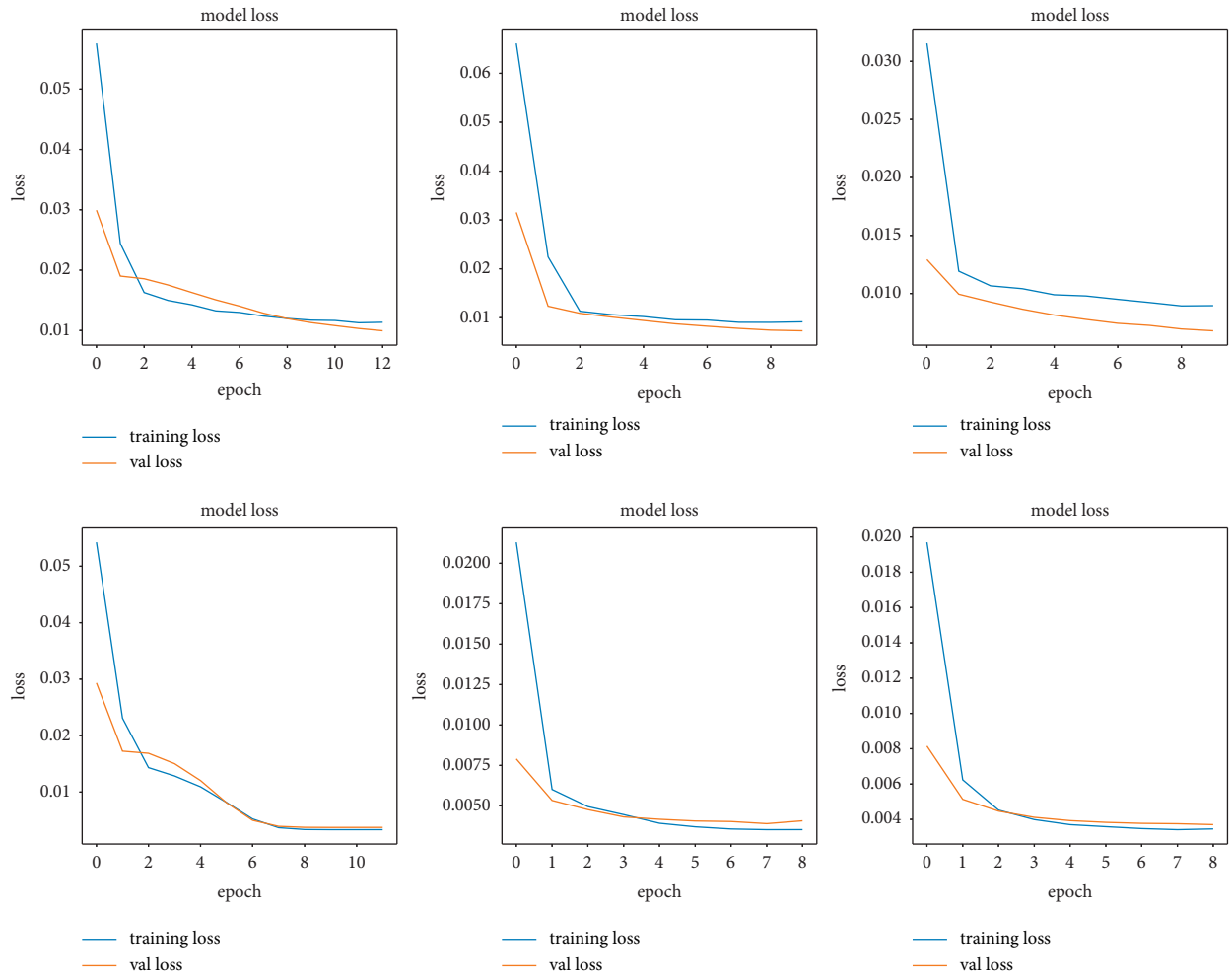
FIGURE 7: Model training loss under different parameter combinations.
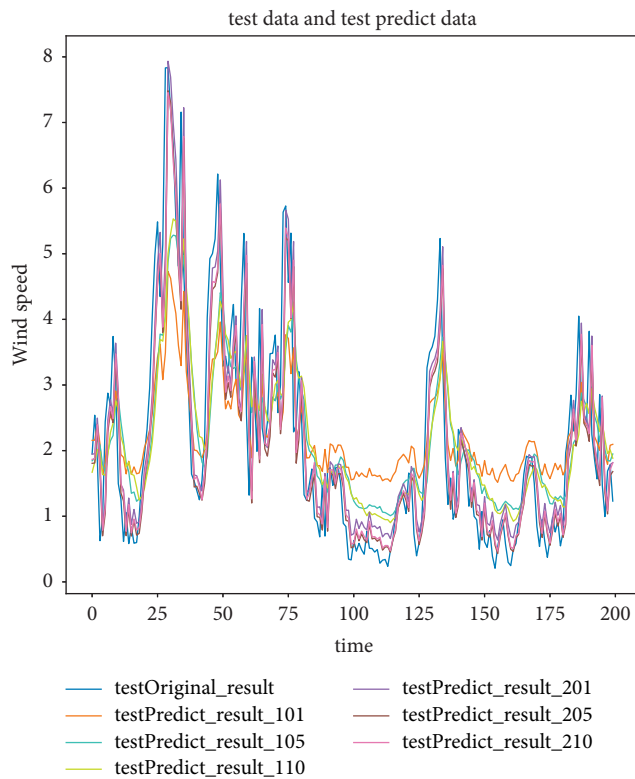
FIGURE 8: Test results of partial data.

TABLE 1: Errors of LSTM-based wind speed prediction models under different parameter combinations.

Model	Parameters	RMSE	MAE	MAPE (%)
LSTM101	(look_back, LN) = (1,1)	1.18	0.96	94.77
LSTM105	(look_back, LN) = (5,1)	0.98	0.74	66.51
LSTM110	(look_back, LN) = (10,1)	0.96	0.71	63.23
LSTM201	(look_back, LN) = (1,2)	0.73	0.51	42.09
LSTM205	(look_back, LN) = (5,2)	0.73	0.58	33.28
LSTM210	(look_back, LN) = (10,2)	0.72	0.58	35.34
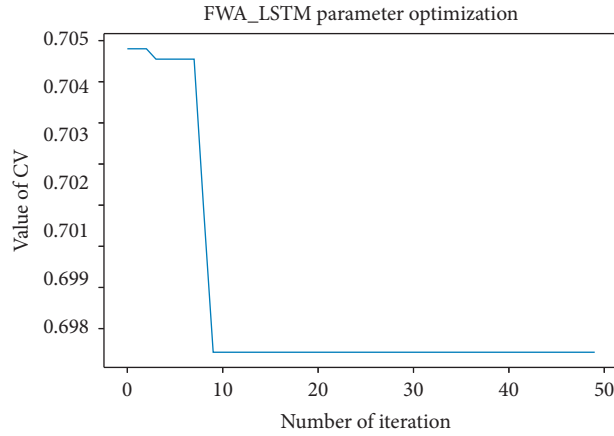
FIGURE 9: The change of the fitness value.

(a)

(b)
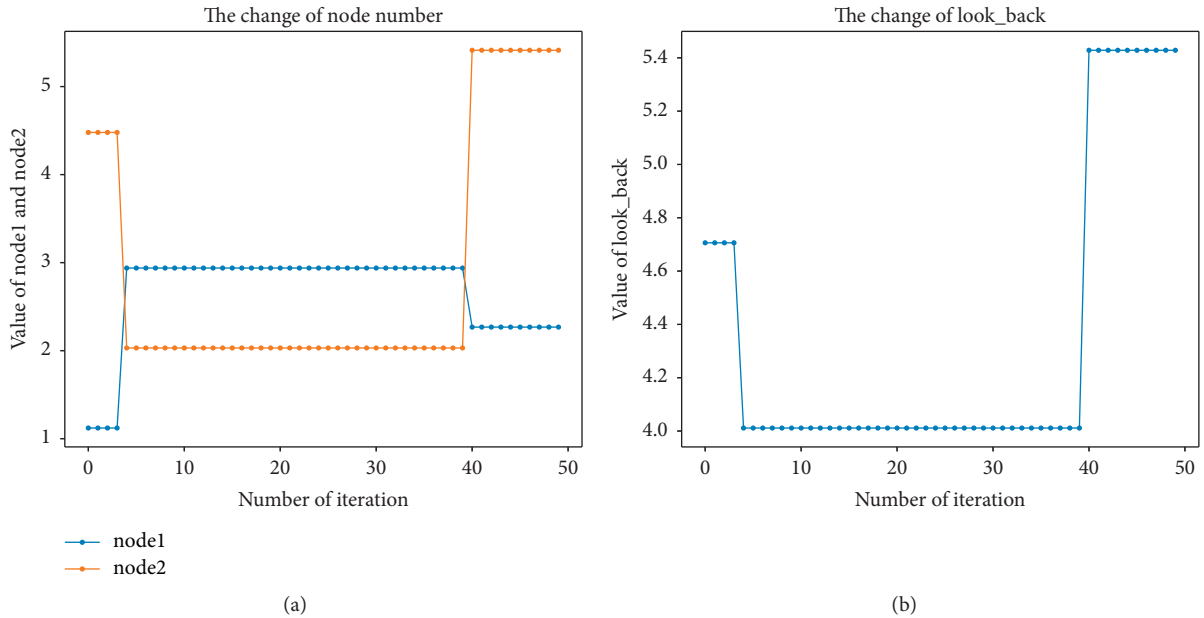
FIGURE 10: The change of parameters during FWA iteration. (a) The change of node number. (b) The change of time step.

performance of the three methods more clearly, their prediction performance evaluation index values are calculated and shown in Table 2.

It can be seen from Table 2 that compared with the PSO-LSTM and the basic LSTM, the FWA-LSTM has slightly smaller prediction errors of RMSE and MAPE, while the MAE is close to PSO-LSTM. On the whole, FWA-LSTM is considered to be superior to the PSO-LSTM and the basic LSTM.

To further verify the prediction effect of the improved FWA-LSTM prediction model, it is compared with other neural network prediction methods, such as Gated Recurrent Unit (GRU), Simple Recurrent Neural Network (SimpleRNN), and Bidirectional Recurrent Neural Network (BiRNN), and other predictive models such as SVR and ARIMA were also compared. Similarly, using 200-time points of wind speed data samples for verification, their
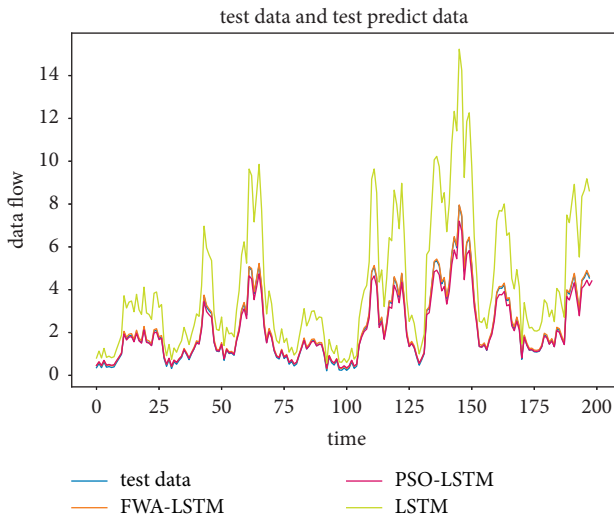
FIGURE 11: Prediction results of FWA-LSTM and other prediction methods.

TABLE 2: The comparison of prediction error index values of the eight models.

Method	RMSE	MAE	MAPE (%)
FWA-LSTM	0.64	0.46	30.05
PSO-LSTM	0.69	0.46	33.07
LSTM	0.76	0.68	38.43

TABLE 3: The comparison of prediction error index values of the six models.

	FWA-LSTM	GRU	SimpleRNN	BiRNN	SVR	ARIMA
RMSE	0.64	0.71	0.74	0.73	0.89	0.83
MAE	0.46	0.51	0.51	0.52	0.68	1.09
MAPE (%)	30.05	30.22	32.13	31.42	38.43	60.16

prediction performance evaluation index values were obtained, respectively, and the results are shown in Table 3.

It can be seen from Table 3 that the prediction errors of RMSE, MAE, and MAPE of the FWA-LSTM model optimized by FWA are all less than those of other tested prediction methods such as GRU, SimpleRNN, BiRNN, SVR, and ARIMA, so it is said that the FWA-LSTM prediction model has a better prediction effect in wind speed prediction. Therefore, it is said that the FWA-LSTM is more suitable for dealing with the real-time sudden change of wind speed data.

In summary, the proposed FWA-LSTM method has a better prediction effect and higher reliability for the future prediction of wind speed.

5. Conclusions

Wind speed prediction can be applied to wind energy optimization and has important reference significance for wind power planning and the stable operation of the power system. This paper first established a wind speed prediction model based on the nonparametric model LSTM neural network, optimized the hyperparameters of the established LSTM prediction model with the firework algorithm, and reduced the prediction Root Mean Square Error compared to the empirical method of obtaining parameters, and the FWA-LSTM is better than the double-layer LSTM in the wind speed data prediction.

The improved model FWA-LSTM is applied to wind speed prediction and compared with the prediction effects of other neural network prediction methods and regression methods. The experimental results show that compared to other prediction models and the traditional LSTM model, the FWA-LSTM method reduces the prediction errors, which significantly reduces the prediction error and improves the accuracy of wind speed prediction. The next step will continue to combine a variety of prediction methods to improve the prediction accuracy of wind speed prediction.

Data Availability

The data used to support the findings of this study are available from the corresponding author upon request.

Conflicts of Interest

The authors declare no conflicts of interest.

Acknowledgments

References

[1] S. Samadianfard, S. Hashemi, K. Kargar et al., "Wind speed prediction using a hybrid model of the multi-layer perceptron and whale optimization algorithm," *Energy Report*, vol. 6, pp. 1147–1159, 2020.

[2] X. Ma, Y. Chen, W. Yi, and Z. Wang, "Prediction of extreme wind speed for offshore wind farms considering parametrization of surface roughness," *Energies*, vol. 14, no. 4, 2021.

[3] R. Jing, Z. Zhang, Z. Liang et al., "Review of wind speed and wind power prediction methods," *Journal of Applied Sport Manageinent*, vol. 39, no. 6, pp. 1045–1059, 2020.

[4] X. Liu, Z. Lin, and Z. Feng, "Short-term offshore wind speed forecast by seasonal ARIMA - a comparison against GRU and LSTM," *Energy*, vol. 227, 2021.

[5] N. Bokde, A. Feijóo, D. Villanueva, and K. Kulat, "A review on hybrid empirical mode decomposition models for wind speed and wind power prediction," *Energies*, vol. 12, no. 2, 2019.

[6] E. B. Ssekulima, M. B. Anwar, A. A. Hinai, and M. S. E. Moursi, "Wind speed and solar irradiance forecasting techniques for enhanced renewable energy integration with the grid: a review," *IET Renewable Power Generation*, vol. 10, no. 7, pp. 885–989, 2016.

[7] J. Wang, Y. Song, F. Liu, and R. Hou, "Analysis and application of forecasting models in wind power integration: a review of multi-step-ahead wind speed forecasting models," *Renewable and Sustainable Energy Reviews*, vol. 60, pp. 960–981, 2016.

[8] L. Xiang and Z. Deng, "Short-term wind speed forecasting based on improved empiricalwavelet transform and least

squares support vector machines," *Acta Energiae Solaris Sinica*, vol. 42, no. 02, pp. 97–103, 2021.

[9] S. Zhang, C. Liu, W. Wang, and B. Chang, "Twin least square support vector regression model based on gauss-laplace mixed noise feature with its application in wind speed prediction," *Entropy*, vol. 22, no. 10, 2020.

[10] A. Khosravi, L. Machado, and R. O. Nunes, "Time-series prediction of wind speed using machine learning algorithms: a case study Osorio wind farm, Brazil," *Applied Energy*, vol. 224, pp. 550–566, 2018.

[11] Y. Dong, J. Niu, Q. Liu et al., "A hybrid prediction model for wind speed using support vector machine and genetic programming in conjunction with error compensation," *Stochastic Environmental Research and Risk Assessment*, vol. 11, pp. 1–14, 2021.

[12] O. Karakuş, E. E. Kuruoğlu, and M. A. Altınkaya, "One-day ahead wind speed/power prediction based on polynomial autoregressive model," *IET Renewable Power Generation*, vol. 11, no. 11, pp. 1430–1439, 2017.

[13] A. Xie, H. Yang, J. Chen, L. Sheng, and Q. Zhang, "A short-term wind speed forecasting model based on a multi-variable long short-term memory network," *Atmosphere*, vol. 12, no. 5, p. 651, 2021.

[14] Z. Gan, C. Li, J. Zhou et al., "Temporal convolutional networks interval prediction model for wind speed forecasting," *Electric Power Systems Research*, vol. 191, Article ID 106865, 2021.

[15] C. Liang, Y. Liu, J. Zhou et al., "Wind speed prediction at multi-locations based on combination of recurrent and convolutional neural networks," *Power System Technology*, vol. 45, no. 2, pp. 534–542, 2021.

[16] H. Fan, X. Zhang, S. Mei et al., "UItra-short-term wind speed prediction model for wind farms based on spatiotemporal neural network," *Automation of Electric Power Systems*, vol. 45, no. 1, pp. 28–35, 2021.

[17] J. Wang, Y. Wang, Z. Li, H. Li, and H. Yang, "A combined framework based on data preprocessing, neural networks and multi-tracker optimizer for wind speed prediction," *Sustainable Energy Technologies and Assessments*, vol. 40, Article ID 100757, 2020.

[18] H. Liu, X. Mi, and Y. Li, "Smart deep learning based wind speed prediction model using wavelet packet decomposition, convolutional neural network and convolutional long short term memory network," *Energy Conversion and Management*, vol. 166, pp. 120–131, 2018.

[19] Z. ZhangL. Ye et al., "Wind speed prediction method using shared weight long short-term memory network and Gaussian process regression," *Applied Energy*, vol. 247, pp. 270–284, 2019.

[20] M.-R. Chen, G.-Q. Zeng, K.-D. Lu, and J. Weng, "A two-layer nonlinear combination method for short-term wind speed prediction based on ELM, ENN, and LSTM," *IEEE Internet of Things Journal*, vol. 6, no. 4, pp. 6997–7010, 2019.

[21] J. Ding, G. Chen, Y. Huang et al., "Short-term wind speed prediction based on CEEMDAN-SE-improved PIO-GRNN model," *Measurement and Control*, vol. 54, no. 1-2, pp. 73–87, 2021.

[22] Y. Jiang, S. Liu, N. Zhao, J. Xin, and B. Wu, "Short-term wind speed prediction using time varying filter-based empirical mode decomposition and group method of data handling-based hybrid model," *Energy Conversion and Management*, vol. 220, Article ID 113076, 2020.

[23] D. Xiong, W. Fu, K. Wang, P. Fang, T. Chen, and F. Zou, "A blended approach incorporating TVFEMD, PSR, NNCT-based multi-model fusion and hierarchy-based merged

[24] M. D. Liu, L. Ding, and Y. L. Bai, "Application of hybrid model based on empirical mode decomposition, novel recurrent neural networks and the ARIMA to wind speed prediction," *Energy Conversion and Management*, vol. 233, Article ID 113917, 2021.

[25] S. W. Fei, "The hybrid model of empirical wavelet transform and relevance vector regression for monthly wind speed prediction," *International Journal of Green Energy*, vol. 17, no. 10, pp. 583–590, 2020.

[26] Y. Liu, J. Zhou, J. Yan et al., "Wind speed real-time prediction method based on multi-task learning," *Renewable Energy Resources*, vol. 39, no. 04, pp. 481–487, 2021.

[27] Y. Li, X. Chen, C. Li, G. Tang, Z. Gan, and X. An, "A hybrid deep interval prediction model for wind speed forecasting," *IEEE Access*, vol. 9, pp. 7323–7335, 2020.

[28] Y. J. Natarajan and D. S. Nachimuthu, "New SVM kernel soft computing models for wind speed prediction in renewable energy applications," *Soft Computing*, vol. 24, pp. 1–18, 2019.

[29] Y. Xie, C. Li, G. Tang, and F. Liu, "A novel deep interval prediction model with adaptive interval construction strategy and automatic hyperparameter tuning for wind speed forecasting," *Energy*, vol. 216, Article ID 119179, 2021.

[30] M. Li, Z. Zhang, T. Ji, and Q. H. Wu, "Ultra-short term wind speed prediction using mathematical morphology decomposition and long short-term memory," *CSEE Journal of Power and Energy Systems*, vol. 6, no. 4, pp. 890–900, 2020.

[31] S. Zhang, Y. Chen, J. Xiao, W. Zhang, and R. Feng, "Hybrid wind speed forecasting model based on multivariate data secondary decomposition approach and deep learning algorithm with attention mechanism," *Renewable Energy*, vol. 174, pp. 688–704, 2021.

[32] L. Lopez, I. Oliveros, L. Torres et al., "Prediction of wind speed using hybrid techniques," *Energies*, vol. 13, no. 23, 2020.

[33] N. Zeng, Z. Huo, X. U. Chang et al., "Minute-scale ultra-short-term wind speed prediction based on improved HHT," *Journal of Chinere Society of Power Engineering*, vol. 41, no. 4, pp. 309–315, 2021.

[34] Y. Zhang, G. Pan, Y. Zhao, Q. Li, and F. Wang, "Short-term wind speed interval prediction based on artificial intelligence methods and error probability distribution," *Energy Conversion and Management*, vol. 224, Article ID 113346, 2020.

[35] W. Xu, P. Liu, L. Cheng et al., "Multi-step wind speed prediction by combining a WRF simulation and an error correction strategy," *Renewable Energy*, vol. 163, pp. 772–782, 2021.

[36] Z. Liu, R. Hara, and H. Kita, "Hybrid forecasting system based on data area division and deep learning neural network for short-term wind speed forecasting," *Energy Conversion and Management*, vol. 238, Article ID 114136, 2021.

[37] T. Fu and M. Yang, "Mixed wind speed prediction based on ensemble empirical mode decomposition and improved cuckoo algorithm to optimize BPNN," *Journal of Qufu Normal University*, vol. 47, no. 2, pp. 27–34, 2021.

[38] L. Bingchen, Y. Huijun, D. Huaxuan et al., "Short-term wind speed prediction based on ceemd and lstm-arima," *China Measurement and Test*, IEEE, vol. 47, pp. 1–6, 2021.

[39] X. Huang, J. Wang, and B. Huang, "Two novel hybrid linear and nonlinear models for wind speed forecasting," *Energy Conversion and Management*, vol. 238, Article ID 114162, 2021.

[40] X. Chen, C. S. Lai, W. W. Y. Ng et al., "A stochastic sensitivity-based multi-objective optimization method for short-term wind speed interval prediction," *International Journal of Machine Learning and Cybernetics*, vol. 12, no. 9, pp. 1–12, 2021.

[41] F. Han, Y. Han, J. Lu et al., "Wind speed prediction based on nested shared weight long short-term memory network," *The Journal of China Universities of Posts and Telecommunications*, vol. 28, no. 1, 2021.

[42] Y. Tan and Y. Zhu, "Fireworks algorithm for optimization," in *Proceedings of the International Conference in Swarm Intelligence*, pp. 355–364, Springer, Beijing, China, June 2010.

[43] Y. Tan and Z. Shaoqiu, "Recent advances in fireworks algorithm," *CAAI Transactions on Intelligent Systems*, vol. 9, no. 05, pp. 515–528, 2014.

[44] X. Han, L. Zheng, L. Wang, Z. Hong, and X. Wang, "Fireworks algorithm based on dynamic search and tournament selection," *International Journal of Computers and Applications*, vol. 43, pp. 1–12, 2019.

[45] J. Zhao, D. Ting, and C. Bo, "AQI prediction based on long short-term memory model with spatial-temporal optimizations and fireworks algorithm," *Journal of Wuhan University (Natural Science Edition)*, vol. 65, no. 3, pp. 250–262, 2019.

[46] Y. Xu, M. Wang, and W. Fan, "Parameter optimization of secondary system fault correlation analysis based on AFWA," *Journal of North China Electric Power University*, vol. 48, no. 4, pp. 1–8, 2021.

[47] X. Li, K. Peng, J. Peng, and D. Hou, "Effect of thermal damage on mechanical behavior of a fine-grained sandstone," *Arabian Journal of Geosciences*, vol. 14, no. 1212, pp. 1–12, 2021.

Research Article

Preliminary Evaluation of Nanobacteria on Crystal Retention, CaSR, and Claudin-14 Expression in HK-2 Cells

Gang Xu,[1] **Biao Qian,**[1] **and Liying Zheng** (ID)[2]

[1]*Department of Urology, The First Affiliated Hospital of Gannan Medical College, Ganzhou 341000, Jiangxi, China*
[2]*Postgraduate Department, The First Affiliated Hospital of Gannan Medical College, Ganzhou 341000, Jiangxi, China*

Correspondence should be addressed to Liying Zheng; zhengliying@gmu.edu.cn

To evaluate cell morphology, crystal adhesion, cell damage, Calcium sensitive receptor (CaSR), and Claudin protein-14 (Claudin-14) expression at different time intervals and explore the role of nanobacteria in the formation of urinary calculi. In this experiment, HK-2 cells were cocultured with nanobacteria (NB) in the absence or presence of tetracycline (Tet). Cells treated with calcium oxalate monohydrate (COM) crystals were used as a positive control of urinary stone-induced cell damage. After which, cell morphology was evaluated by hematoxylin-eosin staining in comparison to untreated HK-2 cells (negative control). Use different methods to assess cell damage, crystal adhesion, and protein expression. (The degree of cell damage, crystal adhesion, and protein expression were evaluated by various methods). It was found that the degree of cell damage observed in Tet + NB-treated cells was significantly lower than that in NB-treated cells. Lactate dehydrogenase (LDH) leakage was higher in COM-exposed than in control cells ($P < 0.05$). However, LDH release from both NB- and Tet + NB-treated cells was significantly lower than from COM-treated cells ($P < 0.05$). The relative expression of CaSR and Claudin-14 proteins was higher in NB, COM, and TET + NB cells than in control cells ($P < 0.001$) and was lower in Tet + NB than in NB cells ($P < 0.01$). And $P < 0.05$ means that the difference was statistically significant, and $P < 0.001$ means that there was a significant difference between the both things. From the cell morphology, the cell damage in the COM group was greater than that in the NB group, and the cell damage markers in the COM group and the NB group were elevated. NB caused damage to HK-2 cells by inducing lipid peroxidation, and the degree of damage was increased in processing time. The adhesion of HK-2 cells to COM crystals increased after injury and was proportional to the duration of NB coculture. NB upregulated the expression of CaSR and Claudin-14 in HK-2 cells.

1. Introduction

The occurrence of urinary calculi is a common phenomenon worldwide. The average prevalence in China is 6.5%, and the prevalence in some areas is as high as 11.6%. Urinary calculi are among the most common urological conditions in China [1]. Kidney calculi are the most common type of urinary calculi. Urolithiasis is a very complex process. In recent years, an important role of nanobacteria (NB) in the pathogenesis of urinary stones has emerged [2–4]. NB have a diameter of about 80–500 nm and are Gram-negative bacteria. Their shape is mostly spherical or rod-shaped, with a thicker cell wall. The detection rate of NB in blood, urine, and calculi in patients with

kidney calculi is above 90% [5–7]. NB have a unique ability to produce hydroxyapatite minerals in the human body and deposit them in tissues and organs. Therefore, they can adhere to the epithelial cells of the collecting ducts and the papillary cells, destroy the membrane structure of the cells, and form apatite crystals as reaction centers, further inducing the formation of calculi [8].

It was reported that, after treatment with traditional extracorporeal lithotripsy, the 5-year recurrence rate in patients with urinary calculi is still as high as 41.8% [9], causing patient suffering and increasing socioeconomic costs [10]. Therefore, the elucidation of the mechanisms responsible for urinary calculi formation and the development of new treatments are

urgent needs. Tetracycline is one of the few antibiotics that can kill NB at physiological concentrations. Shoskes et al. showed that a 3-month treatment with Tet greatly alleviated the symptoms in 80% of patients [11]. However, at present, we do not know exactly how NB play their unique role in the formation of kidney calculi, let alone treatment for NB.

Hypercalciuria is another risk factor for the formation of calcium stones. It is reported that approximately 33% of patients with kidney stones develop urinary calcium reabsorption disorders. The activation of calcium-sensing receptor plays an important role in this process by upregulating, in the thick ascending limb (TAL), the downstream molecule Claudin-14, which in turn inhibits the resorption of calcium.

The purpose of this study was to investigate the mechanism of NB-induced crystal retention in renal tubular epithelial HK-2 cells. An interesting question to be addressed was whether calcium signaling pathways contribute to the development of NB-induced kidney stones. Therefore, the influence of NB on the expression of CaSR and Claudin-14 was investigated.

2. Materials and Methods

2.1. Clinical Data of Patients.
Patients ($n = 10$) (average age 49.2 ± 14) with nephrolithiasis were enrolled for sample collection (Urine is more likely to reflect the environment of NB-induced urinary calculi, and more conducive to NB bacteria growth). They had not been treated with drugs or undergone surgery. The inclusion criteria were (1) diagnosis of upper urinary tract stones; (2) male patients; (3) no antibiotics used before surgery. I have unified the diagnosis of the selected patients with the inclusion criteria, and all patients were from the Department of Urology, the First Affiliated Hospital of Shihezi University School of Medicine. Prior written and informed consent was obtained from every patient and the study was approved by the ethics review board of the First Affiliated Hospital of Shihezi University School of Medicine.

2.2. Culture and Identification of NB.
Urine samples (2 ml) were collected from patients with nephrolithiasis and diluted five times with saline under aseptic conditions. After centrifugation at 4°C for 45 min ($14,000 \times g$), the pellet was resuspended in 2 ml saline and filtered with a 0.45 μm filter. The filtered sample was diluted 5 times with saline and centrifuged at 4°C for 45 min ($14,000 \times g$). Next, the pellet was resuspended in 1 ml of saline and filtered with a 0.22 μm filter. Then, 1 mL of the filtered sample, containing NB, was collected and transferred to a cell culture flask containing Dulbecco's modified Eagle's medium (DMEM) (GIBCO, USA), 10% γ-FBS (Hyclone, USA), and 1% HEPES (Hyclone, USA). The NB were cultured at 37°C and 5% CO_2 for 5 to 7 days. Inverted phase contrast microscopy was used to monitor NB growth. NB was collected by centrifugation at $14,000 \times g$ for 20 min at 4°C and washed three times with sterile water. The calcium-specific von Kossa staining and scanning transmission electron microscopy were used to identify NB.

2.3. Cell Culture and Treatments.
HK-2 cells were obtained from Wuhan University Collection Center and cultured in 10% fetal bovine serum 1640 medium, at 37°C, 5% CO_2. Cells were divided into four different subpopulations corresponding to the following treatments: control, NB, COM, and Tet + NB. Control cells were cultured with medium only. For NB exposure, HK-2 cells were cultured with an NB suspension (OD = 0.7) and culture medium. COM cells (positive control) were cultured with a 5 mmol/L suspension of calcium oxalate monohydrate crystals (COM) (Sigma, USA) and culture medium. Tet (tetracycline) +NB cells were treated with 5 mg/L Tet and an NB suspension (OD = 0.7). The cells were cultured for 6 h, 12 h, and 24 h.

2.4. HE Staining.
After treatments, slides in 12-well plates were removed, rinsed 3 times with PBS, and fixed with 95% alcohol for 20 min. After washing with PBS 3 times, the cells were stained with Harris hematoxylin for 1 min and then rinsed with tap water for 2 min. Then, it was differentiated for 5 s in 1% hydrochloric acid and stained with eosin for 5 min. Finally, after gradient alcohol dehydration and xylene transparency, a neutral resin was used to seal the slides and cell morphology was observed under an optical microscope.

2.5. Detection of H_2O_2, MDA, LDH, Na^+/K^+ ATPase, and Ca^{2+}/Mg^{2+}ATPase Activity.
After treatments, the cell supernatants were collected and the content of H_2O_2, malondialdehyde (MDA), and LDH were measured according to the instructions provided in the relevant kits (H_2O_2/MDA/LDH assay kits, Nanjing Jiancheng Institute of Biological Engineering, Nanjing, China).

The activities of Na^+/K^+ ATPase and Ca^{2+}/Mg^{2+}ATPase were measured by an ATPase kit (colorimetric method; Nanjing Jiancheng Institute of Biological Engineering, Nanjing, China).

2.6. Laser Confocal Microscopy for Detection of Crystal Retention.
HK-2 cells were seeded in a 24-well plate containing clean coverslips. After 6, 12, and 24 h of cocultivation, a COM suspension was added at a final concentration of 200 mg/L per well and gently shaken for 5–10 s, so as to allow for proper contact between the COM crystals and the bottom cells. After 3 min, the liquid above the cover glass was moved and the coverslips rinsed three times with saturated sodium oxalate solution. The coverslips were removed from the wells, fixed in 4% paraformaldehyde for 20 min, washed in PBS twice for 5 min, and shaken in a rocker. Then, 50 μL of 5 mg/L phalloidin-FITC were added and incubation was performed in 20°C in the dark for 20 min. After 2 PBS rinses, 5 min each, the slides were observed with an LSM800 microscope (Carl Zeiss, Germany) with 488 nm and 633 nm excitation light, followed by image acquisition.

2.7. Observation of Cell Crystal Retention.
Cells were seeded in 24-well plates containing clean coverslips in RPMI 1640 medium supplemented with FBS and EGF and then treated

with NB or COM in medium. After 6, 12, and 24 h of treatment, the COM suspension was added to each well (200 mg/L) and incubations continued for 3 min. Then cells were rinsed 3 times with a saturated calcium oxalate solution. After fixation with 4% paraformaldehyde for 20 min and incubation with phalloidin-FITC for 20 min, the coverslips were examined with a laser scanning confocal microscope with 488 nm and 633 nm excitation light to evaluate the crystal retention by cells.

2.8. The Detection of CaSR and Claudin-14 mRNA Expression in HK-2 Cells by Quantitative Real-Time PCR.

HK-2 cells were seeded in 6-well plates, and total RNA was extracted by Trizol method after coculture for 6, 12, and 24 h, and the purity and concentration were determined. The extracted RNA was reverse-transcribed into cDNA and then subjected to CaSR and Claudin-14 and PCR detection of the GAPDH gene. The reaction conditions were set according to the kit instructions. The relative expression levels of the genes of CaSR and Claudin-14 were obtained by GAPDH correction. The primer sequences are shown in Table 1.

2.9. Western Blotting.

Lysates were prepared from the treated cells using a RIPA lysis buffer. The protein samples were separated by 10% SDS-PAGE and then transferred onto PVDF membranes. Next, 5% nonfat dried milk was used to block the nonspecific binding sites at 20°C. Subsequently, the membrane was incubated with a primary antibody overnight at 4°C. After four 5-min washes with TBST, the membrane was incubated with the secondary antibody conjugated with horseradish peroxidase for 2 h at 20°C. The signals were captured using an ECL advanced system. The bands were quantified through Quantity One software and normalized to GAPDH.

3. Statistical Analysis

SPSS 24.0 statistical software (SPSS Inc., Chicago, IL) was used for statistical analysis. Measured data were expressed as mean ± standard deviation (SD). One-way ANOVA was used to compare the effects of the different treatments, followed by LSD-t test. One-way ANOVA was used for quantitative comparison between multiple groups, and the S-N-K method was used for pairwise comparison. The test level $\alpha = 0.05$, and the statistical graph was drawn using GraphPad Prism 6.

4. Results

4.1. Impact of Treatments on Cell Morphology.

HE staining was performed to evaluate the morphology of HK-2 cells after the different treatments. HE staining results are shown in Figure 1. The control cells exhibited a uniform morphology, clear nuclei, dense cytoplasm, and no obvious abnormalities. The number of COM-treated cells was significantly reduced, and the nuclei were loose. Some of the nuclear membranes were dissolved and the nucleoli were not visible. After 6 h of coculture with NB, some cells exhibited enlarged cell bodies,

loose nuclei, and blurred nuclear membranes. Finally, most of the cells that had been exposed to Tet + NB were morphologically regular, dense, and presented clear nuclei. Some cells showed cell body swelling and a loose nucleus.

4.2. ATPase Activity, LDH, H_2O_2, and MDA in the Medium of HK-2 Cells.

As shown in Table 2, after 12 h and 24 h of incubation in the presence of NB and COM, the activities of Na^+/K^+ ATPase and Ca^{2+}/Mg^{2+} ATPase in HK-2 cells were significantly lower than in the control cells ($P < 0.05$). Notably, both enzyme activities were significantly higher in the Tet + NB-treated cells, compared to the NB-treated cells, at all time points ($P < 0.05$).

As shown in Table 3, at each time point, the LDH release from the COM-exposed cells was significantly higher than from control cells ($P < 0.05$). The LDH released from the NB- and Tet + NB-exposed cells was lower than from the COM-treated cells ($P < 0.05$). After 12 h and 24 h, the content of H_2O_2 and MDA in the extracellular medium of NB- and COM-treated cells was significantly higher than in that of the control cells at the corresponding time points ($P < 0.05$). On the other hand, the release of H_2O_2 and MDA from the Tet + NB-treated cells was significantly lower than from the NB-treated cells ($P < 0.05$).

4.3. Assessment of Crystal Adhesion by Laser Scanning Confocal Microscopy.

To observe the adhesion of crystals to cells, a confocal microscope was used. As shown in Figure 2, after cocultivation for 6 hours, a small amount of crystal adhesion was observed in the NB group and the COM group, and no crystal adhesion was observed in the blank group. After 12 h of coculture, the crystal adhesion of the NB group and COM group increased significantly compared with 6 h, and there was no significant change in the blank group. After 24 hours of cocultivation, the crystal adhesion of the NB group and COM group was further increased than that of 12 h, and there was no significant change in the blank group. At all-time points, Tet + NB treated crystal adhesion was significantly reduced compared to NB treated cells.

4.4. The Expression of CaSR and Claudin-14 in HK-2 Cells.

qRT-PCR and western blotting assays were employed to detect CaSR and Claudin-14 in HK-2 cells. The relative levels of mRNA are shown in Figure 3. At 6, 12, and 24 h, the treatment with both NB and COM resulted in a significant increase in CaSR and Claudin-14 mRNAs as compared to control cells ($P < 0.001$). As shown in Figure 4, Western blotting confirmed a remarkably higher level of both proteins under the treatment with both NB and COM (24; $P < 0.001$). Both protein levels were lower in the TET + NB-treated than in the NB-treated cells ($P < 0.01$).

5. Discussion

The etiology of urinary calculi is very complex, involving genetic, environmental, and dietary factors, among others. It has been reported that calcium-containing stones account

TABLE 1: Primer sequences.

Gene		bp
CaSR	5′TATGCCTCCTCCAGCAGACT3′	122
	5′TTCCAGCGGAAATACTCGAT3′	122
Claudin-14	5′CTACCTGAAAGGGCTCTGGA3′	132
	5′AGGCAGGAGATGACCATGAG3′	132
GAPDH	5′ACGGCAAGTTCAACGGCACAG3′	129
	5′CGACATACTCAGCACCAGCATCAC3′	129
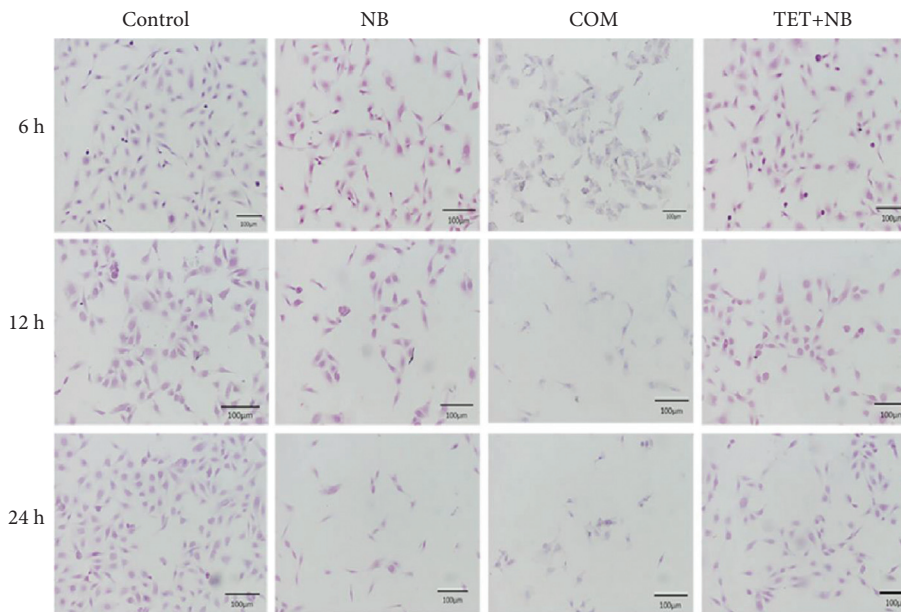
FIGURE 1: HE staining of HK-2 cells after the different treatments (200x).

TABLE 2: Comparison of Na+/K + ATP and Ca2+/Mg2+ATPase activities in HK-2 cells after the different treatments ($n = 3$).

Groups	Na^+/K^+ATP			$Ca^{2+}/Mg^{2+}ATP$		
	6 h	12 h	24 h	6 h	12 h	24 h
Control	13.74 ± 3.50	12.88 ± 1.80	3.40 ± 1.43	9.91 ± 2.80	11.84 ± 2.38	6.26 ± 1.26
NB	9.73 ± 1.90	$6.56 \pm 1.59^*$	$0.60 \pm 0.40^*$	8.22 ± 2.52	$3.78 \pm 0.78^*$	$1.45 \pm 1.50^*$
COM	$7.16 \pm 2.03^*$	$2.01 \pm 1.07^*$	$0.45 \pm 0.30^*$	5.25 ± 1.86	$2.48 \pm 1.61^*$	$0.25 \pm 0.17^*$
TET + NB	11.37 ± 2.08	$10.45 \pm 2.04^\#$	$2.85 \pm 0.60^\#$	7.81 ± 2.86	$7.31 \pm 2.70^\#$	$3.85 \pm 0.75^\#$

Note. *Compared with control cells, $P < 0.05$. #Compared with NB-treated cells, $P < 0.05$.

for the majority of urinary calculi, and about 33% of patients have abnormal urinary calcium metabolism [12]. In recent years, a damaging effect of calcium oxalate monohydrate (COM) on animal renal tubular epithelial cells has been reported [13, 14]. For example, Li et al. [15] have found that after the addition of 5 mmol/L calcium oxalate monohydrate (COM) crystals to cultured renal tubular epithelial cells from Wistar rats, a large amount of cell-adhered crystals could be observed. Therefore, in this study, calcium oxalate monohydrate (COM) treatment (5 mmol/L) was used as a positive control. Nanobacteria (NB) are commonly found in human blood, urine, tissues, and organs and form a calcium phosphate shell.

The results of this study are consistent with previous reports [16], demonstrating that calcium oxalate monohydrate (COM) crystals cause more damage to cell membranes than other groups. HE staining showed that the degree of the cell damage caused by Nanobacteria (NB) was higher than that associated with cell exposure to TET + NB. Although, in HK-2 cells, as assessed by transmission electron microscopy and by the detection of cell damage markers. After cell injury, the degree of crystal adhesion was much higher in HK-2 cells cocultured with NB than in the Tet + NB-treated cells. Tet prevents the Nanobacteria (NB) effects on this process, suggesting that the dominant role in cell damage and subsequent crystal

Table 3: Comparison of LDH, H_2O_2, and MDA levels in culture fluids after treatment at the different time points ($n = 3$).

Groups	H_2O_2			MDA			LDH		
	6 h	12 h	24 h	6 h	12 h	24 h	6 h	12 h	24 h
Control	17.85 ± 6.11	11.67 ± 1.71	8.31 ± 3.33	7.73 ± 0.27	8.21 ± 0.29	7.99 ± 0.31	972.01 ± 207.51	597.40 ± 124.4	884.50 ± 210.23
NB	20.86 ± 3.25	$17.30 \pm 2.49^*$	$22.13 \pm 5.70^*$	$18.40 \pm 0.73^*$	$16.47 \pm 2.28^*$	$25.70 \pm 1.47^*$	1363.00 ± 441.30	1124.35 ± 292.84	1418.79 ± 264.00
COM	15.60 ± 2.39	$17.88 \pm 3.27^*$	$20.60 \pm 3.40^*$	$25.46 \pm 4.29^*$	$29.50 \pm 5.72^*$	$61.74 \pm 13.50^*$	$1581.23 \pm 279.00^*$	$2392.08 \pm 734.78^*$	$2009.19 \pm 754.95^*$
TET + NB	13.59 ± 3.54	$10.72 \pm 1.79^{\#}$	$10.81 \pm 1.38^{\#}$	$8.46 \pm 2.09^{\#}$	$9.27 \pm 1.36^{\#}$	$9.41 \pm 2.30^{\#}$	$713.36 \pm 388.01^{\#}$	738.81 ± 410.49	809.98 ± 196.22

Note. * Compared with control cells, $P < 0.05$. $^{\#}$Compared with NB-treated cells, $P < 0.05$.
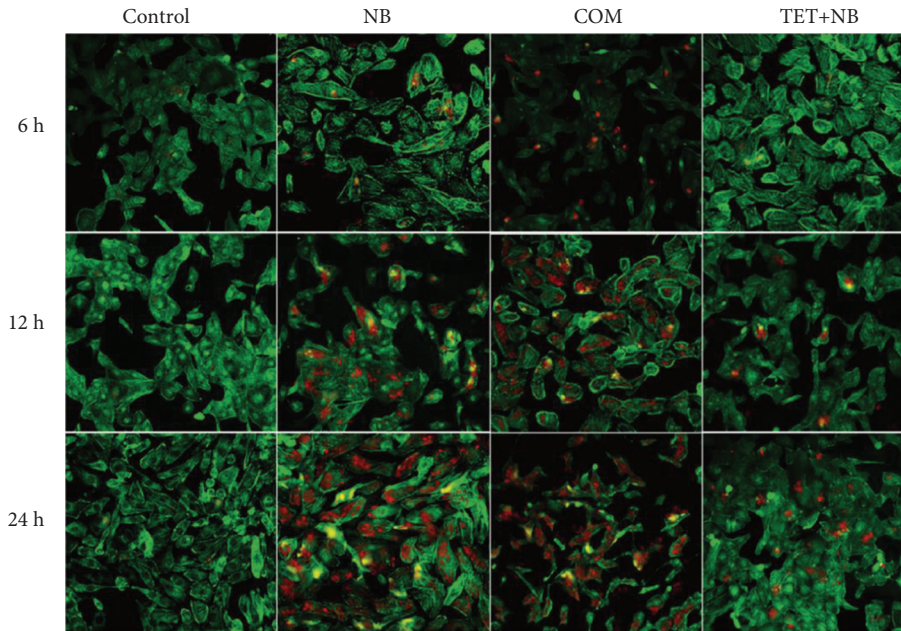
Figure 2: Adhesion of HK-2 cells to COM crystals by laser scanning confocal microscopy (200x).

adhesion may be played by the bacterial body itself rather than the calcium phosphate shell.

Cell damage is a key factor in the formation of stones, and the exposure of basement membranes can attract crystal adhesion. Necrotic cell debris can further exacerbate the formation of stones, leading to the development of kidney stones [17, 18]. It has been reported that calcium oxalate monohydrate (COM) crystals cause damage renal tubular epithelial cells by inducing lipid peroxidation reactions that generate large amounts of reactive oxygen species [16, 19]. Thamilselvan et al. [20] observed that the extracellular concentration of LDH and MDA was significantly increased after culturing LLC-PK1 cells with 500 mg/L calcium oxalate monohydrate (COM) crystals for 4 h. However, antioxidants within a certain concentration range can effectively inhibit lipid peroxidation [20], thus reducing the damage to cells caused by reactive oxygen species. In this study, the release of H_2O_2 and MDA was increased after cell exposure to COM and NB. On the other hand, the release of malondialdehyde(MDA) and H_2O_2 was not significantly increased by Nanograde hydroxyapatite (nHAP) treatment and was lower in the Tet + NB-treated than in the NB-treated cells. Thus, lipid peroxidation may be one of the mechanisms by which NB damage HK-2 cells and Tet inhibited this process.

Tet is one of the few antibacterial agents that can kill NB at physiological concentrations. It penetrates the calcium crust of NB and thus exerts its antibacterial action. The efficacy of Tet in the treatment of NB-associated chronic prostatitis and interstitial cystitis [20] has been reported. Hu Weiguo et al. [3] established a rat kidney stone model by tail vein injection of NB and found that Tet gavage reduced, in 24 h, urinary Lactate dehydrogenase (LDH) and the number of renal tubular crystals, suggesting an inhibiting effect on the formation of kidney stones. To date, however, there is still no evidence of such an effect from in vitro experiments.

In this study, in vitro coculturing NB and HK-2 cells revealed that Tet inhibited NB-induced injury to HK-2 cells and reduced crystal retention after injury. These results further confirmed the effectiveness of Tet in the prevention and treatment of kidney stones and emphasized its potential relevance for both diagnosis and treatment of nephrolithiasis in clinical practice.

Calcium sensitive receptor (CaSR), a member of the G protein-coupled receptor family, commonly expressed in organs such as the parathyroid, gastrointestinal tract, and kidney, plays an important role in the regulation of calcium secretion in the kidney [21]. The paracellular calcium reabsorption in TAL is tightly regulated by Calcium sensitive receptors (CaSR) in response to circulating calcium levels [22]. Increases in urinary calcium levels as a consequence of hypercalciuria can activate Calcium sensitive receptors (CaSR) to inhibit calcium-sensitive potassium channels and reduce calcium reabsorption [23]. Calcium-sensitive receptor (CaSR) overexpression increases the sensitivity to extracellular calcium and disrupts calcium metabolism, eventually resulting in the formation of kidney stones. Calcium sensitive receptor (CaSR) and Claudin protein-14(Claudin-14).

A recent large cohort study of patients with kidney stones has identified Claudin protein-14 (Claudin-14) as a major risk gene for hypercalciuria stones through genome-wide association analysis [24]. Gong et al. [25] demonstrated that calcium sensitive receptor (CaSR) regulates the expression of Claudin protein-14 (Claudin-14) in TAL through microRNA (miR-9 and miR-374)-mediated gene silencing. Claudin protein-14 (Claudin-14) inhibits the permeability of paracellular cation channels made of Claudin-16 and Claudin-19, which, in turn, regulate the metabolism of urinary calcium. When the level of urinary calcium increases, the Calcium sensitive receptor (CaSR)
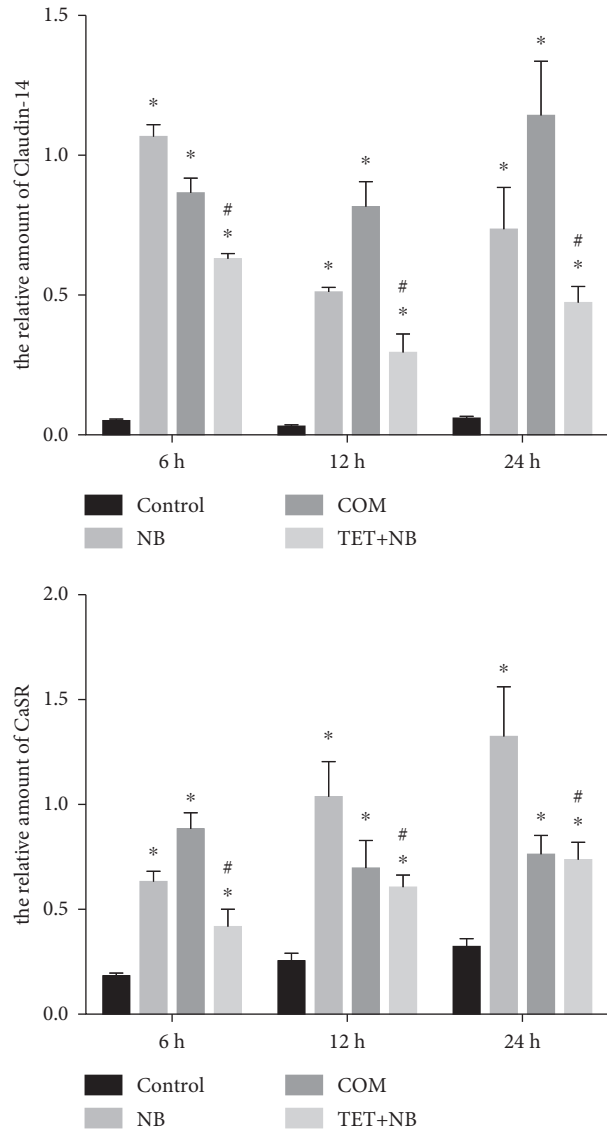
Figure 3: RT-PCR detection of Relative protein levels of CaSR and Claudin-14 in HK-2 cells.
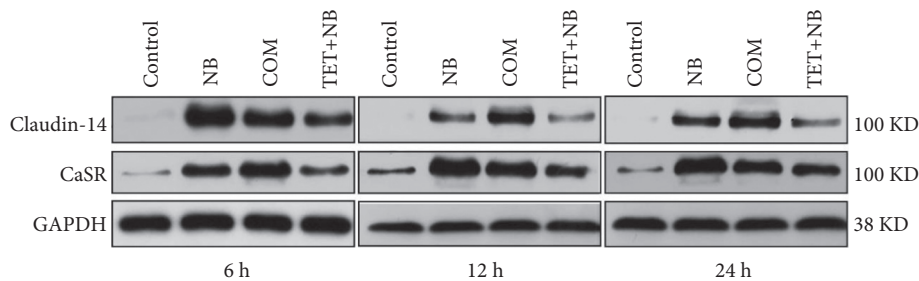
Figure 4: Western blot detection of CaSR and Claudin-14 in HK-2 cells.

and Claudin protein-14 (Claudin-14) axis is activated, inhibiting the reabsorption of calcium and ultimately resulting in hypercalciuria. Another study of the same group further described a CaSR-NFATc1-microRNA-Claudin protein-14 (Claudin-14) signaling pathway tightly modulating the metabolism of calcium in the kidney. Notably, the knockout of Claudin protein-14 (Claudin-14) abolished the transport of calcium induced by calcium sensitive receptor(CaSR), indicating that Claudin protein-14(Claudin-14) is required for calcium sensitive receptor (CaSR)-regulated calcium metabolism in the kidney [26]. A previous study from our laboratory also demonstrated that calcium

sensitive receptor (CaSR) induces the formation of stones by activating Claudin-14 in a calcium oxalate rat model [27]. Enhanced activity of calcium sensitive receptor (CaSR) and Claudin protein-14 (Claudin-14) regulatory channels may play an important role in the formation of calculi by nanobacteria [28].

However, to date, the relationship between NB and the CaSR-Claudin-14 axis has not been explored. In this study, HK-2 cells were cocultured with NB or exposed to calcium oxalate monohydrate (COM) crystals, revealing that both the mRNA and protein expression of CaSR and Claudin-14 were significantly upregulated under both conditions, compared to control cells, indicating that the CaSR-Claudin-14 axis may be involved in the process of NB-induced crystal adhesion in HK-2 cells.

In summary, NB may damage HK-2 cells by inducing lipid oxidation. The extent of damage and crystal retention is proportional to the duration of NB action. NB may lead to the formation of kidney stones through the following mechanism: after the damage of tubular epithelial cells by NB infection, crystals adhere to the exposed basement membrane. The CaSR-Claudin-14 axis may be involved in the process of crystal adhesion, which leads to stone formation in conjunction with NB and necrotic cell debris. To some extent, one experiment is to judge whether tetracycline has certain positive and negative effects on HK-2 cells on the basis of previous studies, and the results show that tetracycline can reduce the damage of NB to HK-2 cells [29].

List of abbreviations

CaSR: Calcium sensitive receptor
Claudin-14: Claudin protein-14
Tet: tetracycline
COM: calcium oxalate monohydrate
LDH: Lactate dehydrogenase
TAL: thick ascending limb
DMEM: Dulbecco's modified Eagle's medium
MDA: Malondialdehyde.

Data Availability

The datasets used or analyzed during the current study are available from the corresponding author on reasonable request.

Ethical Approval

This study was ethically approved by Medical Ethics Committee of the First Affiliated Hospital of Shihezi University Medical College (A-2019-037-01).

Disclosure

Gang Xu and Biao Qian and should be considered co-first authors.

Conflicts of Interest

The authors declare that they have no conflicts of interest.

Authors' Contributions

The two first authors contributed equally to this work.

References

[1] Y. Yang, Y. Deng, and Y. Wang, "Major geogenic factors controlling geographical clustering of urolithiasis in China," *The Science of the Total Environment*, vol. 571, pp. 1164–1171, 2016.

[2] N. Abrol, A. Panda, N. Kekre, and A. Devasia, "Nanobacteria in the pathogenesis of urolithiasis: myth or reality?" *Indian Journal of Urology*, vol. 31, no. 1, pp. 3–7, 2015.

[3] H. Ansari, A. Akhavan Sepahi, and M. Akhavan Sepahi, "Different approaches to detect "nanobacteria" in patients with kidney stones: an infectious cause or a subset of life," *Urology Times*, vol. 14, no. 5, pp. 5001–5007, 2017.

[4] H. Yan, Q. Wang, S. Wu, Q. Cheng, Y. Wang, and B. Qian, "Dynamic study on the formation time of kidney stones in rat model of nano-bacterial kidney stones," *Chinese Journal of General Medicine*, vol. 20, no. 21, pp. 2613–2618, 2017.

[5] E. O. Kajander, N. Ciftcioglu, K. Aho, and E. Garcia-Cuerpo, "Characteristics of nanobacteria and their possible role in stone formation," *Urological Research*, vol. 31, no. 2, pp. 47–54, 2003.

[6] W. G. Hu, X. F. Wang, T. Xu, J. X. Li, and X. B. Huang, "Establishment nephrolithiasis rat model induced by nanobacteria and analysis of stone formation," *Beijing Da Xue Xue Bao Yi Xue Ban*, vol. 42, no. 4, pp. 433–435, 2010.

[7] N. Ciftçioglu, R. S. Haddad, D. C. Golden, D. R. Morrison, and D. S. Mckay, "A potential cause for kidney stone formation during space flights: enhanced growth of nanobacteria in microgravity," *Kidney International*, vol. 67, no. 2, pp. 483–491, 2005.

[8] N. Rahman, M. Meng, and M. Stoller, "Infections and urinary stone disease," *Current Pharmaceutical Design*, vol. 9, no. 12, pp. 975–981, 2003.

[9] E. Garcia Cuerpo, K. A. J. A. N. D. E. R. E. Olavi, N. Ciftcioglu, F. L. Castellano, and A. E. Barrilero, "Nanobacteria,An experimental neo-lithogenesis model," *Archivos Españoles de Urología*, vol. 53, no. 4, pp. 291–303, 2000.

[10] G. E. Tasian, A. E. Kabarriti, A. Kalmus, and S. L. Furth, "Kidney stone recurrence among children and adolescents," *The Journal of Urology*, vol. 197, no. 1, pp. 246–252, 2016.

[11] D. A. Shoskes, K. D. Thomas, and E. Gomez, "Anti-nanobacterial therapy for men with chronic prostatitis/chronic pelvic pain syndrome and prostatic stones: preliminary experience," *The Journal of Urology*, vol. 173, no. 2, pp. 474–477, 2005.

[12] C. Y. Pak, "Nephrolithiasis," *Current Therapy in Endocrinology and Metabolism*, vol. 6, pp. 572–576, 1997.

[13] K. K. Frick and D. A. Bushinsky, "Molecular mechanisms of primary hypercalciuria," *Journal of the American Society of Nephrology*, vol. 14, no. 4, pp. 1082–1095, 2003.

[14] H. Dimke, P. Desai, J. Borovac, A. Lau, W. Pan, and R. T. Alexander, "Activation of the Ca2+-sensing receptor increases renal claudin-14 expression and urinary Ca2+ excretion," *American Journal of Physiology—Renal Physiology*, vol. 304, no. 6, pp. F761–F769, 2013.

[15] C. Li, G. Sun, Y. Deng, and S. Li, "Experimental study on the damage of renal tubular epithelial cells induced by calcium oxalate crystals," *Journal of Modern Urology*, vol. 11, no. 2, pp. 75–77, 2006.

[16] H. Xin, X. Wang, W. Tian, C. Yu, and L. Hui, "Role of nanobacteria in the pathogenesis of kidney stone formation," *The American Journal of Translational Research*, vol. 8, no. 7, pp. 3227–3234, 2016.

[17] J. C. Lieske and F. G. Toback, "Regulation of renal epithelial cell endocytosis of calcium oxalate monohydrate crystals," *American Journal of Physiology*, vol. 264, no. 5, pp. F800–F807, 1993.

[18] N. Cíftçíoglu, M. A. Miller-Hjelle, J. T. Hjelle, and E. O. Kajander, "Inhibition of nanobacteria by antimicrobial drugs as measured by a modified microdilution method," *Antimicrobial Agents and Chemotherapy*, vol. 46, no. 7, pp. 2077–2086, 2002.

[19] S. Wang, X. Huang, Q. Xu, H. Ye, K. Ma, and X. Wang, "Protective effects of tea polyphenols on oxalic acid and calcium oxalate monohydrate-induced injury in HK-2 cells," *Journal of Peking University*, vol. 45, no. 4, pp. 567–574, 2013.

[20] S. Thamilselvan, S. R. Khan, and M. Menon, "Oxalate and calcium oxalate mediated free radical toxicity in renal epithelial cells: effect of antioxidants," *Urological Research*, vol. 31, no. 1, pp. 3–9, 2003.

[21] Z. Zhou, L. Hong, X. Shen et al., "Detection of nanobacteria infection in type III prostatitis," *Urology*, vol. 71, no. 6, pp. 1091–1095, 2008.

[22] Q.-H. Zhang, X.-C. Shen, Z.-S. Zhou, Z.-W. Chen, G.-S. Lu, and B. Song, "Decreased nanobacteria levels and symptoms of nanobacteria-associated interstitial cystitis/painful bladder syndrome after tetracycline treatment," *International Urogynecology Journal*, vol. 21, no. 1, pp. 103–109, 2010.

[23] E. M. Brown, "Clinical lessons from the calcium-sensing receptor," *Nature Clinical Practice Endocrinology & Metabolism*, vol. 3, no. 2, pp. 122–133, 2007.

[24] D. Riccardi and E. M. Brown, "Physiology and pathophysiology of the calcium-sensing receptor in the kidney," *American Journal of Physiology - Renal Physiology*, vol. 298, no. 3, pp. F485–F499, 2010.

[25] N. Spurr, "Genetics of calcium-sensing—regulation of calcium levels in the body," *Current Opinion in Pharmacology*, vol. 3, no. 3, pp. 291–294, 2003.

[26] G. Thorleifsson, H. Holm, V. Edvardsson et al., "Sequence variants in the CLDN14 gene associate with kidney stones and bone mineral density," *Nature Genetics*, vol. 41, no. 8, pp. 926–930, 2009.

[27] Y. Gong, V. Renigunta, N. Himmerkus et al., "Claudin-14 regulates renal Ca++transport in response to CaSR signalling via a novel microRNA pathway," *The EMBO Journal*, vol. 31, no. 8, pp. 1999–2012, 2012.

[28] M. Shen, Q. Wang, C. Qian, H. Xu, Z. Hao, and P. L. B. Qian, "Dynamic study on the expression of CaSR and Claudin-14 in nanobacterial kidney stone formation," *Journal of Medical Graduate Students*, vol. 31, no. 5, pp. 466–469, 2018.

[29] M. Shen, C. Gao, and L. Zheng, "Effects of tetracycline on expression of CaSR and Claudin-14 in human renal tubular epithelial cells HK-2 infected with nanobacteria," *Chinese pharmacy*, vol. 29, no. 19, pp. 2607–2611, 2018.

Research Article

Light Industry Technology of Chiral Perovskite Nanomaterials Construction and Photoelectric Properties

Jie Sun ⓘ

Department of Construction Engineering and Office, Yantai Vocational College, Yantai 264670, Shandong, China

Correspondence should be addressed to Jie Sun; 20140912@stu.nun.edu.cn

Perovskite nanomaterials have become a new research hotspot due to the many novel physical properties of quantum effects and have good application prospects in the field of optoelectronics. Among them, the realization of controllable fabrication of perovskite nanomaterials is the basis of performance studies and applications and is also a difficult point. Reducing production costs to improve manufacturing methods, further improve product controllability, promote advantages, or improve disadvantages will be very important for further application of perovskite nanomaterials. Therefore, this paper studies the construction of titanium ore nanomaterials by designing a novel preparation process and, at the same time, analyzes the related optoelectronic properties of the obtained materials. In this paper, a triangular PbI_2 nanosheet having a uniform and controllable shape and size was successfully fabricated by physical vapor deposition through the introduction of a limited space, and related characterization was performed to show uniform controllability and high crystallinity. Using PbI_2 nanosheets as the substrate, $MAPbI_3$ nanosheets were further prepared and related characterizations proved that the obtained nanosheets had high crystallinity and excellent optical properties. The experiment proves that the peak position of the fluorescence spectrum obtained by Gaussian fitting is 800 nm and the half-peak width is about 45 nm. At the same time, $MAPbI_3$ exhibits strong light absorption characteristics when the wavelength is less than 800 nm. This shows that this enclosed space deposition method can improve the uniformity and controllability of PbI_2 and $MAPbI_3$ nanosheet fabrication, which provides the basis for further research on $MAPbI_3$ nanomaterials and references to the controllable growth of other nanomaterials.

1. Introduction

As a direct band gap semiconductor, perovskite has many advantages, such as designable structure, continuously adjustable band gap, high light absorption and emission efficiency, high carrier mobility, and low preparation cost. It has become a star material that has attracted much attention. When the perovskite is further made into nanomaterials, due to the quantum effect, it will exhibit many novel physical and chemical properties, further expanding its application range. Perovskites also have excellent electrical properties, high hole mobility, and carrier diffusion lengths up to the millimeter level. When perovskites form nanomaterials, they have newer properties due to quantum effects. Because of these outstanding optical and electrical properties, perovskites, especially perovskite nanomaterials, have been extensively studied.

The study of the structure and optoelectronic properties of perovskite nanomaterials abroad is much faster than in China, the discovery of perovskite nanomaterials is also faster than in China, and the construction technology of nanomaterials is rapidly developing and updating. The construction and optoelectronic properties of perovskite nanomaterials have been greatly improved and developed. It is believed that the application of perovskite nanomaterials in light industry will become more and more extensive in the near future. Ha et al. synthesized a series of tantalate compounds with Dion–Jacobson layered perovskite structure by solid-phase method. These compounds can photocatalytically decompose water to produce hydrogen and oxygen under the irradiation of ultraviolet light [1]. Halford studied the Ruddlesden-Popper layered perovskite structure compound and found that it can effectively degrade

rhodamine B solution under ultraviolet light irradiation and have a wide range of applications in photocatalytic sterilization, water purification treatment, and conversion of solar energy to hydrogen energy [2]. Riba et al. prepared a series of perovskite nanoparticles with different compositions and realized the continuous adjustment of its fluorescence spectrum from 410 nm to 710 nm in the visible light region [3].

The application of perovskite nanomaterials in light industry began in western countries. Research on perovskite nanomaterials in our country started late compared to western countries, and the development speed is relatively slow. With the continuous development of science and technology and the maturity of nanomaterials, studying the construction and photoelectric properties of perovskite nanomaterials can greatly promote the development of our country's light industry. Shang et al. successfully prepared a new and highly active solid solution catalyst, which can effectively degrade the organic pollutant acetaldehyde in response to visible light [4]. Han et al. synthesized perovskite nanosheet structures of different thicknesses through the solution method and tested the PL of samples with different thicknesses. The results found that as the nanosheets increased from a single layer to 10 layers, the PL peak position shifted significantly from 724 nm [5]. Kong et al. observed ionic conductivity higher than electron conductivity in perovskite nanomaterials, indicating the importance of ion transport in perovskite [6].

This paper improves the perovskite vapor phase synthesis method, reduces the cost of preparing the vapor phase method, and obtains a uniform and controllable perovskite nanomaterial. Although we have achieved some results from the preparation of the material, there are still aspects that require further development. Although the uniform and controllable PbI_2 and $MAPbI_3$ nanosheets have been obtained by the confined space method, there is a lack of in-depth research on the method and the materials obtained. The dynamic instability in the growth process of nanomaterials is universal. This experiment only improves the preparation of PbI_2 nanosheets to overcome this phenomenon, but the same problems existing in the preparation of other nanomaterials have not been explored in depth.

2. Construction and Photoelectric Properties of Chiral Perovskite Nanomaterials

2.1. Optical and Electrical Properties of Perovskite

2.1.1. Optical Properties. Perovskite is a direct band gap semiconductor with a high absorption coefficient, so it has excellent optical properties. In addition, the perovskite band gap position is appropriate, between 1.4 and 3.0 eV, and the light absorption and emission can just cover the entire visible light region, which has broad application prospects. The optical performance adjustment can be achieved between the same type of perovskite through ion exchange, and the same can be achieved between different types of perovskite. When perovskite forms nanomaterials, due to the existence of quantum effects, its optical properties will also

change with the thickness of perovskite nanomaterials [7, 8]. From the single layer to the bulk phase, the bandgap offset can reach 100 meV, which shows that the thickness of the perovskite nanosheets has a great influence on the optical properties.

2.1.2. Electrical Properties. In addition to excellent optical properties, perovskite has good electrical properties, and perovskite has high ionic conductivity. The conductivity of perovskite is not only related to temperature and I_2 partial pressure, but also related to light [9, 10]. As the light intensity increases, the ionic and electronic conductivities continue to increase. Second, perovskites also have a longer carrier diffusion distance and lower defect concentration. The optical and electrical properties of $MAPbX_3$ single crystal have a carrier diffusion distance exceeding $10 \mu m$, and the crystallinity is the same as the highest crystalline quality of single crystal silicon.

2.1.3. Application of Perovskite Nanomaterials in the Field of Optoelectronics. Among them, perovskite nanomaterials such as nanowires and nanosheets generally have very high crystallinity and better performance. At the same time, its small size makes it particularly suitable for applications in the field of micronano optoelectronic devices. The principle of photodetectors is based on the photoelectric effect of semiconductor materials. The photoelectric effect can be divided into the photoconductive effect and the photovoltaic effect [11, 12]. A good photodetector needs to meet the conditions of high spectral selectivity, high sensitivity, fast response speed, high signal-to-noise ratio, and good cycle stability.

2.2. Preparation of Perovskite Nanomaterials.
Perovskite has the advantages of simple method and low cost in preparation, which is also an important reason for its large-scale application in the field of optoelectronics. The raw materials for perovskite synthesis are usually AX and BX_2. The one-step method refers to the direct reaction of the two to obtain perovskite nanomaterials. The two-step method refers to the synthesis of BX_2 precursor nanomaterials and then further conversion with AX into perovskite [13, 14]. No matter which method is used to prepare the corresponding nanorods and nanosheets of perovskite nanomaterials, machine learning models need to be used to detect their optoelectronic properties.

2.2.1. Decision Tree. In the process of constructing the decision tree model, the most important thing is the feature selection of the node. Through the feature selection, the standard for constructing the split judgment is reached and the tree is further split. The Gini index is the main method to select the optimal feature in the decision tree model [15]. When the decision tree model is used for classification, if there are i categories and p_i is the probability that the sampling point belongs to the i category, then the Gini index formula is

$$\text{Gini}(p) = \sum_{i=1}^{I} p_i (1 - p_i) = 1 - \sum_{i=1}^{I} p_i^2. \tag{1}$$

When the decision tree performs two classifications, assuming that the probability of the sample point being classified into the first class is q, then the Gini index of the probability distribution is

$$\text{Gini}(q) = 2q(1 - q). \tag{2}$$

For a given sample set M, its Gini index is

$$\text{Gini}(M) = 1 - \sum_{i=1}^{I} \left(\frac{|C_i|}{|M|} \right)^2. \tag{3}$$

Here, C_i is the subset of samples in M that is the class i and M is the number of classes.

2.2.2. Logistic Regression.

Taking X as a continuous random variable, which obeys the logistic distribution, its distribution function and density function are

$$F(x) = P(X \le x)$$

$$= \frac{1}{1 + e^{-(x-\mu)/\gamma}},$$

$$f(x) = F'(x) \tag{4}$$

$$= \frac{e^{-(x-\mu)/\gamma}}{\gamma \left(1 + e^{-(x-\mu)/\gamma} \right)^2}.$$

Binomial logistic regression in logistic regression can be used as a classification, with conditional probability $P(Y|X)$ as a model function. In the model, the value of random variable X can be any real number, and the corresponding Y value is 1 or 0 [16, 17]. Its conditional probability distribution is

$$P(Y = 1 \mid x)$$

$$= \frac{\exp(\omega x + b)}{1 + \exp(\omega x + b)},$$

$$P(Y = 0 \mid x) \tag{5}$$

$$= \frac{1}{1 + \exp(\omega x + b)}.$$

Here, $x \in R^n$ is the input, $Y \in \{0, 1\}$ is the output, $\omega \in R^n$ and $n \in R^n$ are the parameters. We call ω the weight vector and b the bias. Let

$$P(Y = 1 \mid x) = \pi(x),$$

$$P(Y = 0 \mid x) = 1 - \pi(x). \tag{6}$$

The likelihood function is

$$\prod_{i=1}^{N} [\pi(x_i)]^{y_i} [1 - \pi(x_i)]^{1 - y_i}. \tag{7}$$

The log likelihood function is

$$L(w) = \sum_{i=1}^{N} [y_i (wx) - \log(1 + \exp(wx))]. \tag{8}$$

Find the maximum value of $L(w)$ to get the estimated value of w. Assuming that the maximum likelihood estimate of w is $\widehat{w}$, the regression model obtained by training is

$$P(Y \mid X) = \frac{\exp(\widehat{\omega}x)}{1 + \exp(\widehat{\omega}x)}. \tag{9}$$

2.2.3. Support Vector Regression Algorithm.

(1) *Linear Support Vector Regression Machine.* Suppose the sample data set is represented as $\varphi: R^n \longrightarrow H\{x_k, y_k\}_{k=1}^{N}$, where N is the number of samples, the input data $x_k \in R^n$ is n dimensional, and the output data $y_k \in R^n$ corresponds to the input data x_k [18, 19]. Suppose the linear regression function is

$$f(x) = w^T x + b, \tag{10}$$

where $w \in R^n$, $b \in R$, and w are normal vectors. The loss function is used as follows:

$$|y - f(x)|_\varepsilon = \begin{cases} 0, & \text{if } |y - f(x)| \le \varepsilon, \\ |y - f(x)| - \varepsilon, & \text{otherwise.} \end{cases} \tag{11}$$

Among them, ε is the preset tolerable loss function, and the distance between the two dotted lines is $2/\|w\|$. The optimization goal of the algorithm is to maximize the distance, that is, minimize the reciprocal of the logarithmic distance [20, 21]. Finally, the process of finding the most suitable regression function is transformed into

$$\min \frac{1}{2} \|w\|^2. \tag{12}$$

The penalty parameter C and the relaxation factor ξ_i, ξ_i^* are introduced, and the optimization problem corresponding to the regression estimation is transformed into

$$\min_{w,b} P = \min \frac{1}{2} \|w\|^2 + C \sum_{i=1}^{N} (\xi_i + \xi_i^*). \tag{13}$$

The constraints that should be met are

$$\begin{cases} y_i - w^T x_i - b \le \varepsilon + \xi_i, & i = 1, \dots, N, \\ w^T x_i + b - y_i \le \varepsilon + \xi_i, & i = 1, \dots, N, \\ \xi_i, \xi_i^* \ge 0, & i = 1, \dots, N. \end{cases} \tag{14}$$

Lagrangian dual functions are usually introduced to solve the above convex quadratic programming problem [22]. The Lagrangian dual function is constructed as follows:

$$L(w, b, \xi_i, \xi_i^*, a, a^*, \eta, \eta^*) = \frac{1}{2}\|w\|^2 + C \sum_{i=1}^{N} (\xi_i + \xi_i^*)$$

$$- \sum_{i=1}^{N} a_i (\varepsilon + \xi_i - y_i + w^T x_i + b)$$

$$- C \sum_{i=1}^{N} (\eta_i \xi_i + \eta_i^* \xi_i^*). \tag{15}$$

The Lagrangian multiplier is introduced, which turns the problem into a solution:

$$\max_{a, a^*, \eta, \eta^*} \min_{w, b, \xi, \xi^*} L(w, b, \xi, \xi^*, a, a^*, \eta, \eta^*). \tag{16}$$

Taking the Lagrangian dual function to differentiate $w, b, \xi,$ and ξ^* equal to zero, the dual problem can be transformed into a convex quadratic programming problem:

$$\max_{a, a^*} J_D(a, a^*) = -\frac{1}{2} \sum_{k,i=1}^{N} (a - a^*)(a_k - a_k^*) x_i^T x_k$$

$$- \varepsilon \sum_{i=1}^{N} (a_i + a_i^*) + \sum_{i=1}^{N} y_i (a_i + a_i^*). \tag{17}$$

The conditions are

$$\sum_{i=1}^{N} (a_i - a_i^*) = 0, \quad a_i a_i^* \in [0, c]. \tag{18}$$

The final target fitting regression function is expressed as

$$f(x) = \sum_{i=1}^{N} (a_i - a_i^*) x_i^T x + b. \tag{19}$$

Through deduction, it can be seen that the number of support vectors in SVM is limited. The input samples x_i corresponding to those a_i are not zero. Only input vectors that meet this condition can contribute to the SVM model. This is the sparsity of the SVM solution [23, 24].

(2) *Nonlinear Support Vector Regression Machine.* Polynomial kernel functions have better generalization power and belong to global kernel functions, but the price paid is an unsuitable effect on nonlinear problems. The nonlinear SVM problem can be expressed as solving the following problem:

$$\max_{a, a^*} J_D(a, a^*) = -\frac{1}{2} \sum_{k,j=1}^{N} (a_i - a_i^*)(a_k - a_k^*) K(x_i, x_k)$$

$$- \varepsilon \sum_{i=1}^{N} (a_i - a_i^*) + \sum_{i=1}^{N} y_i (a_i - a_i^*). \tag{20}$$

The conditions are

$$\sum_{i=1}^{N} (a_i - a_i^*) = 0, \quad a_i a_i^* \in [0, c]. \tag{21}$$

The final target fitting regression function is expressed as

$$f(x) = \sum_{i=1}^{N} (a_i - a_i^*) K(x_i, x) + b. \tag{22}$$

When there is a lack of prior knowledge in the relevant fields of sample data, the radial basis kernel function is generally selected as the kernel function, which can better balance the fitting effect and generalization ability than other kernel functions [25]. The expression of the radial basis kernel function is as follows:

$$K(x', x) = \exp\left(\frac{-\|x - x'\|^2}{\sigma^2}\right), \tag{23}$$

where σ is a parameter that characterizes the width of the core.

3. Construction of Perovskite Nanomaterials and Experimental Design of Photoelectric Properties

3.1. Purpose

(1) Research on the construction of perovskite nanomaterials

(2) Study of the optoelectronic properties of perovskite nanomaterials

3.2. Preparation of PbI$_2$ Nanosheets.
PbI_2 is an important precursor material in the process of preparing perovskite nanomaterials by the two-step method, and PbI_2 itself is a layered structure, and it is easy to prepare a two-dimensional nanosheet structure through regulation. The two-dimensional PbI_2 preparation is prepared by vapor deposition method. As shown in Figure 1, this preparation method can meet the requirements of productivity and crystallinity at the same time. Based on the high-quality PbI_2 nanosheets obtained, the vapor deposition method is further used to transform it into $MAPbI_3$ perovskite nanosheets.

3.3. Experimental Method.
(1) *X-Ray Diffraction Analysis.* The X-ray diffraction test method is based on the diffraction effect of a polycrystalline sample on X-ray and analyzes and determines the presence of each component in the sample. X-ray powder diffraction can not only analyze the phase of the sample, but also determine the unit cell parameters of the crystal structure, the lattice pattern, and the atomic coordinates of simple structures.

(2) *Scanning Electron Microscope Morphology Analysis.* Scan the different positions on the sample by scanning electron beams, collect this information, and send it to the imaging system after being magnified. The information emitted at any point in the sample surface scanning process can be recorded to obtain image information. The distribution of the surface morphology of the sample can be obtained through the correspondence between the

FIGURE 1: Schematic diagram of PbI$_2$ nanosheets prepared by vapor deposition method (https://image.baidu.com/).

information and the sample position. First glue the conductive glue on the sample stage, then put an appropriate amount of sample on the conductive glue, use the blowing rubber ball to blow gently to blow off the excess sample, and make the sample evenly distributed on the conductive glue; finally, the sample stage is put into the gold spraying equipment, and the sample is sprayed gold and then taken out, to be tested.

(3) *Analysis of the Morphology of the Transmission Electron Microscope.* The electrons transmitted out of the sample are magnified and projected on the phosphor screen for observing the graph by the three-stage magnetic lens of the objective lens, the intermediate mirror, and the projection lens. Therefore, the image corresponding to the morphology, organization, and structure of the sample is displayed on the fluorescent screen.

3.4. Establishment of the Model Evaluation Index System. The evaluation index is a specific evaluation item that is determined according to the evaluation purpose and can reflect the basic characteristics of the evaluation target. Indicators are specific and measurable and are the observation points of your target. Clear conclusions can be drawn from the actual observation of the object. Typically, the metrics system includes three levels of metrics. This is the relationship between progressive decomposition and improvement. Among these, the first-stage evaluation index and the second-stage evaluation index are relatively abstract and cannot be used as direct evaluation criteria. The three-level assessment indicator should be specific, measurable, and action-oriented and can be used as a direct basis for assessment.

3.5. Statistical Processing. Statistical analysis was performed with SPSS 13.0 statistical software, the significance test of the difference was performed by one-way analysis of variance, the difference between the two groups was tested by LSD-t, and the photoelectric properties of perovskite nanomaterials were performed by group t-test. $P < 0.05$ is considered to be statistically significant.

4. Construction and Photoelectric Properties of Perovskite Nanomaterials

4.1. Evaluation Index System Based on Index Reliability Testing. Here we perform reliability analysis on all reliability indicators of each object. The reliability indicators we choose for each object are slightly different. The results are shown in Table 1.

It can be seen from Figure 2 that the morphology control of the PbI$_2$ nanosheets, the growth mechanism of PbI$_2$, the characterization of the composition, and the data obtained from the optical properties have a very good effect on this experiment ($\alpha > 0.8$); the influence of the data obtained from various indicators of the optical performance of MAPbI3 nanosheets on this experiment is acceptable ($\alpha > 0.7$). This shows that the indicators are reasonable when studying the composition and photoelectric properties of the five selected chiral perovskite nanomaterials in this paper. It provides the basis for subsequent experiments.

4.2. Evaluation Index System Based on Inspection Data. (1) *PbI$_2$ Nanosheet Morphology Control.* Keeping the growth temperature and substrate unchanged, the size of the confinement space and the distance between the substrate and the furnace center are important factors affecting the growth of PbI$_2$ nanosheets. Therefore, the size of the confinement space (the height between the sandwich quartz plates) is compared here. The results of the experiment are shown in Figure 3.

Figure 3 shows the synthesized PbI$_2$ nanosheets synthesized under different confinement space heights. The confinement space heights are 1 mm, 2 mm, and 3 mm, respectively. The crystal size and nucleation density of these samples were counted, and the results are shown in Table 2.

It can be seen from Figure 4 that as the height of the confined space increases from 1 mm to 3 mm, the average crystal size increases from 4 μm to 8 μm. But when the height of the confined space is 3 mm, the synthesized PbI$_2$ nanosheets are no longer uniformly distributed: many small particles and linear structures appear on the substrate. This is similar to the sample obtained without the confined space, indicating that as the height of the confined space increases, the confinement effect decreases. However, PbI$_2$ nanosheets with uniform shape and crystal size distribution can be obtained at both 1 mm and 2 mm limit heights. The nucleation density gradually increases as the height of the confinement space increases, from 36.14 * 10^4 cm^2 at 1 mm to 125.48 * 10^4 cm^2 at 3 mm, indicating that the size of the confinement space is positively correlated with the nucleation density. When the height of the confinement space increases to 3 mm, the uniformity of the PbI$_2$ nanosheets is reduced, and the confinement effect is weakened. Therefore, the effect is best when the height of the confined space is 2 mm, and a uniform and relatively large PbI$_2$ triangular nanosheet can be obtained.

(2) *PbI$_2$ Growth Mechanism.* It can be seen from Figure 5 that for the case of no confined space, PbI$_2$ has both

TABLE 1: Data sheet of evaluation index system for index reliability testing.

	Very clear	Clear	General	Not clear	Chaotic	Alpha
PbI$_2$ nanosheet morphology control	3.98	3.81	4.51	0.79	0.47	0.7281
PbI$_2$ growth mechanism	3.55	3.65	4.45	0.47	0.54	0.7349
Component structure characterization	3.87	3.86	4.76	0.66	0.49	0.7425
Optical properties	3.58	4.14	4.70	0.52	0.41	0.7762
Optical properties of MAPbI$_3$ nanosheets	3.62	3.98	4.52	0.53	0.42	0.8294
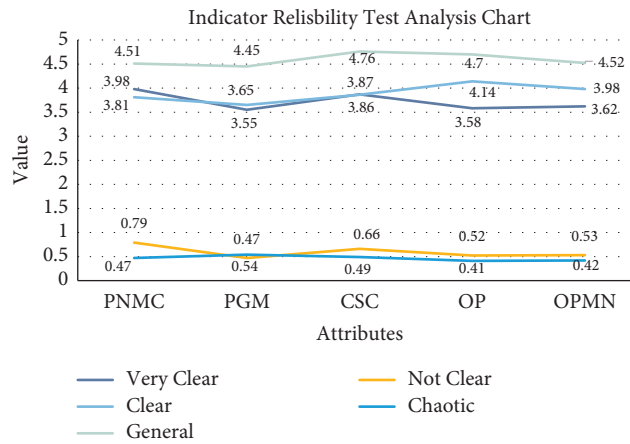
FIGURE 2: Indicator reliability test analysis chart.

(a) (b) (c)
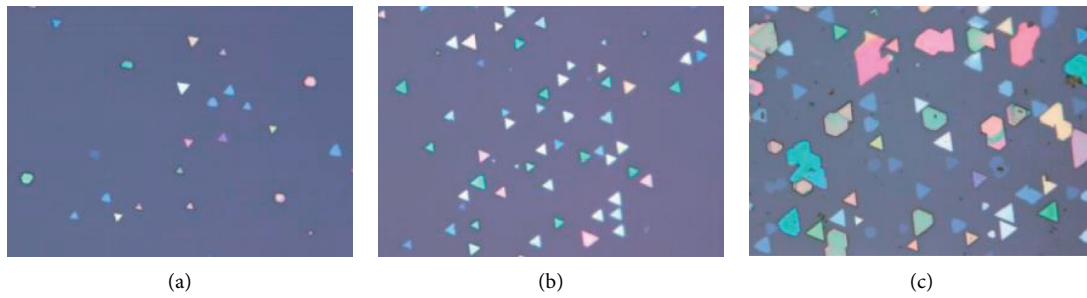
FIGURE 3: Influence of the height of the confined space on the morphology of PbI$_2$ nanosheets (https://image.baidu.com/). (a) PbI$_2$ nanosheets under the restricted space height of 1 mm. (b) PbI$_2$ nanosheets under the restricted space height of 2 mm. (c) PbI$_2$ nanosheets under the restricted space height of 3 mm.

TABLE 2: Data sheet of evaluation index system for index reliability testing.

Restricted space height	Average crystal size (μm)	Nuclear density ($*10^4$ cm^2)
1 mm	4	36.14
2 mm	6	67.78
3 mm	8	125.48

triangular and hexagonal morphologies, indicating that the growth process has dynamic instability, and the concentration and flow rate of the gaseous source of PbI$_2$ are constantly changing. This greatly limits the controllable growth of PbI$_2$, thus limiting their further applications. When the sandwich quartz plate is introduced as the confined space, it cannot only ensure that the PbI$_2$ gaseous source can be successfully transferred to the substrate, but also produce a stable gaseous source concentration delivery process, so that the gas source concentration is evenly distributed on the substrate. In the nucleation stage, the low source concentration in the confined space effectively reduces the nucleation density; in the epitaxial growth stage, it can provide a stable source supply and realize the uniform growth of PbI$_2$ nanosheets. As the substrate distance increases, the PbI$_2$ concentration gradually decreases, resulting in thinner nanosheets. The confined space reduces nucleation density and provides a relatively stable gas source
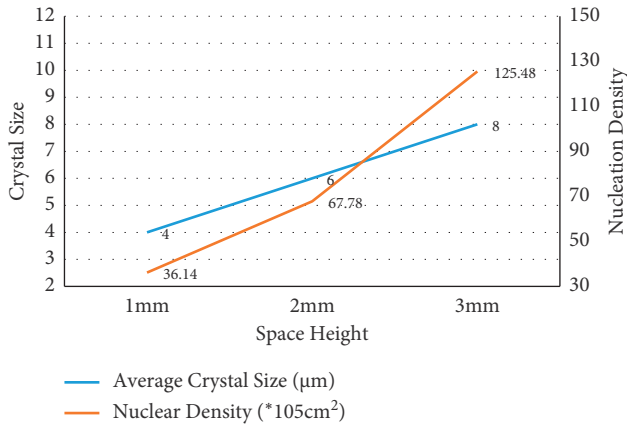
FIGURE 4: Relationship between crystal size and nucleation density and confinement space height.
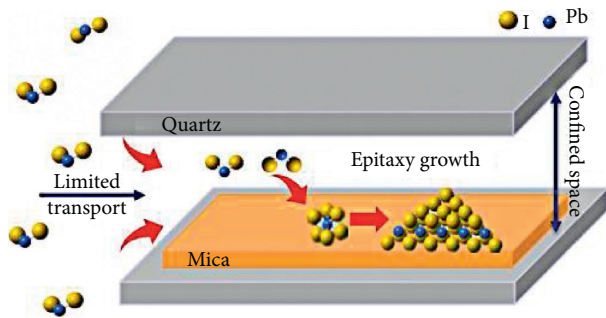
FIGURE 5: Schematic diagram of the growth mechanism of PbI$_2$ nanosheets in a confined space (https://image.baidu.com/).

TABLE 3: Component structure characterization data sheet.

Degree	(001)	(002)	(003)	(004)
10	1.29	2.59	2.31	2.75
20	2.68	2.70	2.80	3.39
30	3.43	3.97	3.47	4.20
40	3.45	4.24	3.76	4.78
50	4.46	4.44	4.96	5.38
60	4.32	5.02	4.94	5.51
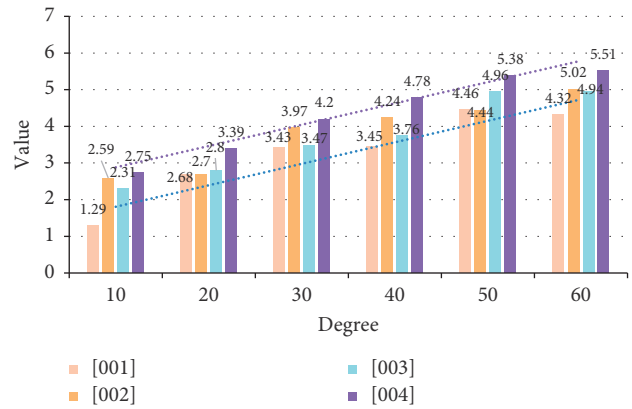
FIGURE 6: Component structure characterization analysis diagram.

supply environment, which can overcome dynamic instability during PbI$_2$ growth and achieve uniform and controllable preparation for the shape and thickness of PbI$_2$ nanosheets.

(3) *Characterization of Composition Structure.* Through X-ray diffraction pattern, X-ray photoelectron spectroscopy, the phase structure, and chemical state of PbI$_2$ nanosheets were studied. The X-ray diffraction pattern was used to determine the crystal phase structure of the sample, and the results are shown in Table 3.

It can be seen from Figure 6 that all the peak positions in the figure are in good agreement with the hexagonal phase PbI$_2$, and only the (001) plane diffraction peak appears, which indicates that the out-of-plane growth direction of PbI$_2$ nanosheets is the [001] direction.

We conducted transmission electron microscopy analysis of the PbI$_2$ crystal structure, and the transmission electron microscopy sample was obtained by sample transfer. The result is shown in Figure 7.

The high-resolution electron microscope image of the PbI$_2$ nanosheet is shown in Figure 7(a). The distance between the crystal planes is 0.228 nm, which corresponds to the (110) plane of PbI$_2$. The selected area electron diffraction pattern in Figure 7(b) also proves that the high-resolution exposed crystal plane is the PbI$_2$ (110) crystal plane, and the direction perpendicular to the crystal plane is the [001] crystal orientation. The results obtained are also consistent

with the X-ray diffraction pattern results. These all indicate that the obtained PbI$_2$ nanosheets are single crystals with high quality and uniformity.

(4) *Optical Property Analysis.* The optical properties of PbI$_2$ nanosheets were studied, and the Raman peak positions of samples with different thicknesses were studied. The results are shown in Table 4.

It can be seen from Figure 8 that the Raman peak of the mica substrate is relatively weak, and its influence on the test results can be ruled out. All samples have characteristic peaks at 75, 100, and 125, which are attributed to the three vibration mode peaks of E_g, A_{1g}, and A_{2u} in PbI$_2$, respectively. As the thickness of PbI$_2$ increases, the peak intensity of all peaks becomes stronger and the half-width becomes narrower, but the position of the characteristic peak remains unchanged.

(5) *Study on Gas Phase Transformation and Optical Properties of MAPbI$_3$ Nanosheets.* Through precise control of reaction conditions and related characterization, we have obtained high-quality PbI$_2$ nanosheets with uniform morphology and controllable size, which provides an important basis for the two-step preparation of MAPbI$_3$ nanosheets. The obtained MAPbI$_3$ nanosheets were characterized by related optical properties, and the results are shown in Table 5.

It can be seen from Figure 9 that the peak position of the fluorescence spectrum obtained by Gaussian fitting is 800 nm, and the half-value width is about 45 nm. The half-value width can reflect the crystalline properties of the material, and the smaller the value, the better, which fully indicates that the obtained nanosheets have high crystallinity and at the same time indicates that the converted perovskite

PbI$_2$ high resolution
transmission spectrum

(a)

PbI$_2$ high-resolution corresponding selected
area electron diffraction pattern

(b)
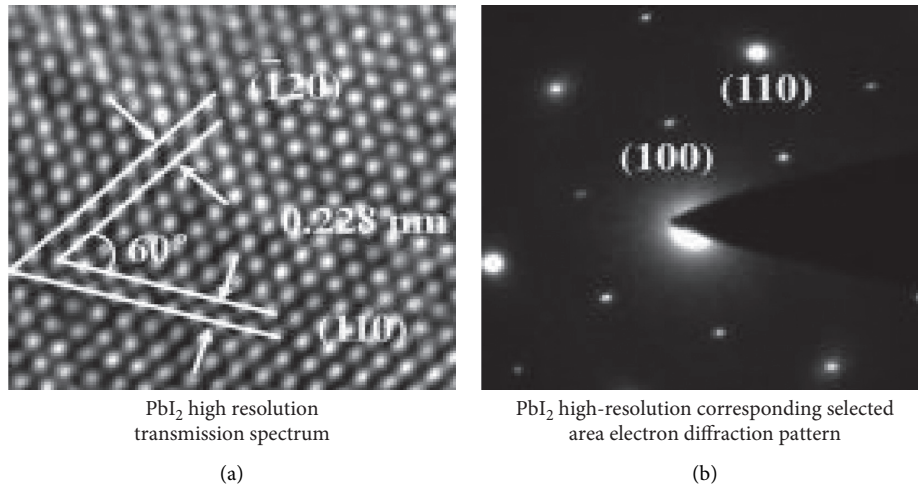
FIGURE 7: Transmission electron microscope analysis chart (https://image.baidu.com/).

TABLE 4: Optical properties data sheet.

Raman shift	Mica	5 nm	10 nm	30 nm	40 nm	80 nm	100 nm
50	2.58	2.46	2.98	2.34	2.98	2.36	2.58
75	2.73	3.17	3.53	2.73	2.83	3.43	3.04
100	2.57	2.97	2.77	2.76	2.68	2.45	2.95
125	3.95	3.21	3.5	3.85	3.58	3.51	3.79
150	2.79	2.71	2.86	3.07	3.42	3.06	2.96
175	2.66	2.84	2.78	2.63	2.66	2.87	2.97
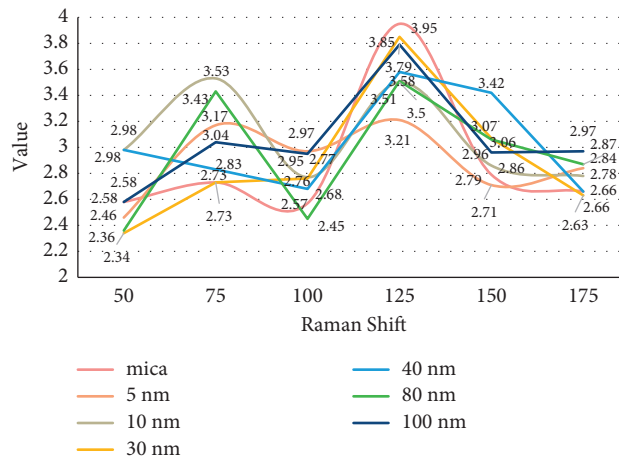
FIGURE 8: Optical property analysis chart.

TABLE 5: MAPbI$_3$ nanosheet optical performance data sheet.

Wavelength	MAPbI$_3$	PbI$_2$	Mica
550	0.1	0.3	0.5
600	0.1	0.3	0.5
650	0.1	0.3	0.5
700	0.1	0.3	0.5
750	0.4	0.6	0.8
800	1.0	1.4	2.0
850	0.4	0.6	0.8
900	0.1	0.3	0.5
950	0.1	0.3	0.5
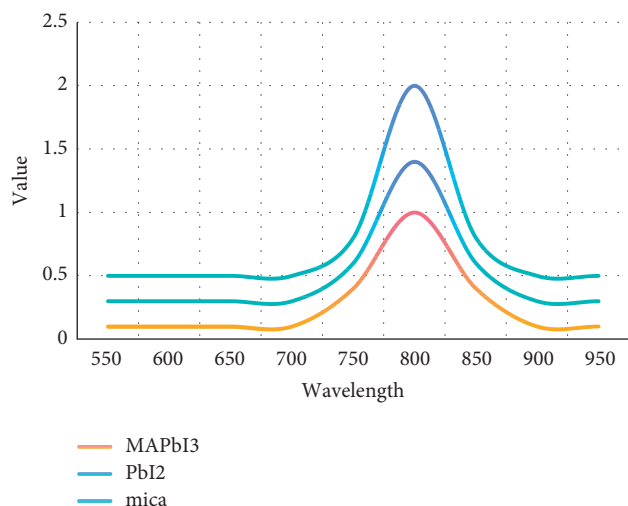
FIGURE 9: MAPbI$_3$ nanosheet optical performance analysis diagram.

nanosheets have good uniformity. MAPbI$_3$ exhibits strong light absorption characteristics when the wavelength is less than 800 nm, which also proves that MAPbI$_3$ not only has good fluorescence spectrum luminescence properties, but also has strong light absorption characteristics.

5. Conclusions

The gas phase method is an important method for preparing high-quality perovskite nanomaterials. Improving the controllability of the gas phase method and reducing the production cost are of great significance for further performance research and commercial application of the perovskite. This paper takes organic perovskite MAPbI$_3$ nanosheets as the research object, through the improvement of the gas phase method and the introduction of limited space to improve the controllability of the preparation of precursor PbI$_2$ nanosheets, then obtain uniform MAPbI$_3$ nanosheets, and further explore its growth mechanism and study its photoelectric performance. By introducing a limited space, the PbI$_2$ nanosheets with uniform and controllable morphology, size, and thickness were successfully prepared by physical vapor deposition. The confined space is the key to realize the uniform growth of PbI$_2$ nanosheets. It provides a relatively stable growth environment and avoids the dynamic instability during the growth of PbI$_2$. This confined space vapor deposition method can improve the uniformity and controllability of the preparation of PbI$_2$ and MAPbI$_3$ nanosheets, which provides a basis for further research of MAPbI$_3$ nanomaterials and also has reference significance for the controllable growth of other nanomaterials.

The introduction of chirality into the optical communication system can not only increase another new dimension of high-speed optical information transmission, but also significantly increase the information capacity. Therefore, chiral perovskite nanomaterials provide broad application prospects in this regard. This paper mainly introduces a limited space to suppress the dynamic instability during the PbI$_2$ vapor deposition process, so as to obtain high-quality PbI$_2$ nanosheets with uniform and controllable morphology and thickness. At the same time, PbI$_2$ can be converted into MAPbI$_3$ nanosheets by chemical vapor deposition, which provides a method for the uniform and controllable synthesis of two-dimensional perovskite and also provides a basis for its performance research. The current field of chiral perovskites is a brand-new research field, which is both an opportunity and a challenge. A lot of basic and applied work needs to be carried out.

This paper improves the perovskite vapor phase synthesis method, reduces the cost of preparing the vapor phase method, and obtains a uniform and controllable perovskite nanomaterial. Although we have achieved some results from the preparation of the material, there are still aspects that require further development. Although uniform and controllable PbI$_2$ and MAPbI$_3$ nanosheets were obtained with a limited space method, in-depth studies on that method and the material obtained are lacking. Movement instability during growth of nanomaterials is universal. This experiment improves the preparation of PbI$_2$ nanosheets and overcomes this phenomenon. However, the same problems that exist in the fabrication of other nanomaterials have not been explored in depth.

Data Availability

No data were used to support this study.

Conflicts of Interest

The author declares that there are no conflicts of interest regarding the publication of this article.

References

[1] S. T. Ha, R. Su, J. Xing, Q. Zhang, and Q. Xiong, "Metal halide perovskite nanomaterials: synthesis and applications," *Chemical Science*, vol. 8, no. 4, pp. 2522–2536, 2017.

[2] B. Halford, "Nanomaterials Chiral gold nanoparticles," *Chemical and Engineering News: \"news Edition\" of the American Chemical Society*, vol. 96, no. 17, pp. 10-11, 2018.

[3] M. M. Riba, C. G. Oliveras, D. B. Amabilino, and A. C. González, "Supramolecular block copolymers incorporating chiral and achiral chromophores for the bottom-up assembly of nanomaterials," *Journal of Porphyrins & Phthalocyanines*, vol. 23, no. 07n08, pp. 916–929, 2019.

[4] X. Shang, I. Song, H. Ohtsu et al., "Supramolecular nanostructures of chiral perylene diimides with amplified chirality for high-performance chiroptical sensing," *Advanced Materials*, vol. 29, no. 21, pp. 1605828.1–1605828.7, 2017.

[5] B. Han, L. Shi, X. Gao et al., "Ultra-stable silica-coated chiral Au-nanorod assemblies: core–shell nanostructures with enhanced chiroptical properties," *Nano Research*, vol. 9, no. 2, pp. 451–457, 2016.

[6] H. Kong, X. Sun, L. Yang, X. Liu, H. Yang, and R. H. Jin, "Chirality detection by Raman spectroscopy: the case of enantioselective interactions between amino acids and polymer-modified chiral silica," *Analytical Chemistry*, vol. 92, no. 21, pp. 14292–14296, 2020.

[7] S. Wang, J. Yu, J. Li, and Y. Lin, "Prevalence and imaging features of superior canal dehiscence based on HRCT," *Chinese Journal of Medical Imaging Technology*, vol. 34, no. 10, pp. 1465–1468, 2018.

[8] V. Y. Gus'kov and V. N. Maistrenko, "New chiral stationary phases: preparation, properties, and applications in gas chromatography," *Journal of Analytical Chemistry*, vol. 73, no. 10, pp. 937–945, 2018.

[9] X. Wang, B. Liu, Y. Yu et al., "Application value of chest multi-detector spiral CT in diagnosis and follow-up of corona virus disease 2019," *Chinese Journal of Medical Imaging Technology*, vol. 36, no. 3, pp. 400–404, 2020.

[10] M. C. Weidman, A. J. Goodman, and W. A. Tisdale, "Colloidal halide perovskite nanoplatelets: an exciting new class of semiconductor nanomaterials," *Chemistry of Materials: A Publication of the American Chemistry Society*, vol. 29, no. 12, pp. 5019–5030, 2017.

[11] M. Jiang, W. Guo, T. Jiao, and Q. Xu, "Metal ion substitution effect and component regulation of perovskite-type $La_{1-x} Ca_x CrO_3$ nanomaterials," *Science of Advanced Materials*, vol. 9, no. 7, pp. 1231–1235, 2017.

[12] N. A. Gibson, B. A. Koscher, A. P. Alivisatos, and S. R. Leone, "Excitation intensity dependence of photoluminescence blinking in CsPbBr3 perovskite nanocrystals," *The Journal of Physical Chemistry, C. Nanomaterials and Interfaces*, vol. 122, no. 22, pp. 12106–12113, 2018.

[13] A. S. Alsubaie, "Recent advances in bismuth ferrite nanomaterials: synthesis, characterization and application," *Journal of Chemical, Biological and Physical Sciences*, vol. 11, no. 2, pp. 101–111, 2021.

[14] M. Yamauchi, Y. Fujiwara, and S. Masuo, "Slow anion-exchange reaction of cesium lead halide perovskite nanocrystals in supramolecular gel networks," *ACS Omega*, vol. 5, no. 24, pp. 14370–14375, 2020.

[15] H. Wang, Y. Liang, L. Liu, J. Hu, P. Wu, and W. Cui, "Enriched photoelectrocatalytic degradation and photoelectric performance of BiOI photoelectrode by coupling rGO," *Applied Catalysis B Environmental*, vol. 208, pp. 22–34, 2017.

[16] B. Hu, Y. Wang, C. Hu, and X. F. Zhou, "Design, fabrication and high efficient visible-light assisted photoelectric-synergistic performance of 3-D mesoporous DSA electrodes," *Materials and Design*, vol. 91, pp. 201–210, 2016.

[17] Y. Jun, Y. Li, Z. Jia, and Z. Dong, "Enhanced photoelectric performance of composite nanostructures combining monolayer graphene and a RbAg4I5 film," *Applied Physics Letters*, vol. 110, no. 21, pp. 1–4, 2017.

[18] W. Luan, C. Zhang, L. Luo, B. Yuan, L. Jin, and Y. S. Kim, "Enhancement of the photoelectric performance in inverted bulk heterojunction solid solar cell with inorganic nanocrystals," *Applied Energy*, vol. 185, no. 2, pp. 2217–2223, 2016.

[19] H. Li and W. Gao, "Detection sensitivity calculation model and photoelectric detection performance analysis on laser light screens," *IEEE Sensors Journal*, vol. 16, no. 11, pp. 4258–4264, 2016.

[20] Y. Deng, Z. Ma, F. Ren, and G. Wang, "Improved photoelectric performance of DSSCs based on TiO2 nanorod array/ Ni-doped TiO2 compact layer composites film," *Journal of Solid State Electrochemistry*, vol. 23, no. 11, pp. 3031–3041, 2019.

[21] F. Li, G. Chen, and X. Fu, "Erratum to: comparison of effect of gear juicer and colloid mill on microstructure, polyphenols profile, and bioactivities of mulberry (morus indica L.)," *Food and Bioprocess Technology*, vol. 9, no. 7, pp. 1246–1248, 2016.

[22] Y. S. Shmaliy, S. H. Khan, S. Zhao, and O. M. Ibarra, "General unbiased FIR filter with applications to GPS-based steering of oscillator frequency," *IEEE Transactions on Control Systems Technology*, vol. 25, no. 3, pp. 1141–1148, 2017.

[23] N. Rozzani, I. S. Mohamed, and S. A. N. S. Yusuf, "Technology for Islamic microfinance's disbursement and repayment system," *International Journal of Social Economics*, vol. 43, no. 12, pp. 1271–1283, 2016.

[24] A. Abburi, M. Ali, and P. V. Moriya, "Synthesis of mesoporous silica nanoparticles from waste hexafluorosilicic acid of fertilizer industry," *Journal of Materials Research and Technology*, vol. 9, no. 4, pp. 8074–8080, 2020.

[25] K. Reals, "Industry urges improved access to aircraft cabins for the disabled," *Aviation Week & Space Technology*, vol. 180, no. 13, pp. 70-71, 2018.

Research Article

Carbon Dot Functionalized Papers for the Selective Detection of 2,4,6-Trinitrophenol in Aqueous Solutions

Wenli Peng, Li Gan, Weihan Li, and Shixiong Deng ⬤

Laboratory of Forensic Medicine & Biomedical Informatics, Chongqing Medical University, #1 Yixueyuan Road, Chongqing 400016, China

Correspondence should be addressed to Shixiong Deng; dengshixiong1963@163.com

The development of probes for the testing of the carcinogenic pollutant 2,4,6-trinitrophenol (TNP) is of great importance for environmental protection and human health. In this paper, a new rapid and sensitive fluorescence detection method based on carbon dots (CDs) was designed for the detection of TNP. The CDs were synthesized by simple pyrolysis using citric acid as raw material and characterized by various advanced techniques. The addition of TNP caused a significant turn off in the fluorescence of the CDs. The fluorescence quench intensity and TNP concentration exhibited a good linear correlation in the range of 0–$80\,\mu$M with a minimum detection limit of $0.48\,\mu$M and a related coefficient of 0.994. The analytical method was applied to the determination of trace TNP in river water and tap water with recoveries in the range of 98%–110% and relative standard deviations less than 5%. Importantly, carbon dots functionalized papers (CDFPs) were prepared using the synthesized CDs and successfully applied to the determination of TNP in aqueous solutions, demonstrating the promising application of the method.

1. Introduction

2,4,6-Trinitrophenol (TNP) is a nitroaromatic compound that is widely used in the preparation of military explosives, pharmaceuticals, matches, insecticides, leather, glass, dyes, and fireworks [1–3]. Due to its high explosive velocity and low safety factor, TNP has more intense explosive properties than the well-known TNT [4, 5]. In addition, its widespread use in several industries has led to soil and water contamination due to its high water solubility [6–9]. Furthermore, TNP is also a highly carcinogenic agent with hepatic and renal toxicity [10–12]. Once TNP enters the body, it can cause damage to the eyes, skin, respiratory system, nervous system, liver, and kidneys and even induce a series of health problems such as anemia, cyanosis, male infertility, and cancer [13–17]. Given the impact of TNP on human health, the surrounding environment, and social and public safety issues, there is an urgent need to establish a rapid and sensitive method that can be used for on-site trace TNP detection. So far, many methods applied to TNP detection such as electrochemistry [18], mass spectrometry [19],

surface-enhanced Raman spectroscopy [20], and colorimetric methods [21] have been able to meet market demand, but their application is limited by time-consuming, pretreatment processes, expensive instruments, complex operations, and low sensitivity and selectivity. In contrast, fluorescence-based detection methods are of interest because of their simplicity of operation, sensitivity, and low cost [22–25]. The common fluorescence analysis methods for TNP detection are mainly based on metal nanoclusters [26], photoluminescent polymers [27], organic frameworks [28–30], and semiconductor quantum dots doped with heavy metals [31, 32], which have low stability and environmental pollution problems. Therefore, a new fluorescent material that overcomes these limitations is needed for the rapid and sensitive detection of TNP.

Currently, carbon dots (CDs), as a novel nanomaterial, have been extensively applied in bioimaging, chemical sensors, drug delivery, and photocatalysis due to their outstanding water solubility, biocompatibility, low toxicity, and ease of synthesis [33–35]. In this study, we prepared fluorescent CDs by a simple hydrothermal route using

citric acid as a precursor. The synthesis process is shown in Scheme 1. After the addition of TNP, the fluorescence of CDs was apparently quenched because of the internal filter effect (IFE). Therefore, the detection of TNP was achieved by the fluorescence quench of synthetic CDs. In addition, the effects of pH, ionic strength, incubation time, nitro analogs, and common metal ions on the fluorescence intensity of the synthesized CDs were discussed. Using the optimized parameters, the prepared fluorescent probes were validated and succeeded in the application for the detection of TNP in tap and river water. Importantly, the carbon dot functionalized papers prepared using CDs as probes showed good selectivity and sensitivity for trace amounts of TNP in water samples, demonstrating their remarkable potential for real-time and in situ detection of environmental pollutants.

2. Experiments

2.1. Materials. 2,4,6-Trinitrophenol (TNP) was purchased from Beijing Zhongke Yingchuang Biotechnology Co. p-Nitrophenol (NP), p-nitrochlorobenzene (NC), nitrobenzene (NB), 1-chloro-2,4-dinitrobenzene (CDNB), and 1,3-dinitrobenzene (DNB) were purchased from Aladdin Co. Water samples were taken from tap water and Jialing River. All chemicals were of analytical grade and utilized directly without further purification.

2.2. Characterization. The morphological profile and particle size distribution of the CDs were assessed using an FEI Tecnai G2 F20 transmission electron microscope (TEM). Diffraction patterns of the CDs were recorded with an X-ray diffractometer (XRD) (X'Pert PRO MPD) at an accelerating voltage of 40 kV. The chemical composition of the CDs was obtained by X-ray photoelectron spectroscopy (XPS) (Thermo ESCALAB 250XI) analysis. Fourier transform infrared (FT-IR) spectroscopy was carried out using a Bruker Vertex 70 spectrometer at 4000–500 cm^{-1}. Fluorescence experiments on the prepared fluorescent CDs and mixtures of CDs with TNP were recorded on an FS5 fluorescence spectrophotometer in the wavelength range 300–600 nm. UV-Vis absorption spectra were recorded on a UV-2600 UV spectrophotometer in the wavelength range 200–600 nm. Absolute fluorescence quantum yields were determined on an Edinburgh FLS9800 (steady-state transient spectrometer). The CDs and CDs-TNP complexes were evaluated using a fluorescence lifetime system.

2.3. Preparation of CDs. 1.0507 g of citric acid was added to 10 mL of deionized water. The mixed solution was then transferred to an autoclave (30 mL) lined with Teflon and heated for 5 hours at 200°C. It was cooled to room temperature, filtered through a microporous filter (0.45 μM), and purified using a dialysis bag (MWCO = 3500) for 24 h. Finally, the resulting solution was freeze-dried under a vacuum to obtain the purified CDs.

2.4. Detection of TNP. A mixture of CDs and TNP was obtained by mixing 1 ml of CDs solution (0.2 mg/ml) with 1 ml of different concentrations of TNP (0, 1, 2, 10, 20, 40, 60, and 80 μM). The solution was kept at room temperature with shaking for 3 min. The fluorescence quenching effect of CDs was observed with a fluorescence spectrometer under 340 nm excitation.

2.5. Sample Pretreatment. Tap water and river water samples were taken locally from Chongqing. Water samples were centrifuged and filtered through 0.45 μM microporous filters.

2.6. Preparation of CDFPs. The CDFPs were prepared as described in the previous literature [36]. In brief, a wax printer was used to print a circular hole pattern on one side and wax on the other side of the chromatography paper. The wax-imprinted chromatography paper was put on a heating table and heated at 150°C for 1 min to melt the wax to form a hydrophobic layer. The prepared carbon dot solution (4 μl) was placed in each circular hole of the wax-printed paper. The excess solvent was evaporated in an oven at 50°C.

3. Results and Discussion

3.1. Synthesis and Characterization of CDs. The XRD diffraction pattern (Figure 1(a)) shows a broad peak located at $2\theta = 24.1°$, comparable to the graphite lattice spacing (002), which is consistent with previous reports, and confirms that the synthesized CDs have a similar graphene structure [37]. The morphology and dimensions of the prepared CDs were characterized by TEM, as shown in Figure 1(b). The synthesized CDs are subspherical in shape and have good dispersion in aqueous solution. Figure 1(c) shows the lattice spacing of the prepared CDs. The particle size distribution of the CDs (Figure 1(d)) shows a narrow range of diameters from 1.49 to 3.09 nm, with an average diameter of 2.2 nm. We then investigated the optical properties of the synthesized fluorescent CDs using fluorescence spectroscopy and UV absorption spectroscopy. As shown in Figure 2(a), CDs do not have a prominent absorption peak in the visible region, but there is significant absorption at 200–300 nm. The fluorescence emission spectra of CDs were obtained at 10 nm intervals at different excitation wavelengths in the range of 310–400 nm. As shown in Figure 2(b), the fluorescence spectrum is red-shifted with increasing excitation wavelength. The carbon dot shift between the emission and excitation wavelengths is 80 nm, indicating that the synthesized CDs could be used as a candidate analytical material. The fluorescence quantum yield, an important property of synthetic CDs, is calculated to be 5.9%, which is comparable to the previously reported yield of undoped quantum dots [38]. The chemical bonding and functional groups at the carbon sites were further investigated using FT-IR spectroscopy (Figure 3(a)). The broad and strong peak at 3490 cm^{-1} is attributed to the –OH stretching vibration [39]. The vibrational peak at 1724 cm^{-1} is thought to be the C=O stretching vibration [40]. The stretching peak at
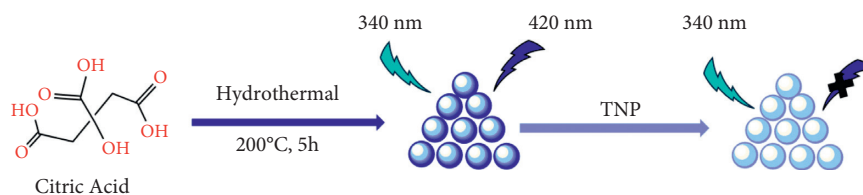
SCHEME 1: Synthesis of fluorescent CDs and detection of TNP.

(a)

(b)

(c)

(d)
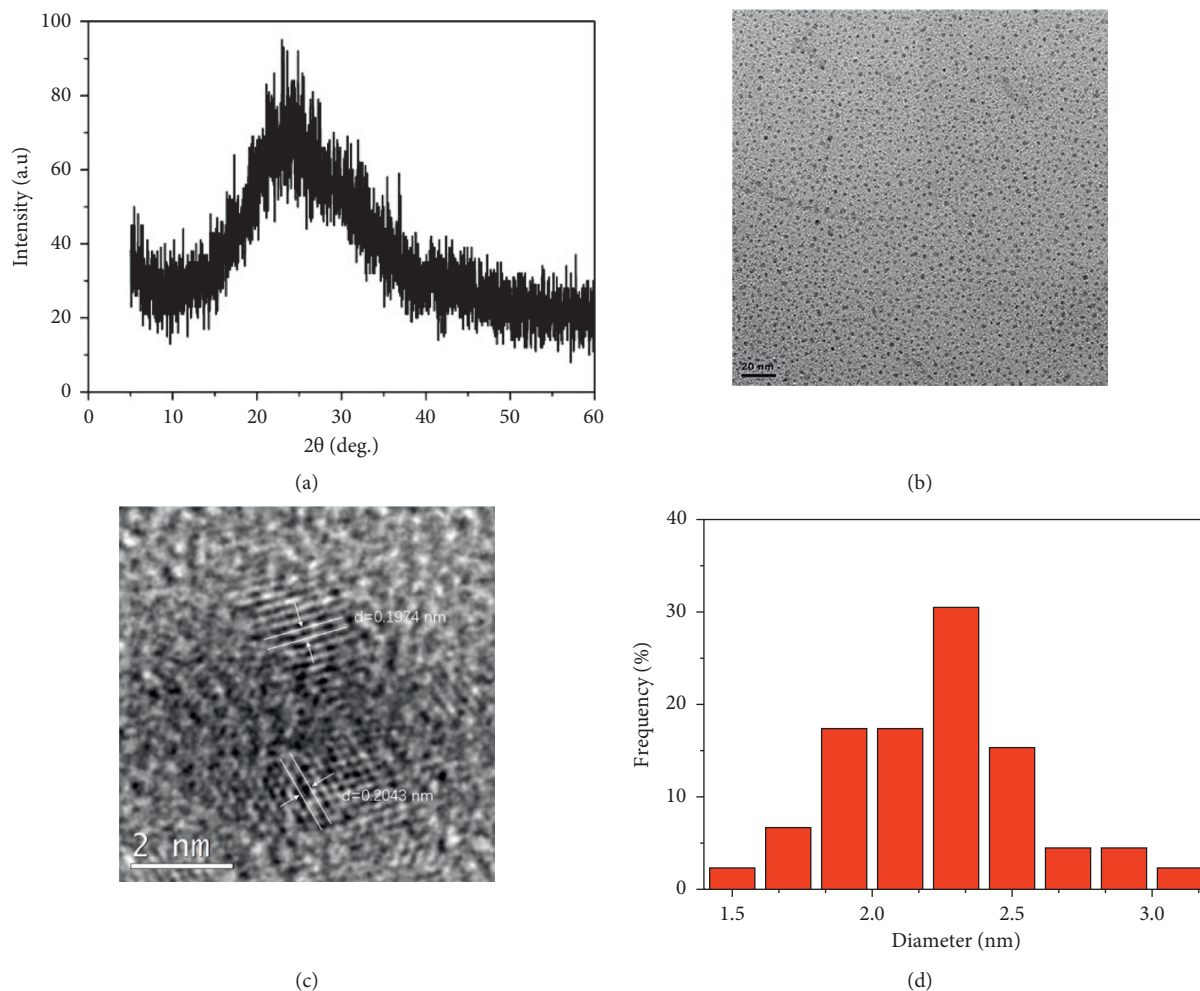
FIGURE 1: (a) XRD of CDs, TEM image (b), HR-TEM and lattice fringes image (c), and the size distribution (d) of CDs.

$1187 \, cm^{-1}$ is attributed to C-O [41]. The bands at $920 \, cm^{-1}$ and $780 \, cm^{-1}$ are identified as out-of-plane bending vibrations of the O-H bond. To further investigate the elemental composition of the CDs, they were subjected to further XPS assays. As shown in Figure 3(b), the wide scan XPS spectrum shows two peaks centered at 285.3 eV and 533.2 eV, attributed to the C 1s and O 1s signals, respectively [42]. The C 1s (Figure 3(c)) show three peaks, which correspond to C−C (284.8 eV), C-O (286.6 eV), and O=C-O (288.8 eV), respectively [43]. The O 1s peak (Figure 3(d)) can be deconvoluted into two peaks, C-O (531.7 eV) and O-C=O (532.9 eV) [44]. The peaks associated with the hydroxyl and carboxyl functional groups in the XPS analysis results are consistent with the FT-IR spectra of the CDs, favoring

solubility and stability in water. The above results indicate that the blue fluorescent probes are successfully synthesized and can be further analyzed for applications.

3.2. Parameter Optimization. Various factors such as buffer pH, ionic strength, and incubation time can affect the fluorescence intensity of CDs, so a series of experiments were carried out to optimize the parameters for the analysis of CDs. Firstly, the influence of PH on the fluorescence of CDs was studied, and the findings are illustrated in Figure 4(a). The fluorescence intensity of CDs remained relatively stable at pH 7.0–9.0. Therefore, we chose the pH 7.0 buffer for the sensitive detection of TNP. The effect of ion

(a)

Excitation wavelength
— 310 nm   — 360 nm
— 320 nm   — 370 nm
— 330 nm   — 380 nm
— 340 nm   — 390 nm
— 350 nm   — 400 nm

(b)
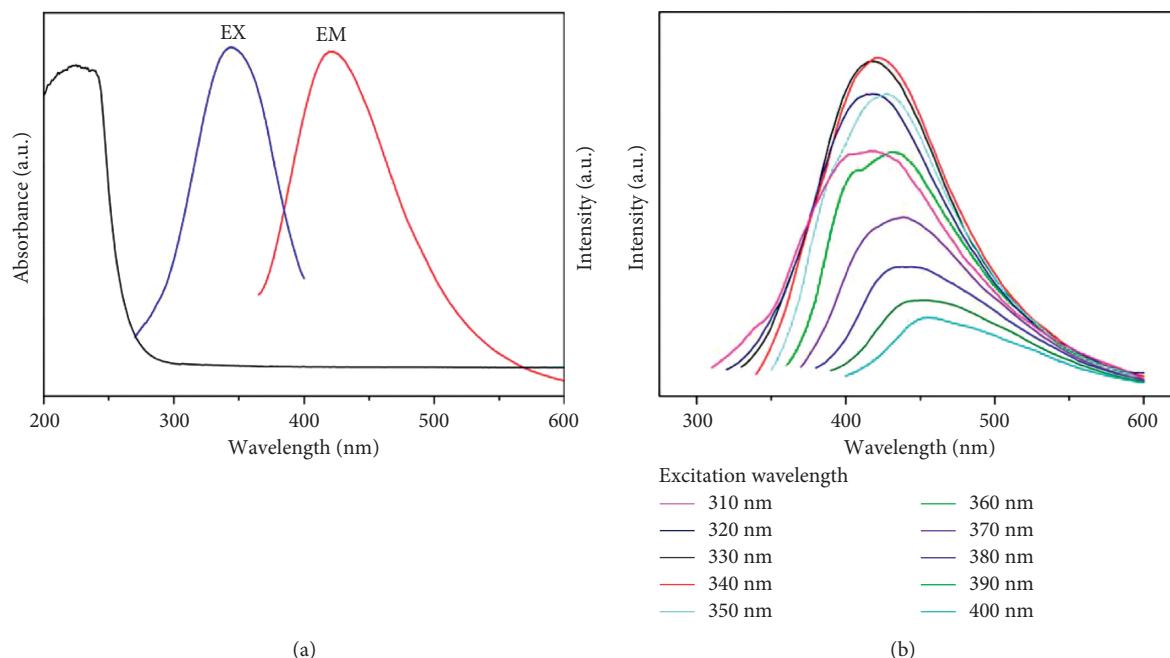
FIGURE 2: (a) UV absorption spectra and fluorescence excitation (Ex) and emission (Em) spectroscopy. (b) Fluorescence spectra of CDs at different excitation wavelengths.

concentration was then explored, as shown in Figure 4(b). The fluorescence intensity remained essentially constant at different concentrations of NaCl solution, which demonstrates that CDs can be detected at stronger ionic concentrations. In addition, the relationship between incubation time and carbon dot fluorescence was investigated to ascertain the altered kinetics of the probes. As shown in Figure 4(c), the fluorescence of the CDs was effectively burst during 7 minutes after the incorporation of $20\,\mu$M TNP, indicating that the 7-minute incubation time could be used for further analytical studies. Therefore, we chose a pH 7.0 buffer incubated for 7 minutes at room temperature for the sensitive detection of TNP.

3.3. Analysis of Performance.

The above optimized analytical parameters were adopted to detect different concentrations of TNP and to evaluate the analysis properties of the presented fluorescent probes. Figure 5(a) shows the fluorescence spectra of the fluorescent CDs at 340 nm excitation under the effect of different levels of TNP. It can be seen that the fluorescence of the CDs is gradually quenched as the concentration of TNP increased. We plotted the Stern–Volmer curve between log (I_0/I) and TNP (Figure 5(b)), where I_0 and I represent the fluorescence intensity of CDs in the absence and presence of TNP. It showed a good linear relationship between the burst of fluorescence and TNP concentration in the 0–80 μM range with a regression coefficient (R^2) of 0.994. The regression equation is log $(I_0/I) = 0.007c$ (μM) $- 0.014$. The limit of detection (LOD) was 0.48 μM ($3\sigma/k$, $n = 3$), which was calculated from the standard deviation (SD) of the response and the slope of the calibration curve (S), which is

comparable to previous studies (Table 1) in the literature. As the concentration of TNP increased, the bright blue fluorescence of the CDs-TNP mixture was gradually quenched under the UV lamp, while a change in colour could be seen in the CDs-TNP mixture, visually demonstrating the quenching phenomenon (Figure 5(c)). Therefore, our proposed analytical method has high affinity and sensitivity for the detection of trace amounts of TNP.

3.4. Study of Possible Mechanisms.

To investigate the mechanism of quenching of the prepared fluorescent probes, we investigated the optical properties of CDs and CDs-TNP complexes. In the recently published literature, three common mechanisms of fluorescence quenching include fluorescence resonance energy transfer, photoinduced electron transfer, and fluorescence internal filtration [45]. As shown in Figure 6(a), the emission spectra of CDs clearly superimpose on the absorbance spectrum of TNP, suggesting that the fluorescence quenching mechanism may be IFE or FRET [46]. As shown in Figure 6(b), the addition of TNP ($20\,\mu$M) changed the fluorescence lifetime from 2.222 ns to 2.198 ns, which showed little change in fluorescence lifetime, in agreement with previous reports [47], ruling out the possibility of a quenching mechanism for FRET and PET [48]. Therefore, the fluorescence quenching mechanism of CDs was attributed to the IFE between TNP and CDs.

3.5. Selective Detection.

An important factor in the evaluation of the prepared fluorescent probes is selectivity. It was possible to detect the selectivity of the proposed fluorescent probes by assessing the change in the fluorescence intensity

(a)

(b)

(c)

(d)
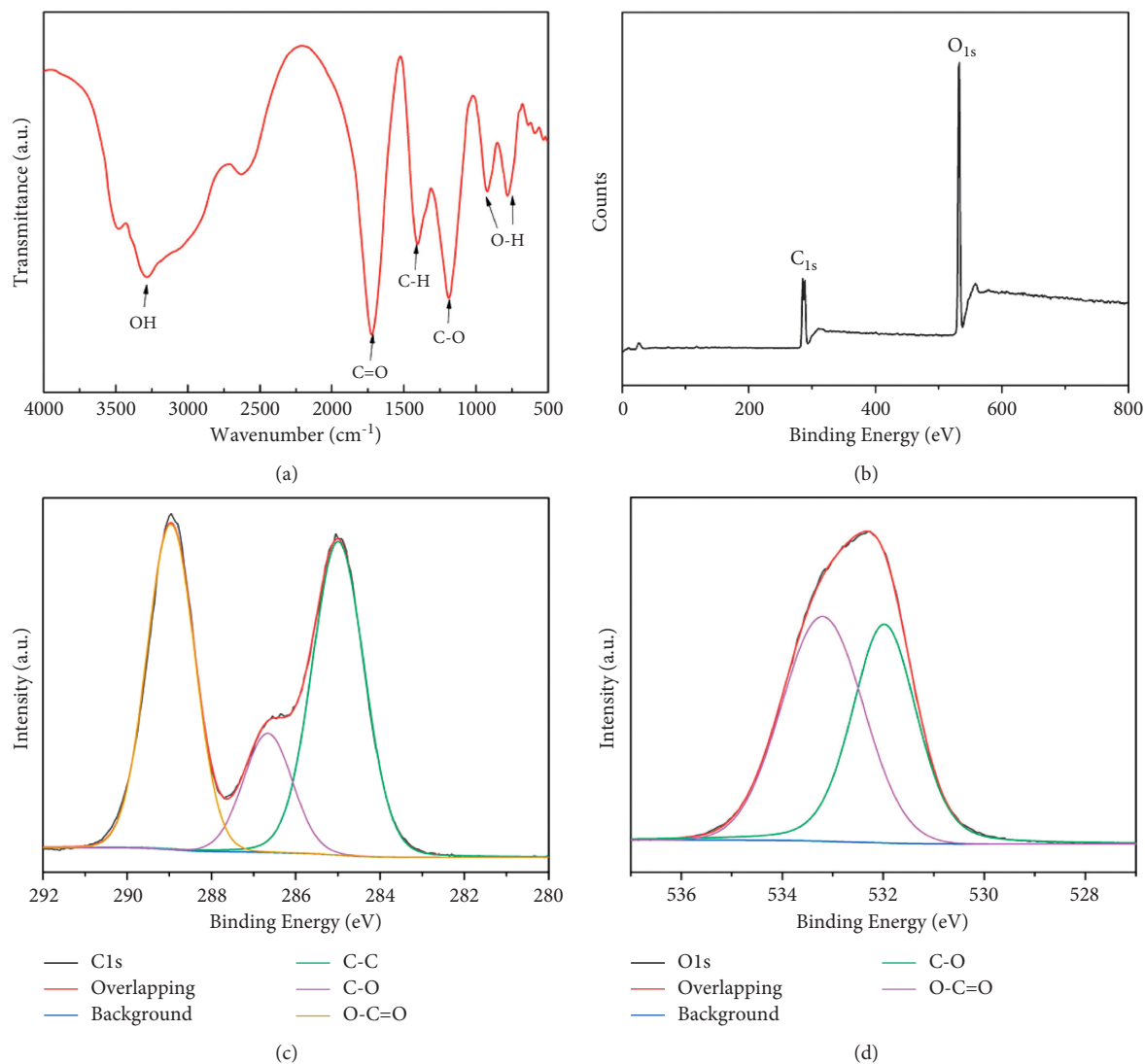
FIGURE 3: (a) FT-IR spectra of the CDs. (b) XPS survey of CDs. The high resolution of C 1s (c) and O 1s (d) spectra of the CDs.

(a)

(b)

(c)
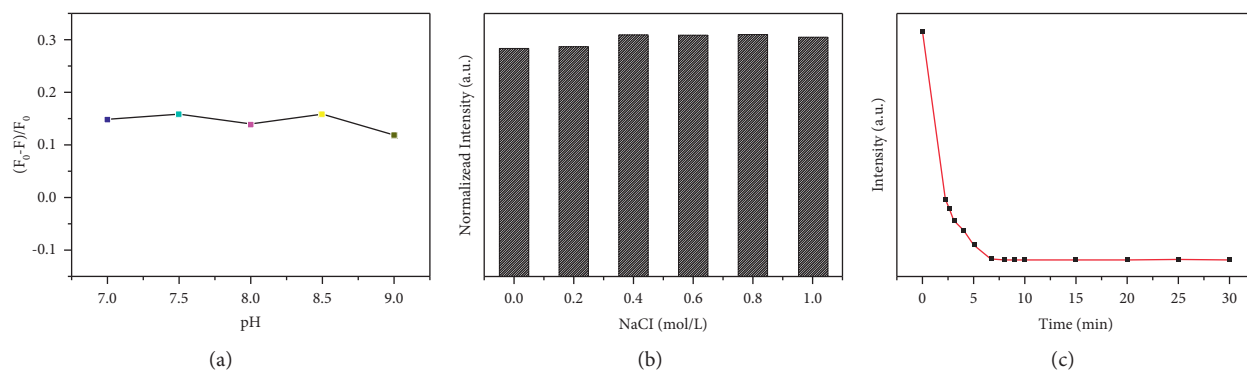
FIGURE 4: (a) Fluorescence quenching efficiency at different pH values. Normalized fluorescence intensity of CDs added to TNP at different NaCl concentrations (b) and incubation periods (c).

of the prepared CDs in the presence of TNP and other similar nitroaromatic compounds (NP, NC, NB, and CDNB). As shown in Figure 7(a), the fluorescence intensity of the CDs was significantly quenched by the addition of TNP compared to the other nitro compounds, showing the good selectivity of the prepared fluorescent probes for TNP.

(a)

(b)

(c)
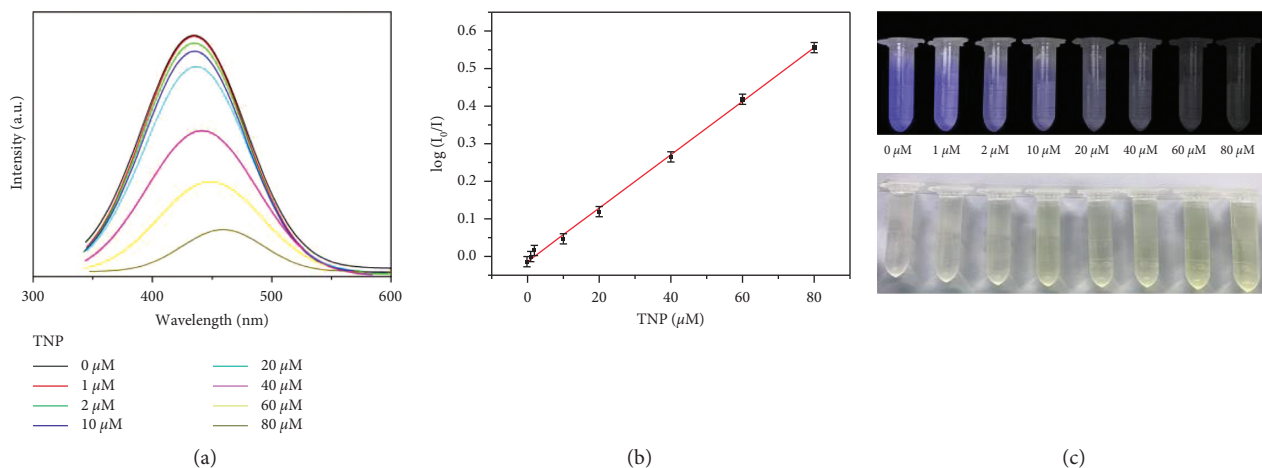
FIGURE 5: (a) Fluorescence emission spectra of CDs added with different concentrations of TNP. (b) Relationship between relative fluorescence intensity ($\log I_0/I$) (I_0 and I represent the fluorescence intensity of CDs in the absence and presence of TNP, respectively) and different concentrations of TNP. (c) Changes in fluorescence under UV light and visible to the naked eye after the addition of different concentrations of TNP.

TABLE 1: Comparison of different methods for the determination of TNP.

Material	Linear range (μM)	LOD (μM)	Reference
CQDs	1–110	1.8	[49]
N-GQDs	1–60	0.3	[50]
BNQDs	0.25–100	0.14	[51]
CDs	0–100	0.02	[52]
CDs	0.5–200	0.2	[53]
CNPs	0.5–100	0.25	[54]
CDs	0–80	0.48	Present work

(a)

(b)
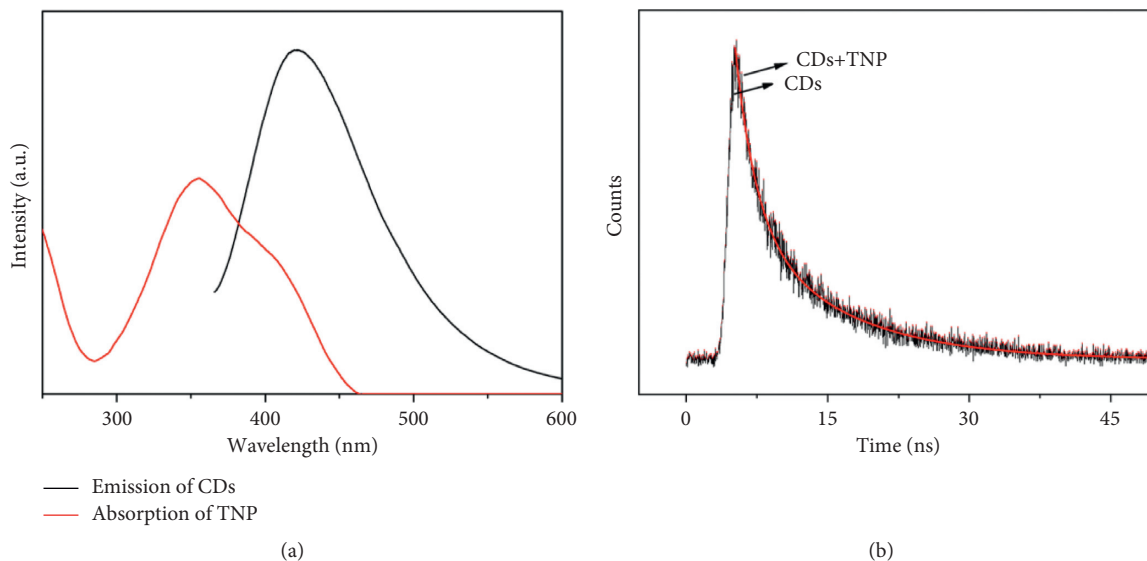
FIGURE 6: (a) The UV absorption spectrum of TNP and fluorescence spectrum of CDs. (b) The fluorescence lifetime and fitting curve of CDs.

The selective detection of TNP was also applied to common metal ions. The results are shown in Figure 7(b). The effect of metal ions is almost negligible compared to TNP, indicating that the prepared probes still have good selectivity despite the interference of metal ions.

3.6. *Assaying TNP in Real Aqueous Samples.* To test the practical application of the prepared probes, the prepared CDs were used to detect TNP in actual samples. We collected Jialing River water and tap water locally in Chongqing, and after adding different concentrations of TNP, the recoveries

(a)

(b)
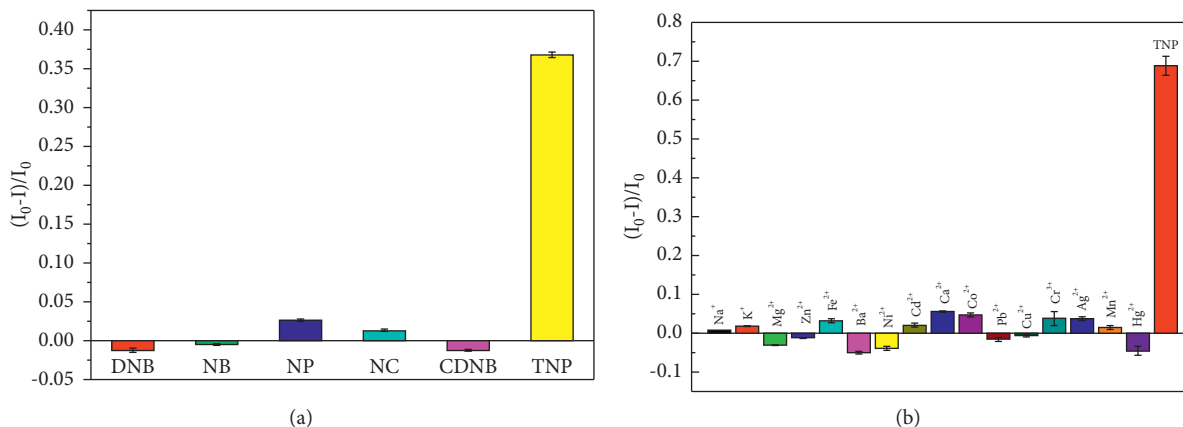
FIGURE 7: (a, b) The efficiency of fluorescence quenching of CDs in the presence of different analytes. I_0 and I represent the fluorescence intensity of CDs in the absence and presence of different analytes, respectively.

TABLE 2: Results of the recovery analysis of TNP in water samples.

Samples	Added (μmol/L)	Founded (μmol/L)	Recovery (%)	RSD ($n = 3$) (%)
Tap water	0.5	0.53	106	2.8
	1	1.03	103	2.7
	2	2.2	110	3.4
River water				
	0.5	0.49	98	2.8
	1	1.01	101	3.2
	2	2.04	102	2.6

(a)

(b)
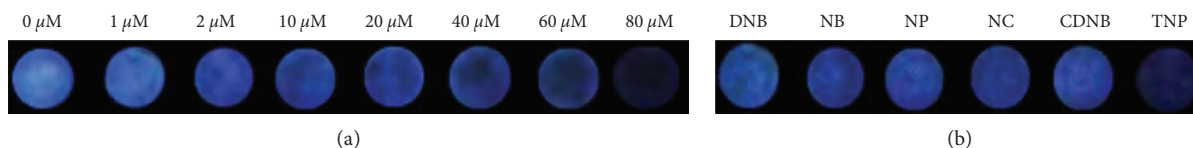
FIGURE 8: Sensitivity (a) and selectivity (b) of CDFPs to TNP detection.

were analyzed and the findings are demonstrated in Table 2, where the recoveries of the samples ranged from 98% to 110% with relative standard deviations of less than 5% for each sample for three experiments. The analytical method proved to have good accuracy and recovery. Therefore, the sensor can be implemented for the detection of real samples.

3.7. Detection of TNP by CDFPs. To demonstrate the rapid sensitivity and easy portability of CDs for TNP detection, the CDFPs were prepared by immersing filter paper in solutions of different concentrations of CDs and drying at room temperature. It was found that the functionalized paper immobilised with 400 μg/mL CDs showed the strongest fluorescence under UV light. Therefore, a carbon dot concentration of 400 μg/mL was chosen as the optimum concentration for the preparation of CDFPs. The functionalized paper immobilised with 400 μg/mL CDs was treated with different concentrations of TNP, as shown in Figure 8(a). The fluorescence intensity of the indicator paper gradually decreased as the TNP concentration increased from 0 to

80 μM, indicating a rapid and naked-eye sensitive detection of TNP. Because of the relatively low emission backdrop of the chromatography paper, we chose a portable laser lamp at 254 nm, although the photoluminescence of the CDs was stronger at 360 nm excitation. In addition, we examined common nitro analogs using the prepared carbon dot functionalized paper. The results are shown in Figure 8(b), where the fluorescence quench of TNP on CDs is visible to the naked eye under UV lamp irradiation, demonstrating its potential application in the field for the detection of TNP.

4. Conclusion

In summary, we synthesized environmentally friendly CDs using citric acid as the precursor. The prepared CDs showed excitation-dependent behavior at 310 nm–400 nm with a fluorescence QY of 5.9%. The results show that the synthesized CDs can be used as detection probes for TNP with high selectivity and sensitivity in the range of 0–80 μM TNP concentration and a detection limit of 0.48 μM. More

importantly, the CDFPs we prepared were effectively used in actual water samples, showing promising potential for field monitoring of environmental water samples.

Data Availability

The data that support the findings of this study are available from the corresponding author upon reasonable request.

Conflicts of Interest

The authors declare no conflicts of interest.

Authors' Contributions

Li Gan and Weihan Li helped to revise manuscript. Shixiong Deng revised the manuscript and coordinated the study.

Acknowledgments

References

[1] S. Lu, M. Xue, A. Tao et al., "Facile microwave-assisted synthesis of functionalized carbon nitride quantum dots as fluorescence probe for fast and highly selective detection of 2,4,6-trinitrophenol," *Journal of Fluorescence*, vol. 31, no. 1, pp. 1–9, 2021.

[2] S. Kumar, N. Venkatramaiah, and S. Patil, "Fluoranthene based derivatives for detection of trace explosive nitro-aromatics," *Journal of Physical Chemistry C*, vol. 117, no. 14, pp. 7236–7245, 2013.

[3] N. Li, S. G. Liu, Y. Z. Fan et al., "Adenosine-derived doped carbon dots: from an insight into effect of N/P co-doping on emission to highly sensitive picric acid sensing," *Analytica Chimica Acta*, vol. 1013, pp. 63–70, 2018.

[4] Y. J. Ju, N. Li, S. G. Liu et al., "Green synthesis of blue fluorescent P-doped carbon dots for the selective determination of picric acid in an aqueous medium," *Analytical Sciences*, vol. 35, no. 2, pp. 147–152, 2019.

[5] J. H. Liu, F. F. Wu, A. Xie, C. F. Liu, and H. J. Bao, "Preparation of nonconjugated fluorescent polymer nanoparticles for use as a fluorescent probe for detection of 2,4,6-trinitrophenol," *Analytical and Bioanalytical Chemistry*, vol. 412, no. 5, pp. 1235–1242, 2020.

[6] J. Wang, Y. Yang, G. Sun, M. Zheng, and Z. Xie, "A convenient and universal platform for sensing environmental nitro-aromatic explosives based on amphiphilic carbon dots," *Environmental Research*, vol. 177, Article ID 108621, 2019.

[7] V. Srinivasan, M. Asha Jhonsi, M. Kathiresan, and A. Kathiravan, "Nanostructured graphene oxide dots: synthesis, characterization, photoinduced electron transfer studies, and detection of explosives/biomolecules," *ACS Omega*, vol. 3, no. 8, pp. 9096–9104, 2018.

[8] J. Li, N. Zhang, Y. Yuan et al., "A luminescent Cd(II)-metal organic frameworks combined of TPT and H3BTC detecting 2,4,6-trinitrophenol and chromate anions in aqueous," *Spectrochimica Acta Part A: Molecular and Biomolecular Spectroscopy*, vol. 242, Article ID 118790, 2020.

[9] K. C. Remani and N. N. Binitha, "Fluorescence sensing of picric acid by ceria nanostructures prepared using fenugreek extract," *Journal of the Iranian Chemical Society*, 2021.

[10] Y. Meng, Y. Jiao, Y. Zhang et al., "Multi-sensing function integrated nitrogen-doped fluorescent carbon dots as the platform toward multi-mode detection and bioimaging," *Talanta*, vol. 210, Article ID 120653, 2020.

[11] M. Tian, Y. Wang, and Y. Zhang, "Synthesis of fluorescent nitrogen-doped carbon quantum dots for selective detection of picric acid in water samples," *Journal of Nanoscience and Nanotechnology*, vol. 18, no. 12, pp. 8111–8117, 2018.

[12] Y. Zheng, S. Wang, R. Li, L. Pan, L. Li, and Z. Qi, "Highly selective detection of nitroaromatic explosive 2,4,6-trinitrophenol (TNP) using N-doped carbon dots," *Research on Chemical Intermediates*, vol. 47, no. 6, pp. 2421–2431, 2021.

[13] B. Chen, S. Chai, J. Liu et al., "2,4,6-Trinitrophenol detection by a new portable sensing gadget using carbon dots as a fluorescent probe," *Analytical and Bioanalytical Chemistry*, vol. 411, no. 11, pp. 2291–2300, 2019.

[14] X. Wang, X. Zhang, H. Cao, and Y. Huang, "A facile and rapid approach to synthesize uric acid-capped Ti3C2 MXene quantum dots for the sensitive determination of 2,4,6-trinitrophenol both on surfaces and in solution," *Journal of Materials Chemistry B*, vol. 8, no. 47, pp. 10837–10844, 2020.

[15] Y. L. Wang, Y. L. Wan, Y. P. Zhou, Y. H. Li, and C. P. Liu, "A luminescent Zn(II)-Organic framework: selective sensing of 2,4,6-trinitrophenol and curing importance combined with ginsenoside on sepsis mice," *Journal of Cluster Science*, 2021.

[16] R. R. Gao, J. H. Wang, H. Wang, W. Dong, and J. W. Zhu, "Fluorescent nucleotide-lanthanide nanoparticles for highly selective determination of picric acid," *Microchimica Acta*, vol. 188, no. 1, p. 18, 2021.

[17] J. Liu, T. Fu, C. Liu, F. Wu, and H. Wang, "Sensitive detection of picric acid in an aqueous solution using fluorescent nonconjugated polymer dots as fluorescent probes," *Nanotechnology*, vol. 32, no. 35, Article ID 355503, 2021.

[18] J. Z. Wei, X. L. Wang, X. J. Sun et al., "Rapid and large-scale synthesis of IRMOF-3 by electrochemistry method with enhanced fluorescence detection performance for TNP," *Inorganic Chemistry*, vol. 57, no. 7, pp. 3818–3824, 2018.

[19] Y. Liu, T. L. Zhang, L. Yang, B. D. Wu, and R. Liu, "QuEChERS-ultra performance liquid chromatography-tandem mass spectrometry for determination of 2,4,6-trinitrophenol, 2,4,6-trinitroresorcinate and 2,4,6-trinitrophloroglucinol in soil," *Chinese Journal of Analytical Chemistry*, vol. 42, no. 8, pp. 1183–1188, 2014.

[20] V. Sivaprakasam and M. B. Hart, "Surface-enhanced Raman spectroscopy for environmental monitoring of aerosols," *ACS Omega*, vol. 6, no. 15, pp. 10150–10159, 2021.

[21] Y. Peng, A. J. Zhang, M. Dong, and Y. W. Wang, "A colorimetric and fluorescent chemosensor for the detection of an explosive-2,4,6-trinitrophenol (TNP)," *Chemical Communications*, vol. 47, no. 15, pp. 4505–4507, 2011.

[22] S. Dey, A. Maity, M. Shyamal et al., "An antipyrine based fluorescence "turn-on" dual sensor for Zn(2+) and Al(3+) and its selective fluorescence "turn-off" sensing towards 2,4,6-trinitrophenol (TNP) in the aggregated state," *Photochemical and Photobiological Sciences*, vol. 18, no. 11, pp. 2717–2729, 2019.

[23] S. Xiong, L. Marin, L. Duan, and X. Cheng, "Fluorescent chitosan hydrogel for highly and selectively sensing of p-nitrophenol and 2, 4, 6-trinitrophenol," *Carbohydrate Polymers*, vol. 225, Article ID 115253, 2019.

[24] S. Y. Zong, B. L. Wang, W. Y. Ma, Y. Yan, and J. Y. Li, "Carbon dots derived from coffee residue for sensitive and selective detection of picric acid and iron(III) ions," *Chemical Research in Chinese Universities*, vol. 37, no. 3, pp. 623–628, 2021.

[25] J. Liu, H. Bao, C. Liu, F. Wu, and T. Fu, ""Turn-on" fluorometric probe for hydroquinone and catechol based on an in situ reaction between protamine sulfate and dihydroxybenzene isomers and the formation of fluorescent polymer nanoparticles," *Sensors and Actuators B: Chemical*, vol. 333, Article ID 129565, 2021.

[26] S. S. Ding, C. Y. Liu, D. Y. Fu, G. Y. Shi, and A. W. Zhu, "Coordination of ligand-protected metal nanoclusters and glass nanopipettes: conversion of a liquid-phase fluorometric assay into an enhanced nanopore analysis," *Analytical Chemistry*, vol. 93, no. 3, pp. 1779–1785, 2021.

[27] M. Wang, M. J. Gao, L. L. Deng et al., "A sensitive and selective fluorescent sensor for 2,4,6-trinitrophenol detection based on the composite material of magnetic covalent organic frameworks, molecularly imprinted polymers and carbon dots," *Microchemical Journal*, vol. 154, Article ID 104590, 2020.

[28] X. Zhang, Y. Yan, F. Q. Chen, G. X. Bai, H. Xu, and S. Q. Xu, "A fluorescent titanium-based metal-organic framework sensor for nitro-aromatics detection," *Zeitschrift für Anorganische und Allgemeine Chemie*, vol. 647, no. 7, pp. 759–763, 2021.

[29] S. Z. Du, Z. Sun, L. Han, M. Qing, H. Q. Luo, and N. B. Li, "Two 3d-4f metal-organic frameworks as fluorescent sensor array for the discrimination of phosphates based on different response patterns," *Sensors and Actuators B: Chemical*, vol. 324, Article ID 128757, 2020.

[30] X. C. Chen, F. Xi, R. Liu, and J. W. Zhou, "A Eu(III)-based metal organic framework: selective sensing of picric acid and nursing application values on the cerebral edema induced by cerebral hemorrhage via reducing the coagulation factor II activity," *Journal of Fluorescence*, vol. 31, no. 2, pp. 385–392, 2021.

[31] M. Amjadi and R. Jalili, "Molecularly imprinted mesoporous silica embedded with carbon dots and semiconductor quantum dots as a ratiometric fluorescent sensor for diniconazole," *Biosensors and Bioelectronics*, vol. 96, pp. 121–126, 2017.

[32] S. Liao, F. W. Zhu, X. Y. Zhao, H. Yang, and X. Q. Chen, "A reusable P, N-doped carbon quantum dot fluorescent sensor for cobalt ion," *Sensors and Actuators B: Chemical*, vol. 260, pp. 156–164, 2018.

[33] F. F. Zhao, T. Y. Zhang, Y. Yang, and C. L. Lu, "A facile synthesis of multifunctional carbon dots as fluorescence "turn on" and "turn off" probes for selective detection of Al(3+) and 2,4,6-trinitrophenol," *Luminescence*, vol. 35, no. 8, pp. 1277–1285, 2020.

[34] A. Kathiravan, A. Gowri, V. Srinivasan, T. A. Smith, M. Ashokkumar, and M. Asha Jhonsi, "A simple and ubiquitous device for picric acid detection in latent fingerprints using carbon dots," *Analyst*, vol. 145, no. 13, pp. 4532–4539, 2020.

[35] Q. Ye, F. Yan, D. Shi et al., "N, B-doped carbon dots as a sensitive fluorescence probe for Hg(2+) ions and 2,4,6-trinitrophenol detection for bioimaging," *Journal of Photochemistry and Photobiology B*, vol. 162, pp. 1–13, 2016.

[36] Y. T. Yen, Y. S. Lin, T. Y. Chen, S. C. Chyueh, and H. T. Chang, "Carbon dots functionalized papers for high-throughput sensing of 4-chloroethcathinone and its analogues in crime sites," *Royal Society Open Science*, vol. 6, no. 9, Article ID 191017, 2019.

[37] L. Cai, Z. Fu, and F. Cui, "Synthesis of carbon dots and their application as turn off-on fluorescent sensor for mercury (II) and glutathione," *Journal of Fluorescence*, vol. 30, no. 1, pp. 11–20, 2020.

[38] H. Li, X. He, Z. Kang et al., "Water-soluble fluorescent carbon quantum dots and photocatalyst design," *Angewandte Chemie International Edition in English*, vol. 49, no. 26, pp. 4430–4434, 2010.

[39] J. Wei, J. Shen, X. Zhang et al., "Simple one-step synthesis of water-soluble fluorescent carbon dots derived from paper ash," *RSC Advances*, vol. 3, no. 32, Article ID 13119, 2013.

[40] Y. Zhao, S. Zou, D. Huo et al., "Simple and sensitive fluorescence sensor for methotrexate detection based on the inner filter effect of N, S co-doped carbon quantum dots," *Analytica Chimica Acta*, vol. 1047, pp. 179–187, 2019.

[41] J. Hou, W. Wang, T. Zhou, B. Wang, H. Li, and L. Ding, "Synthesis and formation mechanistic investigation of nitrogen-doped carbon dots with high quantum yields and yellowish-green fluorescence," *Nanoscale*, vol. 8, no. 21, pp. 11185–11193, 2016.

[42] Y. Dong, H. Pang, H. B. Yang et al., "Carbon-based dots co-doped with nitrogen and sulfur for high quantum yield and excitation-independent emission," *Angewandte Chemie International Edition in English*, vol. 52, no. 30, pp. 7800–7804, 2013.

[43] Z. Yang, M. Xu, Y. Liu et al., "Nitrogen-doped, carbon-rich, highly photoluminescent carbon dots from ammonium citrate," *Nanoscale*, vol. 6, no. 3, pp. 1890–1895, 2014.

[44] X. Chen, Q. Jin, L. Wu, C. Tung, and X. Tang, "Synthesis and unique photoluminescence properties of nitrogen-rich quantum dots and their applications," *Angewandte Chemie International Edition in English*, vol. 53, no. 46, pp. 12542–12547, 2014.

[45] Z. Liang, M. Kang, G. F. Payne, X. Wang, and R. Sun, "Probing energy and electron transfer mechanisms in fluorescence quenching of biomass carbon quantum dots," *ACS Applied Materials and Interfaces*, vol. 8, no. 27, pp. 17478–17488, 2016.

[46] Y. Z. Fan, Y. Zhang, N. Li et al., "A facile synthesis of water-soluble carbon dots as a label-free fluorescent probe for rapid, selective and sensitive detection of picric acid," *Sensors and Actuators B: Chemical*, vol. 240, pp. 949–955, 2017.

[47] Y. Ling, J. X. Li, F. Qu, N. B. Li, and H. Q. Luo, "Rapid fluorescence assay for Sudan dyes using polyethyleneimine-coated copper nanoclusters," *Microchimica Acta*, vol. 181, no. 9-10, pp. 1069–1075, 2014.

[48] M. Rong, L. Lin, X. Song et al., "A label-free fluorescence sensing approach for selective and sensitive detection of 2,4,6-trinitrophenol (TNP) in aqueous solution using graphitic carbon nitride nanosheets," *Analytical Chemistry*, vol. 87, no. 2, pp. 1288–1296, 2015.

[49] F. Cheng, X. An, C. Zheng, and S. Cao, "Green synthesis of fluorescent hydrophobic carbon quantum dots and their use for 2,4,6-trinitrophenol detection," *RSC Advances*, vol. 5, no. 113, pp. 93360–93363, 2015.

[50] L. Lin, M. Rong, S. Lu et al., "A facile synthesis of highly luminescent nitrogen-doped graphene quantum dots for the detection of 2,4,6-trinitrophenol in aqueous solution," *Nanoscale*, vol. 7, no. 5, pp. 1872–1878, 2015.

[51] D. Peng, L. Zhang, F. Li, W. R. Cui, and J. D. Qiu, "Facile and green approach to the synthesis of boron nitride quantum dots for 2,4,6-trinitrophenol sensing," *ACS Applied Materials & Interfaces*, vol. 10, no. 8, 2018.

[52] X. Deng and D. Wu, "Highly sensitive photoluminescence energy transfer detection for 2,4,6-trinitrophenol using photoluminescent carbon nanodots," *RSC Advances*, vol. 4, no. 79, pp. 42066–42070, 2014.

[53] A. B. Siddique, A. K. Pramanick, S. Chatterjee, and M. Ray, "Amorphous carbon dots and their remarkable ability to detect 2,4,6-trinitrophenol," *Entific Reports*, vol. 8, no. 1, p. 9770, 2018.

[54] X. Sun, J. He, Y. Meng et al., "Microwave-assisted ultrafast and facile synthesis of fluorescent carbon nanoparticles from a single precursor: preparation, characterization and their application for the highly selective detection of explosive picric acid," *Journal of Materials Chemistry*, vol. 4, no. 11, pp. 4161–4171, 2016.

Research Article

Pollution Characteristics and Risk Assessment of Heavy Metal Elements in Sediment in the West Lake of Hengshui Lake

Zhongqiang Zhang [iD],[1] **Shuzhen Wei,**[2] **and Jianxiao Liu**[3]

[1]*Department of Applied Chemistry, Hengshui University, Hengshui, Hebei 053000, China*
[2]*Wetland Conservation Research Center, Hengshui University, Hengshui, Hebei 053000, China*
[3]*Department of Physics, Hengshui University, Hengshui, Hebei 053000, China*

Correspondence should be addressed to Zhongqiang Zhang; zhangzhongqiang@126.com

21 sampling points were set in the West Lake of Hengshui Lake including 20 fish ponds and 1 natural pond to analyze the contents distribution of heavy metal elements including Cr, Zn, Pb, Cu, Cd, Hg, As, and Sb in sediment. The degree of heavy metal pollution was evaluated by the geoaccumulation index (I_{geo}) method. The results showed that the concentrations of Cr, Zn, Pb, Cu, Cd, and Hg at in all sampling points of the fish ponds were lower than soil risk screening values of agricultural land in soil environmental quality: risk control standard for soil contamination of agricultural land (trial) (GB 15618-2018). The concentrations of As at 5 sampling points were higher than soil risk screening values and lower than soil risk control values of agricultural land in GB 15618-2018. The concentrations of Sb were lower than soil risk screening values of construction land in soil environmental quality: risk control standard for soil contamination of development land (trial) (GB 36600-2018). The evaluation results of the geo-accumulation index method showed that the pollution degrees of Cd, Pb, and Hg were moderately contaminated in general, the pollution degree of Cu was uncontaminated to moderately contaminated in general, the pollution degrees of Cr and As were uncontaminated to moderately contaminated in some sampling points, and Zn and Sb could be regarded as uncontaminated in sediment of the fish ponds in the West Lake of Hengshui Lake. Otherwise, the average contents of other heavy metal elements in sediment of the fish ponds in the West Lake of Hengshui Lake were higher than the background value of soil in Hebei Province (BVSH) except for Zn and Sb. The average contents of seven heavy metal elements in sediment of the natural pond in the West Lake of Hengshui Lake were lower than BVSH except for Cr. The result can be regarded as no pollution in the natural pond because the values of I_{geo} were all lower than 0. The heavy metal pollution in the sediment of the West Lake of Hengshui Lake may be due to the introduction of feeding. The water environment of the West Lake of Hengshui Lake can be effectively improved by cleaning up the sediment of fish ponds and "returning fishing to wetland."

1. Introduction

The heavy metal pollution has the characteristics of strong toxicity, easy accumulation, and nondegradation, which is one of the key points in the current environmental pollution prevention and control work. The sediment in the lake usually has a strong accumulation effect on heavy metal elements because heavy metal elements in lake can be enriched in sediment through a variety of biological and physicochemical processes. The contents of the heavy metal elements in sediment in lake are often much higher than that in the water itself, which may be hundreds or even tens of thousands of times of its content in the water. The heavy metal elements in sediment may be released into water under the certain conditions. It may lead to the secondary pollution of water body [1–5]. The polluted condition of sediment is one of the important factors to evaluate the quality of lake water environment [6, 7]. So, it is great significance to study the endogenous pollution release of heavy metal in lake water environment through the characteristics, and risk of heavy metal pollution was assessed in lake sediment.

Hengshui Lake is located in Hengshui City, Hebei Province, with an area of about 75 km^2. It is a typical inland fresh water lake. It is the main source of drinking water and industrial and agricultural production in Hengshui City and its surrounding areas. It is also a gathering place of animals and plants in the north temperate zone and a transit place for rare and endangered migratory birds. The maximum storage capacity is 188 million m^3. It is the first National Wetland Nature Reserve in North China Plain.

Hengshui Lake is divided into East Lake and West Lake. The West Lake covers an area of about 32.5 km^2, with scattered water surface including many fish ponds and a natural pond. Due to historical reasons, there is a risk of heavy metal enrichment in sediment. In recent years, there have been studies on the pollution characteristics and ecological risk of heavy metal elements in the sediment of Hengshui Lake [8–11] and mainly focusing on the East Lake, while the study on the West Lake of Hengshui Lake has not been reported. In this study, the sediment of the West Lake of Hengshui Lake has been sampled and analyzed, and heavy metal pollution in sediment has been evaluated by using the geoaccumulation index (I_{geo}) method, so as to provide scientific basis for the effective control of heavy metal pollution, ecological environment protection, and risk management and control of Hengshui Lake.

2. Materials and Methods

2.1. Sampling Point Setting.
The water area of the West Lake of Hengshui Lake is relatively scattered, and the distribution is uneven including many fish ponds and a natural pond. Therefore, according to the geographical location of the West Lake of Hengshui Lake, 21 sampling points had been set up in the West Lake of Hengshui Lake, including 20 fish ponds and 1 natural pond. The study area is located at longitude 115.5511726–115.580819°E and latitude 37.56 968–37.637332°N.

2.2. Sample Collection and Analysis.
According to the field investigation of the sediment and the disturbance in the West Lake of Hengshui Lake, 21 sampling points were selected in the West Lake of Hengshui Lake. The water depth of the sampling points is 1–5 M. The TC-600 the grab dredger was used to collect the sediment samples with the depth of 0–50 cm, the sampling area was 50×50 cm^2, and the sampling points were located by GPS, July 15–17, 2019. The sediment volume of each sampling point was about 1-2 L. The collected sediment samples were sealed and stored in polyethylene plastic bags and transported back to the laboratory for low temperature storage.

The sediment samples were air-dried. The dried sediment samples were homogenized with an agate mortar and sieved in a 0.5 mm mesh nylon sieve to obtain a fine homogeneous powder in the laboratory. Then, the samples were dried in an oven at 105°C to constant weight for the experiment.

The sediment samples were digested by a microwave digester (Model Mars6, CEM, U.S.A). The contents of Cr,

Zn, Pb, Cu, Cd, and Sb were determined by the atomic absorption spectrometry (Model TAS-990, Beijing Puxi General Instrument Co., Ltd., China), and the contents of Hg and As were determined by the atomic fluorescence spectrometry (Model SA7/5, Beijing Puxi General Instrument Co., Ltd., China).

2.3. Data Processing and Assessment Methods.
In 1969, German scholar Mulr proposed the geoaccumulation index (I_{geo}) method [12], which was widely used to evaluate heavy metal pollution in water and sediment. Therefore, the geoaccumulation index method has been used to evaluate the heavy metal pollution degree of the West Lake of Hengshui Lake in this study.

The calculation formula of the geoaccumulation index method is expressed as

$$I_{geo} = \log\left(\frac{C_i}{kB_i}\right), \tag{1}$$

where C_i is the content of the element i in sediment (unit: mg/kg), and B_i is the geochemical background value of the element i. In this study, the background value of soil heavy metal elements content in Hebei Province (BVSH) [13] was used as the reference value. Coefficient k is the rectification coefficient due to the difference of the regional background value, generally 1.5. According to the value of I_{geo}, the heavy metal pollution degrees are divided into 7 classes (Table 1).

2.4. Statistical Analysis.
The experimental data were processed by Excel software and were plotted by ArcGIS 10.3 software.

3. Results and Discussion

3.1. Distribution Characteristics of Heavy Metal Elements in the Sediment of the West Lake of Hengshui Lake.
The contents of heavy metal elements in the sediment of the West Lake of Hengshui Lake are given in Table 2. Based on the background value of the soil heavy metal elements content in Hebei Province (BVSH), the pollution of eight heavy metal elements in the sediment of the West Lake of Hengshui Lake was evaluated. In natural ponds, the contents of the other seven heavy metal elements were all lower than BVSH except for Cr.

In the fish ponds sediment, only the average contents of Zn and Sb were lower than BVSH. In all sampling points, the contents of Sb were all lower than BVSH, while the contents of Zn were slightly higher than BVSH at 7 sampling points. The contents of Cr, Pb, Cu, Cd, Hg, and As were higher than BVSH. The average contents of Cd, Hg, and Pb were 2.37, 2.24, and 2.00 times of BVHB, respectively. It indicated that the pollution of Cd, Hg, and Pb in the sediment of fish ponds in the West Lake of Hengshui Lake was relatively serious. The average contents of Cu, Cr, and As were 1.72, 1.47, and 1.47 times of BVSH, respectively. It indicated that there was slight pollution of Cu, Cr, and As in the sediment of fish ponds in the West Lake of Hengshui Lake.

TABLE 1: I_{geo} and classification of sediment pollution degree.

I_{geo}	≦0	0~1	1~2	2~3	3~4	4~5	>5
Class	0	1	2	3	4	5	6
Pollution degree	Uncontaminated	Uncontaminated to moderately contaminated	Moderately contaminated	Moderately to heavily contaminated	Heavily contaminated	Heavily to extremely contaminated	Extremely contaminated

TABLE 2: Contents of heavy metal elements in the sediment at various sampling points in the West Lake of Hengshui Lake (mg/kg).

Sampling point	Longitude (°E)	Latitude (°N)	Cr	Zn	Pb	Cu	Cd	Hg	As	Sb
1	115.57972	37.637332	110.8	81.4	45.9	39.5	0.22	0.067	20.8	0.19
2	115.580235	37.632706	96.3	64.2	38.6	44.7	0.13	0.092	16.4	0.08
3	115.580819	37.625911	128.6	82.3	58.9	63.1	0.37	0.112	23.2	0.13
4	115.577401	37.615455	74.7	53.8	25.6	36.5	0.19	0.043	14.4	0.07
5	115.578115	37.613281	86.4	62.7	45.1	29.9	0.13	0.051	13.8	0.11
6	115.577711	37.61342	71.3	58.5	31.6	40.3	0.17	0.038	15.3	0.09
7	115.576741	37.613887	88.6	71.5	28.9	31.3	0.16	0.042	14.9	0.15
8	115.57612	37.613968	94.2	58.7	37.6	48.8	0.18	0.097	18.1	0.12
9	115.57448	37.614382	102.1	79.5	50.8	39.6	0.15	0.093	22.6	0.16
10	115.572681	37.608833	79.4	51.3	29.8	31.2	0.11	0.082	16.2	0.06
11	115.570792	37.614233	81.5	69.6	38.7	34.1	0.22	0.098	15.5	0.09
12	115.575772	37.608444	86.3	75.2	26.5	22.3	0.14	0.049	13.9	0.05
13	115.575105	37.609114	78.6	79.7	31.4	32.8	0.18	0.055	14.8	0.07
14	115.569049	37.607871	139.7	79.5	68.3	59.5	0.35	0.151	28.3	0.31
15	115.5511726	37.56968	162.6	95.8	76.4	53.1	0.48	0.134	30.4	0.26
16	115.573043	37.596982	103.6	62.1	38.6	23.3	0.29	0.081	17.4	0.12
17	115.570848	37.592124	115.9	76.4	53.4	31.4	0.32	0.126	25.8	0.14
18	115.570396	37.591182	97.1	63.2	50.8	29.6	0.21	0.064	30.7	0.11
19	115.569973	37.587342	127.5	87.6	46.1	33.2	0.34	0.087	28.2	0.35
20	115.571514	37.577032	89.3	58.4	35.7	23.8	0.12	0.054	19.7	0.09
Average			100.725	70.570	42.935	37.400	0.223	0.081	20.020	0.138
Natural pond	115.578324	37.615915	61.9	67.3	18.6	16.7	0.13	0.029	8.2	0.07
The background value of the soil in Hebei Province			68.3	78.4	21.5	21.8	0.094	0.036	13.6	1.22

The results showed that the contents of Cr, Zn, Pd, Cu, Cd, and Hg were 71.3–162.6 mg/kg, 51.3–95.8 mg/kg, 25.6–76.4 mg/kg, 22.3–63.1 mg/kg, 0.11–0.48 mg/kg, and 0.038–0.151 mg/kg in the sediment of fish ponds in the West Lake of Hengshui Lake, respectively. The contents of all sampling points were lower than the screening values of soil pollution risk of agricultural land in soil environmental quality: risk control standard for soil contamination of agricultural land (trial) (GB 15618-2018)[14].

The contents of As were 13.8–30.7 mg/kg, and the 14th, 15th, 17th, 18th, and 19th sampling points were higher than the screening value of soil pollution risk, but lower than the risk control value in GB 15618-2018.

The contents of Sb were 0.05–0.35 mg/kg. Since there are no relevant contents standard of Sb in GB 15618-2018, the contents of Sb were analyzed in soil environmental quality: risk control standard for soil contamination of development land (trial) (GB 36600-2018) [15]. The content of each sampling point was lower than the screening value of soil pollution risk of development land in GB 36600-2018.

3.2. Pollution Assessment by the Geoaccumulation Index (I_{geo}).
The results of I_{geo} of heavy metal elements in the sediment of the West Lake of Hengshui Lake are given in Table 3. It showed that I_{geo} of eight heavy metal elements in natural pond was all less than 0, which can be regarded as uncontaminated in natural pond.

In the fish ponds sediment, the I_{geo} values of Zn and Sb in all sampling points were less than 0, as given in Table 3, which could be regarded as uncontaminated. The areas with higher I_{geo} values of Zn and Sb concentrated in the south of the West Lake of Hengshui Lake, as shown in Figure 1 (the black spots are fish ponds, and the black regular triangular is natural pond), are adjacent to Jizhou District of Hengshui City. The higher contents of Zn and Sb may be related to high population density and more social activities of human beings.

The average values of I_{geo} about Cr, Zn, As, and Sb were less than 0 in all sampling points of the fish ponds. The average I_{geo} value of Cr was −0.0594. But the I_{geo} values of seven sampling points were higher than 0, and the I_{geo} values

TABLE 3: I_{geo} of heavy metal elements elements in the sediment at various sampling points in the West Lake of Hengshui Lake.

Sampling point	Cr	Zn	Pb	Cu	Cd	Hg	As	Sb
1	0.113037897	−0.530787361	0.509194993	0.272562018	0.641808361	0.311201688	0.028014376	−3.267772325
2	−0.089312281	−0.873242858	0.259301687	0.450984196	−0.117183539	0.768674454	−0.314873337	−4.515699838
3	0.327970658	−0.514923724	0.868968474	0.948349369	1.391830108	1.05246742	0.185555653	−3.81526012
4	−0.455739836	−1.128209982	−0.33315535	0.158605828	0.430304256	−0.328622747	−0.502500341	−4.708344916
5	−0.245816767	−0.907350712	0.483828273	−0.129145151	−0.117183539	−0.08246216	−0.563900885	−4.05626822
6	−0.522946003	−1.00737953	−0.029374602	0.301489203	0.269839584	−0.506959989	−0.415037499	−4.345774837
7	−0.20954138	−0.717872913	−0.158229668	−0.063127979	0.182376742	−0.362570079	−0.453256822	−3.608809243
8	−0.121121019	−1.002455652	0.221433501	0.577590512	0.352301744	0.84502534	−0.172579455	−3.930737338
9	−0.004937118	−0.564861295	0.655529336	0.276209795	0.089267338	0.784271309	0.14775362	−3.515699838
10	−0.367709072	−1.196857329	−0.11398683	−0.067744607	−0.358191639	0.602664502	−0.332575339	−4.930737338
11	−0.33004802	−0.756728849	0.263034406	0.060481104	0.641808361	0.859822342	−0.396300937	−4.345774837
12	−0.24748752	−0.645083493	−0.283306801	−0.552246926	−0.010268335	−0.140177658	−0.553484269	−5.193771743
13	−0.382318767	−0.561236431	−0.038534601	0.004405179	0.352301744	0.026472211	−0.462971976	−4.708344916
14	0.447412036	−0.564861295	1.082586418	0.863599033	1.311659759	1.483517237	0.472232901	−2.561503528
15	0.666407273	−0.295790499	1.244273478	0.699421225	1.767339243	1.311201688	0.575502171	−2.81526012
16	0.016104019	−0.921222887	0.259301687	−0.488960681	1.040357738	0.584962501	−0.229481846	−3.930737338
17	0.177960582	−0.622243517	0.727540581	−0.058526077	1.182376742	1.222392421	0.338801913	−3.708344916
18	−0.077376784	−0.895891597	0.655529336	−0.14369346	0.574694165	0.245112498	0.589669503	−4.05626822
19	0.315577263	−0.424885285	0.51546759	0.021892606	1.269839584	0.688055994	0.46712601	−2.386416821
20	−0.198187904	−1.009847786	0.146624914	−0.458329062	−0.232660757	$3.20343E − 16$	−0.050373523	−4.345774837
Average	−0.059403637	−0.75708665	0.346801341	0.133690806	0.533130883	0.468252449	−0.082134004	−3.937365064
Natural pond	−0.218821314	−0.242392258	−0.239016775	−0.291831282	−0.03527576	−0.269995762	−0.395816315	−1.41735305
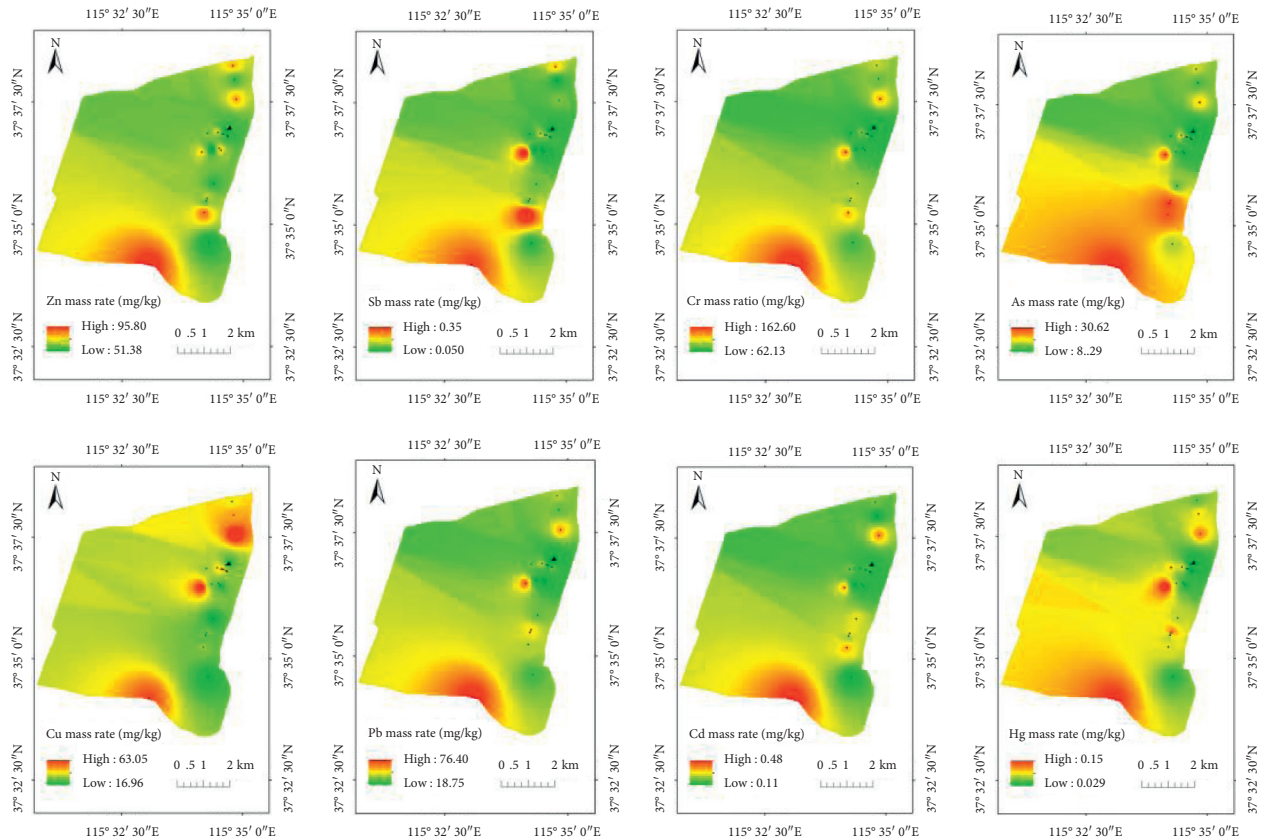
FIGURE 1: Spatial distribution of contents of 8 kinds of heavy metal elements in sediment at 0–50 cm depth in the West Lake of Hengshui Lake.

of Cr were 0.0161–0.66641, so the pollution class was 1. It indicated that the seven sampling points were uncontaminated to moderately contaminated by Cr.

The average I_{geo} values of As was −0.0821 in the fish ponds. But the I_{geo} values of 8 sampling points were higher than 0, and the I_{geo} values of As were 0.02801–0.58067, so the pollution class was 1. It indicated that the eight sampling points were uncontaminated to moderately contaminated by As. Similarly, the areas with higher I_{geo} values of Cr and As also concentrated in the south of the West Lake of Hengshui Lake, that is, the higher contents of Cr and As may be related to high population density and more human social activities too.

The average I_{geo} values of Pb, Cu, Cd, and Hg were higher than 0 in the fish ponds. The average I_{geo} value of Pb was 0.3468. The I_{geo} values of six sampling points were less than 0, and the I_{geo} values of other sampling points were 0.14662–1.24427. The I_{geo} values of the 14th and 15th sampling points were higher than 1, so the pollution class was 2. It indicated that the two sampling points were moderately contaminated by Pb. The I_{geo} values of the other 12 sampling points were 0-1, and the pollution class was 1. It indicated that the twelve sampling points were uncontaminated to moderately contaminated by Pb. Therefore, the pollution degree of Pb was moderately contaminated in general in the fish ponds. The areas with a higher I_{geo} value of Pb also concentrated in the south of the West Lake of Hengshui Lake, which means that the higher content of Pb was also related to the high population density and more human social activities.

The average I_{geo} value of Cu was 0.13369 in the fish ponds. The I_{geo} values of 8 sampling points were less than 0, and the other sampling points were 0.00441–0.94835. The I_{geo} values of these 12 sampling points were 0-1, and the pollution class was 1. It indicated that the twelve sampling points were slightly polluted. So, the pollution degree of Cu was uncontaminated to moderately contaminated in general in the fish ponds. The areas with a high I_{geo} value of Cu were scattered. The highest I_{geo} value was in the northeast corner of the West Lake. It is the junction of Hengshui City and the East Lake and the West Lake of Hengshui Lake, where the traffic flow is large and the population is concentrated. Therefore, it may be related to more human social activities and automobile exhaust.

The average I_{geo} value of Cd was 0.53313 in the fish ponds. The I_{geo} values of 5 sampling points were less than 0. The other sampling points were 0.08927–1.76734. The I_{geo} values of the 3th, 14th, 15th, 16th, 17th, and 19th sampling points were higher than 1, and the pollution class was 2. It indicated that the six sampling points were moderately contaminated. The I_{geo} values of the other 9 sampling points were 0-1, and the pollution class was 1. It indicated that the nine sampling points were uncontaminated to moderately contaminated. Therefore, the pollution degree of Cd was moderately contaminated in general in the fish ponds. The areas with a high I_{geo} value of Cd still concentrated in the south of the West Lake of Hengshui Lake, that is, the high contents of Cd were also related to the high population density and more human social activities.

The average I_{geo} value of Hg was 0.46825 in the fish ponds, and the I_{geo} values of 5 sampling points were less than 0. The I_{geo} values of other sampling points were 3.2×10^{-16}–1.48352. The I_{geo} values of the 3th, 14th, 15th, and 17th sampling points were higher than 1, and the pollution class was 2. It indicated that the four sampling points were moderately contaminated. The I_{geo} values of the other 11 sampling points were 0-1, and the pollution class was 1. It indicated that the eleven sampling points were uncontaminated to moderately contaminated. Therefore, the pollution degree of Hg was moderately contaminated in general in the fish ponds. The areas with a high I_{geo} value of Hg were scattered, mainly concentrated in the high-population density areas such as villages and around the city. So, it was also related to more human social activities.

4. Conclusion

(1) In natural ponds, the contents of the other seven heavy metal elements were all lower than BVSH except for Cr, and the contents of eight heavy metal elements were all lower than the soil risk screening value of agricultural land in GB 15618-2018 or the soil pollution risk screening value of development land in GB 36600-2018.

(2) The average contents of Cr, Zn, Pb, Cu, Hg, and As were higher than BVSH except for Zn and Sb in sediment of the fish ponds at various sampling points in the West Lake of Hengshui Lake. It showed a small amount of heavy metal elements pollutants.

In the fish ponds, the contents of Cr, Zn, Pb, Cu, Cd, and Hg were all lower than the standard of the soil risk screening value of agricultural land in GB 15618-2018. The contents of As in the sediment samples were 8.2–30.7 mg/kg. The contents of As in 5 sampling sites were higher than the screening value of soil pollution risk of agricultural land, but lower than the risk control value in GB 15618-2018. The contents of Sb were 0.05–0.35 mg/kg, which was lower than the screening value of soil pollution risk of development land in GB 36600-2018.

(3) The results of I_{geo} pollution assessment showed that the sediment samples of the fish ponds in the West Lake of Hengshui Lake were mainly polluted by Cr, Pb, Cu, Cd, Hg, and As. And the pollution degrees of Cd, Pb, and Hg were moderately contaminated in general, the pollution degree of Cu was uncontaminated to moderately contaminated in general, and the pollution degree of Cr and As was uncontaminated to moderately contaminated in some sampling sites. While in the sediment of natural ponds, the I_{geo} values of Cr, Zn, Pb, Cu, Cd, Hg, As, and Sb were −1.41735305 to −0.03527576, which could be regarded as uncontaminated.

The heavy metal pollution in the sediment of the West Lake of Hengshui Lake mainly concentrated in the southern edge area, which is close to Jizhou District of Hengshui City. It may be related to the high population density and more

human social activities. Therefore, it is necessary to strengthen the discharge control of heavy metal pollutants, the treatment of heavy metal pollutants in sediment, and the long-term monitor of heavy metal pollutants in the sediment. In addition, the analysis showed that the heavy metal pollution in the sediment of the West Lake of Hengshui Lake was mainly concentrated in the fish ponds. There was no heavy metal pollution in the natural pond. So, heavy metal pollution in the fish ponds may be due to the introduction of feeding [16, 17]. Therefore, the water environment of the West Lake of Hengshui Lake can be effectively improved by cleaning the sediment of fish ponds and "returning fishing to wetland." In the future, several aspects of research should be reinforced, such as the correlation study in the heavy metal pollution in between the West Lake of Hengshui Lake and the surrounding environment, the association of heavy metal pollution between sediment and water in the West Lake of Hengshui Lake, and the comparison of heavy metal pollution between East Lake and West Lake in Hengshui Lake. In addition, the emphasis should be placed on the detection of heavy metal content in sediment, water, and surrounding soil in the Hengshui Lake region.

Data Availability

The data used to support the findings of this study are available from the corresponding author upon request.

Conflicts of Interest

The authors declare that they have no conflicts of interest.

Acknowledgments

References

[1] J. Guo, L. Q. Li, D. Z. Huang et al., "Assessment of heavy metal pollution in surface water and sediment of Dongting Lake," *Research of Environmental Sciences*, vol. 29, no. 1, pp. 44–51, 2016.

[2] L. El Bilali, P. E. Rasmussen, G. E. M. Hall, and D. Fortin, "Role of sediment composition in trace metal distribution in lake sediments," *Applied Geochemistry*, vol. 17, no. 9, pp. 1171–1181, 2002.

[3] J. J. Rothwell, M. G. Evans, and T. E. H. Allott, "Sediment-water interactions in an eroded and heavy metal contaminated peatland catchment, Southern Pennines, UK. Water," *Air and Soil Pollution: Focus*, vol. 6, no. 5/6, pp. 669–676, 2006.

[4] L. I. Min, H. Chen, Z. Sun, and M. A. Gouwei, "Electrokinetic combination remediation of sediment contaminated with complex heavy metals," *Chinese Journal of Environmental Engineering*, vol. 15, no. 5, pp. 1652–1661, 2021.

[5] D.-R. ai, T. Zhang, J.-S. Bao et al., "Pollution distribution and ecological risk assessment of heavy metals in river sediments from the ancient town of suzhou," *Environmental Sciences*, vol. 42, no. 7, pp. 3206–3214, 2021.

[6] Z. C. Xu, X. Y. Yang, Y. Wen, G.-H. Chen, and J.-D. Fang, "Evaluation of the heavy metals contamination and its potential ecological risk of the sediments in Beijiang River's upper and middle reaches," *Environmental Sciences*, vol. 30, no. 11, pp. 3262–3268, 2009.

[7] S. N. Sin, H. Chua, W. Lo, and L. M Ng, "Assessment of heavy metal cations in sediments of Shing Mun River, Hong Kong," *Environment International*, vol. 26, no. 5, pp. 297–301, 2001.

[8] N. Wang, *Distribution and Seasonal Variability of Mercury in Environment-Medium and Phragmites Australis in Hengshuihu Wetland*, China Academy of Forestry Sciences, Beijing, China, 2016.

[9] H. N. Wang, M. Y. Zhang, Z. L. Guo, D. A. Wang, and W. W. Liu, "Distribution of contents of 7 kinds of heavy metal elements in the sediments of Hengshui Lake and their ecological risk assessment," *Wetland science*, vol. 18, no. 2, pp. 191–199, 2020.

[10] L. Liu, J. W. Zhang, F. F. Chen, S. Sheng, Z. Q. Tian, and J. Wang, "Pollution characteristics and ecological risk assessment of heavy metals in sediment of Hengshui Lake," *Journal of Environmental Engineering Technology*, vol. 10, no. 2, pp. 205–211, 2020.

[11] M. Zhang, L. Cui, L. Sheng, and Y.-F. Fang, "Pollution and ecological risk assessment of heavy metals in the Hengshuihu Wetland," *Wetland science*, vol. 5, no. 4, pp. 362–369, 2007.

[12] G. Muller, "Index of geoaccumulation in sediments of the rhine river," *GeoJounal*, vol. 2, no. 3, pp. 109–118, 1969.

[13] China environmental monitoring station, *Background Values of Soil Elements in China*, pp. 330–380, China Environmental Science Press, Beijing, China, 1990.

[14] Ministry of ecological environment, *Soil Environmental Quality: Risk Control Standard for Soil Contamination Agricultural Land (Trial): GB 15618-2018*, China Environment Press, Beijing, China, 2018.

[15] Ministry of ecological environment, *Soil Environmental Quality: Standard for Soil Pollution Risk Control of Construction Land (Trial): GB 36600-2018*, China Environment Press, Beijing, China, 2018.

[16] S. Qinxuan, Z. Han-qu, J. Wang, Z. Min, and Y. Wei-zhong, "Potential ecological risk assessment and source analysis of heavy metals in surface sediments from aquaculture ponds in Huzhou city," *Freshwater Fisheries*, vol. 45, no. 6, pp. 80–84, 2015.

[17] S. Xue, "Health innovation," *OECD Science, Technology and Industry Scoreboard*, vol. 33, no. 6, pp. 156-157, 2013.

Research Article

Rainfall Erosion Predictions for Artificial High-Filled Embankment with Reinforcement

Shangwei Wu [ID],[1] **Dongming Wu** [ID],[2] **Xiaofei Jing** [ID],[1] **Xuanyi Chen** [ID],[1] **Yijun Wang**,[1] **and Luhua Ye**[1]

[1]*School of Safety Engineering, Chongqing University of Science and Technology, Chongqing 401331, China*
[2]*Jinzhu Subsidiary Company of Zhejiang Communications Construction Group Co Ltd, Hangzhou, China*

Correspondence should be addressed to Dongming Wu; wdm94124@163.com and Xiaofei Jing; xfjing@cqust.edu.cn

In recent years, rainstorm disasters caused by global warming have frequently occurred in China. It has caused serious damage to artificial high embankments. In this paper, the influence of rainfall intensity, slope, and reinforced layers on the erosion and destruction of the artificial high embankment is deeply analyzed. Through the model test, the rainfall erosion prediction model is established. The results show that (1) the gully width, depth, and erosion amount increased with the increase in rainfall intensity and slope and decreased with the increase in reinforcement layers; (2) the final ditch shape of the embankment is influenced by steel bars; and (3) according to the model test data, the mathematical model of dike scouring is established. Rainfall intensity and the coupling between slope and reinforced layers are considered in the model. It can be used for predicting erosion during rainfall.

1. Introduction

In recent years, there have been many rainstorms in China that are affected by global warming. Especially in the south of China in 2020, a large number of floods, mudslides, and landslides were caused by rainfall. The rainfall in Chongqing is 19% higher than the previous average level [1]. Due to the construction of a ground transportation network in Southwest China, a large number of artificial high embankments have been formed. In this case, deformation, instability, landslides, and other accidents are easy to occur.

In the past, 80% of landslide accidents were caused by rainfall. Therefore, many scholars have done a lot of research on rainfall. Some scholars analyzed the erosion effect of different rainfall modes and types on embankments [2–5]. The influence of rainfall intensities on sediment yield and embankment stability was also studied [6–8]. The results show that the greater the rainfall intensity is, the greater the sediment yield is, the greater the displacement is, and the lower the stability of the embankment is. Some scholars have studied the influence of slope gradient on erosion failure.

The larger the slope is, the faster the runoff speed is and the greater the rainfall erosion is. The greater the slope is, the greater the influence of rainfall on slope erosion is [9–12]. When the slope gradient exceeds a certain value, the rainfall erosion of the embankment is inversely proportional to it. Many scholars have conducted a large number of experimental studies on the critical slope, and the results show that the critical slope range is $10°\sim45°$ [13–15]. Due to the limitation of topography, the stability of some fill embankments is not high, and the reinforcement method is usually adopted to reinforce fill embankment. Because of this situation, many scholars have studied the impact of reinforcement on embankment erosion. The influence of different reinforcement materials and methods on the stability of subgrade was studied. The results show that reinforcement can improve the stability of embankment [16–19]. When the quantity of reinforcement materials changes in a certain range, the stability of the slope will be improved with the increase in the quantity. When the amount of reinforcement materials exceeds a certain value, it will not affect the stability of the slope [20, 21].

The erosion process of reinforced embankment induced by rainfall is very complex, and the blocking rule of reinforced belts in the erosion process is unclear. The research on artificial embankment has been focused on rainfall and reinforcement (materials and methods) and achieved fruitful results. However, there are few research reports on erosion damage under the coupling condition of reinforcement and rainfall. Based on the test of rainfall erosion on the reinforced embankment, this paper deeply analyzed the influence of rainfall intensity, slope, and reinforcement layers on the erosion of artificial embankment and established a prediction model of rainfall erosion on the reinforced artificial embankment under multifactor coupling. The research results can provide a reliable scientific basis for effectively forecasting rainfall landslide disasters of the reinforced artificial high embankment and have important theoretical value.

2. Model Test of Rainfall Erosion on the Reinforced High Embankment

2.1. Testing Equipment. The model test equipment is a self-designed model test equipment for embankment rainfall, as shown in Figure 1. The model groove is tempered glass, and the geometric size is 2 m × 0.6 m × 0.5 m (length × width × height). After pretest, this size is large enough to avoid size influence. Above the model trough, the rainfall system is composed of a water supply system and sprinkler. The data monitoring system consists of the following parts: BX-2 resistance earth pressure sensor and vibrating wire pore water pressure sensor produced by Dandong Electronic Instrument Factory and TST3828EW dynamic strain gauge produced by Jiangsu Tate Electronic Equipment Manufacturing Co., Ltd. A high-resolution camera is arranged in front of the model tank to record the rainfall erosion process.

The glass fiber mesh material is selected to replace geogrid as the reinforcement material, and the reinforcement parameters are shown in Table 1.

A series of rainfall erosion tests were carried out with different reinforcement layers ($N = 0, 1, 2,$ and 4, as shown in Figure 2).

We analyzed the rainfall uniformity in which the rainfall uniformity can be calculated as follows:

$$U = 1 - \frac{\sum (R_i - \overline{R})}{n\overline{R}}. \tag{1}$$

In the formula, U is the rainfall uniformity; R_i is the rainfall of rainfall range point i within the test time; n is the number of test points; and R is the average rainfall of all test points within the rainfall range. As shown in Figure 3(a), 47 cups are evenly placed in the test glass tank, and the rainfall of each cup is collected at a rainfall duration of 60 s to calculate the uniformity. The results are shown in Figure 3(b), and the results show that the uniformity meets the requirements of the rainfall test.

2.2. Experimental Materials and Procedures. To study the law of rainfall erosion damage to the embankment in the Chongqing area, referring to the previous research progress

of embankment in Chongqing [22, 23], combined with the actual project in Chongqing, the test material was selected as the field clay of an embankment in Chongqing. After field sampling, the soil samples were dried and ground. The particle size distribution of soil samples was measured by the Winner3002 laser particle size analyzer. Other physical and mechanical parameters were obtained based on field data (Table 2). The final embankment model is 1.2 m × 0.6 m × 0.5 m.

In the test, the model of reinforced embankment slope should be established first, and all sensors and reinforced belts should be installed completely. Then, rainfall is provided to the embankment through the rainfall system. When the embankment slope is eroded and damaged, the current gully width and depth are measured.

The specific steps of the fill embankment model building are as follows:

(1) The soil with 10% water content was prepared according to the test requirements (as shown in Figure 4(a)). The water content is low, so we can observe the influence of rising water content on the soil.

(2) The layer compaction method was used for constructing embankment with each layer of 8 cm and the compactness of each layer of 85% (as shown in Figure 4(b)). 85% is selected because, in the engineering background, the result of sampling from the site is 85%. To restore the actual site, 85% is done.

(3) The reinforcement and sensors are laid down (as shown in Figure 4(c)).

(4) After the fill embankment model building is completed (as shown in Figure 4(d)), the camera is placed and calibrated.

The experimental model is established by layered compaction. The compacted soil sample of each layer is 8 cm high; it is divided into five floors. To ensure that the compaction degree of each layer is uniform and the end effect is minimized, the surface is burred after each layer is compacted. This operation enables the soil below to be better combined with the upper layer, thus preventing the filling embankment model from stratification. Each layer is rammed with the same quality hammer and from the same height down the same number of compaction. After compaction of each layer, four soil samples were taken from each layer by the ring knife for the density test. After the density test, the sampling vacancy is filled in the above manner. Finally, the soil volume is compared with the expected value through the overall measurement.

2.3. Test Scheme. The slope is made by the layer pressure method, and each layer is piled up into soil piles with the same height according to the same mass of samples, and the soil is compacted from the same height by the compaction
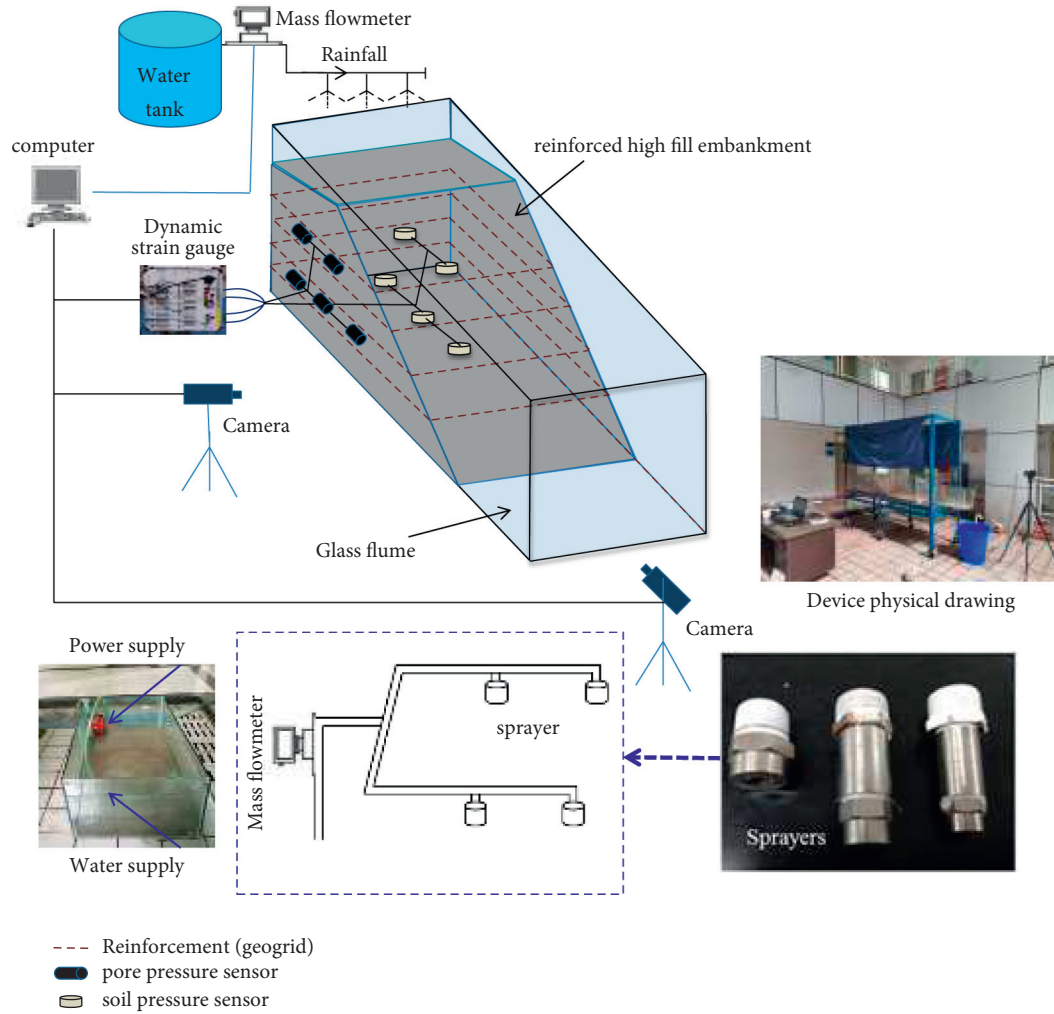
FIGURE 1: Rainfall test system for reinforced artificial high embankment.

TABLE 1: The basic property of reinforcement.

Type	Grid size (mm)		Tensile strength (kPa)		Elongation at break (%)
	Vertical	Horizontal	Longitudinal	Transverse	
JT 11 01	25	25	6.5	6.5	12.7
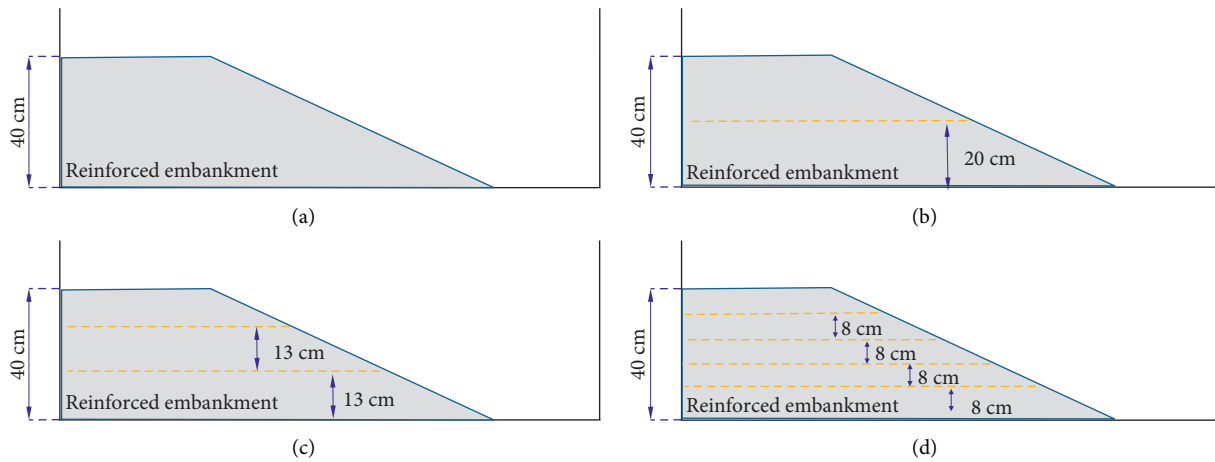
FIGURE 2: The schematic diagram of reinforcement layers: (a) $N = 0$; (b) $N = 1$; (c) $N = 2$; (d) $N = 4$.

(a)

(b)
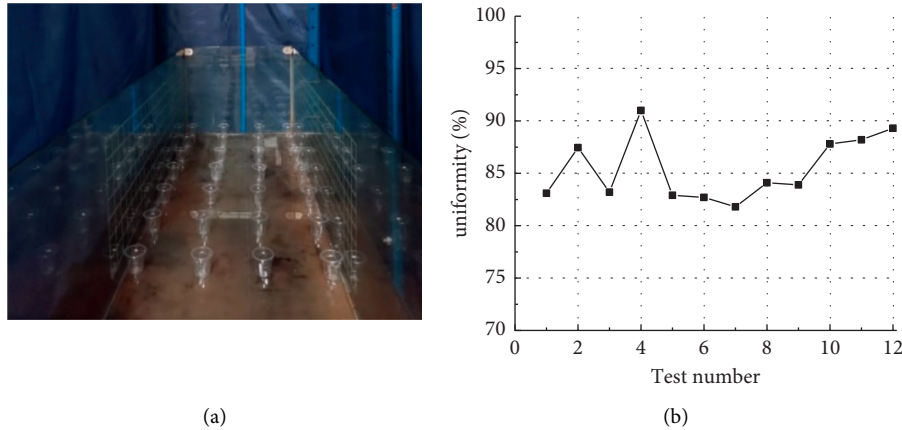
Figure 3: Rainfall dispersion test. (a) Rainfall dispersion experiment. (b) The uniformity of each test.

Table 2: Physical and mechanical parameters of test soil.

Index	Values
Sample layers (g/cm^3)	1.75
Median diameter D_{50} (um)	6.42
Water content (%)	16.8
Cohesion (kPa)	21.5
Internal friction angle (°)	20.16
Poisson ratio	0.254

hammer with the same mass. To ensure the uniformity of soil compaction, a square board is placed under the hammer. After each layer is laid, the ring cutter is sampled, the ring cutter quality is weighed, and the degree of compaction is detected. The top surface of each layer adopts the method of hearing so that the soil can be more closely combined with the upper layer of soil to avoid the end effect between the layers. Finally, the built slope is cut to different angles under the same degree of compaction.

Based on the average rainfall of Chongqing in recent 50 years and rainfall strength of each return period [24], the setting values of rainfall intensity variables are 14, 28, 42, and 70 mm/h; in line with the actual situation of the Chongqing area, the setting values of slope gradient variables are 30, 35, 40, and 45°; according to the size of the indoor test model, the band layers variables are designed as 0, 1, 2, and 4 layers, and the fill embankment model is constructed for the indoor artificial rainfall test. Specific programs are as shown in Table 3.

3. Analysis of Model Test Results

To analyze the slope failure of reinforced artificial high-fill embankment under rainfall, the effects of rainfall intensity, slope gradient, and reinforcement layers on the development of gully on the slope were analyzed. The width and depth of the main gully on the slope were measured by the ruler method and the photography method. The main source of embankment slope erosion is gully erosion, and gully development can characterize the total erosion degree.

3.1. Influence of Rainfall Intensity on Erosion Damage of Embankment. As shown in Figure 5, with a slope gradient of 45°, the 2-reinforced layer is the basic test condition, and different rainfall intensities (14, 28, 42, and 70 mm/h) are the influencing factors. After 90 minutes of rainfall, erosion and damage of embankment were observed. The results show that with the increase in rainfall intensity, the width and depth of the gully on the embankment slope increased significantly, and the amount of soil loss also increased. The main reason is that the rainfall power increases, the runoff erosion is formed earlier, the runoff velocity increases, and the erosion on the embankment slope increases significantly.

With continuous rainfall, the width and depth of the maximum gully on the slope are measured every 10 minutes. Under the influence of rainfall intensity (14, 28, 42, and 70 mm/*h*), the development trend of the embankment gully is shown in Figure 6. It can be seen from the diagram that rainfall strength has a significant impact on the erosion damage of artificial embankments. With the increase in rainfall intensity, the width and depth of the gully and the amount of erosion are increasing. As rainfall intensity increased from 14 mm/*h* to 70 mm/*h*, gully width increased by 13.0 cm, depth increased by 8.1 cm, and erosion increased by 22.0 kg. The main reason is that rainfall intensity increases, the rainfall erosion force increases, and the embankment erosion is more intense.

3.2. Influence of Slope Gradient on Embankment Erosion Damage. As shown in Figure 7, the experimental conditions are as follows: rainfall intensity is 42 mm/h. Two layers of

(a)   (b)   (c)   (d)
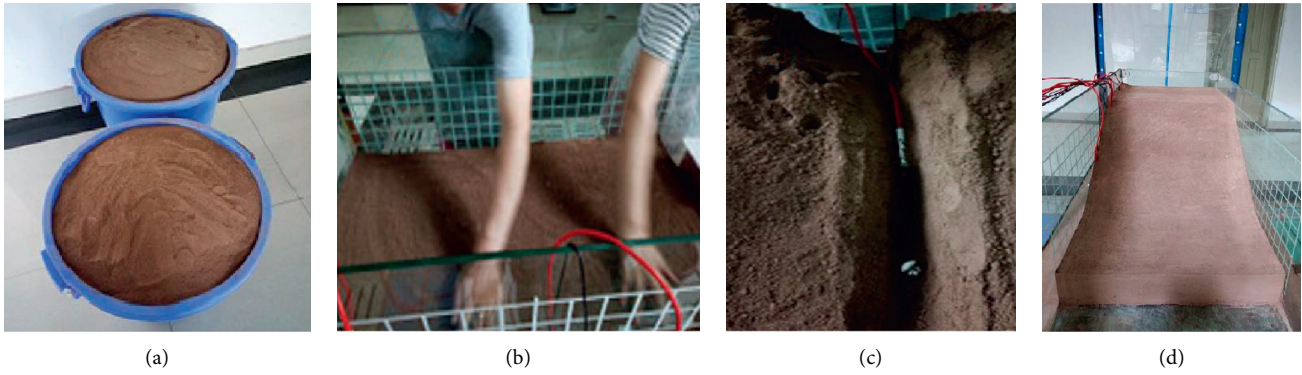
Figure 4: Establishment process of experimental soil sample: (a) soil sample; (b) fill embankment construction; (c) fill embankment construction; (d) final model.

Table 3: Test scheme.

Test variables	Rainfall intensity (mm/h)	Slope gradient (°)	Reinforcement layers (layers)
	1.4	3.0	0
Factor level	2.8	3.5	1
	4.2	4.0	2
	7.0	45	4

(a)   (b)   (c)   (d)
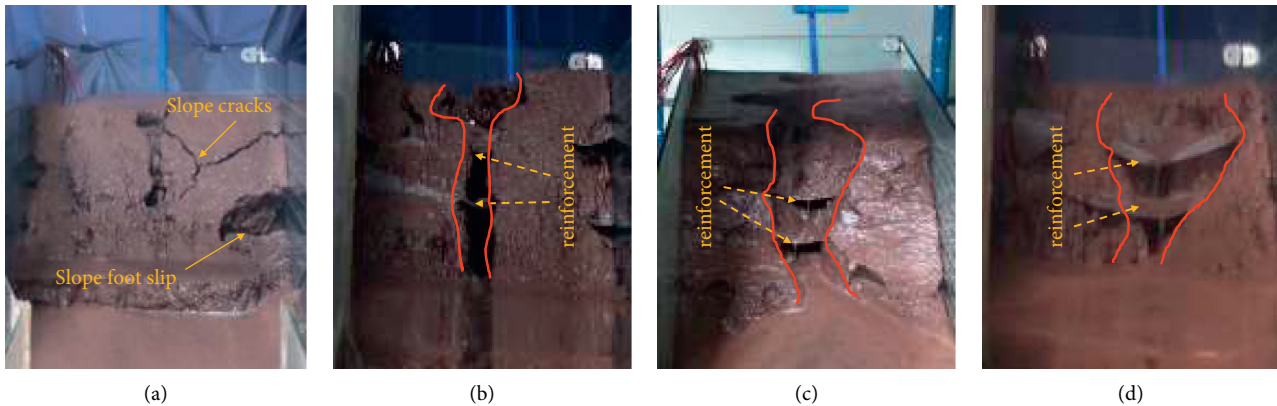
Figure 5: Final erosion failure of reinforced embankment under different rainfall intensities: (a) 14 mm/h; (b) 28 mm/h; (c) 42 mm/h; (d) 70 mm/h.

geogrid shall be laid in the soil. Under the influence of different slopes (30, 35, 40, and 45), the ultimate erosion damage after rainfall which lasts for 90 minutes is observed. The results show that the greater the embankment slope, the more serious the soil erosion, and the larger the sliding area, the more serious the soil erosion. The main reason is that with the increase in slope gradient, the gravity component of soil in the slope direction increases, which leads to the decline of the stability of the slope soil. The runoff speed increases with the increase in slope so do rainfall erosion on the slope.

Figure 8 shows the development trend of dikes and ditches under the influence of slope. It can be seen from the figure that the embankment slope has a significant influence on the erosion and damage of artificial embankments. With the increase in slope gradient, the gully width, depth, and erosion amount increase. When the slope gradient increased from 30° to 45°, the gully width increased by 4.8 cm, the depth increased by 4.5 cm, and the erosion amount increased by 4.8 kg. The main reason is that the slope gradient increases, the slope runoff velocity increases, and the erosion of rainfall on the embankment increases.

3.3. Influence of Reinforcement Layers on Embankment Erosion Damage.

As shown in Figure 9, under the experimental conditions of rainfall intensity of 42 mm/h, the slope of 45, and different reinforcement layers (0, 1, 2, 4), the final erosion failure phenomenon of rainfall lasts 90 min. The phenomenon shows that the width and depth of the gully decrease significantly with the increase in reinforcement layers. The main reason is the combination of reinforcement
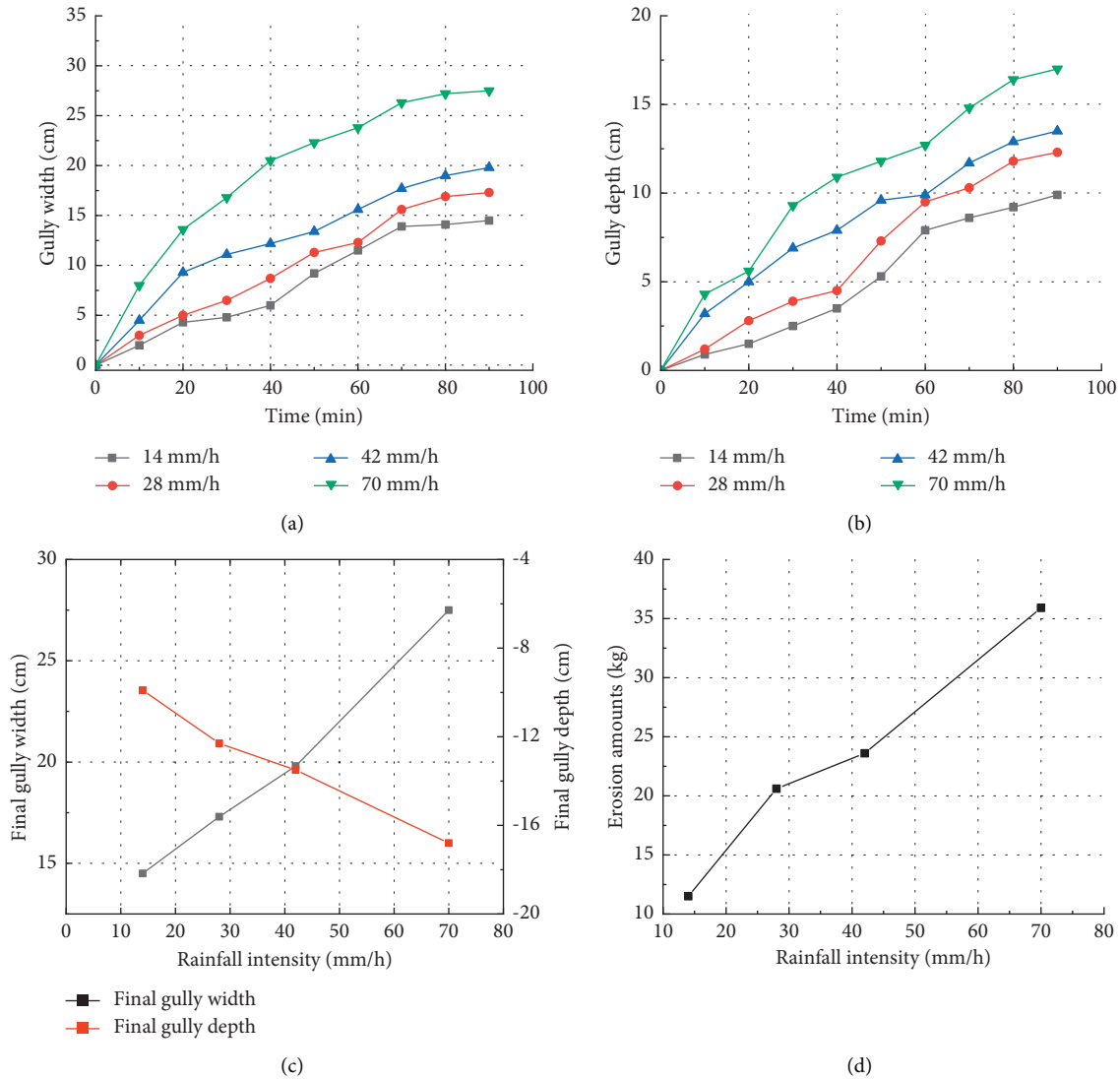
Figure 6: Effect of embankment erosion under different rainfall intensities: (a) gully width changes with time; (b) gully depth changes with time; (c) final gully width and depth; (d) final erosion amount.
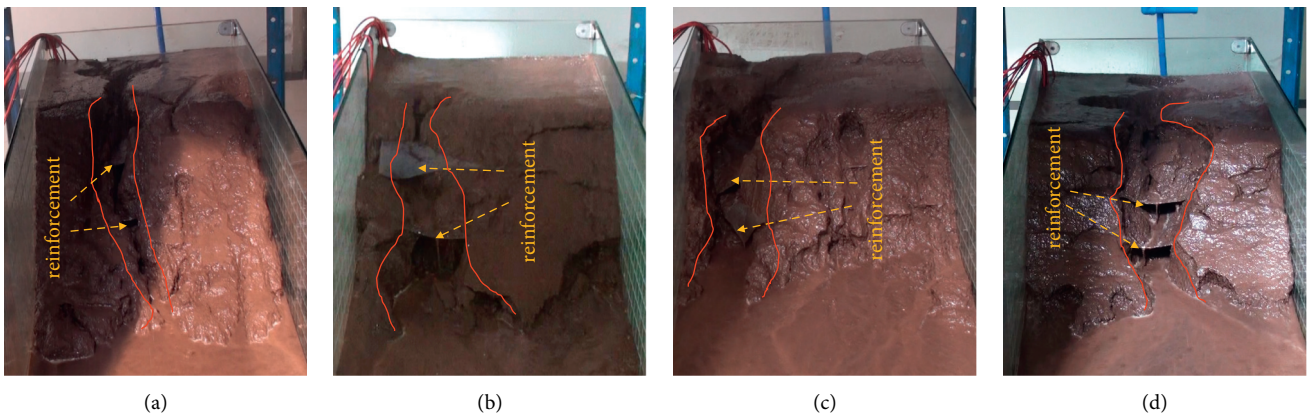
Figure 7: Final erosion failure of reinforced embankment with different slope gradients: (a) 30°; (b) 35°; (c) 40°; (d) 45°.

and soil, which improves the strength of the embankment. With the increase in the number of geogrid layers, the interaction between adjacent layers increases significantly. Thus, the erosion of rainfall on the embankment slope is effectively reduced. When the gully develops to the rib zone, the flow does not damage the rib zone, and it will flow down the rib zone. At this time, the flow passing through the rib zone will be divided into two parts. One part is the seepage water. It penetrates the slope directly through the reinforcement belt, softening the subsoil and reducing the strength of the soil. The other part is the runoff water. It formed along the band breaks the surface. The soil is constantly eroded, and finally a gully with holes is formed on the slope.

Figure 10 is the final erosion damage consequence of embankment under different reinforcement densities (0, 1, 2, and 4 layers). It can be seen from the figure that the reinforcement layers have a significant impact on the gully width of an artificial embankment. The larger the number of reinforcement layers added to the filled embankment is, the smaller the erosion damage consequence under rainfall is. The test shows that when the reinforcement layers increase from 0 layers to 4 layers, the gully width per unit time decreases by 14.5 cm, the depth decreases by 11.5 cm, and the erosion amount decreases by 13.8 kg.

4. Study on Prediction Model of Rainfall Erosion Damage to Reinforced High-Fill Embankment

To discuss the coupling effect of rainfall intensity, reinforced layer, and reinforcement layers on the consequences of rainfall erosion damage to reinforced high-fill embankment, the influence of each factor on the consequences of erosion disaster is analyzed. The relationship between the factor and the final results is obtained. Based on the function form, the function form of the coupling prediction model is determined, and then the parameters are determined.

4.1. Study on the Influence of Various Factors on the Consequences of Erosion Damage

4.1.1. Effects of Rainfall Intensity on the Consequences of Erosion Disasters. Many scholars have also studied the relationship between rainfall intensity and embankment erosion damage, including Shen et al. [14], Jiang et al. [25], Qin et al. [26], and Chen [27]. Based on the rainfall model test, it is found that the amount of soil erosion increases with the increase in rainfall strength. Based on the model test results, the influence function of rainfall intensity on the consequences of erosion disaster is fitted, as shown in Table 4. The results show that with the increase in rainfall

intensity, gully width, gully depth, and erosion amount increase in a power function.

4.1.2. Effect of Slope Gradient on Erosion Disaster Consequences. Referring to previous studies, it is found that the influence of slope on soil erosion was also different. Chen et al. [28] found that the influence of slope on sediment yield was quadratic. Shen et al. [14] and Sheng et al. [29] found that the influence of slope on soil erosion was power function. As shown in Table 5, the influence of slope gradient change on the consequences of rainfall erosion disaster presents that with the increase in slope gradient, the gully width, gully depth, and erosion amount increase in a power function.

4.1.3. Effect of Reinforcement Layers on the Consequence of Erosion Disaster. Because there is little research on reinforced embankments in the past, there is no literature pointing out the functional relationship between the influence of reinforced layers on the consequences of erosion disasters. However, some scholars pointed out that the reinforcement effect of reinforcement materials on the fill embankment has an upper limit [20]. On this basis, we believe that with the increase in the number of reinforcement layers, the trench width, trench depth, and erosion amount decrease in a quadratic polynomial. The influence of the number of reinforcement layers on the consequences of erosion disasters is shown in Table 6. With the increase in the number of reinforcement layers, the trench width, trench depth, and erosion amount show a nonlinear decreasing trend.

4.2. Study on Prediction Model of Rainfall Erosion Damage to Reinforced High-Fill Embankment. The function model considers the influence of the above factors on the consequences of erosion disaster. The coupling prediction model with rainfall intensity, slope gradient, and reinforcement layers as independent variables and gully width and depth as the consequences of erosion disasters was fitted by IBM SPSS Statistics 26 ( ).

According to the output results of SPSS software, the prediction model of rainfall erosion disaster of fill embankment is as follows:

Gully width:

$$L = 0.088tQ^{0.519}S^{0.840}\left(-0.038N^2 - 0.022N + 1.247\right),$$
$$R^2 = 0.829.$$

(2)

Gully depth:

$$H = 0.353tQ^{0.414}S^{0.494}\left(-0.009N^2 - 0.100N + 0.923\right),$$
$$R^2 = 0.917.$$

(3)
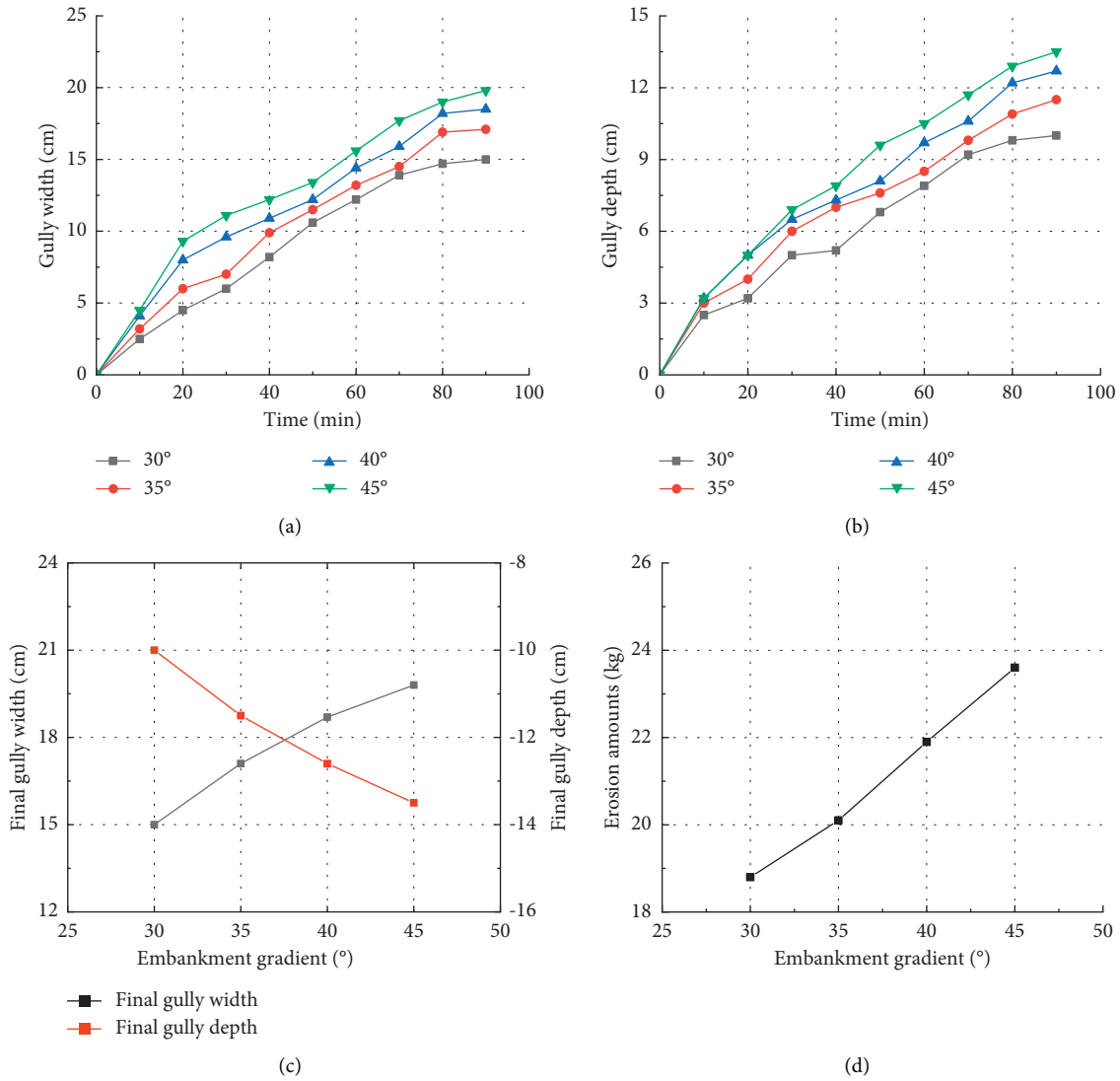
Figure 8: Effect of embankment erosion under different rainfall intensities: (a) gully width changes with time; (b) gully depth changes with time; (c) final gully width and depth; (d) final erosion amount.
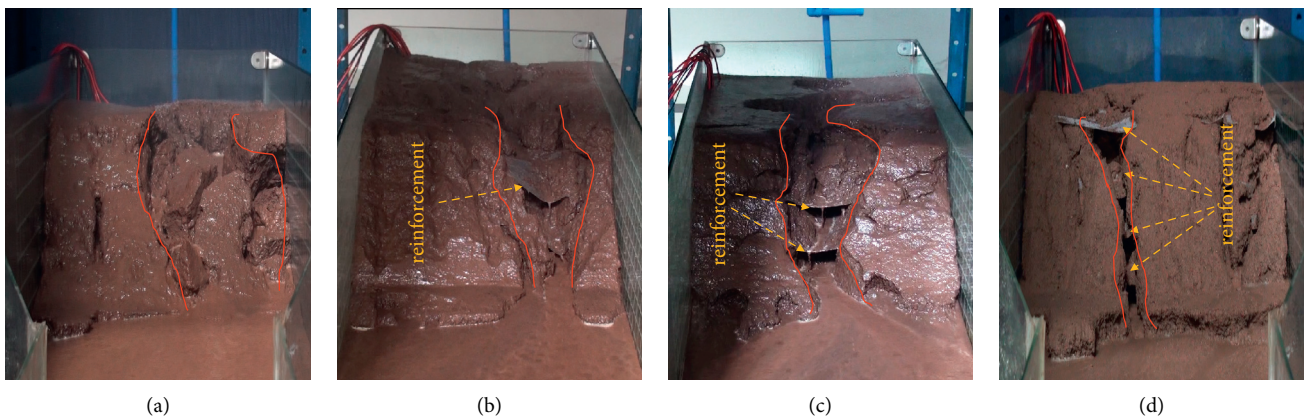
Figure 9: Erosion failure phenomena of different reinforcement layers: (a) $N = 0$; (b) $N = 1$; (c) $N = 2$; (d) $N = 4$.
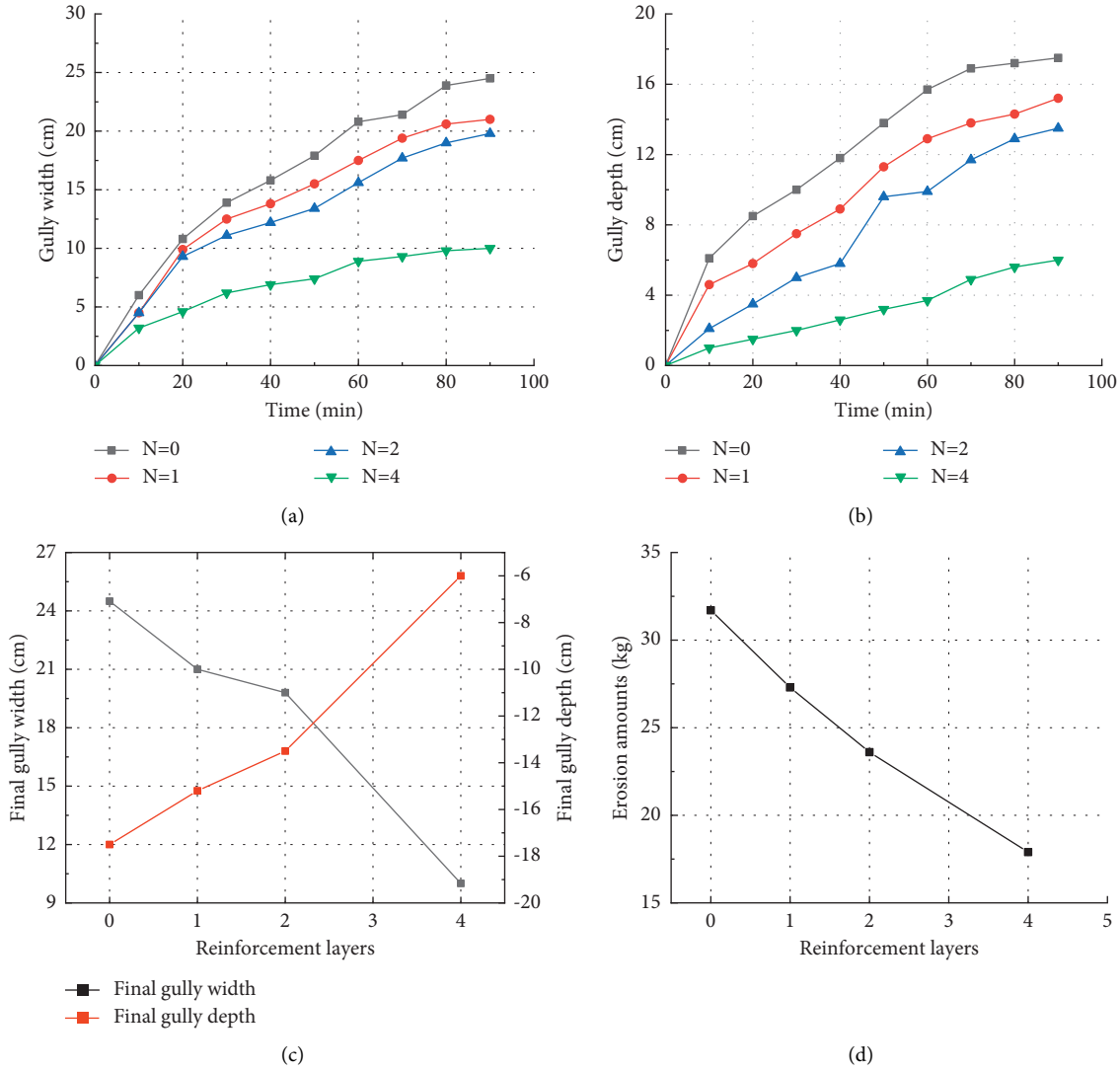
Figure 10: Erosion damage consequences of different reinforcement layers: (a) gully width changes with time; (b) gully depth changes with time; (c) final gully width and depth; (d) final erosion amount.

Erosion amounts:

$$M = 0.975tQ^{0.698}S^{0.701}\left(-0.001N^2 - 0.013N + 0.11\right),$$

$$R^2 = 0.980.$$

(4)

L is the gully width, cm; H is the gully depth, cm; M is the erosion amount, kg; t is the rainfall time, hour; Q is the rainfall intensity, mm/h; S is the slope gradient, °; and N is the reinforcement layers, layer.

It can be seen from the formula that with the increase in rainfall intensity and slope, the consequences of erosion disasters increase in the form of the power function. With the increase in the number of reinforcement layers, the consequences of the disaster decrease nonlinearly. The correlation coefficient R^2 of all formulas exceeds 0.80, indicating that the obtained prediction model formula can accurately fit the results of the indoor model test.

4.3. Verification of Prediction Model of Rainfall Erosion Damage to Reinforced High-Fill Embankment. The data in reference [22] were chosen because they are similar to the experiment in this paper for comparison. In this paper, the rainfall erosion model test of reinforced embankment with similar test materials was also carried out, and the influence of different influencing factors on the erosion damage of embankment was obtained. However, the change of erosion amount was not involved in that paper. To ensure the consistency of the verification data, only the width and depth of the gully were verified but not the scouring amount. The main source of the slope erosion of the embankment was rill erosion, and the rill development could represent the total erosion development. Therefore, the accuracy of the prediction of gully development could roughly determine the accuracy of formulas (2)–(4). As shown in Figure 11, after the test conditions in reference [22] are substituted into the prediction model, the calculated gully width and depth are compared with their test

TABLE 4: Effect of rainfall intensity on erosion disaster consequences.

Influencing factor	Fitting equation of erosion consequence	Correlation coefficient
Rainfall intensity (mm/h)	Gully width: $L = 4.282\,Q^{0.429}$	$R^2 = 0.919$
	Gully depth: $H = 2.312Q^{0.478}$	$R^2 = 0.946$
	Erosion amounts: $M = 1.978\,Q^{0.679}$	$R^2 = 0.975$

TABLE 5: Effect of slope gradient on erosion disaster consequences.

Influencing factor	Fitting equation of erosion consequence	Correlation coefficient
Slope gradient (°)	Gully width: $L = 1.565\,S^{0.668}$	$R^2 = 0.985$
	Gully width: $H = 2.656\,S^{0.3699}$	$R^2 = 0.943$
	Erosion amounts: $M = 2.656\,S^{0.573}$	$R^2 = 0.988$

TABLE 6: Effect of reinforcement layers on erosion disaster consequence.

Influencing factor	Fitting equation of erosion consequence	Correlation coefficient
Reinforcement layers (N)	Gully width: $L = -0.475\,N^2 - 1.595\,N + 24.11$	$R^2 = 0.951$
	Gully depth: $H = -0.370\,N^2 - 1.339\,N + 17.33$	$R^2 = 0.986$
	Erosion amounts: $M = 0.305\,N^2 - 4.664\,N + 31.69$	$R^2 = 0.998$

(a)   (b)
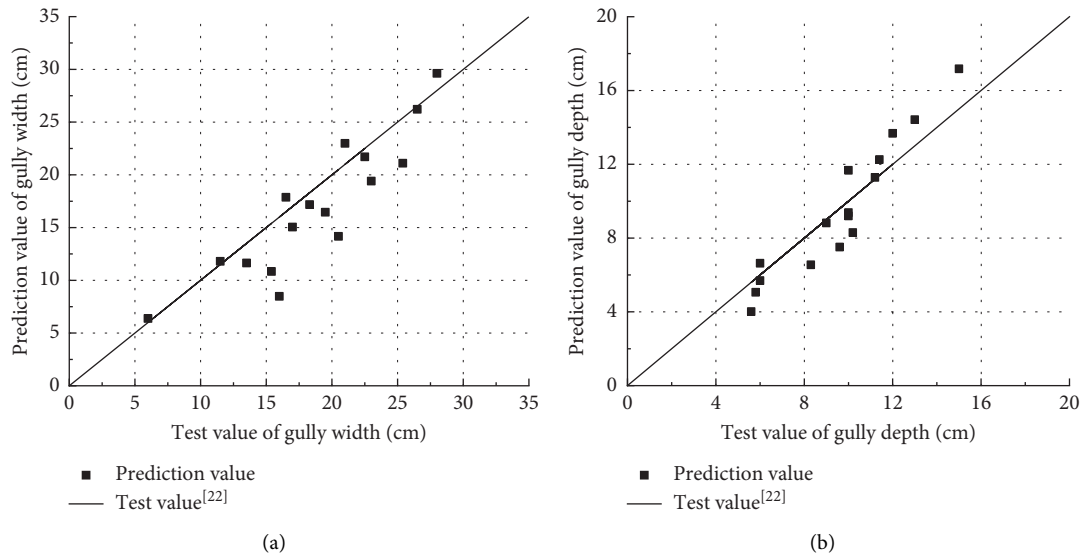
FIGURE 11: Verification and comparison of prediction models: (a) comparison of gully width; (b) comparison of gully depth.

values. The scatter is the predicted value, the slant is the test value, and the distance between the scatter and the slant represents the error.

As shown in Table 7, the absolute error and relative error of prediction calculated by 16 groups of test conditions and test values in reference [22] are compared with the predicted data calculated by the model substituted for the test conditions. The absolute error and relative error of gully width predicted by the model are 2.72 cm and 16.6%, respectively. The absolute error of gully depth is 1.15 cm, and the relative error is 13.7%.

TABLE 7: Prediction error of erosion disaster consequence.

Consequences of erosion disasters	Mean absolute error (cm)	Mean relative deviation (%)
Gully width	2.72	16.6
Gully depth	1.15	13.7

5. Conclusions

This paper takes the reinforcement of artificial high embankment in Chongqing as the research background. Through the combination of model test and theoretical analysis, a prediction model of rainfall erosion damage to reinforced high-fill embankment was established. The influence of rainfall intensity, slope, and reinforcement layer is considered in the model. Concrete conclusions are as follows:

(1) Adding a reinforced belt to fill the embankment will have an impact on the final shape of the ditch and form a stepped ditch on the slope. The more levels, the more meaningful the form.

(2) In the rainfall erosion for artificial high-filled embankment with reinforcement, the width, depth, and erosion amount of the gully increased with the increase in rainfall intensity and slope but decreased with the increase in reinforced layers. When rainfall intensity increased from 14 mm/h to 70 mm/h, the ditch width increased by 13.0 cm, the ditch depth increased by 8.1 cm, and the erosion increased by 24.4 kilograms. When the embankment slope increases from 30 to 45, the three elements increased by 4.8 cm, 4.5 cm, and 4.8 kg, respectively. When the reinforcement layers are increased from 0 to 4 layers, the three elements decreased by 14.5 cm, 11.5 cm, and 13.8 kg, respectively.

(3) A multifactor coupling rainfall erosion prediction model is put forward. With the increase in rainfall intensity and slope, the consequences of erosion disasters present a power function increasing trend. With the increase in the number of reinforcement layers, the consequence of erosion disaster decreases as a quadratic function.

Data Availability

The data used to support the findings of this study are available from the corresponding author upon request.

Conflicts of Interest

The authors declare that there are no conflicts of interest.

Acknowledgments

References

[1] X. Yan, "China climate bulletin released in 2020: higher annual average temperature and more precipitation," 2021.

[2] W. S. d. Almeida, S. Seitz, L. F. C. d. Oliveira, and D. F. d. Carvalho, "Duration and intensity of rainfall events with the same erosivity change sediment yield and runoff rates," *International Soil and Water Conservation Research*, vol. 9, no. 1, pp. 69–75, 2021.

[3] L. Wu, M. Peng, S. Qiao, and X.-Y. Ma, "Effects of rainfall intensity and slope gradient on runoff and sediment yield characteristics of bare loess soil," *Environmental Science and Pollution Research*, vol. 25, no. 4, pp. 3480–3487, 2018.

[4] K. Christofer, R. Harianto, and S. Alfrendo, "Effect of variations in rainfall intensity on slope stability in Singapore," *International Soil and Water Conservation Research*, vol. 5, 2017.

[5] P. W. Zhong, H. L. Zhang, K. L. Tian, H. Chen, and K. Nie, "Study on the influence of continuous rainfall infiltration on the loess slope stability," *Yellow River*, vol. 40, no. 1, pp. 76–81, 2018.

[6] O. Augusto Filho and M. A. Fernandes, "Landslide analysis of unsaturated soil slopes based on rainfall and matric suction data," *Bulletin of Engineering Geology and the Environment*, vol. 78, no. 6, pp. 4167–4185, 2019.

[7] C. Anusron, H. Toshikazu, S. Hirotaka, S. Tomotaka, and K. Yuji, "Experimental tests of slope failure due to rainfalls using physical slope models," *Soils and Foundations*, vol. 58, no. 2, pp. 03–18, 2018.

[8] E. Elkamhawy, H. B. Wang, B. Zhou, and Z. Yang, "Failure mechanism of a slope with a thin soft band triggered by intensive rainfall," *Journal of Environment and Earth Science*, vol. 77, no. 9, pp. 1–15, 2018.

[9] S. E. Cho, "Stability analysis of unsaturated soil slopes considering water-air flow caused by rainfall infiltration," *Engineering Geology*, vol. 211, pp. 184–197, 2016.

[10] N. V. Sobol, I. M. Gabbasova, and M. A. Komissarov, "Effect of rainfall intensity and slope steepness on the development of soil erosion in the southern Cis-Ural region (a model experiment)," *Eurasian Soil Science*, vol. 50, no. 9, pp. 1098–1104, 2017.

[11] T. Li, L. Zhao, H. Duan, Y. Yang, Y. Wang, and F. Wu, "Exploring the interaction of surface roughness and slope gradient in controlling rates of soil loss from sloping farmland on the Loess plateau of China," *Hydrological Processes*, vol. 34, no. 2, pp. 339–354, 2020.

[12] E. Koomson, T. Muoni, C. Marohn, G. Nziguheba, I. Öborn, and G. Cadisch, "Critical slope length for soil loss mitigation in maize-bean cropping systems in SW Kenya," *Geoderma Regional*, vol. 22, 2020.

[13] D. Liu, D. She, S. E. Yu, G. Shao, and D. Chen, "Rainfall intensity and slope gradient effects on sediment losses and

splash from a saline-sodic soil under coastal reclamation," *Catena*, vol. 128, pp. 54–62, 2015.

[14] H. O. Shen, F. L. Zheng, L. L. Wen, Y. Han, and W. Hu, "Impacts of rainfall intensity and slope gradient on rill erosion processes at loessial hillslope," *Soil & Tillage Research*, vol. 155, 2016.

[15] X. Wang, *Research on Slope Surface Erosion under a Rainfall of Artificially Loess Slope*, Chang'a University, Xi'an, China, 2015.

[16] Y. H. Chok, M. B. Jaksa, W. S. Kaggwa, and D. V. Griffiths, "Assessing the influence of root reinforcement on slope stability by finite elements," *International Journal of Geo-Engineering*, vol. 6, no. 1, 2015.

[17] D. Bhattacherjee and B. V. S. Viswanadham, "Effect of geo-composite layers on slope stability under rainfall condition," *Indian Geotechnical Journal*, vol. 48, no. 2, pp. 316–326, 2018.

[18] F. Zhang, D. Leshchinsky, Y. Gao, and S. Yang, "Corner reinforced slopes: r," *Geotextiles and Geomembranes*, vol. 47, no. 3, pp. 408–416, 2019.

[19] G. Zheng, X. Yu, H. Zhou, X. Yang, W. Guo, and P. Yang, "Influence of geosynthetic reinforcement on the stability of an embankment with rigid columns embedded in an inclined underlying stratum," *Geotextiles and Geomembranes*, vol. 49, no. 1, pp. 180–187, 2021.

[20] Lossanima, *Centrifugal Model Test and Finite Element Analysis of Reinforced Soil Slope*, Tsinghua University, Beijing, China, 2011.

[21] X. Jing, Y. Chen, D. Williams, M. Serna, and H. Zheng, "Overtopping failure of a reinforced tailings dam: laboratory investigation and forecasting model of dam failure," *Water*, vol. 11, no. 2, pp. 315–330, 2019.

[22] C. S. Pan, *Study on Stability and Evaluation of Safety Influencing Factors of Reinforced Embankment under Heavy Rainfall*, Chongqing University of Science and Technology, Chongqing, China, 2018.

[23] Y. F. Liu, "Experimental study on rheological properties of lateritic clay in chongqing," *Pearl River*, vol. 38, no. 8, pp. 42–45, 2017.

[24] Q. Guo, R. Li, J. Sun et al., "The calculated design rainstorm in the central districts of chongqing," *Journal of Southwest University (Natural Science)*, vol. 39, no. 5, pp. 170–177, 2017.

[25] M. H. Jiang, J. S. XiE, W. M. Wang, R. Z. Huang, and Y. C. Yang, "Effects of different land use and different rainfall intensities on soil and water loss in northern Fujian province," *Science of Soil and Water Conservation*, vol. 10, no. 4, pp. 84–89, 2012.

[26] W. Qin, C. Q. Zuo, Q. H. Yan, Z. Wang, P. Du, and N. Yan, "Regularity of individual rainfall soil erosion in bare slope land of red soil," *Transactions of the Chinese Society of Agricultural Engineering*, vol. 31, no. 2, pp. 124–132, 2015.

[27] X. A. Chen, *Study on Soil Erosion and Erosion Empirical Model in Hilly Loess Region on the Loess Plateau*, Huazhong Agricultural University, Wuhan, China, 2010.

[28] J. J. Chen, L. Y. Sun, J. T. Liu, and Q. G. Cai, "Effects of slope gradients on rill erosion: study based on three-dimensional laser technology," *Science of Soil and Water Conservation*, vol. 11, no. 3, pp. 1–5, 2013.

[29] H. W. Sheng, *Impacts of Soil Type and Slope Gradient on Sloping Sheet Erosion and Rill Erosion in Loess Region*, Northwest A&F University, Xianyang, China, 2016.

Research Article

Hydraulic Erosion Rate of Reinforced Tailings: Laboratory Investigation and Prediction Model

Xuanyi Chen [ID],[1] **Xiaofei Jing** [ID],[1] **Hai Cai,**[2] **Yijun Wang,**[1] **and Luhua Ye**[1]

[1]*School of Safety Engineering, Chongqing University of Science and Technology, Chongqing 401331, China*
[2]*Sichuan Provincial Bureau of Geological and Mineral Exploration Geological Team 202, Sichuan 610000, China*

Correspondence should be addressed to Xuanyi Chen; 2584304676@qq.com and Xiaofei Jing; xfjing@cqust.edu.cn

Tailings dams are high-potential-energy dams built to store various ore tailings, and the overtopping failure caused by hydraulic erosion is one of the most common failure modes. The characteristics of hydraulic erosion of the reinforced tailings were studied by using the self-made erosion apparatus with four kinds of reinforcement spacing 2.5, 1.7, 1.3, and 1.0 cm, respectively. The test results show a positive correlation between the reinforcement spacing and erosion rate of tailings. Based on the sediment scouring theory, the scouring constant in the erosion rate formula is determined to be 0.056 mm/s; a prediction model for the hydraulic erosion rate of reinforced tailings is established by introducing the collapse coefficient into the results of the overflow test of reinforced tailings. This model can provide a reference for the prediction of overtopping-induced erosion failure of the reinforced tailings dam.

1. Introduction

Tailings dam is a sizeable high potential energy facility used to store the waste after beneficiation, and the primary process is to discharge the slurry precipitation into the tailings dam. However, the tailings dam is a dangerous source of artificial debris flow with high potential energy. Once the dam break occurs, the safety of downstream residents and facilities will be threatened. Tailings dam accidents frequently occurred in recent years, including dam liquefaction, overtopping erosion, and collapse, which has brought serious disaster to the life of downstream people [1–6]. At present, most researchers take unreinforced tailings dam as the research object, and there are few studies carried out on the erosion failure of the reinforced tailings dam. Sun et al. [7] proposed a failure evolution model of unreinforced tailings dam overtopping through the physical model test. Dang et al. [8] divided the dam failure evolution stages of the tailings dam during flood overtopping with different accumulation densities. Wang et al. [9] discussed the physical characteristics, mode, and development regularity of dam break in the process of water level rise through

the flood overtopping dam-break test of the tailings dam. Zhang et al. [10] used the self-made dam-break model test platform of a tailings dam to carry out the dam-break model test of the tailings dam with a similarity ratio of 1 : 100. The evolution of dam displacement, infiltration line, maximum velocity, and dam failure was also analyzed. It found that the collapse of the tailings dam first occurs at the foot of the slope, showing traceability failure. Some scholars [11, 12] studied the dam failure causes and dam failure evolution process of tailing dams under different rainfall conditions, as well as the causes of flood overtopping dam failure. None of the above researchers studied the overtopping of the reinforced tailing dams, failure analysis of tailings dam failure mode, failure mechanism and cause of dam failure, and reinforced tailings dam analysis of the impact of few scholars to study. Geosynthetics have been widely used in tailing dam engineering. Adding geogrid in tailings can effectively improve the shear strength of soil and reduce the erosion of water flow during flood overtopping. In the process of hydraulic erosion, the influence of reinforcement on tailings dam particles is worth studying [13, 14]. Jing [15] and Zhou [16] revealed that the increase of reinforcement density

could improve the mechanical strength of tailing dams by studying the effect of band density on the overtopping failure of the tailings dam, and the difference of the development model of the reinforced and unreinforced tailing dam breach is also analyzed. The interpretation of the influence of geogrid density on tailing dam failure provides the scientific basis for the research of tailing dam reinforcement.

At present, there have been studies on sediment incipient motion, sediment scouring, viscous sediment scouring, and overtopping failure of the reinforced tailings dam, but few researchers studied the multifactors coupling of the viscous tailings scouring and the geogrid. Overtopping failure is the leading cause of erosion damage of tailings dam. To predict the failure process of overtopping erosion of tailings dam, it is necessary to obtain the erosion rate, that is, the erosion height per unit area per unit time. In addition, it is also essential to establish semitheoretical or semiempirical formulas of the hydraulic erosion rate of tailings dam based on the formula of incipient motion velocity of the tailings dam, to analyze the force of cohesionless sediment particles under the action of water flow. Zhao et al. [17] analyzed the influence of microtopography on hydraulic erosion and its change during rainfall by comparing the smooth surface with the rough surface and analyzed the effect of the surface morphology on runoff and sediment transport. Briaud [18] measured the shear stress and erosion rate of water flow at different flow velocities through a self-developed erosion test device. Wang and Wu [19] introduced a new viewpoint of flow bed-moving force and analyzed the functional relationship between the fluctuation of near-bottom water flow. The results showed that the flow of bed-moving force and the fluctuation intensity of water flow is positively correlated. Kandiah [20] obtained the nonlinear relationship between the sediment erosion rate and the relative residual shear stress through the silt scouring test and established the formula of the sediment scouring rate by the dimensionless method. Researchers such as Zhang et al. [21], Osman and Thorne [22], Krone [23], and Sanford and Maa [24] established the erosion formula of cohesive sediment through the results of erosion tests. Different from Kandiah [20], Li et al. [25] obtained the nonlinear relationship between the sediment erosion rate and the relative residual shear stress through the silt erosion test. The physical and chemical properties index l was proposed according to the dimensionless method, and Li established the formula of sediment erosion rate.

In this paper, the self-made hydraulic erosion test device for reinforced tailings is used to carry out the erosion test of reinforced tailings dams. The erosion rate formula is established, referring to a similar idea in sediment research [26–34]. The erosion rate model of tailings dam with various reinforcement spacing is obtained by fitting the erosion constants and physicochemical indices in the formula with test data. Through the results of the overtopping failure test of the reinforced tailings dam, the collapse coefficient $K(d)$ is introduced to establish the formula of the hydraulic erosion rate of the reinforced tailings dam, which can provide a reference for the study of microscopic characteristics of hydraulic erosion damage of the reinforced tailings dam.

2. Experimental Method

2.1. Experimental Facilities.
The experimental erosion facilities consist of a glass flume, a rectangular horizontal acrylic tube with the diameter of a sample hole of 5 cm under the bottom of the tube, sample tube, electromagnetic flowmeter, water pump, and overflow tank (as shown in Figure 1).

An aluminum alloy sample tube with an inner diameter of 5 cm is used as the sample tube. Then Vaseline is smeared on the inner wall of the tube to keep the degree of compaction constant when the sample is jacked up. The piston has good sealing performance and can be vertically reinforced in the sample tube. In order to reduce the hydraulic roughness, the horizontal tube made of organic glass is used for observation tests. And the horizontal tube size is 180 cm × 8 cm × 5 cm (length × width × height). The size of the water storage tank is 2 m × 0.6 m × 0.6 m (length × width × height). The circulating water supply power device adopts a water pump with a power of 1.5 kW and a flow rate of 40 m³/h. The high-resolution cameras (SONY, Beijing, China, resolution: 1920 × 1080/50p) are used as observation devices. Finally, the water level is kept constant through the overflow tank.

2.2. Materials and Experimental Procedures.
The particle size, gradation, and compactness of silt will influence the constant scouring K of erosion. The tailings soil cover of a tailings pond in Yunnan is used in this test. And the particle size range of the tailings pond is 0.005~0.30 mm. The cumulative distribution curve of the particle size is shown in Figure 2. Next the raw tailings are sieved into four-particle size grades, which are 0~0.038 mm, 0.038~0.075 mm, 0.075~0.109 mm, and 0.109~0.27 mm. Then the tailings soil of the four-particle size grades is proportioned according to different quality percentage requirements. Finally, eight groups of tailings soil samples with different particle sizes are formed, shown in Table 1.

2.3. Test Method.
The test is carried out on a reinforced tailings erosion device. The tailings with 15% water content were prepared according to the test requirements, and the reinforcement spacing is 2.5 cm, 1.7 cm, 1.3 cm, and 1.0 cm, respectively. The tube with a diameter of 2.5 cm is inserted into 1, 2, 3, and 4 layers glass fiber window screen [26] as reinforcement, respectively. The reinforcing geogrid specification is 1.5 mm × 1.5 mm aperture. As shown in Figure 3, before carrying out the erosion test, the quality and height of the test tailings samples are measured first.

2.3.1. Test Process.
The detailed procedures of the erosion test of reinforced tailings are listed as follows:

① Using the lifting jack pushes the reinforced tailings in the sample tube into the horizontal tube for 1~3 mm as shown in Figure 4.

② Close the valve of the horizontal tube and slowly inject water into the horizontal tube until it is filled with water.
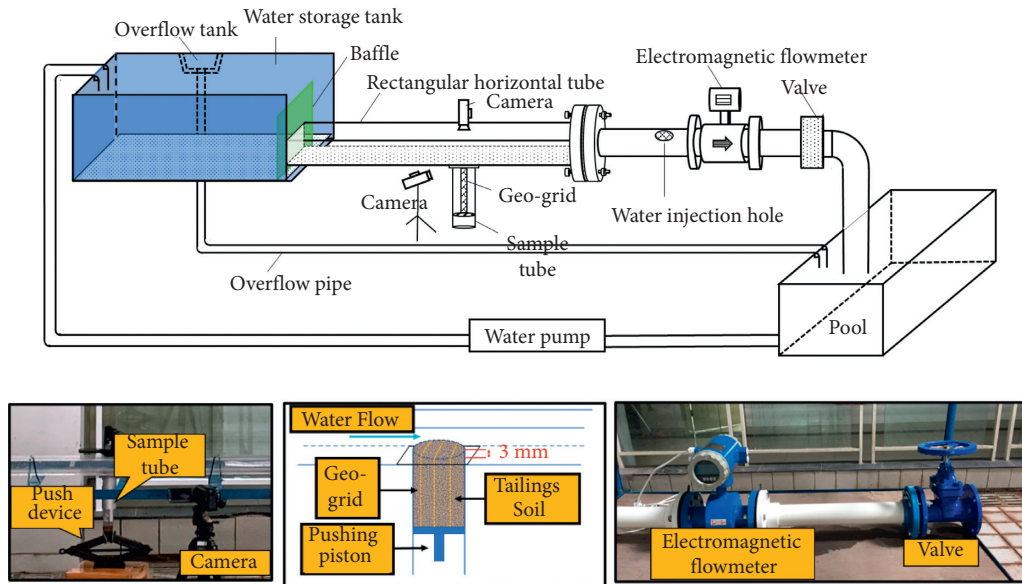
FIGURE 1: Erosion apparatus to measure erodibility.
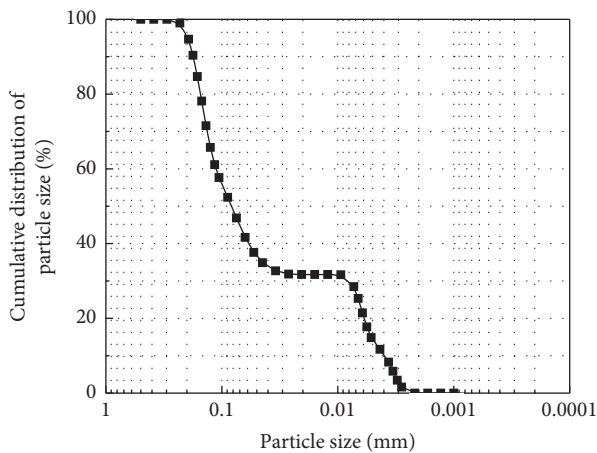
FIGURE 2: The cumulative size distribution curve of the tailings sample.

③ Open the valve, adjust the size of the valve to ensure that the flow velocity is greater than the incipient motion velocity of tailings.

④ Pull out the piston blocking the valve to start the erosion test. This method can reduce the erosion and damage of the sample as much as possible when the flow velocity increases.

⑤ The total erosion time of the reinforced tailings is 120 seconds.

2.3.2. Reading of Erosion Velocity. The erosion test needs to measure the average velocity of the water flow in a fixed erosion time, but not the instantaneous threshold incipient motion velocity test. Because the reading of the electromagnetic flowmeter fluctuates in the order of 0.01 m³/h, the average velocity calculated by the average flow rate is used as the erosion velocity. The flow rate is recorded by an electromagnetic flowmeter, and then the average flow rate is obtained by comparing the flow rate with the cross-sectional area of the horizontal tube.

2.3.3. Determination of Erosion Height. In the test process, the height of the reinforced tailings sample eroded in a fixed time was measured. When the valve knob reaches the correct position, the erosion test starts, and the erosion of the sample is recorded until the end of the fixed erosion time. The erosion height of the corroded reinforced tailings samples was measured at several positions, and the average value was adopted.

3. Results and Discussion

3.1. Test Phenomenon and Analysis. The tailings sample 4 and the reinforcement number of 2 (the reinforcement spacing is 1.7 cm) are taken as an example to show the phenomenon of the erosion test, as shown in Figure 5. The erosion test starts after the reinforced sample is pushed 2 mm into the horizontal tube, and the valve is opened with five and a half cycles (flow rate of 4.5 m³/h). As can be seen from Figure 5(a), the front end of the sample pushed into the horizontal tube is far away from the band, and there is no geogrid affecting the soil. The front end of tailings soil is first impacted by water flow and erodes quickly, just like that without reinforcement. With the continuous erosion of the water flow, the tailings in front of the band (the first side affected by the water flow) are gradually eroded completely, making the tailings level to the bottom of the horizontal tube. However, the tailings behind the second layer of the rear reinforcement are blocked by the reinforcement and gradually accumulated to form sand ridges, as shown in Figure 5(b). As the test continues, the tailings far behind the second layer of the reinforcement gradually increase. The sample area near the rear of the first layer of the geogrid is

TABLE 1: Proportioning of tailings samples.

Tailings samples	Quality percentage of tailings with various particle sizes				Median diameter (mm)
	<400 mesh (<0.038 mm) (%)	400~200 mesh (0.038~0.075 mm) (%)	200~140 mesh (0.075~0.109 mm) (%)	140~50 mesh (0.109~0.27 mm) (%)	
1	50	30	20		0.0071
2	20	50	30		0.0426
3	30	20	50		0.0476
4	20	10	60	10	0.0487
5	10	10	20	60	0.0508
6	10	20	50	20	0.0826
7	20	50	10	20	0.0971
8	25	25	25	25	0.1536
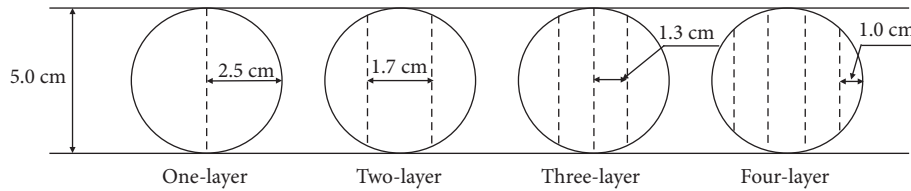
FIGURE 3: Diagrams of different geogrid arrangements and reinforcement space.
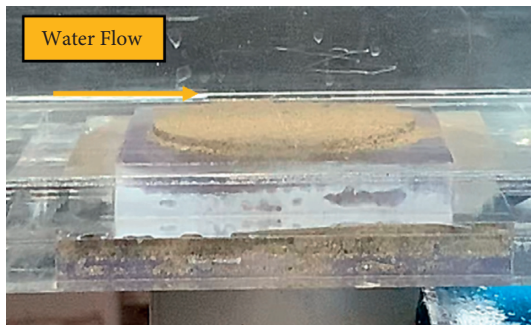
FIGURE 4: Schematic of sample pushing into a horizontal tube.

exposed in the flow, which forms a vortex and a deep concave in the flow, as shown in Figure 5(c). With the test continuing, a gradual increase occurs in the concave behind the first layer of reinforcement. The sand ridge behind the second layer of the geogrid also gradually increases and moves backward along the flow direction. At this time, the tailings near the front of the first layer are progressively eroded. Finally, with the increase of erosion time, the sand ridge formed behind the band is gradually eroded as well, as shown in Figure 5(d).

When the exposed length of the reinforced tailings is short, it is hard for the reinforced tailings to bend, which can be regarded as the situation of the local scour of the pier. Therefore, the erosion phenomenon of the reinforced tailings under hydraulic action can be explained by the local scour theory of piers. Therefore, the scouring phenomenon of reinforced tailings under hydraulic action can be explained by the local flushing mode of bridge piers studied by Briaud [18]. Due to the influence of water flow, the flow structure near the pier is divided into descending flow, horseshoe vortex, and wake vortex [27]. As shown in

Figure 6, in the erosion process, a part of the flow and the longitudinal reinforcement can be seen as the pier erosion, which makes the wake vortex behind the reinforcement cause tailings erosion. The tailings in front of the longitudinal reinforcement also erode the tailings due to the horseshoe vortex. In the other parts, descending flow is formed due to the influence of the transverse geogrid. After converging with the flow passing through the geogrid, a vortex is formed behind the geogrid. Therefore, the tailings behind the first layer of reinforcement is the most seriously eroded due to the combined action of two parts of water flow.

For the tailings samples with other reinforcement spacing, the erosion test process is the same as the above process. It can be seen from the erosion process that the reinforced tailings samples will not be eroded to the uniform horizontal height by water flow, but there are pits of varying degrees. Therefore, in the reinforced tailings erosion tests with 1, 2, 3, and 4 layers of reinforcement, the reinforcement spacing is 2.5, 1.7, 1.3, and 1.0 cm, respectively. The erosion height is measured at several positions of the final tailings sample and the average erosion height is taken; then, we use the fixed time to calculate the erosion rate.

3.2. Results and Analysis. In the erosion process, the quality, total thickness, flow rate (Q), erosion time (t), and erosion height (h) are measured, and the flow velocity and erosion rate of reinforced tailings are calculated. The erosion rate is shown in Tables 2–5.

Figure 7 shows the erosion rate of the tailings in the middle of the particle size range of 8 samples under different reinforcement spacing of 2.5, 1.7, 1.3, and 1.0 cm, respectively. It can be seen from Figure 7 that the reinforcement spacing has a noticeable effect on the erosion rate of tailings. With the increase of the reinforcement spacing, the erosion rate of the reinforced tailings increases; the test results show

(a)

(b)

(c)

(d)
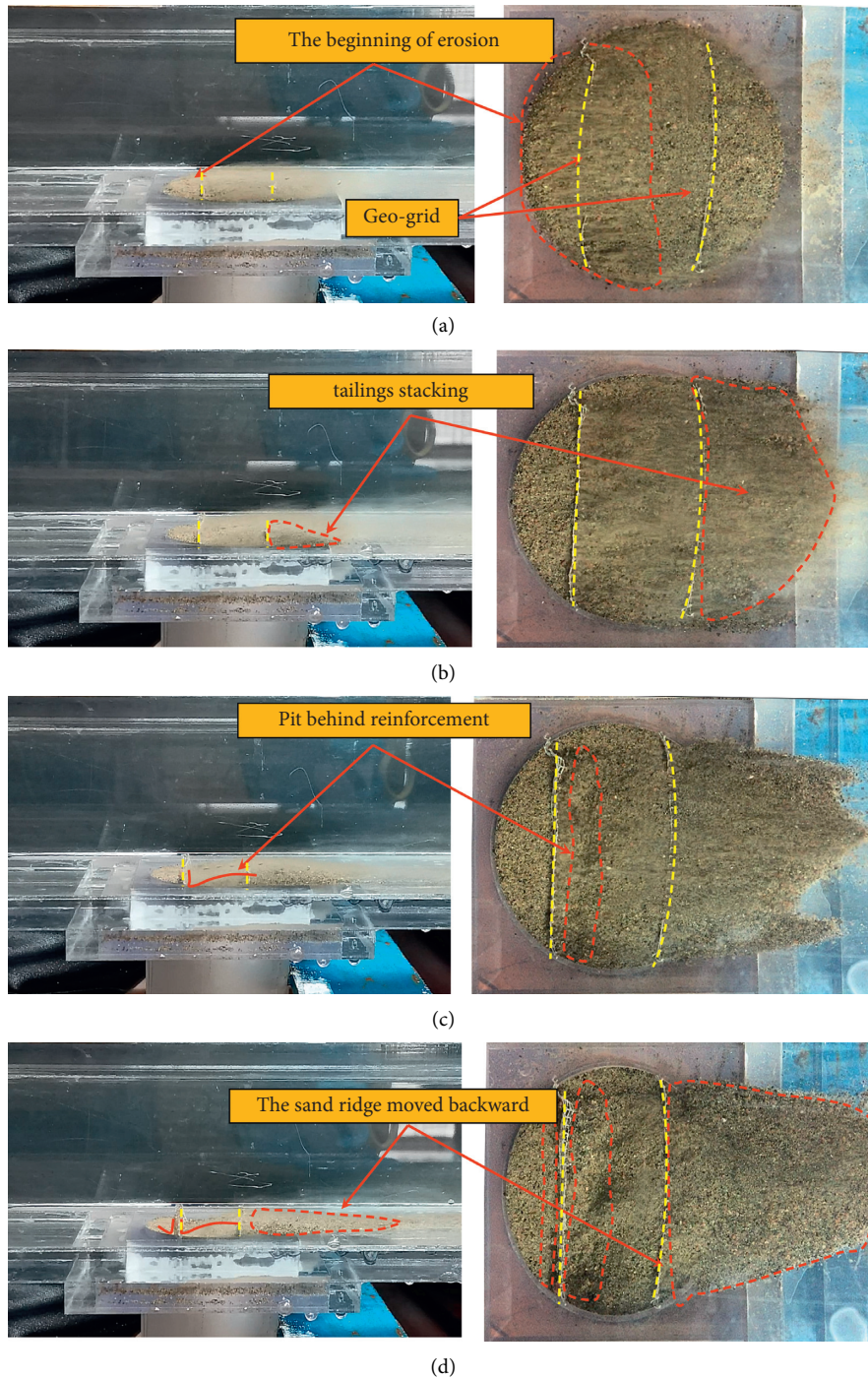
FIGURE 5: Tailings erosion phenomena with different geogrid spacing. (a) The front end of the sample begins to erode. (b) The front end of the sample is flushed, and the tailings behind the second layer of reinforcement are stacked. (c) Concavity of tailings behind the first layer of the band. (d) Backward movement of tailings ridge behind the second layer.

that when the reinforcement spacing is 1.0 cm, the corrosion rate of the reinforced tailings Sample 2 is 0.025 mm/s, while when the reinforcement spacing is 2.5 cm, the erosion rate of reinforced tailings is 0.058 mm/s. Therefore, it can be seen that the closer the reinforcements are, the smaller the erosion rate is. The main reason is that the existence of the reinforcement slows down the corrosion rate of the tailings sample. Based on the theory of quasicohesive reinforcement

of geogrid, it can be concluded that the effect of adding of geogrid will increase the pseudocohesive force c_1 of tailings, which can enhance the antiscour performance of the sample. However, with the increase of the reinforcement spacing of reinforced tailings, the pseudocohesive force of geogrid decreases gradually. It is shown that the reinforcement range of the geogrid is limited when it is used in the tailings. Therefore, only the particles near the reinforcement will be
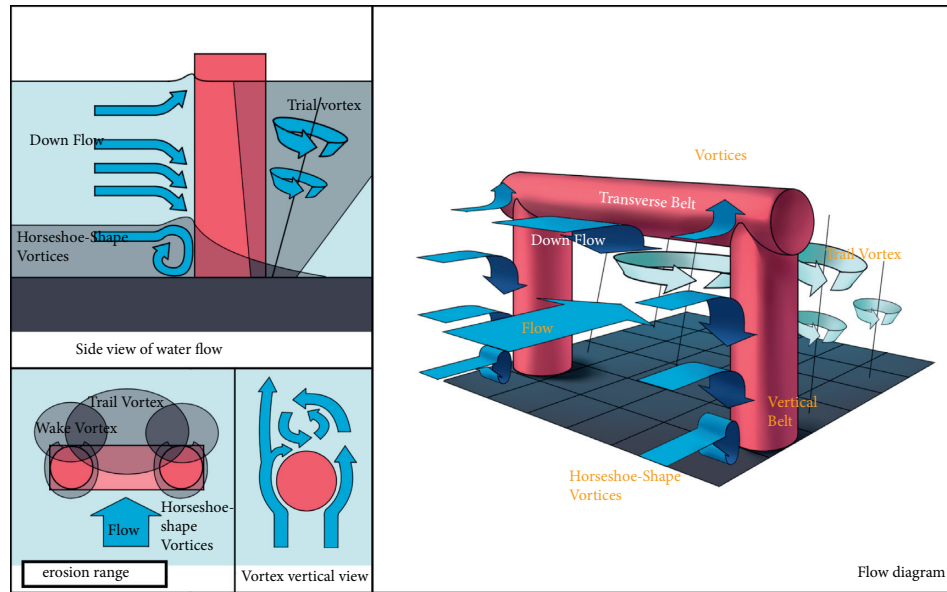
FIGURE 6: The flow structure at the geogrid.

TABLE 2: Experimental data of tailings erosion with the reinforcement spacing of 2.5 cm.

Geospacing d (cm)	Sample number	Flow rate Q (m³/h)	Flow velocity U(m/s)	Erosion time t (s)	Erosion height h (mm)	Erosion rate E (mm/s)
	1	12.1	0.840	120	7.4	0.062
	2	3.8	0.264	120	7.0	0.058
	3	3.8	0.264	120	5.8	0.048
2.5	4	3.8	0.264	120	8.0	0.067
	5	3.8	0.264	120	8.5	0.071
	6	3.8	0.264	120	9.0	0.075
	7	3.8	0.264	120	6.8	0.057
	8	3.8	0.264	120	6.5	0.054

TABLE 3: Experimental data of tailings erosion with the reinforcement spacing of 1.7 cm.

Geospacing d (cm)	Sample number	Flow rate Q (m³/h)	Flow velocity U (m/s)	Erosion time T (s)	Erosion height h (mm)	Erosion rate E (mm/s)
	1	12.1	0.840	120	6.2	0.052
	2	3.8	0.264	120	5.7	0.048
	3	3.8	0.264	120	5.0	0.042
1.7	4	3.8	0.264	120	6.3	0.053
	5	3.8	0.264	120	7.0	0.058
	6	3.8	0.264	120	6.5	0.054
	7	3.8	0.264	120	5.3	0.044
	8	3.8	0.264	120	5.2	0.043

TABLE 4: Experimental data of tailings erosion with the reinforcement spacing of 1.3 cm.

Geospacing d (cm)	Sample number	Flow rate Q (m³/h)	Flow velocity U (m/s)	Erosion time t (s)	Erosion height h (mm)	Erosion rate E (mm/s)
	1	12.1	0.840	120	4.7	0.039
	2	3.8	0.264	120	4.5	0.038
	3	3.8	0.264	120	3.7	0.031
1.3	4	3.8	0.264	120	5.0	0.042
	5	3.8	0.264	120	5.8	0.048
	6	3.8	0.264	120	6.0	0.050
	7	3.8	0.264	120	4.2	0.035
	8	3.8	0.264	120	4.0	0.033

TABLE 5: Experimental data of tailings erosion with the reinforcement spacing of 1.0 cm.

Geospacing d (cm)	Sample number	Flow rate Q (m³/h)	Flow velocity U (m/s)	Erosion time t (s)	Erosion height h (mm)	Erosion rate E (mm/s)
1.0	1	12.1	0.840	120	3.2	0.027
	2	3.8	0.264	120	3.0	0.025
	3	3.8	0.264	120	1.8	0.015
	4	3.8	0.264	120	3.9	0.033
	5	3.8	0.264	120	4.5	0.038
	6	3.8	0.264	120	5.0	0.042
	7	3.8	0.264	120	2.8	0.023
	8	3.8	0.264	120	2.5	0.021
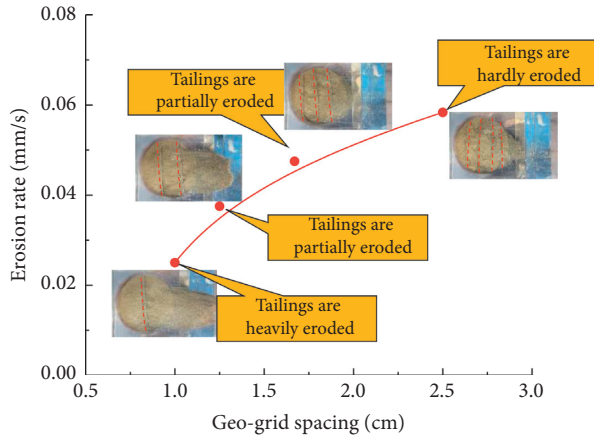
FIGURE 7: Relationship between erosion rate and geogrid spacing.

strengthened, with the antiscour performance improved. In summary, the reduction of the reinforcement spacing in tailings can improve the antiscouring ability, which reduces the water flow erosion on tailings and overtopping.

4. Prediction Model of Hydraulic Erosion Rate of Reinforced Tailings

4.1. Establishment of Erosion Rate Based on Erosion Test. Liu [28] introduced the concept of geogrid coefficient $f(d)$ and established the calculation formula of incipient motion velocity of reinforced tailings particles. Then, through the test data of incipient motion velocity of reinforced tailings, the specific expression of geogrid coefficient $f(d)$ is fitted. Finally, the calculation formula of incipient motion velocity of tailings particle reinforcement is established. V'_c is shown in the formula:

$$V_c^{'} = \left(1 + e^{(-d/0.73)}\right) \cdot V_c, \tag{1}$$

where V_c is the incipient motion velocity of tailings.

$$\frac{V_c}{\sqrt{\gamma_s - \gamma/\gamma g \ D} (R/D)^{1/6}} = 0.0035 \left(\frac{\mathrm{NR}^{1/6}}{\sqrt{g} \ n\mathrm{Re_{vd}}}\right)^2 + 1.5. \tag{2}$$

In the formula, N is a constant, usually 11.6; R is the hydraulic radius; $R = ab/2(a + b)$, where a and b are the height and width of rectangular pipes; n is roughness; $\mathrm{Re_{vd}}$ is the starting Reynolds number of sediment; γ_s is sediment

bulk density; γ is the bulk density of water; D is sediment particle size.

Li [11] and Kandiah [20] obtained the nonlinear relationship between the sediment erosion and relative residual shear stress through the silt scouring test. The physical and chemical characteristic index l was proposed by the dimensionless method, and the formula of sediment scouring rate was established:

$$E = M\left(\frac{\tau_b}{\tau_c} - 1\right)^l. \tag{3}$$

In the formula, E is a sediment erosion rate; τ_b is the flow shear stress; τ_c is the critical starting shear stress of tailings; M is a dimensional scouring constant, with the unit of mm/s, which varies with the sediment type and various physicochemical properties; $\tau_b/\tau_c - 1$ represents the relative residual shear stress; the value of index l is related to the properties of the sediment.

To obtain the incipient motion velocity V'_c of the reinforced tailings particles with different geogrid spacing, eight tailings samples were calculated according to (1). The flow velocity U in the erosion rate test data of the reinforced tailings from Tables 2–5 is used to calculate the relative residual shear stress of reinforced tailings under different geogrid spacing according to (3) ($U^2/V_c^{'2} - 1$). Finally, the flow velocity U, the incipient motion velocity V'_c, the relative residual shear stress τ', and the erosion rate E of the reinforced tailings particles are obtained as listed in Table 6, along with the erosion rate of tailings corresponding to relative residual shear stress under different geogrid spacing.

According to the erosion rate of various reinforced tailings spacings, the erosion constant M and physicochemical property index l in the erosion rate (3) of the reinforced tailings are fitted. The erosion rate curve of the reinforced tailings is plotted, as shown in Figure 8. The abscissa represents the relative residual shear stress under different geogrid spacing, and the ordinate represents the erosion rate of the reinforced tailings.

In the fitting process of the erosion rate formulas of different geogrid spacings, since the geogrid spacing has been considered in τ_c, namely V'_c, the erosion constant and physicochemical index in the erosion rate formula will no longer be considered as the functions of geogrid spacing. In summary, the erosion rate formula of the reinforced tailings can be fitted as follows:

TABLE 6: Value of relative residual shear stress τ' and corrosion rate E of reinforced tailings.

Geospacing d(cm)	Sample	U (m/s)	V_c' (m/s)	τ'	E (mm/s)
2.5	1	0.840	0.559	1.001	0.062
	2	0.264	0.187	0.768	0.058
	3	0.264	0.203	0.504	0.048
	4	0.264	0.162	1.356	0.067
	5	0.264	0.160	1.421	0.071
	6	0.264	0.158	1.485	0.075
	7	0.264	0.190	0.718	0.057
	8	0.264	0.192	0.673	0.054
1.7	1	0.840	0.560	0.785	0.052
	2	0.264	0.186	0.585	0.048
	3	0.264	0.201	0.365	0.042
	4	0.264	0.161	1.120	0.053
	5	0.264	0.159	1.194	0.058
	6	0.264	0.160	1.142	0.054
	7	0.264	0.190	0.521	0.044
	8	0.264	0.193	0.474	0.043
1.3	1	0.840	0.561	0.595	0.039
	2	0.264	0.186	0.430	0.038
	3	0.264	0.201	0.226	0.031
	4	0.264	0.162	0.875	0.042
	5	0.264	0.160	0.928	0.048
	6	0.264	0.159	0.957	0.050
	7	0.264	0.191	0.360	0.035
	8	0.264	0.192	0.347	0.033
1.0	1	0.840	0.698	0.450	0.027
	2	0.264	0.234	0.269	0.025
	3	0.264	0.253	0.089	0.015
	4	0.264	0.205	0.653	0.033
	5	0.264	0.199	0.753	0.038
	6	0.264	0.199	0.757	0.042
	7	0.264	0.237	0.238	0.023
	8	0.264	0.243	0.181	0.021

$$E = 0.056 \, (U^2/V_c'^2 - 1)^{0.503}$$
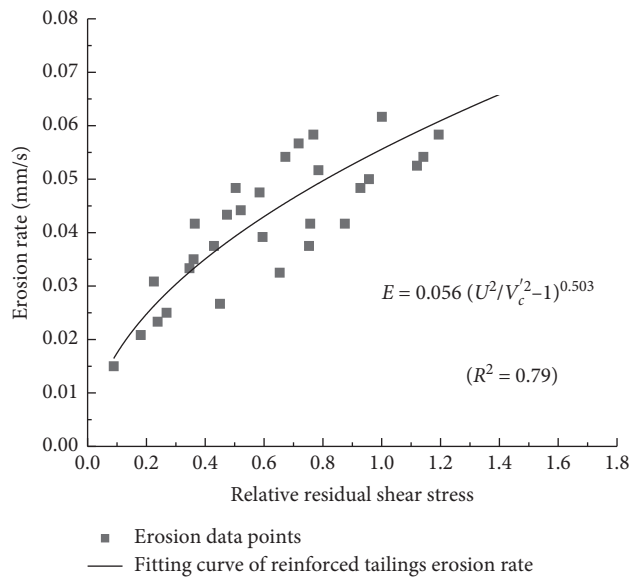
$$(R^2 = 0.79)$$

FIGURE 8: Relationship between erosion rate of reinforced tailings and relative residual shear stress.

$$E = 0.056 \left(\frac{U^2}{V_c'^2} - 1 \right)^{0.503} \left(R^2 = 0.79 \right). \tag{4}$$

Equation (4) is a formula for calculating the erosion rate of reinforced tailings selected near the geogrid d_x. However, it is not considered that the actual reinforced tailings pond will collapse in the whole process of overtopping. When establishing a hydraulic erosion rate model for reinforced tailings dam, the formula of reinforced tailings erosion rate needs to be further modified through the overtopping erosion test of the reinforced tailings dam.

4.2. Correction of Collapse Coefficient Based on Overtopping Test.

To modify the formula of erosion rate of the reinforced tailings, the overtopping erosion test of reinforced tailings dam with different geogrid spacing is carried out to obtain the overtopping erosion amount. The experimental value of the erosion amount is compared with the calculated value of (4), and the collapse coefficient is introduced to modify (4). The overtopping erosion test of the reinforced tailings dam adopts the simulation test bench of tailings dam failure designed by the authors, which mainly includes water supply system, tailings dam test groove, and dam failure monitoring system. The test tank is made of acrylic material, with the length, width, and height of 50, 30, and 30 cm, respectively.

Taking into account the size of the test platform, the size of the reinforced tailings dam overtopping erosion test is $48 \, \text{cm} \times 30 \, \text{cm} \times 24 \, \text{cm}$ (length × width × height); the slope ratio of the model is 1 : 1.5; the slope ratio of the inner slope is 1 : 2.0; and the slope top height is 24 cm. In this study, a total of five groups of overtopping dam failure tests of reinforced tailings reservoirs with geogrid spacings of 3.0, 4.0, 4.5, 6.0, and 7.5 cm (i.e. the number of geogrid layers is 6, 5, 4, 3, and 2) are designed. The test illustration of the reinforced tailings dam with the geogrid spacing of 6.0 cm is shown in Figure 9.

① Samples with 15% moisture content are prepared as required and sealed for 12 h

② The layered compaction method is adopted to compact the samples, with the thickness of 6 cm and the compaction degree of 90%

③ The reinforced strip is laid according to the spacing of 3.0, 4.0, 4.5, 6.0, and 7.5 cm, respectively, by using a glass fiber screen window

4.2.1. Steps of Reinforced Tailings Dam Overtopping Erosion Test

① It is standstill after the water injection height of the tailings dam reaches 6 cm through the water supply system, so that the reservoir water infiltrates into the dam body. And water is injected into the reservoir again to keep the water level unchanged; then, the flood dam test is started.

② The color foam balls are put into the tailings dam as a tracking point, and the high-resolution camera is used
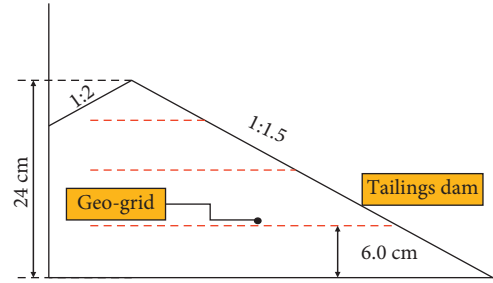
FIGURE 9: Illustration of geogrid arrangement with 6.0 cm spacing.

to capture the motion of the foam ball frame by frame to calculate the overtopping flow velocity.

③ Control flow rate at 22.73 cm³/s for 4 min, collect eroded tailings to sedimentation, and dry and determine their quality.

4.2.2. The Phenomenon of the Overtopping Erosion Test in the Reinforced Tailings Pond.

The erosion failure process of the dam embankment is described as follows: after 4 min overtopping of the reinforced tailings dam, erosion failure with different degrees of gully, width, and depth of breach has appeared on the surface of the dam embankment, as shown in Figure 10.

From Figure 10, it can be seen, in the progressive erosion and failure process of the reinforced tailings dam overtopping, with the decrease of geogrid spacing, the width of gully formed on the surface of the dam body is gradually reduced, and the dam collapses disappear progressively. It can be seen that the geogrid can effectively reduce the erosion and failure of the tailings dam when the flood is overtopping.

4.2.3. Correction of Collapse Coefficient Based on Macro-Overtopping Test.

In the process of overtopping erosion of the reinforced tailings dam, the dam will collapse due to its gravity under the action of water flow. Therefore, the collapse coefficient $K(d)$ is introduced into the erosion rate formula, i.e., (4), of the reinforced tailings, where d is the geogrid spacing. The modified hydraulic erosion rate model of the reinforced tailings dam is

$$E = K(d) \cdot 0.056 \left(\frac{U^2}{V_c'^2} - 1 \right)^{0.503}. \tag{5}$$

By collecting, drying, and weighing the overtopping erosion amount of the five groups of reinforced tailings dams, the erosion amounts of the reinforced tailings with the geogrid spacing of 3.0, 4.0, 4.5, 6.0, and 7.5 cm are obtained, with the unit of g. Because the unit of the fitting formula of the reinforced tailings erosion rate is mm/s, considering the difference of erosion units, the erosion rate formula is multiplied by the slope area of the dam body to obtain the calculated value of the erosion amount formula in g. In addition, the ratio of erosion amount is the ratio of erosion rate, so the collapse coefficient $K(d)$ can be calculated by the percentage of the overtopping test erosion to calculate
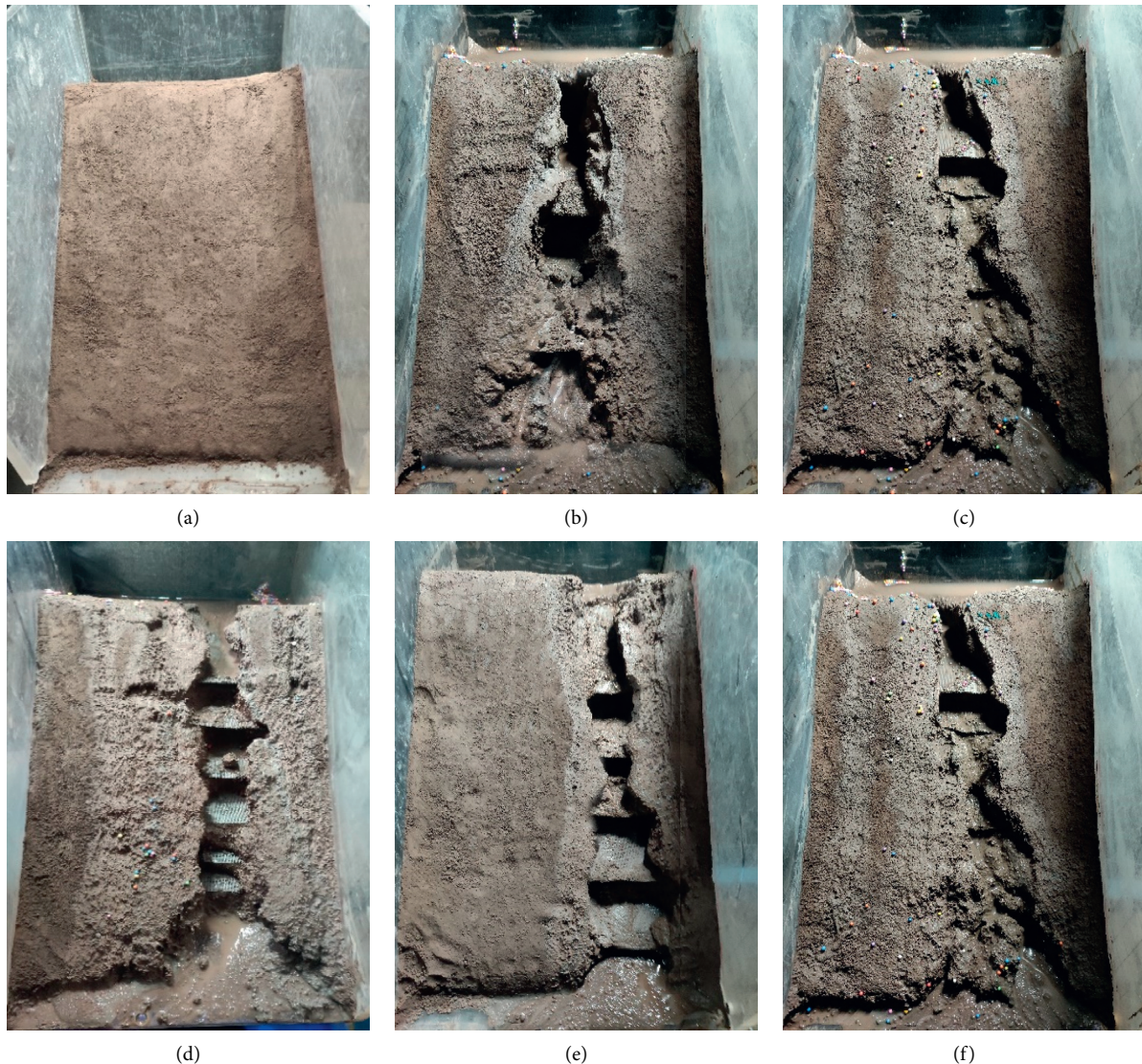
FIGURE 10: Diagrams of reinforced tailings dam failure. (a) Front of reinforced tailings. (b) $d = 7.5$ cm. (c) $d = 6.0$ cm. (d) $d = 4.5$ cm. (e) $d = 4.0$ cm. (f) $d = 3.0$ cm.

erosion from the formula. The values of flow Q, erosion time t, overtopping erosion amount, and collapse coefficient $K(d)$ are listed in Table 7.

Erosion is calculated by the formula of overtopping erosion and erosion rate of the reinforced tailings dam, as shown in Figure 11. It can be seen from Figure 11 that the calculated value of the erosion rate formula of the reinforced tailings is close to that of the reinforced tailings dam when the geogrid spacing is small (the spacing is 3.0~4.5 cm). When the geogrid spacing is larger (spacing >4.5 cm), the erosion caused by the overtopping of the reinforced tailings dam is greater than the calculated value of the erosion rate formula. When the spacing between the reinforcing bars is large, the reinforcing bars' effect only acts near the reinforcing bars of the tailings dam. There is a specific range of influence, so there still will be a small amount of collapse.

From Table 7, it can be seen that the collapse coefficient $K(d)$ is greater than 1 at different geogrid spacings. When the geogrid spacing is less than 4.5 cm, that is, when the geogrid spacing is small, the overtopping erosion of the reinforced tailings reservoir is close to the calculated value of (4). The reinforced tailings pond can be approximately regarded as no collapse occurred during the whole process of overtopping erosion, and the collapse coefficient is close to 1, which is consistent with the phenomenon of the overtopping erosion test of the tailings pond with the geogrid spacing of 3.0~4.5 cm. Figure 12 is fitted by collapse factor $K(d)$ and geogrid distance d.

When the spacing d is less than or equal to 4.5 cm, the collapse coefficient $K(d)$ is close to 1, so when the spacing d is less than 4.5 cm, the collapse coefficient $K(d) = 1$. Linear fitting of the collapse coefficient $K(d)$ and the geogrid spacing d is adopted when geogrid spacing d is greater than

TABLE 7: Erosion amount of the overtopping test of the reinforced tailings pond.

Geospacing d(cm)	Flow rate Q (cm^3/s)	Erosion time t (s)	Erosion amount (g)	Formula calculation value (g)	Error percentage	Collapse coefficient $K(d)$
3.0	22.73	240	653	621	4.92	1.05
4.0	22.73	240	731	724	0.98	1.01
4.5	22.73	240	812	802	1.29	1.01
6.0	22.73	240	998	842	15.59	1.18
7.5	22.73	240	1191	843	29.18	1.41
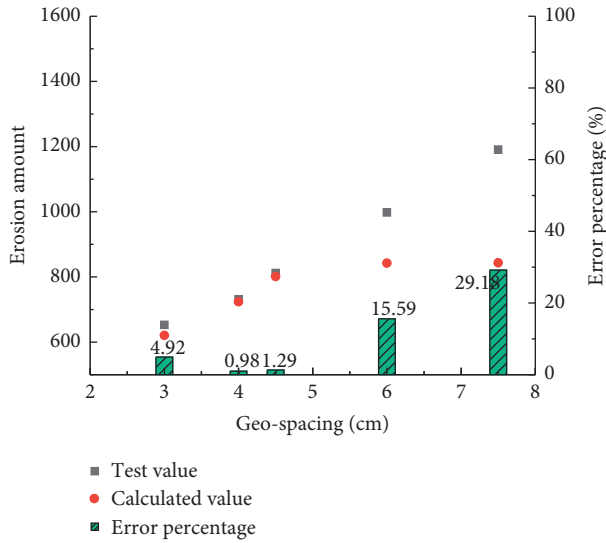
FIGURE 11: Comparison of calculated and measured erosion amounts of reinforced tailings.
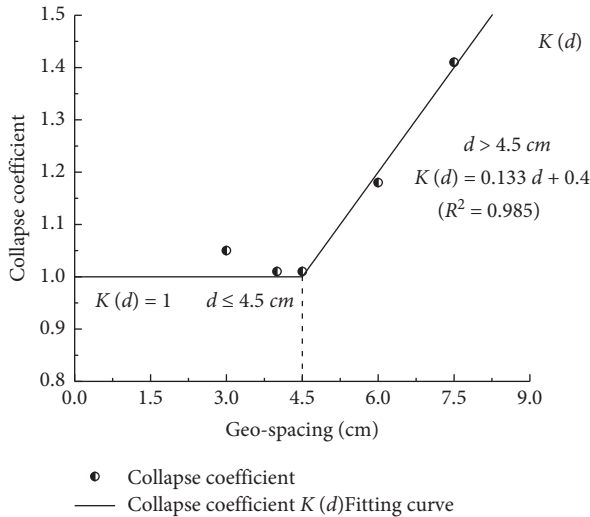
FIGURE 12: Fitting diagrams of collapse coefficient $K(d)$.

4.5 cm, and the collapse coefficient $K(d)$ is expressed by formula (6).

By substituting the collapse coefficient $K(d)$ in (6) into the reinforced tailings erosion rate of (4), the hydraulic erosion rate equation of the reinforced tailings considering collapse factors can be obtained:

$$K(d) = \begin{cases} d \cdot \left(0.133 \text{ cm}^{-1}\right) + 0.4, & d > 4.5 \text{ cm } \left(R^2 = 0.985\right) \\ 1, & d \leq 4.5 \text{ cm} \end{cases},$$

(6)

$$E = \begin{cases} 0.056\,(0.133\,d + 0.4) \cdot \left(\dfrac{U^2}{V_c'^2} - 1\right)^{0.503}, & d > 4.5 \text{ cm} \\ 0.056\left(\dfrac{U^2}{V_c'^2} - 1\right)^{0.503}, & d \leq 4.5 \text{ cm} \end{cases}$$

(7)

5. Conclusions

In this paper, the influence of geogrid spacing on the erosion rate of reinforced tailings is analyzed through a series of erosion and overtopping tests. Based on the existing erosion rate formula, the effects of the erosion constant and physicochemical property index on the erosion rate are considered. The following conclusions can be drawn:

(1) The hydraulic erosion test of tailings with different geogrid spacing (1.0, 1.3, 1.7, 2.5 cm) was carried out by self-made reinforced tailings hydraulic erosion test device. It was found that with the decrease of geogrid spacing, the erosion rate of reinforced tailings particles is gradually reduced. The test results show a positive correlation between the reinforcement spacing and erosion rate of tailings.

(2) Through the tailings reinforced erosion test, the erosion test data were obtained. By considering the influence of erosion constant and physicochemical property index on the erosion rate, the formula of reinforced erosion rate was obtained by combining with the erosion rate.

(3) Based on the theory of sediment scouring, the scouring constant M in the erosion rate formula was determined as 0.056 mm/s by the reinforced tailings erosion test. They were considering that there was a certain collapse in the process of overtopping erosion of reinforced tailings dam. Overtopping erosion tests of the tailings dam with different geogrid spacing (3.0, 4.0, 4.5, 6.0, 7.5 cm) were carried out. The collapse coefficient $K(d)$ was introduced into the formula of reinforced tailings erosion rate, and the formula of hydraulic erosion rate of the reinforced tailings dam was established. When the geogrid spacing $d \leq 4.5$ cm, the collapse coefficient $K(d) = 1$.

When the geogrid spacing $d > 4.5$ cm, the collapse coefficient $K(d)$ is linearly related to the geogrid spacing d.

Data Availability

The data used to support the findings of this study are available from the corresponding author upon request.

Conflicts of Interest

The authors declare that there are no conflicts of interest.

Acknowledgments

References

[1] G. M. Yu, C. W. Song, Y. Z. Pan, and L. Li, "Review of new progress in tailings dam safety in foreign research and current state with development trent in China," *Chinese Journal of Rock Mechanics and Engineering*, vol. 33, no. S1, pp. 3238–3248, 2014.

[2] V. S. Quaresma, A. C. Bastos, M. D. Leite, and A. Costa, "The effects of a tailings dam failure on the sedimentation of the eastern Brazilian inner shelf," *Continental Shelf Research*, vol. 205, Article ID 104172, 2020.

[3] X. Zheng, X. H. Xu, and K. L. Xu, "Study on the risk assessment of the tailings dam break," *Procedia Engineering*, vol. 26, pp. 2261–2269, 2011.

[4] J. R. Owen, D. Kemp, É. Lèbre, and K. Svobodova, "Catastrophic tailings dam failures and disaster risk disclosure," *International journal of disaster risk reduction*, vol. 42, Article ID 101361, 2020.

[5] M. Rico, G. Benito, A. R. Salgueiro, A. Díez-Herrero, and H. G. Pereira, "Reported tailings dam failures," *Journal of Hazardous Materials*, vol. 152, no. 2, pp. 846–852, 2008.

[6] X. S. Li, K. Peng, J. Peng, and D. Hou, "Effect of thermal damage on mechanical behavior of a finegrained sandstone," *Arabian Journal of Geosciences*, vol. 14, no. 1212, 2021.

[7] E. Sun, X. Zhang, Z. Li, and Y. Wang, "Tailings dam flood overtopping failure evolution pattern," *Procedia Engineering*, vol. 28, no. 8, pp. 356–362, 2012.

[8] X. Z. Dang, M. S. Gao, L. T. Zhang, X. Wang, and S. Zhang, "Experimental study on the model of flood overtopping and dam break of a tailing pond under different deposit compactness," *Marine Geology Frontiers*, vol. 34, no. 9, pp. 79–84, 2018.

[9] G. J. Wang, Y. J. Tang, C. Du, and X. Kong, "Experimental study on dam break under water level variation in reservoir," *Journal of Sedimentary Research*, vol. 43, no. 4, pp. 67–73, 2018.

[10] X. K. Zhang, E. J. Sun, and Z. X. Li, "Experimental study on evolution law of tailings dam flood overtopping," *China Safety Science Journal*, vol. 21, no. 7, pp. 118–124, 2011.

[11] H. G. Li, *Study on the Influence of Rainfall Factors on Tailings Dam Break and its Safety Warning Technology*, PhD thesis, University Of Science & Technology Beijing, Beijing, China, 2017.

[12] X. Li, *Experimental Study on Rainfall Induced Collapse of Tailings Pond*, Kunming University of Science and Technology, Kunming, China, 2015.

[13] J. B. Zhao, J. Li, X. H. Bai, C. Miao, and J. Zhang, "Influence of particle orientation on the performance of geogrid reinforced ballast," *Advances in Materials Science and Engineering*, vol. 2020, Article ID 6758059, 12 pages, 2020.

[14] J. Zhang, Z. Y. Zhao, and Z. J. Sun, "Study on long-term performance of geogrid-reinforced and pile-supported embankment at bridge approach," *Advances in Materials Science and Engineering*, vol. 2021, Article ID 5567391, 11 pages, 2021.

[15] X. F. Jing, X. Zhou, Y. S. Zhao, K. Liu, C. Ye, and C. Pan, "Study on influence of reinforcement density on overtopping failure of tailings dam," *Journal of Safety Science and Technology*, vol. 12, no. 8, pp. 68–74, 2016.

[16] X. Zhou, *Study on the Over-topping Evolution Law and Disaster Consequences of Reinforcement Tailings Dam*, Chongqing University of Science and Technology, Chongqing, China, 2016.

[17] L. Zhao, C. Huang, and F. Wu, "Effect of microrelief on water erosion and their changes during rainfall," *Earth Surface Processes and Landforms*, vol. 41, no. 5, pp. 579–586, 2015.

[18] J.-L. Briaud, "Case histories in soil and rock erosion: woodrow wilson bridge, brazos river meander, normandy cliffs, and new orleans levees," *Journal of Geotechnical and Geoenvironmental Engineering*, vol. 134, no. 10, pp. 1425–1447, 2008.

[19] Z. Y. Wang and Y. S. Wu, "A preliminary study on sediment-removing capacity and river motion dynamics," *Journal of Hydraulic Engineering*, vol. 3, pp. 6–11, 2002.

[20] A. Kandiah, *Fundamental Aspects of Surface Erosion of Cohesive Soils*, PhD thesis, University of California, Davis, Calif, 1975.

[21] Q. Zhang, Y. Wang, and C. B. Chen, "Experiment on incipient motion and scour features of artificial filling clay," *Advances in Science and Technology of Water Resources*, vol. 32, no. 6, pp. 75–78, 2012.

[22] A. M. Osman and C. R. Thorne, "Riverbank stability analysis. I: theory," *Journal of Hydraulic Engineering*, vol. 114, no. 2, pp. 134–150, 1988.

[23] R. B. Krone, "Effects of bed structure on erosion of cohesive sediments," *Journal of Hydraulic Engineering*, vol. 125, no. 12, pp. 1297–1301, 1999.

[24] L. P. Sanford and J. P.-Y. Maa, "A unified erosion formulation for fine sediments," *Marine Geology*, vol. 179, no. 1-2, pp. 9–23, 2001.

[25] H. G. Li, M. Q. Yuan, and X. Q. Zhang, "Study on Critical motion and erosion of cohesive sediment," *Journal of Waterway and Harbor*, vol. 3, pp. 20–26, 1995.

[26] J. X. Tang, G. Z. Yin, Z. A. Wei et al., "Model test study about fine grained tailings dam of longdu tailings pone," *China Mining Magazine*, vol. 13, no. 1, pp. 54–56, 2004.

[27] Y. L. Zhou and Y. L. Wang, "Forecast of the bridge local scour depth," *Journal of Xi'an Highway University*, vol. 19, no. 4, pp. 48–50, 1999.

[28] K. H. Liu, H. Cai, X. F. Jing et al., "Study on hydraulic incipient motion model of reinforced tailings," *Water*, vol. 13, no. 15, 2021.

[29] H. A. Einstein, "Formulas for the transportation of bed load," *Transactions of the American Society of Civil Engineers*, vol. 107, no. 1, pp. 561–577, 1942.

[30] Å. Sundborg, "The river Klarälven a study of fluvial processes," *Geografiska Annaler*, vol. 38, no. 2-3, pp. 125–316, 1956.

[31] R. A. Kuhnle, "Incipient motion of sand-gravel sediment mixtures," *Journal of Hydraulic Engineering*, vol. 119, no. 12, pp. 1400–1415, 1993.

[32] H. W. Zhang, "A unified formula for incipient velocity of sediment," *Journal of Hydraulic Engineering*, vol. 43, no. 12, pp. 1387–1396, 2012.

[33] B. R. Li, "Calculation method of threshold velocity of sediment," *Journal of Sedimentary Research*, vol. 1, pp. 73–79, 1959.

[34] R. R. Cai, L. H. Zhang, and H. W. Zhang, "Modifications to Li Baoru's sediment incipient velocity formula," *Journal of Hydraulic Engineering*, vol. 50, no. 5, pp. 547–554, 2019.

Research Article

Research on the Energy-Saving Design Path of Rural Farmhouses under the Background of Ecological Livability

Jingyuan Shi[1] and Qiuna Li [ID][2]

[1]*College of Architecture and Urban Planning of Chongqing, Jiaotong University, Yuzhong District, Chongqing 400074, China*
[2]*Chongqing College of Architecture and Technology, Shapingba District, Chongqing 401331, China*

Correspondence should be addressed to Qiuna Li; 990201900031@cqjtu.edu.cn

Different from the state of large-scale energy use and concentrated energy conservation in urban areas, the state of energy use and energy conservation in rural areas has its own characteristics and typical problems. Rural areas have been concentrated on the multiple differences in economic, social, and construction characteristics such as mountain and peace dam topography, natural and artificial construction, developed and underdeveloped, rapid urban development, and relatively backward rural development. It has practical problems that need to be solved urgently, such as the "insufficient savings" in the construction of farmhouses and the "insufficient open source" of clean energy applications. The discussion will be conducted from three aspects: the planning and layout design of rural houses in Chongqing, the performance of the enclosure structure of rural houses in key seasons, and the application of renewable clean energy in rural houses. Then put forward is the energy-saving design path of Chongqing farmhouse. It aims to improve the indoor and outdoor thermal environment of farmhouses, saving heating energy consumption in winter and air-conditioning energy consumption in summer and effectively benefit users to use renewable energy such as biogas, straw, and solar energy. Finally, explore the adaptability between the design methods of farmhouses and the local characteristics of Chongqing's rural areas. In the work of Chongqing Design Going to the Countryside, we create a contemporary farmhouse case that is not only energy-saving but also has good indoor and outdoor space quality. It also provides a reference for the energy-saving design of farmhouses in Chongqing and other regions in China.

1. Introduction

The farmhouse is the basic unit of rural residential environment and is the daily living space for rural residents to rest and prepare for work. Its construction process has particularity and complexity. It not only contains part of the traditional ecological adaptation wisdom, but also reflects the conflicts between the ecological planning and construction process and the ecological environment. The core problem of rural farmhouses is that the state of planning and construction is still at a relatively low level on the ecological level. It is necessary to carry out appropriate ecological guidance and improvement work in light of the regional characteristics and actual conditions of rural areas.

Compared with the consensus on urban energy consumption, the energy consumption of the rural construction environment is actually not small. Due to the expansion of the construction base and the insufficient energy conservation of the enclosure structure, the rural farmhouses have caused serious energy waste. In 2018, rural residential buildings accounted for 14% of the energy consumption for civil building construction. According to China's Annual Development Research Report on Building Energy Conservation 2020 (Rural Housing Special), the total energy consumption of rural farmhouses in 2020 will reach 311 million tce (Figure 1). Chongqing's natural environment has inherent advantages in ecological resources. And in the process of traditional village construction, the ecological adaptability of the mountain environment will be considered
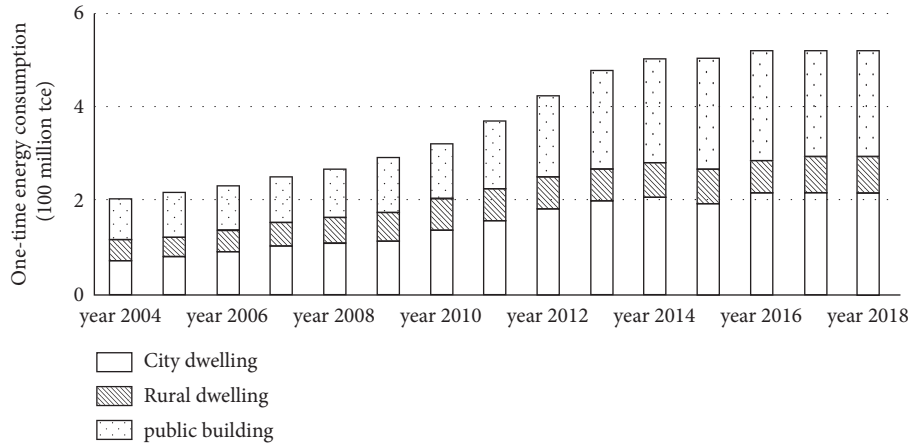
FIGURE 1: China's civil building construction energy consumption (2004–2018). Data source: estimated by the Building Energy Research Center of Tsinghua University.

spontaneously. However, in recent years, there has been a lack of ecological awareness in the process of rural planning and construction in Chongqing. The closedness of rural farmhouses is generally weak. Its energy-saving effect and thermal comfort are obviously different from those of urban houses. Take power consumption as an example. The electricity consumption per unit construction area in rural areas in Chongqing is 27.7 kW·h/m². It is significantly higher than the average electricity consumption level of 17.6 kW·h/m² for urban residential buildings in the Yangtze River Basin. In addition, energy utilization is insufficient, and clean energy utilization is insufficient. These are all typical problems in Chongqing's farmhouses [1, 2].

In recent years, the research on energy conservation of rural residential buildings in China has been focused on the life cycle analysis of rural residential energy consumption (Li Rong, 2006); the energy consumption status and optimization strategy of Henan rural housing (Lumeijun, Zhangshaowei, 2010); analysis of the influence of indoor thermal environment and energy consumption on rural residential buildings in cold areas (Donghailong, 2010); the indoor thermal environment index of rural residential buildings in Northwest China in winter (Zhuyiyun, Liujiaping, 2010); the three directions of applying ecological energy-saving technology in rural houses in Chongqing include optimization of building envelope structure, building partition and indoor environment, and improvement of energy-saving of ecological building equipment to rural houses (Guanjian, 2017); and the application of biomass energy and solar energy resources is the basis of rural renewable energy technology. The application possibility of solar water heater, solar stove, and biomass energy heating furnace technology is proposed (through investigation and monitoring of biogas project in some rural areas of Chongqing, the paper puts forward the cooking lighting mode suitable for scattered farming of farmers and hot water heating mode suitable for centralized cultivation of residential areas). Based on previous research, this paper proposes innovative research focusing on rural areas of Chongqing, further discovering the scientific problems of

energy use and saving of rural housing and summarizing the possible path of energy conservation of agricultural houses from the perspective of architectural design [3, 4].

2. Energy Problems in Chongqing's Farmhouses

2.1. Insufficient Throttling—Energy-Saving Problem of Farmhouse Construction. The planning, design, and construction of urban residential buildings in Chongqing are in compliance with relevant energy-saving standards. And by improving the energy saving efficiency of air-conditioning, refrigeration, heating, and heating equipment, reduce all kinds of energy consumption in the operation of air-conditioning, lighting, hot water, and other equipment. At the same time, insufficient attention has been paid to energy conservation in the planning and construction of rural farmhouses. In the mid-1980s, rural areas in Chongqing began to be electrified, and electrical appliances such as lighting fixtures entered farmhouses. In recent years, with the improvement of villagers' living standards, high-power household appliances have become popular. According to statistics, in 2017, on average, one in two households in Chongqing rural areas used air conditioners and water heaters. The fan usage rate is as high as 90%. In the survey of villages such as Zhongliang Town in Shapingba District, Yudong Town in Banan District, and Luohuang Town in Jiangjin District, it was found that every household had 2 to 4 air conditioners. Some farmers have as many as 6–8. The utilization rate of heating equipment such as electric heaters and water heaters has also continued to increase [5].

Rural houses in Chongqing are mostly brick-concrete structures. There is no energy-saving control in design and construction. This situation is reflected in the fact that the walls and other enclosure structures are basically not treated with thermal insulation and have poor thermal performance. The ratio of the figure coefficient of the farmhouse to the area of the window and wall is too large without control. The air tightness of door and window components such as single-layer ordinary glass windows is poor. No thermal bridge condensation treatment has been performed. Poor indoor

thermal environment in winter and summer leads to high-power consumption of air conditioners and so on. Therefore, only by paying attention to the energy conservation in the planning and construction of rural houses in Chongqing, can the total energy consumption be effectively reduced and energy "saving" can be achieved.

2.2. Insufficient Open Source—The Application of Clean Energy.

The effective use of clean energy such as household biogas, solar energy, and straw can broaden energy sources while saving traditional energy sources such as electricity and realize the "open source" of energy problems in rural areas of Chongqing. The survey found that the clean energy application of Chongqing's farmhouses presents the following problems [6].

2.2.1. Household Biogas Is Difficult to Construct, with Low Efficiency and Simple Application.

Household biogas digesters were once the main content of Chongqing's rural clean energy construction. In 2015, Chongqing has built more than 5,700 biogas project villages, with a total of 1.557 million users. But now the construction of household biogas has cooled down. Except for Wanzhou, Wulong, and other places, many districts and counties no longer even use it. According to the survey, it takes about 10 man-days to complete a household biogas digester. In recent years, most of the young and middle-aged laborers in Chongqing's rural areas have gone out to work, and left-behind farmers are unable to build pools. In terms of cost, Chongqing's rural areas are mostly in typical mountainous areas with many mountains and steep slopes. The transportation is inconvenient and the economy is relatively backward. Some farmers and farms gave up building ponds due to financial difficulties. In addition, there are problems: the biogas application system is not perfect, the efficiency of biogas production is low, the development of centralized biogas is slow, the operation of follow-up service outlets is weak, the responsible organization is lacking, and the management work is difficult to carry out, the single purpose of biogas which is only used for cooking and lighting, and so on.

2.2.2. Pollution Caused by Straw Burning—Potential Resources Are Not Utilized.

Straw is a common agricultural waste and one of the main energy sources in rural areas of Chongqing. Most of the current disposal measures are used for fuel energy or incineration. However, the thermal efficiency of direct combustion is very low. The emission of a large amount of smoke and ash will make the rural living environment worse. It also causes a series of problems such as waste of resources, damage to farmers' health, and impact on traffic safety. According to incomplete statistics, straw and firewood accounted for 83% of Chongqing's rural energy use. The thermal efficiency of direct combustion is only 10%–20%, being inefficient and uneconomical [7].

2.2.3. Misunderstandings Exist in Solar Energy Applications, and the Types of Applications Are Not Sufficient.

Chongqing has more rainy weather and not enough sunshine. On the surface, there is a misunderstanding that solar technology cannot be used at all. However, during the investigation, it was discovered that there is actually the possibility of solar energy utilization in various districts and counties. For example, rural solar energy applications in Yongchuan District are more common, and more than half of the residents choose to use solar energy equipment. Therefore, the possibility of solar energy application should be sorted out and analyzed according to the regional characteristics of Chongqing. In addition, we need to summarize the different types of solar energy applications and implement suitable equipment such as solar water heaters and solar street lights in suitable areas to effectively use sunshine, an inexhaustible clean energy [8].

2.3. Summary of the Problem.

All the above problems show that the rural houses in Chongqing area exist because of their actual characteristics. It is even more necessary to introduce ecological methods and strategies in planning and construction to truly achieve the ultimate goal of rural ecological livability. Therefore, it is urgent to consider the ecological problems of Chongqing's farmhouses in terms of saving resources, protecting the environment, reducing residential energy consumption, and improving residential comfort, so as to maintain ecological adaptability to the natural environment. The basic attitude of improving the living standards of villagers and optimizing the rural living environment should be followed, guided by ecological thinking, supported by ecological laws, and ecological design as a path to promote the dependence and coordination between people, architecture, and the environment.

The energy-saving design path of the farmhouse is to improve the energy efficiency of the farmhouse. On the premise of ensuring a comfortable living environment for rural residents, plan and guide measures for rational utilization and effective energy saving. Different from the state of large-scale and concentrated energy use in urban areas, the state of energy use and energy conservation in rural areas has its own characteristics and typical problems. Based on the actual situation, the energy utilization links involved in rural farmhouses in Chongqing are mainly embodied in three aspects: overall layout planning of farmhouses; the performance of the enclosure structure of farmhouses in the two key seasons of winter and summer; and the application of renewable clean energy in farmhouses. The specific energy-saving design path can be developed from some key points, for example, the rational layout of the overall planning environment of the farmhouse; the construction process of the farmhouse, especially the optimization and improvement of the enclosure structure; and the suitable application method of rural renewable energy, etc.

3. Energy-Saving Planning of Farmhouses

3.1. The Impact of Wind Direction on Farmhouse Energy Consumption and Reasonable Planning. The summer wind direction has a greater impact on the natural ventilation of farmhouses. Its effective organization can enhance the degree of air convection in the farmhouse and accelerate the heat exchange inside and outside the farmhouse at night. In this way, the purpose of saving energy for air-conditioning is achieved. The direction of the winter wind will bring heat loss to the farmhouse and will also affect the total amount of energy used for heating. Therefore, the reasonable design of the wind direction is very necessary.

The wind direction design mainly includes two aspects: on the one hand, the farmhouse can achieve good ventilation through the reasonable organization of spacing and layout; on the other hand, the direction is conducive to the smooth entry of the summer wind and avoid the invasion of winter wind. Through a good natural ventilation organization, the cooling and heating energy consumption of farmhouses can be effectively reduced [9].

3.2. The Impact of Farmhouse Layout on Energy Consumption and Reasonable Planning. The overall layout of rural farmhouses in Chongqing generally adopts determinant, staggered, oblique, peripheral, and free style. The following principles should be followed in the layout: the layout of the farmhouse community should be conducive to ventilation in summer and shelter from wind in winter. Meet the requirements of sunshine, environmental vision, and hygiene standards through suitable farmhouse spacing. In addition, the layout of farmhouses can also make full use of the surrounding water bodies, greening, and other natural resources to form a microclimate environment with good ecological benefits.

In the design of the plan, elevation, section, doors, and windows of rural farmhouses, consideration should be given to making them conducive to natural ventilation and natural lighting, avoid rain, snow, and wind, and effectively reduce energy consumption. The main rooms should be arranged in the south or south as far as possible. Make full use of the winter sun for heating and avoid direct sunlight in summer. Controlling the room area can effectively save energy for cooling or heating. The exhaust vents of the kitchen and bathroom spaces should be ventilated to avoid backflow and oil fume pollution. Controlling the depth of the daylighting room within 6 meters can effectively save lighting and daylighting energy.

3.3. The Impact of Farmhouse Orientation on Energy Consumption and Reasonable Planning. In winter, compare the same farmhouses. The east-west farmhouses consume about 5.5% more energy than the north-south farmhouses. The heat gained by solar radiation and the heat loss by air penetration through the gaps between doors and windows are also related to the orientation of the building. Therefore, in order to reduce building energy consumption in winter, the orientation of farmhouses should be north-south or close to north-south. The main facade should avoid the prevailing wind direction in winter. In summer, air-conditioning energy consumption is closely related to factors such as the orientation of farmhouses and the heat gain from solar radiation. Research data shows that when the window-to-wall area ratio of a farmhouse is 30%, the air-conditioning load of the east-west room is 24% to 26% larger than that of the south-facing room. Therefore, east-west air-conditioned rooms should be avoided as much as possible in the layout design of farmhouses to promote effective energy conservation [10].

3.4. The Impact of Natural Ventilation on Energy Consumption and Reasonable Planning. In spring and autumn, the effective use of natural ventilation can save equipment energy and improve the thermal comfort environment in the farmhouse. At night in summer, the effective organization of natural ventilation can introduce cold outside air. On the one hand, it reduces the cooling energy consumption inside the farmhouse at night, and on the other hand, it can also avoid excessive heat storage on the walls and roof, creating conditions for a cool indoor environment during the next day.

3.5. The Impact of Greening the Environment on Energy Consumption and Reasonable Planning. In Chongqing, summer temperatures are high, humidity is high, wind speed is low, and the climate is muggy. Comprehensive heat protection planning measures should be adopted for farmhouses, including the strengthening of the envelope structure, especially the thermal insulation effect of the roof and the west facade. Ensure the natural ventilation of the room. And do a good job of window shading. Practice has shown that suitable planning and layout of green landscape can effectively improve the thermal environment and reduce the impact of outdoor heat on farmhouses. The general greening landscape of farmhouses mainly includes two categories: courtyard greening and wall greening (Figure 2) [11].

The greening of the courtyard can effectively heat insulation. First, trees absorb solar radiant heat and absorb water from the roots to evaporate through the leaves, thereby reducing the air temperature. Secondly, lush trees have a good shading effect in summer. According to statistics, it can block 50%–90% of solar radiant heat. At the same time, because the ground is shady, the heat radiated from the ground to the farmhouse is also reduced. Therefore, the surface temperature and indoor temperature of the farmhouse shaded by trees will decrease. Thirdly, trees also have the function of guiding and blocking the wind. Proper planting can effectively improve the indoor and outdoor thermal environment.

In terms of wall greening, Chongqing is suitable for planting wall climbing plants such as creeper and ivy. In addition, climbing plants such as grapes, melons, beans, morning glory, wisteria, firecrackers, or coral vines are also suitable for planting. These plants grow luxuriantly in summer and are used to block solar radiation and absorb solar heat. In winter, plants will shed their leaves and will not prevent the farmhouse from receiving sunlight. Set up a
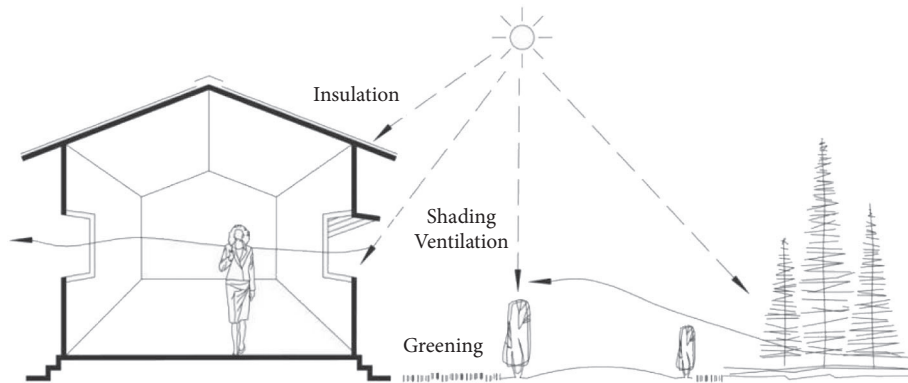
FIGURE 2: Schematic diagram of comprehensive heat protection planning for farmhouses. Chart source: the authors, organized according to relevant data.

scaffold in front of the door, window, or balcony of the farmhouse, so that the climbing plants can grow on the frame, which can form a baffle or horizontal shading. According to statistics, this method of shading can reduce the temperature of the outer surface of the wall by 4-5 degrees Celsius in the summer season. The indoor temperature can also be reduced by about 1 degree Celsius [12].

4. Energy-Saving Design of Farmhouses Adapted to the Season

The energy-saving design of the residential environment of Chongqing's farmhouses uses more energy-efficient materials and electrical equipment in the design of farmhouses to improve the thermal insulation performance of the envelope structure and the energy efficiency ratio of heating and air-conditioning equipment. In this way, the energy consumption of heating, cooling, lighting, and other aspects in the use of farmhouses can be reduced. Ultimately improve energy efficiency. Summer is generally hotter in rural areas of Chongqing. In winter, the indoor temperature is low, and energy consumption mainly occurs in these two periods. Therefore, the guiding design of heating and heat preservation in winter and cooling and heat insulation in summer are the core tasks of the energy-saving planning and design of the residential environment of rural houses in Chongqing.

4.1. Energy-Saving in the Residential Environment of Farmhouses in Winter. The rural areas of Chongqing cover hot summers and cold winters, hot summers and warm winters, and mild areas. It is a nonuniform heating area. In winter, rural farmhouses often use the combined effect of household heating equipment such as electric heaters, other heat-receiving equipment, and envelope structure to keep the indoor environment at a suitable temperature. Due to the objective existence of indoor and outdoor temperature differences, heat will inevitably flow from a higher-temperature indoor environment to a lower-temperature outdoor environment, and heat loss will occur through structural parts such as doors, windows, and enclosure structures.

In winter, the overall gains and losses of the farmhouse living environment have a relatively stable structure. When the total gain and loss of the indoor environment of the farmhouse reach a balance, the room temperature can be maintained. Therefore, the main way to save heating energy consumption in farmhouses in winter is to reduce the overall external surface area of farmhouses as much as possible. Improve the thermal insulation performance and air tightness of structural parts such as walls, roofs, doors, and windows. Reduce the heat loss of the enclosure structure of the farmhouse and the air infiltration part in the heat transfer process in order to make full use of the heat gained from the internal environment of the farmhouse and the heat gained by solar radiation. In the specific planning and design, it can be further summarized as optimizing the body shape coefficient, reasonably selecting the types of doors and windows, and applying thermal insulation walls in order to effectively solve the condensation problem [13].

4.1.1. Optimization of the Body Shape Coefficient. The larger the area of the enclosure structure that participates in heat transfer, the greater the heat transfer and heat loss of the rural residential environment. Flat facades and complex farmhouses are not conducive to energy conservation due to their larger envelope structure area. However, farmhouses with regular flat facades, simple shapes, and small body coefficients are beneficial to energy conservation. Therefore, it is necessary to optimize the design of the shape of the farmhouse to reduce the convexity and concavity of the shape of the farmhouse, so as to reduce the body shape coefficient, reduce heat loss in winter, and save energy. Based on the experience of hot summer and cold winter regions, the shape coefficient of rural houses in Chongqing can be controlled within 0.35.

4.1.2. Selection of Door and Window Types. The airtightness and thermal insulation of doors and windows will greatly affect the heating energy consumption of the residential environment. In residential buildings, the heat loss of heat transfer through doors and windows is added to the heat loss of air infiltration, accounting for about 50% of the total loss. Among them, heat transfer and air infiltration account for

about half. However, traditional steel windows in rural farmhouses have poor performance in these two aspects, causing a waste of energy. In recent years, new types of doors and windows such as plastic steel doors and windows with good heat preservation and air tightness, single-frame double glass color plate steel windows and aluminum alloy windows have emerged. It has a significant effect on saving heating energy consumption, which can be selected according to the actual situation. In addition, according to the economic situation of different regions, you can choose more economical sealing strips to fill the gaps between doors and windows, or replace with single and double insulating glass with better airtight and heat preservation.

4.1.3. Application of the Thermal Insulation Wall.
The exterior walls of rural houses in Chongqing are mostly built with traditional materials such as clay bricks and concrete blocks, which have poor thermal insulation performance. The current technology mature, economical, and reliable thermal insulation wall includes two categories: single-material thermal insulation wall and composite thermal insulation wall. The single-material thermal insulation wall adopts a single material with good thermal insulation performance, such as aerated concrete blocks and other masonry walls, without additional thermal insulation. Therefore, the process is simple and the cost is saved. The composite thermal insulation wall is a composite thermal insulation material added to the structural wall, which can be subdivided into external wall internal thermal insulation practices, external wall thermal insulation practices, and sandwich thermal insulation practices.

4.1.4. Solving the Problem of Condensation.
The exterior walls and roofs of farmhouses in Chongqing are generally thin, and there are many obvious thermal bridges. Condensation in winter is quite common, which seriously affects farmers' daily life and health. On the one hand, the cause of condensation is due to the low room temperature and the high humidity of the indoor environment due to the closed doors and windows of residents. On the other hand, because there is no central heating in Chongqing, the uneven temperature difference is caused by the use of equipment for heating. Condensation can be avoided by strengthening the thermal insulation of the thermal bridge, adding thermal insulation materials to the ground and external walls, using double-layer glass and thermal insulation doors and windows, and improving the room temperature and humidity. In the dew-condensed farmhouse, the thermal insulation performance of the enclosure structure can be improved by replacing the windows and applying thermal insulation mortar on the inside of the outer wall, so as to alleviate the problem of condensation [14].

4.2. Summer Energy Saving in the Residential Environment of Farmhouses.
With the improvement of the living standards of rural residents and the full coverage of Chongqing's rural power grid transformation, the utilization rate of air-conditioning has increased year by year. The key task of energy-saving in summer in the residential environment of farmhouses is to optimize the enclosure structure and effectively save energy consumption of air-conditioning.

4.2.1. Ways for Save Air-Conditioning Energy Consumption in Summer.
The ways to save air-conditioning energy consumption in the residential environment of rural houses in Chongqing in summer include adopting an appropriate indoor temperature, using energy-saving air-conditioning equipment with low power consumption in combination with national subsidy policies, choosing energy-saving appliances and lamps and reduce the room temperature by improving the kitchen's heat dissipation performance, and measures such as reasonable layout of air-conditioned rooms. These measures can effectively reduce the external heat gain of the residential environment of the farmhouse and achieve the purpose of saving energy consumption of air-conditioning.

4.2.2. Wall Structure and Air-Conditioning Energy Saving in Summer.
The wall structure of the farmhouse plays a major role in saving energy consumption of air-conditioning in summer. From the perspective of different number of floors, under the same conditions, the effect of reducing the air-conditioning load after increasing the thermal resistance of the outer wall of the top room is more significant. From the perspective of internal and external wall structure, if lightweight materials with lower heat capacity are selected for external walls, the energy-saving effect of air-conditioning will be significant. If heavy materials with higher heat capacity are selected for the inner wall, the indoor heat can be effectively collected and stored, and the energy consumption of the air conditioner can be significantly reduced.

4.2.3. Farmhouse Doors and Windows and Air-Conditioning Energy-Saving in Summer.
The control of the window area and the window-to-ground ratio, especially the control of the east-west room window-to-ground ratio, can greatly reduce the air-conditioning load and save energy consumption. Window shading facilities, especially those facing west, will have a greater impact on air-conditioning load. This has a major impact on the air-conditioning load. In addition, the air penetration in the room also has a certain impact on the air-conditioning load. In summary, in order to effectively save the energy consumption of farmhouse air-conditioning in summer, we should strive to open windows in the north-south direction to reduce the window area and improve its air tightness. In summer, the number of air changes in the room should be reduced.

In addition, take necessary window shading facilities, such as external shading facilities and internal shading facilities. The former shading effect is more remarkable. The latter is widely used because of its convenient construction. Shading facilities can be divided into two categories: fixed shading and movable shading. Fixed sunshades, such as eaves, etc., are neat and beautiful and do not require routine maintenance. Movable awnings, blinds, window shutters,

and other movable sunshade facilities are all flexibly adjustable. The shading efficiency can reach 100%. It is needed to pay attention to daily maintenance and unified planning. Previous studies have compared the intersubject effect of external sunshades on the indoor natural lighting and building energy consumption of rural residential buildings in Chongqing, that is, the difference F value, to obtain the influence effect degree of sunshades. Based on this, the combination scheme of external sunshade of rural residence in Chongqing is given to meet the natural lighting and reduce air-conditioning energy consumption.

4.2.4. Selection and Application of Energy-Saving Roofing Technology.

The use of energy-saving roofing technology can effectively insulate and save energy in summer. This applies to the types of rural areas in Chongqing, including reflective roofs, ventilated roofs, ecological green roofs, and water storage roofs.

Reflective roofing is to design the farmhouse roof in white, light gray, and other light colors to reduce solar radiation heat and lower the roof temperature. The internal structure of the ventilated roof is provided with a hollow ventilation layer to take away heat through the wind.

Ecological green roofs can be planted with grass, flowers, shrubs, covering soil planting, and soilless planting in order to effectively reduce solar radiation heat. And radiant heat energy is converted into biological energy and oxygen. Improve the microenvironment (Table 1). Water storage roof is to store a thin layer of water on the roof, use the effect of evaporative heat dissipation to absorb solar radiant heat, and improve the roof thermal insulation capacity. The impounding roof used in some farmhouses in Changhe Village, Luohuang Town, Jiangjin District, Chongqing, has achieved good results. In the construction case of rural residence in Fuling District, Chongqing, the sloping roof with good heat insulation and leakage prevention effect is selected, which has achieved good energy-saving effect.

5. Effective Utilization of Household Renewable Energy

Renewable energy is a type of energy that is recycled and inexhaustible. Under the background that national laws and regulations clearly propose to make full use of various types of renewable energy in rural areas, combined with the local characteristics of Chongqing, it is proposed to realize the effective use of renewable energy for households in Chongqing's rural houses from three aspects: biogas, straw energy, and solar energy. This is done to increase the energy flow in the agricultural ecosystem, improve the rural ecological environment and village appearance, and promote the energy-saving and clean energy use of villagers' homes.

5.1. Effective Utilization of Household Biogas Energy in Chongqing's Rural Houses.

Household biogas is the earliest technical method used for the treatment of household waste in Chongqing's rural households and the production of gas fuel. It has undergone a long-term development process.

Connect the three major links. Involve six major areas (Figure 3). It plays an important role in the coordination of three children in rural areas. After the system and technology are updated, it can be selectively used in suitable rural areas in the future [15].

5.1.1. Construction of the Household Biogas Application System.

Chongqing rural household biogas can establish a complete and efficient application system. Five important links are included, including household biogas management and promotion, technical support, financial subsidies, production and operation, and social group services (Figure 4). On July 15, 2021, the Department of Science, Technology and Education of the Ministry of Agriculture and Rural Areas organized an exchange meeting on the investigation and guidance activities of rural biogas safety production. Five investigation and guidance groups made future work ideas, measures and countermeasures for rural household biogas digesters, biogas projects, biogas safety production, and industrial development in 10 provinces and regions such as Chongqing.

5.1.2. Selection and Update of Household Biogas Digesters.

According to the characteristics of Chongqing, in addition to centralized biogas supply in mountainous areas, new thermostatic biogas digesters based on renewable energy can also be used in applicable areas. This type of biogas digester can effectively use solar energy to keep the biogas digester at a constant temperature to ensure biogas production. The water can be heated by solar energy to increase the temperature in the pool, or solar radiation can be directly used to increase the temperature in the pool to ensure the normal operation of the biogas digester in winter (Figure 5) [16, 17].

5.2. Effective Utilization of Rural Straw Energy in Chongqing.

Rural straw yields are relatively high, which can be converted into energy use according to local conditions. For example, the use of biomass conversion technology can increase the thermal efficiency by 35%–40%. In this way, waste materials can be fully utilized, and environmental pollution caused by straw incineration can be avoided.

5.2.1. Centralized Gas Supply by Gasification.

The mountain villages in Chongqing are relatively scattered in space, the scale of agricultural land is limited, and the straw yield is not high. Household equipment such as a new type of straw gasifier can be used. However, rural areas with relatively flat land and concentrated scale have larger straw yields. It can be used as a raw material to supply gas to farmers through a centralized gas supply method suitable for gasification in Chongqing. Through cooking and other application methods, the original energy consumption structure of farmers based on fuelwood will be improved. The basic model is as follows: set up gasification stations and deliver gas to farmers through the gas pipeline network (Figure 6). The gasification centralized gas supply system uses natural

TABLE 1: Thermal measured values with and without planting layer.

Project	Unit	No planting layer	Planted roof	Difference value
Maximum temperature of the outer surface	Celsius	61.6	29.0	32.6
Amplitude of outer surface temperature	Celsius	24.0	1.6	22.4
Maximum temperature of the inner surface	Celsius	32.2	3.02	2.0
Internal surface temperature fluctuation	Celsius	1.3	1.2	0.1

Chart source: the authors, organized according to relevant data.
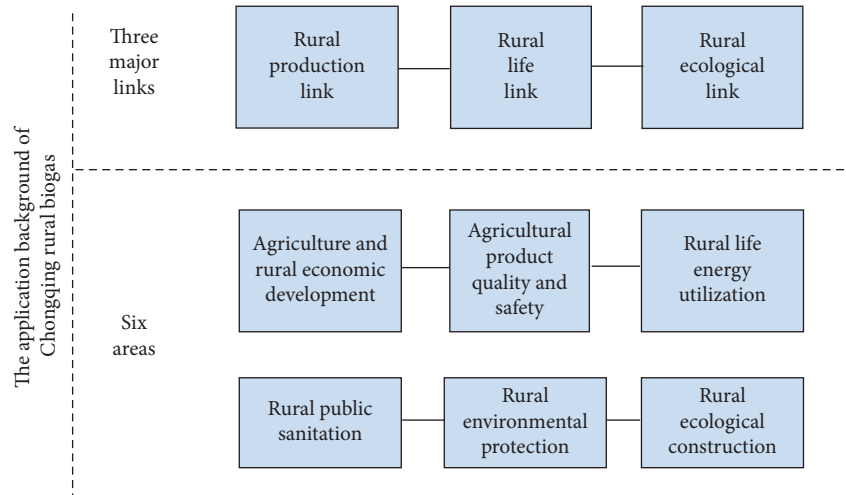
FIGURE 3: Schematic diagram of the application background of Chongqing rural biogas energy. Chart source: the authors.
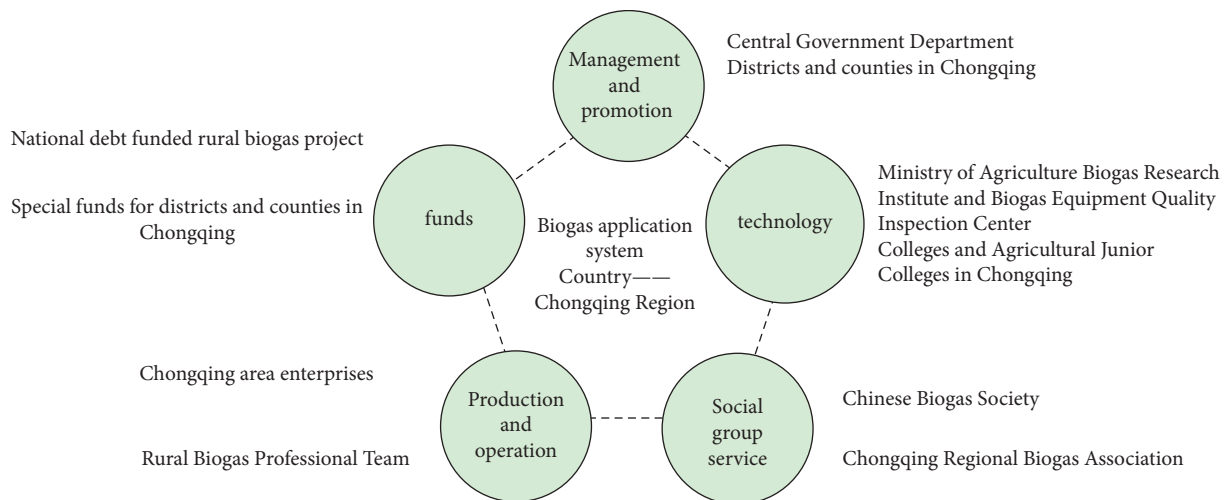
FIGURE 4: "National level-Chongqing area" rural biogas energy application system composition diagram. Chart source: the authors.

villages as the unit, and its gas cost is only 60% of the liquefied gas [18].

5.2.2. Application of Gasification Power Generation. Straw gasification power generation is to convert the biomass energy of straw into heat energy through anoxic combustion to generate combustible gas and drive a steam turbine generator to generate electricity. The current "biomass generator set" with newer technology has improved many disadvantages of the traditional furnace structure. It adopts a new structure of compartmental combustion, which can ensure full combustion of biomass and effectively reduce flue gas emissions, improve heat conversion efficiency, can continuously feed large amounts of materials and generate electricity, and process straw with high efficiency (Figure 7). Same as above, the site selection, scale and construction method of
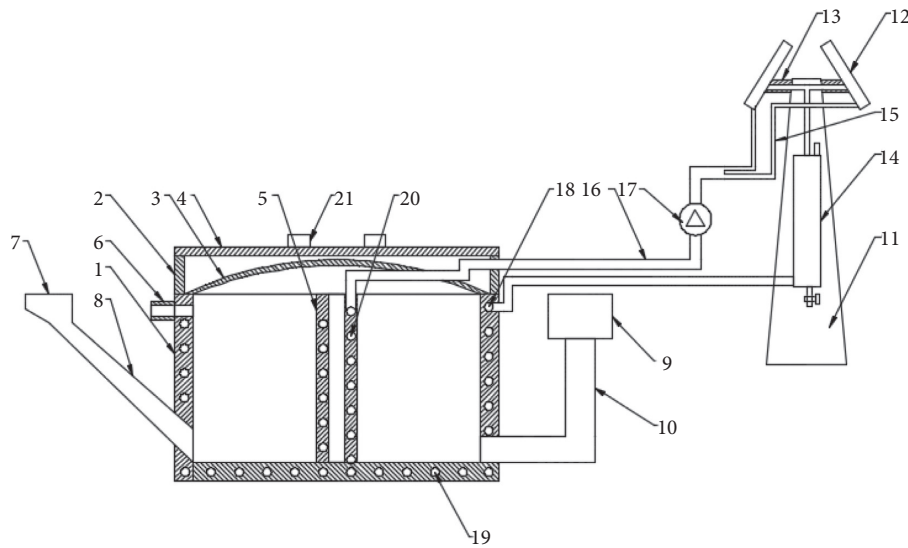
FIGURE 5: Design drawing of a new constant temperature biogas digester based on renewable energy. Chart source: the authors. 1: biogas digester, 2: heightening sealing edge, 3: inner sealing cover, 4: outer sealing cover, 5: central column, 6: biogas outlet pipe, 7: feeding port, 8: feeding pipe, 9: overflow port, 10: overflow pipe, 11: high tower, 12: solar collector, 13: support, 14: insulation water tank, 15: first water pipe, 16: second water pipe, 17: water pump, 18: first heating pipe, 19: second heating pipe, 20: third heating pipe, and 21: handle.
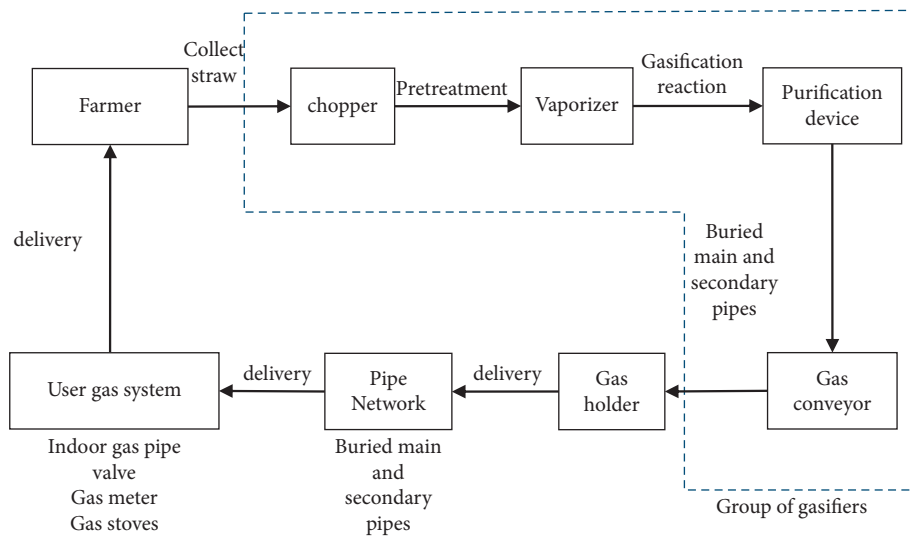
FIGURE 6: Planning flowchart of Chongqing rural straw gasification centralized gas supply mode. Chart source: the authors, organized according to relevant data.
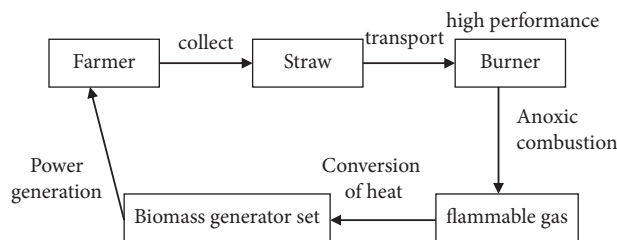
FIGURE 7: Flowchart of the application planning model of Chongqing rural straw gasification power generation. Chart source: the authors.

straw gasification power generation application should also be adapted to the characteristics of Chongqing's rural areas [19]. As early as 2007, the pilot project of straw gasification centralized gas supply has been built in the villages of Yongchuan District and Dianjiang District of Chongqing.

TABLE 2: Analysis of the distribution and promotion of solar energy resources in southwest China.

Area category	Solar resource	Southwest region	Daily radiation (kWh/m^2)	Solar promotion
First category	The richest	Western Tibet	5.1–6.4	Suitable for promotion Solar energy
Second category	Richer	Southeastern Tibet	4.5–5.1	
The third category	Medium	Yunnan	3.8–4.5	
The fourth category	Poor	—	3.2–3.8	Partial promotion of solar energy
The fifth category	Least	Chongqing, Sichuan, Guizhou	3.2–3.5	

Chart source: the authors, organized according to relevant data.

FIGURE 8: Photovoltaic power generation scene in Bade Village, Bashan Town, Zhong County, Chongqing. Chart source: Xinhua News Agency.

TABLE 3: Comparison and analysis table of the advantages of energy storage solar stoves and traditional energy sources.

Category	One-time input cost	The cost	Absolute carbon emission value	Life	Whether to run automatically	Whether it has heat storage capacity	Thermal power
Biomass such as wood, etc.	Low	Low	Zero	Very long	No	Yes, stored as chemical energy	Larger
Liquefied petroleum gas, natural gas, etc.	Medium	Relatively high	High	Very long	No	Yes, a chemical energy storage	Larger
Electrothermal	Low	Relatively high	High	Very long	Yes	No	Smaller
Traditional solar cooker	Medium	Low	Zero	Very long	No	No	Smaller
Energy storage solar cooker	Relatively high	Low	Zero	Very long	Yes	Yes	Great, direct heat conduction

Chart source: the authors, compiled according to "Tibet Department of Agriculture and Animal Husbandry Department. Tibet Rural Household Solar Energy Supply Project Feasibility Report[R] 2015."

5.3. Effective Use of Solar Energy. The distribution of total solar radiation in the southwest is uneven. There are both high-resource areas and low-resource areas. The daily radiation dose in Chongqing is relatively low (Table 2). However, even in areas with poor solar energy resources, the total solar radiation in some towns and villages is relatively large. As far as a small area is concerned, it is still an area rich in solar energy resources, and the use of solar energy technology can also be promoted. Therefore, the situation of rural solar energy in Chongqing is "if there is more, there will be more usage, and if there is less, there will be less usage." Solar energy should be used effectively according to local conditions(Figure 8).

The solar energy utilization types applicable to rural areas in Chongqing mainly include solar water heaters, solar lights, solar photovoltaics, solar stoves, solar greenhouses, and solar houses. Take Chongqing as an example: farmers in 6 towns including Shuangfeng and Zouma in Hechuan and Wanzhou districts have installed more than 1,600 solar water heaters and achieved good results. Gaofengsi Village,

Fuling District, located in the Wujiang Gorge, is sunny. Install low-cost independent household solar photovoltaic. The area is about 30 square meters. It can generate 5000 kilowatt-hours of electricity every year. The installation of 200 solar street lights in the high mountain ecological relocation site of Zhongxin Temple in Qianjiang District has effectively improved the lighting environment of the village and saved electricity. Bishan area uses solar greenhouses of flowers, breeding, fruit trees, vegetables, and ecological sightseeing to increase the temperature in the sheds in winter and effectively promote high-value agricultural production activities. In addition, energy storage solar stoves are a new type of combined heat and power system popularized in rural areas in Tibet in recent years. It can automatically complete solar thermal energy collection and storage and electrical energy conversion and storage. The use cost is relatively low, the continuous use time is relatively long, and its thermal power is relatively high. It can be verified to explore the possibility of its application in suitable rural areas in Chongqing (Table 3)[19, 20].

6. Conclusions and Prospects

This chapter summarizes the energy-saving design path of rural farmhouses in Chongqing, aiming to enhance the coherence between the artificial construction environment, the natural ecological environment, and the socioeconomic and cultural environment. In view of the author's limited theoretical ability and practical experience, this article only constructs a comprehensive research framework. Its specific research content, research depth and working methods still need to be gradually adjusted and improved in the future study, research and practice process. Looking to the future, there are the following aspects that need attention:

(1) Further regional and targeted research

The geographical features of Chongqing area, such as topography, climatic environment, history and humanities, are more distinctive. The planning methods and actual construction conditions of rural human settlements have their own characteristics. The same applies to the energy-saving design path of farmhouses. Part of the research content in this article still presents universality and generality. The regionality and pertinence can be further strengthened.

(2) Strengthen the in-depth study of the energy-saving design path of rural houses in Chongqing

Part of the theoretical research on the surface and middle level will be promoted to a deeper level. Further strengthen the research work of induction, summary and analysis. Strengthen the logic construction process. Promote the highlights and innovative thinking in theoretical research.

(3) Establish a relevant evaluation system for the energy-saving design path of Chongqing's farmhouses

This article puts forward the overall research framework of Chongqing's rural house energy-saving design path and can further try to establish an evaluation system for Chongqing's rural house energy-saving design. With the support of necessary data, various ecological index factors, scoring rules, and weighting basis are set in the evaluation standards. This can more effectively improve the standardization and scientificity of the energy-saving design path of Chongqing's farmhouses and provide a basis for the initiation and evaluation of related construction work.

(4) Strengthen practicality and gradualism

Rural work is a task of "being grounded and alleviating people's worries." This article conducts guided research more from the level of theoretical understanding and guiding path. In the future work, the actual needs of the villagers should be the core, and specific issues should be analyzed in detail, so that theory can be combined with practice. Under the background of the rural revitalization strategy that satisfies the ecological and livable environment, we will better serve the peasants.

Data Availability

No data were used to support this study.

Conflicts of Interest

The authors declare that they have no conflicts of interest regarding the publication of this paper.

Acknowledgments

References

[1] Research Center for Building Energy Efficiency, *China Annual Development Research Report on Building Energy Efficiency 2020 (Rural Housing Project)*, Tsinghua University, Beijing, China, 2020.

[2] Energy Consumption Special Committee of China Building Energy Conservation Association, *China Building Energy Consumption Research Report*, Energy Consumption Special Committee of China Building Energy Conservation Association, Beijing, China, 2020.

[3] X. Wang and H. Hong, *Green Village and Town Construction in China*, Springer, Berlin, Germany, 2021.

[4] Y. Yan, W. Jiao, K. Wang, Y. Huang, J. Chen, and Q. Han, "Coal-to-gas heating compensation standard and willingness to make clean energy choices in typical rural areas of northern China," *Energy Policy*, vol. 145, no. 10, Article ID 111698, 2020.

[5] Q. Du, X. Han, Y. Li, Z. Li, B. Xia, and X. Guo, "The energy rebound effect of residential buildings: e," *Energy Policy*, vol. 153, no. 7, Article ID 112235, 2021.

[6] K. O'Sullivan, O. Golubchikov, and A. Mehmood, "Uneven energy transitions: understanding continued energy peripheralization in rural communities," *Energy Policy*, vol. 138, no. 3, Article ID 111288, 2020.

[7] Z. Hu, "When energy justice encounters authoritarian environmentalism: the case of clean heating energy transitions in rural China," *Energy Research & Social Science*, vol. 70, no. 12, Article ID 101771, 2020.

[8] X. Zeng, Y. Zhao, and Z. Cheng, "Development and research of rural renewable energy management and ecological management information system under the background of beautiful rural revitalization strategy," *Sustainable Computing: Informatics and Systems*, vol. 30, no. 7, Article ID 100553, 2021.

[9] Q. Zhang, M. Luo, and S. Sun, "Research on energy-saving renovation of rural houses in hot summer and cold winter area," *Building Energy Efficiency*, vol. 1, no. 2, pp. 87–91, 2019.

[10] J. Shi and Q. Li, "Energy saving performance evaluation and planning OptimizationDesign of rural residential building environment," *Argos*, vol. 36, no. 73, 2019.

[11] D. Li, X. An, and H. Li, "Preliminary study on the energy-saving renovation of existing rural houses in hot summer and cold winter areas: taking rural houses in Deyang city, Sichuan province as an example," *Building Energy Conservation*, vol. 1, no. 4, pp. 87–92, 2020.

[12] C. Jia, A. Feng, Li Zhong et al., "The impact of the renovation of existing farm buildings in southern Fujian on the indoor thermal environment," *Building Energy Conservation*, vol. 1, no. 1, 2019.

[13] B. Zou and A. K. Mishra, "Appliance usage and choice of energy-efficient appliances: e," *Energy Policy*, vol. 146, no. 11, Article ID 111800, 2020.

[14] C. Zi, M. Qian, and G. Baozhong, "The consumption patterns and determining factors of rural household energy: a case study of Henan Province in China," *Renewable and Sustainable Energy Reviews*, vol. 146, no. 8, Article ID 111142, 2021.

[15] H. Roubík and J. Mazancová, "Suitability of small-scale biogas systems based on livestock manure for the rural areas of Sumatra," *Environmental Development*, vol. 33, no. 3, Article ID 100505, 2020.

[16] J. Shi and Q. Li, "A new type of constant temperature biogas digester based on renewable energy," National Utility Model Patent, 2016.

[17] M. R. Shaibur, H. Husain, and S. H. Arpon, "Utilization of cow dung residues of biogas plant for sustainable development of a rural community," *Current Research in Environmental Sustainability*, vol. 3, Article ID 100026, 2021.

[18] Z. Liu, M. Wang, Q. Xiong, and C. Liu, "Does centralized residence promote the use of cleaner cooking fuels? evidence from rural China," *Energy Economics*, vol. 91, no. 9, Article ID 104895, 2020.

[19] F. Huang, Z. Wang, J. Liu, C. Shuai, and W. Li, "Exploring rural energy choice from the perspective of multi-dimensional capabilities: e," *Journal of Cleaner Production*, vol. 283, no. 2, Article ID 124586, 2021.

[20] O. Kaya, A. M. Klepacka, and W. J. Florkowski, "Achieving renewable energy, climate, and air quality policy goals: rural residential investment in solar panel," *Journal of Environmental Management*, vol. 248, no. 10, Article ID 109309, 2019.

Research Article

Application Calibration Based on Energy Consumption Model in Optimal Design of Green Buildings

Feiran Xue and Jingyuan Zhao (iD)

Coll Architecture, Changan University, Xi'an 710016, Shaanxi, China

Correspondence should be addressed to Jingyuan Zhao; zjyqtt@chd.edu.cn

Buildings will generate considerable resource and energy consumption, environmental impact, and costs throughout their entire life cycle. Life cycle assessment and life cycle cost methods have become widely used building sustainability evaluation methods internationally due to their long-term comprehensive evaluation perspectives and scientific quantitative calculation methods. In response to energy consumption management issues in green buildings, a questionnaire survey was conducted to investigate the concepts of sustainable development, green environmental protection, and energy consumption management of construction enterprise personnel. Through the survey, it can be seen that corporate executives generally have a sense of sustainable development and pay more attention to sustainable competition and the green development of enterprises. Approximately 90% of executives understand energy consumption models. Only 10% of employees do not understand, but they are acquired by the company's frontline employees. The result of the feedback is just the opposite. Frontline workers pay little attention to the long-term development of the company. Only about 5% of employees are proficient in the energy management system, but the proportion of completely unknown is as high as 20%, indicating that the overall energy management awareness of Chinese enterprises still needs to be strengthened. Secondly, through design experiments, the energy-saving management effect of the energy consumption model was observed and analyzed. From the power saving and load test, we found that the monitoring of the energy consumption model is helpful for companies to choose more energy-efficient building circuit designs, achieving an average annual energy-saving effect of about 8%, so as to achieve the purpose of energy saving.

1. Introduction

With the rapid development of China's industrialization and urbanization, the construction industry has become a pillar industry of China's economic development. In the rapid development of the construction industry, environmental problems are becoming increasingly prominent, and the exhaustion of resources and energy threatens the survival of mankind. Countries around the world have proposed the concept of green energy saving in order to seek harmony between architecture and nature. Green building is an inevitable choice for China to develop a low-carbon circular economy.

From the perspective of sustainable development, the evaluation of environmental emissions and energy consumption during the life cycle of a building is an important aspect of the physical performance of a building. Due to its long-term comprehensive evaluation perspective, scientific quantitative calculation method and scientific database statistical method, the life cycle assessment method has become an important supplement to the existing building physical environment performance analysis method, which can more comprehensively evaluate the whole life of the building. Material inputs and outputs in the process support decision makers to make scientific decisions at different stages.

In the management of green buildings, Liao studied the application of energy management systems in green buildings. Energy management systems (EMS) are special computers that program them to control all energy-related systems of buildings, including heating and cooling, ventilation, hot water, indoor lighting, external lighting, on-site power generation, and mechanization of systems for shading equipment, window actuators, and dual facade elements [1].

Recently, a new module for EMS simulation has been added to EnergyPlus' entire building energy simulation program. The basic part of the EMS module is EnergyPlus Runtime Language (ERL), which is a simple programming language used to specify EMS control algorithms. Vimpari and Junnila are focused on the research of smart home energy management systems. The smart home energy management system (IHEMS) can control the energy consumption of equipment and household appliances and the best energy distribution and management [2]. Its characteristics can not only avoid inefficient energy consumption but also alternately coordinate the use of existing energy and renewable energy. The project focuses on the development of IHEMS embedded energy-saving and management systems. Neyestani introduced the design of the EMS2000 energy management system on the basis of example projects [3]. The functions of the submeter energy-saving management system are analyzed from the aspects of overall building energy consumption analysis, power distribution system information monitoring, and power load analysis. It is pointed out that the EMS2000 energy consumption management system can accurately discover wasted energy and energy-saving potential in large public buildings and judge the actual energy-saving effect of management or technical measures, which is of great significance for energy-saving supervision.

Based on the concept of sustainable development and green building, this paper analyzes the environmental protection concept and awareness of China's construction enterprises, and the application of consumption management system in green building, specifically the application of power saving, explains the energy The use effect of the energy consumption management system is hoped to provide more basis for the application of the energy consumption management system in green building.

2. Proposed Method

2.1. Sustainable Development and Green Building. Sustainable development is the sustainability of a people-oriented ecological-social-economic composite system [4, 5]. The strategic evolution of enterprise development will inevitably experience four stages of predatory mining and production, passive pollution control, proactive prevention and control, and the formation of environmental competitiveness, reflecting the different historical stages of enterprises' understanding of sustainable development and market environment change. At present, under the global green trend, construction companies should also realize strategic evolution, shape environmental competitiveness under the concept of sustainable development, develop the ecological economy and circular economy, and achieve green growth. To study how construction companies abandon the traditional high-energy consumption and high-pollution construction company business model and carry out research on green strategic innovation of construction companies has important contemporary and practical significance [6, 7].

In China, there are many opinions on the understanding of green buildings, but a unified consensus has been reached on the sustainability of green buildings. The relatively comprehensive concept of green buildings in China is more than its affirmation of "full lifespan." The concept of "cycle" [8]. The full life cycle of green buildings is not limited to the construction period. The traditional concept of the construction period only considers comfort and economy. The construction period of green buildings emphasizes the extension of the front and back, giving green buildings a complete life period. According to the "Green Building Technical Guidelines," the green building is defined in the whole life cycle of the building to minimize pollution, save resources (commonly known as "four sections" of land saving, energy saving, water saving, and material saving), and protect the environment. It is also a kind of building that can provide humans with health, comfort, and high-efficiency space utilization and live in harmony with humans. In addition, there is a more popular concept, emphasizing the physical health of the occupants, focusing on the saving of the whole process of the building, and at the same time also involving reducing the interference to the environment; that is, green buildings provide human health and comfort, safe, used for living, working and living space, throughout the entire life cycle of the building (from the design and planning of the building to the production and transportation of building materials, to construction and maintenance, and finally the entire process of scrapping and dismantling the raw materials for recycling), a building that affects the surrounding environment to a minimum and uses various resources (land, energy, water, raw materials) efficiently [9, 10].

Compared with developed countries, China's green building started relatively late. Since the development of green buildings in China, the evaluation standard evaluation label system has been promulgated. Although the progress has been significant, there are also many problems, mainly including the following 4 points: (1) Green: there are misunderstandings in the construction personnel, especially in the economic aspect; there is a deviation in investment perception, and a mistaken believe that green buildings are high-cost high-tech buildings. It just ignores the economic, social, and environmental benefits brought by green buildings, leading to the development of green buildings into a misunderstanding [11]. The green building concept and green consumption concept need to be properly guided. (2) There are misunderstandings in the application of green building technology, blindly stacking new technologies, resulting in high costs and high repetition rate of green building technology, and lack of flexibility to adapt to local conditions. (3) The incentive and enforceability of government incentive policies are not strong, lack of adjustment of incentive policies, and legislation and regulations also need to be further improved. (4) There are few participants in the promotion, and the promotion of green buildings requires the participation and cooperation of the whole society in order to truly penetrate the hearts of the people [12, 13]. Due to the lack of comprehensive analysis and research on the cost and benefit of green buildings in China, the promotion of green buildings is often not persuasive. A cost-effective database should be established on the basis of the investigation of green building evaluation and labeling

projects, and different green building technologies should be analyzed according to different regions. The resulting costs and benefits have made society more comprehensively aware of the benefits of green buildings [14]. Compared with developed countries, China has insufficient per capita resources and is a country with high energy consumption. Therefore, the demand for green buildings is more urgent than in other countries. At present, China's green building is still in the development stage. The evaluation standard currently adopted in China is GB/T 50378-2014 "Green Building Evaluation Standard." This standard is divided into seven categories of indicators, namely: land conservation and external environment, energy-saving and renewable resources utilization, water resources conservation and utilization, construction materials conservation and utilization, building environmental quality, building construction process management, and building commissioning management. Among various indicators, energy conservation and energy utilization are inseparable from the major of electrical engineering, and the weight in the design evaluation accounts for 0.28. Among them, the submetering of energy consumption and the power density value of lighting are the control items and the evaluation of green buildings [15, 16]. The characteristics of green buildings are neither general greening nor specific buildings but a comprehensive evaluation of building energy efficiency, comfort, and environmental protection. Its characteristics can be summarized as follows: (1) emphasis on the concept of the full life cycle, emphasizing the harmony between man and nature. (2) Reflecting the concept of circular economy and having minimal impact on the environment. Emphasis on obtaining the maximum benefit with the smallest cost. (3) The integration of man and nature. (4) The use of renewable energy, energy-saving technologies, green and environmentally friendly recyclable materials, and other means to achieve high efficiency and low cost.

2.2. Ecological Building and Energy Management System.

In the 1960s, American architects put forward the concept of ecological architecture, for the first time linking architecture and ecological environment, which is also the origin of the concept of green architecture. After the oil crisis in the 1970s, some countries began to pay attention to the research on energy conservation in buildings. With the emergence of new concepts and technologies such as geothermal energy, wind energy, and solar energy, and investment in the field of construction, green buildings have been used on a large scale [17]. The "LEED" standard evaluation system in the United States has been widely recognized in the construction industry worldwide and has become an important standard for global green building certification. LEED certification levels from low to high are certification level, silver level, gold level, and platinum level, of which 6 major scoring systems are sustainable site, energy and atmosphere, water efficiency, construction materials and resources, indoor environment, and innovation design [18, 19]. In addition, the more well-known green building evaluation systems in the world include BREEAM in the United Kingdom, CASBE in Japan,

and Blue Angel in Germany. Each of them has developed relevant scoring schemes based on their own national conditions and technological development status. The development of green energy projects requires electrical designers to apply relevant technologies and adopt effective energy management solutions during the building design phase [20]. For the first time, an Italian architectural designer proposed the direction of architectural research combining ecology and architecture, which made people rerecognize the new development characteristics of architecture. After that, the West developed ideas such as sustainable architecture and green architecture [21]. In 2006, the China Academy of Building Research and other construction units prepared the "Green Building Evaluation Standard." The "standard" defines green building as follows: during the life cycle, the resources and energy are saved and used to the maximum extent to protect the environment and reduce pollution, providing a beautiful living environment and achieving harmony between man and nature [22]. The following can be seen from the definition: (1) Focus on the entire life cycle of the building. Now people pay more and more attention to the entire life cycle of the building, so the early stage of the analysis of the surrounding terrain and environment to avoid the waste of space can also reduce the environmental pollution caused by the later demolition and fully reflect the sustainable development of green buildings idea. (2) Promote natural harmony. The energy consumption of traditional buildings puts tremendous pressure on the environment, and green buildings emphasize that under the premise of having a healthy and comfortable use space, energy consumption can be reduced and people and nature can live in harmony. (3) Emphasize economic benefits. Technology and form make full use of advanced technologies such as informatization, automation, new processes, and new materials to achieve optimal social and economic benefits. There will be a certain incremental cost during the construction phase, but from the perspective of the whole process of the life cycle, various costs are saved. In April 2014, the State Department of Housing and Urban-Rural Development revised the 06 edition of the "Green Building Evaluation Standards" and added new evaluation content on green construction. Green building evaluations are implemented with a more quantitative evaluation system. In May 2017, the "Thirteenth Five-Year Plan" for the development of the construction industry requires that by 2020, all new urban civil buildings in China will meet the energy-saving standards. Green urban buildings will account for 50% of new buildings and 40% of green building materials. In April 2018, the International Green Construction Conference was successfully held in Zhuhai. Topics include green design, energy-saving renovation of existing buildings, development of green ecological urban areas, building big data, and BIM technology [23].

The application of building energy management technology in various countries has experienced long-term development: (1) The technical application measures adopted by the United Kingdom in building energy management are mainly in three aspects: First, the use of structural (wall, door, window, roof) improvement

measures to improve the internal insulation function indirectly reduce the energy required for heating; the second is the use of solar energy; the third is the transformation of the heating system. At present, the United Kingdom is vigorously promoting passive solar houses, which use building heat absorption and insulation materials as a medium and use the natural exchange of cold and hot air to achieve the use of solar energy. In solar houses, the total energy provided by solar energy accounts for 30%–40% of the total energy. In order to fully promote sustainable development, the British government implemented a million-dollar "green housing" project to encourage residents to use environmentally friendly technologies and building materials to build and renovate housing and build new environmentally friendly housing. This new house mainly uses solar panels and water recovery equipment. (2) Germany is in a leading position in the field of energy management, mainly involving the heat energy of building envelopes, indoor environmental quality, and energy consumption of construction equipment. The energy-saving of buildings can be obtained through the thermal insulation function of the enclosure structure, the airtightness of the doors and windows, the operating efficiency of the boiler, the natural lighting of the building, and natural ventilation. Under the leadership of government policies, renewable resources such as solar energy and natural gas are gradually applied to various types of building heating. (3) The United States promotes building energy efficiency in two major ways. One is the thermal performance of the building, which can achieve energy saving and emission reduction by providing the insulation of the building envelope, the sealing of the doors and windows, and the rational use of light, ventilation, and environment; the second is to improve the energy consumption equipment in the building (including heating, Air conditioning, lighting, water resources, and office automation systems). The United States is a world leader in the development of new energy sources, the use of pollution-free energy, and energy management (such as energy conservation and emission reduction). At present, the United States is popularizing the conversion of solar energy into electrical energy to provide effective energy for buildings such as homes, schools, and public buildings. It mainly converts solar energy into electrical energy and stores it in batteries, which are then directly used in lighting systems, hot water supply, indoor ventilation, etc. The solar energy technology in the United States has gradually matured, and it has formed a complete building industrialization system for building design, construction, or operation. China's building energy management work started late. After years of development, the central and local management centers have been established to carry out building energy management work in accordance with laws, regulations, and regulatory documents and basically form a building energy-saving design standard system [24, 25].

EMS energy management system is the general term of modern power grid dispatching automation system (including hardware and software). Its main functions are composed of two parts: basic functions and application functions. Basic functions include computer, operating system, and EMS support system. Application functions include data acquisition and monitoring (SCADA), automatic generation control (AGC) and planning, and network application analysis. Based on the application of the energy management system in green buildings, this article uses a questionnaire survey to understand the public's understanding of the energy management system. Through experimental research, it mainly verifies the energy-saving effect of the energy management system on electrical aspects [26].

3. Experiments

3.1. Questionnaire Survey Method

3.1.1. Theoretical Basis. A questionnaire survey is the most common research method in the field of management. It is in the form of a questionnaire to allow respondents to fill in the questions and respond to the actual situation and real ideas. According to the research scope, research objects, research time, research funding, response rate, and other factors of the researchers, different forms of questionnaires are issued, such as field visits, e-mails, on-site unified organization, and answering, etc. This article uses the questionnaire survey method, mainly because it has the following advantages: First, the cost of questionnaire survey is low, especially the popularity and convenience of online tools, so that the use of online questionnaire survey tools, e-mail, and other forms is more efficient, saving time, manpower, and material resources. Electronic questionnaires save paper, are more environmentally friendly, shorten the time of the entire questionnaire survey process, and improve the overall efficiency of empirical research. Second, by answering the questionnaire anonymously, the surveyed can express their wishes faithfully according to the real situation of the enterprise and avoid the interference of other external factors, making the survey results more reliable. Third, the questionnaire survey is time-sensitive. After the questionnaire is recovered, the survey results can be quantitatively analyzed in time, and the data analysis can be performed through various statistical software to obtain more accurate data hypothesis results.

3.1.2. Questionnaire Design. The questionnaire mainly includes the following three parts: First, the purpose of the investigation. Before filling in the questionnaire formally, the research should explain the objectives, significance, precautions, and confidentiality measures of the survey in detail. Since the content of the questionnaire involves corporate environmental protection behavior, special emphasis should be placed on protecting the rights and interests of those who answer the questionnaire. The results of this survey are only used for academic research, not for any commercial purposes, and are anonymous. Fill in; Second, corporate characteristics and personal characteristics. The characteristics of the enterprise include the nature, size, industry category, and years of the enterprise, and the personal characteristics include gender, education, age, and working years. Third, measure various variables in the

theoretical framework. It mainly includes five aspects: enterprise sustainable development strategy, green building, sustainable competitive advantage, stakeholders' environmental pressure, and understanding of energy consumption management system. Based on previous research and suggestions from multiple management experts and scholars, this article follows the following process and steps to design the questionnaire: First, based on the existing literature at home and abroad, the study fully draws on multiple empirical tests and has high reliability. According to the connotation of variables, theoretical basis, and applicable situation, the scale of validity is designed to match the measurement scale most suitable for this study. Second, indepth interviews with companies. Before the initial questionnaire was generated, we selected some companies to conduct in-depth interviews to understand the regulatory system and actual implementation of the company's environmental strategy and green innovation, listen to the suggestions of multiple entrepreneurs and executives, and ensure that the questionnaire is more in line with the presentation—the context of Chinese organizations. Third, listen to expert opinions and participate in academic seminars. On the basis of literature reading and in-depth interviews with enterprises, in order to increase the content validity of the questionnaire, the author consulted professors and experts in the field of corporate social responsibility of corporate management in multiple universities by e-mail and telephone and asked them to question the questionnaire. Make assessments and modifications. At the same time, the author participated in relevant academic discussions on green building energy consumption management and revised and adjusted the measurement items based on these opinions and suggestions. Fourth, preinvestigation. Before conducting the preliminary survey, ask five experts and scholars in the field to evaluate and modify the questionnaire, adjust and modify the measurement items appropriately according to the situation in China, and then distribute the questionnaire to 50 senior executives of the construction enterprises in the economic park. Conduct research with 100 frontline staff.

3.2. Experimental Research on Energy Consumption Management System.

The energy-saving design of the electrical part of the EMS energy consumption management system can adopt different schemes, starting from multiple aspects, multiple levels, and multiple perspectives, to achieve the goal of open source and throttling. Different buildings should adopt an electrical design that matches the function and characteristics of the building and balances energy-saving effects and investment budget. Designers should grasp the overall needs of builders and make reasonable designs in accordance with green building standards and energy conservation and emission reduction goals.

3.2.1. Power Supply and Distribution System Planning.
The low-voltage voltage level in the building is 380/220 V, and the high-voltage side voltage levels are 6 kV, 10 kV, and 35 kV, in the form of overhead lines or cable entry. Because

the loss of the transmission line is proportional to the current density and transmission distance and inversely proportional to the transmission voltage and power factor, reducing the current density or increasing the transmission voltage will increase the investment cost of the transmission equipment. Therefore, it is necessary to seek a technically and economically reasonable voltage level.

3.2.2. Green Building Load Estimation.
Peak electricity consumption occurs in summer and winter in China. For industrial and commercial buildings, peak power consumption will cause overloaded operation of lines and transformers, thereby reducing the reliable operation of the power grid and impairing the operation of equipment. At the same time, if the long-term operation is in a state where the peak-valley gap is large, it will result in the long-term noneconomic operation of the transformer, which is very unfavorable for energy-saving operation. Therefore, in a green building, it is necessary to manage and intervene in the internal load of the building and determine the time period of peak load and trough by monitoring the load statistics of the equipment. The load estimation of the project can provide a basis for the selection of distribution transformers, the economic and safe operation of the distribution system, and the selection of wires and cables. If the load estimation value is too small, the equipment and cables selected based on this may be overloaded, which causes the equipment cable to heat up, generating unnecessary energy consumption and affecting the service life of the equipment; if the load estimation is too large, it will cause waste of equipment investment. In green building load estimation, the following three estimation methods are generally used: First, the coefficient method is needed: the ratio of the actual power consumption of electrical equipment to the rated power of the equipment is the coefficient of need. This value is usually a statistical value. The rated power multiplied by the required coefficient can be regarded as the calculated load of the equipment. Second, the use of the coefficient method: based on the utilization coefficient, the average power in the maximum load platform shift is obtained, and the number of effective electrical equipment in the power supply area. Use the coefficient to find the maximum coefficient and then multiply it by the average power to calculate the load; third, the power method per unit area: the area of the load calculation area is multiplied by the load density of the power supply area. The load density of various civil and industrial buildings can be found in the related tables. However, when applied to green buildings, these load densities will be too large. Since green buildings are not yet popular, the sample of load density is not large enough, so the power per unit area method is not recommended. This experiment uses the coefficient method to calculate the load.

3.2.3. EMS Energy Consumption Management Software System.
The interface system of the software adopts B/S architecture, and users can access browsing data through browser software such as IE and Firefox. By visiting the website, users can monitor building energy consumption

data at any time. Different users can access different building areas, format types, and energy consumption data by using accounts with different permissions. The software system functions include energy consumption analysis, energy consumption comparison, indicators and parameters, power distribution monitoring, report printing, and energy-saving diagnosis. After the user accesses the web server through a browser and enters the correct user name and password, the system will navigate to the corresponding function page according to the user's authority and display the data within the user's authority. Different users have different access rights. The data authority system can configure and adjust in the background, for different users can also set different device system permissions and format permissions. Through the energy management system software to monitor the entire building and building lines, analyze the building electricity load, analyze the building electricity report and energy consumption, analyze the energy consumption data in-depth, conduct energy-saving analysis, and finally perform user analysis to evaluate energy. Use effect of consumption management system.

4. Discussion

4.1. Analysis of Questionnaire Survey Results. The questionnaire is shown in Table 1:

It can be seen from Table 1 that this questionnaire answers the question from the five aspects of enterprise sustainable development strategy, green building, sustainable competitive advantage, environmental pressure of stakeholders, and understanding of energy consumption management system. Overall view, options 1–5, respectively, indicate the degree of conformity of the options, 1 represents complete noncompliance or complete ignorance, and the degree of representation is deepened in turn, 5 represents complete compliance or complete understanding, of which the third stakeholder environmental pressure, from 1 to 5 means that the pressure comes from the outside, and the pressure comes from the inside.

The results of the questionnaire survey are shown in Figures 1 and 2.

As can be seen from Figure 1, most of the senior executives of the company believe that their company is more in line with the company's sustainable development strategy, green building, sustainable competitive advantage, and that the environmental pressure of stakeholders mainly comes from the external environment, The proportion of them all reached more than 80%, and in terms of understanding the energy management system, most of the personnel have a certain understanding of it, accounting for about 80%, and a few people who are proficient and completely ignorant, each accounting for 10%.

As can be seen from Figure 2, most of the frontline staff believe that the company is in line with the company's sustainable development strategy, green building, and has a certain sustainable competitive advantage and that the environmental pressure of stakeholders mainly comes from internal management. It accounts for about 50%. In

terms of understanding the energy management system, most people do not understand it or even do not understand it at all. The number of people who do not understand it is as high as 20%, while only 5% are proficient. From Figures 1 and 2, in a comprehensive view, the managers of the surveyed enterprises pay more attention to green building and energy consumption management, but the frontline staff of the company does not pay much attention to it. Consumption management is still lacking in understanding, and the focus of our next work should be on enhancing the sustainable development concept of the enterprise and saving energy and reducing consumption.

4.2. Analysis of Experimental Results of EMS Energy Consumption Management System. The relationship between the power supply system voltage level, power supply capacity, and power supply range is shown in Figures 3 and 4.

It can be seen from Figures 3 and 4 that under the same incoming line type, the loss of the transmission line is proportional to the transmission distance and inversely proportional to the transmission voltage, and reducing the current density or increasing the transmission voltage will increase the power transmission equipment's investment cost. Therefore, it is necessary to seek a technically and economically reasonable voltage level. Monitoring the feedback data through the energy consumption management system is helpful for enterprises to choose a reasonable circuit and incoming line type so as to achieve the purpose of saving electricity.

See Table 2 for the green building load calculation table.

It can be seen from Table 2 that the installed capacity of the engineering equipment is 33.66 kW, the active load is 17.12 kW, the reactive power compensation capacity is 7.98 kvar, and the apparent power is 19.40 kVA. This data saves about 8% of power consumption compared with the conventional situation.

From the comprehensive data analysis of Figures 3 and 4 and Table 2, the overall analysis report of the EMS energy consumption management system can be obtained.

(1) Analysis of overall energy consumption of buildings. The EMS energy consumption management system detects the entire building and various power supply and distribution systems, detects the data running track, and performs real-time data analysis and energy consumption interpretation.

(2) Building power distribution information monitoring. The EMS energy consumption management system can enter the operation interface of the power supply route through the operating system, view the working status of the power supply system in real time, check the status of the corresponding circuit, and analyze the data.

(3) Analysis of building electricity load. The EMS energy consumption management system provides data support for managers and analyzes the building's electricity load to understand the electricity load,

TABLE 1: Questionnaire about green building energy management system.

Number	Description	Not match<-----> match 100%
Corporate sustainable development strategy	Do you think your company meets the sustainable development strategy	1 2 3 4 5
Green building	Do you think your company is a green building	1 2 3 4 5
Sustainable competitive advantage	What do you think of your company's sustainable competitive advantage	1 2 3 4 5
Stakeholder environmental pressure	Do you think the pressure of the enterprise mainly comes from the external environment or internal management	1 2 3 4 5
Knowledge of energy management system	How well do you know the energy management system	1 2 3 4 5
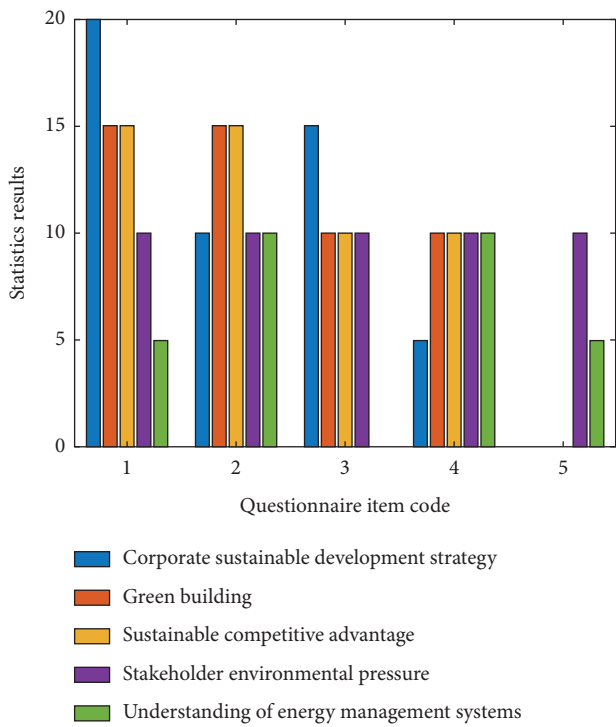
FIGURE 1: Survey results of 50 senior executives of enterprises.
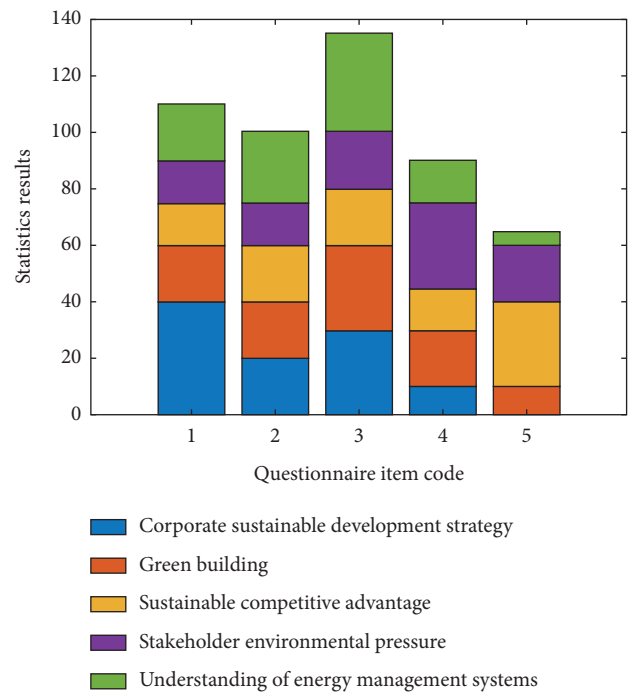
FIGURE 2: Results of the questionnaire survey of 100 frontline staff in the enterprise.

which provides great convenience for the centralized management of the building.

(4) Building electricity consumption report and financial analysis of energy consumption. The report generation function of the EMS energy consumption management system and the financial analysis function of building electricity use the financial analysis of building electricity according to local characteristics and combine the characteristics of itemized energy consumption comparison to provide distribution management data for managers.

(5) In-depth analysis and energy-saving diagnosis of energy consumption data of building subprojects are mainly for daily energy-saving monitoring of equipment and provide suggestions for daily equipment management and system energy-saving renovation work.
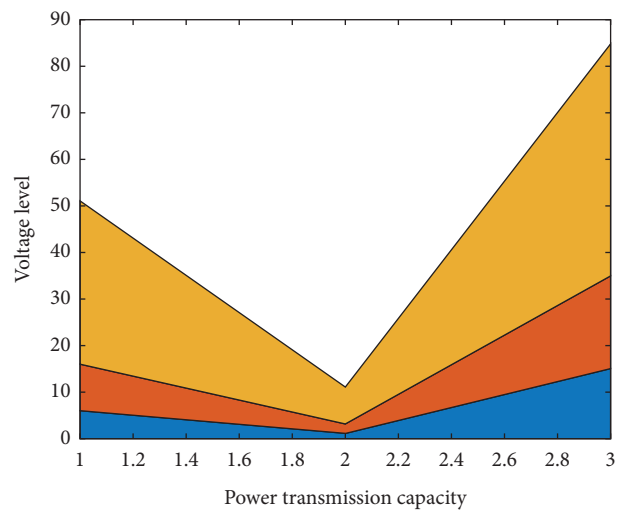
FIGURE 3: The relationship between voltage level, power supply capacity, and power supply distance under overhead line type.
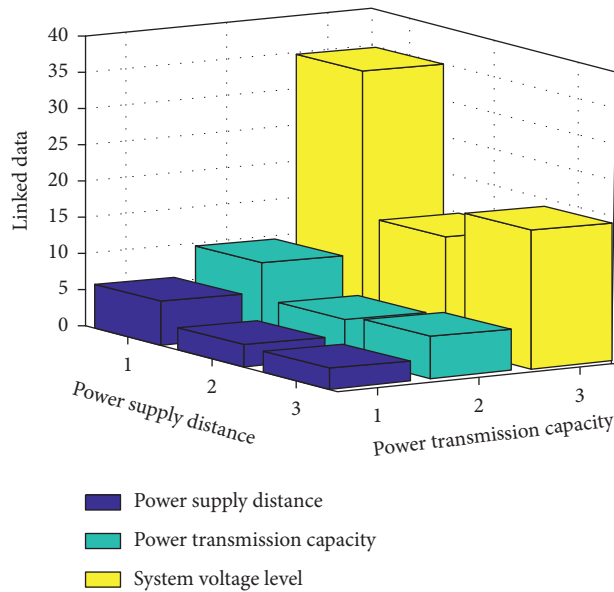
FIGURE 4: The relationship between voltage level, power supply capacity, and power supply distance under cable type.

TABLE 2: Load calculation table.

Load name	Electricity load (kW)	Need factor (ke)	Power factor	Active power (kW)	Reactive power (kvar)	Inspecting power (kVA)
Illumination	3.23	1.13	0.91	2.31	1.46	2.65
Air conditioning system	19.66	1.43	1.54	12.96	12.10	16.60
Weak current system	9.01	1.27	1.39	5.13	4.52	6.71
Subtotal	33.25	0.64	—	19.34	17.67	23.11
Multiplied by the coefficient	—	0.89	—	17.04	14.87	21.65
After power factor compensation	33.66	—	0.88	17.12	7.98	19.40

(6) User energy consumption analysis. The EMS energy consumption management system can combine the actual situation of the entire project to rationally divide the use units, such as separate measurement and management of rental stores. According to the standardized management of the energy-saving analysis report of the EMS2000 energy consumption management system, energy savings of 8% to 10% can be achieved each year. If a major energy consumption loophole is found, the energy consumption of the building can also be greatly reduced. In addition, due to the comprehensive monitoring and professional maintenance guidance of the main equipment of the building, the service life will reach the expected effect.

5. Conclusions

With the increase of consumers' awareness of environmental protection and energy conservation, consumers have gradually realized that a harmonious ecological environment and a healthy and efficient lifestyle are the most profound essence of architecture. Combined with the actual application of the energy consumption model, the energy-saving management effect of the energy-saving management system is analyzed. This article starts from the concept of corporate sustainable development and green building and uses a questionnaire survey method to understand the environmental protection concepts and awareness of my country's construction companies. Through the application in practice, the use effect of the energy management system is explained, and conclusions are drawn. Compared with developed countries, my country's green building started late, and the understanding of sustainable development, green ecological building, and environmental protection is not strong and deep. This requires our long-term efforts. Enhancing the environmental protection awareness of the enterprise, the energy consumption model analyzes the overall energy consumption of the enterprise through remote monitoring of the entire building and various low-voltage power distribution branches while monitoring the distribution information, analyzing the power load, and generating system report functions and building using electricity financial analysis, itemized energy consumption management, and energy-saving monitoring. Finally, the user analysis is summarized according to user usage. Through standardized management, an average annual energy saving of 8%–10% can be achieved. It is feasible to apply energy management systems to green buildings.

Data Availability

No data were used to support this study.

Conflicts of Interest

There are no potential conflicts of interest in our paper.

Acknowledgments

References

[1] W. Liao, "Application of hadoop in the document storage management system for telecommunication enterprise," *International Journal of Interdisciplinary Telecommunications & Networking*, vol. 8, no. 2, pp. 58–68, 2017.

[2] J. Vimpari and S. Junnila, "Valuing green building certificates as real options," *Journal of European Real Estate Research*, vol. 7, no. 2, pp. 181–198, 2016.

[3] Neyestani, "A review on sustainable building (green building)," *Mpra Paper*, vol. 6, no. 1, pp. 451–459, 2017.

[4] A. Das, B. M. Al-Hashimi, and G. V. Merrett, "Adaptive and hierarchical runtime manager for energy-aware thermal management of embedded systems," *ACM Transactions on Embedded Computing Systems*, vol. 15, no. 2, pp. 1–25, 2016.

[5] L. Zhao, Q. Zhang, and Y. Ji, "The relationship between green building and regional economy: a case study in Guangdong, China," *The Open Civil Engineering Journal*, vol. 11, no. 1, pp. 216–234, 2017.

[6] N. Aghili, A. H. B. Mohammed, and L. Sheau-Ting, "Management key practices for improving green building performance," *Advanced Science Letters*, vol. 23, no. 9, pp. 8874–8876, 2017.

[7] S. Abhinaya, V. R. Prasath Kumar, and L. Krishnaraj, "Assessment and remodelling of a conventional building into a green building using BIM," *International Journal of Renewable Energy Resources*, vol. 7, no. 4, pp. 1675–1681, 2017.

[8] A. Andrea, "California adopts nation's first statewide green building code," *International Journal of Oncology*, vol. 1, no. 2, p. 121, 2016.

[9] S. Xiaofeng and K. Song, "Exploration and practice of green building management in Sino-Singapore Tianjin Eco-City," *China City Planning Review*, vol. 25, no. 3, pp. 50–57, 2016.

[10] N. Bin Yasin, A. H. Bin Abdullah, and R. B. Yunus, "Potential retrofit of universiti tun hussein onn Malaysia existing building towards green building," *Social Sciences*, vol. 11, no. 11, pp. 2726–2731, 2016.

[11] Isa, M. Abu Bakar, and M. Sufian Hasim, "Data quality control for survey instrument of office investors in rationalising green office building investment in Kuala Lumpur by the application of Rasch analysis," *Facilities*, vol. 35, no. 4, 2017.

[12] A. T. Syed and A. A. Abdou, "A model of a near-zero energy home (NZEH) using passive design strategies and PV technology in hot climates," *Journal of Green Building*, vol. 11, no. 1, pp. 38–70, 2016.

[13] S. Pushkar, "Environmental damage and saving benefit of external shading devices via photovoltaic (PV) energy generation," *Journal of Green Building*, vol. 11, no. 3, pp. 95–109, 2016.

[14] N. A. Azmi, M. Z. Kandar, and D. H. C. Toe, "Daylight optimization for green office building: a study of west facing window design and configuration," *Advanced Science Letters*, vol. 23, no. 9, pp. 9177–9182, 2017.

[15] M. Kensek, "Teaching visual scripting in BIM: a case study using a panel controlled by solar angles," *Journal of Green Building*, vol. 13, no. 1, pp. 115–137, 2018.

[16] B. Raji, M. J. Tenpierik, and A. van den Dobbelsteen, "A comparative study: design strategies for energy-efficiency of high-rise office buildings," *Journal of Green Building*, vol. 11, no. 1, pp. 134–158, 2016.

[17] A. Roetzel, "Variability of building simulation results depending on selected weather files and conditioning set points-a case study for a residential building in Victoria, Australia," *Journal of Green Building*, vol. 11, no. 4, pp. 91–108, 2016.

[18] W. A. Miller, P. Boudreaux, S. Pallin et al., "A field study setup of four homes having non-ventilated and semi-conditioned sealed attics," *Journal of Green Building*, vol. 11, no. 3, pp. 1–20, 2016.

[19] S. Pushkar and O. Verbitsky, "Environmental damage from wall technologies for residential buildings in Israel," *Journal of Green Building*, vol. 11, no. 4, pp. 154–162, 2016.

[20] D. Phillips, M. Guaralda, and S. Sawang, "Innovative housing adoption: modular housing for the Australian growing family," *Journal of Green Building*, vol. 11, no. 2, pp. 147–170, 2016.

[21] C. Peng, J. Yang, and J. Huang, "Case study of the operational energy consumption and carbon emissions from a building in Nanjing based on a system dynamics approach," *Journal of Green Building*, vol. 11, no. 3, pp. 126–142, 2016.

[22] O. Sukalo, "Conceptual narratives, ecological heeds, social purposes and subjective ends of natural building movement," *Facta Universitatis - Series: Architecture and Civil Engineering*, vol. 14, no. 2, pp. 201–221, 2016.

[23] F. Xiong, Y. Lin, and S. Tu, "Value assessment of green buildings based on CASBEE," *Journal of Shenzhen University Science and Engineering*, vol. 33, no. 2, p. 194, 2016.

[24] L. Malys, M. Musy, and C. Inard, "Direct and indirect impacts of vegetation on building comfort: a comparative study of lawns, green walls and green roofs," *Energies*, vol. 9, no. 1, p. 32, 2016.

[25] B. A. Kayan, A. M. Forster, and P. F. G. Banfill, "Green Maintenance for historic masonry buildings: an option appraisal approach," *Smart & Sustainable Built Environment*, vol. 39, no. 2, pp. 654–664, 2016.

[26] R. Yadav, A. Kumar Dokania, and G. Swaroop Pathak, "The influence of green marketing functions in building corporate image," *International Journal of Contemporary Hospitality Management*, vol. 28, no. 10, pp. 2178–2196, 2016.

Research Article

Experimental Research on Coal and Gas Delay Outburst and AE Characteristics under Conditions of Geostress and Gas Pressure Disturbance

Geng Jiabo,[1,2] Liu Jiangtong,[1] Li Xiaoshuang [1,2,3,4] Nie Wen,[1] Zhang Dongming,[1] and Xu Jiang[5]

[1]*School of Resources and Environmental Engineering, Jiangxi University of Science and Technology, Ganzhou 341000, China*
[2]*State Key Laboratory of Safety and Health for Metal Mines, Sinosteel Maanshan General Institute of Mining Research Co., Ltd., Maanshan 243000, China*
[3]*School of Civil Engineering, Shaoxing University, Shaoxing 312000, China*
[4]*College of Civil Engineering, Qilu Institute of Technology, Jinan 250200, China*
[5]*State Key Laboratory of Coal Mine Disaster Dynamics and Control, Chongqing University, Chongqing 400044, China*

Correspondence should be addressed to Li Xiaoshuang; xsli2011@126.com

Adopting yellow mud as barrier layer materials, coal and gas delay outburst experiments under conditions of geostress and gas accumulation disturbance were carried out by using self-developed simulation system, to find out roles of geostress and gas pressure played in the process of the delay outburst and ways to predict it, through analysis of variations of gas pressure, and AE characteristics during the process. The results show that after the geostress increased by 0.11 MPa from 1.80 MPa, an outburst occurs, while in gas accumulation situations, the gas pressure increase of 0.27 MPa from 0.67 MPa induces an outburst; hence, geostress is one of the dominant factors impacting an outburst occurrence. The lasting time of the outburst triggering under geostress disturbance is shorter than that under gas accumulation disturbance, while the duration of the outburst development under gas accumulation conditions is longer than that under geostress conditions. Coal seam breakage by geostress is the precondition for an outburst risk, and gas expansion energy is the dominant parameter influencing the duration of the outburst development. The AE signals show distinctive features in different stages of the outburst under geostress disturbance. At the preparation stage of the outburst, the AE signals increase sharply but have a low intensity and then drop to a lower balance level. At the triggering stage, the AE signals become active and increasing until up to the peak where the outburst occurs, and the intensity is highest.

1. Introduction

The coal and gas delay outburst (hereinafter referred to as the delay outburst) is considered as one of the main patterns of the dynamic disaster, the coal and gas outburst. It is an outburst accident that does not occur during blasting or extracting operations, but takes place sometime after the operations at the blasting or working site. Bearing the characteristics of time delay and imperceptibility, the delay outburst poses a serious risk to coal mine safety [1–3].

Sufficient achievements have been made in the study of instantaneous outbursts [4–6], while positive research results on delay outbursts are relatively few up to now. In the 1950s, Hodote, an expert from the former Soviet Union, found the phenomenon of the delay outburst and analyzed the reason from the duration of the blasting breakage propagating from the blasting source to the deep coal seam. According to the actual situation, Jiang and Guo [7] analyzed various reasons for the delayed outburst and carried out a simulation test for the delayed outburst according to the analysis results. Some researchers [8, 9]

discussed the reasons for the delay outburst in terms of the coal bearing capacity decreasing with time and the poor gas diffusion capacity in the pressure relief zone of the coal seam. Bao [10] analyzed a large number of in situ cases and found that the majority of delay outburst accidents occur after the increasing damage or even rupture of the pressure relief zone, as well as in the circumstances of engineering disturbances at the blasting or mining sites. Several scholars investigated the mechanism of the delay outburst through physical simulation experiments. Xu et al. [11] and Li et al. [12] conducted physical simulation experiments with different materials as the barrier layer and believed that the delay outburst results from either the creep deformation of the hard coal barrier layer or the decreasing of the supporting force in the pressure relief zone.

On the other hand, due to the influence of geostress and gas pressure during the outburst process, crack initiation and development behaviors inside the coal rocks produce the acoustic emission (AE) phenomenon. As a result, AE monitoring which is a research method for studying and predicting deformation and failure of materials is introduced into monitoring and forecasting coal and gas outburst incidents [13, 14]. It is proved to be an effective method to analyze the mechanism of coal and gas outbursts.

Efforts on delay outburst mechanism are mainly focused on several aspects. The bearing force of coal rock masses decreases with time under the action of geostress. The role of gas played in the delay outburst remains unclear and few physical simulations discuss the variation rules of gas pressure, temperature, and AE characteristics during the entire delay outburst process whereas these parameters are indispensable to understanding the mechanism and prediction of delay outburst risks. Using yellow mud as the barrier materials, delay outbursts caused by geostress disturbance and gas accumulation in front of the working face are separately simulated in this work. The influences of geostress and gas pressure on delay outbursts and evolution rules of the above-mentioned parameters during the delay outburst process are also discussed.

2. Experiment Method

2.1. Experiment Equipment.
Self-developed large-scale coal and gas outburst simulation platform was used to simulate the delay outbursts [15]. The temperature sensor and gas pressure sensor installed in the device can synchronously detect the variations of the temperature and gas pressure in the coal body, and gas pressure sensor is installed in the middle area inside the test box. When the temperature and gas pressure in the box change, the temperature sensor and gas pressure sensor will transmit the temperature and gas pressure change to the analysis equipment through digital signals and electrical signals for storage. Figure 1 shows the picture of the simulation system.

Additionally, the PCI-2 AE system produced by American Physical Acoustics Company (PAC) was selected to collect the AE signals in the process of coal and gas outbursts. The AE threshold value was set at 35 dB, and two AE sensors were symmetrically arranged at the central part of the external board of the outburst chamber, as shown in Figure 2.

FIGURE 1: Picture of coal and gas outburst simulation system.
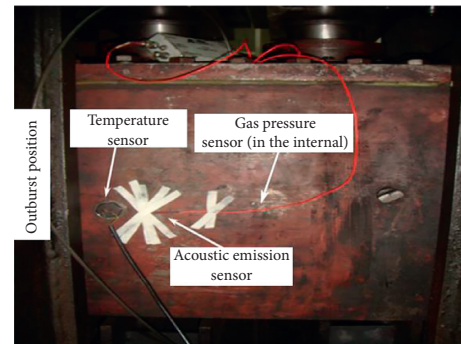
FIGURE 2: Layout of AE and temperature sensors.

2.2. Experiment Design.
Through comprehensive analysis of coal and gas delay outburst cases, it is found [16] that the majority outbursts generally occur within 100 meters range of the outburst crater at which the stress concentration is caused by blasting or/and coal mining operations, and the gas emission increases sharply before in situ outburst occurrence. It can be seen that both the disturbances of geostress and the increase of gas pressure are likely to stimulate the delay outburst. To understand the influence of geostress disturbance and gas pressure increases on delay outbursts, simulation experiments for coal and gas delay outbursts under two different conditions including geostress disturbance and gas accumulation disturbance are designed separately, i.e., by increasing the $P3$ after uncovering the baffle plate to simulate the delay outburst caused by in situ stress disturbance in the coal seam in front of the working face, and by increasing the gas pressure after the baffle plate opened to simulate the delay outburst caused by gas accumulation in the coal seam ahead of the work face.

In the experiments, a series of physical simulation tests are carried out against the background of coal seam occurrence conditions at 265 m; the coal specimens were sampled from coal seam 9# of Linhua Coal Mine, Guizhou Province, China. The moisture content of the specimens was constant at 4%.

Referring to China's empirical formula [17] for geostress stress changing with buried depth, the vertical stress (σ) of coal seam can be obtained as follows:

$$\sigma = 0.0208H + 2.195 = 7.7 \text{ MPa}. \tag{1}$$

To calculate the geometric similarity constant (C_L) and volume force similarity constant (C_ρ),

$$\text{CL} = \frac{L_p}{L_m},$$

$$C_\rho = \frac{\rho_p}{\rho_m}, \tag{2}$$

where L_p is the prototype size, m; L_m is model size, m; ρ_p is the prototype density, kg/m^3; and ρ_m is the model density, kg/m^3.

The stress similarity constant can be calculated as follows:

$$C_\sigma = C_L * C_\rho. \tag{3}$$

Gas pressure calculation [18] is as follows:

$$Y = 1E - 5 * H^2 + 0.0022H + 0.005, \tag{4}$$

where H is depth, m, and Y is the gas pressure, MPa.

The original vertical stress $\sigma = 4.0$ MPa and gas pressure $P = 0.67$ MPa were calculated. According to the stress distribution law in front of the working face, the three indenters above the box are set to provide transverse principal stress, named $P1 \sim P3$, respectively. An indenter behind the box provides the axial principal stress, named $P4$; and the pressure was constant at 4.00 MPa. The constant values of $P1$, $P2$ threshold $P3$, and $P4$ were 1.80 MPa, 3.60 MPa, 1.80 MPa, and 2.40 MPa, respectively. The initial gas pressure was constant at 0.67 MPa. Vacuum extraction time was 2 hours and gas adsorption time was 24 hours.

2.3. Layout of Yellow Mud Barrier Layer.

After the roadway excavation and coal mine extraction, the coal around the working face steps into a plastic state due to stress concentration. Wold et al. [19, 20] and some other researchers believed that the outburst is caused by plastic deformation and failure of the coal seam. Bao [10] analyzed in situ delay outburst cases and concluded that the delay outburst is the result of the development of coal seam plastic deformation under the action of external force.

In this study, hard-plastic yellow mud was selected to simulate the plastic coal seam near the outburst crater. The hard yellow mud has a certain strength that can bear some degree of stress changing inside the coal mass to prevent an outburst accident. Moreover, it can maintain in the plastic state under existing loading conditions and realistically simulate the plastic deformation and failure of the coal seam. The yellow mud was finely ground and mixed with water for being in a hard-plastic state; afterwards, it was filled into the coal and compacted. The layout of yellow mud in the chamber is shown in Figure 3. The cohesive force C of the compacted yellow mud was about 0.15 MPa, and the internal friction angle φ was about 45° [21–23].

The force applied to the yellow mud barrier layer in the coal chamber is shown in Figure 4(a) and is simplified as the shear force model in Figure 4(b) for calculation. There is a PVC plate with a radius of 50 mm bonded outside the outburst crater by silicone rubber; hence, it can provide an adhesive force (F_a) to prevent the outburst. Since the radius
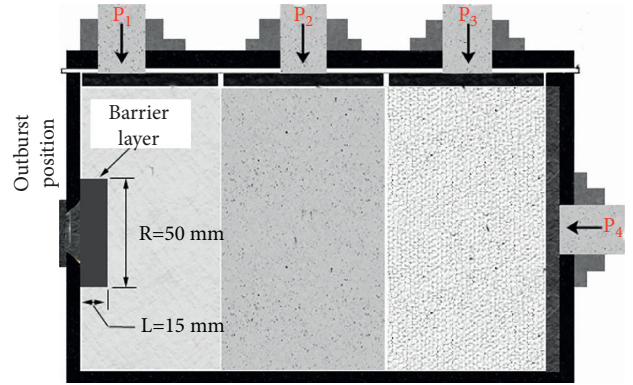
FIGURE 3: Stress distribution loaded on coal specimens and layout of yellow mud.

of the outburst crater (r) is 30 mm, the equivalent stress provided by the adhesive force F_a is represented by σ_e. The adhesive force is taken as 0.4 MPa; hence, the value of σ_e is 0.71 MPa, i.e., $\sigma_e = 0.4 \times \pi \times (50^2 - 30^2)/(\pi \times 30^2) = 0.71$ MPa. P is the gas pressure, taken as 0.7 MPa; σ_1 is the normal stress of yellow mud transmitted by the coal mass, taken as 1.8 MPa; σ_h is the shear force of yellow mud transmitted by the coal mass, taken as 2.4 MPa. The ultimate stress (F) causing yellow mud deformation and failure can be calculated by the following equation:

$$F = (\sigma_h + P - \sigma_e) \times \pi \times r^2 = 2 \times \pi \times r \times \tau \times L, \tag{5}$$

where τ is the shear strength of yellow mud, derived by the equation, $\tau = C + (\sigma_1 + P) \times \tan\varphi$, and L is the thickness of yellow mud.

The simulation experiments were carried out for three times, and the actual gas pressure was 0.67 MPa. The instantaneous outburst occurred when the thickness of the yellow mud was 10 mm, and delay outbursts took place when the thickness was 15 mm. The two simulation experiments under the conditions of 15 mm thickness of the yellow mud were mainly discussed in this work.

3. Delay Outburst Simulation Experiment

3.1. Delay Outburst under Geostress Disturbance.

Based on the description of the coal and gas outburst process in the literature [6] and combined with the screenshots of the outburst videos (Figure 5), the delay outburst process can be divided into four stages, including preparation, triggering, development, and termination stages, in which the term termination is defined as the end of coal ejection. Figure 6 shows the variation curve of the geostress vertically applied to the coal mass. The red point a in Figure 6 represents the moment where no outburst occurred after the baffle plate was opened. 42 seconds later after this opening, while $P3$ was gradually increased to 1.91 MPa from 1.80 MPa, the barrier materials began to break and were stepping into the outburst triggering stage. If the stress condition remained unchanged, the barrier layer constantly deformed and was destroyed until it encountered an outburst; afterwards it came to the outburst development stage. Figure 6 shows the

(a)   (b)
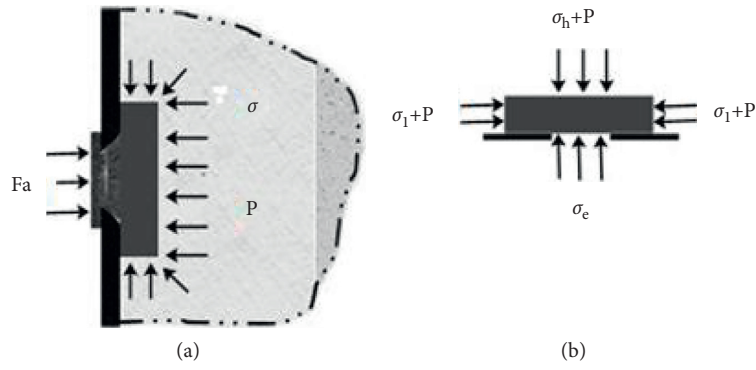
FIGURE 4: Bearing model of yellow mud barrier layer.
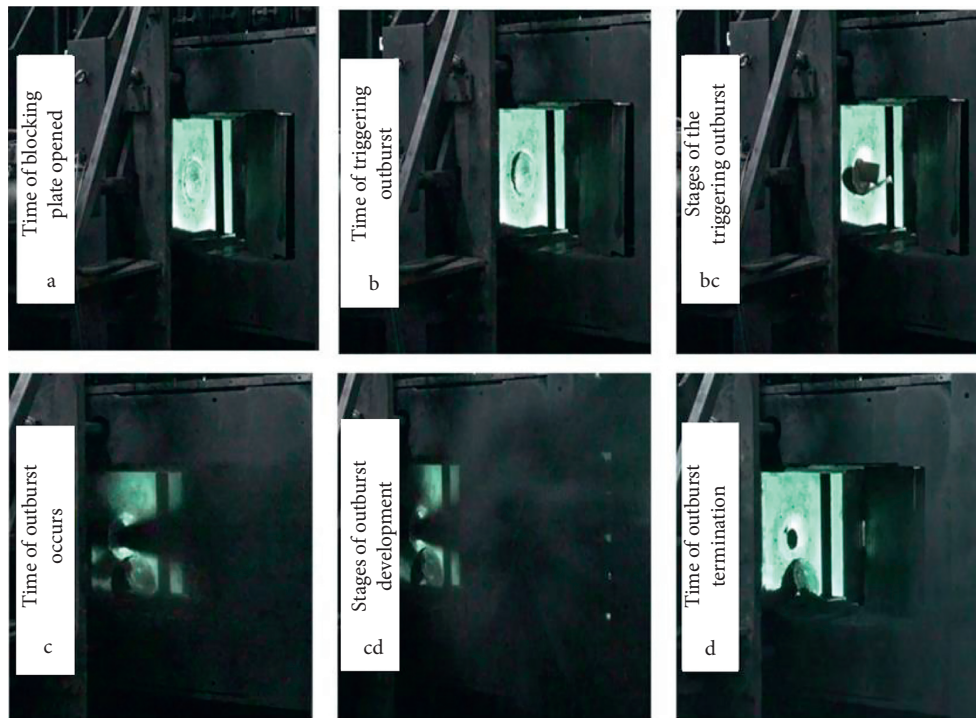
FIGURE 5: Video screenshots of the delay outburst caused by geostress disturbance.
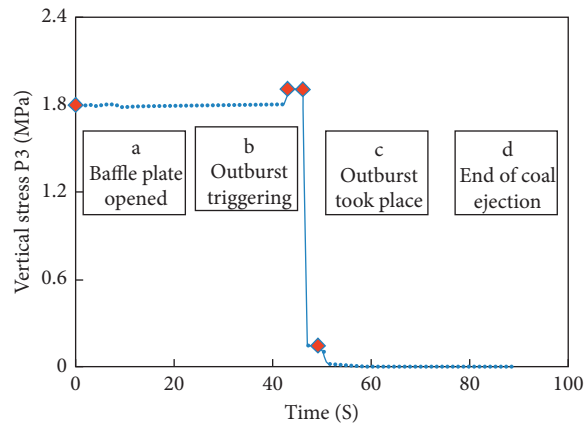
FIGURE 6: Variation curve of stresses loaded vertically.
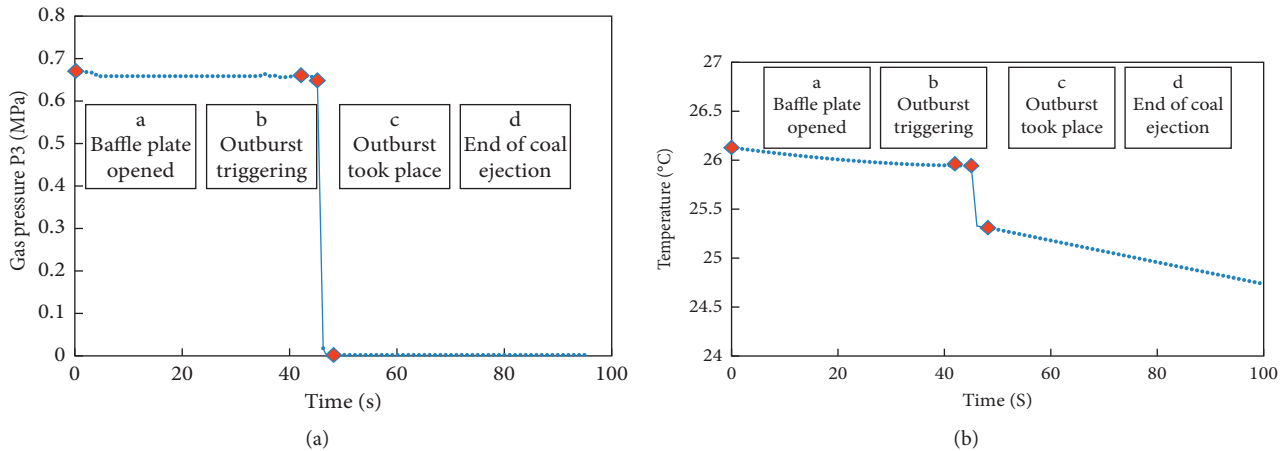
FIGURE 7: Gas pressure (a) and temperature (b) change curves during the delay outburst caused by geostress disturbance.

corresponding gas pressure and temperature evolution curves in the experiment, and Figure 7 provides the corresponding video screenshots at different outburst moments. The entire initiation process of the outburst is analyzed in terms of stages (Figures 5–7).

At the outburst preparation stage (Stage ab), when the baffle plate was quickly opened (moment a in Figures 5 and 7), equivalent to the completion of mining operations at the work face, the stress state of the coal seam was subjected to a change, the gas pressure only had a slight decrease, and the temperature declined slowly. However, no deformation or failure occurred in the barrier layer, and there were no signs of damage at the outburst crater. At this stage, the stresses inside the coal rocks were altered after the completion of mining activities; physical and mechanical properties, gas pressure, and other parameters of the coal seam were changed. Nevertheless, the coal and rock masses were still able to bear these changes and keep in a new balance state due to the presence of the barrier layer.

During the outburst triggering stage (Stage bc), namely, 42 seconds after the baffle plate was uncovered, the coal and rock masses were disturbed by geostress disturbance, namely, gradually increasing the $P3$ loading by 0.11 MPa (from 1.8 MPa to 1.91 MPa), corresponding to moment b in Figures 5 and 7, the outburst hole was destructed, and the barrier layer materials were constantly ejected from the outburst chamber. During this period, the gas pressure and temperature decreased slowly. When the residual barrier materials were not enough to resist the coal failure and ejected out, an outburst occurred, corresponding to moment c in Figures 5 and 7. In the triggering stage (Stage bc), due to the increase of vertical loading, the coal rock masses were further destroyed and the elastic potential energy largely increased. The energy inside the coal and rocks was sufficient to destroy the barrier layer and initiate an outburst, leading to the coal seam breakage and ejection. The triggering of the outburst produced an early outburst cavity, adsorbed gases in the coal seam had the behavior of desorption, and the gas pressure and temperature were also reduced accordingly. The triggering process lasted only 3 seconds.

At the outburst development stage (Stage cd), after the outburst took place, the accumulated energy was released instantaneously, and the broken coal and rocks were constantly destroyed and ejected out until the outburst terminated. During this stage, the gas pressure declined instantaneously, and the adsorbed gas continued to desorb and expand power rapidly. The temperature dropped significantly. The duration time of the development stage (Stage cd) was only 3 seconds.

3.2. Delay Outburst under the Disturbance of Gas Accumulation.
In the same way combined with the gas pressure and temperature change curves during the delay outburst under gas accumulation conditions (Figure 8) and the outburst video screenshots (Figure 9), the delay outburst process under the disturbance of gas accumulation is discussed in stages.

At the outburst preparation stage (Stage ab), after opening the baffle plate (corresponding to moment a in Figures 8 and 9), the stress conditions of the coal and rocks became worse. As a result of the presence of the barrier layer, the stress state of coal rocks was able to reach a new balance. When the gas pressure was gradually improved by 0.27 MPa from 0.67 MPa to 0.94 MPa, the total energy inside the coal rocks soared to the threshold of triggering an outburst; subsequently, the outburst crater was deformed and an outburst was initiated (corresponding to moment b in Figures 8 and 9). Stage ab is equivalent to the period of stress changing in the coal seam after coal mining, during which gas accumulated ahead of the work face and energy accumulated in the coal seam.

At the outburst triggering stage (Stage bc), after the outburst took place, the elastic energy and gas expansion energy accumulated in the coal rock masses squeezed out the barrier materials, unstable coal particles were separated from solid coal, the bearing capacity of the barrier layer reduced drastically, and finally an outburst occurred (corresponding to moment c in Figures 8 and 9). Stage bc was the triggering stage of the outburst and lasted for 33 seconds, where the
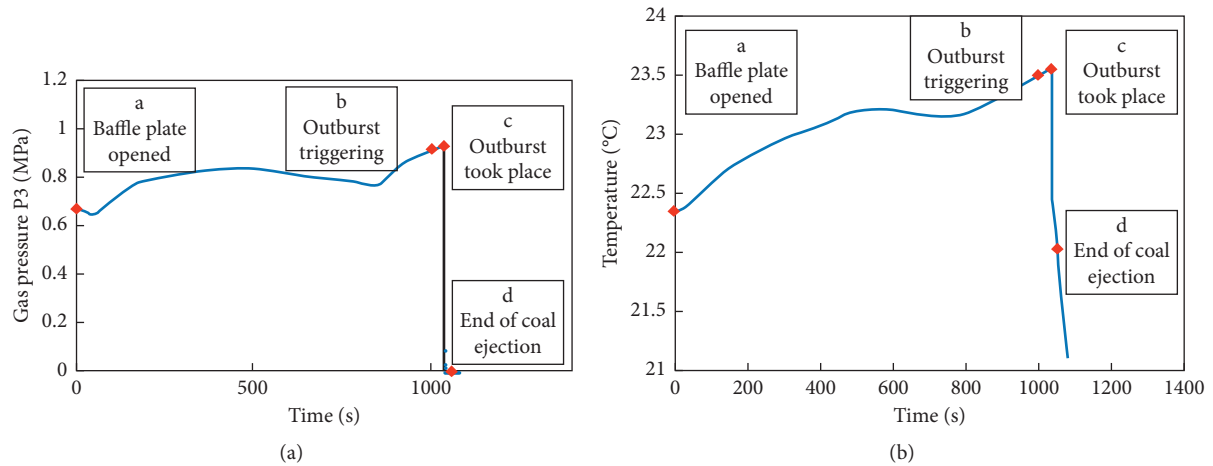
FIGURE 8: Gas pressure (a) and temperature (b) change curves during the delay outburst caused by gas accumulation ahead of the work face.

FIGURE 9: Video screenshots of the delay outburst caused by gas accumulation in front of the working face.

barrier layer was destroyed under the combined action of geostress and gas pressure.

In the process of outburst development (Stage *cd*), a large amount of pulverized coal was quickly ejected from the chamber, the gas pressure decreased instantly, the accumulated energy in the coal seam fractured the coal and ejected them out, the adsorbed gas continuously desorbed into the free state and constantly broke the coal masses, and the temperature also declined significantly. Here the development stage, *cd*, lasted for 21 seconds.

From Figures 7(b) and 8(b), it can be concluded that the change of coal temperature is consistent with the change of gas pressure, indicating that the gas in the coal seam is almost simultaneously desorbed in large quantities, resulting in the decrease of coal temperature during the outburst process.

3.3. Comparison of Delay Outburst under Two Disturbance Conditions. According to the video screenshots and comparison analysis of the results of the delay outburst simulation experiments under two disturbance conditions (Table 1), it can be concluded that the outburst takes place when the geostress gradually increases from 1.80 MPa to

TABLE 1: Comparison of delay outburst under two disturbance conditions.

Test types	Parameter threshold value (MPa)	Increment (MPa)	Degree (%)	Preparation time (s)	Triggering time (s)	Development time (s)
Geostress disturbance	1.80	0.11	6.1	42	3	3
Gas accumulation disturbance	0.67	0.27	38.6	1002	33	21

(a)

(b)

(c)
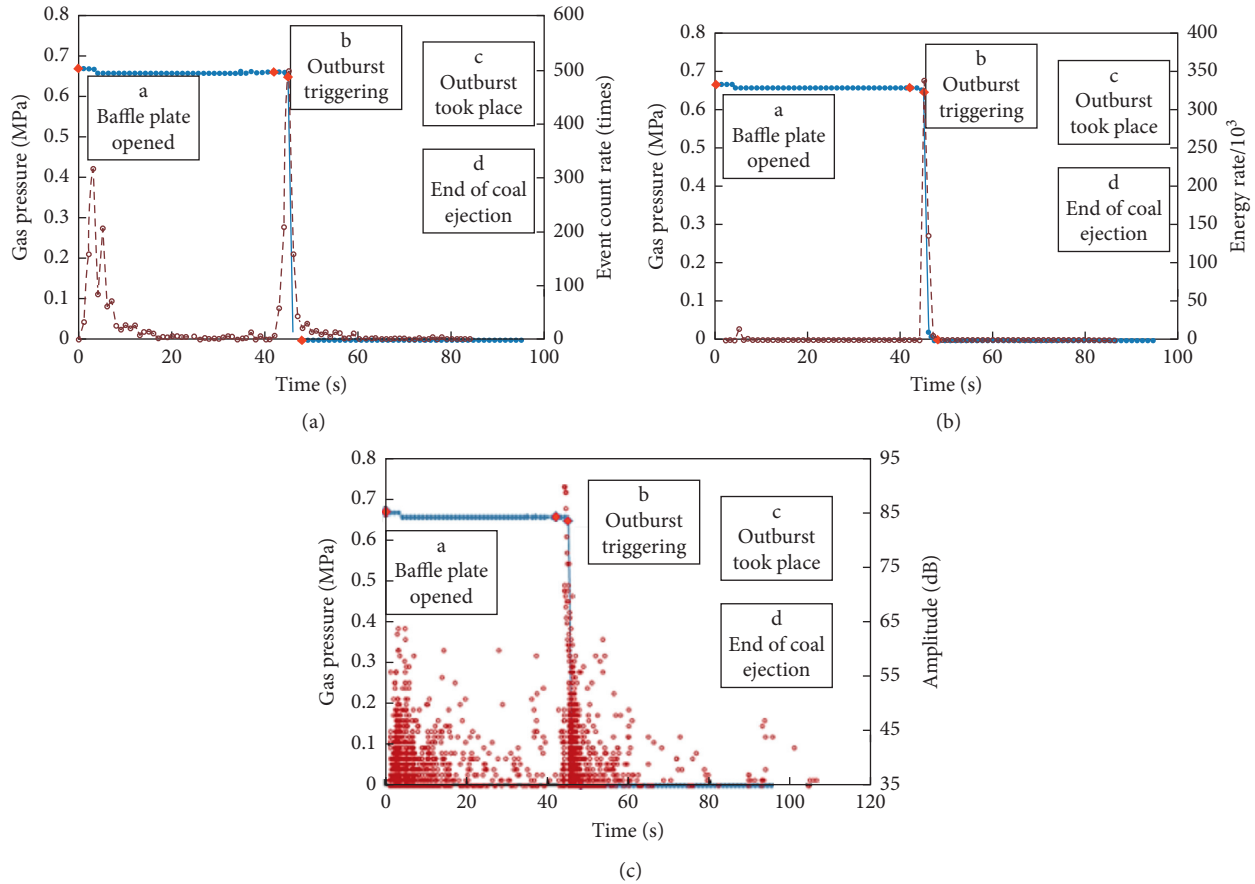
FIGURE 10: AE characteristics of the delay outburst under the geostress disturbance. (a) AE event count rate variation; (b) AE energy rate variation; (c) AE amplitude variation.

1.91 MPa (namely, an increase of 6.1 percent), but through gas accumulation, it needs to gradually increase 38.6 percent of the gas pressure from 0.67 MPa to 0.27 MPa to stimulate the occurrence of an outburst. This indicates that geostress disturbance is more likely to induce an outburst and geostress is the dominant factor affecting the initiation of an outburst since coal rock masses are constantly breaking with the increasing geostress. In addition, the preparation time of an outburst is associated with the disturbed conditions of the coal seam. Specifically, the geostress disturbance is mainly related to the coal seam loading pressure and engineering activities, while the gas accumulation disturbance is relevant to the gas accumulation velocity and seam gas release ability. When the stress disturbance is applied to the coal seam, the yellow mud barrier layer begins to deform and break. When the bearing force of the remaining barrier layer cannot maintain the original balance, an outburst occurs. The

duration of the outburst development lasts only 3 seconds under the disturbance of geostress, while it lasts for 21 seconds under the disturbance of gas pressure. Therefore, it can be considered that gas expansion energy is the dominant factor affecting the outburst development. The failure of coal and rock masses by geostress is the precondition of an outburst. Gas expansion can promote the development of the outburst. The duration of ejecting pulverized coal can indirectly reflect the intensity of an outburst; thus, the outburst intensity caused by gas pressure disturbance is higher than that caused by geostress disturbance.

In terms of predicting a delay outburst, the triggering time of the outburst caused by gas accumulation is relatively longer (33 seconds), and the outburst is initiated more slowly. Moreover, gas accumulation ahead of the work face generally induces corresponding changes in the gas emission amount and coal seam temperature; hence, the warning

signs are more obvious for an outburst under gas accumulation disturbance. The geostress disturbance causes high velocity of an outburst and the outburst is initiated more quickly. As a result, it is critical to strengthen the supporting of coal and rocks and adopt reasonable roof caving methods, as well as employ other means to in situ monitor coal seam changes for coal mine safety production.

4. AE Characteristics

As to AE parameters, this study selected the AE count rate reflecting the frequency of the AE events, the AE energy rate reflecting the change of the energy released in the AE events, and the AE amplitude reflecting the magnitude of the AE signals to investigate the AE characteristics in the process of the delay outburst under the condition of geostress disturbance, and the results are shown in Figure 10 [24, 25].

Further analysis of Figure 10 shows that after the blocking plate was opened, the stress state of the coal rocks at the outburst crater began to change. The coal and rock masses were deformed and damaged under the action of geotress and gas pressure, resulting in high AE events. Due to the restricting function of the barrier layer, broken coal and rocks would not immediately eject out, and the gas pressure slightly decreased. With the adjustment of the internal stress of the coal rocks reaching a new balance, the number of the AE events stabilized at a low level. Although the AE count rate was high after opening the baffle plate, the energy rate was relatively low. At the same time, the AE amplitude was basically at a low level. When the geostress disturbance was applied to the coal seam, original internal balance was destroyed, the stress was redistributed, and the coal and rock masses continued to fracture. The gas stored in the coal seam desorbed to a free state and continuously expanded. The rapid expansion of gas in the chamber further fractured the coal particles. At this stage, the AE count rate began to increase, but the AE energy and amplitude were still at a relatively low level. With the continuous coal damage and increase of free gas content, the barrier layer was unable to maintain the balance, finally resulting in an outburst occurrence. The accumulated energy of the coal rock masses was released instantly. Under the action of geostress and gas pressure, the coal and rock masses were continuously destructed and ejected out. When the AE count rate reached the maximum of 498 times per second, the AE energy and amplitude were up to the peak.

After the coal ejection terminated, the gas in the residual coal rock masses continued to desorb and expand, and the AE signals were still detected. Fractures and cracks still propagated in the coal seam at this time, but the energy was not enough to eject the broken coal and rocks. During this stage, the energy was rather low and the AE amplitude returned to a lower level with few AE events still generating.

During the entire process of the delay burst, the AE signals increased sharply and then decreased to a lower level when the blocking plate was opened. After the triggering of the outburst, the AE signals increased again and reached the peak value. Namely, if an outburst does not occur immediately after the completion of mining operations, a

significant increase in AE signals after a certain stable period may indicate the arrival of an outburst. Therefore, AE monitoring can be used as a device to predict the coal and gas delay outburst.

5. Conclusion

(1) It is appropriate to divide the entire process of the coal and gas delay outburst into four stages, including preparation, triggering, development, and termination stages. Both the temperature and gas pressure decline under the two different disturbance conditions in the preparation stage. Due to different inducing mechanisms of the outbursts during the triggering stage, the gas pressure and temperature change rules show different features under the two different disturbances.

(2) The triggering and development time of the outburst caused by gas accumulation in the coal seam ahead of the work face are longer than those by geostress disturbance. Geostress and gas pressure play different roles in the process of the outburst. The coal seam destruction by geostress is the precondition for an outburst, and the gas expansion energy is the main dominant factor for the duration time of an outburst.

(3) According to the AE characteristics in the process of the coal and gas delay outburst, if the AE signals increase significantly from a lower level with no occurrence of an outburst after the completion of mining operations, it may indicate the arrival of a delay outburst.

Data Availability

The data of this study are from Jiangxi University of Science and Technology and Chongqing University.

Conflicts of Interest

The authors declare no conflicts of interest.

Acknowledgments

References

[1] B. Zhao, "Analysis of delayed coal and gas outburst and its prevention measures," *Hunan safety and disaster prevention*, vol. 6, no. 157, pp. 44-45, 2008.

[2] B. Lin, F. Yan, C. Zhu et al., "Cross-borehole hydraulic slotting technique for preventing and controlling coal and gas outbursts during coal roadway excavation," *Journal of Natural Gas Science and Engineering*, vol. 26, pp. 518–525, 2015.

[3] F. Yan, B. Lin, C. Zhu et al., "A novel ECBM extraction technology based on the integration of hydraulic slotting and hydraulic fracturing," *Journal of Natural Gas Science and Engineering*, vol. 22, pp. 571–579, 2015.

[4] J. Xu, D. Liu, S. J. Peng et al., "Coal and gas outburst analogous test under the different diameter of exposed coal seam surface," *Journal of China Coal Society*, vol. 38, no. 1, pp. 09–14, 2013.

[5] J. Xu, Y. Q. Tao, G. Z. Yin et al., "Development and application of coal and gas outburst simulation test device," *Chinese Journal of Rock Mechanics and Engineering*, vol. 27, no. 11, pp. 2354–2362, 2008.

[6] S. J. Peng, W. J. Yang, B. Zhou et al., "Study on the evolution law of gas pressure in the process of coal and gas outburst under true triaxial stresses," *Chinese Journal of Rock Mechanics and Engineering*, vol. 39, no. 09, pp. 39–49, 2020.

[7] C. L. Jiang and L. W. Guo, "Mechanism and simulation test of delayed outburst," *Journal of China Coal Society*, vol. 24, no. 4, pp. 373–378, 1999.

[8] X. R. Luo, N. N. Xia, and Z. Z. Jia, "Research on Stress Simulation and Mechanism of Delaying Coal and Gas Outburst in Coal Driving," *Journal of China university of mining and technology*, vol. 35, no. 5, pp. 571–575, 2006.

[9] F. Nie, H. Wang, and L. Qiu, "Research on the disaster-inducing mechanism of coal-gas outburst," *Advances in Civil Engineering*, vol. 2020, pp. 1–12, 2020.

[10] Z. J. Bao, "Examples and analysis of delayed outburst of coal and gas," *Coal engineer*, vol. 6, pp. 49–56, 1992.

[11] L. H. Xu, H. N. Jiang, and Z. C. Feng, "Effect analysis of barrier layer thickness on outburst delay time based on combination model," *Safety In Coal Mines*, vol. 7, pp. 9–13, 2018.

[12] X. Q. Li, G. Z. Yin, B. Cai et al., "Simulation and analysis of mechanics of coal and gas delay outburst," *Journal of Chongqing University*, vol. 34, no. 4, pp. 13–19, 2011.

[13] J. Xu, W. J. Zhou, D. Liu et al., "Temperature and acoustic emission characteristics of coal in the process of outburst under the influence of mining," *Journal of China Coal Society*, vol. 38, no. 2, pp. 239–244, 2013.

[14] C. Wang, J. Xie, and J. Liu, "Deformation and acoustic emission characteristics of cracked granite during creep," *Advances in Materials Science and Engineering*, vol. 2020, pp. 1–11, 2020.

[15] T. Ai, R. Zhang, J. F. Liu et al., "Space-time evolution rules of acoustic emission locations under triaxial compression," *Journal of China Coal Society*, vol. 36, no. 12, pp. 2048–2057, 2011.

[16] G. Z. Yin, X. Q. Li, C. B. Jiang et al., "Simulation experiments of coal and gas delay outburst in rock cross-cut coal uncovering," *Journal of University of Science and Technology Beijing*, vol. 32, no. 7, pp. 827–832, 2010.

[17] X. P. Li, B. Wang, and G. L. Zhou, "Research on distribution rule of geostress in deep stratum Chinese mainland," *Chinese Journal of Rock Mechanics and Engineering*, vol. 31, pp. 2875–2880, 2012.

[18] C. B. Lian and W. Li, "Exploration on the enhance of gas pressure prediction accuracies in coal seam," *Journal of Henan Polytechnic University (Natural Science)*, vol. 27, no. 2, pp. 12–20, 2008.

[19] M. B. Wold, L. D. Connell, and S. K. Choi, "The role of spatial variability in coal seam parameters on gas outburst behaviour during coal mining," *International Journal of Coal Geology*, vol. 75, no. 1, pp. 1–14, 2009.

[20] S. Xue, Y. C. Wang, J. Xie et al., "A coupled approach to simulate initiation of outbursts of coal and gas —model development," *International Journal of Coal Geology*, vol. 86, no. 2-3, pp. 222–230, 2011.

[21] Z. J. Zhou and R. S. Yang, "Studies of engineering properties of compaction loses," *Journal of Ningxia University*, vol. 28, no. 3, pp. 241–244, 2007.

[22] Y. Zhang, H. He, Z. Y. Zeng et al., "Comparison of strength characteristics of fly ash-lime Improved loess and compacted loess," *Science Technology and Engineering*, vol. 21, no. 8, pp. 3265–3273, 2021.

[23] X. S. Li, K. Peng, J. Peng et al., "Effect of thermal damage on mechanical behavior of a fine-grained sandstone," *Arabian Journal of Geosciences*, vol. 14, Article ID 1212, 2021.

[24] E. Y. Wang, Z. H. Li, D. X. Li et al., "Application of electromagnetic radiation monitoring equipment in monitoring and warning of coal and gas outburst," *Safety In Coal Mines*, vol. 51, no. 10, pp. 46–51, 2020.

[25] J. P. Tang, N. Hao, Y. S. Pan et al., "Experimental study on precursor characteristics of coal and gas outburst based on acoustic emission energy analysis," *Chinese Journal of Rock Mechanics and Engineering*, vol. 40, no. 1, pp. 31–42, 2021.

Research Article

Building Thermal Comfort Research Based on Energy-Saving Concept

Feiran Xue and Jingyuan Zhao 🆔

Coll Architecture, Changan University, Xian 710016, Shaanxi, China

Correspondence should be addressed to Jingyuan Zhao; zjyqtt@chd.edu.cn

Under the trend of building green and comfortable development, effective control of building energy consumption has become one of the problems that countries are actively facing to solve. People's demand for residential buildings has changed from the past survival type to a comfortable and livable type. The high level of heating energy consumption is worthy of in-depth study. In order to reduce energy consumption, realize the mapping of energy-saving concepts in buildings, and understand the energy consumption of different building materials and the influence of external factors on human thermal comfort, this book has conducted research on building thermal comfort based on energy-saving concepts. First of all, this article introduces the concept and application mode of energy-saving concepts in buildings and the concept of thermal comfort and the SET index of standard effective temperature, including the two-node model and the algorithm involved in the Fanger heat balance equation. In the experimental part, a model based on the concept of energy saving was designed to predict and analyze the energy consumption and thermal comfort effects of the building. In the analysis part, a comprehensive analysis of the effects of temperature, humidity, wind speed, and gender on thermal comfort, methods to improve thermal comfort, cumulative load changes with the heat transfer coefficient of windows, and the effects of windows of different materials on energy consumption was performed. At the same temperature, the wind speed is different, and the degree of heat sensation is also different. When the wind speed is 0.18 m/s and the temperature is 28°C, the thermal sensation is 0.32, and the human sensation is close to neutral. When the wind speed increases to 0.72 m/s, the heat sensation drops to −0.45, and the human body feels neutral and cool. It can be seen that the increase in wind speed has a certain compensation effect on the thermal sensation of the human body. When the wind speed does not change, increase the air temperature. For example, when the wind speed is 0.72 m/s, the temperature is 28°C, and the thermal sensation is −0.45, and when the temperature is increased to 29°C, the thermal sensation is 0.08, which shows that the temperature is improving the thermal sensation of the human body which has a certain offsetting effect. By studying the thermal comfort of buildings based on energy-saving concepts, it is possible to obtain the effect of external factors on thermal comfort, thereby optimizing building materials and using building materials with lower heat transfer coefficients to reduce heating energy consumption.

1. Introduction

Building based on the energy-saving concept is a brand-new architectural design concept. On the basis of providing comfortable activity space, it provides more healthy living quality and efficient working environment for building users. Its development goal is to maximize the building, optimize efficiency, while protecting the surrounding environment and increasing the value of resource utilization, minimize the negative impact of the building on the surrounding environment, effectively reduce operating costs, and achieve the highest cost performance [1]. The concept of green building should be embodied in the entire life cycle of a building, from material transportation, processing, and production to new construction, operation and maintenance, and final demolition. In addition to introducing many advanced energy-saving and environmentally-friendly technologies,

it is more important for energy-saving buildings to closely integrate natural sciences and the human environment, showing a people-oriented development concept and allowing people, environment, and buildings to develop harmoniously. Therefore, energy-efficient buildings have undoubtedly become one of the most influential development trends in the world today.

The evaluation of comfort is inseparable from architecture. Architectural comfort includes two specific concepts, namely, the comfort of the building and the comfort of the physical environment. The comfort of the building mainly focuses on its use function, including good living experience and convenience of living facilities, including the barrier-free design of the building. In comparison, the comfort of the physical environment largely depends on the individual's state, and it will change with different feelings. With the promotion of intelligent buildings, the endless emergence of intelligent equipment and integrated systems not only provides great convenience for our lives but also improves the comfort of the living environment to a large extent [2].

Based on the above background of energy-saving concept buildings, many scholars at home and abroad have conducted related research. Meyer W believes that energy-efficient building renovation aims to save energy and, thereby, reduce carbon dioxide emissions. The increase in energy efficiency of buildings usually means a reduction in air exchange, coupled with other indoor air quality issues, which may lead to an increase in indoor radon concentration (Rn-222). To investigate the severity of this problem, the author measured the radon concentration in energy-efficient renovation and low-energy houses (passive houses). In a period of 1 year, the orbital etching detector was exposed to every type of building. The author draws reference samples of nonrefurbished nonpassive buildings from the national radon database for comparison, selects buildings with the same radon-related characteristics, and builds them on a geological subsoil equivalent to the geological subsoil of the survey. The compilation method of the reference sample adopted is that the measured values of the refurbished house and the bottom room of the passive house are assigned a measured value from the database. Statistical analysis shows that compared with unrenovated houses, houses renovated to improve energy efficiency have a wider range of indoor radon concentration. In buildings renovated to improve energy efficiency, the average and median radon concentrations have almost doubled. On the contrary, there is no significant difference in the distribution of passive houses and houses that have not undergone energy-efficient renovations. The author's research on energy conservation has a certain significance for improving the energy efficiency of buildings, but the author has no control variables, and a blank control group should be set up for comparative analysis [3]. Middel A pointed out that, in hot desert cities, shading plays an important role in designing outdoor spaces suitable for pedestrians. The study investigated the impact of photovoltaic canopy shading and tree shade on thermal comfort through meteorological observations and field surveys on the pedestrian streets of Arizona State University Tempe Campus. During the course of the year, on selected sunny and calm days representing each season, the researcher conducted a meteorological section every hour from 7:00 in the morning to 6:00 in the afternoon and investigated the heat of 1284 people. On the 9-point semantic difference system, the shadow reduces the thermal sensation vote by approximately 1 point, thereby increasing thermal comfort in all seasons except winter. The type of shading (tree or sun canopy) has no significant effect on perceived comfort, indicating that artificial and natural shading are equally effective in hot and dry climates. Earth's temperature is the reason for the 51% difference in thermal sensation voting, and it is the only statistically significant meteorological predictor. Important nonmeteorological factors include adaptation, thermal comfort voting, thermal preference, gender, season, and time of day. The return of thermal sensation to the physiologically equivalent temperature produces a neutral temperature of 28.6°C, the acceptable comfort range is 19.1°C–38.1°C, and the preferred temperature is 20.8°C. Respondents believe that being exposed to temperatures above neutral and being in the air conditioner will make them feel more comfortable, indicating that they are lagging in response to outdoor conditions. The author's research emphasizes the importance of active solar energy access management to reduce thermal stress in hot urban areas. The study conducted a research on thermal comfort and used PMV voting indicators to illustrate. The survey samples are referenced, but they did not make reasonable suggestions on how to improve thermal comfort [4]. The scope of D Kioupis' research is to propose an effective method for the experimental design and development of geopolymer products that can meet a wide range of end-user requirements. The method involves the application of a multifactor experimental design model through Taguchi's method, which allows the combined effect of selected parameters in the response of the experimental system to be studied by conducting a minimum number of experiments, thus significantly reducing the time and cost of the entire process. The results showed that the use of various raw materials and additives, as well as controlled changes in synthesis parameters and manufacturing conditions, led to the production of geopolymers with a wide range of final properties. This method is used to develop geopolymers with compressive strength, density, and thermal conductivity in the range of 2–55 MPa, 0.6–2.0 g/cm^3, and 0.09–0.40 W/mK, respectively. The author studied the relevant characteristics of the abovementioned building materials, but did not analyze the application prospects of these materials, such as the compressive strength and density of these materials, which make them applicable to buildings [5].

This paper studies the thermal comfort of buildings based on the concept of energy saving. First, this article introduces the concept and application mode of energy-saving concepts in buildings and the concept of thermal comfort and the SET index of standard effective temperature, including the two-node model and the algorithm involved in the Fanger heat balance equation. In the experimental part, a model based on the concept of energy saving was designed to predict and analyze the energy

consumption and thermal comfort effects of the building. In the analysis part, it comprehensively analyzes the effects of temperature, humidity, wind speed, and gender on thermal comfort, methods to improve thermal comfort, cumulative load changes with the heat transfer coefficient of windows, and the impact of windows of different materials on energy consumption. The innovation of this article is to integrate energy-saving concepts into modern buildings to increase people's awareness of green and environmental protection, select multiple external indicators for thermal comfort research, select materials with the best energy efficiency, and conduct an in-depth analysis of the thermal comfort of the human body in the building from multiple angles.

2. Building Thermal Comfort Methods Based on Energy-Saving Concepts

2.1. Energy-Saving Concept. The main content of the energy-saving concept is to reduce energy consumption and improve energy efficiency, which is mainly reflected in green buildings in terms of buildings. Green building, as its name implies, is to build an economical, comfortable, energy-saving, efficient, reliable, safe, and healthy living environment at the level of low environmental load by reducing energy consumption, maximizing the use of existing resources, and realizing people and the environment. The purpose of the building is to be mutually beneficial for symbiosis, sustainable development, and harmonious coexistence. With the continuous progress of economy and society, the sustained and rapid development of the national economy, and the improvement of the current social living standards, the society's demand for living environment and management standards continues to rise, and there are new and higher demands for the functions of buildings. Nowadays, a variety of electrical equipment are installed in green buildings. The wide application of electrical automation technology in green buildings has increased the economy, reliability, and living comfort of buildings and improved the ability of building equipment operation and management [6, 7].

Green buildings can indeed reduce energy consumption by about 40% or more, but the initial investment is too much. From the inside of the building, it is necessary to consider heating, ventilation, water supply and drainage, lighting, etc.; from the outside of the building, it is to consider the natural resources that can replace these as much as possible [8]. And, we must comprehensively consider their mutual cooperation. This makes the process of building construction complicated. Another concept of green building is that the consumables of the building itself must also meet the requirements of environmental protection. At present, most building materials cannot be recycled and cannot be reused when buildings are demolished. This wastes resources and even causes pollution. In addition to being recyclable, environmentally-friendly alternative materials can also increase the lifespan of buildings.

The schematic diagram of energy-saving building HVAC is shown in Figure 1. It can be seen that the HVAC of energy-saving buildings involves multiple aspects of heat transfer

and is based on resource conservation, reuse, recycling, and development and utilization of renewable resources. Therefore, the choice of building envelope structure materials in practice also requires the above four characteristics. Materials such as building walls should be environmentally friendly and save energy [9, 10]. Energy-saving buildings need to use green building materials, and the heat resistance of these materials can enable buildings to meet the requirements of minimizing energy consumption. For example, the outer wall of the building with the largest heat dissipation. At present, 60% of the outer wall materials in the construction market have used a large number of green building materials, and the energy-saving effect is very obvious. In addition to heat preservation, it can meet energy-saving requirements, and the weight is also small.

2.2. Thermal Comfort. Comfort is a broad concept. It is not determined by a single factor, but a subjective feeling produced by the human body under the image of comprehensive environmental factors. Since the psychological level has many effects on comfort or not, everyone's feelings are different, so the general understanding is that 80% of people are satisfied with the current environmental comfort conditions, that is, they think they have reached comfortable state. The human body must maintain internal thermal balance under any environmental conditions. Since humans are warm-blooded animals, they need to maintain their own body temperature at a constant state. Therefore, the human body can maintain the heat balance in the body when the surrounding environment fluctuates greatly, and its regulating ability is very strong [11]. When the body's heat production and heat dissipation are maintained in a balanced state, the body temperature can be maintained within the normal range. The human body produces energy mainly through metabolism. This energy is converted into two parts: heat and mechanical work. The human body mainly radiates heat to the surrounding environment through the skin. There are usually three ways: convective heat exchange, radiation heat exchange, and evaporative heat dissipation [12].

The body's heat balance can only be maintained when the body's heat production and heat dissipation are maintained in a balanced state. In a certain thermal environment, when the heat exchange between the surface of the human body and the external environment is not maintained in a balanced state, the human body will use its own physiological regulation functions and effective behaviors to adjust the human body's thermal sensation, and these behaviors' regulation is affected by regional climate and geographical environment, climatic conditions, and living conditions. In addition, psychological thermal adaptation is also significantly related to human thermal comfort. Psychological thermal adaptation is, under the influence of microclimate, an individual's thermal experience and thermal history of a certain environment, as well as the thermal expectations and thermal stimuli that arise from it. Climate experience, regional background, and psychological adaptation affect the human body's level of adaptation to the thermal
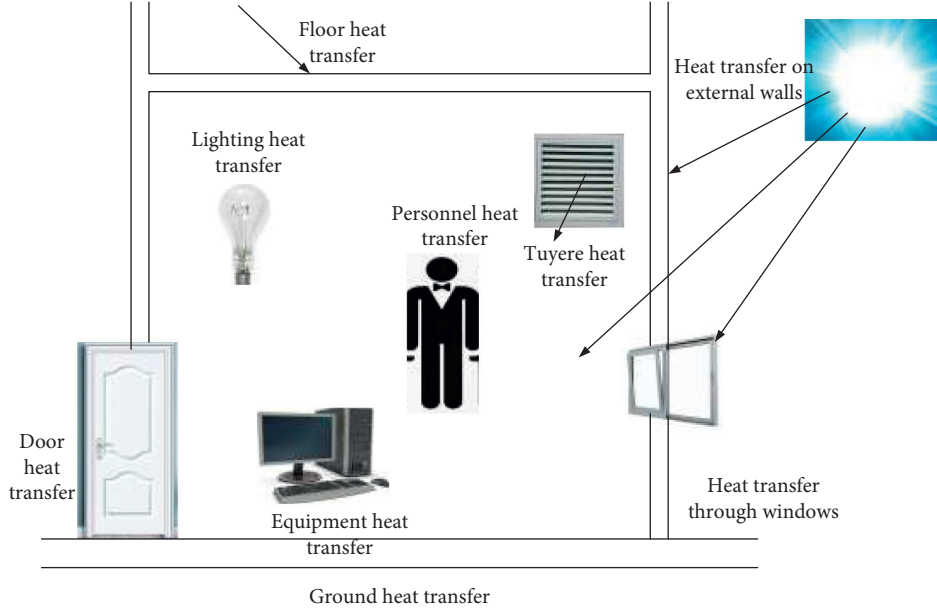
Figure 1: Schematic diagram of energy-saving building HVAC (pictures from Baidu Picture).

environment. Therefore, many physical and psychological factors affect the thermal comfort of the human body [13].

2.3. SET Index of Standard Effective Temperature.

The standard effective temperature was proposed late. It is based on the effective temperature and the new effective temperature. It is a comfort index that has been continuously verified and revised by several generations of researchers [14].

2.3.1. Two-Node Model.

Gagge proposed a two-node human body temperature regulation model, in which the human body is divided into two layers, namely, the core layer and the skin layer [15, 16]. Metabolic heat is generated in the core layer, and then, the metabolic heat is transferred from the core layer to the environment. During this process, a part of the heat will be directly lost to the environment due to human respiration, and the remaining heat will continue to spread to the surface of the skin. Due to evaporation, part of the heat transferred to the surface of the skin will be lost, and the remaining heat will be transferred to the surface of the clothes through the clothes and then transferred to the surrounding environment through radiation and convection. This heat transfer model between people and environment can be expressed by the core layer heat balance equation and the skin layer heat balance equation [17]. The heat balance equation of the core layer is

$$
\begin{aligned}
Q + \Delta Q - W = & P_{a,\text{res}} + P_{b,\text{res}} \\
& + (L + Q_{c1}D_{c1})(m_{dv} - m_{a1}) \\
& + Q_{dv}D_{dv}\frac{bm_{dv}}{b\varsigma}.
\end{aligned}
\tag{1}
$$

Among them, ΔQ represents the heat generated per unit human body surface area regulated by chills, L represents the thermal conductivity between the core layers of the skin, D_{c1} represents the specific heat capacity of the blood, m_{dv} represents the temperature of the core layer, m_{al} represents the temperature of the skin layer, and ς represents the transmission time. The skin layer heat balance equation is

$$
(L + Q_{c1}D_{c1})(m_{dv} - m_{al}) = P_{al} + Q_{al}D_{al}\frac{bm_{al}}{b\varsigma},
\tag{2}
$$

where m_{al} represents the temperature of the skin layer and P_{al} represents the mass per unit human body surface area of the skin layer. Q_{c1} is used to express the blood flow between the core layer and the skin, and the specific equation is

$$
Q_{c1} = \frac{6.3 + 200(m_{dv} - 36.8)}{1 + 0.1(33.7 - m_{al})}.
\tag{3}
$$

The amount of perspiration U_{kf} is mainly determined by the average temperature of the human body after it rises above the set temperature. After the skin surface temperature increases above its reference temperature, it will promote sweat secretion [18], namely,

$$
U_{kf} = 136\|M_c - 36.34\|\exp\left(\frac{\|M_{al} - 34\|}{10.7}\right).
\tag{4}
$$

The tremor occurs when the temperature of the core layer and the temperature of the skin layer are both lowered, and the increase in the metabolic rate is calculated as follows:

$$
\Delta Q = 19.4\|34 - M_{al}\| \times \|36.6 - M_{dv}\|.
\tag{5}
$$

Either vasodilation or vasoconstriction will cause changes in the body's heat transfer coefficient [19]. The heat flow calculation formula from the core layer to the skin layer is

$$P_{al} = L(M_{dv} - M_{al}). \tag{6}$$

Among them, L, as the heat transfer coefficient from the core layer to the skin layer, includes two parts: variable and constant. The constant part is the heat transfer coefficient term, and the other variable part is caused by blood flow. The increase in the temperature of the core layer causes vasodilation, and the decrease in the temperature of the skin layer causes vasoconstriction [20]. The heat transfer coefficient is expressed as follows:

$$L = 5.28 + \frac{7.33 + 175\|M_{dv} - 36.6\|}{1 + 0.5\|34 - M_{al}\|}. \tag{7}$$

These control functions, together with the human body's heat flow and heat mass equations, establish a model of temperature changes with time and can predict skin temperature and skin humidity, which are the two main parameters for calculating SET. Its advantage is that, under any environmental conditions, human skin temperature and humidity can be calculated by the two-node model [21].

2.3.2. Fanger Heat Balance Equation. Professor P. O. Fanger of Denmark proposed a comprehensive comfort index based on the following: the parameters that determine the comfort state of the human body have nothing to do with the environment, but only with the human body. Fanger believes that what a person feels is not the temperature of the surrounding air, but the temperature of his own skin [22]. On the basis of theory, Fanger conducted experiments with subjects and then used regression analysis to determine the relationship between the average human skin temperature, sweat evaporation heat loss, and metabolic rate:

$$M_{\text{hal}} = 35.7 - 0.028(Q - V),$$
$$U_{rsw,\text{req}} = 0.42(Q - V - 58.15). \tag{8}$$

Among them, Q represents the body's metabolism rate and V represents the amount of external work done.

Subsequently, the expression of each quantity in the heat balance equation is summarized, and each term is introduced into the heat balance equation, and the following formula is obtained:

$$Q - V - 3.05 \times 10^{-3} \left[256M_{\text{hal}} - 3373 - R_b \right] - U_{rsw,rwq}$$
$$- 1.73 \times 10^{-5} Q(5867 - R_b) - 1.4 \times 10^{-3} Q(34 - M_b) \tag{9}$$
$$= 3.96 \times 10^{-8} s_{dv} \left[(M_{dv} + 273)^4 - (M_{mrt} + 273)^4 \right] + s_{dv} g_d (M_{dv} - M_b).$$

In the above formula, S_{dv} represents the area coefficient of clothes, R_b represents the saturation partial pressure of water vapor at ambient air temperature, M_{dv} represents the average temperature of the human body surface, M_b represents the surrounding air temperature, and g_b represents the convective heat transfer coefficient between the human body and the air. In addition, the convective heat transfer coefficient can be divided into natural convection and forced convection [23].

When $\sqrt[4]{2.38(M_{dv} - M_b)} > 12.1\sqrt{P_{bh}}$, the coefficient of natural convection was

$$g_d = \sqrt[4]{2.38(M_{dv} - M_b)}. \tag{10}$$

When $\sqrt[4]{2.38(M_{dv} - M_b)} < 12.1\sqrt{P_{bh}}$, the forced convection coefficient had

$$g_d = 12.1\sqrt{P_{bh}}. \tag{11}$$

For the clothing area coefficient s_{dv}, when $F_{dv} \leq 0.078$,

$$s_{dv} = 1.00 + 1.29F_{dv}. \tag{12}$$

When $F_{dv} > 0.078$,

$$s_{dv} = 1.05 + 0.645F_{dv}. \tag{13}$$

Then, the heat balance equation is combined with the two comfort requirements to meet the three comfort conditions proposed by Fanger, and the famous Fanger comfort equation is obtained:

$$H = Q - V - 3.05 \times 10^{-3} \left[5733 - 6.99(Q - V) - R_b \right] - 0.42(Q - V - 58.15)$$
$$- 1.73 \times 10^{-5} Q(5867 - R_b) - 1.4 \times 10^{-3} Q(34 - M_b) \tag{14}$$
$$= 3.96 \times 10^{-8} s_{dv} \left[(M_{dv} + 273)^4 - (M_{mrt} + 273)^4 \right] + s_{dv} g_d (M_{dv} - M_b).$$

2.3.3. Forecast the Average Comfort Level Voting Index PMV. PMV is a comprehensive index that considers many factors of thermal comfort, and it is also a more authoritative and representative thermal comfort evaluation index. The PMV model is a comfort equation, which points out the basic influencing factors for thermal environmental evaluation, namely, air temperature, average irradiation temperature, relative humidity, wind speed, clothing amount, and activity

level. They evaluate indoor thermal comfort and occupy an important position [24]. Professor Fanger found the relationship between the six, created the relationship between each other, and formed the judgment equation, the PMV indicator. The PMV index divides the human body's thermal comfort into 7 levels, including cold, cool, slightly cool, moderate, comfortable, slightly warm, warm, and hot, as shown in Table 1, where each different PMV value represents a different value. The degree of hot and cold, such as 0, means moderate. The PMV evaluation model comprehensively considers the effects of six types of indoor environment factors (temperature, relative humidity, air flow rate, average radiation temperature, clothing thermal resistance, and metabolic rate) on the thermal comfort of the human body [25, 26].

The control method of the environmental thermal comfort system is to directly use the PMV index as the control basis and realize the separate control of each environmental variable through the set PMV index, that is, the PMV index and each environmental variable must be used as the controlled parameter. This control method uses PMV as two functions, one is the evaluation index of the system, and the other is the input of the control system. The temperature is no longer regarded as a single control parameter, but a variety of parameters affecting the room are regarded as control objectives. In the actual control process, because the control system directly uses the PMV value as the control basis, when the indoor environmental factors change, it will have an impact on the PMV value [27].

As shown in Figure 2, the control system directly regards the PMV index as the control basis. The control principle is to monitor the thermal comfort PMV index of the home environment in real time and compare it with the preset thermal comfort mode to obtain the corresponding operation judgment result. Then, according to the judgment result, the control system issues an order, and the actuator regulates the indoor temperature, wind speed, and humidity and also adjusts indoor thermal comfort.

3. Building Thermal Comfort Experiment Based on Energy-Saving Concept

3.1. Experimental Protocol. With the development and popularization of information technology, computers can realize automated management in many fields. On the one hand, it can save labor costs, and on the other hand, it can avoid loopholes in human management. Due to the large amount of energy consumption data, complicated classification, and complex systems in office buildings, traditional human management methods are no longer suitable and inefficient. Based on computer technology, the establishment of a building energy-saving management system can help managers grasp the accurate distribution and level of energy consumption and find out the problems with high energy consumption at the first time so that targeted countermeasures can be taken to truly achieve quantitative energy consumption and energy saving to achieve active and accurate energy management. The database used in this article must manage and store massive amounts of energy consumption data and can realize functions such as querying basic building energy consumption information and energy consumption status of key equipment and establish a building energy consumption database system based on a local server to realize energy consumption statistics and analysis of related buildings in a designated area, including lighting, heating, and air conditioning.

3.2. Demand Analysis of Energy-Saving Management System. The purpose of designing the building energy-saving management system is to realize the automatic storage and management of energy consumption data, realize the query and analysis of energy consumption data in a visual way, and then provide data support for energy-saving work. The corresponding functional requirements are as follows:

(1) Visual query of energy consumption data: the management system connects with the database to store, manage, and analyze the collected energy consumption data

(2) Statistics and analysis of energy consumption data: the management system can classify and subitem statistics on energy consumption data, including hourly, daily, monthly, and year-by-year statistics of energy consumption, and can output energy consumption reports, and the data can be printed

(3) Energy consumption forecast: based on the building energy consumption database, using the predictive average comfort level voting index PMV, it can predict the short-term energy consumption and thermal sensation trends and realize the advance planning and scientific scheduling of energy use

3.3. Experimental Environment. In order to further study the related strategies of intelligent control, we need to study the relationship between environmental variables and thermal comfort. Thermal comfort needs to control a certain objective environment. Its core variables are indoor air temperature, relative humidity, air flow rate, and average radiation temperature. However, the control of radiation temperature is more difficult to achieve and does not take control considerations. Therefore, we will study the first three environments here. The influence between variables and comfort. Table 2 shows the metabolic rate of the human body under different activities. This study uses this as the experimental environment.

4. Building Thermal Comfort Analysis Based on Energy-Saving Concepts

4.1. Influence of Temperature, Humidity, and Wind Speed on Thermal Comfort. This study uses the method of controlling variables to compare and analyze the effects of temperature, humidity, and wind speed on thermal comfort. First, the influence of temperature and wind speed on PMV is analyzed. The humidity is fixed at 50%, the air temperature is 27°C, 28°C, 29°C, and 30°C, and the wind speed is 0.18 m/s, 0.72 m/s, and 1.21 m, respectively.

TABLE 1: Thermal comfort level 7 index.

Hot sensation	Cold	Cool	Slightly cool	Comfortable	Slightly warm	Warm	Heat
PMV	−3	−2	−1	0	+1	+2	+3
PPD	100%	66%	33%	0	33%	66%	100%
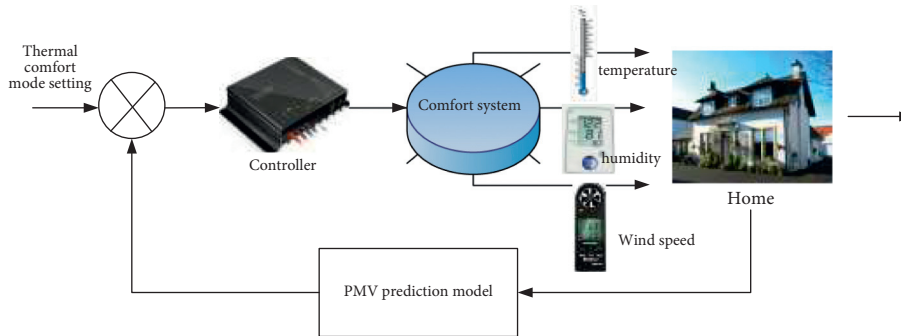
FIGURE 2: Thermal comfort control method (pictures from Baidu Picture).

TABLE 2: Reference table of human activity and metabolic rate.

Human activity	Metabolic heat production rate M	
	W/m^2	Met
Lying down	42	0.6
Sit relaxed	53	0.8
Sit and work	67	1.0
Relax and stand	67	1.0
Standing with light activity	88	1.4
Standing with moderate activity	102	1.8
Heavy activity	155	2.5

FIGURE 3: The influence of different wind speeds on human thermal comfort.

Figure 3 shows the effect of different wind speeds on the thermal comfort of the human body when the humidity is 50%. It can be seen from Figure 1 that, at the same temperature, the wind speed is different, and the degree of thermal sensation is also different. When the wind speed is 0.18 m/s and the temperature is 28°C, the thermal sensation is 0.32, and the human sensation is close to neutral. When the wind speed increases to 0.72 m/s, the heat sensation drops to −0.45, and the human body feels neutral and cool. It can be seen that the increase in wind speed has a certain compensation effect on the thermal sensation of the human body. When the wind speed does not change, increase the air temperature. For example, when the wind speed is 0.72 m/s, the temperature is 28°C and the thermal sensation is −0.45, and when the temperature is increased to 29°C, the thermal sensation is 0.08, which shows that the temperature is improving the thermal sensation of the human body which has a certain offsetting effect. In addition, the influence of temperature on PMV is more significant than the influence of wind speed on PMV. When the wind speed is 0.18–1.213 m/s, the maximum value of PMV change is −0.32−(−1.63) = 1.31, and the temperature rises from 27°C to 30°C, the maximum value of PMV change is −0.01−(−1.63) = 1.62. It can be seen that compared to the temperature, the wind speed has a weaker influence on PMV.

In addition, this study also studied the influence of humidity and wind speed on PMV. The fixed temperature was 25°C, the humidity was set to 40%, 50%, and 60%, and the wind speed was 0.1, 0.2, 0.3, 0.4, and 0.5 m/s.

Figure 4 shows the effect of humidity and wind speed on temperature. As the wind speed continues to increase, the PMV value continues to decrease, and the decrease is small. The maximum change in the thermal comfort value PMV is 0.51–0.02 = 0.49. Similarly, as the humidity increases, the PMV value also continues to decrease, but the impact is still not significant. The maximum change range of PMV is 0.51–0.23 = 0.28. It can be seen that compared with wind speed, humidity has a smaller impact on thermal comfort. From the analysis of the above two aspects, among the three external factors of wind speed, temperature, and humidity, temperature has the most obvious effect on thermal comfort,
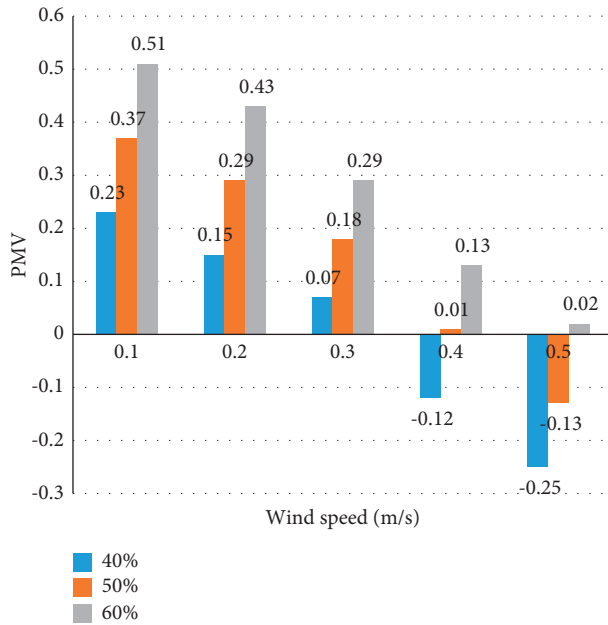
FIGURE 4: The influence of humidity and wind speed on PMV.

followed by wind speed, and humidity has less effect on thermal comfort.

4.2. Influence of Gender on Thermal Comfort. It can be seen from Table 3 that there are obvious differences in the skin surface temperature values of various parts of the male and female bodies. In the test, under normal circumstances, the temperature of the arms, hands, legs, and feet of men is significantly higher than that of women, and the temperature of the head and torso is similar to that of women. In the torso, the male temperature is 34.53, while the female temperature is 34.52, which is not much different. On the legs, the male temperature is 34.05 and the female temperature is 33.69.

Table 4 shows the differences in thermal comfort between men and women. Among them, in each season, there is no significant difference in neutral temperature and average heat sensation from a gender perspective. From the perspective of thermal dissatisfaction, in summer, the thermal dissatisfaction rates of men and women are 31.9 and 29.8, which are significantly higher than those of the other three seasons. Regarding the effect of gender on thermal comfort, the difference in clothing has no obvious effect, but there is a gender difference in the use of fans. In summer, the fan usage rate of men is 72.9%, while that of women is 66.3%. In addition to the fact that the fan usage rate of both is zero in winter, the frequency of use of fans by men is higher than that of women.

4.3. Ways to Improve Thermal Comfort. Figure 5 shows a method to improve its thermal comfort. In winter, most people choose to go indoors to improve their thermal comfort, accounting for 43%. In addition, some people choose to exercise and sunbathe to increase the heat sensation. In the summer, those who choose to enter the room

and improve their thermal comfort in the shade account for a considerable proportion, 47% and 39%, respectively. In the transitional season, people basically choose to exercise and increase the feeling of heat in the sun or shade. In this season, fewer people choose to enter the room, and everyone prefers outdoor activities.

4.4. Accumulative Load Changes with the Heat Transfer Coefficient of the Window. Cooling load refers to the amount of cold supplied to the room at a certain time by continuously maintaining a constant temperature and humidity in an air-conditioned room; heat load refers to the amount of heat that needs to be provided to the room to compensate for the loss of heat in the room.

Figure 6 shows the cumulative cooling and heating load and the total load change with the heat transfer coefficient of the window. It can be seen from Figure 3 that the cumulative heat load of heating increases with the increase of the thermal conductivity of the window, and the increase is more significant. With the increase of the thermal conductivity of the windows, the cumulative cooling load of the air conditioner does not change significantly, and the range of change is small. Judging from the changes in the total load accumulated throughout the year, as the thermal conductivity of the windows increases, the total load has shown a clear upward trend. It can be seen that windows can affect building energy consumption, and the degree of impact is relatively large.

4.5. Impact of Windows of Different Materials on Energy Consumption. As a part of the indoor building environment, the role of windows in energy conservation should not be underestimated. This study selects windows as the object for performance analysis and window renovation.

In addition, this study also analyzed the performance of windows and their impact on energy consumption. Due to the poor thermal insulation effect of the inner windows in some buildings and the weak shading performance, the indoor solar radiation is higher in summer, which increases the heat perception and generally feels more tan; while in winter, due to the poor thermal insulation effect of the outer window, part of the heat loss is large, so the transformation of the window is very important to reduce the heating load and air conditioning cooling load. Here are four commonly used windows performance, as shown in Table 5. Obviously, the energy efficiency of the hollow glass window with inert gas is the best, at 24.03%, and the heat generated is lower than that of the windows of the other three materials, at 79854 J. At the same time, this study also compared the energy consumption effects before and after the window transformation to determine the energy-saving effects of these types of windows.

Figure 7 is a comparison of energy consumption after window transformation. When the hollow glass window with inert gas is used, the heat transfer coefficient is 1.7 and the energy consumption is 75922 J. When the ordinary single-layer window is used, the heat transfer coefficient is 5.2 and the energy consumption is 90238 J. The heat transfer

TABLE 3: Skin surface temperature of various parts of the body.

Gender body parts	Head (°C)	Torso (°C)	Arm (°C)	Hand (°C)	Leg (°C)	Foot (°C)
Male	34.39	34.53	34.01	34.49	34.05	34.62
Female	34.41	34.52	33.66	34.03	33.69	34.13

TABLE 4: Gender differences.

	Spring		Summer		Autumn		Winter	
	Male	Female	Male	Female	Male	Female	Male	Female
Thermal neutral temperature (°C)	24.1	24.5	25.4	25.1	23.9	24.5	22.4	22.9
Average heat sensation	−0.19	−0.07	0.08	0.10	0.02	−0.01	−0.02	−0.09
Percentage of unsatisfied forecasts (%)	4.5	4.3	31.9	29.8	3.5	4.4	3.0	6.4
Clothing thermal resistance (clo)	0.77	0.70	0.51	0.49	0.88	0.89	0.94	0.99
Fan usage rate (%)	13.9	2.8	72.9	66.3	11.4	2.4	0	0
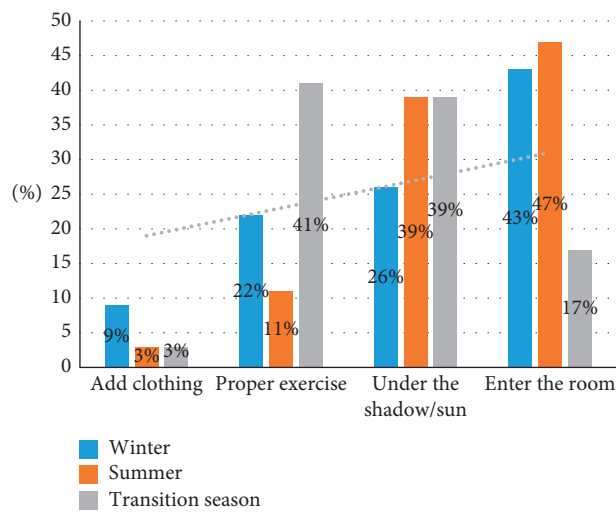
FIGURE 5: Ways to improve your own thermal comfort.
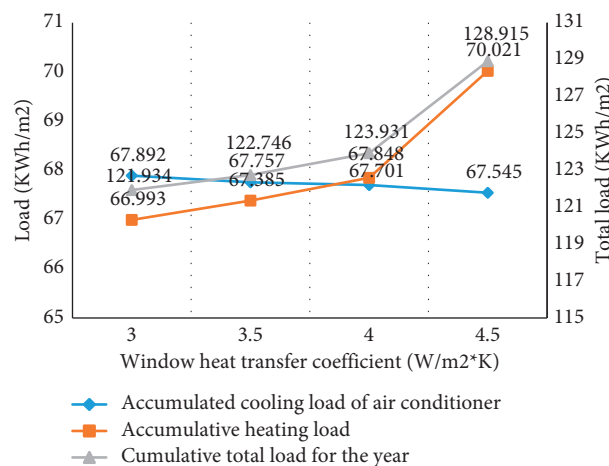
FIGURE 6: Accumulative load changes with the window heat transfer coefficient.

coefficient can achieve obvious energy-saving effect. At the same time, comparing single-layer windows and three-layer insulating glass windows, although the heat transfer coefficient and energy consumption are reduced, the heat transfer coefficient of three-layer insulating glass is slightly higher than that of insulating glass windows with inert gas (1.7). It is 2.2. Although the airtightness is better, the reduction of heating energy consumption is limited.

TABLE 5: Performance comparison of several typical windows.

	6 mm single window	6Low-E+12 + 6 hollow glass window	6Low-E+12 + 6 hollow glass window (inert gas)	Three-layer hollow glass window
Heat transfer coefficient	4.3	2.0	1.6	1.8
Shading coefficient	0.91	0.81	0.57	0.85
Heating	98432	84325	79854	80359
CO_2	79378	63875	56798	60953
Energy saving efficiency	—	15.98%	24.03%	20.11%
Price	200	350	400	≥500
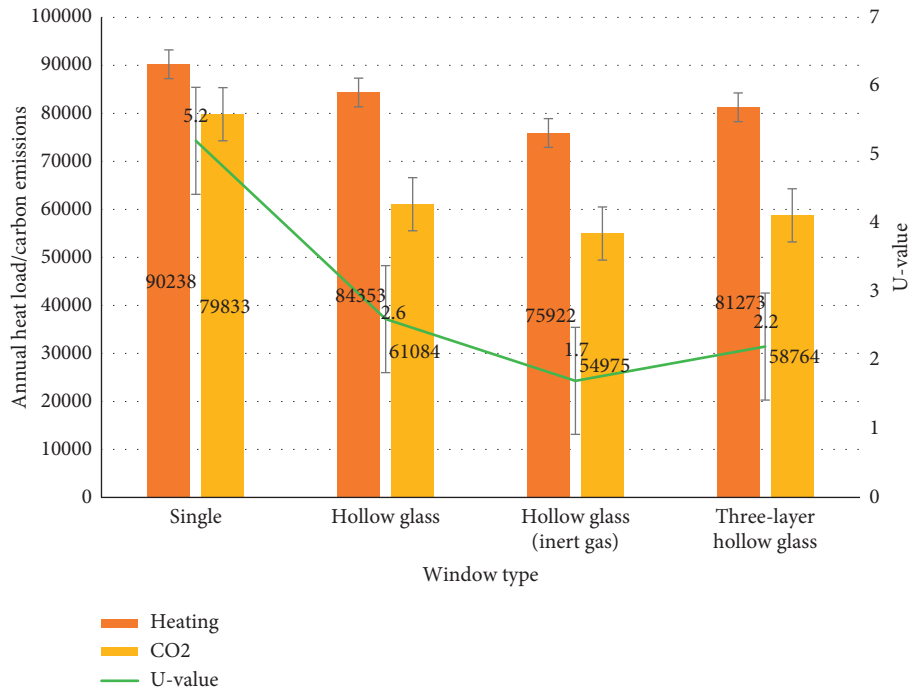
FIGURE 7: Comparison of energy consumption after window renovation.

5. Conclusion

With the continuous development of the national economy and the continuous development of the construction of energy-saving resources, building energy-saving has become an increasingly important part of engineering projects. Due to prejudice and misunderstandings about building energy-saving, the development of energy-saving buildings is hindered to a certain extent. Based on the concept of energy-saving, this paper conducts an in-depth study on the thermal comfort of buildings and concludes that external factors such as wind speed, temperature, and humidity have different degrees of influence on the thermal comfort of the human body. Among them, temperature has the greatest impact, and the choice of building materials is also required, considering the heat transfer coefficient and energy consumption. At the same time, there are some shortcomings in this article. The study of materials in this article only selects the form for transformation research, which is not comprehensive enough. It can also start from

other aspects of the building, and the selected material samples are also relatively small; in addition, for energy conservation, the combination of the concept and the building is also not in place, and there is no certain optimization plan for energy saving. The authors hope that, with the in-depth study of building materials, this research can be further improved. This article's research on the thermal comfort of buildings based on energy-saving concepts has certain significance for the realization of energy-saving and emission reduction in buildings in China. China is now in the industrialization stage of rapid urbanization. The problems of energy scarcity and ecological destruction will be further aggravated. Therefore, it is necessary to continuously improve the level of Chinese energy conservation and environmental protection technology to provide technical support for large-scale energy conservation and emission reduction work. Therefore, building energy efficiency is an inevitable choice for our country to transform the form of development and adjust the economic structure.

Data Availability

The data used to support the findings of this study are available from the corresponding author upon reasonable request.

Conflicts of Interest

The authors declare that they have no conflicts of interest.

Acknowledgments

References

[1] S.-B. Tsai and K. Wang, "Using a novel method to evaluate the performance of human resources in green logistics enterprises," *Ecological Chemistry and Engineering S*, vol. 26, no. 4, pp. 629–640, 2019.

[2] A. Zl, A. Dc, A. Rl, and B. Aa, "Artificial intelligence for securing industrial-based cyber–physical systems," *Future Generation Computer Systems*, vol. 117, pp. 291–298, 2021.

[3] W. Meyer, "Impact of constructional energy-saving measures on radon levels indoors," *Indoor Air*, vol. 29, no. 4, pp. 680–685, 2019.

[4] A. Middel, N. Selover, B. Hagen, and N Chhetri, "Impact of shade on outdoor thermal comfort-a seasonal field study in Tempe, Arizona," *International Journal of Biometeorology*, vol. 60, no. 12, pp. 1–13, 2016.

[5] D. Kioupis, S. Tsivilis, and G. Kakali, "Development of green building materials through alkali activation of industrial wastes and by-products," *Materials Today: Proceedings*, vol. 5, no. 14, pp. 27329–27336, 2018.

[6] W. Poortinga, L. Steg, and C. Vlek, "Environmental risk concern and preferences for energy-saving measures," *Environment and Behavior*, vol. 34, no. 4, pp. 455–478, 2016.

[7] U. M. Namil and H. Tetsuji, "A hydrometallurgical method of energy saving type for separation of rare earth elements from rare earth polishing powder wastes with middle fraction of ceria," *Journal of Rare Earths*, vol. 34, no. 5, pp. 536–542, 2016.

[8] C. Armando, A. Lauro, G. Umberto et al., "Energy saving in a water supply network by coupling a pump and a pump as turbine (PAT) in a turbopump," *Water*, vol. 9, no. 1, p. 62, 2017.

[9] B. M. Todorović and D. Samardžija, "Road lighting energy-saving system based on wireless sensor network," *Energy Efficiency*, vol. 10, no. 1, pp. 1–9, 2016.

[10] G. Fei, C. Shi, C. Zhang, and L. Hongjie, "Printed smart photovoltaic window integrated with an energy-saving thermochromic layer," *Advanced Optical Materials*, vol. 3, no. 11, pp. 1524–1529, 2016.

[11] T. H. Arimura, H. Katayama, and M. Sakudo, "Do social norms matter to energy-saving behavior? Endogenous social and correlated effects," *Journal of the Association of Environmental and Resource Economists*, vol. 3, no. 3, pp. 525–553, 2016.

[12] W. Nie, F.-C. Zheng, X. Wang, W. Zhang, and S. Jin, "User-centric cross-tier base station clustering and cooperation in heterogeneous networks: rate improvement and energy saving," *IEEE Journal on Selected Areas in Communications*, vol. 34, no. 5, pp. 1192–1206, 2016.

[13] O. Arouk, A. Ksentini, and T. Taleb, "Group paging-based energy saving for massive MTC accesses in LTE and beyond networks," *IEEE Journal on Selected Areas in Communications*, vol. 34, no. 5, pp. 1086–1102, 2016.

[14] Y. Guo, L. Duan, and R. Zhang, "Optimal pricing and load sharing for energy saving with cooperative communications," *IEEE Transactions on Wireless Communications*, vol. 15, no. 2, pp. 951–964, 2016.

[15] P. Xu, Y. Shen, L. Chen, J. Mao, E. Chang, and Y. Ji, "Assessment of energy-saving technologies retrofitted to existing public buildings in China," *Energy Efficiency*, vol. 9, no. 1, pp. 67–94, 2016.

[16] J. Wang, Y. Wang, D. Zhang, and S. Helal, "Energy saving techniques in mobile crowd sensing: current state and future opportunities," *IEEE Communications Magazine*, vol. 56, no. 5, pp. 164–169, 2017.

[17] W. Zhou and W. Huang, "Contract designs for energy-saving product development in a monopoly," *European Journal of Operational Research*, vol. 250, no. 3, pp. 902–913, 2016.

[18] R. Khan and S. U. Khan, "Achieving energy saving through proxying applications on behalf of idle devices," *Procedia Computer Science*, vol. 83, no. 2, pp. 187–194, 2016.

[19] A. Novikova, T. Csoknyai, and Z. Szalay, "Low carbon scenarios for higher thermal comfort in the residential building sector of South Eastern Europe," *Energy Efficiency*, vol. 11, no. 4, pp. 1–31, 2018.

[20] M. Dhahri and H. Aouinet, "CFD investigation of temperature distribution, air flow pattern and thermal comfort in natural ventilation of building using solar chimney," *World Journal of Engineering*, vol. 17, no. 1, pp. 78–86, 2020.

[21] K. Xu, D. Chen, F. Yang, and Z. Zang, "Sub-10 nm nanopattern architecture for 2D material field-effect transistors," *Nano Letters*, vol. 17, no. 2, pp. 1065–1070, 2017.

[22] Z. Chen, D. Chao, M. Chen, and Z. Shen, "Hierarchical porous LiNi1/3Co1/3Mn1/3O2 with yolk-shell-like architecture as stable cathode material for lithium-ion batteries," *RSC Advances*, vol. 10, no. 32, pp. 18776–18783, 2020.

[23] Y. Benjelloun, J. D. Sigoyer, J. Carlut et al., "Characterization of building materials from the aqueduct of Antioch-on-the-Orontes (Turkey) - Sciencedirect," *Journal of Field Robotics*, vol. 33, no. 5, pp. 561–590, 2016.

[24] S. Shaw, B. Yuan, X. Tian et al., "Building materials from colloidal nanocrystal arrays: preventing crack formation during ligand removal by controlling structure and solvation," *Advanced Materials*, vol. 28, no. 40, pp. 8892–8899, 2016.

[25] S. Shaw, J. L. Colaux, J. L. Hay, F. C. Peiris, and L. Cademartiri, "Building materials from colloidal nanocrystal arrays: evolution of structure, composition, and mechanical properties upon the removal of ligands by O2 plasma," *Advanced Materials*, vol. 28, no. 40, pp. 8900–8905, 2016.

[26] T. Azamov, "Temperature models of technological processes in the production of ceramic building materials," *Acta of Turin Polytechnic University in Tashkent*, vol. 8, no. 1, p. 5, 2018.

[27] S. V. Piddubnyi, H. O. Tatarchenko, and V. M. Sokolenko, "Express method for the evaluation of the frost resistance of silicate building materials," *Materials Science*, vol. 56, no. 2, pp. 240–246, 2020.

Research Article

Compatibility of Composite Biomaterials in Sports Injury Repair

Mo Xing 🄳

School of Physical Education, Hulunbuir University, Hulunbuir 021000, Inner Mongolia, China

Correspondence should be addressed to Mo Xing; xingmo@hlbec.edu.cn

With the rapid development of sports, sports injuries have become an inevitable problem in sports. Repairing sports injuries has always been the focus of attention in the field of sports and medicine. The wide application of biomedical materials leads to the innovation and development of medical technology. It is of great significance to use them to repair sports injuries, but the current research results are not ideal. In this paper, the biocompatibility of composite biomaterials used to repair sports injuries was studied. First, the rat bone marrow mesenchymal stem cells were cultured to prepare a cell suspension. Then, the tricalcium phosphate-gelatin composite scaffold material and the collagen material were scraped into powder to make the material extract, which are, respectively, the experimental group and the control group. An apoptosis detection kit and a flow cytometer were used to detect apoptosis rate and survival rate of all samples, and a CKK-8 kit was used to detect cytotoxicity and calculate cell proliferation activity. The absorbance value was read with a microplate reader, and the coagulation performance and hemolysis rate of different groups were calculated. The experimental results showed that the cell survival rate of the experimental group was 91.41%, the early apoptosis rate was 2.81%, the stem cell proliferation activity was 0.83, and the anticoagulant performance and hemolysis rate were 64.8% and 0.28%, respectively. This indicates that although the anticoagulant performance of the tricalcium phosphate-gelatin composite scaffold is weak, its cell proliferation activity is strong, which is more suitable for cell adhesion and proliferation, and the cell apoptosis and hemolysis rate are lower. Therefore, it has better biocompatibility than a single collagen material.

1. Introduction

1.1. Background Significance. Sports injury not only endangers the health of athletes, but also has an irreversible impact on their life and sports career. Therefore, it is necessary not only to prevent sports injury in advance, but also to take scientific and effective repair methods after the injury occurs [1]. When sports injury is serious, it is necessary to implant biomaterials to replace damaged tissues or organs for repair. At present, many biomaterials have been used to repair sports injury [2]. Especially for the composite biomaterials which combine the advantages of a variety of materials, it is necessary to study the biocompatibility of these new composite materials, so as to ensure that there will be no new damage to the human body after implantation. Bioremediation materials include the following categories: (1) biomedical metal materials: medical metal materials are metals or alloys used as biomedical materials, which have

high mechanical strength and fatigue resistance, and are the most widely used clinically for load-bearing implants. The materials mainly include artificial joints and artificial bones made of cobalt alloy (Co-Cr-Ni), titanium alloy (Ti-6Al-4V), and stainless steel. Nitinol shape memory alloy has the intelligent characteristics of shape memory and can be used in orthopedics and cardiovascular surgery. (2) Biomedical polymer materials: there are two types of biomedical polymer materials: natural and synthetic. The fastest growing is synthetic polymer medical materials. Through molecular design, many biomaterials with good physical and mechanical properties and biocompatibility can be obtained. Among them, soft materials are often used as substitutes for human soft tissues such as blood vessels, esophagus, and knuckles; synthetic hard materials can be used as artificial dura mater, spherical valves of cage-shaped artificial heart valves, etc.; liquid synthetic materials such as room temperature vulcanization silicone rubber can be used as an

injectable tissue repair material. (3) Biomedical composite materials: biomedical composite materials are biomedical materials composed of two or more different materials. They are mainly used to repair or replace human tissues and organs or enhance their functions and the manufacture of artificial organs. Among them, titanium alloy and polyethylene tissue prostheses are often used as joint materials; carbon-titanium synthetic materials are good artificial femoral heads for clinical applications; polymer materials and biopolymers (such as enzymes, antibodies, antibodies, and hormones) can be combined as a biosensor.

1.2. Related Work. The repair of sports injuries has always been the focus of the sports world. Scillia et al. proposed a surgical technique including rectus abdominis repair and long adductor muscle lengthening, aimed at patients with sports muscle injuries that are incurable by conservative treatment [3]. Their research only focused on muscle injuries. In fact, many sports injuries can cause bone tissue damage. Composite biomaterials have attracted the attention of researchers from various countries due to their unique properties. Wang et al. reviewed the application of nano-hydroxyapatite and its composite biomaterials in bone defect repair. They discussed whether the application of composite materials and polymer biomaterials can overcome the brittleness and poor mechanical properties of nano-hydroxyapatite [4]. Pieniak et al. discussed the quantitative fatigue assessment of polymer-ceramic composites for dental restorations and simulated thermal fatigue using a dedicated computer control device with thermal cycling algorithm [5]. Li et al. prepared a bio-scaffold material by melt fusion/particle leaching process and analyzed the biocompatibility of the material [6]. Their experiments provide a reference for the research of composite biomaterials, but when conducting research, they either tend to explore the physical properties of the materials, or prefer biocompatibility without combining the two.

1.3. Innovative Points in This Paper. This paper studies the compatibility of composite biomaterials in sports injury repair, combined with the role of biomaterials in injury repair; this paper innovatively uses flow cytometry to detect the cells of tricalcium phosphate-gelatin composite scaffolds and collagen materials. In observing cell proliferation activity, this article selects the CKK-8 kit, which is more suitable as an environment for cell proliferation than traditional kits.

2. Sports Injury Repair and Compatibility of Composite Biomaterials

2.1. Sports Injury Repair

2.1.1. Cause of Damage. Different sports will cause different parts of the injury. Common sports injuries include periostitis, fractures, muscle strains, and ankle sprains. Injuries that occur during sports activities can be divided into acute injuries and chronic injuries [7]. Acute injuries happen

suddenly, and if improper treatment at the time leads to recurrence of later illnesses, it will turn into chronic injuries.

The main cause of sports injuries is technical errors or irregularities during the exercise. Professional athletes also make mistakes in their movements, let alone ordinary people. Their exercise time is not long, and they cannot master some difficult movements. These wrong movements violate the physiological characteristics and biomechanical principles of the human body and can easily lead to sports injuries. In addition, improper preparation activities and failure to allow the body to adapt to exercise will increase the probability of muscle strain and joint sprain. Exercise load exceeds the level that the body can withstand, which can easily lead to body fatigue and minor injuries. If it is not repaired in time, it will induce serious sports injuries [8].

After a sports injury occurs, it is also important to take a reasonable first aid plan to minimize the degree of sports injury. Some sports coaches have insufficient training experience, fail to reasonably convey the essentials of sports movements, or do not arrange training content according to the actual situation, which will lead to sports injuries.

Sports venues and equipment facilities will also affect the formation of sports injuries. The geology of the site is excellent, the cushioning performance is poor, and the equipment is outdated, which cannot guarantee the safety of the athletes and bring safety risks [9].

2.1.2. Damage Prevention. There are different preventive measures for damage caused by different reasons. Starting from the athletes themselves, improve the athletes' ideological understanding, publicize basic sports knowledge, and make them aware of the importance of preventing sports injuries. Do adequate preparation activities, which is often said to warm up before exercise to improve the excitability of the human nervous system. Appropriate relaxation should be carried out after exercise to eliminate fatigue caused by exercise [10].

Sports coaches or physical education teachers must put safety first and arrange training scientifically and reasonably according to the physical fitness of the athletes. The intensity and difficulty of exercise must be well controlled to reduce sports injuries caused by improper training plans or excessive exercise [11]. The coach or teacher himself should strengthen the learning of sports health knowledge and guide the athletes to treat sports injuries correctly.

In terms of sports conditions, it is necessary to strengthen the maintenance of venues and equipment, conduct regular inspections, repair and replace damaged equipment in time, and eliminate safety hazards [12]. Athletes themselves should conduct a general safety inspection of the venue and equipment before exercising, and avoid exercising on unsafe venues.

2.1.3. Damage Repair. There are different repair methods for different parts of the injury. After an acute knee injury occurs, it is necessary to quickly apply ice to find the cause of the injury for further examination and treatment. Rehabilitation training is carried out on the second day after

injury to prevent muscle atrophy around the injury. In the recovery period of the exercise range, you must first start training the surrounding muscle strength, and you must do it slowly to avoid excessive stimulation. If you experience discomfort after training, you should stop using ice immediately [13]. In the strength recovery phase, attention should be paid to load control and protection during training period, and training equipment with a constant angle and speed should be selected. In the functional recovery period, increase the intensity of training, pay attention to the recovery of the neuromuscular system of the athlete's knee joint, and the methods of strength training should be diversified and flexible.

You also need to apply ice immediately after acute ankle injury to reduce the congestion and swelling of the injured area. At the same time, try to avoid activities and raise the limbs to relieve pain. Those with severe injuries need to be sent to the hospital for examination and treatment immediately, and acupuncture and drug treatment can be performed later, with functional recovery training.

The directional repair process of fatigue damage of bone tissue is completed by bone cells, and the directional bone reconstruction work is achieved by osteoclasts and osteoblasts [14]. There is a threshold effect in the perception and repair of fatigue damage of bone tissue, and bone cells can induce the subsequent directional bone reconstruction process through apoptosis or non-apoptosis. The degree of fatigue damage will directly determine its specific response.

2.2. Composite Biomaterials in Damage Repair

2.2.1. Basic Elements of Composite Biomaterials. To be implanted into the human body as a qualified implant, the composite biomaterial must meet the following requirements. First of all, it must have biocompatibility. The basic concept is nontoxic effects. The premise of nontoxic effect is that the chemical structure of the material is stable and the raw material is pure [15]. It will not cause irritation and damage to the tissues, or immune interference and rejection, and will not cause hemolysis or coagulation.

The second is biomechanics, because many biocomposite materials will be used to replace the load-bearing tissues in the human body. If there are not enough mechanical properties, it will easily break. Good mechanical properties include the elasticity, wear resistance, strength, and aging resistance of the material itself, as well as the compatibility with the elastic modulus of the surrounding tissues.

An important sign of biological stability is whether the material can exhibit a good proliferation response phenomenon [16]. After the material is moved into the living body and contact with the recipient tissue, it will form a different structural state after a period of time. The ideal material will have a proliferation reaction phenomenon on the surface, thereby forming a cell layer dominated by fibrocytes. As time goes by, fibrocytes gradually increase, and a good tissue envelope is formed.

Biodegradability requires that the material be slowly degraded after implantation in the organism and replaced by cells, and the rate of degradation and tissue growth must be consistent. Regardless of whether the materials that have been formed in the tissue have not been degraded, or the tissue is degraded before it is completely formed, it is said that it is not conducive to tissue repair. At the same time, some small molecular impurities will inevitably remain in the preparation process of the material. Once it becomes a body fluid exudate, it will cause a serious physiological reaction. Therefore, attention must be paid to its biological exudation [17, 18].

The natural fiber used as the raw material of bio-based composite materials includes various types of natural polysaccharides such as cellulose, hemicellulose, tannins, etc. From the physical properties, the surface is hydrophilic, while bio-based composite materials are another large class of raw materials. It is an organic synthetic polymer resin with hydrophobic surface. The surface properties of the two have a huge difference. Due to the weak interface interaction force and easy defects, it is not good for the formation of composite materials. Using these two types of raw materials to produce composite materials can improve the performance of composite materials by modifying fibers and resins to increase the interaction force between the interfaces. However, after the interface performance of the composite material has been improved, the impact and other properties have declined, and the best solution has not been found in a variety of modification treatment methods. From the perspective of biocompatibility, if the use of the material is different, the scale of the evaluation of biocompatibility will be different. For example, in vitro and in vivo (comparison of debridement materials and some materials used for transplantation to help regeneration), debridement materials do not cause inflammation, are nontoxic, and are antibacterial. Regeneration materials may also need to promote cell growth. It still depends on the specific problem. The repair materials used in orthopedics may promote the adhesion and growth of bone cells, and the vascular repair materials must promote the adhesion and growth of endothelial cells, avoid calcification, and also have anti-coagulation to avoid thrombosis.

2.2.2. Seed Cells and Growth Factors. Seed cells can help tissue construction and organ regeneration, so they must meet certain criteria to become qualified seed cells. The source of seed cells should be extensive, sufficient in number, and relatively easy to obtain. Seed cells should be easy to cultivate, have strong proliferation, and be expanded in large numbers. Cells with stable genetics and specific biological functions, and with specific functions, should dominate. The immune rejection reaction is minimal or absent, so as to avoid rejection. The molecular structure and function of the seed cell must be similar to that of the normal cell of the regenerated tissue, so as to be better adapted.

At present, seed cells can be divided into stem cells, bone cells, fibroblasts, and endothelial cells [19]. Mesenchymal stem cells have the potential to differentiate into bone and

adipose tissue. Fibroblasts have the advantages of strong function, rapid proliferation, and low immunogenicity. Endothelial cells can accelerate the process of vascularization and vascular system reconstruction.

Growth factors can combine with specific and high affinity receptors on cell membrane to induce and stimulate cell proliferation and maintain cell survival. The role of growth factors is specific, so it needs to be selected for different cells, tissues, and organs. Fibroblast growth factor can promote angiogenesis and repair. Transforming growth factor can induce cartilage differentiation and promote bone healing and anticancer. Epidermal growth factor can promote cell migration to the wound and accelerate wound healing.

2.2.3. Support Material. The scaffold material provides a platform and support for the growth of seed cells, maintains the original shape and integrity of the tissue, and provides a good environment to promote cell growth, proliferation, and differentiation. The qualified scaffold has a three-dimensional porous structure and simulates the natural microenvironment. The current scaffold materials are divided into three types: natural biological materials, synthetic materials, and composite materials.

Chitosan, collagen, and fibrin are more commonly used in natural biomaterials. These materials have no toxic and side effects, can help cells better adhere to, proliferate, and differentiate, and can also fight infection and promote the recovery of immune function [19]. But it has a certain degree of immunogenicity, and the degradation rate is not very stable. Synthetic materials mainly include polyvinyl alcohol, polystyrene, and polycaprolactone, etc., which have the advantages of many varieties, strong plasticity, and good mechanical properties, and can be mass-produced. However, the biocompatibility and hydrophilicity of these materials are relatively poor, and the degradation products may be toxic and interfere with tissue regeneration. Composite materials combine the excellent properties of different materials to meet different needs. Currently, the composite scaffold materials that have been put into use include chitosan-calcium polyphosphate composite scaffold, tricalcium phosphate-gelatin composite scaffold, and hydroxyapatite polycaprolactone [20].

In order to ensure the safety and effectiveness of scaffold materials during use, physical and chemical performance tests, biological performance tests, and cell and histocompatibility tests must be carried out before clinical use. The physical property test should be carried out in a simulated body fluid environment to test tensile strength, viscoelasticity, hardness, and melting point [21]. The chemical performance test is aimed at pH, hydrophilicity, adsorption, etc. The biological performance test detects the toxicity of the material to the receptor, including cell compatibility and tissue compatibility.

2.3. Evaluation of Biocompatibility. Various biological materials implanted in the body will have different degrees of contact with collective tissues or body fluids, and the

reactions caused by contact are divided into two types. One is to prevent reactions, toxic reactions and allergic reactions, local or systemic effects caused by the pH of the material, residual or adsorbed toxic low-molecular substances, etc. [22]. The second is the reaction of various factors in the body to the deformation, aging, or degradation of the implanted material. Therefore, no matter what kind of biological material, it must meet the requirements of biocompatibility. The methods of evaluating the biocompatibility of biological materials are mainly divided into in vitro cell biology evaluation and in vivo histological evaluation [23]. In vitro cell biology evaluation studies the cell adhesion and growth on the surface of the material, while in vivo histological evaluation observes tissue growth.

2.3.1. Detection Method of Cytotoxicity. A common method for testing biocompatibility is to conduct a cytotoxicity test. Through in vitro cell culture, the effect of biomedical materials on cell growth is detected to evaluate whether the materials are toxic. The use of cytotoxicity testing for biocompatibility evaluation has the advantages of simple operation, rapidity, low cost, and good repeatability.

Cytotoxicity test can be divided into MTT method, agar covering hair, molecular filtration method, cell morphology, and LDH release method according to the standard [24, 25]. The MTT method is generally used to detect the toxicity of the material's eluate. It has the advantages of being simple and accurate and having a high degree of automation. However, the use of the material extract will produce colored precipitates, and fading will occur in a short time. The agar covering method is suitable for large quantities of materials with high toxicity and has the advantages of simple operation and wide application types, but its sensitivity will be affected by the degree of diffusion of the material's eluate on the agar.

The molecular filtration method is suitable for materials with small molecular weights of toxic components. It has the advantage of simultaneously observing the primary and secondary cytotoxicity of the material, but it will forcefully affect the diffusion of the precipitated product in the material. The cell morphology method is suitable for mass testing and has the advantages of simple operation and intuitive results, but the result is an estimate and not very convincing [26]. The LDH release method is suitable for small batch testing and has the advantages of good objectivity, easy detection, and no labeling process, but it is easily affected by the activity of lactate dehydrogenase and is not easy to control.

2.3.2. Evaluation Method of Blood Compatibility. Blood compatibility requires that the material does not produce hemolysis or clots on the surface of the material when it comes into contact with blood, and the material neither destroys the blood components nor changes the blood physiological environment. At present, the blood compatibility of biomaterials is mainly studied through the hemolysis rate, dynamic clotting time, and the number of platelets attached to the surface of the material.

The blood compatibility of biomaterials is affected by the structure, morphology, composition, and surface free energy of biomaterials [27]. The coagulation properties are also related to the structure of the materials, and also to the contents of platelets, plasma proteins, and coagulation factors in the blood. The hemolysis rate of the material can be determined by detecting the absorbance of the material. After contact with the material, the more hemoglobin released from the blood, the higher the absorbance, the higher the hemolysis rate. The hemolysis rate meeting the biomaterial standard must be lower than 5%; otherwise the material will have hemolytic effect and cannot be implanted into the body [28].

The blood compatibility of the material can be improved to varying degrees through certain surface treatment methods. The surface of hydrophilic materials has weak interaction with platelets, which will reduce the degree of adhesion and prevent the formation of platelet thrombus.

3. Experiments on Compatibility Testing of Composite Biomaterials

3.1. Experimental Materials, Instruments, and Reagents

3.1.1. Experimental Materials.
In the experimental group, tricalcium phosphate-gelatin composite scaffolds were used in sports injury repair. The control group used collagen, a natural biomaterial. The biomaterials were provided by the hospital without preparation. The experimental animals included 4 clean SD rats, weighing about 210 g. The cells were rat bone marrow mesenchymal stem cells. Rats used in the experiment were also provided by the hospital.

3.1.2. Experimental Equipment.
Experimental instruments included multifunctional ultrapure water machine, electronic balance, filter, CO2 incubator, digital display constant temperature water bath, inverted optical microscope, ultraclean workbench, microplate reader, centrifuge, magnetic stirrer, and micropipette.

3.1.3. Experimental Reagents.
They included 75% alcohol, fetal bovine serum, trypsin, CKK-8 kit, 4% paraformaldehyde, penicillin and streptomycin, collagenase, PBS solution, DMEM medium, and apoptosis detection kit.

3.2. Cell Culture.
The two rats were killed by severed necks, the thigh bones were removed after disinfection, and the bone marrow mesenchymal stem cells were flushed out from the bone marrow with a syringe. The cells were cultured in DMEM medium, which contained 10% fetal bovine serum and $100 \, \mu g/ml$ penicillin and streptomycin. They were incubated in a CO_2 incubator at 37°C, and the medium was changed every 2 days. When the number of monolayer cells exceeded 75%, they were digested with trypsin, centrifuged in a centrifuge, and resuspended in culture medium. After the primary cells were obtained, the cells were passaged and the second and third generation cells were obtained for use.

3.3. Biocompatibility Testing

3.3.1. Flow Cytometry Detection of Cell Apoptosis Rate.
Take the third generation of stem cells in the logarithmic growth phase, and add 1.5 ml trypsin to the culture flask. Put the culture flask in a CO_2 incubator at 37°C for 3 min. After digestion, pipette the solution with a pipette to become a uniform suspension, centrifuge at 1200 r/min for 3 min, and remove the supernatant.

The tricalcium phosphate-gelatin composite scaffold material and collagen material were scraped into powder, soaked in 75% alcohol for 48 hours, then air-dried, and sterilized by ultraviolet radiation. It was made into a material suspension with PBS solution with a concentration of 0.05 g/ml. Tricalcium phosphate-gelatin composite scaffold material suspension was added to the cell suspension of the experimental group, collagen material was added to the cell suspension of the control group, and PBS solution was added to the cell suspension of the blank group. After culturing for 48 hours, they were washed with PBS solution to remove residual trypsin.

All samples were tested for cell apoptosis rate with a cell apoptosis detection kit and flow cytometer, and the operation process was carried out in accordance with the kit instructions.

3.3.2. Cytotoxicity Test.
The treatment of MSCs and materials was the same as that of the other materials. Use CKK-8 kit and operate according to the instructions. But it should be noted that the bubble should be punctured with a hot needle in order to avoid affecting the experimental results. The absorbance values in different sample holes were read by the 450 nm wavelength of enzyme standard instrument. The calculation method of cell proliferation activity is shown as follows:

$$\text{RGR} \, (\%) = \frac{E_0 - N_0}{C_0 - N_0} \times 100\%. \tag{1}$$

Among them, E_0, N_0, and C_0 are the absorbance of experimental group, blank group, and control group.

3.3.3. Evaluation of Blood Compatibility.
Take 4 ml of fresh blood from the rat, add it to a centrifuge tube containing anticoagulant, and add physiological saline for dilution. The tricalcium phosphate-gelatin composite scaffold material and the collagen material were scraped into powder, and PBS solution was added after 24 hours of ultraviolet irradiation to prepare a material suspension with a concentration of 0.2 g/ml, and then filtered. They were also divided into 3 groups, the tricalcium phosphate-gelatin composite scaffold material was the experimental group, the collagen material was the control group, and only the PBS solution was the blank group.

Add $200 \, \mu l$ of anticoagulated whole blood to the three groups of material suspensions, and place them in a 37°C water bath for 5 minutes. Then start timing and take them out in four time periods of 15 min, 30 min, 60 min, and 120 min. Centrifuge at a speed of 1200 r/min for 3 minutes.

Use the 450 nm wavelength of the microplate reader to read the absorbance values in different sample wells. The calculation method of the anticoagulant ability of the material is shown as follows:

$$\text{BCI} = \frac{E_n}{C_n} \times 100\%. \tag{2}$$

Among them, E_n and C_n represent the absorbance value of the experimental group and the control group, respectively.

The preparation process of the material suspension for the hemolysis test is the same as that of the coagulation test. 1 ml of fresh rat blood is collected and centrifuged at 2500 r/min in 12 minutes, and the supernatant is removed and washed with saline. After obtaining the red blood cells, add 5 ml of normal saline for dilution. Set up the experimental group, the control group, the negative control group, and the blank group, respectively, adding tricalcium phosphate-gelatin composite scaffold material extract, collagen material extract, physiological saline, and distilled water. There are 3 parallels for each group. After adding the red blood cell suspension in a water bath at a constant temperature for 25 minutes, let it stand for 60 minutes for observation. Centrifuge at a speed of 1800 r/min for 8 min, take the supernatant, puncture the bubbles with a heating needle, and read the absorbance value at 540 nm with a microplate reader. The calculation method of the hemolysis rate of the material is shown as follows:

$$\text{HR} = \frac{E_1}{N_1} \times 100\%. \tag{3}$$

Among them, E_1 and N_1 are, respectively, the absorbance values of the experimental group and the blank group.

4. Discussion on Composite Biomaterial Compatibility

4.1. Test Results of Apoptosis Rate. Use flow cytometry to observe the apoptosis of experimental group E, control group C, and blank group N. $F1$ represents cells that die from debris and damage, $F2$ represents late-stage apoptotic or necrotic cells, $F3$ represents living cells, and $F4$ represents early-stage apoptotic cells. The apoptosis rates of the three groups are as follows.

Figure 1 shows the apoptosis rate of the three groups of experiments. Among them, the experimental group has the highest content of living cells, which is 91.41%. The viable cells of the control group and the blank group were 86.6% and 77.7%, respectively, indicating that the experimental group had the largest number of cells that survived under the same conditions. In addition, the amount of apoptosis in the experimental group was also significantly lower than that in the control group. Since the experimental group has the highest number of living cells and a lower apoptosis rate, it indicates that the experimental group has a higher cell survival rate and better biocompatibility. For apoptosis, the early apoptosis rate is used to represent the overall apoptosis of the sample.

As shown in Figure 2, the early apoptosis rate of the experimental group was the lowest at 2.81%, the blank group was 8.17%, and the control group was the highest at 11.9%. The difference between the three groups is obvious. This also shows that the tricalcium phosphate-gelatin composite scaffold material of the experimental group has higher biocompatibility.

4.2. Cytotoxicity Test Results. The cytotoxicity of bone marrow mesenchymal stem cells in experimental group E, control group C, and blank group N was tested, and the cell proliferation activity (RGR) was calculated. The results are as follows.

As shown in Figure 3, the proliferation activity of bone marrow mesenchymal stem cells in the experimental group, control group, and blank group showed significant differences. The cell proliferation activity of the tricalcium phosphate-gelatin composite scaffold in the experimental group was the highest, at 0.83 at 120 min, the cell proliferation activity of the collagen material in the control group was 0.79 at 120 min, and the blank group was the lowest. This indicates that the tricalcium phosphate-gelatin composite scaffold material is more suitable for cell adhesion and proliferation.

4.3. Hemocompatibility Evaluation Results

4.3.1. Coagulation Performance. The greater the absorbance value, the more free hemoglobin in the solution, and the better the anticoagulant performance. Calcium chloride is added to the blood to start the blood coagulation mechanism, and the blood compatibility of the material is evaluated by observing the dynamic coagulation time in vitro. In vitro dynamic coagulation test results of tricalcium phosphate-gelatin composite scaffold material and collagen material are as follows.

As shown in Figure 4, with the increase of time, the absorbance of the two groups of materials showed an overall downward trend, indicating that the coagulation mechanism was activated by sodium chloride, and the content of thrombus began to increase. In the first 45 minutes, the rate of decline is relatively fast, which shows that the degree of activation of coagulation factors is relatively high. However, as time continues to increase, between 60 min and 120 min, the rate of decline continues to slow down, showing a certain degree of anticoagulant performance. Finally, in the control group with high absorbance, the collagen material has better anticoagulant performance at 68.8%, while the tricalcium phosphate-gelatin composite scaffold material may have a certain cytotoxicity during the crosslinking process, which is related to the phosphoric acid on the cell membrane surface. The combination of bilayers aggravates blood coagulation, and its anticoagulant performance is 64.8%.

4.3.2. Hemolysis Rate. The greater the value of the hemolysis rate is, the more serious the red blood cells will be destroyed. The state stipulates that the hemolysis rate must be less than
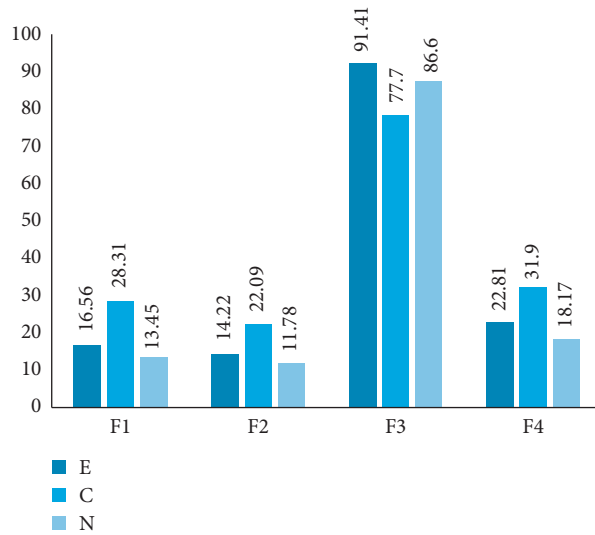
FIGURE 1: Comparison of cell apoptosis rate.
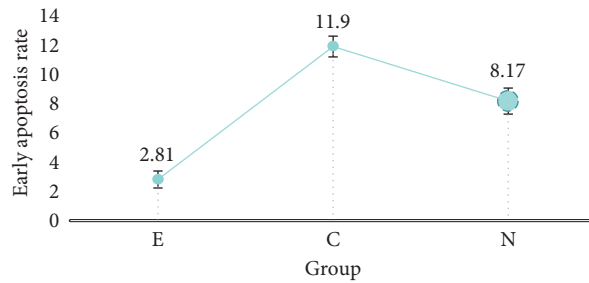
FIGURE 2: Early apoptosis rate of different groups.
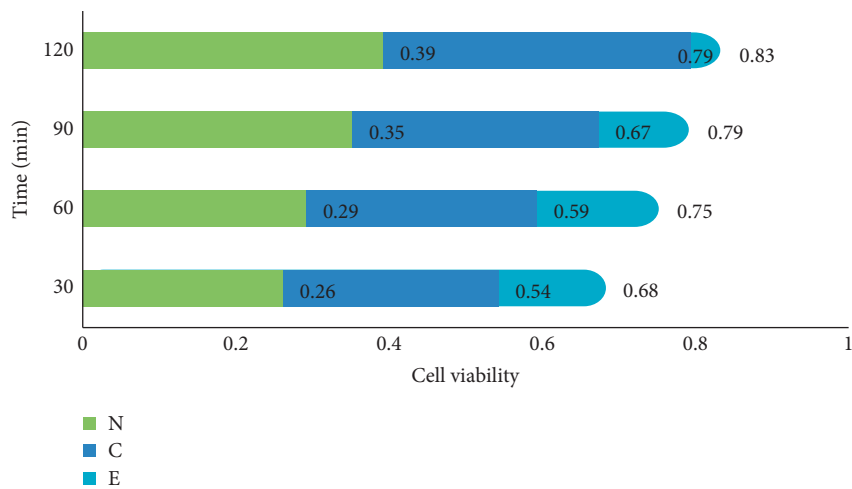
FIGURE 3: Stem cell proliferation activity detection.

5%. The material hemolysis rate of experimental group E, control group C, negative control group $C1$, and blank group N was tested and compared. The results are as follows.

As shown in Table 1, there were significant differences in absorbance among the four groups, with an average of 0.0566, 0.0572, 0.0516, and 0.2248, respectively. The hemolysis rate of tricalcium phosphate-gelatin composite scaffold was 0.28% in the experimental group and 0.33% in the control group. Both of them are lower than the national standard of 5%, and the hemolysis rate of composite materials in the experimental group is lower, and the damage degree of red blood cells is also lower.
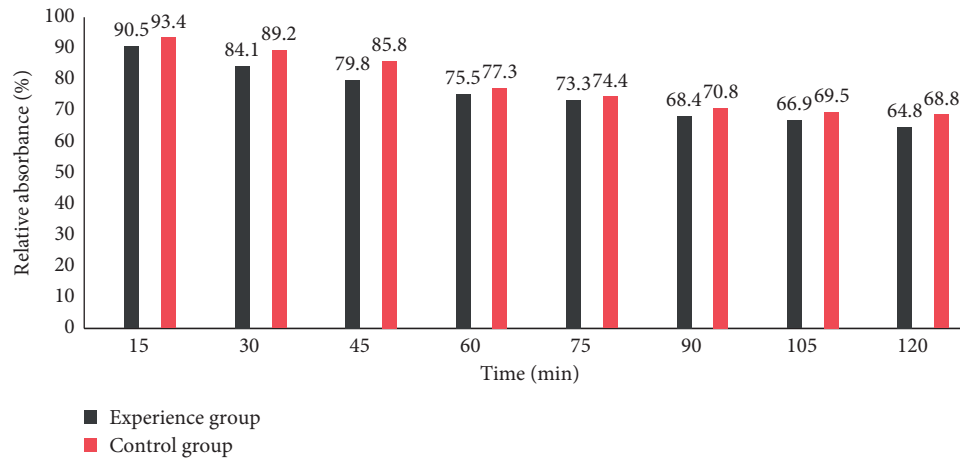
Figure 4: In vitro dynamic coagulation test results of the two groups.

Table 1: Red blood cell hemolysis rate of different groups.

Group	Absorbance				
	1	2	3	Average value	HR
E	0.0541	0.0569	0.0587	0.0566	0.28%
C	0.0548	0.0570	0.0599	0.0572	0.33%
C_1	0.0511	0.0523	0.0515	0.0516	—
N	0.2117	0.2274	0.2352	0.2248	—

5. Conclusions

Composite biomaterials have been gradually used in the process of sports injury recovery, but the use of this material must consider the compatibility with the individual injury site. This paper studies the biocompatibility of composite biomaterials used to repair sports injuries. First, the rat bone marrow mesenchymal stem cells are cultured to prepare a cell suspension. Then, the tricalcium phosphate-gelatin composite scaffold material and collagen material are scraped into powder to make material extracts, which are the experimental group and the control group, respectively. Apoptosis detection kit and flow cytometer detect the apoptosis rate and survival rate of all samples, and CKK-8 kit detects cytotoxicity and calculates cell proliferation activity. Read the absorbance value with a microplate reader to calculate the coagulation performance and hemolysis rate of different groups. The biocomposite of tricalcium phosphate-gelatin has a good effect on injury recovery and also has high compatibility. Since there are many factors affecting biocompatibility, how to solve the cytotoxicity of composite biomaterials during the crosslinking process is the next problem to be solved in this research. The disadvantage of this study is that this article only conducted preliminary tests on the biocompatibility of the tricalcium phosphate-gelatin composite scaffold, but the long-term biological function needs more experiments to test.

Data Availability

The data used to support the findings of this study are available from the corresponding author upon reasonable request.

Conflicts of Interest

The author declares no conflicts of interest with respect to the research, authorship, and/or publication of this article.

References

[1] K. W. Young, K. C. Park, J. S. Hwang, and H. S. Lee, "Peroneal Tendon repair in sports injury," *Journal of Korean Foot and Ankle Society*, vol. 23, no. 3, p. 100, 2019.

[2] C. Wang, J. Liu, Y. Liu, B Qin, and D He, "Study on osteogenesis of zinc-loaded carbon nanotubes/chitosan composite biomaterials in rat skull defects," *Journal of Materials Science. Materials in Medicine*, vol. 31, no. 2, pp. 15–10, 2020.

[3] A. J. Scillia, T. P. Pierce, E. Simone, R. C. Novak, and B. A. Emblom, "Mini-open Incision sports hernia repair: a surgical technique for Core muscle injury," *Arthroscopy Techniques*, vol. 6, no. 4, pp. e1281–e1284, 2017.

[4] C. Wang, Y. Wang, H. Meng et al., "Research progress regarding nanohydroxyapatite and its composite biomaterials in bone defect repair," *International Journal of Polymeric Materials and Polymeric Biomaterials*, vol. 65, no. 12, pp. 601–610, 2016.

[5] D. Pieniak, K. Przystupa, A. Walczak et al., "Hydro-thermal fatigue of polymer matrix composite biomaterials," *Materials*, vol. 12, no. 22, pp. 3650-3651, 2019.

[6] X. Li, S. Zhang, X. Zhang et al., "Biocompatibility and physicochemical characteristics of poly(-caprolactone)/poly(lactide-co-glycolide)/nano-hydroxyapatite composite scaffolds for bone tissue engineering," *Materials & design*, vol. 114, pp. 149–160, 2016.

[7] Y. Gu, J. Fernandez, J. S. Baker, and J. Awrejcewicz, "A special Section on Informatics of medical image application in sports

injury," *Journal of Medical Imaging and Health Informatics*, vol. 9, no. 3, pp. 540–542, 2019.

[8] Y. Zhang, W. Ni, and Y. Li, "Effect of siliconizing temperature on microstructure and phase constitution of Mo-MoSi2 functionally graded materials," *Ceramics International*, vol. 44, no. 10, Article ID 11166, 2018.

[9] J. N. Harr and F. Brody, "Sports hernia repair with adductor tenotomy," *Hernia*, vol. 21, no. 1, pp. 1–9, 2016.

[10] B. Gao, N. Xu, and P. Xing, "Shock wave induced nano-crystallization during the high current pulsed electron beam process and its effect on mechanical properties," *Materials Letters*, vol. 237, no. 15, pp. 180–184, 2019.

[11] D. Kaul, J. Kahn, L. Huizing et al., "Mid-term functional Outcome and Return to sports after Proximal Hamstring Tendon repair," *International Journal of Sports Medicine*, vol. 37, no. 7, pp. 570–576, 2016.

[12] F. Alaee, J. Apostolakos, H. Singh et al., "Lateral clavicle fracture with coracoclavicular ligament injury: a biomechanical study of 4 different repair techniques," *Knee Surgery, Sports Traumatology, Arthroscopy*, vol. 25, no. 7, pp. 2013–2019, 2017.

[13] S. Akahane, Y. Sakai, T. Ueha et al., "Transcutaneous carbon dioxide application accelerates muscle injury repair in rat models," *International Orthopaedics*, vol. 41, no. 5, pp. 1007–1015, 2017.

[14] D. Steffen and K. Baar, "Loading to Optimize Patellar Tendon repair after injury," *Medicine & Science in Sports & Exercise*, vol. 52, no. 7S, p. 90, 2020.

[15] Z.-D. Meng, C.-J. Wang, Y.-Q. Zhang, C. Luo, Z.-Y. Wang, and W.-C. Li, "Porous hydroxyapatite/Strontium Oxide composite ceramic preparation and properties of biomaterials," *Journal of Biomaterials and Tissue Engineering*, vol. 9, no. 6, pp. 783–788, 2019.

[16] B. Koodziejska, A. Kaflak, and J. Kolmas, "Biologically Inspired collagen/Apatite composite biomaterials for potential Use in bone tissue regeneration—a review," *Materials*, vol. 13, no. 7, p. 1748, 2020.

[17] O. M. Otychenko, "Some physico-mechanical properties of composite biomaterials on the basis of biogenic hydroxyapatite with magnetic additives," *Functional Materials*, vol. 25, no. 4, pp. 695–701, 2018.

[18] S. Chen, M. K. Hassanzadeh-Aghdam, and R. Ansari, "An analytical model for elastic modulus calculation of SiC whisker-reinforced hybrid metal matrix nanocomposite containing SiC nanoparticles," *Journal of Alloys and Compounds*, vol. 767, pp. 632–641, 2018.

[19] T. Yokoi, "The development of novel calcium phosphate–polymer composite biomaterials with macro- to nano-level controlled hierarchical structures," *Journal of the Ceramic Society of Japan*, vol. 127, no. 10, pp. 715–721, 2019.

[20] I. A. Neacsu, A. P. Serban, A. I. Nicoara, R. Trusca, V. L. Ene, and F. Iordache, "Biomimetic composite scaffold based on naturally Derived biomaterials," *Polymers*, vol. 12, no. 5, p. 1161, 2020.

[21] "Water-based, surfactant-free cytocompatible nanoparticle-microgel-composite biomaterials–rational design by laser synthesis, processing into fiber pads and impact on cell proliferation," *Nephron Clinical Practice*, vol. 18, no. 3-4, pp. 740–746, 2017.

[22] X. Wang, G. Wang, L. Liu, and D. Zhang, "The mechanism of a chitosan-collagen composite film used as biomaterial support for MC3T3-E1 cell differentiation," *Scientific Reports*, vol. 6, no. 1, Article ID 39322, 2016.

[23] P. P. Özyol, E. Özyol, and F. Karel, "Biocompatibility of intraocular lenses," *Türk Oftalmoloji Dergisi*, vol. 47, no. 4, pp. 221–225, 2017.

[24] I. Palmer, J. Nelson, W. Schatton, N. J. Dunne, F. J. Buchanan, and S. A. Clarke, "Biocompatibility of calcium phosphate bone cement with optimized mechanical properties," *Journal of Biomedical Materials Research Part B: Applied Biomaterials*, vol. 104, no. 2, pp. 308–315, 2016.

[25] V. Kalidasan, X. L. Liu, T. S. Herng, Y. Yang, and J. Ding, "Bovine serum Albumin-Conjugated Ferrimagnetic Iron Oxide nanoparticles to enhance the biocompatibility and magnetic Hyperthermia performance," *Nano-Micro Letters*, vol. 8, no. 1, pp. 80–93, 2016.

[26] K. H. Hussein, K.-M. Park, K.-S. Kang, and H.-M. Woo, "Biocompatibility evaluation of tissue-engineered decellularized scaffolds for biomedical application," *Materials Science and Engineering: C*, vol. 67, pp. 766–778, 2016.

[27] D. Algul, A. Gokce, A. Onal, E. Servet, A. I. Dogan Ekici, and F. G. Yener, "In vitrorelease andIn vivobiocompatibility studies of biomimetic multilayered alginate-chitosan/β-TCP scaffold for osteochondral tissue," *Journal of Biomaterials Science, Polymer Edition*, vol. 27, no. 5, pp. 431–440, 2016.

[28] M. Catauro, R. A. Renella, F. Papale, and S. Vecchio Ciprioti, "Investigation of bioactivity, biocompatibility and thermal behavior of sol-gel silica glass containing a high PEG percentage," *Materials Science and Engineering: C*, vol. 61, pp. 51–55, 2016.

Research Article

Research on the Evolution Characteristics of Rock Mass Response from Open-Pit to Underground Mining

Jiabo Geng,[1] Qihang Li [ID],[1] Xiaoshuang Li [ID],[2,3,4,5] Tao Zhou,[1] Zhifang Liu,[1] and Yulin Xie[1]

[1]*School of Resources and Environmental Engineering, Jiangxi University of Science and Technology, Ganzhou 341000, China*
[2]*School of Civil Engineering, Shaoxing University, Shaoxing 312000, China*
[3]*College of Civil Engineering, Qilu Institute of Technology, Jinan 250200, China*
[4]*Sinosteel Maanshan General Institute of Mining Research Co. LTD., Maanshan 243000, China*
[5]*State Key Laboratory of Safety and Health for Metal Mines, Maanshan 243000, China*

Correspondence should be addressed to Xiaoshuang Li; xsli2011@126.com

This study is based on the engineering background of pit no. 2 in Jinning Phosphate Mine, China. In order to systematically analyze the movement, deformation, and failure laws of surrounding rocks in underground stopes. The room and pillar method is used to excavate and stop the ore bodies in the mining area. Combined with the similar physical model experiments and discrete element MatDEM numerical simulations, it reveals the deformation and failure laws and evolution characteristics of the surrounding rock of the stope in the process of converting from open-pit to underground mining. The results show the following: (1) Along the inclination of the ore body, the farther the horizontal and vertical displacements are from the underground stope, the less the impact of mining stress. On the other hand, along the inclined vertical direction of the ore body, the farther the measuring point is from the stope, the smaller the range of mining influence will be. (2) In the process of ore body recovery, the rupture of the overlying strata of the stope has an obvious layered structure, with collapse zones, fissure penetrating zones, and microfracture loosen zones appearing from the bottom to top. In addition, the movement and destruction of the overlying strata of the entire stope is an "elliptical arch." Therefore, the results of similar simulation experiments and numerical simulation are basically consistent.

1. Introduction

China is one of the largest phosphate mining countries, and its total resources rank second in the world, but the burial is deeper, mostly in inclined deposits. Compared with other open-pit mines, it has the characteristics of difficult mining and high cost [1–3]. In addition, as the country pays more and more attention to environmental governance, open-pit mines have gradually lost the advantages of fast production and high safety index [4, 5]. Because of this, it is urgent to switch to underground mining. Affected by the mining stress and the gravity of the overlying rock, the stability of the open-pit slope of the underground stope is about 20% lower than that of the single open-pit mining, which seriously endangers the safety of the open-pit and underground stope

[6]. Therefore, the response of slope rock mass coupled with underground mining is the key issue that affects safe production.

Many scholars have conducted a large number of studies on the instability mechanism, deformation and failure characteristics of open-pit slopes, and deformation and failure characteristics of underground surrounding rocks [7–9]. Jakubec et al. discussed the failure structure of the rock mass on the slope of the Ekati Diamond Mine after open-pit mining was converted to underground mining [10]. Bakhtavar and Shahriar used mathematical economic theory models to predict and analyze the stripping rate and optimal mining time period of open-pit and underground combined mining, which greatly improved the mining efficiency [11]. Brummer et al. used 3DEC (3 Dimension Distinct Element

Code) to simulate the instability and failure of the high and steep slope on the north side of Palabora Mine during the process of converting from open-pit to underground mining [12]. Mass et al. analyzed the mechanism of the upper pit in the goaf after the Plabora Mine was converted to underground mining [13]. With the continuous improvement of rock mass testing methods, coupled with the introduction of various interdisciplinary advanced theories. Some researchers have conducted a more in-depth discussion on the mechanical mechanism and deformation mechanism of open-pit transfer to an underground stope. Li et al. established a rock slope deformation model for the transition from open-pit to underground mining and analyzed the nonlinear relationship between underground mining disturbance and slope deformation in open-pit mining [14]. Based on the combination of theoretical analysis and numerical simulation, Zhang et al. systematically studied the deformation mechanism of the slope rock mass in the Jinchuan Longshou mining area [15]. Song et al. used similar physical model tests and numerical simulation methods to study the degree of rock deformation during the converting of the Panzhihua Jianshan Iron Mine to underground mining [16]. Jia used similar material simulation tests and a noncontact strain analysis system to monitor the displacement of iron ore from open-pit to underground mining and obtained the effect of underground stopes on open-pit slopes [17]. Wang et al. used numerical simulation methods to study the stress and deformation and failure laws of the slope rock mass under the action of underground mining [18].

The above-mentioned methods are mainly used in the mining of open-pit and steeply inclined open-pit to underground ore bodies and rarely involve gently inclined thin to medium-thick layered nonmetallic phosphate ore. On the other hand, they mainly focused on the actual technical issues of the project, and there is little research on the effect of the open-pit slope on the underground stope and the mechanical mechanism. In short, it is a difficult problem to systematically study the mechanic mechanism and mining response characteristics of the slope rock mass coupled with underground mining after the open-pit to underground mining.

To overcome these challenges, we took the deep ore body of no. 2 pit of Jinning Phosphate Mine as the engineering background and conducted in-depth investigations on the geological characteristics of the mines, the occurrence characteristics of the ore bodies, and the current status of mining in the area. On this basis, MatDEM numerical simulation test, similar physical simulation experiment, and theoretical analysis methods were used to study the evolution characteristics of rock mass response in open-pit mining to underground mining. The comparison of a similar simulation experiment and numerical simulation test verified that the direct roof of the underground stope was destroyed in an "elliptical arch" after the phosphate ore body was converted from open-pit to underground mining. When the internal stress value of the pressure arch exceeds the ultimate strength of the rock layer itself, the rock layer will have four failure modes: compression failure, shear failure, tensile failure, or combined failure.

2. Engineering Background

2.1. Mine Profile. As shown in Figure 1, the phosphate mining area is located 72 kilometers southwest of Kunming, China, 2 kilometers on both sides of the southern end of Dianchi Lake. The geographical coordinates are 103°22′16″–103°34′42″ east longitude and 24°41′40″–24°44′07″ north latitude. The mining area is about 9.2 square kilometers, with county-level highways, quasigauge railways, and expressways nearby, and the transportation is very convenient. According to the preliminary design of the Jinning Phosphate Mine Phase I expansion project, the Jinning Phosphate Mine (III and IV mine sections) #34~#130 exploration line is divided into ten open-pit mining from north to south. In this study, we choose the no. 2 mining area (between the #52~#66 exploration lines) as the study area. This area is located in the hinterland of the Yunnan Plateau, belonging to the Jinsha River system, and adjacent to the Nanpan River watershed in the south. The mine is a mid-mountain landform, with cold winters, no sweltering summers, foggy all year round, and an average annual rainfall of 925.4 mm. Currently, affected by open-pit mining and natural weathering, the study area has fully developed fissures, and the ore body is relatively loose (Figure 2).

2.2. Mining Area Structure. The no. 2 mining area (between the #52~#66 prospecting line) squeezed from east to west in the early stage, forming the F1-1, F1-2, and F10-01 faults with a nearly north-south strike. Later, it was extruded from the NW-SSE direction to form the F2-4 fault in the NEE-SW direction. The structure is simple, and no folds are developed. In addition, the stratum and the ore layer slope to the east and produce monoclinic.

2.2.1. Near North-South Faults

F1-1 Fault. It is a regional large fault (a reverse fault), which runs through the entire Jinning Phosphate Mine in a nearly north-south direction, distorting the stratum and ore layers and forming two major ore bodies (layers) in the east and west. The fault plane is inclined to the east, with a dip angle of 65°~70°, and a length of about 9530 m.

F1-2 Fault. The reverse fault strike is N15°W, and the total length is about 2588 m. Among them, the extension length in the area is about 584 m, and the curvature is relatively large near the #57 exploration line. The fault plane is inclined to the east, with a dip angle of 63°~70°. The fault has no effect on the continuity of the ore body, which is located on the east side.

F10-01 Fault. The length of the reverse fault is about 107 m, the fault plane is inclined to the east, and the dip angle is about 68°~71°. The extension is short and the scale is small, causing failure to the ore bodies in a small area on the north and south sides of ZK54-2.

2.2.2. Northeast-Southwest Fault

F2-4. The fault is a flat-reverse fault with a length of about 129 m. After geological investigation, the north-west plate slides in the southwest direction, and the
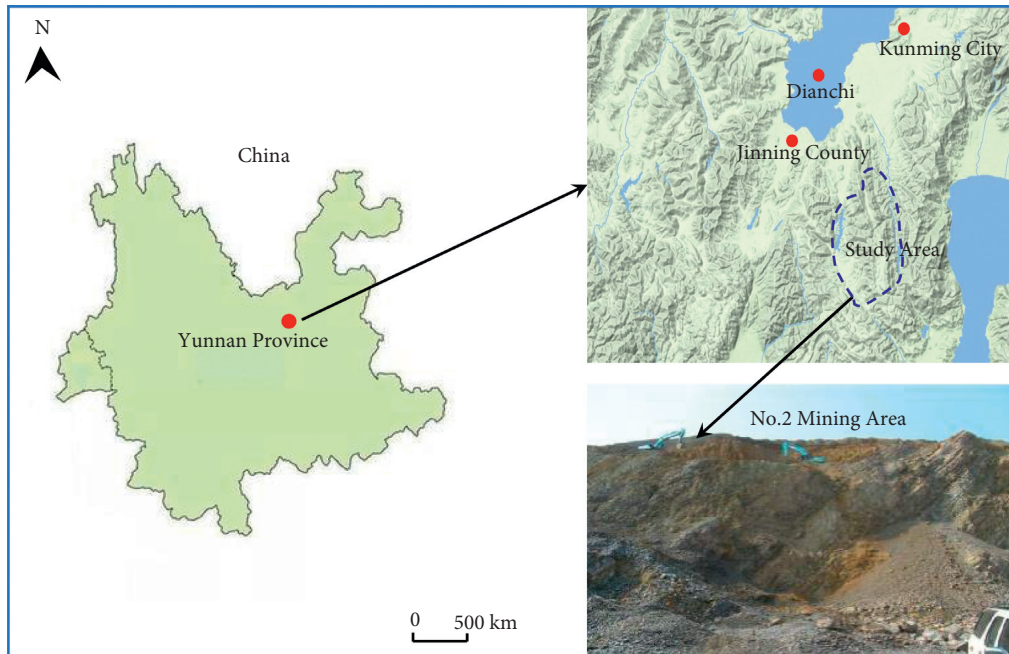
FIGURE 1: Geographical map of no. 2 mining area of Jinning Phosphate Mine.

(a)   (b)

FIGURE 2: The mining status of Jinning Phosphate Mine no. 2 pit. (a) Current status of surface mining. (b) Development of fissures in open-pit mining at this stage.

southeast plate slides in the northeast direction. The sliding distance is about 29 m. Affected by this, the ore body outcrops between #62 and #63 exploration lines formed dislocation.

2.3. Stope Stability Investigation. According to the direction of the investigated dominant structural surface, a stereographic projection map is drawn. As shown in Figure 3(a), the azimuth angle of the strip arrangement can be roughly divided into five regions. Based on the stereographic projection map (Figures 3(b)–3(f)), the stability of the stope was judged and analyzed in five areas:

  (1) As shown in Figure 3(b), the stope axis of Zone 1 is obliquely intersected with the strikes of the two sets of structural planes, and the inclination angle of the

structural plane l_1 is relatively slow. The distribution of structural planes has a greater impact on the stability of the stope. The main deformation forms may be gangsters and roof failures.

  (2) As shown in Figure 3(c), the stope axis of Zone 2 is almost orthogonal to l_2, and the l_2 structure has little effect on the stability of stope strips. The stope axis in Zone 2 is almost parallel to l_1, and the inclination of the structural plane of l_1 is relatively slow. Thus, the distribution of structural planes has a greater impact on the stability of the stope, and roof fall is prone to occur.

  (3) In Figures 3(d)–3(f), the stope axis of Zone 3, Zone 4, and Zone 5 obliquely intersect with the direction of the two sets of structural planes, which is easy to

(a)

(b)

(c)

(d)

(e)

(f)
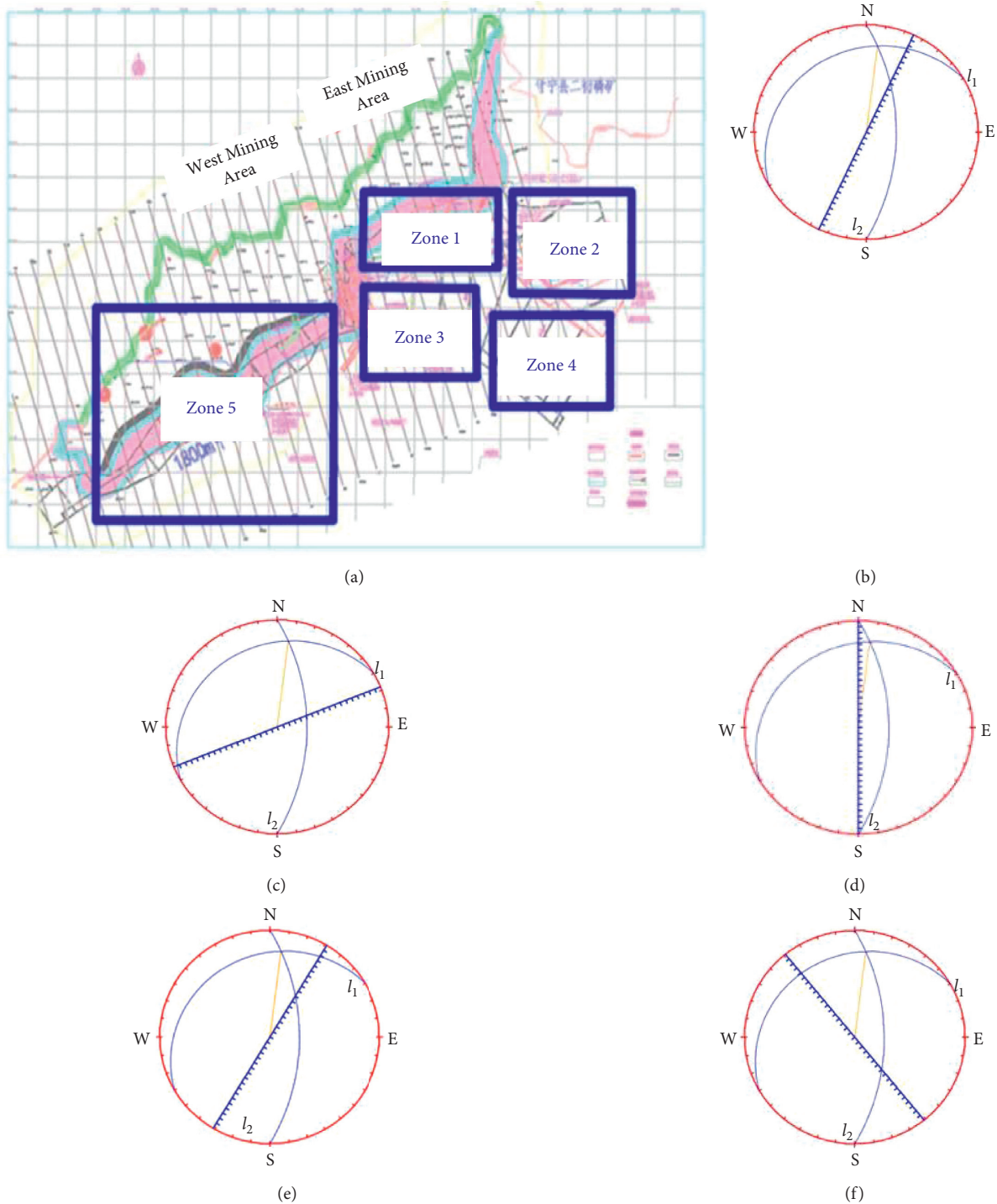
FIGURE 3: Stereographic projection of different regions. (a) Area division map; (b) stereographic projection in zone 1; (c) stereographic projection in zone 2; (d) stereographic projection in zone 3; (e) stereographic projection in zone 4; (f) stereographic projection in zone 5.

form unstable bodies and cause the occurrence of roof fall and film gang.

3. Similar Material Experiments

3.1. Model Design. As shown in Figure 4(a), the similar physical experiment model frame is composed of a pressurized lever, pressurized panel, top beam, side beam, bottom beam, and model surface steel plate. The model size is $2.00 \, m \times 0.3 \, m \times 1.5 \, m$ (length × width × height), the lever loading range is 0.1~200 MPa. In this test, the ground stress was simulated by self-weight loading. To better simulate actual mining, this test finally selected the hanging wall section of the #59 exploration line as the study area, with a dip angle of 14° and a layer thickness of 3.4 m (Figure 4(b)). Table 1 shows the rock mechanical parameters measured by

(a)

(b)
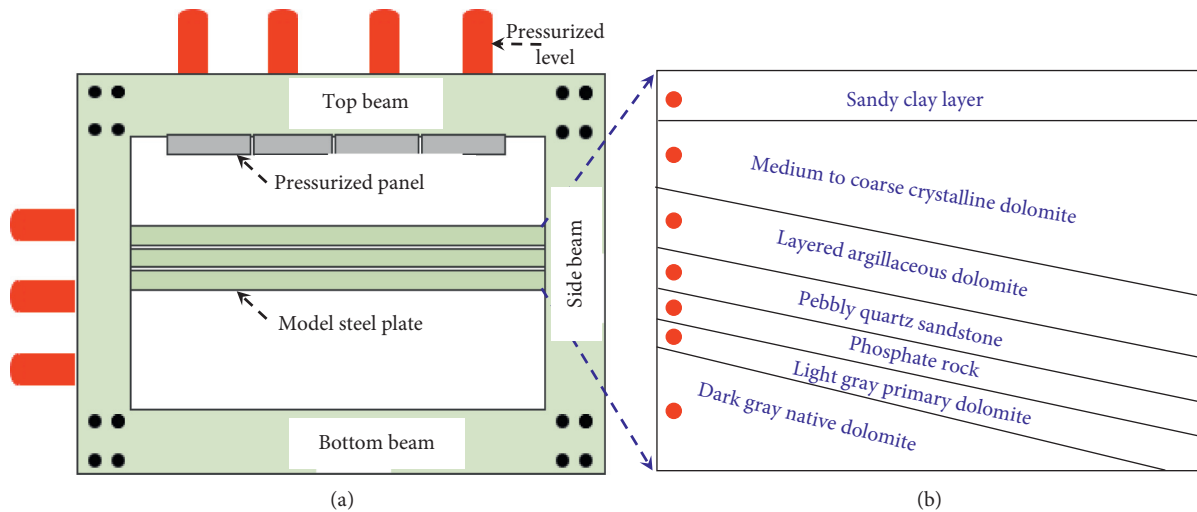
FIGURE 4: (a) Similar model; (b) similarity simulation experiment profile.

TABLE 1: Rock mechanics parameters table.

Rock name	Uniaxial compressive strength (MPa)	Elastic modulus (GPa)	Tensile strength (MPa)	Poisson's ratio	Cohesion (MPa)	Internal friction angle (°)
Sandy clay layer	45.68	24.32	4.65	0.26	18.63	32.12
Medium to coarse crystalline dolomite	48.25	35.43	6.38	0.15	14.69	34.22
Layered argillaceous dolomite	74.12	32.54	7.87	0.17	18.60	44.36
Pebbly quartz sandstone	78.41	49.12	6.61	0.25	22.53	49.75
Phosphate rock	87.49	45.36	12.73	0.32	28.70	54.78
Light gray primary dolomite	63.71	46.72	11.59	0.19	18.42	53.17
Dark gray native dolomite	88.62	52.49	14.37	0.10	25.94	44.25

laboratory physical tests after field sampling, which reflects the mechanical properties of rock, and the similar physical model experiment material ratio is also based on the mechanical parameters [19].

Based on the principle of similar material simulation, the similarity parameters for each simulation test are as follows: intensity similarity ratio = 1 : 500, Poisson's ratio, strain, internal friction angle = 1 : 1, time similarity ratio = 1 : 17, and bulk density similarity ratio = 5 : 8. A plane stress model was used in the present work to simulate similar materials along the dip materials, sand, gypsum, calcium carbonate, mica powder, soft glue, engine oil, fine wood chips, and water [20–22]. The final selection of the ratio of the measured value of the material parameters and the theoretical value of the least error are combined with the measured actual rock mechanics parameters (Table 2).

3.2. Measuring Point Layout. In this experiment, the design slope height of the final slope after open-pit excavation is 200 m, and the slope angles is 65°. The purpose is to systematically analyze the law of rock mass movement and deformation. As shown in Figure 5, the similar model is

along the direction of the ore body, dividing the 24 m boundary pillar and the three-stage mine rooms and pillars (the size of the mine room is 10 m, the pillar size is 6 m, and the continuous pillar is 15 m). In detail, each stage of the excavation is divided into two steps, and the excavation time interval of each mining room is 2.5 h. The mining sequence of the pillars is as follows: the three-stage excavation is completed, and the pillars shall be recovered in sequence (the interval of mining is 2 h). In addition, a total of 5 displacement measuring lines are arranged along the normal direction of the ore body at the displacement measuring points, which are, respectively, arranged above each stope and above the pillars.

3.3. Experimental Phenomena. After the first-stage excavation of the model with a slope height of 200 m and a slope angle of 65°, affected by the mining stress of the underground stope, arc-shaped separation fissures of varying degrees appeared above the roof. The roof collapsed in the upper left corner of mine room #1 (Figure 6(a)). After second stage of excavation, pillar #1 has a shear fracture fissure. In addition, the pillars tended to fall, and

TABLE 2: Similar material ratio scheme.

Lithology	Simulated thickness (cm)	Actual strength (kPa)	Simulation strength (kPa)	Material ratio (sand : lime : gypsum)
Sandy clay layer	10	2.19	4.38	6 : 7 : 3
Medium to coarse crystalline dolomite	69.7	35.16	70.32	2.5 : 1.4 : 8.8
Layered argillaceous dolomite	23.5	24.78	49.56	2.8 : 3.5 : 6.5
Pebbly quartz sandstone	8	22.87	45.74	3 : 1 : 9
Phosphate rock	4.3	38.54	71.68	2.4 : 1.2 : 9
Light gray primary dolomite	2.3	39.35	78.7	2.4 : 1 : 9
Dark gray native dolomite	50.0	34.17	68.34	2.45 : 1.5 : 8.5
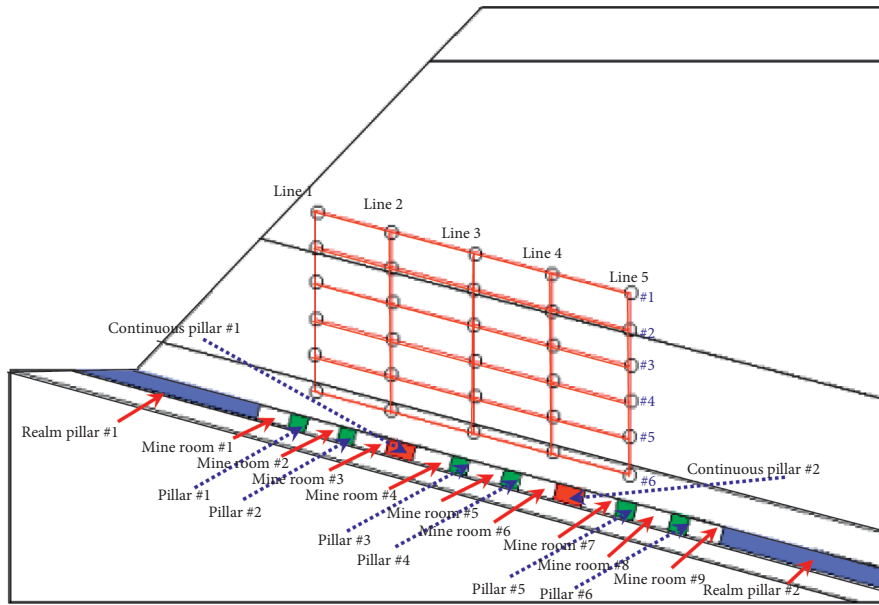
FIGURE 5: Displacement survey line monitoring diagram of a similar physical model.

(a)

(b)

FIGURE 6: Continued.

(c)

FIGURE 6: Failure characteristics of underground stope after (a) first-stage excavation, (b) second-stage excavation, and (c) third-stage excavation under the model of slope height of 200 m and slope angle of 65°.

microfissures appeared inside the direct roof. With the gradual advancement of the working face, the microfissures developed into arc-shaped through fissures (Figure 6(b)). The reason is that due to the mining stress of the entire stope and the weight of the overlying r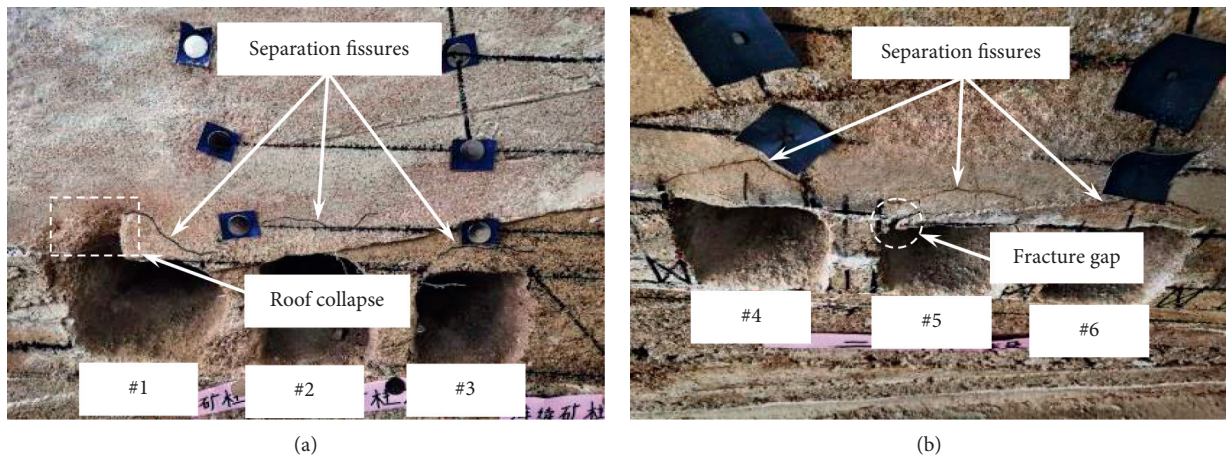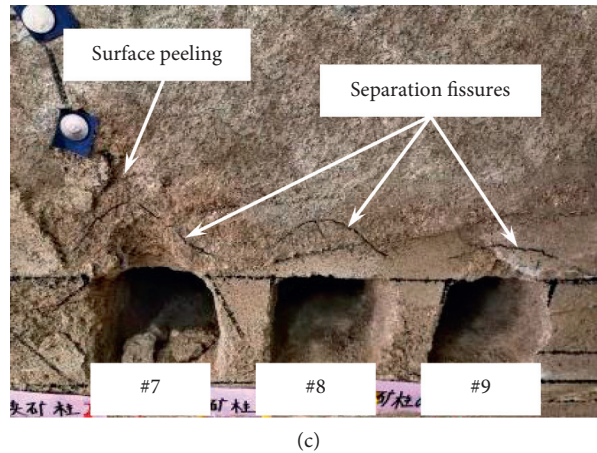ock mass, the roof center has been unloaded and collapsed. However, the stress transfers to the surrounding rocks and pillars of the stope, resulting in a phenomenon of pressure arch, which maintains the stability of the stope. During the third-stage excavation, the redistribution of stress will cause the span of the pressure arch to become larger, a large-scale collapse occurs, and a small pressure arch will be formed behind the neighboring stope. Among them, the surface layer of the overlying rock began to fall off, and the collapse was the most obvious (Figure 6(c)).

To better clearly understand the deformation and failure characteristics of the surrounding rock in the underground stope of room and pillar mining, we recovered the isolated pillars in the stope in turn (Figure 7). As shown in Figure 7, after the recovery of the pillars was completed, the overburden failure of the stope caused a large-scale sliding failure trend, with a typical "domino effect." According to the degree of deformation and failure, it can be divided into roof collapse zone, fissure penetration zone, and microfracture loose zone. In other words, under the influence of the superimposed force of mining, the pillars of the stope are in a critical failure state. When any pillar is mined, it will cause plastic failure to its surroundings, thereby threatening the stability of the stope.

3.4. Physical Modeling Result Analysis. As shown in Figure 8, the vertical displacement of the surrounding rock and overlying strata at various stages of the model excavation was measured using a digital camera system. Figures 8(a)–8(c) are the subsidence displacements after the first, second, and third excavation stages of the similar material model, respectively. Here, the distance from the beginning of the ore body and the extent of subsidence are plotted as negative values [23].

These experimental results indicate that the deformation of the surrounding rock underground and the overlying strata during mining occurs in the following stages: (1) A small area of the roof fell off during the first excavation stage (Figure 8(a)). (2) In the second excavation stage, the microfissures developed into perforated fissures and collapsed (Figure 8(b)). (3) Large-scale collapse occurred during the third excavation stage (Figure 8(c)).

In detail, after the completion of the first stage of excavation, it advanced 27 cm in the inclined direction of the ore body (actual engineering 81 m). The roof above mine room #1 began to show fissures caused by the bending and sinking of the separation layer, and the direct roof on the upper left side collapsed, forming an arched structure. Among them, the maximum horizontal displacement was −0.164 mm (−4.92 cm), and the maximum vertical displacement was −0.283 mm (−8.50 cm) (Figure 8(a)). It continued to advance 73 cm (actual engineering 219 m) along the inclined direction of the ore body (the second excavation stage). At this time, the separation fissures extended from the top of the stope from bottom to top, and the upper left corner of mine room #5 had a fall, and pillar #5 had broken microfractures. The maximum horizontal displacement and the maximum vertical displacement were increased to −0.376 mm (−11.29 m) and −0.775 mm (−23.27 cm), respectively (Figure 8(b)). When the third excavation stage advanced to 119 cm (actual engineering 357 m), the space of the stope was further enlarged, causing a large-scale collapse of the overlying rock of the stope. Meanwhile, the maximum horizontal displacement and the maximum vertical displacement reached −0.423 mm (−12.68 cm) and −0.999 mm (−29.97 cm), respectively (Figure 8(c)).

In a word, due to the influence of the mining stress in the underground stope, different degrees of separation fissures appeared on the roof at different stages. After the initial stage of excavation, the overall model was in a stable state, but the roof collapsed in the upper left corner of mine room #1. After the second stage of excavation, a shear fracture fissure appeared in pillar #1, and a microfracture

(a)

(b)
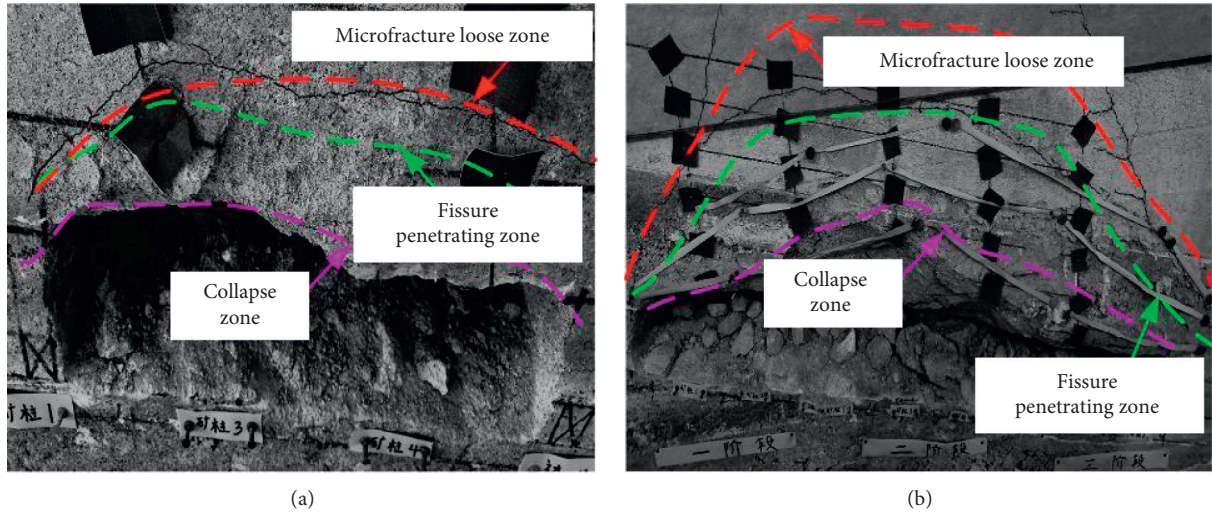
FIGURE 7: The failure characteristics of the overlying rock mass at the stage of recovering the pillars. (a) Recover pillar #3 and pillar #4; (b) recover the continuous pillar #2.

(a)

(b)

(c)

(d)
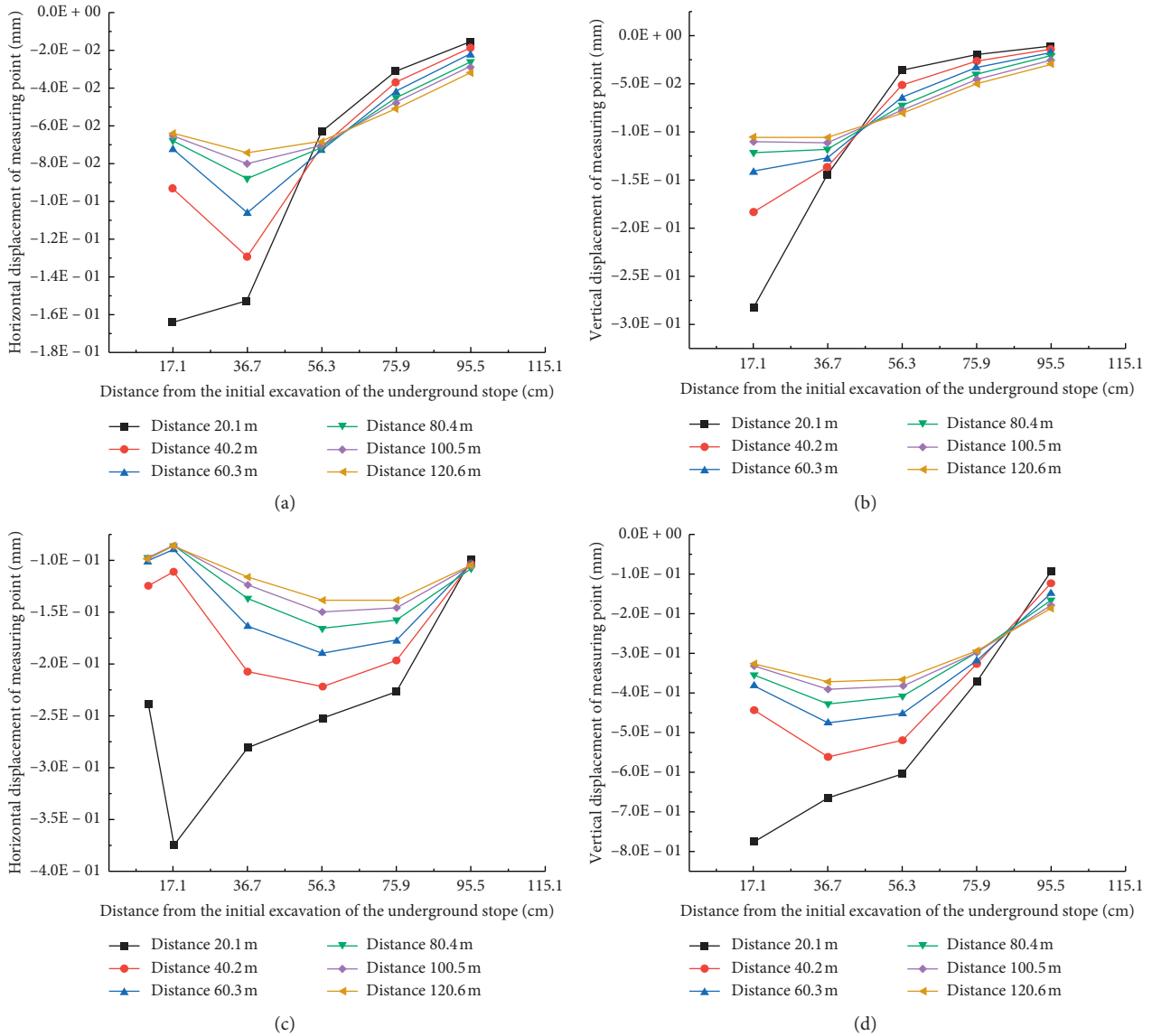
FIGURE 8: Continued.

(e)

(f)
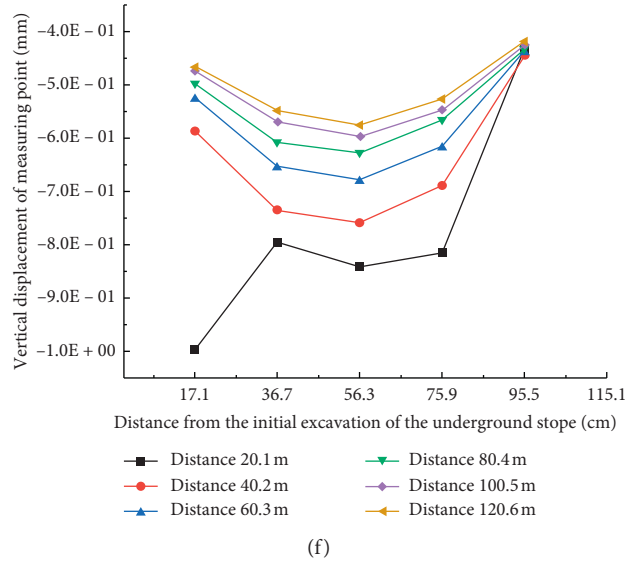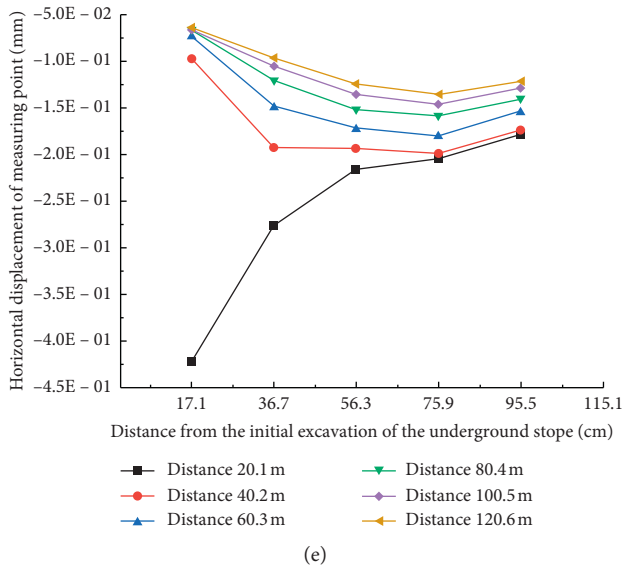
FIGURE 8: The model with a slope height of 200 m and a slope angle of 65°; the three-stage mining displacement curve of the underground stope. Mining displacement curve in (a) the first stage, (b) the second stage, and (c) the third stage.

appeared in the direct roof. With the continuous advancement of the working face, the microfractures developed into arc-shaped through fissures. The reason was that due to the mining stress of the entire stope and the self-weight of the overlying rock mass, there was unloading in the center of the roof, causing caving [24, 25]. When the last stage of excavation is carried out, the redistribution of stress will cause the span of the pressure arch to become larger, until the mining reaches a certain span, and a large-scale collapse occurs.

4. Numerical Simulation of Rock Mass Movement Characteristics

4.1. Model Establishment and Assumptions. In recent 20 years, computer technology has developed rapidly, and numerical simulation has become an important research method [26–28]. Based on the measurement results of rock mechanics parameters (Table 1), the following assumptions are made for the numerical model: (1) The ore body model is an ideal elastoplastic body under the ideal Mohr-Coulomb criterion. (2) Each layer of rock is made of homogeneous and homogeneous materials. (3) Ignore the influence of ore body groundwater and other geological structures. Figure 9(a) shows the MatDEM model diagram, and Figure 9(b) shows the initial state of the model.

4.2. Physical and Mechanical Parameters of the Rock. The mesomechanical parameters of the MatDEM model were based on the measured mechanical properties of rock samples obtained on-site. Whether the numerical simulation results are reliable or not mainly depends on the determination of rock mass mechanical parameters. In order to solve this problem, this paper introduced the Hoek–Brown empirical formula to weaken the upper and lower rock layers of

the ore layer. The mechanical parameters of the weakened rock mass after numerical simulation are as shown in Table 3.

4.3. Numerical Simulation Model Excavation Scheme. As shown in Figure 9(a), the boundary pillar, the main mine room, and the continuous pillar were divided along the direction of the ore body. Open the mining rooms in order from left to right. Among them, the width of each mine room was 10 m, and the thickness of the boundary pillar was 24 m. To meet the safety requirements of underground mining, each of the three mine rooms was regarded as a mining stage (a total of three stages), and a 6-meter-wide interval pillar (a total of 6) was set between each mine. In addition, two continuous pillars (15 m wide) were reserved after each stage of mining is completed. On the other hand, in order to further study the change law of the overlying rock stress field and displacement field of the stope, we arranged a monitoring line composed of 25 monitoring points 20 m above the stope (the area circled in black).

4.4. MatDEM Simulation Results and Analysis

4.4.1. Rock Mass Stress Distribution Law. In the physical model with a slope height of 200 m and slope angle of 65°, under the influence of mining stress, some small arch-shaped microfissures appeared on the top of the stope at the first stage, and the rock mass was in a stable state (Figure 10(a)). With the unfolding of the second stage of excavation, the overhang area of the roof gradually increased, and the unloading range of the stope roof is further expanded. Later, the microfissures in the roofs of various mine rooms gradually penetrated to form multiple macrofissures, and these macrofissures gradually extended to the

(a)

(b)
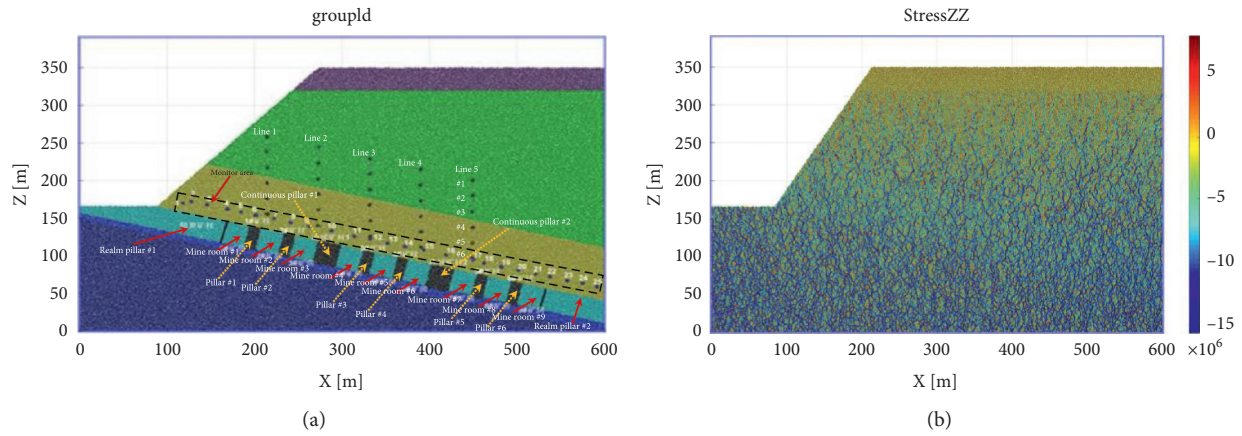
FIGURE 9: Numerical simulation physical model. (a) Schematic diagram of the layout of monitoring points for mine rooms and pillars. (b) Stress distribution in the initial state of rock mass.

TABLE 3: Rock mechanics parameters.

Rock name	Compressive strength (MPa)	Elastic modulus (GPa)	Tensile strength (MPa)	Poisson's ratio	Cohesion (MPa)	Internal friction angle (°)
Sandy clay layer	2.19	9.96	1.25	0.15	1.51	19.0
Medium to coarse crystalline dolomite	35.16	35.43	1.25	0.28	3.86	29.85
Layered argillaceous dolomite	24.78	25.84	0.92	0.25	4.08	29.66
Pebbly quartz sandstone	22.87	17.52	0.67	0.26	5.25	29.52
Phosphate rock	37.96	28.40	0.88	0.3	5.64	30.53
Light gray primary dolomite	39.35	30.19	1.66	0.21	6.05	30.17
Dark gray native dolomite	34.17	26.80	0.72	0.23	5.42	30.32

(a)

(b)

FIGURE 10: Continued.

FIGURE 10: The stress distribution of the excavated rock mass in (a) the first stage, (b) the second stage, (c) the third stage, and (d) the stoping stage.

old roof and the load layer. After the completion of the second stage of excavation, the exposed area of the stope roof further increased. Affected by the mining stress and the weight of the overlying rock, the ore pillars and their boundary ore pillars bear more and more loads [29]. When the ultimate load borne by the ore pillars is reached, the ore pillars will appear to fracture fissures (Figure 10(b)). After the completion of the third excavation stage, the stope at this time collapsed on a large scale, and stress concentration occurred in the boundary pillars on both sides of the stope (Figure 10(c)). In addition, after the end of the pillar stoping stage, the overlying rock strata collapsed in a large area, and its shape was similar to the "elliptical arch" type (Figure 10(d)).

4.4.2. Law of Rock Mass Movement, Deformation, and Failure. In Figure 11, the top and bottom plates of the stope had undergone displacement changes at different stages, and the subsidence of the surrounding rock of the stope roof was significantly greater than the displacement at the bottom plate. As each ore body was mined, the stope floor begun to arch upwards, the roof was bent downwards and sank, and the largest sinking area appeared in the center of the stope. In addition, due to the soft and inclination of the floor of the ore body, during the excavation process, the floor of the ore body was uplifted in the direction of the goaf. The pillars of various stopes and mine rooms had a tendency to break [30]. After the first stage ore body was excavated, the overlying rock of mine room #1 and #2 begun to sink, and the roof center had a downward bending and sinking trend (Figure 11(a)). After the second stage ore body was mined, the deformation of the stope will be further increased. Among them, the deformation and destruction areas of the stope were concentrated in the first stage mine rooms #1, #2, and the second stage (Figure 11(b)). After the three-stage ore body was mined, the maximum deformation area of the stope was concentrated in the second stage ore body, and the

pillars of each stage have different degrees of shear displacement, and the maximum displacement was about −1.2 m (Figure 11(c)). After the mining of the pillar, the overlying rock of the model stope collapsed on a large scale, and the collapse shape was similar to the stress distribution in Figure 10(d), which was "elliptical arch" (Figure 11(d)).

In summary, after each stage of ore body excavation, the maximum subsidence displacement occurred in the central area of the overlying rock, and stress concentration occurred at the pillar and stope boundary, resulting in shear deformation. At the synchronous distance, along the normal direction of the goaf, the farther away from the goaf, the smaller the displacement. In addition, at the same level in the horizontal direction, the displacement above the goaf is much greater than the displacement of the rock above the pillar. With the increase of the exposed roof span, the settlement of the overlying rock on the old roof of the stope also increases. On the other hand, the bulging phenomenon of the floor below the field is also moving forward dynamically. Thus, this phenomenon is consistent with the test results of similar materials [31–33].

4.4.3. Analysis of the Rock Mass Plastic Zone. As shown in Figure 12, after the first stage of mining was completed, the plastic zone mainly occurred near the toe of the open slope, the roof of the goaf, and the topsoil layer (Figure 12(a)). After the second stage of excavation was completed, the scope of the goaf will increase, resulting in a substantial increase in the scope of the stope's plastic zone, causing the production of plastic through the zone, which gradually extends upward into the indirect roof. In addition, with the mining of the mine room, each pillar had yielded. Due to the support of the pillar, the overlying rock had yielded, but the overall stability was basically stable. The reason is that the upper part of the ore body has a huge thick hard rock layer (medium to coarse crystalline dolomite), which has the ability to resist the tensile deformation of the rock body

(a)

(b)

(c)

(d)
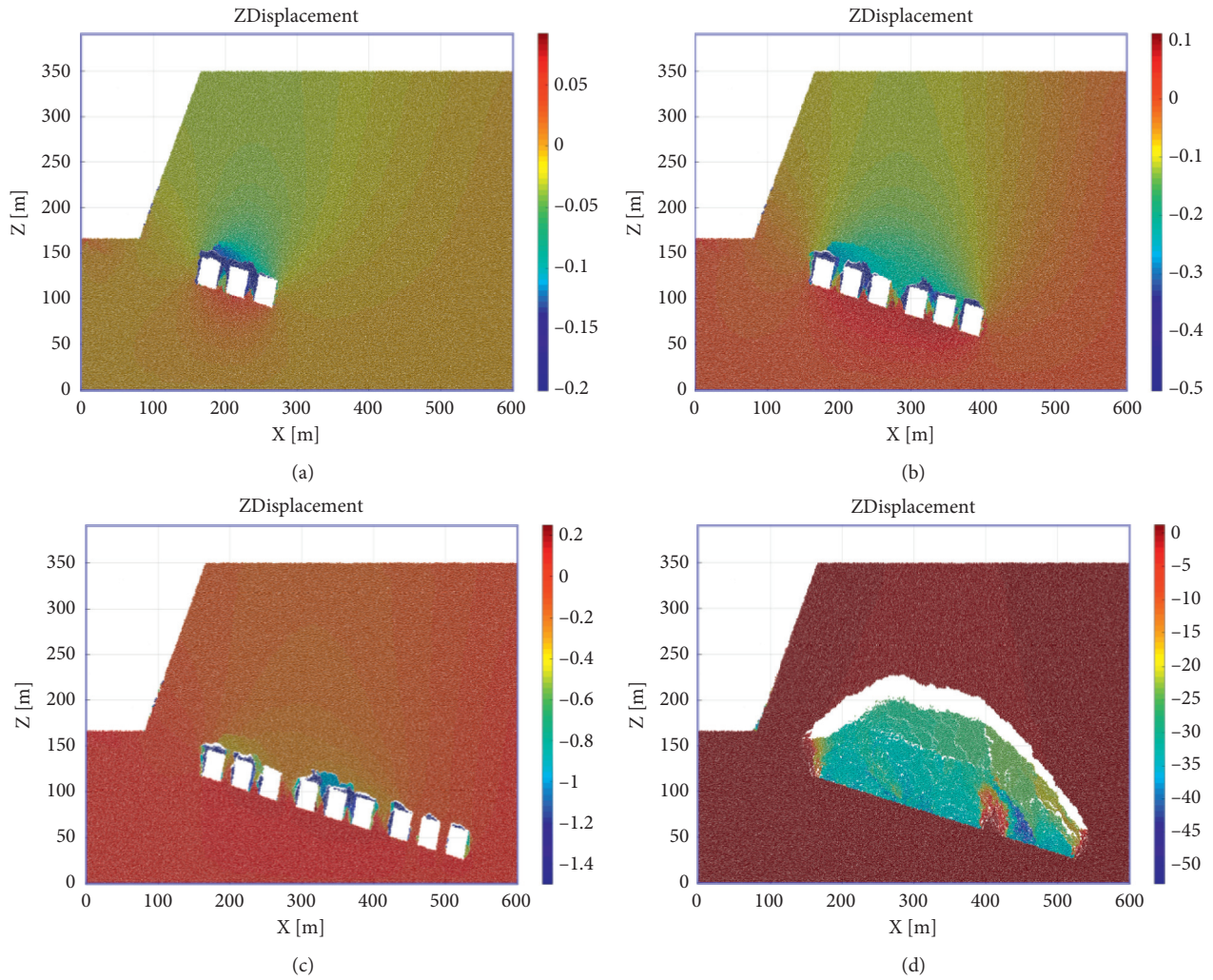
Figure 11: Displacement distribution of excavated rock mass in (a) the first stage, (b) the second stage, (c) the third stage, and (d) the stoping stage.
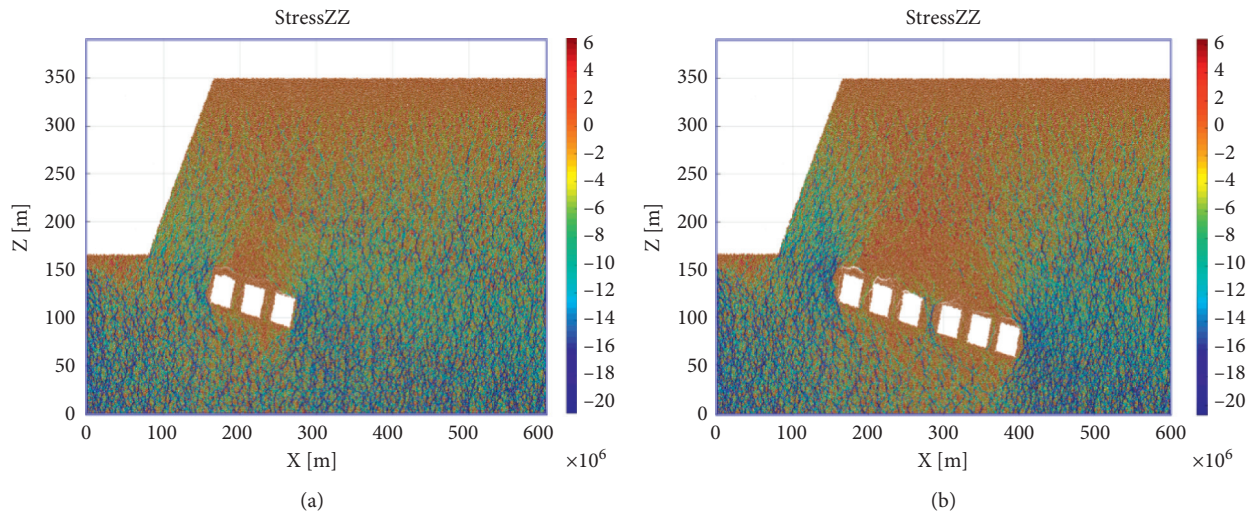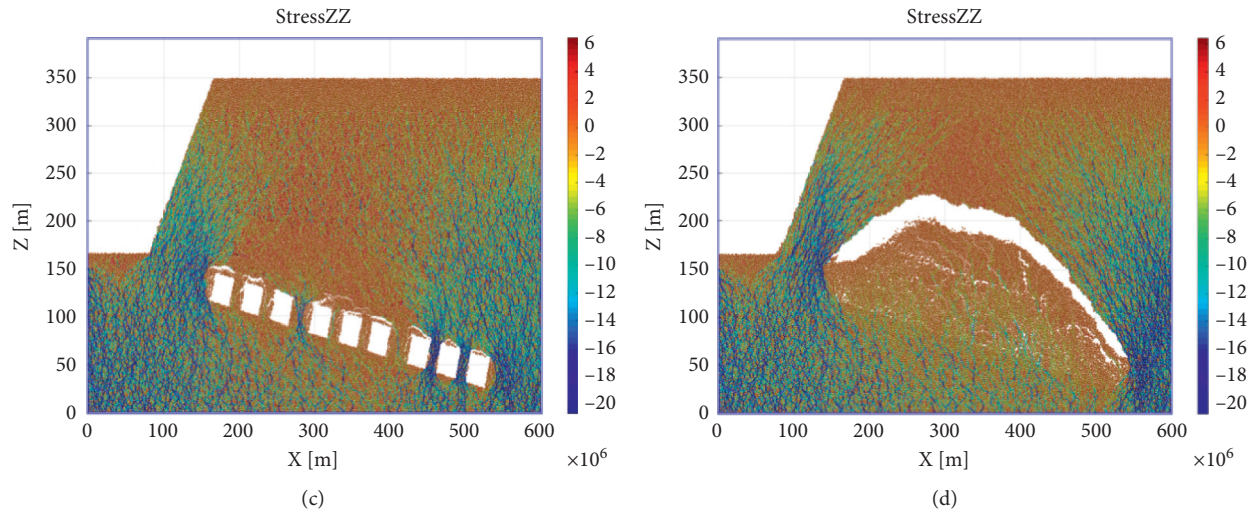

(a)

(b)
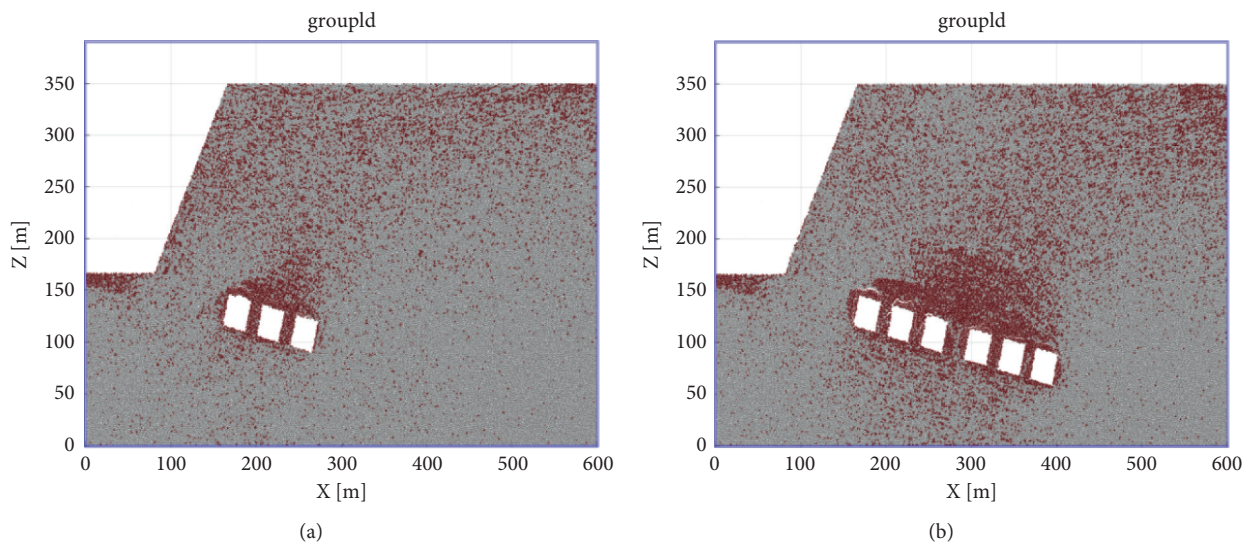
Figure 12: Continued.

(c)

(d)
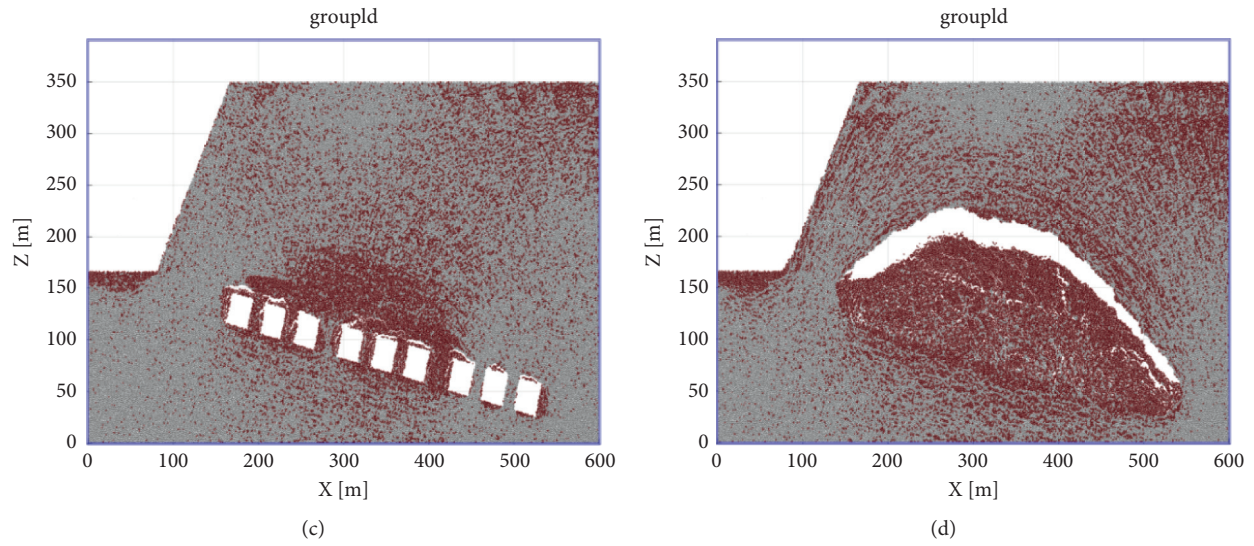
FIGURE 12: The plastic zone of excavated rock mass in (a) the first stage, (b) the second stage, (c) the third stage, and (d) the stoping stage.

(a)

(b)
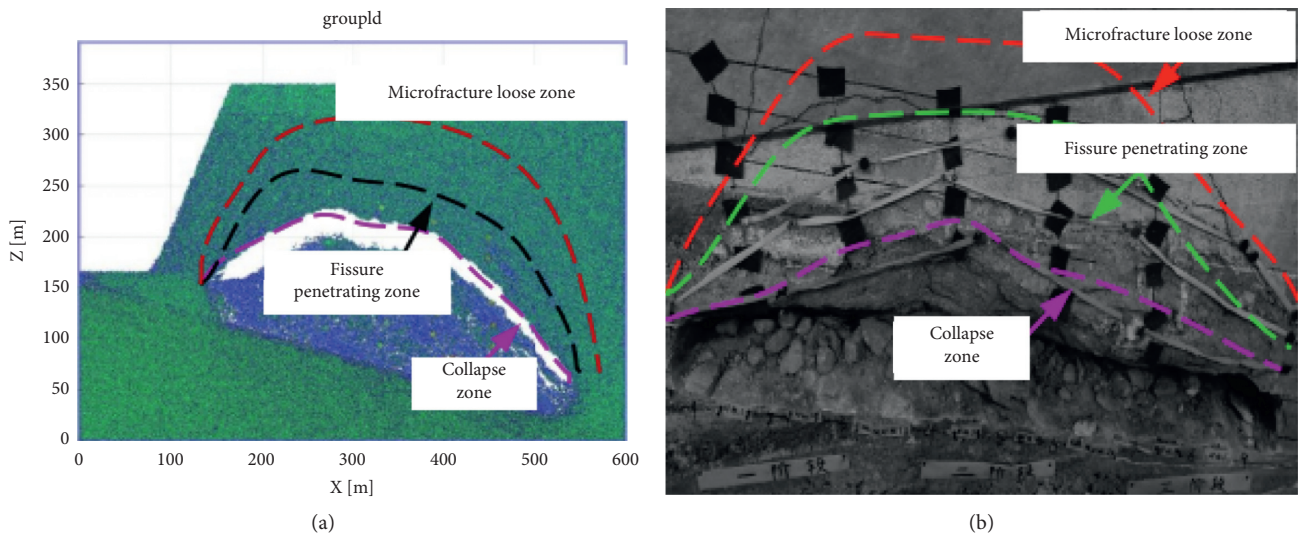
FIGURE 13: Comparison of collapse characteristics between numerical simulation and similar simulation under the slope height of 200 m and slope angle of 65°.

[34–37]. Therefore, the plastic penetration zone of the overlying strata does not form a penetration at the medium to coarse crystalline dolomite layer (Figure 12(b)). After the end of the third stage of mining, the plastic zone of the stope continued to increase, and part of the overlying rock above the pillar collapsed (Figure 12(c)). Finally, when all the pillars were stopped, the plastic zone above the stope was penetrated and the entire stope collapses in a large area. At this time, it can be found that the bottom floor of the stope is uplifted and destroyed (Figure 12(d)).

4.5. Comparison and Analysis with Similar Simulation Experiment Results. Similar model experiments and numerical simulation results show that when the room-pillar method is used to mine gently inclined phosphate ore bodies, the direct roof of the mined-out area collapses, a large number of fissures and separation layers are generated inside the indirect roof, and the rock formation is structurally damaged. In particular, the recovery of the two central pillars caused a sharp increase in the deformation area of the roof. However, due to the presence of medium to coarse-grained dolomite layers (large thickness and high strength) in the overlying rock, the direct roof and the lower part of the indirect roof in the mined-out area have a certain degree of plastic penetration. The upper part of the indirect roof and the overlying rock have no major failure. The linear elastic contact model built in MatDEM software follows Hooke's law and Moore-Coulomb strength criterion, which cannot well reflect the rheological properties of real rock masses. Therefore, the

numerical simulation results are different from similar simulation experiments (Figure 13), but the penetration position of the fissure and the deformation and failure range of the rock mass are basically consistent.

5. Conclusions

In this paper, through engineering geological survey, rock mechanics test, similar material experiment and MatDEM numerical simulation, the deformation and failure law and evolution characteristics of surrounding rock of open-pit converted underground stope were studied systematically. The following conclusions were drawn:

(1) Based on the law of rock mass movement, deformation, and failure, the direction of the underground stope rock layer movement points to the goaf, and the maximum horizontal displacement and vertical displacement appear at the upper boundary of the goaf (gravel-containing quartz sandstone). Along the inclination of the ore body, the farther the horizontal and vertical displacements are from the underground stope, the less the impact of mining stress. On the other hand, along the inclined vertical direction of the ore body, the farther the measuring point is from the stope, the smaller the range of mining influence.

(2) Numerical simulation results show that during the recovery process of the ore body, the rupture of the overlying strata of the stope has an obvious layered structure, with collapse zones, fissure penetrating zones, and microfracture loosen zones appearing from bottom to top. In addition, the movement and destruction of the overlying strata of the entire stope are an "elliptical arch."

(3) The results of similar simulation tests and numerical simulation are basically consistent. Specifically, after the phosphate ore body is converted from open-pit mining to underground mining, the direct roof of the underground stope is destroyed in an "elliptical arch." When the internal stress value of the pressure arch exceeds the ultimate strength of the rock layer, the rock layer will undergo compression failure, shear failure, tensile failure, or combined failure.

Data Availability

The data used to support the findings of this study are included within the article.

Conflicts of Interest

The authors declare that there are no conflicts of interest regarding the publication of this paper.

Acknowledgments

References

[1] Z. G. Agioutantis, "Automated downtime recording and processing for continuous surface mining systems," *International Journal of Surface Mining, Reclamation and Environment*, vol. 8, no. 4, pp. 159–162, 1994.

[2] P. Liu, W. Zhou, Q. X. Cai, X. Shi, and G. Xu, "The thin coal seam (TCS) mining technology for open pit mines in China," *Geotechnical & Geological Engineering*, vol. 36, no. 6, pp. 3627–3637, 2018.

[3] E. Bakhtavar and H. Mahmoudi, "Development of a scenario-based robust model for the optimal truck-shovel allocation in open-pit mining," *Computers & Operations Research*, vol. 115, Article ID 104539, 2020.

[4] J. C. Branco, R. Rebbah, J. Duarte, and J. S. Baptista, "Risk assessment in the open pit mining industry-a short review," *Studies in Systems, Decision and Control*, vol. 202, pp. 13–21, 2019.

[5] S. Singgih, Y. M. Rahman, V. Vega, and S. Herry, "Rock mass classification for sedimentary rock masses in Indonesia coal mining areas," *AIP Conference Proceedings*, vol. 2245, no. 1, pp. 1–15, 2020.

[6] S. Xu, Y. H. Li, L. An, and Y. J. Yang, "Study on high and steep slope stability in condition of underground mining disturbance," *Journal of Mining and Safety Engineering*, vol. 29, no. 6, pp. 888–893, 2012.

[7] Q. H. Li, X. S. Li, J. B. Geng, and L. Luo, "FLAC3D numerical simulation of open-pit transformation to underground slope and stope stability," *Nonferrous Metals*, vol. 73, no. 2, pp. 5–10, 2021.

[8] Z. W. Wang, G. F. Song, and K. Ding, "Study on the ground movement in an open-pit mine in the case of combined surface and underground mining," *Advances in Materials Science & Engineering*, vol. 2020, Article ID 8728653, 13 pages, 2020.

[9] M. James and D. Roussos, "A stochastic optimization formulation for the transition from open pit to underground mining," *Optimization and Engineering*, vol. 18, no. 3, pp. 793–813, 2017.

[10] J. Jakubec, L. Long, T. Nowicki, and D. Dyck, "Underground geotechnical and geological investigations at Ekati Mine-Koala north: case study," *Lithos*, vol. 76, no. 1–4, pp. 347–357, 2005.

[11] E. Bakhtavar and K. Shahriar, "Economical-mathematical analysis of transition from open-pit to underground mining," *International Journal of Rock Mechanics and Mining Sciences*, vol. 52, no. 9, pp. 79–88, 2015.

[12] R. K. Brummer, H. Li, A. Moss, and T. Casten, "The transition from open pit to underground mining: an unusual slope failure mechanism at Palabora," in *Proceedings of the International Symposium on Stability of Rock Slopes in Open Pit Mining and Civil Engineering*, pp. 411–420, Cape Town, Africa, April 2006.

[13] A. Mass, S. Diachenko, and P. Townsend, "Interaction between the block cave and the pit slopes at Palabora mine," *Journal of the South African Institute of Mining and Metallurgy*, vol. 106, no. 7, pp. 479–484, 2006.

[14] C. H. Li, Y. F. Wang, M. F. Cai, S. J. Miao, and L. P. Fan, "Slope deformation model of metal mines transferred underground mining from open-pit based on support vector machines,"

Journal of University of Science and Technology Beijing, vol. 31, no. 8, pp. 945–950, 2009.

[15] Y. M. Zhang, F. S. Ma, J. M. Xu, and H. Zhao, "Deformation laws of rock mass due to transform from open-pit to underground mining in high stress area," *Rock and Soil Mechanics*, vol. 32, no. S1, pp. 590–595, 2011.

[16] W. D. Song, J. X. Fu, and D. X. Wang, "Study on physical and numerical simulation of failure laws of wall rock due to transformation from open-pit to underground mining," *Journal of China Coal Society*, vol. 37, no. 2, pp. 186–191, 2012.

[17] T. B. Jia, "The Dynamic prediction on environment damage induced by the excavation from open-pit into underground mine," *Journal of Safety Science and Technology*, vol. 11, no. 3, pp. 99–104, 2015.

[18] Y. F. Wang, C. H. Li, and F. Cui, "Evolution mechanism of dynamic shock disaster caused by slope instability in transition from open-pit to underground mining," *Mining and Metallurgical Engineering*, vol. 33, no. 5, pp. 13–16, 2013.

[19] R. Wang, S. Yan, and J. B. Bai, "Theoretical analysis of damaged width & instability mechanism of rib pillar in open-pit highwall mining," *Advances in Civil Engineering*, vol. 2019, Article ID 6328702, 15 pages, 2019.

[20] X. S. Li, Y. C. Li, and S. S. Wu, "Experimental investigation into the influences of weathering on the mechanical properties of sedimentary rocks," *Geofluids*, vol. 2020, pp. 1–12, 2020.

[21] X. S. Li, Z. F. Liu, and S. Yang, "Similar physical modeling of roof stress and subsidence in room and pillar mining of a gently inclined medium-thick phosphate rock," *Advances in Civil Engineering*, vol. 2021, Article ID 6686981, 17 pages, 2021.

[22] X. S. Li, S. Yang, Y. M. Wang, W. Nie, and Z. Liu, "Macro-micro response characteristics of surrounding rock and overlying strata towards the transition from open-pit to underground mining," *Geofluids*, vol. 2021, Article ID 5582218, 18 pages, 2021.

[23] X. S. Li, Y. M. Wang, K. Zhao, and S. Yang, "Research progress on the key problems in transition from open-pit to underground mining for metal mines," *Metal Mine*, vol. 2019, no. 12, p. 20, 2019.

[24] N. X. Xu, J. Y. Zhang, H. Tian, G. Mei, and Q. Ge, "Discrete element modeling of strata and surface movement induced by mining under open-pit final slope," *International Journal of Rock Mechanics and Mining Sciences*, vol. 88, pp. 61–76, 2016.

[25] Y. Zhao, T. H. Yang, M. Bohnhoff et al., "Study of the rock mass failure process and mechanisms during the transformation from open-pit to underground mining based on microseismic monitoring," *Rock Mechanics and Rock Engineering*, vol. 51, no. 5, pp. 1473–1493, 2018.

[26] X. S. Li, J. B. Geng, Q. H. Li, W. Tian, and T. Zhou, "Behaviors and overlying strata failure law for underground filling of a gently inclined medium-thick phosphate deposit," *Advances in Civil Engineering*, vol. 2021, Article ID 3275525, 17 pages, 2021.

[27] X. S. Li, Y. M. Wang, S. Yang, J. Xiong, and K. Zhao, "Research progress in the mining technology of the slowly inclined, thin to medium thick phosphate rock transition from open-pit to underground mine," *Applied Mathematics and Nonlinear Sciences*, vol. 6, no. 1, pp. 319–334, 2021.

[28] X. S. Li, Y. M Wang, and K. Zhao, "Study on the law of ground pressure obliquity effect with gently inclined thin to medium thickness phosphate body from open-pit to underground," *Solid State Technology*, vol. 63, no. 4, pp. 6773–6781, 2020.

[29] A. K. Mohammad and M. Ali, "Slope stability analysis of sarcheshmeh copper mine west wall under seismic loads," *Geotechnical & Geological Engineering*, vol. 37, no. 4, pp. 3141–3155, 2019.

[30] S. Vongpaisal, G. Li, and R. Pakalnis, "New development of expert system module for a decision-making on mine stope stability in underground blasthole mining operations," *International Journal of Mining, Reclamation and Environment*, vol. 25, no. 1, pp. 41–51, 2011.

[31] K. Zhao, X. Yu, S. J. Gu et al., "Stability of stope structure under different mining methods," *Journal of Vibroengineering*, vol. 21, no. 7, pp. 1945–1960, 2019.

[32] S. L. Ren, Z. G. Tao, M. C. He, S. H. Pang, M. N. Li, and H. T. Xu, "Stability analysis of open-pit gold mine slopes and optimization of mining scheme in inner Mongolia, China," *Journal of Mountain Science*, vol. 17, no. 12, pp. 2997–3011, 2020.

[33] X. S. Li, K. Peng, J. Peng, and D. Hou, "Effect of thermal damage on mechanical behavior of a fine-grained sandstone," *Arabian Journal of Geosciences*, vol. 14, p. 1212, 2021.

[34] M. Li, J. X. Zhang, G. H. Meng, Y. Gao, and A. Li, "Testing and modelling creep compression of waste rocks for backfill with different lithologies," *International Journal of Rock Mechanics and Mining Sciences*, vol. 125, Article ID 104170, 2020.

[35] M. Li, A. L. Li, J. X. Zhang, Y. Huang, and J. Li, "Effects of particle sizes on compressive deformation and particle breakage of gangue used for coal mine goaf backfill," *Powder Technology*, vol. 360, pp. 493–502, 2019.

[36] M. Li, J. X. Zhang, A. L. Li, and N. Zhou, "Reutilisation of coal gangue and fly ash as underground backfill materials for surface subsidence control," *Journal of Cleaner Production*, vol. 254, Article ID 120113, 2020.

[37] X. S. Li, Y. M. Wang, and K. Zhao, "Research on deformation and failure character of underground surrounding rock and overlying strata transition from open-pit to underground mining," *Solid State Technology*, vol. 63, no. 4, pp. 6732–6757, 2020.

Research Article

Sustainable Development of Tourism under the Background of Low-Carbon and Green Economy

Lirong Han[1] and Lei Li [ID] [2]

[1]*Tourism Management and Geographical Science College, Hulunbeier College, Hulunbeier 021000, Inner Mongolia, China*
[2]*College of Tourism, Xinyang Normal University, Xinyang 464000, Henan, China*

Correspondence should be addressed to Lei Li; stanley9065@126.com

The development of tourism industry not only promotes social and economic progress and the improvement of people's happiness index but also causes resource damage and environmental pollution, which not only affects our living environment but also directly threatens the survival and development of mankind. Therefore, how tourism will develop in the context of low-carbon green economy has become the main problem of tourism development. Based on the above background, in order to solve the development problem of tourism in the future under the low-carbon green economy, based on the research results at home and abroad, starting from the starting point of sustainable development of tourism, this paper introduces the concept of "tourism consumption separation rate" and uses Kaya traditional accounting method. The structural decomposition analysis method and cointegration relationship test method are used to calculate, analyze, and test the tourism carbon emissions and influencing factors at the overall level of China and the middle, western, and eastern regions. Through this method, the accuracy of the calculation results is improved by 30%, which increases the accuracy of the experimental data and is more practical.

1. Introduction

With the continuous development of human society and economy, the actual problems caused by carbon emissions to people all over the world are gradually increasing. The frequent occurrence of extreme weather and natural disasters caused by carbon emissions has brought great losses to the survival and life of people all over the world, as well as the shortage of energy supply. China's economic development is very dependent on energy. The extensive use of primary energy will eventually lead to insufficient energy supply and an energy crisis, which will affect China's economic and social development. Sustainable environmental development will be challenged. Extensive economic growth mode has destroyed forests and caused serious air pollution. Therefore, to find out the key factors affecting China's carbon emissions is an inevitable choice for China's social and economic sustainable development, it is of theoretical and practical significance to study the carbon emission

factor and its mechanism. Therefore, how to reduce the impact of human activities on global climate change has become an important task to achieve sustainable development in the future.

Due to the importance of low-carbon and green economy to the future development strategy of tourism, many research teams have begun to study this and achieved good results. For example, tourism is one of the sources of carbon dioxide emissions, and tourism activities will cause pressure on the ecological environment. Zha et al. research constructs the evaluation framework of tourism direct and indirect carbon dioxide emissions and puts the carbon dioxide emission factors into the efficiency evaluation framework based on the SBM bad model. On this basis, taking Hubei Province as an example, this paper evaluates the tourism carbon dioxide emission as a case study, measures the development efficiency and dynamic fluctuation of the low-carbon tourism economy in various cities from 2007 to 2013, and makes analysis [1]. Wu et al. pointed out that the

calculation of tourism carbon dioxide emissions is a pre-requisite for the formulation of energy-saving emission reduction targets in some regions of our country, and it is essential for the sustainable development of tourism in certain regions [2]. Shuxin w established a new method to analyze the characteristics and influencing factors of EETT in China from 1994 to 2013. Shuxin w found that the CO_2 emission per unit person time (CETTU) increased from 26.07 kg in 1994 to 14.01 kg in 2013. The decline of energy intensity, scale effect, and policy promotion is the key factor affecting energy consumption. Although the research results are relatively rich, there are still many deficiencies, which are mainly reflected in the fact that the above research results are more focused on a certain aspect of research and are not systematic and comprehensive [2].

In the calculation and research of tourism carbon di-oxide emissions, tourism consumption stripping coefficient and Kaya traditional accounting method are good methods, which can solve the problem of large deviation in the cal-culation data of tourism carbon emissions in the past. Therefore, it is used in the calculation and analysis of tourism carbon dioxide emissions in China. The calculation of tourism carbon dioxide emissions is the premise of formulating energy conservation and emission reduction targets in some regions of China. It is also important for the sustainable development of tourism in some areas. Based on the concept of "tourism consumption stripping coefficient," Wu et al. proposed the calculation method of tourism emissions in Beijing, Shandong, Zhejiang, Hubei, and Hainan. The results show that, from 2009 to 2011, the total tourism emissions of the five provinces and cities increased continuously, and the per capita tourism emissions de-creased from 56.569 kg to 54.088 kg. During this period, Hainan's tourism emissions are still the lowest. Hubei's tourism emissions soared from the third place in 2009 to the first in 2011. Beijing is the only downward trend that has not been disturbed. Hainan has the lowest total emissions, but the highest per capita emissions. Only Beijing and Hainan's per capita emissions continued to decline in 2009 and 2011 [3]. The emission of the tourism industry in Zhejiang Province shows an inverted U-shaped trend, while that of Shandong and Hubei Province shows a U-shaped trend. In the future, China should promote energy conservation and emission reduction by formulating action programs, inno-vating energy-saving technologies, strengthening environ-mental awareness, and developing regional tourism cooperation.

In order to solve the future development of tourism in the low-carbon green economy, this paper introduces the separation rate of tourism consumption and takes Kaya traditional accounting method as the first step, structural decomposition analysis method as the second step, and cointegration relationship test method as the third step to establish an analysis model to study how to develop a low-carbon economy and low-carbon tourism in response to global climate change, so as to achieve the goal of saving energy. Under the common requirement of environmental responsibility, we are actively promoting the construction of a green economy and the development of low-carbon tourism and exploring the future route of low-carbon tourism, which is also one of the hotspots of future research [4, 5]. How to develop tourism in the future is a com-prehensive problem, including the transformation of social, economic, resource, and environmental values. There is little research on carbon tourism in China. At present, low-carbon tourism is only at the level of theoretical discussion and strategic positioning. Based on the classification of relevant research results at home and abroad, according to the relevant theories, such as the theory of sustainable development and the stripping coefficient of tourism consumption, this paper makes an in-depth and multi-faceted evaluation and empirical analysis on the carbon dioxide emissions of tourism cities. The research results have certain practical significance and guiding practical value.

Sustainable development can protect the ecological environment and is a key issue that needs to be considered in the development of tourism.

2. Sustainable Development Strategy of Tourism under Low-Carbon and Green Economy

2.1. Tourism Consumption Separation Rate. It means "sep-aration rate of tourist consumption" [6–8]. It is the added value of tourist consumption deducted from tourism related industries. The original intention is to refer to the percentage of tourism consumption in the added value provided by service sectors including tourism consumption. As the products of tourism industry only account for a part of the products of tourism consumption, it is necessary to deduct a certain proportion of its growth value. The idea of calcu-lating this ratio is to convert the total value of market production, supply, transportation, and other industries into total tourism income with added value according to the percentage of the added value of tourism related industries and calculate the passenger consumption separation rate based on industry value-added words [9–11].

According to this calculation method, the calculation formula is set as follows:

$$E_N = \frac{V_N}{C_N}. \tag{1}$$

In formula (1), E_N represents the separation rate of tourism consumption of n industry, V_N represents the growth number of n industry; and C_N represents the tourism growth number of n industry, multiplying the growth rate of n industry by the tourism revenue of n industry, where the growth rate of n industry is the ratio of the growth number of n industry to the total revenue of n industry [12, 13].

2.2. Kaya Traditional Accounting Method. In order to clarify the contribution efficiency of China's overall and regional tourism carbon emission influencing factors, this paper adopts the Kaya traditional accounting method, namely, Kaya's accounting identity, which is used to analyze the key

factors affecting the change of national carbon emissions [14, 15].

The expression is as follows:

$$C = \frac{C}{R} \times \frac{R}{\text{GDP}} \times \frac{\text{GDP}}{\text{POP}} \times \text{POP}. \tag{2}$$

In formula (2), W is carbon emission, R is energy consumption, GDP is GDP, and pop is household population (100 million). W/R is the energy structure, representing the carbon emissions per unit of energy consumption; w/GDP is the energy intensity, representing the energy consumption per unit of GDP; and GDP/Pop is the per capita GDP [16].

2.3. Structural Decomposition Analysis Method.

The method of structural decomposition analysis (IDA) is used to analyze the changes of energy intensity, structure, economic scale, and industrial structure of national and cross-city structures based on industry data [17, 18]. In a word, IDA methods can be divided into two types: Divisia exponential decomposition analysis (Dida) and Laspeyres exponential decomposition analysis (Lida). This method can be divided into two types: arithmetic mean divisor index (AMDI) and logarithmic average divisor index (LMDI). The former model was weighted by arithmetic mean. The deduction process is relatively easy, but the residual value is too large to be calculated when the value is zero [19, 20]. The latter model uses logarithms instead of arithmetic based on the weight ratio and performs zeroing using analysis constraints. Avoid situations that cannot be calculated.

2.4. Cointegration Test Method.

It is necessary to investigate whether there is a stable long-term relationship between various influencing factors before empirical research is carried out to ensure that the database is more stable. Therefore, it is inevitable to use the cointegration relationship test method to verify the periodic time series data. Whether there is a stable long-term relationship [21]. At present, there are two common cointegration testing methods: one Engle Granger (EG), mainly based on the stationarity test of regression residuals, followed by the j-j test.

Johansen Juselius mainly uses vector autoregression and VaR to verify the cointegration relationship. Before conducting an empirical study on the overall level and responsible regions of the influencing factors of carbon emissions in tourism industry, this paper examines whether there is a long-term cointegration relationship between the influencing factors on the basis of the JJ likelihood ratio test. In order to ensure that individual factors are taken into account, it is meaningful to analyze the decomposition of the influencing factors later [22, 23].

The expression of the j-j likelihood ratio test is as follows:

$$T_Y = \alpha + \prod_1 q_{t-1} + \cdots + \prod_k y_{k-1} + \mu = \alpha + \sum_{j=1}^{k} \prod_j y_{t-j} + \mu_t. \tag{3}$$

However, the best method to analyze the fragmentation of index has not been established. Among the many IDA methods mentioned above, this article analyzed the theoretical basis, applicability, and functionality of the index decomposition analysis (IDA) in the existing literature and pointed out that the log average degradation index (IDA) LMDI method can eliminate the residual duration, so it is more applicable [24, 25].

3. Research Design

3.1. Accounting Scope of Tourism Carbon Emission.

Tourism industry has the characteristics of a long industrial chain and high business relationship, which leads to the complexity and diversity of energy consumption and carbon dioxide emission measurement indicators. In addition, due to the lack of tourism statistics and the unclear definition of the scope of tourism carbon emission accounting, the measurement of tourism energy consumption and carbon emission has become a recognized problem. Before calculating the carbon dioxide emissions of tourism, it is necessary to determine the accounting scope of carbon dioxide emissions of tourism. Although China has incorporated the tourism industry into the carbon emission system, the five links of "eating, traveling, shopping, and entertainment" in the tourism industry have not been directly reflected. If the carbon emission of tourism is calculated according to this statistical classification, it is actually only a part of the carbon emission in the accommodation process of tourism and tourism service industry, resulting in the formation of "quantity leakage," because other situations are not taken into account. Therefore, domestic researchers believe that the statistical coverage of tourism should include economy, catering, communication and transportation, post and telecommunications, and social services, as well as accommodation and catering industry. They should be put forward independently of each other. Tourism revenue and tourism added value are considered from six aspects of transportation, post and telecommunications, trade, catering and accommodation, and social services.

3.2. Carbon Emission Research Design.

In this paper, the "separation rate of tourism consumption" is used to calculate the "separation rate of tourism consumption," and the energy consumption of tourism industry is separated from tourism related industries.

The calculation formula of "tourism consumption separation rate" and the proportion of energy consumption in tourism related industries are as follows:

$$\text{TVN}_K \equiv \text{TE}_K \times \text{VAE}_K = \text{TE}_K \times \frac{\text{VN}_K}{\text{TPV}_K}. \tag{4}$$

In formula (4), TVN_K is the tourism growth value of tourism related industry K, TE_K is the tourism revenue of tourism related industry K, WAE_K is the growth value of tourism related industry K, TE_K is the growth value of tourism related industry K, and WAE_K is the total revenue of tourism related industry K, where $k = 1, 2, 3, 4$ represent "transport, "transport, and post and telecommunications," "wholesale and retail," "catering and accommodation," and "social service industry."

Based on the statistics of energy consumption of tourism related industries, this paper investigates and calculates the overall level of carbon emission of tourism industry in eastern, central, and western regions of China in accordance with the "reference method" proposed in IPCC "guidelines for greenhouse gas emission inventory." The expression is as follows:

$$k^e = \sum_q k_q^e = \sum_j k_j^e = \sum_j k_{jq}^e = \sum_j \text{DR}_{jqv}^e \times \beta_v. \quad (5)$$

In formula (5), k^e is China's overall tourism carbon emission in e year; k_q^e is tourism carbon emission in q region in e year; k_j^e is tourism carbon emission in e year of J province; k_{jq}^e is tourism carbon emission of tourism related industry q in e year of j province; DR_{jqv}^e is energy consumption of tourism related industry q in e year of J province; and β_v is carbon emission coefficient of energy source v. Among them, $e = 1, 2, 3$ denote eastern, central, and western and $v = 1, 2, 3, \ldots$.

4. Analysis of Simulation Results of Tourism Carbon Emissions in China

4.1. Carbon Emission Algorithm Analysis. According to the calculation formulas (1) and (2) and based on the research data of added value and total revenue of tourism related industries, this paper calculates the transport; post and telecommunications; wholesale and retail; and the east, central, and western regions of China from 2010 to 2019. The "tourism consumption stripping coefficient" of the four tourism related sectors of social services is shown in Table 1. On the basis of calculating the "tourism consumption stripping coefficient" of each industry, according to the calculation formulas (4) and (5) and the energy consumption data of tourism related industries, we can separately calculate the overall level of China and its eastern, central, and western tourism carbon emissions, as shown in Table 1.

As shown in Figure 1, in terms of regions, in the past 10 years, the tourism carbon emission intensity of the industries in the west, the middle, and the east is limited by the energy utilization efficiency, energy consumption composition, management efficiency level, policy regulation environment, and energy conservation and emission reduction technology, which shows a different numerical distribution. On the whole, however, the intensity of tourism carbon emission in the west, middle, and east always shows "catering and acceptance > transport, post, and telecommunications > wholesale and retail > social service industry."

4.2. Analysis on the Results of China's Tourism Carbon Emissions. As shown in Figure 2 and Table 2, the measurement results of tourism carbon emissions of China as a whole and its eastern, central, and western regions show that there are two significant characteristics of China's tourism carbon emissions from 2010 to 2019: (1) the tourism carbon emissions show an upward trend year by year, but the rising range gradually tends to be gentle. In terms of increase, China's overall tourism carbon emissions increased from 48.9114 million tons in 2010 to 198.646 million tons in 2019, an increase of 149734600 tons. From the perspective of the increase rate, the annual growth rate of China's overall tourism carbon emissions increased from 13.56% in 2011 to 17.95% in 2019, an increase of 4.39%. The difference of the rising range of tourism carbon emissions is relatively large. In terms of regions, the carbon emissions of tourism in the east, central, and western regions increased from 37.2162 million tons, 8.142 million tons, and 10.6621 million tons in 2010 to 118.6715 million tons, 63.2364 million tons, and 67.8244 million tons in 2019.

Note: since the tourism carbon emissions in 2010 are taken as the base period data, the annual growth rate of tourism carbon emissions in 2010 is set as 0.

Among them, the carbon emissions of tourism in the central and western regions increased fastest and the growth rate was about 5 times. This shows that although the carbon emissions in the central and western regions are lower than those in the east, the growth rate of carbon emissions caused by the rapid development of tourism industry is obviously higher than that in the east, as shown in Figure 2. However, affected by the factors of regional economic level, tourism carbon emissions in different regions are different. There are also differences in the rebound range of the two-year growth rate. In the more developed eastern region, the rebound amplitude is small and the rebound growth rate is only 6.39%. In the underdeveloped central and western regions, the rebound amplitude is relatively large, and the rebound growth rate reaches 8.24% and 10.37%, as shown in Table 2.

As shown in Table 3 and Figure 3, during the 10 years from 2010 to 2019, China's overall carbon emissions from transport, post, and telecommunications; wholesale and retail; catering and accommodation; and social services show a gradual growth trend. From 48.911 million tons, 10.662 million tons, 8.1422 million tons, and 37.216 million tons in 2010, they will increase to 198.646 million tons, 67.824 million tons, 63.236 million tons, and 118.677 million tons in 2019, with an increase of 306.13%, 536.12%, 676.64%, and 218.88%, respectively.

With 2016 as the change node, tourism carbon emissions of China's overall industries show a transformation from "low and median area" (2010–2015) to "high-value area" (2015–2019), as shown in Figure 3. In the above transformation, the increase rate of tourism carbon emissions of wholesale and retail is significantly higher than that of other industries. Tourism carbon emissions due to wholesale and retail have jumped from the fourth place in 2010 to the second in 2019, and from the "low-value area" of 8.142 million tons in 2010 to the "high-value area" (31.8091 million tons, 2019), as shown in Table 3. Although the carbon

TABLE 1: Stripping coefficient of tourism consumption in China and its regional industries from 2010 to 2019.

Industry	Year									
	2010	2011	2012	2013	2014	2015	2016	2017	2018	2019
Transportation, post, and telecommunications	0.21	0.21	0.45	0.46	0.12	0.32	0.3	0.3	0.73	0.12
Wholesale and retail	0.21	0.26	0.21	0.31	0.36	0.32	0.65	0.12	0.13	0.56
Catering and accommodation	0.35	0.36	0.46	0.44	0.46	0.2	0.12	0.3	0.44	0.62
Social services	0.16	0.05	0.22	0.21	0.05	0.37	0.32	0.58	0.33	0.32
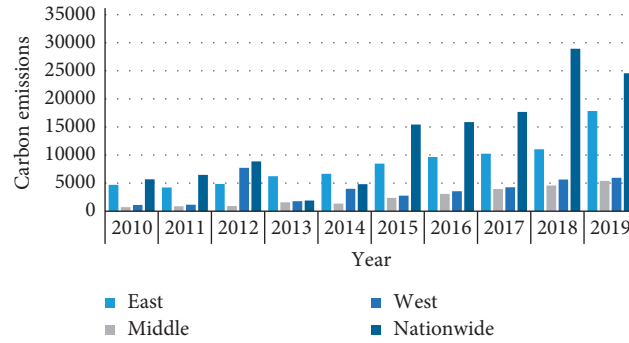
FIGURE 1: Tourism carbon emissions.
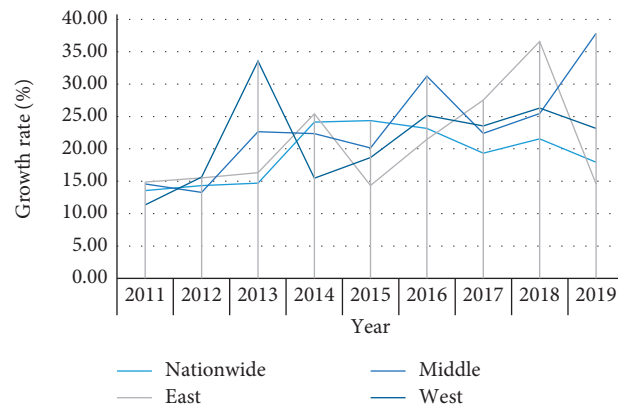
FIGURE 2: Annual growth rate of China's overall and regional tourism carbon emissions from 2010 to 2019.

TABLE 2: Annual growth rate of China's overall and regional tourism carbon emissions from 2010 to 2019.

Content	Year								
	2011 (%)	2012 (%)	2013 (%)	2014 (%)	2015 (%)	2016 (%)	2017 (%)	2018 (%)	2019 (%)
Nationwide	13.56	14.33	14.69	24.16	24.37	23.17	19.32	21.54	17.95
East	14.87	15.50	16.31	25.43	14.35	21.45	27.54	36.58	14.58
Middle	14.58	13.28	22.64	22.34	20.15	31.24	22.38	25.46	37.84
West	11.35	15.64	33.56	15.48	18.65	25.16	23.54	26.31	23.15

TABLE 3: Carbon emissions by industry.

Content	Year									
	2010	2011	2012	2013	2014	2015	2016	2017	2018	2019
Transport	3721.62	3978.5	4823.3	6325.3	5921.44	8288.79	9268.4	10395.6	11087.4	11867.7
Wholesale	814.22	893.16	983.85	1510.6	1765.21	2277.91	3180.9	3948.4	4909.45	6323.64
Catering	1066.21	1366.1	1407.3	1833.6	2194.43	2909.54	4018.4	4268.2	5104.86	6782.44
Social service	4891.14	6327.6	6931.1	9462.5	11342.3	13476.2	15857.	17582.2	21541.8	19864.6
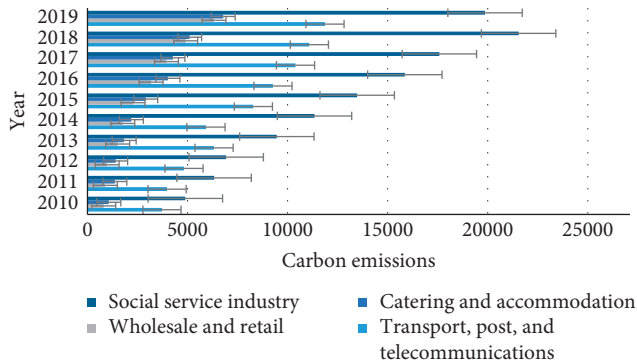
FIGURE 3: Analysis and comparison of carbon emission of China's overall and regional tourism growth rate from 2010 to 2019.

emission of tourism in the wholesale and retail industry is still lower than that of transport, post, and telecommunications, its rising value is obviously higher than that of transport, post, and telecommunications. This shows that when meeting the basic demand of tourism, the tourism motivation of tourists changes, which makes wholesale and retail tourism carbon emissions second only to transport. Another major source of tourism carbon emissions is post and telecommunications, catering, and accommodation, which is expected to exceed the level of tourism carbon emission caused by "food," "housing," and "transportation" in a certain period in the future.

The purpose of the research and analysis of tourism carbon emissions is to understand the current situation of tourism carbon emissions in China as a whole, regions, and industries. To analyze the intensity of tourism carbon emissions is to understand the contribution efficiency of tourism carbon emissions of provinces, cities, and industries. However, the research on the relationship between tourism economic growth and tourism carbon emissions is rare. Existing studies have pointed out that there is a correlation between energy consumption or carbon emissions and economic growth; that is, they are synchronized. This makes how to block the relationship between economic growth and resource consumption and environmental pollution become an important issue in today's academic research. Therefore, to clarify the relationship between tourism economic growth and tourism carbon emissions plays an important role in the realization of low-carbon tourism development under the premise of economic growth. In this context, this paper uses the index decomposition analysis method and cointegration relationship test method to analyze the correlation between China's overall level and its regional tourism carbon emissions.

As shown in Figure 4, combined with the data of the total amount of tourism carbon emissions and the growth rate of the eastern, central, and western industries, the three regions draw the following conclusions and suggestions: (1) the eastern region should focus on wholesale and retail businesses, with social services as the second choice; (2) make transportation, catering, and accommodation the first choice, and social service industry should be the third choice object.
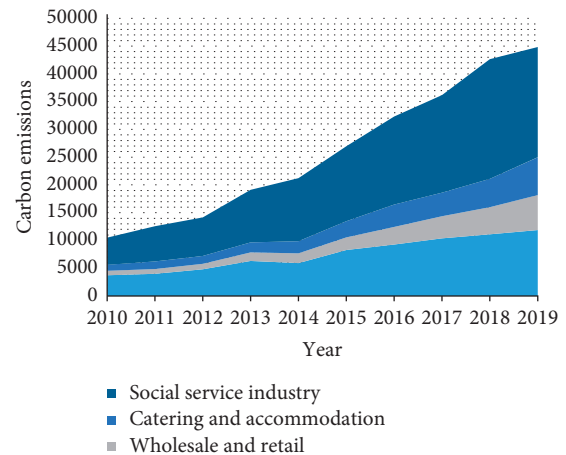
FIGURE 4: Carbon emissions by industry.

The total carbon emissions (including direct and indirect) of China's tourism industry in the research years (2013, 2014, 2015, and 2016) were 140.26 million tons, 135.89 million tons, 148.93 million tons, and 16.978.47 million tons, respectively, accounting for 4.64%, 3.95%, 2.84%, and 2.71% of the total carbon emissions of all industries in China. It accounts for 4.11%, 3.50%, 2.54%, and 2.44% of China's total carbon emissions (including carbon emissions from domestic consumption). In the research year, the proportion of direct carbon emissions, indirect carbon emissions, and total carbon emissions of China's tourism industry in the total carbon emissions of all industries in China and the proportion of China's total carbon emissions (including the carbon emissions of living consumption) decreased in turn. (3) In the study years (2013, 2014, 2015, and 2016), the direct carbon emissions from tourism transportation were the largest, which were 49.9257 million tons, 42.2538 million tons, 36.8809 million tons, and 50.01427 million tons, accounting for 74%, 76%, 67%, and 68% of the total direct emissions of tourism industry. The second is commodity sales, catering, and accommodation. The proportion of tourism, entertainment, post and telecommunications, and other services is small, and the total emissions are also less. Take the tourism departments in 2007 as an example, 68% of transportation, 2% of sightseeing, 6% of accommodation, 6% of catering, 11% of commodity sales, 1% of entertainment, 1% of posts and telecommunications, and 5% of other services. In the study year, the direct carbon emissions of the tourism sector showed a trend of first rising and then decreasing, especially in the tourism transportation sector. In the research years (2013, 2014, 2015, and 2016), the indirect carbon emissions from tourism transportation were the largest, accounting for 39%, 43%, 40%, and 38% of the total indirect carbon emissions of tourism industry, which were 28.5328 million tons, 34.7507 million tons, 37.4926 million tons, and 37.04 million tons, respectively. However, compared with the percentage of direct carbon emissions from tourism transportation, these ratios are relatively small and have a large drop. The second is commodity sales, catering, accommodation, and other services, while the proportion of sightseeing, entertainment, post, and telecommunications is

small. Take the tourism departments in 2010 as an example, the traffic, sightseeing, accommodation, catering, commodity sales, entertainment, posts, telecommunications, and other services were 38%, 6%, 11%, 12%, 16%, 3%, 1%, and 13%, respectively. In the study year, the overall carbon emissions of various sectors of the tourism industry showed an upward trend, while the local changes in various sectors. The direct carbon emission of the tourism transportation sector is higher than indirect carbon emission, while the indirect carbon emission of other tourism sectors is far higher than direct carbon emission. In particular, direct carbon emissions from tourism and entertainment account for only 20% of the total carbon emissions. Besides the ministry of tourism and transportation, the indirect carbon emissions of other tourism sectors are 3 to 4 times their direct carbon emissions. Therefore, the carbon emissions generated by other tourism sectors should also be paid attention to, because it is very important for the path analysis of carbon emission reduction and the formulation of carbon emission reduction policies. Although the direct carbon emission of tourism transportation is large, its relative indirect carbon emission is not as large as that of other tourism sectors.

5. Conclusion

For the total amount of tourism carbon emissions, annual growth has become the development trend, high east and low west has become the normal development. During the 10 years from 2010 to 2019, China's overall and regional tourism carbon emissions show an upward trend year by year, and the growth rate of central and western regions is significantly higher than that of the eastern region; in this upward trend, the tourism carbon emissions and the ability of tourism development to resist the crisis cycle are significant and show a "postcrisis rebound" effect after the end of the crisis to achieve compensatory growth in carbon emissions. In terms of tourism carbon emission intensity, decreasing year by year has become the development trend, and high in the west and low in the east has become the normal development. China's tourism carbon emission intensity is decreasing year by year in time and is high in the west and low in the east in space.

Therefore, combined with the trend chart of tourism carbon emission at the overall and regional level of China, China should take "enhancing the intensity of tourism carbon emission and reducing the total amount of tourism carbon emission" as the action guideline in the process of reducing tourism carbon emission, that is, on the premise of promoting the continuous growth of tourism income at the overall level and the regional level of China. To achieve the continuous reduction of tourism carbon emissions, complete the sustainable development of tourism under the green and low-carbon economy. As for the theme of "strategic research on sustainable development of tourism industry under the background of low-carbon and green economy," due to the restriction of the author's level and practical experience, there are the following research deficiencies and areas that need to be further improved in the future.

The research on the development strategy of tourism under the green and low-carbon economy is a systematic project, which needs to be based on the theories of tourism, geography, ecology, psychology, and economics. At present, the low-carbon concepts such as the low-carbon economy and low-carbon tourism are still in the research stage, and there is no unified theoretical framework The research is less and needs to be further improved. We explained, in this paper, the concept of sustainable development and the development of low-carbon tourism research ideas, combined with the concept of low-carbon economy to supplement and improve. However, under the green and low-carbon economy, the development of tourism strategy is a comprehensive process, and the selection of the index system needs to be further supplemented and improved. With further research in the future, the development of tourism is more in line with the requirements of the low-carbon concept and sustainable development concept and more suitable for practical application.

Data Availability

The data that support the findings of this study are available from the corresponding author upon reasonable request.

Conflicts of Interest

The authors declare that they have no conflicts of interest.

Acknowledgments

References

[1] J. Zha, L. He, Y. Liu, and Y. Shao, "Evaluation on development efficiency of low-carbon tourism economy: a case study of Hubei province, China," *Socio-Economic Planning Sciences*, vol. 66, pp. 47–57, 2019.

[2] P. Wu, Y. Han, and M. Tian, "The measurement and comparative study of carbon dioxide emissions from tourism in typical provinces in China," *Acta Ecologica Sinica*, vol. 35, no. 6, pp. 184–190, 2015.

[3] G. Wu, W. Pedrycz, H. Li, M. Ma, and J. Liu, "Coordinated planning of heterogeneous earth observation resources," *IEEE Transactions on Systems, Man, and Cybernetics: Systems*, vol. 46, no. 1, pp. 109–125, 2017.

[4] R. Li, L. Chen, T. Yuan, and C. Li, "Optimal dispatch of zero-carbon-emission micro energy internet integrated with non-supplementary fired compressed air energy storage system," *Journal of Modern Power Systems and Clean Energy*, vol. 4, no. 4, pp. 566–580, 2016.

[5] L. Qiong, "An index evaluation for planning modern industrial cities: the low carbon concept," *Open House International*, vol. 42, no. 3, pp. 15–19, 2017.

[6] H. Toyoda, T. Kumada, T. Tada et al., "Risk factors of hepatocellular carcinoma development in non-cirrhotic patients with sustained virologic response for chronic hepatitis C virus

infection," *Journal of Gastroenterology and Hepatology*, vol. 30, no. 7, pp. 1183–1189, 2015.

[7] A. J. Venables, "Using natural resources for development: why has it proven so difficult?" *The Journal of Economic Perspectives*, vol. 30, no. 1, pp. 161–184, 2016.

[8] R. B. O. Australia, "Discussion on is our current international economic environment unusually crisis prone?" *Frontiers in Microbiology*, vol. 6, no. 3, pp. 543–553, 2015.

[9] C. L. Payne, P. Scarborough, and L. Cobiac, "Do low-carbon-emission diets lead to higher nutritional quality and positive health outcomes? A systematic review of the literature," *Public Health Nutrition*, vol. 19, no. 14, pp. 2654–2661, 2016.

[10] Y. Han, C. Long, Z. Geng, and K. Zhang, "Carbon emission analysis and evaluation of industrial departments in China: an improved environmental DEA cross model based on information entropy," *Journal of Environmental Management*, vol. 205, no. 1, pp. 298–307, 2017.

[11] Z. Jin, K. Dai, G. Fu, and Y. Li, "Discussion on tourism logistics based on the separation and combination of tourists and items theory," *American Journal of Industrial and Business Management*, vol. 7, no. 4, pp. 537–547, 2017.

[12] C.-Y. Dye and C.-T. Yang, "Sustainable trade credit and replenishment decisions with credit-linked demand under carbon emission constraints," *European Journal of Operational Research*, vol. 244, no. 1, pp. 187–200, 2015.

[13] Z. Zhou, C. Liu, X. Zeng, Y. Jiang, and W. Liu, "Carbon emission performance evaluation and allocation in Chinese cities," *Journal of Cleaner Production*, vol. 172, no. 2, pp. 1254–1272, 2018.

[14] L. Xu, S.-J. Deng, and V. M. Thomas, "Carbon emission permit price volatility reduction through financial options," *Energy Economics*, vol. 53, pp. 248–260, 2016.

[15] Y. Narangajavana, T. Gonzalez-Cruz, F. J. Garrigos-Simon, and S. Cruz-Ros, "Measuring social entrepreneurship and social value with leakage. Definition, analysis and policies for the hospitality industry," *The International Entrepreneurship and Management Journal*, vol. 12, no. 3, pp. 911–934, 2016.

[16] M. Dayarathna, Y. Wen, and R. Fan, "Data center energy consumption modeling: a survey," *IEEE Communications Surveys & Tutorials*, vol. 18, no. 1, pp. 732–794, 2017.

[17] C. Gutiérrez-Martín, M. Borrego-Marín, and J. Berbel, "The economic analysis of water use in the water framework directive based on the system of environmental-economic accounting for water: a case study of the Guadalquivir river basin," *Water*, vol. 9, no. 3, p. 180, 2017.

[18] A. D. A. Tasci, "Added value of a destination brand name calculated by crimmins's method," *Tourism Analysis*, vol. 21, no. 6, pp. 669–673, 2016.

[19] M. Todorovic, A. Mehmeti, and A. Scardigno, "Eco-efficiency of agricultural water systems: methodological approach and assessment at meso-level scale," *Journal of Environmental Management*, vol. 165, no. 1, pp. 62–71, 2016.

[20] A. O'Cass and P. Sok, "An exploratory study into managing value creation in tourism service firms: understanding value creation phases at the intersection of the tourism service firm and their customers," *Tourism Management*, vol. 51, pp. 186–200, 2015.

[21] E. Agyeiwaah, "Exploring the relevance of sustainability to micro tourism and hospitality accommodation enterprises (MTHAEs): evidence from home-stay owners," *Journal of Cleaner Production*, vol. 226, no. 20, pp. 159–171, 2019.

[22] H. Guoqiang, Y. Peng, X. Liu, L. Wei, and X. Zhang, "Compensatory growth of juvenile brown flounder paralichthys olivaceus following low temperature treatment for different periods," *Journal of Ocean University of China*, vol. 16, no. 2, pp. 326–332, 2017.

[23] D. Yan, Y. Lei, L. Li, and W. Song, "Carbon emission efficiency and spatial clustering analyses in China's thermal power industry: evidence from the provincial level," *Journal of Cleaner Production*, vol. 156, no. 10, pp. 518–527, 2017.

[24] M. Ilkyeong, J. Yoon, and S. Subrata, "Fuzzy bi-objective production-distribution planning problem under the carbon emission constraint," *Sustainability*, vol. 8, no. 8, p. 798, 2016.

[25] X. Zhou, X. Guan, M. Zhang, Y. Zhou, and M. Zhou, "Allocation and simulation study of carbon emission quotas among China's provinces in 2020," *Environmental Science and Pollution Research*, vol. 24, no. 8, pp. 7088–7113, 2017.

Research Article

Fiber-Reinforced Magnesium Phosphate Cement-Based Nanocomposites in the Field of Bridge Structure Repair and Strengthening

Wenwei Yang [iD] [1,2]

[1]*Lanzhou University, Ministry of Education of China,*
 Key Laboratory of Mechanics on Disaster and Environment in Western China, Lanzhou 730000, Gansu, China
[2]*Lanzhou University, Civil Engineering & Mechanical College, Department Mechanical & Engineering Science, Lanzhou 730000,*
 Gansu, China

Correspondence should be addressed to Wenwei Yang; yangwenwei@lzu.edu.cn

Currently, fiber-reinforced magnesium phosphate cement-based nanocomposites are being used in various projects. The unique physical properties of this material allow it to bear the load together with the material in the inherent structure, and it will be better used in the field of bridge structure repair and reinforcement. The purpose of this article is to study the application of fiber-reinforced magnesium phosphate cement-based nanocomposites in the field of bridge structure repair and reinforcement. Through the use of finite element analysis software and various stress sensor materials, the mechanical properties of fiber-reinforced magnesium phosphate cement-based nanocomposites are used to analyze the mechanical properties of damaged bridges in our area after reinforcement treatment and establish a control group (using magnesium phosphate cement-based nanocomposite materials) for comparative experiments. The reinforcement effect of the bridge repair structure under different ballast conditions is studied. Studies have shown that fiber-reinforced magnesium phosphate cement-based nanocomposites can provide excellent reinforcement for damaged bridge structures. Compared to the control group, the strength and stiffness of the repaired structure were significantly improved, the strength increased by 15.7%, and the stiffness increased by 12%. The carrying capacity has also been improved compared to the previous one, from the original 120 t to 150 t.

1. Introduction

Now there are more ways to strengthen concrete structures [1]. The design specification for reinforced concrete structures (GB50367-2013) introduces the specific ones: crack repair technology, pre-tensioned steel wire rope net, polymer mortar reinforcement method, anchor bolt technology, and pasted steel plate, and the reinforcement method of prestressed carbon fiber composite materials [2]. In addition, there are additional protection and reinforcement methods, replacement methods, steel wire reinforcement methods, reinforced concrete and prestressed reinforcement methods, reinforcement methods for steel bars and CFRP composite materials, cross-sectional expansion methods, etc. [1, 3].

Magnesium phosphate cement is a new type of environmentally friendly cementitious material. It is composed of magnesium oxide, soluble phosphate, and retarder according to an appropriate mixing ratio. Through acid-base neutralization reaction, a flowing acidic composite brine is generated [4]. In recent years, a new type of environmentally friendly cement material has received more and more attention, especially in the application of rapid restoration. After several years of research, development, and accumulation, MPC can gradually be divided into three categories: phospho-Portland cement (MPSC), magnesium ammonium phosphate cement (MAPC), and potassium magnesium calcium phosphate cement (MKPC) [5]. The cement chosen in this topic is potassium magnesium phosphate cement. The reinforced concrete method of fiber-reinforced potassium phosphate

cement mortar is similar to that of reinforced concrete with enlarged section.

The purpose of this article is to study the effect of fiber-reinforced magnesium phosphate cement-based nanocomposites on bridge structure repair. Among them, Ahmad pointed out in the article that in the repair of damaged bridge structures, the repair effects of various existing materials are not very good, the cost of repair materials is often too high, and new materials are urgently needed in the field of bridge construction to be replaced [6]. Peters' et al. research found that magnesium phosphate cement-based nanocomposites have excellent effects in repairing various damaged beam structures, and the manufacturing cost is still acceptable [7]. Selvakumar et al. conducted various mechanical performance experiments on magnesium phosphate cement-based nanocomposites and found that adding various materials to it can better improve this mechanical performance [8]. Díez -Pascual and Díez-Vicente found through experiments that adding a certain amount of fiber to the magnesium phosphate cement-based nanocomposite material can well increase the tensile and compressive strength of the material [9]. Li et al. found that the fiber-reinforced magnesium phosphate cement-based nano-composite has an excellent repair effect on the bridge structure, the strength and rigidity of the repaired structure are significantly improved, and the bearing capacity is also improved compared with the previous one [10].

In the research on the application of fiber-reinforced magnesium phosphate cement-based nanocomposites in the field of bridge structure repair and reinforcement, this article summarizes and compares the research status and research results of previous scholars and material scientists. This article is innovative. The points are roughly as follows. First, this article uses finite element analysis software and various stress sensor materials for the first time to conduct a detailed analysis of the stress-carrying capacity of the material in the damaged structure of the bridge and verifies the feasibility of the material. The second point is that this paper strictly established a control experiment through the controlled variable method. The experimental group uses fiber-reinforced magnesium phosphate cement-based nanocomposites, and the control group uses magnesium phosphate cement-based nano-composites. A two-month experiment was carried out. Variables are strictly controlled to ensure the accuracy of the experiment. The third point is that this paper not only analyzes the physical properties of the material in detail but also conducts an experimental analysis on the influence of the amount of fiber on the reinforcement effect and examines the fiber ratio of the composite material when the physical properties are optimal.

2. Research Content of Fiber-Reinforced Magnesium Phosphate Cement-Based Nanocomposites

2.1. Characteristics and Application Fields of Magnesium Phosphate Cement.
Magnesium phosphate cement, as an environmentally friendly cementing material with chemical bonding ceramic properties, has characteristics that other existing building materials cannot match, for example, fast setting speed, demoulding within 30 minutes [11], and high strength, the strength can reach more than 40 MPa within 3 hours [12]; at the same time, it has good compatibility with old concrete and high bonding strength. It has excellent wear resistance, which is twice that of ordinary Portland cement products and can be used as a repair material. Under the same conditions, steel bars have better rust resistance, and the corrosion rate of steel bars is only 22.8% of that of ordinary Portland cement [13]. Its excellent salt resistance and antifreeze corrosion properties make the phosphate cement mortar and concrete surface to spall off only after 40 years. It has good heat resistance and can withstand high temperatures of 1300°C [14].

Various waste materials that can be used for cement not only are environmentally friendly but also can reduce costs and improve the performance of cement slurry.

At present, the use and development of MPC are mainly concentrated in the following parts.

2.1.1. As a Quick Repair Material.
In terms of road maintenance, disc acid magnesium cement not only can be quickly set and formed but also has high early strength. The construction process is simple, the maintenance is convenient, and it has superior durability. It can be constructed even in low temperature environments. It is an ideal rapid road repair material; it has become the most common application of magnesium phosphate cement today [15].

2.1.2. Solidified Body as Hazardous Waste.
The nuclear waste produced by magnesium phosphate cement can be treated by radiation curing at room temperature without a special calcining device, which not only reduces fuel costs but also avoids secondary pollution caused by waste components in volatiles. At the same time, the waste product has high strength, good stability, and low dissolution rate of environmental pollution or human body-damaging substances, which is a very promising curing method.

When a material containing harmful substances is added to magnesium phosphate cement, it reacts with the hydration product of magnesium phosphate cement to produce new phosphoric acid. These phosphates have low solubility and are tightly wrapped by the hydrated product of magnesium phosphate cement.

2.1.3. As a New Type of Adhesive Made of Artificial Wood.
Magnesium phosphate cement replaces the existing adhesives for wood-based panels. Compared with the existing production process, magnesium phosphate cement can effectively reduce energy consumption, control the emission of harmful environmental substances, and make wood-based panels more prominent in fire resistance and durability. After mixing magnesium phosphate cement and lignin waste particles uniformly, the hydration reaction generates phosphate, which cements the lignin waste into a network to form a composite material with significant

compactness [16]. This process can quickly cure and harden at room temperature without heating and curing like traditional polymers, and there is no special requirement for environmental humidity.

2.1.4. Production of Biological Bone Cement. Magnesium phosphate cement is non-toxic, has excellent biocompatibility, and has a good gelation effect between biological bones. It enters the biological body without foreign body reaction, so biological bone cement can be made into a rapid repair material for bone fixation of teeth and has a good development prospect in the medical field [17].

2.1.5. As Paint Material. Due to the rapid early strength and excellent fire resistance of magnesium phosphate cement, some American companies have developed sprayed concrete, which can be sprayed directly on the surface of rigid foam polystyrene boards or wood to form a complete wall mode.

2.2. Advantages and Disadvantages of Fiber-Modified Magnesium Phosphate Cement. Carbon fiber-modified magnesium phosphate cement is a magnesium phosphate cement-based composite material based on magnesium phosphate cement, in which discontinuously cut carbon fibers are added as a reinforcing and toughening material. The carbon fiber added to the magnesium phosphate cement matrix has the following function: to improve the tensile strength of the matrix. Internal defects are the predisposing factors leading to the failure of magnesium phosphate cement [1]. In order to improve the tensile strength, it is necessary to minimize the stress concentration at the internal fracture end and limit the fracture propagation. The uniform and arbitrary distribution of short-cut carbon fibers in carbon fiber-modified magnesium phosphate cement improves the matrix structure of magnesium phosphate cement, reduces defects in the matrix, and improves the continuity of the magnesium phosphate cement matrix during concrete hardening [18]. During the stress process of the magnesium phosphate cement, the carbon fiber and the magnesium phosphate cement matrix deform together under the action of the stress, and the bridging effect of the carbon fiber makes the magnesium phosphate cement continuously crack and bear greater load. All these contribute to improving the tensile strength of carbon fiber-modified magnesium phosphate cement [19].

The addition of carbon fiber is like adding a large number of thin strips to the matrix, forming a relatively complete network structure. During the development process, the microcracks are inevitably blocked by carbon fiber, which hinders the propagation of the cracks, thereby playing a role in crack resistance. The fiber is closely combined with the matrix material, which greatly maintains the overall strength of the magnesium phosphate cement [20]. When a wall made of concrete receives an impact, carbon fiber will absorb a lot of energy, thereby effectively reducing the impact of stress concentration. Carbon fiber has a bridging effect on the fracture of magnesium phosphate cement and consumes energy when the fiber is pulled out of the matrix of magnesium

phosphate cement [21]. All of the above effects help improve the toughness of concrete. Carbon fiber is more effective than magnesium phosphate cement, but the surface of the carbon fiber has a graphite structure [22]. Due to its smooth surface, such as inertness, the number and types of active functional groups are small, and the composite with magnesium phosphate cement has poor interface bonding. The interlayer shear strength of cement paste is low, and the pull-out resistance of carbon fiber is poor [2, 23]. Therefore, in order to improve the toughening effect of magnesium phosphate cement fiber, surface modification of carbon fiber is required.

2.3. Effect of Fiber on the Properties of Magnesium Phosphate Cement. Magnesium phosphate cement is composed of reburned magnesium oxide, soluble phosphate, and retarder. The main hydration product is magnesium ammonium phosphate hexahydrate, which has the advantages of fast solidification, fast hardening, and high early strength [24]. It can be used for rapid repair of concrete roads and structures and radioactive and toxic curing treatments [25]. However, since the main cohesive forces of magnesium phosphate cement are ionic bonds and covalent bonds, its brittleness is relatively large, so it needs to be toughened and modified. At present, the main toughening modification measures are polymer emulsion modification and fiber modification. Studies have shown that polymer emulsions can encapsulate magnesium oxide particles, which has an adverse effect on the hydration process and the strength of magnesium phosphate cement, so it is rarely used [26]. Fiber modification mainly uses organic fibers, glass fibers, steel fibers, carbon fibers, etc. Among them, carbon fibers have the advantages of high modulus, high tensile strength, and good corrosion resistance. The toughening effect of magnesium phosphate cement is particularly obvious [27]. In the laboratory, according to the mixing ratio of magnesium phosphate cement mortar and carbon fiber, the length and content of carbon fiber, and the water-cement ratio studied, the expansion degree of magnesium phosphate cement mortar was studied. According to the hardening strength of magnesium phosphate cement, the dispersion of carbon fiber in magnesium phosphate cement mortar was also studied, and its compressive strength, flexural strength, and split tensile strength were analyzed [28].

Since magnesium phosphate cement is not used in industrial production, this article uses a mixture of magnesium phosphate cement for a variety of raw materials, including soluble phosphate using ammonium dihydrogen phosphate, retarder using borax, the proportion of magnesium oxide concrete, and ammonium dihydrogen phosphate = 4 : 1; the sand content of borax (calculated by the mass of magnesium oxide): magnesium oxide = 1 : 10 [29]. Good workability is an important indicator for evaluating the performance of concrete and mortar. The lap and agglomeration of fibers will greatly reduce the fluidity and performance of concrete. This section mainly studies the influence of fiber length, water-cement ratio, and fiber content on the working performance of magnesium phosphate cement mortar, which is characterized by the swelling degree of the mortar. In the

test, the sand-to-cement ratio of the magnesium phosphate cement mortar is 1:1, and the fibers are 3 mm, 6 mm, 10 mm, and 15 mm, respectively [30]. Fiber content is all volume content. The light weight of carbon fiber is less than half the density of magnesium oxide, and the surface is hydrophobic. In addition, the diameter of the fiber is much smaller than that of magnesium oxide and fine aggregate particles, so it is difficult to uniformly mix carbon fiber and magnesium phosphate cement mortar. When carbon fiber is added to magnesium phosphate cement to improve its toughness, in order to give full play to its high modulus and high tensile strength, it must be uniformly dispersed in the mortar. When the dispersion performance of carbon fibers is poor, the strength of magnesium phosphate cement mortar is easily affected by the fiber dispersion state of the worst part and the dispersion of carbon fibers, and the local content of the dominant part is too small. The elongation strength fails to give full play to the advantages of high, so the uniformity of the carbon fiber dispersion determines its effect on improving the toughness of magnesium phosphate cement mortar [31].

3. The Experiment of Fiber-Reinforced Magnesium Phosphate Cement-Based Nanocomposite in Bridge Structure Repair

3.1. Materials Needed for Experimental Cement. The prepared material is calcined at a high temperature to form magnesium oxide. The material is purchased from Jiangsu Huanan Magnesium Industry Co., Ltd., and the production process adopts a two-step calcination method. First, magnesite is processed at about 1000°C to obtain light-burned magnesia and then calcined at a high temperature of 1700°C for 6 hours to obtain reburned magnesia. The recalcined magnesia used in the test was first ground by a ball mill and then sieved through a sieve with an aperture of 0.1 mm to a specific surface area of 310–3202 m/kg. The content of each component of the purchased dead-burned magnesia is shown in Table 1.

In addition, there are two types of potassium dihydrogen phosphate (KDP) raw materials used for testing. The first raw material was purchased from Tianjin Dongsheng Chemical Co., Ltd., the registration number was KDP-1, and the crystal size was 28/600~35/425 mesh/m. The second raw material was provided by Fujian Waiting Chemical Co., Ltd. The crystal size was 48/315~80/180 mesh/m. The phosphate used in the experiment was obtained by uniformly mixing two potassium dihydrogen phosphates at a mass ratio of 1:1. All KDPs used are white crystals, easy to go crazy, and packed in plastic bags.

3.2. Experimental Nanomaterials and Other Admixtures. The nano iron oxide (NF) used in this test has a red powder appearance and was purchased from Ziti Nanometer Technology Co., Ltd. The main component is Fe_2O_3 (≥99.8%), the particle size range is 20–50 nm, and the specific surface area is 80–902 m^2/g. The nano alumina (NA)

TABLE 1: Data of neurotransmitter substances in plasma of control experiment.

Ingredient	MgO	CaO	Fe2O3	Al2O3	SiO2
Content (%)	97.5	0.15	0.05	0.03	0.02

used in the test has an appearance of white powder and was purchased from Ziti Nano Technology Co., Ltd. The main component is Al_2O_3 (≥99%), the particle size range is 30–40 nm, and the specific surface area is 2002 m^2/g [32]. The sodium silicate glass (marked as WG) used in the experiment was white powder and was purchased from Tianjin Davao Chemical Reagent Factory. Its main component is $Na_2SiO_3H_2O$ (≥99%). The fiber (marked as SF) used in the experiment was off-white and was purchased from Jinmen water purification material Co. The main component is SiO_2 (≥85%), the particle size is 2000 mesh, and the specific surface area is 20~282 m^2/g.

Four types of fiber (denoted as F) are used in this test: imitation steel fiber (denoted as ISF), microsteel fiber (denoted as MSF), flat steel fiber (SF), and tail hook steel fiber (HF). The imitation steel fiber was purchased from Ningbo Shake New Material Technology Co., Ltd. The material used is rough polypropylene, the surface is embossed, the cross section is rectangular, and the equivalent diameter is 0.6 mm. The fine steel fiber was purchased from Shanghai Zhenjiang Fiber Co., Ltd. The material is stainless steel, the surface is plated with copper, the surface is smooth, the cross section is circular, and the equivalent diameter is 0.22 mm. The straight steel fiber is obtained by removing the ends of the hook-shaped steel fiber produced by Shanghai Bekaert. The tail hook steel fiber was purchased from Shanghai Bekaert Co., Ltd. It is a row of steel fibers, made of stainless steel, with a straight surface and curved ends.

3.3. Mechanical Performance Test of Magnesium Phosphate Cement Mortar. The compressive strength of magnesium phosphate cement mortar is tested by mechanical performance test, and its compressive strength test refers to ASTM C109 "Standard Test Method for Compression of Hydraulic Cement Mortar." The instruments and equipment used include cement mortar mixer (5 L), pressure testing machine (200 T), concrete magnetic vibration table, etc.

The measurement method of this test is as follows:

(1) The three joints of plastic compressed concrete were tested to form a cement mortar test block with a size of 50 mm × 50 mm × 50 mm, which was taken out after being placed in the room and cured for 2 hours.

(2) Curing to the specified conditions according to the corresponding immersion time.

(3) According to the standard compressive strength test method, the loading speed of the compression testing machine is set to 0.9 kN/s. Three samples are taken from each group to test and record the data.

The load-displacement curve of the bonding performance between the fiber and the magnesium phosphate cement mortar was obtained through the fiber pull-out test. The bonding performance is tested with reference to "Test Method for Steel Fiber Concrete" (CECS13 : 2009). Compared with single fiber pull-out, the result of multi-fiber pull-out test shows that the dispersion is smaller, and too small fiber spacing will reduce the bonding efficiency. Therefore, in this test, four fibers were pulled out in one direction, and the fiber interval was set to 12 mm. The main instruments and equipment used are cement slurry mixer (5 L), electronic universal testing machine (5 KN), pressure sensor (2 KN), strain displacement sensor (30 mm), and No. 3 static strain testing system machine [33].

3.4. The Principle of Experimental FRCC Enhancement.
The strengthening mechanism of FRCC mainly includes fiber spacing theory, composite mechanics theory, and multiple fracture theory. According to mechanics theory, composite materials are a combination of fibers and substrates, and according to the law of mixing, the overall performance of composite materials is equal to the sum of the properties of substrates and fibers. In order to calculate the fiber spacing S, it is considered that the fibers are distributed in a square ratio. On the basis of theoretical and experimental research, an algorithm for the average fiber spacing S is established as shown in the following formula:

$$S = 13.8 * d * \sqrt{\frac{1}{P}}, \tag{1}$$

where D is the diameter of the fiber; P is the percentage of the fiber volume ratio; and V_f is the volume fraction of the fiber.

The concept of effective spacing coefficient not only is a statistical description of the spacing between fiber centers but also points out the bad mode of fiber-matrix interaction, and its expression should include the factor of fiber shape. Therefore, the effective fiber spacing is also determined as shown in the following equation:

$$S = 25.0 * \sqrt{\frac{d}{Pl}}, \tag{2}$$

where S is the length of the fiber.

3.5. Experimental Process and Results.
The surface treatment methods of old concrete are three treatment methods: without surface cleaning, mechanical chiseling to remove laitance, and chisel out by hand. For the mechanical gouging samples, the surface laitance is mainly removed by the gouging machine, while the artificial gouging is the gouging of the cement stone on the concrete surface, so that the coarse aggregate is exposed on the surface. The roughness of concrete measured by sand casting method is 1 mm and 4 mm, respectively. Drilling holes and bolts used for insertion and positioning are MKPC cement positioning bolts, reinforced MKPC cement positioning bolts, and embedded

steel bars. The electric drill is used to drill a 20 mm round hole with a depth of 3 cm on each of the two reinforced surfaces of the old concrete. The sample is B6, which is inserted into the hole and then the rubber is injected. The sampling material is made of steel wire mesh, which is inserted into a hole in old concrete and injected with MKPC grout, and the exposed steel wire is transferred and expanded. After treating the surface of the old concrete, pour MKPC cement mortar on both sides of the sample for double-sided reinforcement. Before pouring the MKPC mortar, the MKPC cement paste with a water-cement ratio of 0.12 was applied to the surface of the old concrete in a thickness of about 5 mm. In order to avoid local breakage of the bonding layer by shearing the experimental pad, the thickness of the entire reinforcement layer is about 30 mm. There are 3 specimens in each group, totaling 18 specimens. After curing for 28 days, a double-sided shear test was performed. At present, China does not have a unified interface shear strength test method standard.

Test Method. Reinforce the sample directly on both sides of the old concrete and conduct a double-sided shear test on the bonding surface between the reinforcement layer and the old concrete. The shear specimen is broken and the test is stopped. In order to eliminate the gap between the sample and the device and set the value of the tester to zero, the data are unreasonably omitted due to the possible stress imbalance during sample loading [34]. Finally, the shear strength of each group is obtained from the average value of each group of data.

4. Effect of Fiber-Reinforced Magnesium Phosphate Cement-Based Nanocomposite on Bridge Structure Repair and Reinforcement

4.1. Analysis of Influencing Factors of Compressive Strength of Fiber-Reinforced Magnesium Phosphate Cement-Based Nanocomposites in Repair and Strengthening of Bridge Structure.
Analysis of influencing factors of compressive strength of fiber-reinforced magnesium phosphate cement-based nanocomposites in repair and strengthening of bridge structure is shown in Table 2.

By comparing the data of each group in the above table, before the reinforcement, the cracking load of each beam is basically the same because it is not reinforced before the failure. By comparing the cracking load of the reinforced layer after A0-1 and A0-2 reinforcement, it can be seen that as the length of the reinforced layer increases, the cracking load of the damaged layer increases by 21.5%. The main reason is that the reinforcement layer and the original structure coordinate share part of the section bending moment, thereby increasing the cracking load. Comparing the ultimate load of beam A0-0, beam A0-1 and beam A0-2 increase by 60.0% and 29.4%, respectively. It can be seen that the longer the reinforced length after reinforcement, the better the lifting capacity of the ultimate load of the beam. Even if the length of the steel bar is

not enough to withstand shear failure, the final load will still increase to a certain extent.

After the pH of the system reaches >7, MKP begins to precipitate rod-shaped crystals, which overlap each other to form a network structure, and the slurry condenses to finally form a hardened body with MgO particles as the skeleton and MKP crystals as a binder. The relevant data are shown in Figure 1.

It can be seen from the data in Figure 1 that P/M affects the compressive strength of fiber-reinforced magnesium phosphate cement-based nanocomposites in the repair and reinforcement of bridge structures [35]. When the P/M value increases to 0.3, the material is used in the bridge structure. The compressive strength in repair and reinforcement was increased from 420 MPa to 485 MPa, and the tensile strength was increased by 18%.

The research results show that for ordinary Portland cement mortar, excessive water-cement ratio will cause seepage segregation of the new slurry, leaving large pores after hardening, which greatly affects the strength of the sample. Although the reaction mechanism of the magnesium phosphate cement system is different from that of ordinary Portland cement, a too large water-cement ratio will cause a large number of holes to be formed after the slurry hardens, and the structure is not dense enough, thereby reducing the strength. As W/C increases from 0.24 to 0.30, the 3D compressive strength of FMPM gradually decreases. The increase in W/C allows the hydration reaction of the slurry to proceed completely, but the evaporation of excess water significantly increases the proportion of harmful pores in the cured product, resulting in a porous structure of the hydrated product. However, a too low water-binder ratio is not only unfavorable to the formation of the slurry but also affects the progress of the test due to the short solidification time of the slurry; the specific data are shown in Figure 2.

It can be seen from the data in Figure 2 that the W/C value affects the compressive strength of fiber-reinforced magnesium phosphate cement-based nanocomposites in the repair and reinforcement of bridge structures. When W/C increases from 0.24 to 0.30, the material is used in bridges. The compressive strength in structural repair and reinforcement was increased from 420 MPa to 490 MPa, and the tensile strength was increased by 19.5%.

4.2. Calculation and Analysis of Flexural Strength of Fiber-Reinforced Magnesium Phosphate Cement-Based Nanocomposite in Repair and Strengthening of Bridge. The reason that affects the bending strength of FMPM is because the two basic mechanical properties of FMPM, namely, flexural strength and compressive strength, are mutually operable. Although there is no direct relationship between the two, the overall trend is similar. The first three factors are the main influencing factors; other factors will not be analyzed temporarily. The flexural strength of FMPM first increases, then decreases with P/M from 1/2 to 1/5, then decreases with W/C from 0.24 to 0.30, and then decreases with S/C from 0.6 to 1.2. Single-doped fibers have similar effects on the bending strength and compressive strength of FMPM. For the bending strength, when the fiber content is 5%, the 3D bending strength of FMPM increases by 4% compared with the reference group.

The strength will increase more obviously, and when the age is 14 days, the bending strength will increase by 17%. When the fiber content is 10%, the 3 d flexural strength of FMPM is increased by 9% compared with the reference group, 36% at 7 d, and the highest value of 9.15 MPa at 14 d, which is 45 higher than the reference group. This also shows that, over time, the bending strength of FMPM will also greatly increase. However, when the fiber content was increased to 20%, the improvement did not increase further, and the value of the flexural strength decreased relative to the group with the fiber content of 10%. As for the compressive strength, when the fiber content is 5%, the 3D compressive strength of FMPM does not change much and is 2% higher than the reference group. However, with the increase of age, the enhancement effect becomes more obvious, and the compressive strength of 14 d increases by 18%. When the fiber content is 10%, the 14 d compressive strength value is 44.35 MPa, which is 22% higher than the reference group. When the fiber content is 20%, the compressive strength decreases to a certain extent. The relevant data are shown in Figure 3.

It can be seen from the data in Figure 3 that as the amount of fiber increases, the flexural strength and compressive strength of magnesium phosphate cement-based nanocomposites in the repair and reinforcement of bridge structures gradually increase, and the tensile strength and flexural strength are increased compared with general materials by 25%.

The flexural strength of concrete beams and columns reinforced with inorganic basalt magnesium phosphate fiber can be increased by 57.5%, and the ultimate axial compressive strength can be increased by 45.4%. Adding an appropriate amount of fly ash to the magnesium phosphate cement can make the structure of the magnesium phosphate cement denser and increase the tensile strength of the fiber reinforced in the MPC matrix by about 10%; at the same time, the binding force between the MPC and the matrix is improved, and the fiber structure is optimized. The specific data are shown in Figure 4.

It can be seen from Figure 4 that the strength and rigidity of the repaired structure have been significantly improved, among which the strength of the structure has increased by 15.7% and the rigidity has increased by 12%. The carrying capacity has also been improved from the previous 120 t to 150 t.

TABLE 2: Summary of damaged beam bearing capacity.

Beam number	Damage-cracking load	Cracking load of reinforcement layer	Ultimate load
AO-0	17.23	—	35.69
AO-1	16.12	28.65	62.15
AO-2	15.23	24.65	45.36

FIGURE 1: Effect of P/M on compressive strength of fiber-reinforced magnesium phosphate cement-based nanocomposites in bridge structure repair and reinforcement.
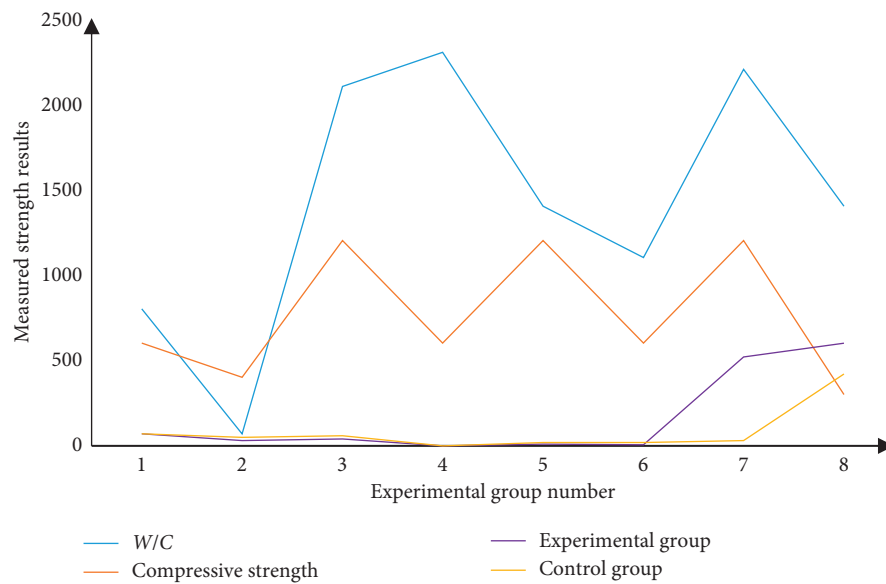
FIGURE 2: The effect of W/C value on the compressive strength of fiber-reinforced magnesium phosphate cement-based nanocomposites in bridge structure repair and reinforcement.
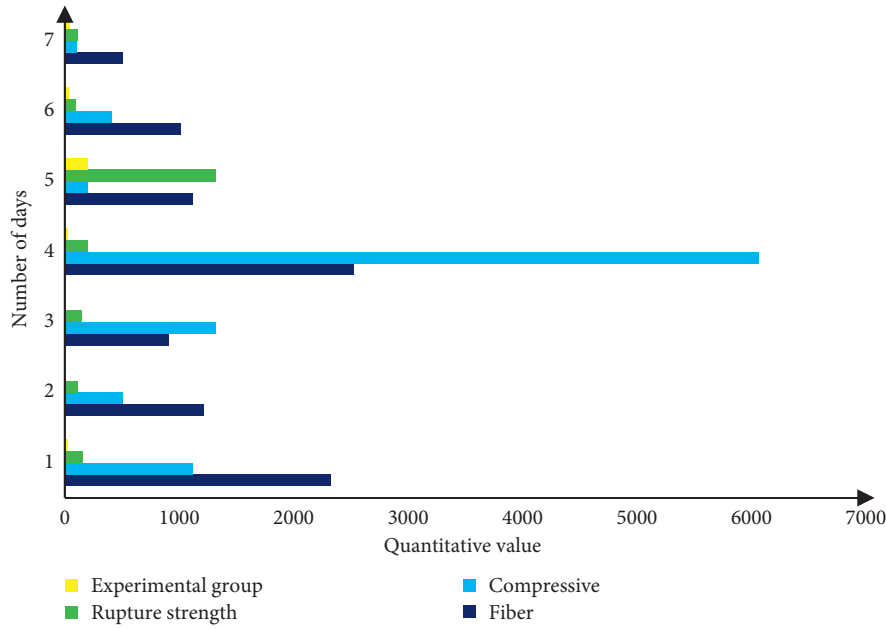
FIGURE 3: The enhancement of the fiber content to the flexural strength and compressive strength of magnesium phosphate cement-based nanocomposites.

FIGURE 4: Repair effect of fiber-reinforced magnesium phosphate cement-based nanocomposite.

5. Conclusions

(1) This paper analyzes the current problems in the application of fiber-reinforced magnesium phosphate cement-based nanocomposites in the field of bridge structure repair and reinforcement, discusses to solve these problems, and proposes corresponding solutions. The common methods and materials for repairing and strengthening bridge structures are introduced, especially the mechanism of using magnesium phosphate cement-based nanocomposites to strengthen and repair bridge structures is discussed and introduced in detail.
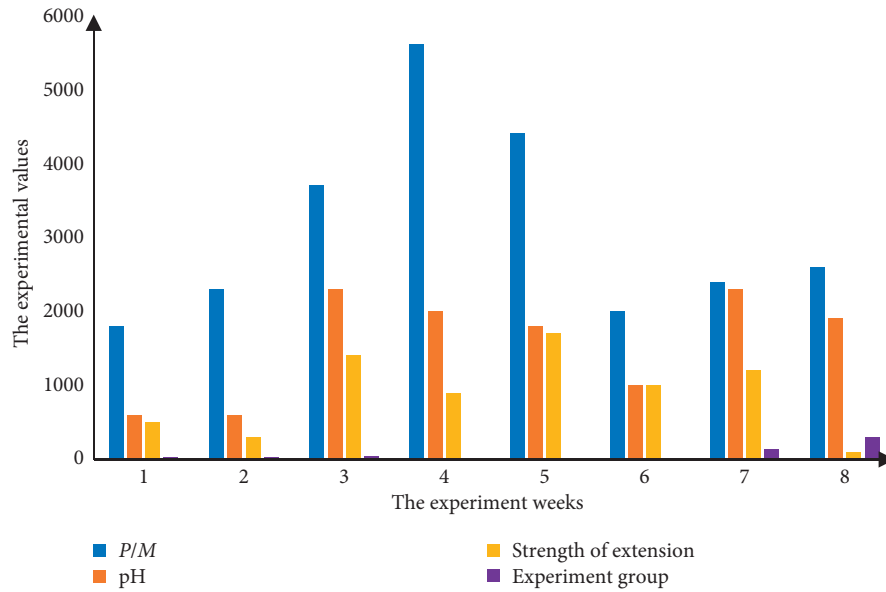
(2) We analyzed the factors affecting the compressive strength of the fiber-reinforced magnesium phosphate cement-based nanocomposites in the bridge structure repair and reinforcement. Experiments have shown that P/M affects fiber-reinforced magnesium phosphate cement-based nanocomposites

with bridge structures. When the *P/M* value increases to 0.3, the compressive strength of the material in the repair and reinforcement of bridge structure increases from 420 MPa to 485 MPa, and the tensile strength increases by 18%.

(3) The calculation of flexural strength of fiber-reinforced magnesium phosphate cement-based nanocomposites in the repair and reinforcement of bridge structures was discussed and verified. Experiments have verified that with the increase of fiber content, the flexural strength and compressive 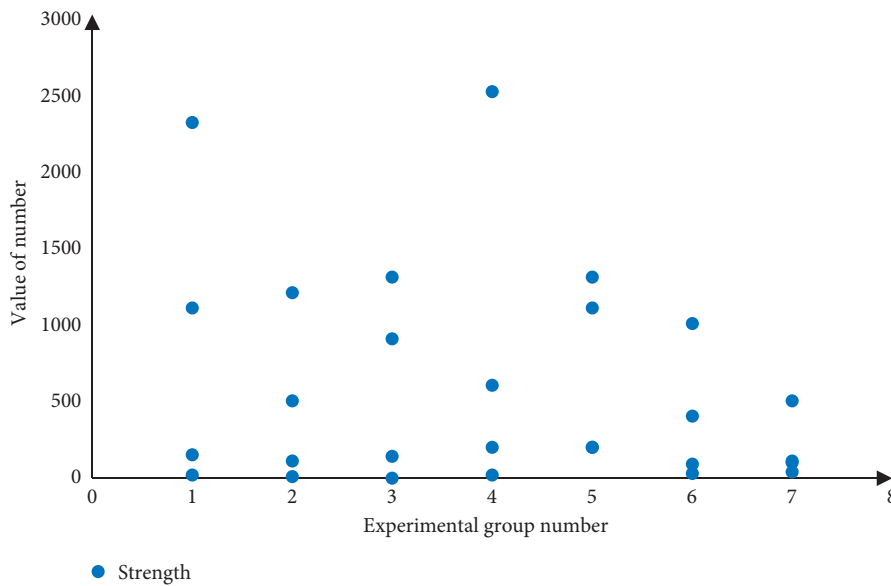strength of magnesium phosphate cement-based nanocomposites in the repair and reinforcement of bridge structures gradually increase, and the tensile strength and flexural strength are increased by 25% compared with ordinary materials.

Data Availability

No data were used to support this study.

Conflicts of Interest

The author declares that there are no conflicts of interest.

Acknowledgments

References

[1] Y. Tang, W. Feng, W. X. Feng, J. Chen, D. Bao, and L. Li, "Compressive properties of rubber-modified recycled aggregate concrete subjected to elevated temperatures," *Construction and Building Materials*, vol. 268, 2020.

[2] R. Pang, B. Xu, Y. Zhou, X. Zhang, and X. Wang, "Fragility analysis of high CFRDs subjected to mainshock-aftershock sequences based on plastic failure," *Engineering Structures*, vol. 206, Article ID 110152, 2020.

[3] H. Feng, G. Chen, D. Gao, K. Zhao, and C. Zhang, "Mechanical properties of steel fiber-reinforced magnesium phosphate cement mortar," *Advances in Civil Engineering*, vol. 2018, no. 1, 11 pages, Article ID 3978318, 2018.

[4] L. Chong, C. Shi, J. Yang, and H. Jia, "Effect of limestone powder on the water stability of magnesium phosphate cement-based materials," *Construction and Building Materials*, vol. 148, no. 1, pp. 590–598, 2017.

[5] M. R. Ahmad, B. Chen, and J. Yu, "A comprehensive study of basalt fiber reinforced magnesium phosphate cement incorporating ultrafine fly ash," *Composites Part B: Engineering*, vol. 168, no. 1, pp. 204–217, 2019.

[6] K. J. Peters, I. K. Tragazikis, and P. T. Dalla, "Nondestructive evaluation of the mechanical behavior of cement-based nanocomposites under bending," in *Proceedings of SPIE–The International Society for Optical Engineering*, vol. 9436, no. 3, pp. 923–964, San Diego, CA, USA, March 2015.

[7] M. Selvakumar, S. K. Jaganathan, G. B. Nando, and S. Chattopadhyay, "Synthesis and characterization of novel polycarbonate based polyurethane/polymer wrapped hydroxyapatite nanocomposites: mechanical properties, osteoconductivity and biocompatibility," *Journal of Biomedical Nanotechnology*, vol. 11, no. 2, pp. 291–305, 2015.

[8] A. M. Díez-Pascual and A. L. Díez-Vicente, "Wound healing bionanocomposites based on Castor oil polymeric films reinforced with chitosan-modified ZnO nanoparticles," *Biomacromolecules*, vol. 16, no. 9, pp. 2631–2644, 2015.

[9] H. Li, T. Du, and H. Xiao, "Crystallization of calcium silicate hydrates on the surface of nanomaterials," *Journal of the American Ceramic Society*, vol. 100, no. 5, pp. 3227–3238, 2017.

[10] G. Riccardo, G. Chiara, B. Gloria et al., "Graphene-based nanomaterials for tissue engineering in the dental field," *Nanomaterials*, vol. 8, no. 5, pp. 349-350, 2018.

[11] Y. Li, W. Bai, and T. Shi, "A study of the bonding performance of magnesium phosphate cement on mortar and concrete," *Construction and Building Materials*, vol. 142, no. 1, pp. 459–468, 2017.

[12] S. Xu, J. Liu, and Q. Li, "Mechanical properties and microstructure of multi-walled carbon nanotube-reinforced cement paste," *Construction and Building Materials*, vol. 76, no. 1, pp. 16–23, 2015.

[13] H. S. Oh, H. Jee, and A. Baev, "Dramatic structural enhancement of chirality in photopatternable nanocomposites of chiral poly(fluorene-alt-benzothiadiazole) (PFBT) in achiral SU-8 photoresist," *Advanced Functional Materials*, vol. 22, no. 24, pp. 5074–5080, 2015.

[14] A. Hakamy, F. U. A. Shaikh, and I. M. Low, "Thermal and mechanical properties of NaOH treated hemp fabric and calcined nanoclay-reinforced cement nanocomposites," *Materials & Design*, vol. 80, no. 7, pp. 70–81, 2015.

[15] N. K. Young, "Characterization and antimicrobial efficacy of Portland cement impregnated with silver nanoparticles," *Journal of Advanced Prosthodontics*, vol. 9, no. 3, pp. 217–223, 2017.

[16] S.-J. Kwon, H.-S. Lee, S. Karthick, V. Saraswathy, and H.-M. Yang, "Long-term corrosion performance of blended cement concrete in the marine environment–a real-time study," *Construction and Building Materials*, vol. 154, no. 15, pp. 349–360, 2017.

[17] Y. Tang, S. Fang, J. Chen, L. Ma, L. Li, and X. Wu, "Axial compression behavior of recycled-aggregate-concrete-filled gfrp–steel composite tube columns," *Engineering Structures*, vol. 216, 2020.

[18] M. Birenboim, R. Nadiv, A. Alatawna et al., "Reinforcement and workability aspects of graphene-oxide-reinforced cement nanocomposites," *Composites Part B: Engineering*, vol. 161, no. 15, pp. 68–76, 2019.

[19] J. Luo, C. Zhang, Z. Duan et al., "Surfactant-assisted processing of carbon nanotube cement-based nanocomposites: microstructural, electrical, and mechanical properties," *Nanoscience and Nanotechnology Letters*, vol. 10, no. 2, pp. 237–243, 2018.

[20] A. Hakamy, F. U. A. Shaikh, and I. M. Low, "Effect of calcined nanoclay on the durability of NaOH treated hemp fabric-reinforced cement nanocomposites," *Materials & Design*, vol. 92, no. 7, pp. 659–666, 2016.

[21] D. Feldman, "Lignin nanocomposites," *Journal of Macromolecular Science, Part A*, vol. 53, no. 6, pp. 382–387, 2016.

[22] P. Wang, T. Yao, Z. Li et al., "A superhydrophobic/electrothermal synergistically anti-icing strategy based on graphene composite," *Composites Science and Technology*, vol. 198, Article ID 108307, 2020.

[23] L.-l. Wang, X. Dong, X.-r. Wang, G.-y. Zhu, H.-q. Li, and D.-j. Wang, "High performance long chain polyamide/calcium silicate whisker nanocomposites and the effective reinforcement mechanism," *Chinese Journal of Polymer Science*, vol. 34, no. 8, pp. 991–1000, 2016.

[24] D. Pinto, L. Bernardo, A. Amaro, and S. Lopes, "Mechanical properties of epoxy nanocomposites using titanium dioxide as reinforcement–a review," *Construction and Building Materials*, vol. 95, no. 8, pp. 506–524, 2015.

[25] M. A. Haque and B. Chen, "Research progresses on magnesium phosphate cement: a review," *Construction and Building Materials*, vol. 211, no. 30, pp. 885–898, 2019.

[26] Z. Jiang, L. Zhang, T. Geng, Y. Lai, W. Zheng, and M. Huang, "Study on the compressive properties of magnesium phosphate cement mixing with eco-friendly coir fiber considering fiber length," *Materials*, vol. 13, no. 14, Article ID 3194, 2020.

[27] L. Lv, P. Huang, L. Mo, M. Deng, J. Qian, and A. Wang, "Properties of magnesium potassium phosphate cement pastes exposed to water curing: a comparison study on the influences of fly ash and metakaolin," *Construction and Building Materials*, vol. 203, no. 10, pp. 589–600, 2019.

[28] K. Yamamoto, H. Shichiri, T. Ishida et al., "Effects of ascorbyl-2-phosphate magnesium on human keratinocyte toxicity and pathological changes by sorafenib," *Biological an Pharmaceutical Bulletin*, vol. 40, no. 9, pp. 1530–1536, 2017.

[29] A. Pedone, F. Palazzetti, and V. Barone, "Models of aged magnesium-silicate-hydrate cements based on the lizardite and talc crystals: a periodic DFT-GIPAW investigation," *Journal of Physical Chemistry C*, vol. 121, no. 13, pp. 7319–7330, 2017.

[30] G. Guan and W. Zhao, "Research progress of fiber-reinforced cement matrix composites," *China Silicate Bulletin*, vol. 10, pp. 3342–3346, 2017.

[31] Y. Li, Y. Su, and J. Mei, "Research progress of Magnesium phosphate cement (MPC) and its application as FRP binder," *Chinese Journal of Silicate*, vol. 38, no. 3, pp. 76–80, 2019.

[32] S. Chen, M. K. Hassanzadeh-Aghdam, and R. Ansari, "An analytical model for elastic modulus calculation of SiC whisker-reinforced hybrid metal matrix nanocomposite containing SiC nanoparticles," *Journal of Alloys and Compounds*, vol. 767, pp. 632–641, 2018.

[33] S. Qu, L. Zhao, and Z. Xiong, "Cross-layer congestion control of wireless sensor networks based on fuzzy sliding mode control," *Neural Computing & Applications*, vol. 32, no. 17, pp. 13505–13520, 2020.

[34] M. Shi, M. Narayanasamy, C. Yang et al., "3D interpenetrating assembly of partially oxidized MXene confined Mn-Fe bimetallic oxide for superior energy storage in ionic liquid," *Electrochimica Acta*, vol. 334, Article ID 135546, 2020.

[35] W. Wu, S. An, C. H. Wu, S. B. Tsai, and K. Yang, "An empirical study on green environmental system certification affects financing cost of high energy consumption enterprises-taking metallurgical enterprises as an example," *Journal of Cleaner Production*, vol. 244, 2020.

Research Article

High-Temperature Environmental Protection Metal Material 3D Printing Equipment Development and Process Research

Jiaofei Huo and Guangpeng Zhang [ID]

School of Mechanical and Precision Instrument Engineering, Xi'an University of Technology, Xi'an 710048, Shaanxi, China

Correspondence should be addressed to Guangpeng Zhang; 20060005@xijing.edu.cn

At present, 3D printing technology is becoming more and more popular, but the traditional learning method has some limitations. The price of 3D printing equipment is expensive, and there are some security risks in the process of learning operation. This paper mainly introduces the development and process research of high-temperature environmental protection metal 3D printing equipment and realizes the design of 3D printing equipment combined with virtual reality technology. In this paper, the whole system of 3D printing equipment is designed and built. The function of motion platform and substrate in mechanical system is analyzed, and the detailed structure design is carried out; the control principle of control system including motion control system and temperature control system is introduced in detail, and the corresponding design and construction work is carried out. In this paper, the pure tin wire with low melting point was used as the experimental material, and the mechanical properties and microstructure of the metal tin forming parts were analyzed. On the basis of tin formation experiment, metal deposition experiment and metal forming error experiment were carried out with H65 high melting copper wire as the raw material. The experimental results show that when the printing speed is 35/mm, the dimensional accuracy of the products is high; the microhardness of the printed tin is close to that of the original material, the surface hardness is 12.50HV$_{0.05}$, and that of the copper alloy is 14.31HV$_{0.05}$; the tensile strength of tin wire after melt deposition is slightly reduced after tensile test for the machined tin parts, the ultimate tensile strength of the first group of specimens is reduced by 1.58%, and that of the second group is reduced by 0.74%. This paper combines virtual reality technology with 3D printing technology and develops 3D printing equipment for high-temperature environmental protection metal using virtual reality technology. The forming and printing performance of the device is analyzed theoretically and experimentally. The experimental results verify the feasibility of the system and the practicability of the device.

1. Introduction

With the in-depth study of manufacturing industry, innovation and product development cycle has become the main contradiction of the product. People put forward rapid prototyping technology, trying to shorten the development cycle and improve the competitiveness of products. 3D printing technology is a kind of rapid prototyping technology; that is, based on the idea of discretization, using plastic or powdered metal as raw materials, using printing equipment to manufacture materials layer by layer and accumulate layer by layer, and finally forming three-dimensional objects [1]. 3D printing combines digital model

technology, control electronics technology, information technology, material science and chemistry, and many other advanced technologies, known as the core technology of the third industrial revolution. Compared with the traditional processing methods such as turning, milling, planning, and grinding, 3D printing is produced and manufactured in the form of addition, which has the characteristics of green environmental protection and is conducive to the manufacture of complex configuration items. It is widely used in automobile, aviation, aerospace, medical, education, electronic products, and other fields. At present, there are a variety of technologies in the field of 3D printing at home and abroad, and the commercialized processes mainly

include melt deposition molding, selective laser sintering, selective laser melting molding, UV curing molding, layered solid manufacturing, laser cladding deposition technology, etc. [2, 3]. All 3D printing technologies are composed of three key factors: first, 3D printing and forming equipment; second, three-dimensional design and modeling of products; third, molding materials to meet product performance requirements. With the development of industrial technology, materials have become the key of 3D printing technology and also the bottleneck restricting the development of 3D printing technology. In recent years, the focus of 3D printing has gradually shifted to metal 3D printing. 3D metal printing technology uses high-energy beam as heat source to melt or powder refractory metal. According to the type of high-energy beam, metal 3D printing can be divided into selective electron beam casting (plane ion beam forming), direct metal laser sintering, selective laser casting, selective laser sintering, etc. The metal 3D printing technology with laser as the heat source is the most mature and widely used [4].

The research on metal 3D printing manufacturing technology started earlier in foreign countries. Since the early emergence of 3D printing technology, researchers have tried to use various postprocessing processes to process nonmetallic models based on rapid prototyping method to prepare the required metal parts. Murr and Johnson reviewed the development of metal 3D printing technology in the past few decades and found that technologies involving direct metal wire or powder deposition and powder bed fusion using laser and electron beam melting are developing continuously, but there is no big breakthrough in the printing technology of direct printing molten metal droplets [5]. Li et al. use 3D printing to produce high-strength metal abrasives. Through the screening of powder materials and preparation methods, the solution with excellent mechanical properties is selected for preparation. The density, hardness, and toughness of three kinds of metal materials are tested. The high-strength drill bit is successfully produced by using the metal abrasive tools manufactured by printing, which proves the feasibility of metal 3D printing technology, but they do not carry out the test. The printing test of their articles cannot be comprehensively analyzed [6]. Buchanan and Gardner believe that metal 3D printing provides a convenient manufacturing method for creating nonprismatic cross sections, openings, functional gradient elements, variable microstructure, and mechanical properties by controlling heating and cooling and thermal induced prestressing. High-temperature environmental protection metal 3D printing also requires more advanced calculation and analysis, structural design, and new verification thinking and pays more attention to inspection and performance testing [7].

This paper will mainly solve several core problems, such as reducing the manufacturing, operating and operating costs of relevant equipment, improving energy utilization, deposition speed, and molding accuracy, and build a group of new high-temperature environmental protection metal material processing equipment and rapid prototyping to provide high-quality and high-efficiency additive processing strategy. It is of great social significance to promote the market application of metal additive technology and promote the transformation and upgrading of traditional industries.

2. Design of High-Temperature Environmental Protection Metal 3D Printing

2.1. Virtual Reality Technology

2.1.1. Definition of Virtual Reality. Virtual reality (VR), also known as fantasy or spirit environment technology, is through computer hardware technology and image processing technology, so that users can realize a kind of perception of virtual environment through visual, auditory, tactile, olfactory, and other sensing means. Users visit the virtual environment with the help of unique output and input devices, and the virtual environment gives feedback to users, so that people feel as if they are in the virtual environment feeling and experience in real environment [8, 9].

The main characteristics of virtual reality system can be summarized into three aspects: immersion, interaction, and imagination. Immersion can make users fully feel the shock brought by the virtual space environment. VR helmets, glasses. and other virtual reality devices separate traditional video and use real-world vision to provide different images of the left and right sides of the eye, making objects have a three-dimensional sense. Interactivity refers to the interaction between user's action and virtual scene in the virtual world. Imagination refers to the fact that when users use virtual reality technology, with the help of virtual reality technology, the effect that reality does not exist is presented to the public, so that people can turn their imagination into reality and enhance their ability to understand and deal with problems [10].

2.1.2. Architecture of Virtual Reality. Virtual reality technology is a comprehensive technology which integrates computer graphics, sensor technology, interactive technology, and network technology. The most basic requirement of virtual reality technology is to realize real-time interaction with users [11]. Therefore, a basic virtual reality system is mainly composed of computer, input and output equipment, application software, and database:

(1) Computer is the carrier of virtual reality world and the core of the whole virtual world. The main work is responsible for the generation of virtual reality world and the processing of interactive information between users and virtual world. According to the complexity of the virtual world, the requirements of computer performance are not the same. When generating complex large-scale scenes, the amount of computation required is very large, which requires the computer to have high computational performance.

(2) The input and output device is the medium of interaction between computer and user. The input device is the interface for users to send instructions to the virtual world. Its function is to receive the

instructions from the users and convert the user's actions into information and data input into the computer. According to different requirements and purposes, the input devices include space tracking locator, data glove, data clothing, etc.

The output device is the medium for virtual reality world to give feedback to users. Its function is to output the feedback information generated by computer to users through different sensory channels. In addition to the traditional display, the output devices include force feedback data glove, digital helmet, stereo surround sound headset, etc.

(3) Database is the repository of all relevant information in the virtual world, such as geometric model, physical model, and captured user action information in virtual reality environment. In the scene of virtual reality world, a large amount of information needs to be stored for use, which requires the database to manage this information.

(4) The software application in virtual reality system is the key to realize the virtual environment. Its specific task is to make the model in the virtual scene, to ensure the fluency of the direct interaction between people and the virtual environment, as well as the synthesis of sound and the positioning of space.

2.1.3. Development Trend of Virtual Reality Technology. At present, industries are increasingly dependent on the Internet, and people's demand for entertainment is also growing. In order to adapt to the development of the times, the continuous integration of virtual reality technology and art is needed. The rapid popularization of video applications has verified that the public's way of receiving information is no longer single, and the content required is also constantly enriched. It will be one of the development trends of virtual reality technology in the future to combine new technology and new equipment to subvert the public's cognitive boundary of information. Due to the unique advantages of virtual reality technology, it can go deep into all walks of life. In the process of virtualization, some traditional industries continue to bring forth new ones, and traditional industries have entered the era of great change [12]. With the vigorous development of virtual reality technology, it will also bring more new challenges to the traditional industrial chain. Various virtual reality derivatives formed by various industries have promoted this change to a certain extent.

2.2. Basic Theory of 3D Printing Technology

2.2.1. Working Principle of 3D Printing Technology. 3D printing technology is also called rapid prototyping and manufacturing (RP or RP & M) or additive manufacturing. It is a new manufacturing method compared with the traditional reduction manufacturing. The principle is to break the original concept of material processing. Instead of cutting the blank, the computer is used to establish the three-dimensional model of the product to be produced, and then it is layered. Each layer is used as the information unit of the product. Then, the 3D printer is used to manufacture layer by layer, and finally the solid model is completed [13, 14]. In the whole 3D printing process, its core technologies include the following aspects.

(1) Building 3D digital model:

Digital model is the premise of printing process. For complex structure products, its model construction form is very important. At present, the mainstream 3d design software can basically realize the design modeling of complex structure and then need to convert the digital model into printing information suitable for 3D printer recognition. The accuracy and scientificity of this information conversion play a decisive role in the printing quality of products.

(2) Printing process parameter selection:

For 3D printing process as an additive manufacturing method, printing materials are added to the printing model layer by layer, so there are strict requirements for printing path, printing speed, printing room temperature, and other process parameters. Process parameters directly affect the manufacturing accuracy and reliability of printed parts. Therefore, the selection of process parameters needs special research and testing to ensure the quality of printed products.

(3) Printing completes the subsequent processing:

Restricted by the performance of printing materials and the accuracy of printers, the surface roughness of models printed by printers developed at this stage cannot meet the requirements of products. Therefore, it is necessary to increase the process of improving the surface quality of products after printing. In addition, in order to improve the reliability of products, some printing products must be heat-treated to eliminate the residual stress generated in the printing and cooling process. Under the current technical level, subsequent treatment is essential [15].

2.2.2. Overview of Temperature Field and Stress Field Theory in 3D Printing Process

(1) Theoretical analysis of temperature field:

In the 3D printing process, with the application of heat source, the energy transfer of the model temperature field is nonlinear, and the laser heat source moves continuously according to the scanning line. Therefore, according to the energy conservation and Fourier law, the energy transfer process is a transient process, and the transfer process satisfies the following equation [16]:

$$\frac{\partial}{\partial x}\left(k\frac{\partial T}{\partial x}\right) + \frac{\partial}{\partial y}\left(k\frac{\partial T}{\partial y}\right) + \frac{\partial}{\partial z}\left(k\frac{\partial T}{\partial z}\right) + \dot{q} = pc_p\frac{\partial T}{\partial t}.$$

(1)

According to formula (1), time is the first-order differential, and the space is the second-order differential. Therefore, we need to provide an initial value for time and two initial values for space to obtain the solution of the above formula and obtain the specific distribution of temperature field. According to the theory of temperature field heat transfer, the boundary conditions to be applied can be roughly divided into the following three types [17, 18]:

The first method is to determine the temperature on all boundaries of an object, that is, when the surface temperature of the object is known and unchanged:

$$\lambda \frac{\partial T}{\partial x} n_x + \lambda \frac{\partial T}{\partial y} n_y + \lambda \frac{\partial T}{\partial z} n_z = q_s(x, y, z, t). \quad (2)$$

The second is that the heat flux density of the object boundary is known:

$$\lambda \frac{\partial T}{\partial a} n_a + \lambda \frac{\partial T}{\partial b} n_b + \lambda \frac{\partial T}{\partial c} n_c = q_s(a, b, c, t). \quad (3)$$

The third is that the heat transfer coefficient between the boundary and the surrounding objects is known:

$$\lambda \frac{\partial T}{\partial x} n_x + \lambda \frac{\partial T}{\partial y} n_y + \lambda \frac{\partial T}{\partial z} n_z = h(T_\infty - T_s). \quad (4)$$

(2) Theoretical analysis of stress field:

In the process of 3D printing, the stress changes of materials are affected by various factors, so it is necessary to combine the temperature field theory with the stress field theory.

When the temperature of the object changes, the intermolecular force also changes, and the change of the molecular gap leads to the volume change and deformation of the object. When the body is not constrained, the thermal deformation can be expressed as [19–21]

$$\varepsilon_T = \frac{\Delta L_T}{L_0} = a(T_1 - T_0). \quad (5)$$

Due to the existence of thermal deformation, when the temperature of the object changes but it cannot deform freely, the original thermal deformation of the object cannot occur normally. If ΔL_e is used to represent the deformation amount of the object after being constrained, the deformation degree of the object is as follows:

$$\varepsilon_T = \frac{\Delta L_e}{L_0}. \quad (6)$$

Since the object cannot deform itself after temperature change, its original deformation is reflected in the object, and the deformation rate can be expressed as follows:

$$\varepsilon_T = \frac{\Delta L}{L_0}. \quad (7)$$

After the temperature changes, the amount of deformation inside the object exceeds the elastic limit. After the temperature returns to the initial value, the material cannot be restored to its original state, and then the residual stress will be generated inside the object. According to the deformation theory, the stress value and strain value of the object satisfy the following relationship:

$$\left(\frac{\partial^2 \varepsilon_x'}{\partial y^2} + \frac{\partial^2 \varepsilon_y'}{\partial x^2} - \frac{\partial^2 \gamma_{xy}'}{\partial x \partial y} \right) + \left(\frac{\partial^2 \varepsilon_x''}{\partial y^2} + \frac{\partial^2 \varepsilon_y''}{\partial x^2} - \frac{\partial^2 \gamma_{xy}''}{\partial x \partial y} \right) = 0,$$

$$R = -\left(\frac{\partial^2 \varepsilon_x''}{\partial y^2} + \frac{\partial^2 \varepsilon_y''}{\partial x^2} - \frac{\partial^2 \gamma_{xy}''}{\partial x \partial y} \right). \quad (8)$$

When $R = 0$, it means that there is elastic sex inside the object and it can be freely retracted and restored to its original state. $R \neq 0$ indicates that there is residual stress in the body.

2.3. Design of the 3D Printing System

2.3.1. Overall Design of the System. The overall design of 3D printing system mainly includes four parts, the main functions of each part are as follows:

(1) *Virtual Reality Interactive Device.* Use virtual reality to display hardware and interact with elements in unity

(2) *Printer Operation Control System.* Realize the control of printer printing, leveling, startup, and cooling

(3) *User Interface Control System.* Set the parameters of the printer and realize the state control

(4) *Model Analysis and Calculation System.* Comprehensively analyze the model to be printed, realize the calculation of the simple base support of the model, and calculate the running track of the printing nozzle [22]

The system realizes interaction through virtual reality equipment and then enters into the user interface to realize control and setting. After completing a series of operations, it realizes model analysis and calculation and determines the trajectory of printing nozzle in each layer of printing process, so as to realize printing. According to the coordinate system used, 3D printer can be divided into polar coordinate system and Cartesian coordinate system, according to the material forming principle. It can be divided into powder binder, sintering and melting, lamination manufacturing, melting deposition molding technology, polymer polymerization reaction, etc. The system designed in this paper is based on the Cartesian coordinate system, which can move in the straight direction of XYZ three axes. Each axis adopts small stepping motor with high precision and good precision and then uses subdivision control stepping motor to make its accuracy reach about 1 mm. The x-axis and y-axis adopt synchronous belt, which can accurately and quickly locate

according to the axial direction, and the z-axis adopts the screw for precise positioning. The main principle of material forming is deposition modeling technology. Simply put, the hot-melt plastic is heated at the designated position, then the thinner plastic wire is extruded, and finally the 3D object is made by depositing the plastic wire.

2.3.2. Design and Construction of the Mechanical System. In essence, 3D printing equipment is a three-axis CNC machine tool. The three-axis motion system is the key executive system of 3D printer mechanical system. The reasonable design of transmission structure and motion mode has a very important impact on the accuracy and efficiency of printing process, which will eventually affect the quality of printed products [23]. Therefore, a reasonable design scheme should be adopted for the three-axis motion system.

The motion platform of 3D printing equipment is composed of X, Y, Z three-axis motion platform, in which x-axis and y-axis coordinate to complete the horizontal movement in xoy plane of substrate, and deposition is mainly realized by the movement of these two axes; z-axis controls the up and down movement of the nozzle, controls the layer thickness, and completes the load-bearing work of the whole nozzle. The movement of the three axes is controlled by the stepping motor. At the same time, two limit switches are installed on each axis, and the sensing distance is 2 mm. It ensures the safety of the platform in the process of motion. Since all the deposition work in the molding process is realized by the movement of the moving platform, the accuracy and stability of the motion platform are the key to ensure the deposition quality. Therefore, the ball screw is selected as the transmission mechanism of the three motion platforms to ensure the stability of the molding process [24]. Among them, the lead of x-axis, y-axis, and z-axis is 10 mm, 10 mm, and 10 mm respectively, and the stroke of three motion platforms is 350 mm, 200 mm, and 250 mm, respectively.

2.3.3. Design and Construction of the Control System. The whole system control framework of the equipment is as follows:

(1) Main control module: this paper uses Mega2560 microcontroller as the lower computer of the control system.

(2) Motor drive module: in this paper, five stepper motors are used to realize the drive function of the control system. The x-axis and y-axis select one stepper motor to realize the precise positioning of the extrusion nozzle; the z-axis uses two stepper motors to drive the working platform to move up and down; the wire feeding mechanism also uses a stepper motor to drive the molten silk material out through the rotation of the stepping motor.

(3) Temperature control module: the module mainly heats the hot bed and extrusion nozzle and collects and feeds back the temperature. The heating temperature of the hot bed ensures that the silk material can stick to the working platform, while the temperature of the extrusion nozzle should ensure that the silk material can melt and print. The real-time temperature feedback ensures that the working environment is in a constant temperature state.

(4) Serial communication module: it is mainly used for data communication between upper computer and lower computer, receiving printing data, controlling command, monitoring printing process, and adjusting printing parameters timely according to feedback results.

(5) Data communication module: this module mainly includes display screen and SD card data reading. The display screen shows the printing status of the printing equipment, including printing speed, printing temperature, printing completion, etc.; the SD card is responsible for receiving and transferring G code in the printing process of 3D model.

In the whole 3D printing process, the microcontroller controls and sends out instructions, the stepper motor executes the received instructions, and the sensor monitors the temperature of the feedback nozzle and working platform in real time, forming a virtuous closed-loop control system [25].

3. Experimental Materials and Methods

3.1. Experimental Materials. The experimental material tin is widely used in various fields, including electronics, information, metallurgy, machinery, and so on. Because the metal tin has a low melting point, tin is used as the experimental material to debug the basic functions of metal 3D printing equipment based on electromagnetic induction heating technology.

Copper, which has conductivity, thermal conductivity, and ductility, plays an important role in human development. H65 brass is a kind of common brass which is widely used. It has good mechanical cutting performance, can be used as solder for brazing and welding, and has good mechanical properties. It is usually used as raw material for pin nut.

The raw materials used in the experiment are pure tin wire and brass wire, and the wire diameter is 4 mm.

As shown in Tables 1 and 2, the chemical compositions of pure tin wire and brass wire are listed.

3.2. Experimental Methods. In this paper, we collect the traffic data in the morning and evening of the same road section in the city. The data collection time is the first three days of the experimental simulation, and the data sampling interval is 5 minutes. This paper randomly selects the monitoring data of six sensors in the traffic section of the city. From the morning peak time (7:00–10:00) and the

TABLE 1: Chemical composition of pure tin.

Element	Sn	Mn
Content	99.1	0.9

TABLE 2: Chemical composition of H65 brass.

Element	Cu	Pb	P	Sb	Bi	Fe	Zn
Content	62.7–68	≥0.01	≥0.01	≥0.005	≥0.003	≥0.05	Allowance

evening peak time (17:00–20:00), each sensor collects and outputs the traffic data every 5 minutes and adds the daily weather data.

3.3. Experimental Evaluation Index

3.3.1. Performing Morphology Experiment. In this study, VK-X200K laser confocal microscope was used to synthesize the depth of field on the surface of the molded part, and the surface morphology, surface roughness, and weld bead overlap were observed.

3.3.2. Mechanical Property Test

(1) Microhardness:

In this experiment, Vickers hardness is used as the hardness test standard. The sample with high density and uniform microstructure is selected for measurement. The upper surface and section of the molded part are selected as the measurement position. After each measurement, after removing the load, the hardness value is calculated by measuring the diamond diagonal length of the measurement point on the sample surface. The calculation formula is shown in the following formula:

$$H_v = 1.8544 \frac{P_{\max}}{d^2}. \tag{9}$$

(2) Tensile property:

In this study, MTS (SANS) cmt5105 microcomputer controlled electronic testing machine is used to test, analyze, and study the static mechanical properties of metal, nonmetal, and composite materials, such as tensile strength, compressive strength, bending strength, modulus, and other parameters under different speed conditions, and according to national standards, ISO and ASTM, and other international standards for testing and data determination.

(3) Microstructure examination:

This experiment is to compare and analyze the metallographic structure of raw materials and formed samples. Therefore, the samples of wire and molded samples are taken and numbered in order, and then the samples are inlaid and the sealing of inlays is checked. The samples with good sealing performance were selected and analyzed by laser

confocal microscope and Fei quanta 250 FEG scanning electron microscope.

4. Experimental Results

4.1. Printing Error Experiment of Metal Materials. In the experimental stage, in order to facilitate the measurement of product size accuracy, standard spline is used to test. During the measurement, the dimensions of X, Y, and Z directions are mainly measured. The length measured in X direction is the total length of spline, Y direction is the original width of parallel length of spline, and Z direction is the thickness of spline. The original size of standard spline: $X = 98$ mm, $Y = 15$ mm, $Z = 3$ mm.

As shown in Figure 1, according to the comparative analysis results of multiple groups of parameters, when the layer thickness is 0.15 mm, the printing product has higher accuracy, and when the thickness of each layer is smaller, the total error of stacking molding is relatively small. When the printing speed is fast, the error of the product will increase. From the measurement results, when the printing speed is 35/mm, the dimensional accuracy of the products is higher.

4.2. Microhardness Test of Metal Materials. As shown in Figure 2, the hardness of the original tin material is $14.82HV_{0.05}$. After printing, the hardness fluctuates in the range of $11.70HV_{0.05}$–$12.50HV_{0.05}$, which is not much lower than that of the original tin material, indicating that the surface microhardness value of the formed parts after this process can basically reach the hardness value of the original material, reaching the casting process level. The hardness of the original copper is $16.20HV_{0.05}$, and the hardness after printing is $12.96HV_{0.05}$–$14.31HV_{0.05}$, which is 11.73% lower than that of the original copper, indicating that the surface microhardness of the copper formed by this process cannot reach the hardness value of the original material. From the metal materials formed after printing, it can be seen that the grains of the original copper wire are slender strips, and the grains of the molded parts are multilateral, and the grain size is larger than that of the original copper wire. At the same time, according to hall Petch formula, in a certain range, the smaller the grain size D, the greater the microhardness HV of the material. This also explains why the hardness of the printed parts becomes smaller.

4.3. Testing of Tensile Properties of Metal Materials. As shown in Figures 3 and 4, the ultimate tensile strength of the tin wire after melt deposition is slightly reduced. Compared
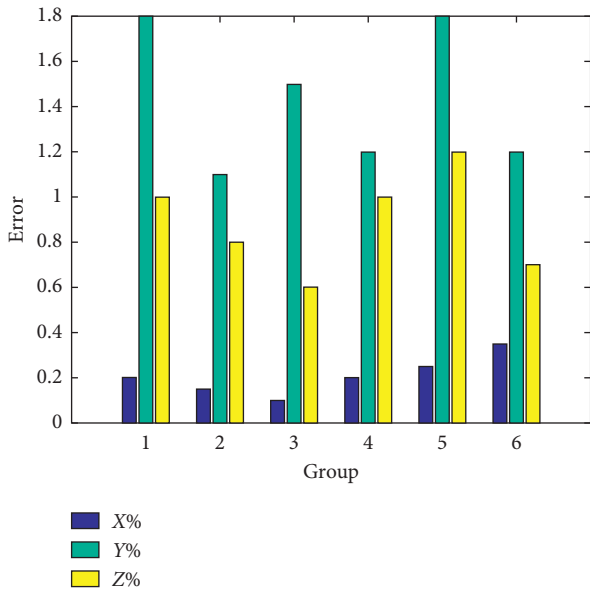
Figure 1: Print error results.

Figure 2: Hardness comparison of metal materials before and after molding.

Figure 3: Pattern stress-strain curve.
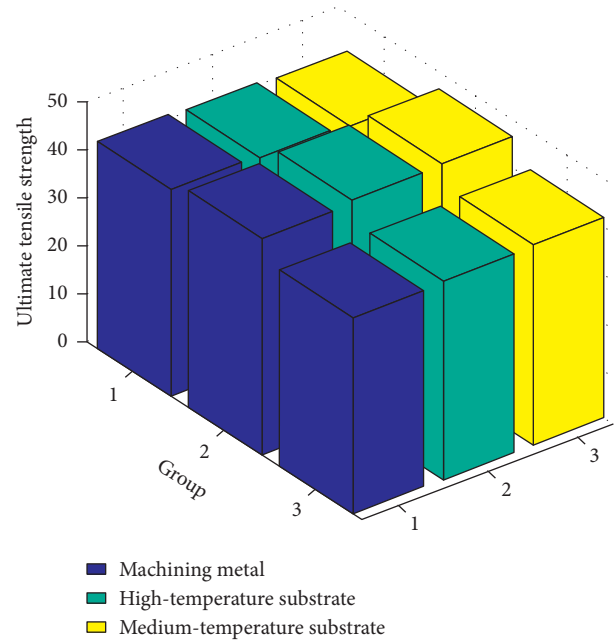
Figure 4: Ultimate tensile strength of tensile specimens.

with the machined tin parts, the ultimate tensile strength of the first group of samples is reduced by 1.58%, and that of the second group of samples is reduced by 0.74%. There are obvious bonding surfaces between the layers of the third group of samples, and the interlayer bonding strength is not high, showing multiple abrupt changes in the stress-strain curve. Value exists. It can be inferred from the test results that the reduction of ultimate tensile strength of the molded parts is mainly due to the influence of interlayer bonding properties. The metal 3D printing equipment based on electromagnetic induction heating technology designed in this paper will slide when the bonding interface between layers is subjected to a certain tensile force during the drawing process. Therefore, if the interlayer bonding is not firm, the overall mechanical properties of the formed parts will slightly decrease.

5. Conclusions

3D printing technology has a decade of development, although it is widely used in the industrial field and has certain achievements. However, due to the rapid development of modern software technology and the Internet, the improvement of 3D printer has attracted much attention. The processing method of 3D printing technology is to accumulate layer by layer, without any mechanical processing and mold. All shape parts can be generated directly through computer graphics data, so as to shorten product development cycle,

improve product productivity, and effectively reduce production costs.

In this paper, the design of 3D printing experience system in virtual reality technology is analyzed. The research results can be used for 3D printer printing design of melt deposition molding and also can be used for the development of virtual printing system of 3D printing technology. In this paper, the overall scheme design of 3D printer is carried out. The motion mode of electromagnetic induction nozzle and printing table, system composition, and design/selection principle of each subsystem are determined. The mechanical structure and electrical system of the equipment are optimized. The feasibility of base metal deposition process is verified by using low melting point pure tin wire and high melting point copper alloy wire as experimental materials. The mechanical properties of the formed parts were studied in terms of strength and microstructure. By testing the system designed in this paper, it shows that the system can provide intuitive, safe, and efficient experience platform for people.

There are many deficiencies in this study. This paper only studies the melting deposition of tin and copper, and it needs to study the properties of many kinds of metal wire materials in the future. It is necessary to optimize the structure of the induction nozzle based on high-temperature environmental protection metal 3D printing equipment, so as to increase the molding speed and improve the molding quality.

Data Availability

The data that support the findings of this study are available from the corresponding author upon reasonable request.

Conflicts of Interest

The authors declare no conflicts of interest.

References

[1] B. G. Compton and J. A. Lewis, "3D-printing of lightweight cellular composites," *Advanced Materials*, vol. 26, no. 34, pp. 5930–5935, 2015.

[2] S. Hong, D. Sycks, H. F. Chan et al., "3D printing: 3D printing of highly stretchable and tough hydrogels into complex, cellularized structures (adv. Mater. 27/2015)," *Advanced Materials*, vol. 27, no. 27, p. 4034, 2015.

[3] J. Edgar and S. Tint, "Additive manufacturing technologies: 3D printing, rapid prototyping, and direct digital manufacturing," *Johnson Matthey Technology Review*, vol. 59, no. 3, pp. 193–198, 2015.

[4] M. Zarek, M. Layani, I. Cooperstein et al., "3D printing of shape memory polymers for flexible electronic devices," *Advanced Materials*, vol. 28, no. 22, p. 4166, 2015.

[5] L. E. Murr and W. L. Johnson, "3D metal droplet printing development and advanced materials additive manufacturing," *Journal of Materials Research and Technology*, vol. 6, no. 1, pp. 77–89, 2017.

[6] R. Li, Y. S. Kim, H. V. Tho, Y. J. Yum, W. J. Kim, and S. Y. Yang, "Additive manufacturing (AM) of piercing punches by the PBF method of metal 3D printing using mold steel powder materials," *Journal of Mechanical Science and Technology*, vol. 33, no. 2, pp. 809–817, 2019.

[7] C. Buchanan and L. Gardner, "Metal 3D printing in construction: a review of methods, research, applications, opportunities and challenges," *Engineering Structures*, vol. 180, no. 1, pp. 332–348, 2019.

[8] U. Ecke, L. Klimek, W. Müller, R. Ziegler, and W. Mann, "Virtual reality: preparation and execution of sinus surgery," *Computer Aided Surgery*, vol. 3, no. 1, pp. 45–50, 2015.

[9] P. H. Cosman, P. C. Cregan, C. J. Martin, and J. A. Cartmill, "Virtual reality simulators: current status in acquisition and assessment of surgical skills," *ANZ Journal of Surgery*, vol. 72, no. 1, pp. 30–34, 2015.

[10] E. Bastug, M. Bennis, M. Medard, and M. Debbah, "Toward interconnected virtual reality: opportunities, challenges, and enablers," *IEEE Communications Magazine*, vol. 55, no. 6, pp. 110–117, 2017.

[11] G. L. Nieder, J. N. Scott, and M. D. Anderson, "Using QuickTime virtual reality objects in computer-assisted instruction of gross anatomy: yorick—the VR Skull," *Clinical Anatomy*, vol. 13, no. 4, pp. 287–293, 2015.

[12] B. Riecke, H. Veen, and H. Bülthoff, "Visual homing is possible without landmarks: a path integration study in virtual reality," *Presence: Teleoperators and Virtual Environments*, vol. 11, no. 5, pp. 443–473, 2015.

[13] L. E. Murr, "A metallographic review of 3D printing/additive manufacturing of metal and alloy products and components," *Metallography Microstructure & Analysis*, vol. 7, no. 3, pp. 1–30, 2018.

[14] L. J. Kumar, P. M. Pandey, and D. I. Wimpenny, "Metal powder based additive manufacturing technologies—business forecast," *3D Printing and Additive Manufacturing Technologies*, vol. 10, pp. 105–118, 2019.

[15] P. Mellin, C. Jönsson, M. Åkermo et al., "Nano-sized by-products from metal 3D printing, composite manufacturing and fabric production," *Journal of Cleaner Production*, vol. 139, no. 15, pp. 1224–1233, 2016.

[16] Z. Baoqing, M. I. Farid, Y. Shuo, C. Cong, and S. Zhang, "Finite element simulation, analysis and research on the influence of 3D printing parameters on forming precision," *Recent Patents on Engineering*, vol. 13, no. 4, pp. 448–454, 2019.

[17] Z.-D. Shan, Z. Guo, D. Du, and F. Liu, "Coating process of multi-material composite sand mold 3D printing," *China foundry*, vol. 14, no. 6, pp. 498–505, 2017.

[18] B. Hu, X. Duan, Z. Xing et al., "Improved design of fused deposition modeling equipment for 3D printing of high-performance PEEK parts," *Mechanics of Materials*, vol. 137, no. Oct., pp. 103139.1–103139.8, 2019.

[19] Y. Ju, L. Wang, H. Xie, G. Ma, Z. Zheng, and L. Mao, "Visualization and transparentization of the structure and stress field of aggregated geomaterials through 3D printing and photoelastic techniques," *Rock Mechanics and Rock Engineering*, vol. 50, no. 6, pp. 1383–1407, 2017.

[20] I. M. Cotabarren, S. Cruces, and C. A. Palla, "Extrusion 3D printing of nutraceutical oral dosage forms formulated with monoglycerides oleogels and phytosterols mixtures," *Food Research International (Ottawa, Ont.)*, vol. 126, no. Dec, pp. 108676.1–108676.11, 2019.

[21] S. C. Park, R. Song, S. Kim, H. K. Kim, S.-H. Kim, and J. Lee, "Fabrication of artificial arteriovenous fistula and analysis of flow field and shear stress by using μ-PIV technology," *Journal of Mechanical Science and Technology*, vol. 30, no. 12, pp. 5503–5511, 2016.

[22] J. An, J. E. M. Teoh, R. Suntornnond, and C. K. Chua, "Design and 3D printing of scaffolds and tissues," *Engineering*, vol. 1, no. 2, pp. 261–268, 2015.

[23] R. J. Mobbs, M. Coughlan, R. Thompson, C. E. Sutterlin, and K. Phan, "The utility of 3D printing for surgical planning and patient-specific implant design for complex spinal pathologies: case report," *Journal of Neurosurgery: Spine*, vol. 26, no. 4, pp. 513–518, 2017.

[24] H. J. Huang, G. D. Zhang, H. B. Ouyang et al., "[Internal fixation surgery planning for complex tibial plateau fracture based on digital design and 3D printing]," *Journal of Southern Medical University*, vol. 35, no. 2, pp. 218–222, 2015.

[25] A. Kantaros, N. Chatzidai, and D. Karalekas, "3D printing-assisted design of scaffold structures," *International Journal of Advanced Manufacturing Technology*, vol. 82, no. 1-4, pp. 559–571, 2016.

Research Article

Treatment Technology of Microbial Landscape Aquatic Plants for Water Pollution

Ming Hu[1] **and Lei Li** [2]

[1]*College of Environment and Life Science, Weinan Normal University, Weinan 714000, Shaanxi, China*
[2]*College of Tourism, Xinyang Normal University, Xinyang 464000, Henan, China*

Correspondence should be addressed to Lei Li; stanley9065@126.com

With the rapid development of industrial and agricultural production, the rapid growth of population, and the acceleration of urbanization, the problem of water pollution is becoming more and more serious. Water shortages and pollution disrupt the balance of ecosystems and seriously limit people's health and rapid economic development. Nowadays, the method of repairing sewage bodies using microbial landscape aquatic plants is attracting more and more attention, and it is a big challenge to maintain the sustainable development of human beings and nature. This paper uses floating rafts to combine microorganisms and landscape aquatic plants to conduct sewage treatment experiments. According to microorganisms, landscape aquatic plants absorb nutrients in the water body, examine the changes in water quality during the restoration of microorganisms' landscape aquatic plants, and establish the growth of microorganisms' landscape aquatic plants. The relationship with changes in water quality aims to provide a theoretical basis for the treatment of slow-flowing water bodies such as lakes, reservoirs, large artificial ponds, and rivers. In this paper, the experiments are divided into four groups (*A* (experimental sewage + microbial inoculant), *B* (experimental sewage + plant), *C* (experimental sewage + microbial inoculant + plant), and *D* (experimental sewage)). It can be divided into the total nitrogen content, total phosphorus content, and COD value data, and chromaticity detection of each group of the test is continuously monitored weekly to comprehensively detect and observe the repair effect on contaminated water bodies. The experiment proved that the water quality of the three treatment groups was significantly clearer than that of the blank control group, and its clarity: microorganism + plant > microorganism > plant > blank control group. This shows that the combination of microorganisms and landscape aquatic plants can effectively reduce the various pollutants contained in sewage and reduce the color of sewage. Treating sewage using plant technology that combines microorganisms is feasible and promising.

1. Introduction

Water is an important resource for human survival, and it is closely related to people's lives. With the continuous development of the society and the increase of industrial production, a large number of pollutants discharged have caused serious damage to drinking water resources, and people's drinking water safety has great hidden dangers. According to monitoring, the groundwater in most domestic cities is currently polluted by point and nonpoint sources to varying degrees, and the degree of pollution is getting worse. For this reason, it has always been a research focus to find a drinking water treatment process with stable effluent and strong applicability. As a major decomposer of ecosystems, microorganisms play an important role in maintaining a stable balance and material cycle of ecosystems. The active growth of microorganisms promotes the decomposition of various pollutants in the water area, optimizes the water environment, and leads to the growth of plants. The two synergies in treating water pollution have good prospects for improving available nutrients.

The use of microbial landscape aquatic plant treatment technology abroad to treat water pollution is much faster than in China, and the development and renewal of water pollution treatment technology are rapid. Water pollution prevention methods have been significantly improved and developed. In the near future, the use of microbial landscape aquatic plants is expected to be an important breakthrough.

Broussard and Devkota found that the turbidity of the effluent of the process was stabilized below 0.1 NTU through the coagulation/ultrafiltration process treatment of a micropolluted water source, and it was not affected by the turbidity of the raw water, and it had strong impact load resistance [1]. Beale et al. have conducted experiments to study the combined process of suspension production biological treatment and ultrafiltration to treat artificially simulated micropolluted source water. The experiment shows that when the hydraulic retention time is 2–4 h, the average removal rate of ammonia nitrogen by the combined process can reach more than 85% [2]. Zheng and Rong conducted indoor simulation experiments using four aquatic plants, targeting water bodies with severe eutrophication. The results show that the four submerged plants have a good reducing effect on total nitrogen and total phosphorus, and the COD content tends to decrease overall [3].

The use of microbial landscape aquatic plant treatment techniques to treat water pollution began in Western countries. Compared to Western countries, our country's water pollution treatment technology started late, and its development is relatively slow. With the continued development of science and technology and the gradual increase in people's awareness of environmental protection, the use of microbial landscape aquatic plants can improve the progress of water pollution research. Stepanov et al. compared direct ultrafiltration and coagulation-ultrafiltration processes on the treatment of micropolluted water containing high ammonia nitrogen. It is found that the direct filtration of ultrafiltration membranes has a poor removal rate of ammonia nitrogen, with a removal rate of only about 7%. This is because the ultrafiltration membrane is only a pure physical filtration process, and it is difficult to remove the soluble ammonia nitrogen in the water [4]. Sokolova et al. used plant floating beds for water environment management. Experiments were conducted for three groups of controls, and different plants were used for control treatment, respectively, showing that the three plants have good degradation effects on total nitrogen, total phosphorus, and COD [5]. Astsaturov et al. used 6 different aquatic plants to treat polluted waters. Studies have shown that six plants have a better phosphorus-removing effect than nitrogen-removing, with no apparent reduction in COD content [6].

This study adopts microbial landscape aquatic plant treatment technology, takes the sewage from the suburban sewage ditch as the target, uses floating raft fixation technology to organically combine microorganisms and landscape aquatic plants to carry out the indoor simulation test of sewage treatment, and uses water exchange to simulate the actual suburban sewage; the discharge of new pollutants into the ditch has been continuously monitored for two weeks. The test achieved good results. At the same time, this article uses fast digestion spectrophotometry to detect the content of major pollutants in sewage and further test other metrics in sewage. It analyzes the quality of the sewage under the test, screens aquatic plants in the microbial landscape, and provides rationale and reference indicators.

2. Treatment Technology of Microbial Landscape Aquatic Plants for Water Pollution

2.1. Support Vector Machine Algorithm to Predict the Degree of Water Pollution Control

2.1.1. Support Vector Regression Algorithm. (1) *Linear Support Vector Regression Machine.* Suppose that the sample dataset is denoted as $\phi: R^n \longrightarrow H\{x_k, y_k\}_{k=1}^N$, where N is the number of samples, the input data $x_k \in R^n$ is n dimensional, and the output data $y_k \in R^n$ corresponds to the input data x_k. Suppose that the linear regression function is

$$f(x) = w^T x + b, \tag{1}$$

where $w \in R^n, b \in R$, and w are normal vectors. The loss function is used as follows:

$$|y - f(x)|_\varepsilon = \begin{cases} 0, & if \, |y - f(x)| \le \varepsilon, \\ |y - f(x)| - \varepsilon, & \text{otherwise.} \end{cases} \tag{2}$$

Among them, ε is the preset tolerable loss function, and the distance between the two dotted lines is $2/\|w\|$. The optimization goal of the algorithm is to maximize the distance, that is, minimize the reciprocal of the logarithmic distance [7, 8]. Finally, the process of finding the most suitable regression function is transformed into

$$\min \frac{1}{2}\|w\|^2. \tag{3}$$

The penalty parameter C and the relaxation factor ξ_i and ξ_i^* are introduced, and the optimization problem corresponding to the regression estimation is transformed into

$$\min_{w,b} P = \min \frac{1}{2}\|w\|^2 + C \sum_{i=1}^N (\xi_i + \xi_i^*). \tag{4}$$

The constraints that should be met are

$$\begin{cases} y_i - w^T x_i - b \le \varepsilon + \xi_i, & i = 1, \dots, N \\ w^T x_i + b - y_i \le \varepsilon + \xi_i, & i = 1, \dots, N \\ \xi_i, \xi_i^* \ge 0, & i = 1, \dots, N \end{cases} \tag{5}$$

Lagrangian dual functions are usually introduced to solve the above convex quadratic programming problem. The Lagrangian dual function is constructed as follows:

$$L(w, b, \xi_i, \xi_i^*, a, a^*, \eta, \eta^*) = \frac{1}{2}\|w\|^2 + C \sum_{i=1}^N (\xi_i + \xi_i^*) - \sum_{i=1}^N a_i (\varepsilon + \xi_i - y_i + w^T x_i + b) - C \sum_{i=1}^N (\eta_i \xi_i + \eta_i^* \xi_i^*). \tag{6}$$

The Lagrangian multiplier is introduced, which turns the problem into a solution:

$$\max_{a,a^*,\eta,\eta^*} \min_{w,b,\xi,\xi^*} L\left(w,b,\xi,\xi^*,a,a^*,\eta,\eta^*\right). \tag{7}$$

Taking the Lagrangian dual function to differentiate $w, b, \xi,$ and ξ^* and equal to zero, this dual problem can be transformed into a convex quadratic programming problem:

$$\max_{a,a^*} J_D\left(a,a^*\right) = -\frac{1}{2}\sum_{k,i=1}^{N}\left(a-a^*\right)\left(a_k-a_k^*\right)x_i^T x_k \tag{8}$$
$$-\varepsilon\sum_{i=1}^{N}\left(a_i+a_i^*\right)+\sum_{i=1}^{N}y_i\left(a_i-a_i^*\right).$$

The conditions are

$$\sum_{i=1}^{N}\left(a_i-a_i^*\right)=0, \quad a_i a_i^* \in [0,c]. \tag{9}$$

The final target-fitting regression function is expressed as

$$f(x) = \sum_{i=1}^{N}\left(a_i-a_i^*\right)x_i^T x + b. \tag{10}$$

Through deduction, it can be seen that the number of support vectors in SVM is limited. It is the input sample x_i corresponding to those a_i which is not zero. Only the input vector that meets this condition can contribute to the SVM model. This is the sparsity of the SVM solution [9, 10].

(2) *Nonlinear Support Vector Regression Machine.* Polynomial kernel functions are highly generalized and belong to global kernel functions, but the price paid is inadequate in adapting to nonlinear problems. The nonlinear SVM problem can be described as solving the following problem:

$$\max_{a,a^*} J_D\left(a,a^*\right) = -\frac{1}{2}\sum_{k,j=1}^{N}\left(a_i-a_i^*\right)\left(a_k-a_k^*\right)K\left(x_i,x_k\right)$$
$$-\varepsilon\sum_{i=1}^{N}\left(a_i+a_i^*\right)+\sum_{i=1}^{N}y_i\left(a_i-a_i^*\right). \tag{11}$$

The conditions are

$$\sum_{i=1}^{N}\left(a_i-a_i^*\right)=0, \quad a_i a_i^* \in [0,c]. \tag{12}$$

The final target-fitting regression function is expressed as

$$f(x) = \sum_{i=1}^{N}\left(a_i-a_i^*\right)K\left(x_i,x\right) + b. \tag{13}$$

When there is a lack of prior knowledge in the relevant fields of sample data, the radial basis kernel function is generally selected as the kernel function, which can better balance the fitting effect and generalization ability than other kernel functions [11, 12]. The expression of the radial basis kernel function is as follows:

$$K\left(x',x\right) = \exp\left(\frac{-\|x-x'\|^2}{\sigma^2}\right), \tag{14}$$

where σ is a parameter that characterizes the width of the core.

2.1.2. Entropy Method for Weight. With m evaluation objects and n evaluation indicators, the original data matrix $X = (x_{ij})_{m\times n}$ can be formed:

$$X = \begin{bmatrix} x_{11} & x_{12} & \cdots & x_{1n} \\ x_{21} & x_{22} & \cdots & x_{2n} \\ \vdots & \vdots & x_{ij} & \vdots \\ x_{n1} & x_{n2} & \cdots & x_{nn} \end{bmatrix}. \tag{15}$$

In the formula, x_{ij} is the evaluation value of the i evaluation object on the j index.

(1) *Standardized Processing of Raw Data.* In the evaluation index system of the new smart city, due to the different meanings of different indicators and different quantification units, it is impossible to directly carry out weighting calculations, and a standardized matrix $Y = (x'_{ij})_{m\times n}$ can be obtained:

$$x'_{ij} = \frac{x_{ij}-\min\{x_{ij}\}}{\max\{x_{ij}\}-\min\{x_{ij}\}}, \quad i=1,2,\ldots,m, \tag{16}$$

where x'_{ij} represents the normalized value of the i evaluation object on the j evaluation index and x_{ij} represents the original data value of the i evaluation object on the i evaluation index.

(2) *Calculate Indicator Weight.* Transform the standardized value of each evaluation index in the standardized matrix $Y = (x'_{ij})_{m\times n}$ to calculate the contribution Z_{ij} of the j index and the i evaluation object:

$$Z_{ij} = \frac{x'_{ij}}{\sum_{i=1}^{m} x'_{ij}}. \tag{17}$$

Calculate the information entropy of each indicator:

$$e_j = -\frac{1}{\ln m}\sum_{i=1}^{m} Z_{ij} \ln Z_{ij}. \tag{18}$$

Among them, when defining $Z_{ij}=0$, $Z_{ij}\ln Z_{ij}=0$. Calculate information entropy redundancy:

$$d_j = 1 - e_j. \tag{19}$$

Calculate the weight of the indicator:

$$\omega = \frac{d_j}{\sum_{j=1}^{n} d_j} = \frac{\left(1-e_j\right)}{n-\sum_{j=1}^{n} e_j}, \quad j=1,2,\ldots,n. \tag{20}$$

2.2. Water Pollution Treatment Technology. As an important element of production and life, water resources are directly related to the sustainable development of mankind. The

water body has a certain purification ability. Through a series of physical, chemical, and biological reactions, the concentration of pollutants in the water body is reduced, and the toxic and harmful substances are decomposed or reduced. When the degree of pollution is greater than the self-purification energy of the water body, the ecological environment of it is damaged, and it is necessary to use appropriate technical means for sewage treatment [13–15].

2.2.1. Water Diversion and Pollution Flushing Technology. Water conversion flushing technology uses engineering techniques to transfer large amounts of clean water to polluted waters and dilute pollutants. Introduced clean water generally has a high dissolved oxygen content, which allows the body of water to flow, reduces the concentration of pollutants, and increases the oxygen content of the body of water to improve its self-purification capacity [16, 17]. No complicated operation techniques or equipment systems are required, and sewage can be treated quickly. It is commonly used for emergency treatment of small contaminated water. However, while flushing the body of water, sedimented pollutants are reintroduced into the body of water, causing two secondary pollutions, affecting the water bodies of the downstream basins and causing specific pollution in the downstream water bodies. On this basis, due to the introduction of a large amount of new water into the water body, the original river water level rise is very likely to cause the river to divert, and the project cost is huge, which further shows that this method cannot solve the fundamental problem [18, 19].

2.2.2. Sediment Dredging Technology. Use the relevant mechanical equipment to discharge the mud at the bottom of the river, and reduce the harmful substances and precipitated pollutants in the water through the mud removal method. Since the rock-containing substances are generally deposited on the surface of the river bottom mud, the mud removal by this method can also effectively reduce the mud and the total rock content and further expand the water capacity of rivers and lakes [20, 21]. It can effectively reduce pollution of rivers and lakes and improve the water quality of rivers and lakes and the surrounding environment. However, this technology has many limitations. It is necessary to consider the depth and area of excavation. Large-scale specialized equipment should be equipped during construction. Narrow rivers cannot be built and require a lot of financial support. Reducing endogenous pollution and controlling pollution in rivers and lakes cannot achieve good results, especially in the treatment of eutrophic lakes, especially when external pollution is not effectively managed.

2.2.3. Masking Isolation Technology. By using sand, clay, and high-aggregate physical materials to cover the bottom mud, it prevents the organic matter and heavy metal pollutants in the bottom mud of the river from entering the upper water body due to the flow of river water and the accumulation of bottom mud, effectively removing the water and polluting

mud from the mud. Isolation has a more obvious effect on improving the quality of water bodies [22, 23]. Masking separation technology is relatively easy to operate, does not require complicated process equipment, and has less potential harm to the surrounding environment. However, adding material originally based on rivers and lakes reduces the effective water capacity of rivers and lakes. Structures that cover and isolate shallow river bottom mud can change the topography of the riverbed. Riverbed mud is an integral part of the entire aquatic ecosystem and is part of the aquatic environment. It is quarantined by the coverage of other sources. Abandoning sediment purification capacity destroys the normal ecological circulation system of the entire body of water, increases the amount of engineering, and requires enormous financial support. Therefore, it is not suitable for uneconomical areas or waters with shallow rivers and small lakes. Its technical limits are better suited for the treatment and repair of deep-sea sediments.

2.2.4. Artificial Oxygen Enhancement Technology. By using the original natural conditions of the river or existing building facilities, on the basis of the pollution and hypoxia of the water body, artificial means are used to increase the amount of dissolved oxygen in the water body, accelerate the metabolism of animals, plants, and microorganisms in the water body, and strengthen the improvement of the purification ability of the water body, thus achieving the purpose of improving water quality [24, 25]. Through mechanical means, adding aeration and oxygenation equipment and improving the purification ability of the polluted water body and the surrounding ecological circle greatly increase the dissolved oxygen content of the water body and have a good effect on the reduction of total nitrogen, total phosphorus, and COD content. The effect is also conducive to the loosening of the river bottom silt to become tighter and to prevent the pollutants in the bottom sludge from entering the upper water body. However, this technology has certain limitations, and the larger energy consumption is not suitable for the pollution control of more water bodies.

2.2.5. Mechanical Algae Removal Technology. This technology uses various mechanical methods to control water pollution caused by the explosive growth of algae. Generally, the technical methods used include artificial arching, ultrasonic method, air flotation technology, and mixed method. This technology method is generally used for the excessive growth of algae. For rivers and lakes that cause eutrophication, the mechanical methods, processes, and equipment vary greatly [26]. It can directly change the growth of algae caused by nutritional temples and effectively avoid secondary pollution. However, the operation cost is expensive and can only be applied to the treatment of small polluted water bodies. It has obvious limitations and serves as an emergency removal. Algae technology cannot fundamentally solve the eutrophication of water bodies caused by algae outbreaks.

3. Experimental Design of Treatment Technology of Microbial Landscape Aquatic Plants

3.1. Test Subject. In order to avoid the difference in the test water samples between the groups, the test water sample selected in this paper is the sewage from the suburban sewage ditch in a district. Through the investigation of the landscape aquatic plant resources, it is better to adapt and purify. The principle of high operability, good landscape effect, and high reuse value comprehensively considers the cost issue, adjusts measures to local conditions, conducts screening tests on the growth characteristics and pollution tolerance of aquatic plants, and checks the domestic and foreign research on the use of aquatic plants to control water pollution. Literature data and analysis select the following 4 common landscape aquatic plants for this test plant, and the types and growth characteristics of the 4 test plants are shown in Table 1. First, each plant was used as a group and a blank control group to conduct a comparative experiment. The total nitrogen content, total phosphorus content, and COD value data of each group were continuously monitored for two weeks. At the same time, this article again divides the experiment into 4 groups (*A* (experimental sewage + microbial inoculants), *B* (experimental sewage + plants), *C* (experimental sewage + microbial inoculants + plants), and *D* (experimental sewage)) for comparison experiments. Continuously monitor the total nitrogen content, total phosphorus content, COD value data, and color detection of each group for two weeks, and comprehensively detect and observe its repair effect on polluted water bodies.

3.2. Experimental Method

3.2.1. Plant Pretreatment. Before the phytoremediation test, the test plant must be pretreated. Divide the four plants into plants, and rinse the root soil with tap water. Based on ensuring the integrity of the root system, the plant should be skillfully pruned to reduce dead branches and leaves to ensure the healthy growth of the plant. The treated plants were cultivated in plastic buckets with sewage, depending on the species. The duration was 3 days, and we chose vibrant plants for the phytoremediation test.

3.2.2. Test Various Indicators. The test was conducted in a room that could be exposed to sunlight. The test time is from November 15th to November 30th, 2020. Room temperature is maintained at 25–30°C for 2 weeks. On the first day of the test, 100 L of fresh sewage was added to each test group in order to simulate that new pollutants were discharged into the actual sewage ditch everyday. After that, each test group changes 10 L of water daily. Total nitrogen, total phosphorus, COD levels, and chromaticity are tested every two days. The sampling time is 8:00 am, and the water is changed after sampling (if there is no sampling test on the water exchange day, the water exchange time is 8:00 am).

TABLE 1: Test plant species and growth characteristics.

Plant	Family name	Ecological habits
Eichhornia crassipes	Yujihuaceae	Perennial floating leaf type
Cyperus alternifolius	Sphagaceae	Perennial emergent
Phragmites communis	Gramineae	Perennial emergent
Scirpus validus vahl	Sphagaceae	Perennial emergent

3.3. Establish a Model Evaluation Index System. A metric is a specific metric that is determined according to several metric goals and can reflect some of the basic characteristics of the valuation target. Indicators are concrete, measurable, and target observation points. By actually observing the object, you can draw clear conclusions. In general, a metric system contains three levels of metric that are related to gradual decomposition and improvement. Among them, the 1st level and 2nd level metrics are relatively abstract and cannot be used as a direct basis for assessment. Third-level metrics need to be concrete, measurable, and behavior-oriented and can be used as a direct basis for teaching assessment.

3.4. Statistical Processing. Statistical analysis was performed with SPSS 13.0 statistical software. The significance test of the difference was performed by one-way analysis of variance. The difference between the two groups was tested by LSD-*t*. The results of total nitrogen, total phosphorus, and COD in sewage were performed by the group *t*-test. $P < 0.05$ is considered to be significant and statistically significant.

4. Treatment Technology of Microbial Landscape Aquatic Plants

4.1. Results of Treatment of Sewage by Experimental Plants

4.1.1. Change Trend of Total Nitrogen Content of Each Group in the Experiment. Through the continuous monitoring of the total nitrogen content of each group of test water bodies for a period of one month, the results are shown in Table 2.

It can be seen from Figure 1 that compared with the blank control group, the four plants all have different degrees of degradation effects on the total nitrogen in the sewage: among them, the water hyacinth group has the best degradation effect on the total nitrogen in the sewage, which is obviously ahead of that in the other groups; after two weeks of the test, the total nitrogen content decreased from 12.2 mg/L at the beginning of the test to 6.78 mg/L, and the degradation rate was 44.43%; the reed group had a better degradation effect on the total nitrogen in the sewage. The content was reduced to 7.62 mg/L, and the degradation rate was 37.54%; then, the water onion group had a poor degradation effect on the total nitrogen in the sewage, the total nitrogen content was reduced to 8.37 mg/L, and the degradation rate was 31.39%; the last was drought. The umbrella grass group reduced the total nitrogen content in the sewage, the total nitrogen content was reduced to 8.73 mg/L, and the degradation rate was 28.44%. The analysis of variance showed that the four treatment groups with added plants had significant differences in the removal effect of total nitrogen in sewage from the blank control group ($P < 0.05$).
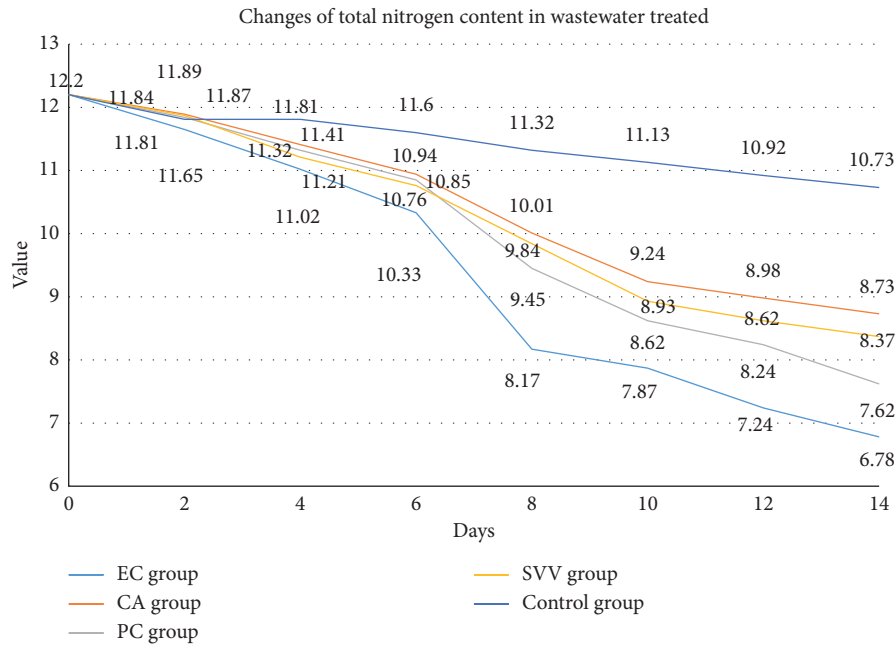
FIGURE 1: Changes of total nitrogen content in wastewater treated by plants.

TABLE 2: Data table of changes in total nitrogen content of wastewater treated by plants.

Day	EC group	CA group	PC group	SVV group	Control group
0	12.20	12.20	12.20	12.20	12.20
2	11.65	11.89	11.84	11.87	11.81
4	11.02	11.41	11.32	11.21	11.81
6	10.33	10.94	10.85	10.76	11.60
8	8.17	10.01	9.45	9.84	11.32
10	7.87	9.24	8.62	8.93	11.13
12	7.24	8.98	8.24	8.62	10.92
14	6.78	8.73	7.62	8.37	10.73

TABLE 3: The change data table of the total content of each plant treated sewage.

Day	EC group	CA group	PC group	SVV group	Control group
0	1.72	1.72	1.72	1.72	1.72
2	1.65	1.68	1.63	1.67	1.72
4	1.59	1.64	1.53	1.62	1.70
6	1.52	1.58	1.40	1.56	1.67
8	1.42	1.52	1.31	1.45	1.71
10	1.30	1.49	1.17	1.34	1.78
12	1.18	1.42	1.09	1.23	1.86
14	1.01	1.35	0.92	1.29	1.95

Therefore, the addition of plants effectively promoted the reduction of total nitrogen in sewage.

4.1.2. The Change Trend of the Total Phosphorus Content of Each Group in the Experiment. Through continuous monitoring of the total phosphorus content of each group of test water bodies for two weeks, the results are shown in Table 3.

Figure 2 shows that all four plants have different levels of degradation effect on total phosphorus in sewage compared to the blank control group. Among them, the reed group has the most decomposing effect on total phosphorus in sewage. Sewage is significantly more advanced than the other groups. Two weeks after the test, the total phosphorus content decreased from 1.72 mg/L at the start of the test to 0.92 mg/L, with a degradation rate of 46.51%. Second, the water hyacinth group showed a better degradation effect on total phosphorus in sewage. The content was reduced to 1.01 mg/L, and the degradation rate was 41.28%. After that, the onion group had a low decomposition effect on total phosphorus in the sewage, the total phosphorus content decreased to

1.29 mg/L, and the decomposition rate was 25.00%. The last was a drought. The umbrella glass group reduced the total phosphorus content in the sewage, the total phosphorus content was reduced to 1.35 mg/L, and the degradation rate was 21.51%. Analysis of variance showed that the four treatment groups with the addition of plants had a significant difference in the effect of removing total phosphorus in sewage from the blank control group ($P < 0.05$). Therefore, the addition of plants effectively helped reduce the total phosphorus content of the sewage.

4.1.3. Test the COD Value Change Trend of Each Group. Through continuous monitoring of the COD value of each group of test water bodies for two weeks, the results are shown in Table 4.

It can be seen from Figure 3 that compared with the blank control group, the four plants all have different degrees of degradation effects on COD in sewage: among them, the water hyacinth group has the best degradation effect on COD in sewage, which is significantly ahead of the other
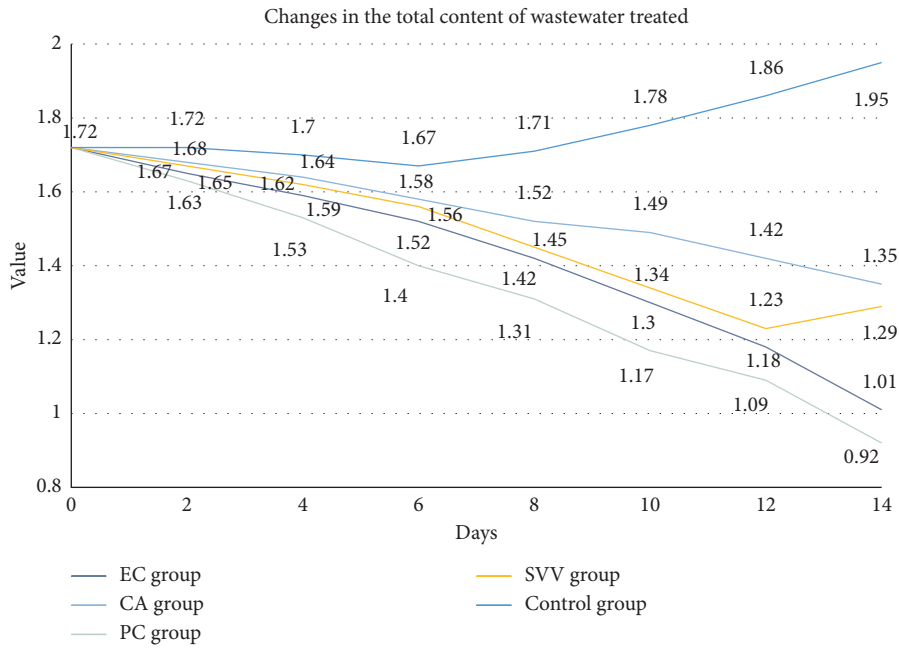
Changes in the total content of wastewater treated

Figure 2: Changes in the total content of wastewater treated by plants.

Table 4: Data table of changes in COD content of sewage treated by plants.

Day	EC group	CA group	PC group	SVV group	Control group
0	196	196	196	196	196
2	189	194	191	194	200
4	181	188	185	188	195
6	172	183	179	181	190
8	157	179	164	176	188
10	144	174	162	170	186
12	140	170	156	166	185
14	137	168	151	163	183

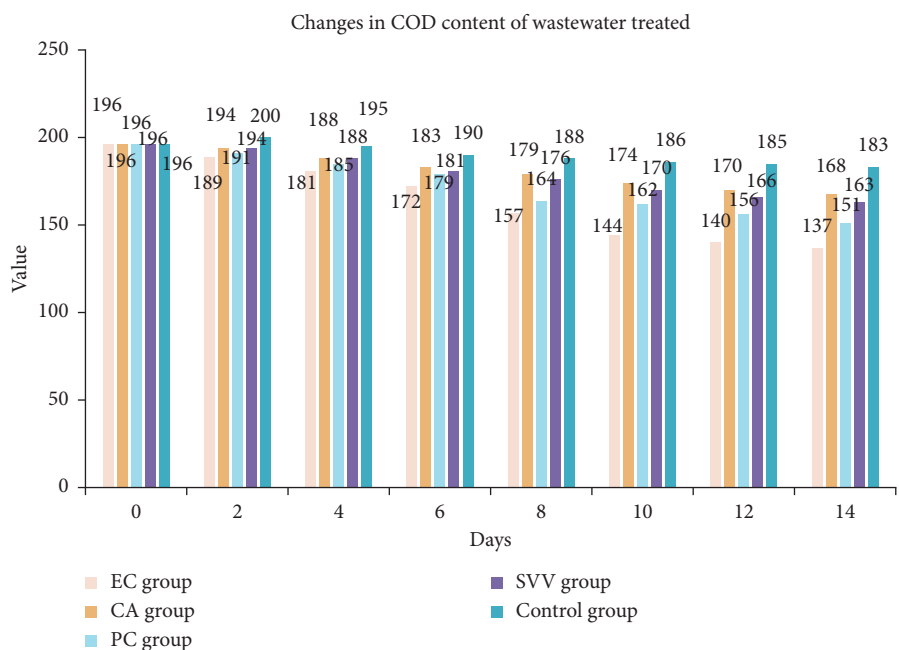Changes in COD content of wastewater treated

Figure 3: Changes in COD content of wastewater treated by plants.

TABLE 5: Microbial-plant combined treatment wastewater total nitrogen content change data table.

Day	A	B	C	D
0	12.20	12.20	12.20	12.20
2	11.54	11.76	11.41	11.81
4	10.13	10.95	9.63	11.81
6	9.06	10.48	8.21	11.60
8	7.72	9.08	6.57	11.32
10	6.34	8.25	5.16	11.13
12	5.12	7.87	3.52	10.92
14	4.29	7.25	2.73	10.73

groups. After two weeks of the test, the COD value was reduced from 196 mg/L at the beginning of the test to 137 mg/L, and the degradation rate was 30.10%; secondly, the reed group had a better degradation effect on COD in sewage, and the COD value was reduced to 151 mg/L. The degradation rate is 22.96%; then, the water onion group has a poor degradation effect on the COD in the sewage, the COD value is reduced to 163 mg/L, and the degradation rate is 16.84%; the last is the dry umbrella grass group on the COD value in the sewage. The COD value is reduced to 168 mg/L, and the degradation rate is 19.39%. The analysis of variance showed that the removal effect of the four treatment groups with plants on the removal of COD in sewage was significantly different from that of the blank control group ($P < 0.05$). Therefore, the addition of plants effectively promoted the reduction of COD in sewage.

4.2. Results of Microbial-Plant Combined Treatment of Sewage

4.2.1. Variation Trend of Total Nitrogen Content in Each Group of Microbial-Plant Joint test. Through two weeks of continuous monitoring of the total nitrogen content of each group of test water bodies in the microbial-plant joint test, the results are shown in Table 5.

It can be seen from Figure 4 that compared with the blank control group, the degradation effect of each treatment test group is significantly different. The total nitrogen degradation effect: microorganism + plant > microorganism > plant > blank control group, and the final degradation rates are 77.67%, 64.85%, and 40.61%, respectively; the combined treatment of sewage with microorganisms and plants has a significantly better effect on reducing the total nitrogen content in sewage than using microorganisms and plants alone, and the effect of microorganisms in reducing the total nitrogen content in sewage is better than that of plants.

4.2.2. Variation Trend of Total Phosphorus Content in Each Group of Microbial-Plant Joint Test. Through continuous monitoring of the total phosphorus content of each group of test water bodies in the microbial-plant joint test for two weeks, the results are shown in Table 6.

It can be seen from Figure 5 that compared with the blank control group, the degradation effect of each treatment test group is significantly different. The total phosphorus degradation effect: microorganism + plant > microorganism > plant > blank control group, the final degradation rates are 71.97%, 61.56%, and 39.23%, respectively; the combined

treatment of sewage with microorganisms and plants has a significantly better effect on reducing the total phosphorus content in sewage than using microorganisms and plants alone, and the effect of microorganisms in reducing the total phosphorus content in sewage is better than that of plants.

4.2.3. The COD Value Change Trend of Each Group in the Microbial Plant Joint Test. Through two weeks of continuous monitoring of the COD value of each group of test water bodies in the microbial-plant joint test, the results are shown in Table 7.

It can be seen from Figure 6 that compared with the blank control group, the degradation effect of each treatment test group is significantly different. The COD degradation effect: microorganism + plant > microorganism > plant > blank control group, and the final degradation rate is 85.95%, 78.64%, and 30.43%, respectively; the combined treatment of sewage with microorganisms and plants has a significantly better effect on reducing the COD value of sewage than using microorganisms and plants alone, and the effect of microorganisms on reducing the COD value of sewage is better than that of plants.

4.2.4. The Color Change of Each Group of Samples in the Microbial-Plant Joint Test. Since sewage contains a lot of pollutants such as organic substances, inorganic substances, and algae that cause sewage turbidity, it is possible to judge the turbidity of the water area by detecting the turbidity of the water area. Water bodies become more turbid, less transparent, and vice versa. The clearer the water, the more transparent it is. Figure 7 shows the results of monitoring the chromaticity of the test water of each group in the joint microbial and plant test for two consecutive weeks.

It can be seen from Figure 7 that the water quality of the three treatment test groups is clear than the blank control group, and its clarity is: microorganism + plant > microorganism > plant > blank control group. In the blank control, the chromaticity of the sewage slightly decreased, which was the result of natural precipitation. In the other treatment groups, the chromaticity of the sewage was reduced. Compared with the blank control, the chromaticity of the plant group was significantly reduced. Therefore, the addition of plants effectively improved the turbidity of the sewage; the microbial chromaticity test results were compared with those of the blank control. The chromaticity is obviously reduced; therefore, the addition of microorganisms is also
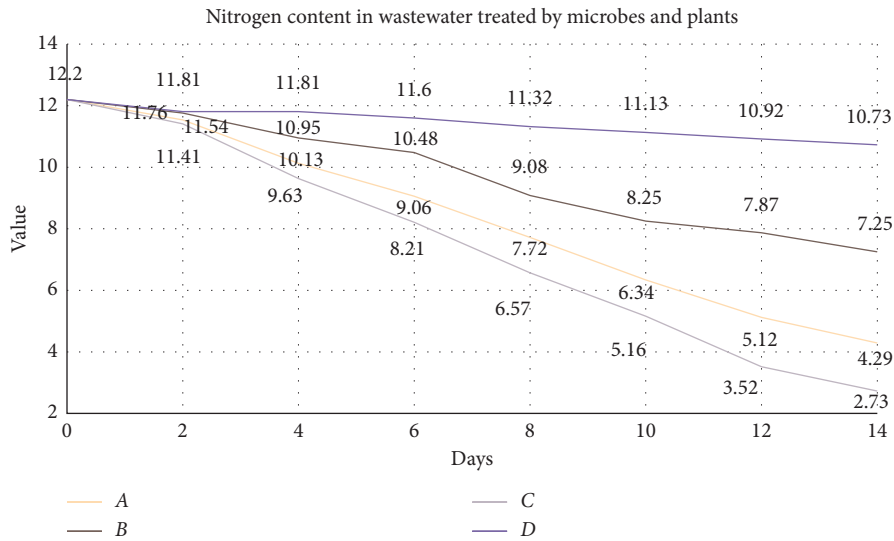
FIGURE 4: Changes of total nitrogen content in wastewater treated by microbes and plants.

TABLE 6: Microbial-plant combined treatment wastewater total phosphorus content change data table.

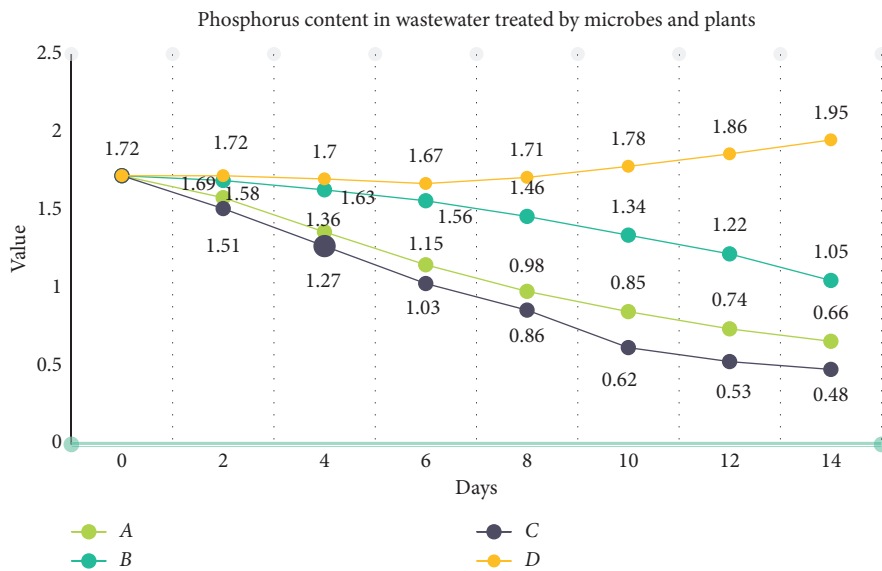| Day	A	B	C	D
0	1.72	1.72	1.72	1.72
2	1.58	1.69	1.51	1.72
4	1.36	1.63	1.27	1.70
6	1.15	1.56	1.03	1.67
8	0.98	1.46	0.86	1.71
10	0.85	1.34	0.62	1.78
12	0.74	1.22	0.53	1.86
14	0.66	1.05	0.48	1.95

FIGURE 5: Changes of total phosphorus content in wastewater treated by the microbe plant.

TABLE 7: The COD value change data table of the combined treatment of microorganisms and plants.

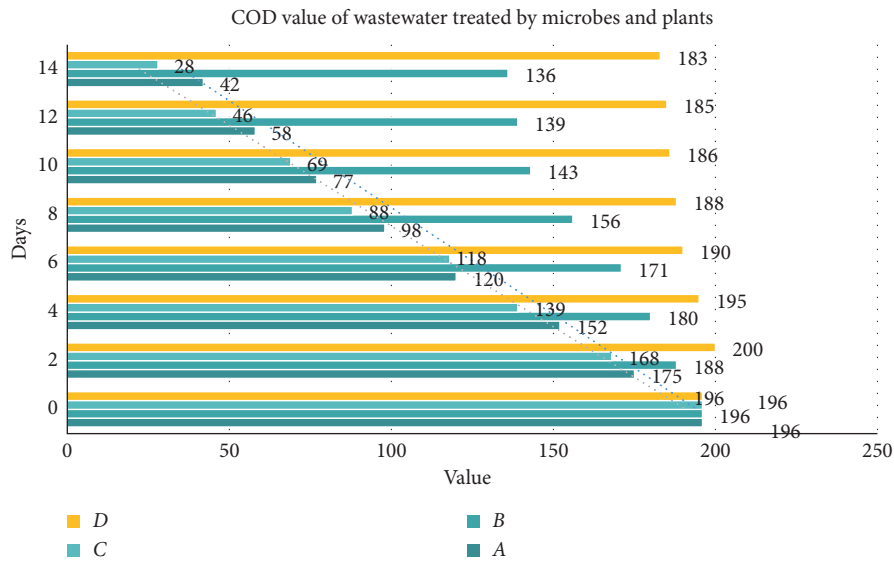| Day	A	B	C	D
0	196	196	196	196
2	175	188	168	200
4	152	180	139	195
6	120	171	118	190
8	98	156	88	188
10	77	143	69	186
12	58	139	46	185
14	42	136	28	183

FIGURE 6: Changes of the COD value of wastewater treated by microbe plants.
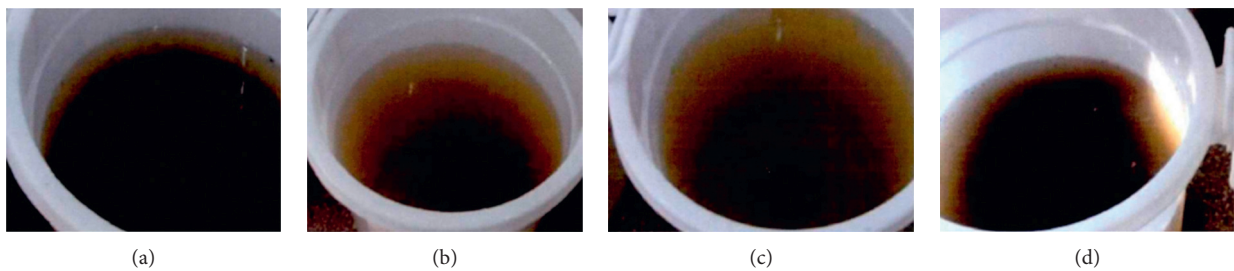
FIGURE 7: Intuitive chart of changes in water quality of each group (https://image.baidu.com/). (a) Microorganisms + plants. (b) Microorganisms. (c) Plants. (d) Control group.

conducive to improving the turbidity of sewage; the combination of microorganisms and plants repairs the sewage to further improve the chromaticity of the sewage.

5. Conclusions

On the basis of a more comprehensive analysis of the pollution of the sewage ditch in the suburbs, a simulation test of microorganism-landscape aquatic plants for sewage treatment was selected to provide a certain theoretical basis for actual sewage treatment on site. In view of the degradation effect of total nitrogen, total phosphorus, and COD in sewage, the effect of combined microorganisms and plants to repair sewage is obviously better than that of using microorganisms and phytoremediation alone, and the effect of microbial repair of sewage is better than phytoremediation of sewage. For the improvement of sewage chroma, the two groups of microorganisms combined with plants have the best effect, followed by the microbiome, and finally the two groups with added plants. By observing the bottom and inner wall of the sewage treatment system, the two groups of microbiome and microbiome combined plant

group, a large number of substances precipitate and attach, which effectively improves the chroma of sewage and makes the test water sample clearer.

In this study, combining the selected microorganisms with landscape aquatic plants for sewage treatment research, the effect of degrading pollutants is good, and the sewage water quality is obviously improved, but there are still many problems that need to be studied in depth. The room temperature is stable and maintained at a temperature where microorganisms can actively reproduce and metabolize. It is impossible to fully analyze the degradation effects of microorganisms and plants under different climatic conditions. At the same time, the growth of plants is limited by the climate. The indoor simulation with the small test scale and low time span cannot meet the requirements. The actual sewage treatment construction needs to be on site. In the indoor simulation test, microorganisms combined with landscape aquatic plants for sewage treatment have the best effect. No in-depth research has been carried out on the mechanism of water purification. In future research projects, attention should be paid to the interaction between microorganisms and plants. The mechanism of water purification is studied and analyzed.

Planting plants in waters not only beautifies the water environment but also purifies the water quality. The subject of this paper's research is sewage from around sewage ditches. Sewage is treated by microorganisms in combination with landscape aquatic plants. By measuring changes in nutrients in water areas, nutrient removal in a combination of microorganisms and landscape aquatic plants has been studied, the nitrogen and phosphorus content of plants and the distribution of microorganisms outside the root zone of plants have been studied, and how to remove nitrogen and phosphorus in water can be studied. The results show that the use of microorganisms and plants alone to treat sewage effectively reduces total nitrogen, total phosphorus, and COD levels in sewage. The combination of these two effects effectively reduces sewage pollutants and reduces chromaticity.

Data Availability

No data were used to support the findings of this study.

Conflicts of Interest

The authors declare that they have no conflicts of interest.

Acknowledgments

References

[1] J. L. Broussard and S. Devkota, "The changing microbial landscape of Western society: diet, dwellings and discordance," *Molecular Metabolism*, vol. 5, no. 9, pp. 737–742, 2016.

[2] D. J. Beale, K. A. Kouremenos, and E. A. Palombo, "Microbial metabolomics," *Exploring the Bioactive Landscape of the Gut Microbiota to Identify Metabolites Underpinning Human Health*, 2016.

[3] Zheng and H. Rong, "Effects of soil salinity on microbial biomass nitrogen of landscape soil," *Journal of Landscape Research*, vol. 55, no. 573, pp. 56–59, 2016.

[4] Y. M. Stepanov, O. M. Vlasova, and I. A. Klenina, "Assessment of microbial landscape and colon cytoprotection indices in patients with chronic constipations," *Gastroenterology*, vol. 54, no. 1, pp. 51–55, 2020.

[5] V. I. Sokolova, D. A. Sychev, E. I. Vasilieva et al., "Analysis of the microbial landscape of infection site and the effectiveness of antibiotic and immunotherapy in patients with diabetic foot," *Antibiotiki i khimioterapīia = Antibiotics and chemoterapy [sic]/Ministerstvo meditsinskoĭ i mikrobiologicheskoĭ promyshlennosti SSSR*, vol. 65, no. 5-6, pp. 25–29, 2020.

[6] H. Y. Astsaturov, O. O. Syzon, and Y. V. Andrashko, "Skin microbial landscape and immune-endocrine parameters in patients with psoriasis by using narrowband UVB phototherapy," *Wiadomoci lekarskie (Warsaw, Poland*, vol. 73, no. 1, pp. 7–11, 1960.

[7] C. Lin and C.-G. Fu, "Study on crack decrease property of high-performance concrete under corrosive environment in subsea metro tunnel," *Science of Advanced Materials*, vol. 11, no. 4, pp. 458–465, 2019.

[8] Z. M. Kulieva, A. I. Gasanov, and L. I. Rustamova, "Microbial landscape of the intestine in outpatients with acute enteric infections," *Kazanskii Meditsinskii Zhurnal*, vol. 99, no. 3, pp. 401–404, 2018.

[9] X. Liu, Y. Sang, S. Ding et al., "Experimental study on the mechanics characteristics of CFRP strengthening of highway tunnels at different damage states," *Geofluids*, vol. 2020, no. 7, pp. 1–11, 2020.

[10] W. A. Hammac, D. E. Stott, D. L. Karlen et al., "Crop, tillage, and landscape effects on near-surface soil quality indices in Indiana," *Soil Science Society of America Journal*, vol. 80, no. 6, pp. 1638–1652, 2016.

[11] W. H. Wang, Y. Wang, L. Q. Sun et al., "Research and application status of ecological floating bed in eutrophic landscape water restoration," *The Science of the Total Environment*, vol. 704, no. Feb.20, pp. 135434.1–135434.17, 2020.

[12] K. E. Kaiser, B. L. Mcglynn, and J. E. Dore, "Landscape analysis of soil methane flux across complex terrain," *Biogeosciences*, vol. 15, no. 10, pp. 3143–3167, 2018.

[13] K. Arbind and Seema, "Monitoring of fluoride contamination and correlation with physicochemical parameters of surface soil and groundwater near tea-garden of thakurganj block of kishanganj, Bihar, India," *American Journal of Environmental Engineering*, vol. 6, no. 2, pp. 38–51, 2016.

[14] X. Xu, D. Cao, Z. Wang et al., "Study on ultrasonic treatment for municipal sludge," *Ultrasonics Sonochemistry*, vol. 57, pp. 29–37, 2019.

[15] I. Kabenge, A. Katimbo, N. Kiggundu et al., "Bioremediation technology potential for management of soil and water pollution from anticipated rapid industrialization and planned oil and gas sector in Uganda: a review," *Journal of Environmental Protection*, vol. 8, no. 11, pp. 1393–1423, 2017.

[16] R. Purnamawati and R. A. Taufikurahman, "The physiological responses of water hyacinth (Eichhornia crassipes (mart). Solms) and water lettuce (Pistia stratiotes L.) as trivalent chromium bioaccumulator," *3BIO Journal of Biological Science Technology and Management*, vol. 2, no. 1, pp. 2655–8777, 2020.

[17] S. K. M. Sa'At, N. Q. Zaman, M. S. Yusoff et al., "The selection of palm oil mill effluent for phytoremediation treatment system using Cyperus alternifolius," *International Journal of Environmental Engineering*, vol. 10, no. 2, pp. 106–117, 2019.

[18] M. P. Carey, S. A. Sethi, S. J. Larsen et al., "A primer on potential impacts, management priorities, and future directions for Elodea spp. in high latitude systems: learning from the Alaskan experience," *Hydrobiologia*, vol. 777, no. 1, pp. 1–19, 2016.

[19] A. K. Ghorai and A. K. Chakraborty, "Sustainable in-situ jute retting technology in low volume water using native microbial culture to improve fibre quality and retting waste management," *International Journal of Current Microbiology and Applied Sciences*, vol. 9, no. 11, pp. 1080–1099, 2020.

[20] V. Ferri, C. Battisti, and C. Soccini, "Bats in a mediterranean mountainous landscape: does wind farm repowering induce changes at assemblage and species level?" *Environmental Management*, vol. 57, no. 6, pp. 1240–1246, 2016.

[21] R. P. Singh, S. Tiwari, M. Singh et al., "Important diseases of greenhouse crops and their integrated management: a review," *Journal of Entomology and Zoology Studies*, vol. 8, no. 1, pp. 962–970, 2020.

[22] F. Ali, "Functional and structural roles of wiry and sturdy rooted emerged macrophytes root functional traits in the abatement of nutrients and metals," *Journal of Environmental Management*, vol. 249, no. 2019, pp. 1–13, 2019.

[23] S. Hemavathi and R. Manjula, "Reduction of wave energy due to monotypic coastal vegetation using response surface methodology (RSM)," *Nature Environment and Pollution Technology*, vol. 19, no. 5, pp. 1965–1971, 2020.

[24] G. M. Chorak and R. A. Thum, "Identification of resistant clones of Eurasian (Myriophyllum spicatum) and hybrid (M. spicatum X M. sibricum) watermilfoil to an operational rate of fluridone," *Invasive Plant Science and Management*, vol. 13, no. 4, pp. 1–20, 2020.

[25] J. Pinthong, V. Kanokkantapong, J. Plengsakul et al., "Integration of aquaculture, aquatic plant and plant cultivation systems," *Journal of Advanced Agricultural Technologies*, vol. 6, no. 3, pp. 226–230, 2019.

[26] D. A. Jay, A. B. Borde, and H. L. Diefenderfer, "Tidal-fluvial and estuarine processes in the lower columbia river: II. Water level models, floodplain wetland inundation, and system zones," *Estuaries and Coasts*, vol. 39, no. 5, pp. 1299–1324, 2016.